Massachusetts Institute of Technology
Center for Space Research
Laboratory for Space Experiments

MIT CSR TR-69-1

The Conceptual Design of a Small Solar Probe (Sunblazer)

January 1969

Research and Development Work Under
NATIONAL AERONAUTICS AND SPACE ADMINISTRATION
Contract Number NASr - 249

List of Contributors

Mr. Richard H. Baker
Mr. Lawrence H. Bannister
Mr. William W. Cooper
Mr. Daniel H. Galvin, Jr.
Dr. John V. Harrington
Mr. William T. Higgins
Mr. Everett A. Johnston
Mr. Hagop J. Nercessian
Mr. Charles A. Peterson
Mr. Rolf Steendal
Mr. Ernest K. Weinschenk
Dr. Robert D. Yates

Edited by:

Mr. Richard H. Baker
Mr. Daniel H. Galvin, Jr.

THE CONCEPTUAL DESIGN OF A SMALL SOLAR PROBE (SUNBLAZER)

ABSTRACT

A scientific experiment to measure the electron density of the solar corona will use apparatus consisting of a small, solar-pressure-oriented spacecraft containing a multiple-frequency, pulsed, 2-kilowatt, solid-state transmitter, and a terrestrial 50-dB dipole phased array receiving antenna.

Included are analyses of the communication system, the 0.63-AU perihelion solar orbit, the semi-passive attitude control system, the spacecraft power and thermal control systems.

The conceptual electrical and mechanical design of the spacecraft hardware covers the basic configuration, RF and digital electronics design and packaging; and includes fundamental stabilization, separation, despin and deployment schemes.

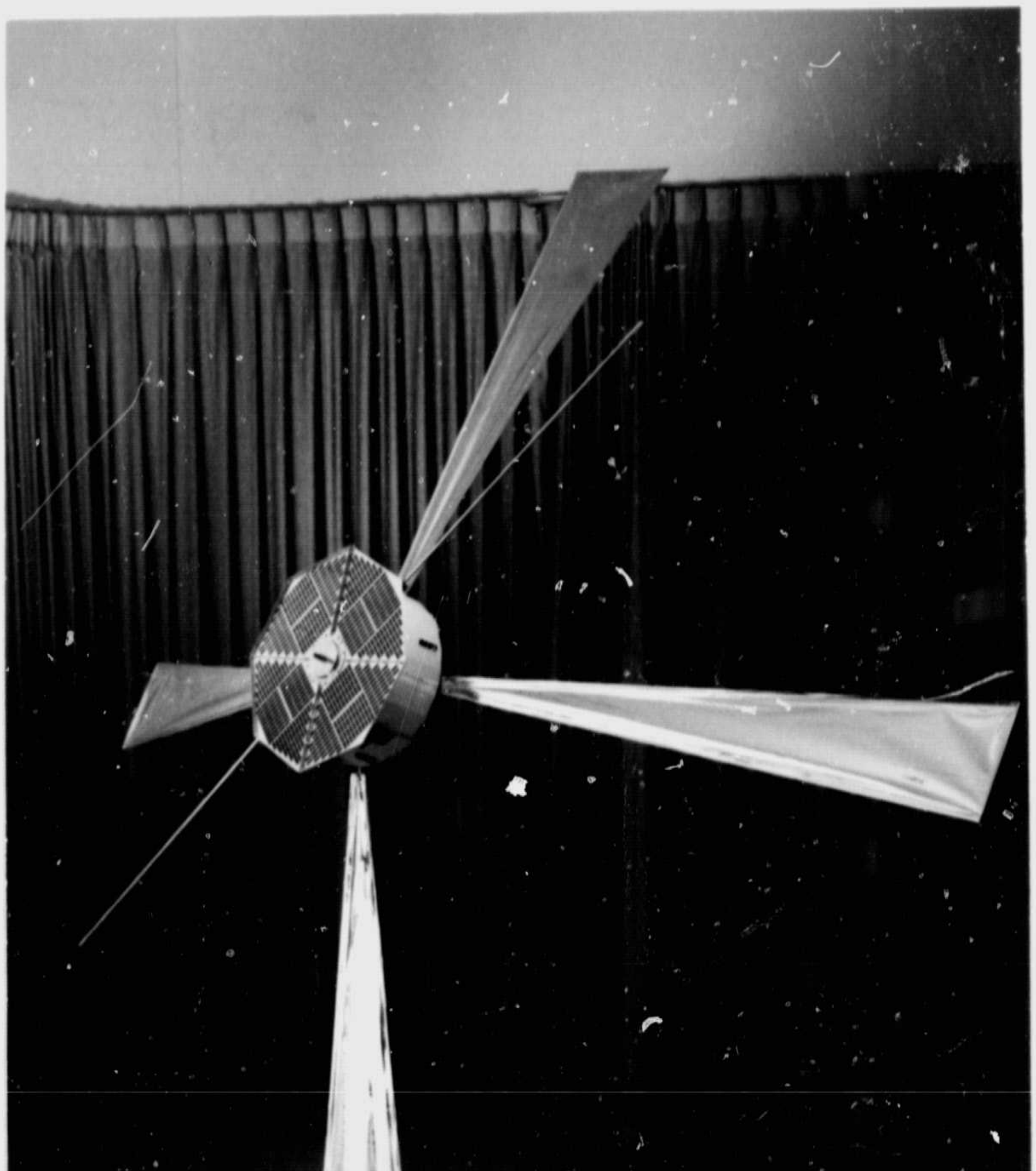

Plate 1 Sunblazer Spacecraft.

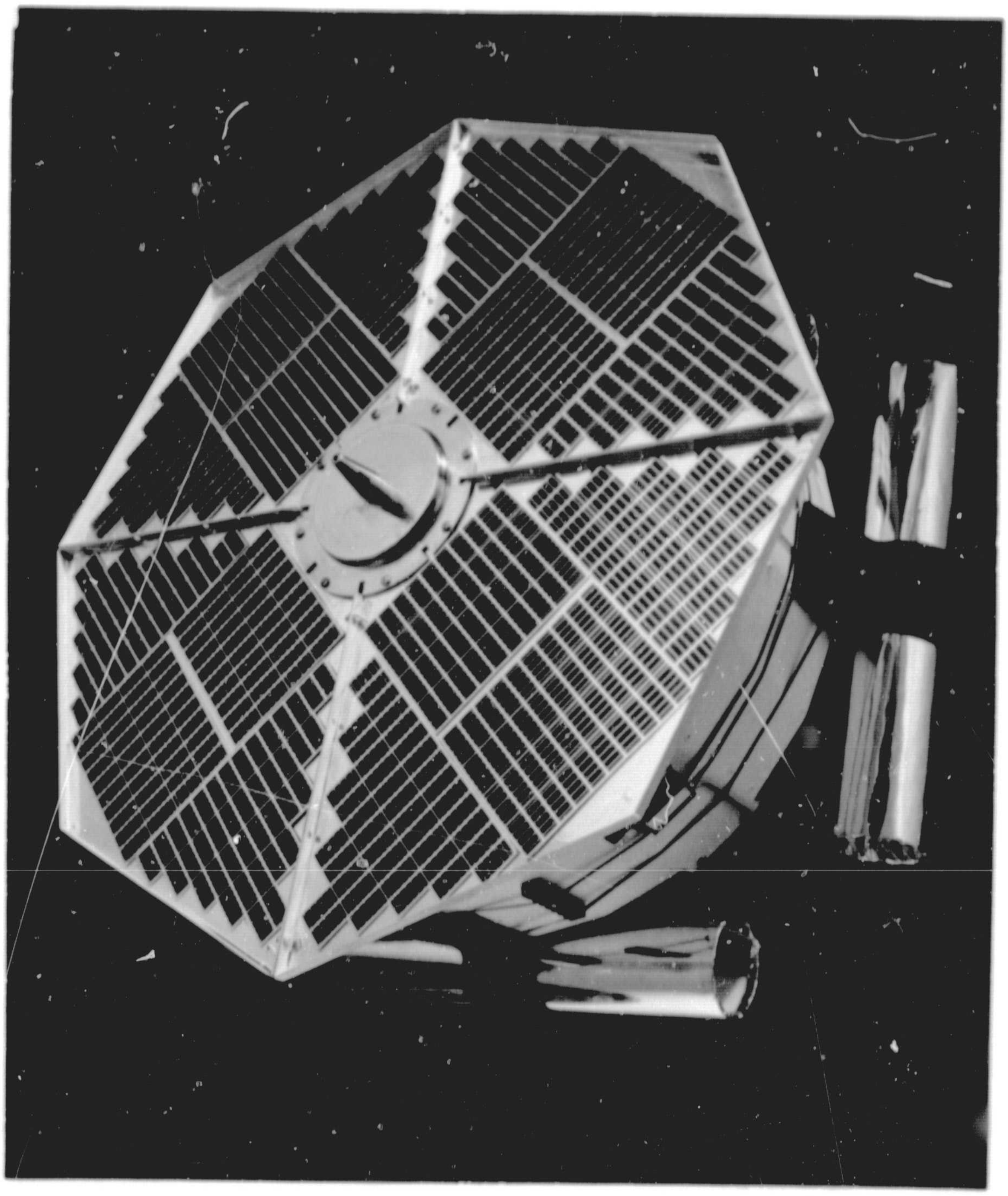

Plate 2 Launch configuration -- front view.

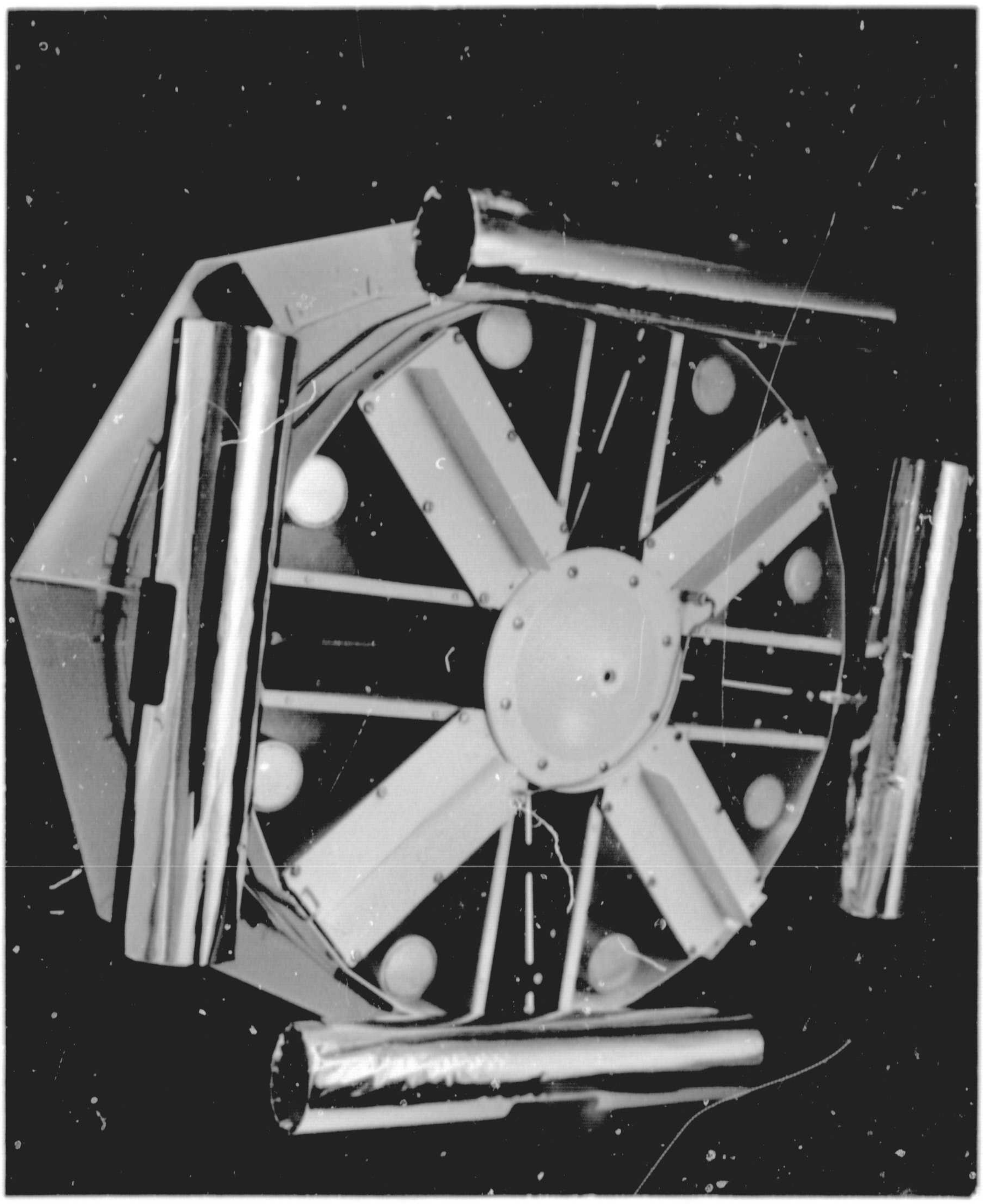

Plate 3 Launch configuration -- rear view.

TABLE OF CONTENTS

TABLE OF CONTENTS (Cont.)

Chapter	TABLE OF CONTENTS (Cont.)	Page

TABLE OF CONTENTS (Cont.)

TABLE OF CONTENTS (Cont.)

TABLE OF CONTENTS (Cont.)

LIST OF ILLUSTRATIONS

LIST OF ILLUSTRATIONS (cont)

LIST OF ILLUSTRATIONS (cont)

LIST OF ILLUSTRATIONS (cont)

LIST OF TABLES

CHAPTER 1

1.0 INTRODUCTORY REVIEW OF THE SUNBLAZER PROGRAM

1.1 Mission Considerations

1.1.1 Scientific Mission Objectives

The primary objective is to measure the electron density profile accurately and unambiguously over the 5-to-100 solar radii distance from the sun, where it has been inferred only with considerable ambiguity from radio star occultation measurements.

A secondary objective is to measure, clearly, the scale of turbulence in the inner corona and the outward-moving velocity of the inhomogeneities in the inner corona by measuring the scintillations in angle and time of arrival of coherent transmissions as occultation progresses.

Other objectives are: to infer some qualitative information about the existence of a general solar magnetic field; and, through observation of Faraday rotation or pulse splitting, to carry a variety of particle and field experiments to the 0.52 AU region of interplanetary space.

1.1.2 Other Flight Program Responsibilities

There appear to be no other NASA flight programs which could, for either economical or technical reasons, satisfy all of the mission objectives of the Sunblazer program. These objectives are: primarily, to make electron density profiles in the region from 5 or so solar radii out to 100 solar radii; and, through the measurement of fluctuation phenomena observed on the ray paths near occultation, to determine the scale of turbulence in the inner corona; and perhaps, through Doppler-broadening measurements, to measure the velocity of the inhomogeneities in a general radial direction.

To accomplish these objectives, one should have spacecraft reaching perihelia of 0.52 to 0.65 AU so that occultations will occur in a reasonable time such as 1 to 1.5 years after launch. To the best of our knowledge, none of the Mariner spacecraft will do this. Similarly, the Pioneer mission, which might have gone into this region, is no longer planned. However, even if it were, the long-term requirement to make not only a simply isolated occultation measurement but perhaps a succession of these, so that the highly variable coronal densities could be more accurately characterized, would underscore the importance of a relatively inexpensive launch vehicle and spacecraft for making such a series of measurements.

1.1.3 Future On-Board Experiments

Our present spacecraft weight is approximately 28 pounds exclusive of any on-board experiments, and the 5-stage Scout is capable of placing a payload of 55 pounds into a 0.65 AU orbit. The word "payload" in this case applies to all weight appended to the fifth-stage rocket casing. There are at least 10 to 15 pounds of excessive telemetry which have been put aboard the 5-stage Scout vehicle as performance-testing telemetry which presumably could be removed on later launches. We would expect that this additional weight could be used for additional science on Sunblazer. A large number of suggestions for quite meritorious experiments have been proposed, relating mostly to particle and field experiments in the 0.52 to 0.65 AU region that Sunblazer will traverse. Dr. Van Allen has proposed a Geiger counter experiment to count energetic particle fluxes in this region. Dr. Simpson has proposed a cosmic ray experiment to determine the cosmic ray gradients in the region closer to the sun; this is also a simple counting experiment. MIT experimenters have proposed placing an x-ray detector on Sunblazer, looking in an antisolar direction, to measure the x-ray sky background over a wide range of angles as Sunblazer orbits the sun, which would be a very rewarding experiment. A simplified plasma probe for measuring the solar wind density and velocity at 0.52 AU is also a possibility, and Dr. Shapiro has discussed with us the possibility of placing aboard Sunblazer a coherent x-band beacon so that his fourth test of general relativity could be undertaken. This is a particularly practical and attractive way to conduct Shapiro's experiment. Weight limitations clearly will not permit all of these being done on any one launch, but combinations, perhaps two at a time, could be done over a succession of launches over several years. It may also be possible to employ a flux gate magnetometer to measure magnetic field strength at 0.52 AU.

All of the experiments listed are typically those that count events over a one-day period and require the contents of a counter to be transmitted back once a day or so for the experiment to be accomplished. These are quite suitable for the low-data-rate transmission system that Sunblazer will have.

1.1.4 Missions and Experiments for a Ten-Year Program

It has always been felt that the great advantage of a light-weight, low-cost spacecraft for interplanetary missions is that it would offer the possibility of repeated measurements of coronal densities and scale sizes through a major portion of a solar cycle. It seems feasible to plan to launch two spacecraft per year over a 10-year period, with the basic propagation experiment being done on all of them, since this is essentially built into the communications system on the spacecraft. Orbital choices and on-board experiments can vary over the time period, depending on the total weight available in each launch. It is believed that the first three missions should probably be 0.65 AU ones with conjunction occurring in 1.5 years. One might regard these as providing exploratory measurements of the corona and as proving out the design of the spacecraft itself. They would also provide, if all three were successful, the opportunity for making spatial and temporal correlations of the coronal densities at different azimuthal positions in the ecliptic. The 0.65 AU orbit provides a very slow passage through conjunction. It would be desirable to return to our original orbit having a perihelion at 0.52 AU and a rapid conjunction passage at one year after launch to make electronic density profile measurements which are more nearly fixed in time, and it is suggested that three 0.52 AU launches be made.

It is also possible, by causing the hyperbolic excess velocity after escape to be almost orthogonal to the ecliptic, to achieve an inclined orbit where the inclination might be as much as 10°. In this case an out-of-plane distance of perhaps 30 million kilometers could be obtained. A number of these launches could be considered partly to make propagation measurements on ray paths out of the ecliptic, but principally to carry on-board experiments significantly far from the ecliptic plane.

On all of these missions, the 0.52 AU, 0.65 AU and the out-of-the-ecliptic inclusion of two out of the five or six possible on-board experiments could also be made, to provide the opportunity for a number of particle and field experiments.

1.2 Propagation and Communication Considerations

1.2.1 The Choice of 75 MHz Frequency

The arguments on choice of frequency, and the belief that a frequency in the 75 MHz is best to use, are complicated but these are the high points of the argument. If it is assumed that the two frequencies used in the experiment are a probing frequency and an infinite reference frequency, then the amount of relative delay between identical signals transmitted on these two carriers varies inversely as the second power of the frequency. At 75 MHz it is predicted the average corona will have a relative delay of 535 μs at 100 solar radii and about 10 ms at 5 solar radii

If, for the sake of reducing the complexity and cost of the ground equipment, and also in the process simplifying the spacecraft, one uses a reference frequency some 10% greater than the probing frequency, then these delays are divided by a factor of 5 and become 2 ms and 107 μs. They are still readily measurable by the pulse techniques which we propose for Sunblazer where the effective pulse definition can be made of the order of 5 μs. If a 150-MHz carrier is used, these delays become reduced by a factor of 4 and become 500 μs and 25 μs which, while still measurable by the same methods, would suggest greatly reduced accuracy. Similarly, if the frequencies used were as high as 2200 MHz, the relative delays become ridiculously small and can no longer be measured by group delay methods.

A similar argument applies to the important scintillations and Doppler-broadening measurements. The angular scintillations at the 4-meter wavelength are fairly readily measurable in the 5 to 20 solar radii range, whereas, with the higher frequencies they would become too small to measure accurately.

1.2.2 The Propagation Experiment

By now, many studies have been made of the extent to which the turbulent coronal plasma would be expected to distort a pulse transmitted through either the frequency broadening which would arise from the motion of the turbulent refractive inhomogeneities or, correspondingly, from the delay distortion which would occur in the time domain through the dispersive nature of the medium or through multipath. It has been concluded, on the basis of both theoretical studies and the examination of the data provided by radio star occultation and by the Mariner 4 frequency-broadening measurements made during its occultation by the sun, that a 3-ms pulse at 75 MHz has an excellent probability of being detected in as close as 5 solar radii, and further that this pulse can be composed of 5-μs elementary pulses distinguished by phase-reversal modulation. In effect, there would be a 5-μs resolution, and any multipath contributions would be identifiable, as well as those contributions arriving on different magnetoionic propagation modes. The large advantage that this pulsed group-delay method has over the kind of sinusoidal modulation employed in the Pioneer propagation experiment is that the periodicity of that modulation precludes the possibility of identifying multipath and other perhaps unanticipated propagation modes, and makes difficult, if not risky, the interpretation of the delay data.

The other, in our view, great deficiency of the Pioneer experiment is that the delay measurements are made on the uplink, for engineering convenience, but the interpretation must be done then by a relatively inept machine, and not by the scientific observer who is available if downlink transmissions are employed. We recognize, as does anyone with space communication experience, that uplink sensitivities can always be made superior, but this is hardly important in view of the great advantage of ground-based interpretation if downlink transmissions can be made adequate, as we believe they are in Sunblazer. In Pioneer, for example, all possibility of scintillation measurements, frequency-broadening measurements and Faraday-rotation measurements are excluded unless an extremely complicated receiver on the spacecraft is postulated. We are convinced from an engineering viewpoint that the MIT propagation measurement has been proved feasible.

1.2.3 Communication Bit-Rates

If the closely-packed 75-MHz frequency-hopping experiment is the one we design for, then with the 45- to 50-dB ground antenna, a bit-rate of approximately 1 bit per second can be expected with low-error probability when Sunblazer is 2 AU from the earth. Assuming that the spacecraft is visible at least two hours per day, this is a capability of 7200 bits, which is more than enough to communicate all of the engineering data such as temperature, battery voltage, orientation angle, etc., as well as the results of any simple on-board experiments. During the summer periods when the visibility is more likely to be six hours per day, a correspondingly greater amount of information can be telemetered. As a matter of interest, the Sunblazer bit-rate of 1 bit per second is a remarkably high bit-rate for such a simple spacecraft, when compared to the Mariner bit-rate of 8 bits per second using directive antennas on the spacecraft, 210-foot antennas, the Goldstone maser receivers, and a much shorter transmission range of only 50 million miles.

1.2.4 Tracking Requirements

Tracking and communications are not a problem if the normal NASA tracking nets are not used. The angle and Doppler information we get on Sunblazer from the phased array will be sufficiently accurate to establish the orbit with enough precision for the propagation experiment. For the propagation experiment, the only important parameter is the displacement of the ray path from the solar center. The actual locations of the terminals, assuming that both are well outside of the region of greatest electron density, are unimportant. Even so, from the angle and Doppler measurements we expect to be able to locate the spacecraft within 10,000 km^3 with high reliability.

There is no uplink contemplated in the Sunblazer mission, and the modest amount of telemetry indicated will be multiplexed on the same 75-MHz carrier emanating from the spacecraft.

1.3 The Ground Receiving Terminal

1.3.1 Initial Proposal

When the Sunblazer experiment was first proposed, it was hoped that the relatively high energy to be transmitted per pulse, consistent with the comparatively long (25-ms) pulse width,[1, 2] would allow one of the existing metric-wave-length radio astronomical telescopes to be employed as the ground-receiving antenna. Several unsuccessful attempts were made to get a commitment of more than a few hours a week of observing time on a number of suitable facilities, such as the Arecibo, P.R. telescope and a local 150-foot paraboloid. It was concluded that the only way in which observing time, consistent with the investment in spacecraft and launch costs, could be guaranteed would be for Sunblazer to have its own receiving antenna. The least expensive means of obtaining a suitable aperture was believed to be through an array of dipoles patterned after the 38-MHz solar radar telescope at El Campo, Texas which had been operated for some time, although design differences were required by the higher 75- and 225-MHz frequencies for the initially proposed two-frequency Sunblazer experiment. It was further proposed to take advantage of new developments in solid-state circuitry to make the array automatically phaseable, as opposed to the time-consuming cable-plugging method then in use at El Campo, and an increase was planned from 1,000 to 4,000 dipole elements to give an improved receiving gain of some 36 dB.[3] This corresponds approximately to the gain in the Arecibo telescope at 75 MHz.

After some considerable amount of laboratory development and test work on the electronic amplifier and phasing package to be associated with each dipole element, the design of these was sufficiently firm so that bids from several electronic manufacturers could be obtained to give realistic cost data on the array's electronic components. These outside estimates indicated two things: 1) That more than 90% of the cost of the two-frequency array was in the electronics, and 2) that the cost of a dual-polarization, two-frequency, 4000-dipole array was likely to be considerably in excess of the $3 million estimate which had earlier been postulated. These somewhat discouraging but realistic conclusions were reported to a group from NASA Headquarters and Langley at a meeting of the Sunblazer coordinating committee held in Cambridge on 22 May 1967.

1.3.2 High-Gain Elements

As a result of this meeting a fundamental redirection of the array program was made. Since the major cost items of the array were in the electronic system, any attempt at significant cost reduction required a less complex electronic system. For a given over-all system gain this implies replacement of the individual 5-dB dipole elements with higher-gain types. A cost a[illegible]lysis, based upon various cost-versus-gain functions indicated that minimum overall system cost results when the element (mechanical) cost and the electronic system cost are approximately equal. It was further indicated that an array of 14-dB to 20-dB elements would yield a reduction of an order of magnitude in electronic system complexity over the previous individual dipole system. Several typical high-gain elements were considered, but no decision was taken as to the final element design.

The approach was discussed at a Sunblazer coordinating committee meeting in Washington on 13 July 1967, and again in Cambridge on 23 August 1967. At the August meeting it was agreed that the 128-element pilot array would continue to be installed at El Campo using dipoles as the radiating element since that work was well along. However, the 225-MHz array would be redesigned to achieve 25-dB gain using an array of high-gain elements. Subsequently the backfire configuration was selected for this array. The 225-MHz array was completely redesigned and typical antenna patterns taken on the element. A complete set of electronic and mechanical hardware was prepared. However, the 225-MHz system was not installed due to a change, dictated in part by budgetary considerations, in the format of the pulse transmitted from the spacecraft. This format is fully described in Section 1.3.3, and was described at the Sunblazer Review meeting on

13-14 March 1968 and 23 July 1968. The closely-packed, single-frequency format eliminates the need for the 225-MHz array and has the additional advantage of higher permissible gain at 75 MHz for constant facility cost.

There remained, however, the question of the element for the 75-MHz array. Although the backfire configuration was satisfactory for the 225-MHz system, it possessed mechanical disadvantages at 75 MHz due to the relatively large (4-meter) wavelength. Based upon cost figures obtained from the construction of an in-house model and estimates obtained from outside vendors, it was determined that the cost-per-unit of gain of this antenna type was inordinately high. The approach to this problem was to keep the element gain constant at 14 dB while investigating other elements of equivalent gain. Details of this evolution are given in the document "History and Design Summary, Sunblazer Phased Array".[4] The fundamental conclusion was: "The best method, in terms of satisfying the Sunblazer tracking requirements (both engineering and science shots) at minimum overall cost (initial installation, operation and maintenance) is to construct a cross-polarized wideband dipole array at El Campo, Texas." In this array the element is realized by the interconnection of six dipoles. Basically, it has been determined that a 14-dB antenna element is less expensive and has better performance when constructed by connecting six dipole elements together as opposed to employing single or multiple backfire or other slow-wave type elements. A detailed description of the 50-dB array using this six dipole (double-tee) interconnection is given in the Sunblazer Ground Antenna Report (February, 1969).

1.3.3 Change to Closely-Packed "Single" Frequency Experiment

The foregoing changes would have been final ones except that information recently gleaned from the Mariner 4 solar occultation experiment[5] suggested some changes in the transmitted-pulse format, which further interacted with the ground antenna design. This experiment measured for the first time the frequency broadening which a coherent signal undergoes when transmitted on ray paths within four to six solar radii of the solar corona. When the 2200-MHz Mariner 4 measurements are scaled to 75 MHz by theoretical methods justified by some recent results in our laboratory[6, 7], they strongly suggest that the 25-ms pulse for Sunblazer earlier proposed should be reduced to a pulse no longer than 3 ms, if coherent integration and coding within the pulse are to be employed. Pulse-coding is desirable to achieve a 5- to 10-μs resolution and accuracy in our time-delay measurements. Without a substantial increase in peak power, the reduced pulse width means a correspondingly reduced energy per pulse which can only be made up by an increase in antenna gain on the spacecraft or on the ground. For reasons associated with the simplicity and the reliability of the spacecraft, we preferred not to change the radiation pattern of its antenna from an essentially omnidirectional one, which meant that to obtain an acceptable signal-to-noise ratio on a single pulse, a ground antenna gain in excess of 36 dB would be required. This, in turn, implied the addition of many more elements and returned the design problem again to one of overcoming a cost constraint.

The solution this time, in an attempt to stay within the $3 million budget, was to simplify the experiment in what was believed to be an acceptable way, by using a separation between the probing and reference frequencies of some 10%, such that both frequencies could be received within the bandwidth achievable in a single array. This reduces somewhat the accuracy of the delay experiment but does not compromise the experimental results. On the other hand the elimination of the 225-MHz array represented a substantial saving in cost which could then be applied to increase the gain of the 75-MHz array to a 50-dB level. This provides an excellent (16-dB) signal-to-noise ratio on the narrow (3-ms) pulse now to be transmitted from the Sunblazer spacecraft, and results, it is believed, in a better and a simpler all-around experiment.

A 50-dB antenna at 75 MHz is a rather remarkable instrument in its own right and is some 14 dB greater than the gain of the telescope at Arecibo at this wavelength. It is also some 14 dB greater than the circular interferometer composed of 96 45-foot-diameter paraboloids operated by CSIRO in Australia. Yet it is believed that the present development and test experience with both the 75-MHz dipole pilot array, and measurement design efforts to date on the high-gain backfire elements at 225 MHz, allow one to say with some degree of confidence that the electronically-phased wideband array of 1024 20-dB, 75-MHz elements with dual polarization is a realistic design and can be built for approximately the $3 million figure.

While, indeed, there have been a number of major changes in the overall Sunblazer propagation experiment and in the receiving array, they have been made for good reasons and are precisely the kind of changes in concept or design that one should expect for work done on supporting research and technology funds. In making these changes, the primary motivation has been to select carrier frequencies and modulation formats which are most likely to lead to the production of useful data in early Sunblazer propagation experiments and, at the same time, are conducive to spacecraft and ground antenna designs which must satisfy serious cost constraints.

1.3.4 Additional Advantages of the 50-dB Broadband Array

A further benefit of the use of a 50-dB ground terminal is the rather high bit-rate (possibly in excess of several bits per second) which can be made available for the telemetry of data from on-board experiments over distances as great as 2 AU. This is a matter of some considerable importance for on-board experimenters, and to the future use of Sunblazer as an interplanetary observatory.

As a radio telescope the array also has important ancillary uses, the most recent and exciting of which concerns the observation of the newly discovered pulsars at a frequency somewhat below that on which they have thus far been observed. The high gain and directivity of this array at 75 MHz may well provide important new information and improved resolution of the signals from the sources observed thus far, and its greater sensitivity may lead to the discovery of still more sources.

The modular nature of the array also makes it practicable to provide small solid-state power amplifiers in the 250- to 1000-watt range on each element, which makes possible conversion of the array into a radar telescope or a future uplink station to Sunblazer of impressive performance. The power amplifiers required are essentially indentical to those developed for the Sunblazer spacecraft and, while some design work is involved in adapting and packaging them for the ground array, their addition to the array is largely a matter of cost. That is, the overall transmitter power could be somewhere between one and four MW, depending on the funds available and the interest in adding the transmitter facility. This was an item in the original proposal, but was eliminated at an early stage because of cost considerations. It is, however, a growth item which should not be forgotten in future planning.

Solar radar echoes have never been observed at 75 MHz, and the reason for this is believed to be that sufficient radar telescope sensitivity has never been available to counteract the additional absorption losses in the corona, which occur along a ray path prior to the reflection point. The great advantage in making solar radar observations with this instrument would be improved sensitivity and a greatly improved angular resolution, which would make it possible to resolve quadrants of the solar disk, and to improve the capability for observing average Doppler and Doppler-broadening of the signals which contain important, and otherwise unobtainable, information on the motion of the solar corona at distances close to the photosphere.

As a planetary radar it would appear to be the first instrument that could detect reflections from the planet Jupiter and could make important observations on Venus and Mars at a much lower frequency than has heretofore been used. The rather surprising oscillation in radio cross section of the planet Venus which James[8] has observed at 38 MHz could be better studied with the additional sensitivity and the greater range of this new instrument.

PRECEDING PAGE BLANK NOT FILMED.

CHAPTER 2

2.0 CHANNEL CHARACTERIZATION

In order to measure the integrated electron density along the communication path and the fluctuation of this density, it is necessary to determine how these two quantities will affect signals propagating through such an ionized medium.

The integrated electron density will cause a transmitted pulse to have an additional delay over the free-space delay and cause it to be dispersed in time. The fluctuations of this integrated electron density will cause the arrival time to be random and fluctuate from pulse to pulse. In addition, it will also cause the received signal to be dispersed in frequency. The bandwidth and duration of the transmitted pulse must be chosen so as to minimize the time and frequency dispersion effects while at the same time allowing the measurement of the pulse delay and delay fluctuation to a reasonable degree of accuracy.

The main reason for the minimization of the dispersion effects is so that a simply near-optimum detection-estimation scheme may be used to make the desired measurements. At present only the frequency and time dispersion of the channel are known. In general complete statistical description of the channel is necessary to design the optimum receiver. However, if the signal duration and bandwidth can be chosen so as to make the channel appear stationary during the pulse duration, a simple detection scheme results. In effect, a transmitted pulse will be received with a random delay, frequency shift, amplitude and phase which are constant over the pulse duration. The optimum detection scheme is then a bank of matched filters, covering the expected frequency shifts; each filter being matched to a frequency shifted version of the transmitted signal and followed by a square-law envelope detector.

2.1 Time Delay

Due to the integrated electron density over the communication path between Sunblazer and the earth, a narrow-band pulse will suffer an additional delay over the space-free delay of:

$$T_d(f) = \frac{1.35 \times 10^{-19} N}{f^2} \text{ sec} \qquad (2.1)$$

where N is the total number of electrons per square meter along the communication path and f is the carrier frequency in MHz. Figure 2-1 shows the additional delay at 75 MHz, and the relative delay between 70 and 80 MHz and between 75 and 80 MHz as a function of the offset distance from the sun for the proposed orbit. The additional delay due to the ionosphere is also shown for comparison.

The variation in the integrated electron density will cause a fluctuation in $T_d(f)$. This has been studied by Hollweg[1] and the standard deviation of $T_d(f)$, noted by $\sigma_d(f)$ is shown in Fig. 2-1. It is assumed that the "blobs" are 200 km in size and that the rms electron density fluctuation is 0.05 times the average electron density.

The measurement of the relative delay will give the value of N, the integrated electron density, while a measurement of the standard deviation of this delay will give a value for $\sqrt{b\,\overline{(\Delta n)^2}}$ where b is the "blob" size and $\sqrt{\overline{(\Delta n)^2}}$ the rms electron density fluctuation.

2.2 Time Dispersion

The integrated electron density along the communication path also causes the time dispersion of a narrow-band pulse; this effect has been studied by Pindyck[2]. The Sunblazer signal will be spread in time by two phenomena. The first is dispersion of the various frequency components of the signal due to the frequency-dependent phase delay in the medium. The second is multipath spreading, due to the random bending of various rays from the transmitter by the coronal refractive index fluctuations, and the resultant varying path lengths of these rays from the transmitter to the receiver.

The behavior of the dispersive time spreading was studied some time ago[2]. Assuming that the medium is constant over the pulse duration, the channel can be modeled by a linear dispersive network with a transfer function $H(\omega) = \exp\{-j\phi(\omega)\}$, where:

$$\phi(\omega) = T_o\left(\omega - \frac{\overline{\omega_p^2}}{\omega}\right) \qquad (2.2)$$

in which T_o is the free-space propagation time and $\overline{\omega_p^2}$ is the average plasma frequency along the path. A study was made of the output signal as a function of the proposed orbit, assuming that the receiver contains a filter matched

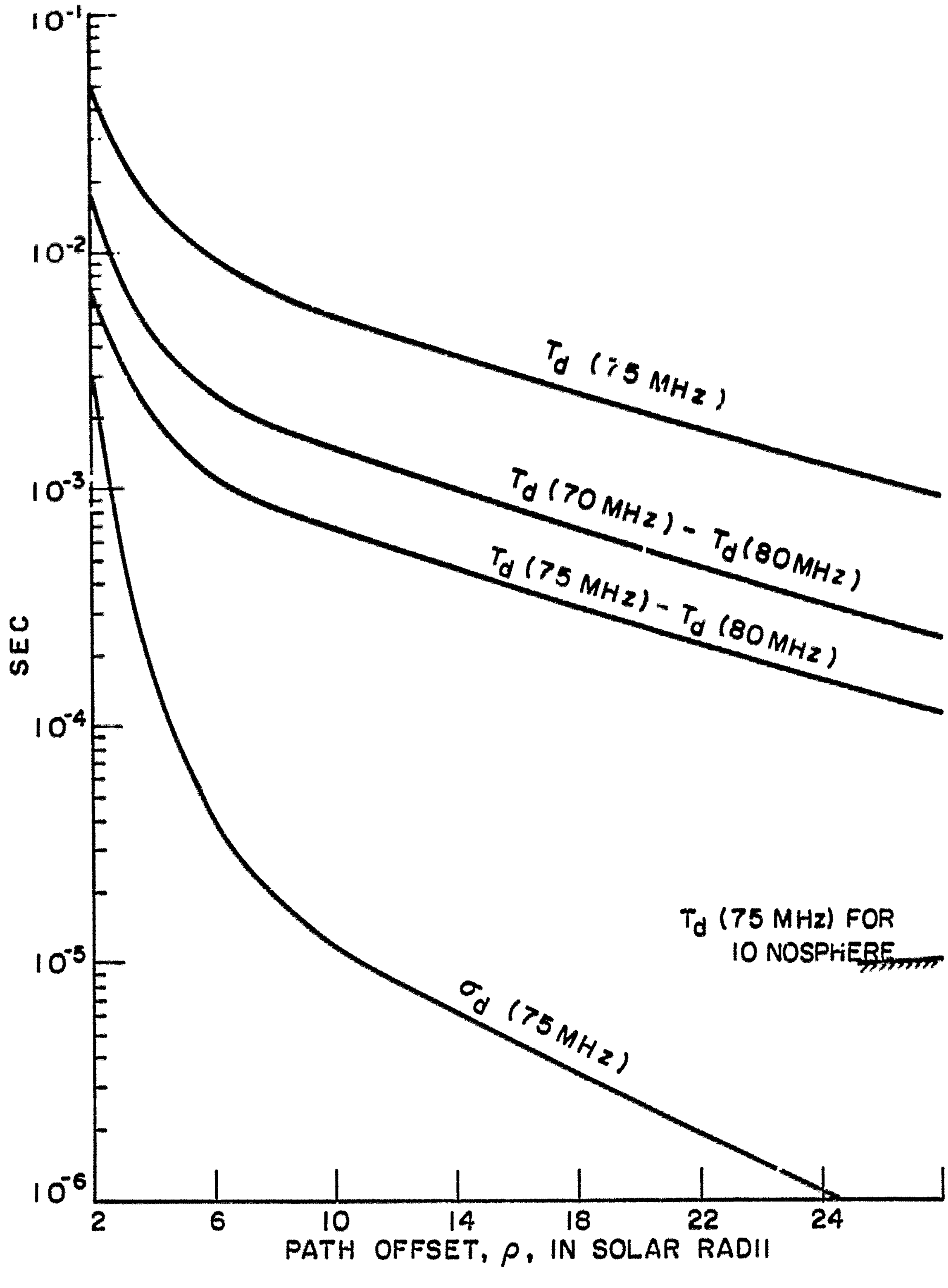

Fig. 2-1 Additional delay $T_d(75)$, relative delay $T_d(f_1) - T_d(f_2)$, and standard deviation of delay $\sigma_d(75)$, vs path offset.

to the transmitted signal, followed by a square-law envelope detector. If the pulse is a binary-phase modulated carrier at ω_o, with a bit time of t_1 the output of the detector is not greatly degraded as long as $t_1 > \tau_o = \sqrt{\pi |\phi''(\omega_o)|}$. In the absence of dispersion (and noise) the output is the square of the envelope of the autocorrelation function of the transmitted pulse (assuming the Doppler has been removed). The correlation peak has a width of $2/t_1$ and reaches a maximum at the arrival time plus the signal duration. With dispersion present, and for $t_1 = \tau_o$, the peak width is doubled, and its maximum value is down 3 dB. The "dispersion time", τ_o, is shown in Fig. 2-2 as a function of the offset distance for the proposed orbit.

Although τ_o gives a good measure for the dispersion of one pulse, it does not include the effects of multipath spreading. This is caused by the arrival of a continuum of delays of the transmitted pulse, over a time comparable to the pulse duration. In all regions where dispersion is noticeable, the multipath spreading is significantly greater than the dispersion. The nature of this time spreading can best be understood from the angular power spectrum of the received electromagnetic signal. It is well known that radiation from a point source will be scattered or randomly bent by the corona, and this radiation will arrive at a receiver with a random angle (or angles) of incidence. If we represent the corona by a thin refracting or phase changing screen at the center of the propagation path, then energy arriving from an angle θ with respect to the line-of-sight path will suffer an additional propagation delay $T_o\theta^2$ with respect to the direct path, where T_o is the line-of-sight propagation time delay from the transmitter to the receiver. Thus, if the mean square angle of arrival fluctuation is θ_o^2, we might expect an average multipath spreading of the signal on the order of $T_o\theta_o^2$. A rigorous analysis of the received field from thin screen has shown that this intuitive result is very nearly correct[3].

A meaningful description of the multipath spreading in the channel is found in the delay scattering function. This function tells us on the average how the power from a very short narrowband pulse is spread out in time by the channel. If a very large number of these short pulses were transmitted through the channel and the received power from each pulses recorded and averaged over the ensemble of pulses, then the result would be the delay scattering function.

For an anisotropic thin screen model of the corona, the delay scattering function has been shown to be:

$$\sigma(\tau) = \frac{4}{T_o\theta_o\theta_i} e^{-\frac{2t'}{T_o}\left[\frac{1}{\theta_o^2}+\frac{1}{\theta_i^2}\right]} I_o\left(\frac{2t'}{T_o}\left[-\frac{1}{\theta_i^2}+\frac{1}{\theta_o^2}\right]\right. \tag{2.3}$$

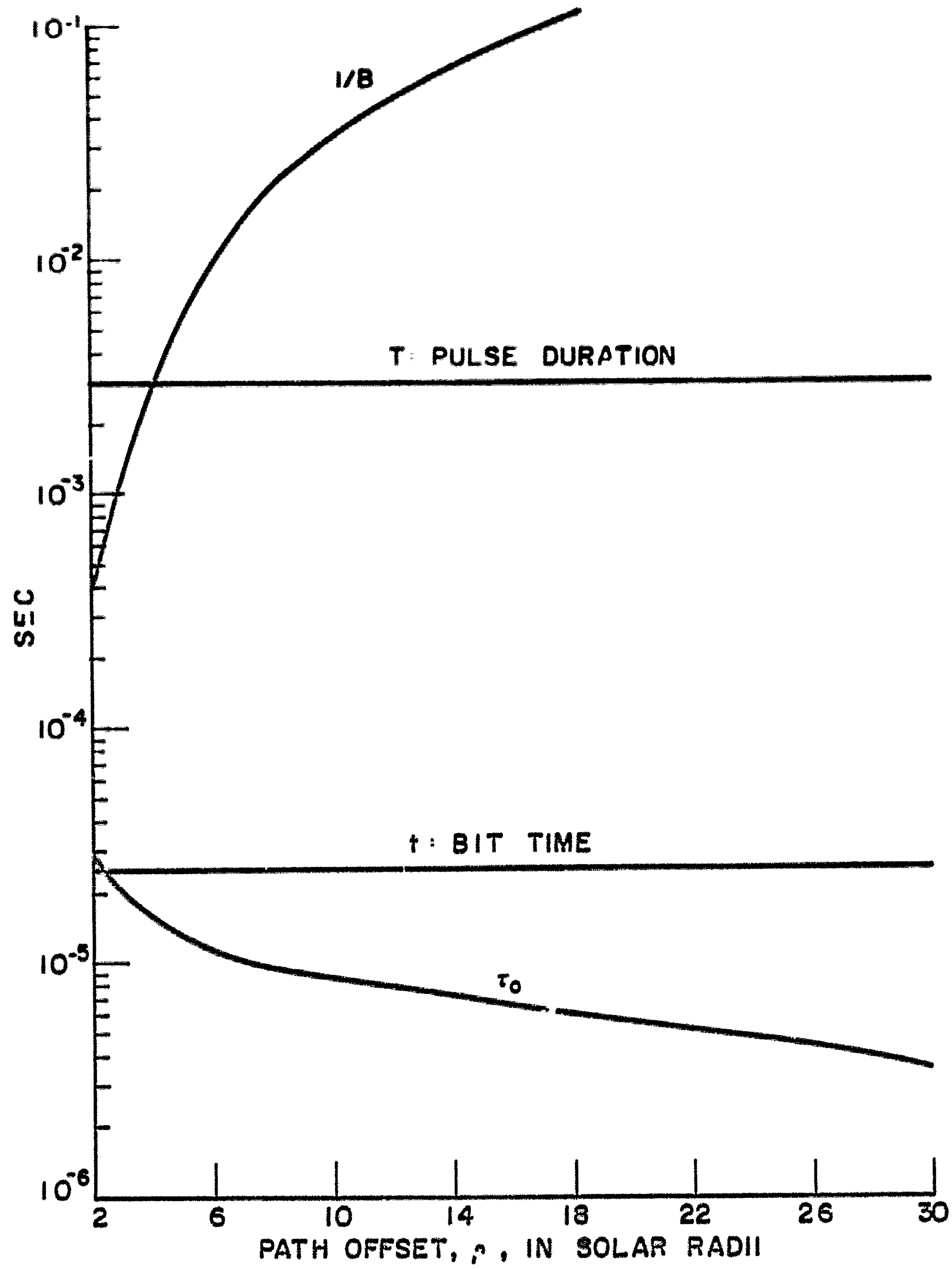

Fig. 2-2 Dispersion time τ_0, and reciprocal frequency spreading 1/B, vs path offset. Frequency : 75 MHz.

where θ_i and θ_o are the rms scattering angles in and out of the plane of the ecliptic. T_o is the propagation time delay from the receiver to the transmitter along the line-of-sight path, $\tau = 0$ is the arrival time of the pulse along this path, and I_o is the zero-order modified Bessel function (Bessel function with an imaginary argument). If the medium is isotropic ($\theta_i = \theta_o$) this expression reduces to an exponential, whereas if $\theta_o \gg \theta_i$ or vice versa the scattering function approaches the chi-squared density. In any case the mean multipath delay is found to be

$$\tau_{ms} = \int_0^{\infty} \tau\, \sigma(\tau)\, d\tau = \frac{T_o(\theta_i^2 + \theta_o^2)}{8} \qquad (2.4)$$

regardless of the anisotropy ratio.

Since the mean square scattering angles are highly variable, we would expect the multipath spreading to vary widely from day to day. Thus when the Sunblazer path offset decreases to the point where the average multipath spread is comparable to the pulse length, operation will probably become intermittent. In this case a measurement of the multipath spreading characteristics of the channel will also yield valuable information.

2.3 Frequency Dispersion

If a long unmodulated carrier is transmitted through the solar corona, the received signal will be spread in frequency. The only experimental data on such phenomena is given by Goldstein[4]. Mariner IV transmitted an unmodulated carrier through the corona and the spectrum of the received signal was estimated. If it is assumed that the received signal is a sample function from a stationary random process, then the power spectrum estimated is the Fourier transform of the statistical correlation function of the process. Analysis of the corona validates this assumption. Hollweg[1] has shown that the spectral broadening is proportional to f^{-1} and Goldstein[4] concluded that for small antenna beamwidths the broadening is proportional to the beamwidth. Scaling the Mariner IV data taken at 2295 MHz with a beamwidth of 0.14 degrees to Sunblazer's 75 MHz and 0.3 degrees, the equivalent noise bandwidth of the received signal is

$$B = \frac{2.2 \times 10^4}{\rho^3} \text{Hz} \qquad 3 \le \rho \le 6 \qquad (2.5)$$

The data are valid only between 3 and 6 solar radii. However, Hollweg's[1] results indicate that for $\rho > 10$ solar radii B is proportional to $\rho^{-1.5}$. 1/B is plotted in Fig. 2-2 with the correct extrapolation made.

2.4 Signal Selection

The correct signal bandwidth and duration can now be deduced from the above data. Since it is desired to make accurate time-of-arrival measurements, the transmitted pulse must possess a good ambiquity function. This can be accomplished by phase modulating a carrier pulse of duration T with a Maximum Length Linear Recurring Sequence of M bits, the bit time being $t_1 = T/M$. The bandwidth of the signal is then $W = 1/t_1$ and the time-bandwidth product $TW = M$.

Considering first the dispersion time τ_0, it is seen that for $t_1 > \tau_0$ the received signal will not be greatly dispersed or distorted in time. By letting $t_1 = 25$ μsec, dispersion will not be noticed until 6 solar radii. At this point the detection loss is 1.5 dB and the correlation peak width is about 1.5 times the undispersed case.

Having fixed the bit time it is now necessary to see if the bandwidth of the signal is reasonably larger than the spread in frequency caused by the medium. As seen in Fig. 2-2 the bandwidth W is at least one hundred times B for $\rho > 4$. Hence, the received signal will not be noticeably dispersed in frequency.

The signal now is not dispersed in time or frequency. However, the pulse duration T has to be adjusted so that the received signal will be coherent. As noted in Section 2.3, B is a measure of the bandwidth of a frequency dispersed carrier. Hence, the signal will tend to be correlated over a time of 1/B sec. By choosing T = 3 msec, it is seen from Fig. 2-2 that the received signal will be coherent up to about 6 solar radii. After this point the signal starts to become distorted and the matched filter square-law envelope detector is no longer optimum.

From the above analysis it appears that based on the present knowledge of the solar corona that a binary phase-modulated pulse of duration 3 msec and a bit time of 25 μsec, in conjunction with a matched-filter, square-law envelope detector receiver, should produce reliable measurements of the electron density and its fluctuations up to about 6 solar radii, or until the multipath spreading begins to dominate.

PRECEDING PAGE BLANK NOT FILMED.

CHAPTER 3

3.0 THE SUNBLAZER ORBIT

3.1 Basic Orbital Objective

In order that the main experiment in the Sunblazer program be conducted properly, it is necessary for the Sunblazer vehicle to be placed in a solar orbit which allows it to pass behind the sun's disc (as seen from the earth) within a reasonably short time after launch. In other words, the orbit must eventually cause the vehicle to line up approximately with the sun and the earth.

3.2 Relative Motions of Spacecraft and Earth

This result can be most reliably accomplished if we first note that, in general, the vehicle's orbit and the ecliptic (i.e., the earth's orbital plane) will be mutually inclined by some small angle, due to errors in injection velocity. Irrespective of these errors, the earth will certainly be in Sunblazer's orbital plane not only at launch, but also after each six-month interval after launch (i.e., after the earth has traversed $n\pi$ radians from the launch point where n is an integer). This means that, if superior conjunction with the sun should be required to occur after the earth has traversed $n\pi$ radians in central angle about the sun, the vehicle must have correspondingly traversed $n\pi \pm \pi$ radians during the same time; thus, the required period of the vehicle's orbit about the sun must be $\frac{n}{n \pm 1}$ times the earth's orbital period (under some additional assumptions given below). If this condition is achieved, then regardless of the inclination of Sunblazer's orbit, after n six-month intervals or $\frac{n}{2}$ years, 1) the earth will be in the vehicle's orbital plane, and 2) the vehicle will have traversed exactly π radians more or less than the earth in that plane.

This condition on the vehicle's orbital period comes out so neatly for all n only because the line of apsides of the vehicle's orbit (the line running through perihelion and aphelion) will nearly coincide with its line of nodes (i.e., the line of intersection of its orbital plane with the ecliptic) for any "reasonable" injection scheme. But this latter restriction applies only if n + 1 is odd, for if n + 1 is even, it is easily shown that any single-impulse injection will bring about the desired result. The important point to be made here is that, if a nominal orbit is selected for Sunblazer with a sidereal period of $\frac{n}{n \pm 1}$ years, then comparatively large launch-vehicle injection errors can be tolerated by the main experiment and the reliability of the mission consequently increased.

3.3 Evaluation of Possible Orbits

Table 3-I

	First-order computations.					
n	sidereal period (yrs)	Semi-major axis (AU)	peri-helion (AU)	aphe-lion (AU)	time to sup. conj. (yrs)	inj. vel. (km/sec)
1	1/2	0.63	0.26	1.00	1/2	10.7
	degenerate	-	-	-	-	-
2	2/3	0.76	0.52	1.00	1	5.1
	2	1.59	1.00	2.17	1	5.1
3	3/4	0.83	0.65	1.00	1 1/2	3.3
	3/2	1.31	1.00	1.62	1 1/2	3.3
4	4/5	0.86	0.72	1.00	2	2.5
	4/3	1.21	1.00	1.42	2	2.4
5	5/6	0.89	0.77	1.00	2 1/2	2.0
	5/4	1.16	1.00	1.32	2 1/2	1.9

These figures assume the earth to be a massless point in a circular orbit about the sun. The actual values depend upon the time of year of launch since the earth is in a slightly eccentric orbit.

Other considerations besides sensitivity to out-of-plane velocity error are displayed in Table 3-I. In calculating the required injection velocity, it is assumed that the most efficient use is made of the launch vehicle by launching it either parallel or anti-parallel to the earth's orbit velocity. It is seen that for each n there is both an orbit which remains entirely outside the earth's orbit (and corresponds to injection parallel to the earth's orbital velocity), and another which remains entirely inside (and corresponds to launching anti-parallel).

However, orbits which remain outside 1 astronomical unit have been rejected for the initial missions because, 1) the available solar power would be decreased, and 2) the corresponding communication distances would be longer.

Of the remaining candidates (which extend no farther than 1 astronomical unit from the sun), the 1/2-year orbit must be rejected. For, despite its appealing property of achieving superior conjunction in only half a year, it not only requires a rather large injection velocity, but also subjects the vehicle to a solar readiation-flux at perihelion 15 times greater than that existing at 1 astronomical unit. On the other hand, although the 5/6-year orbit requires a low injection velocity and subjects the spacecraft to only a small increase in solar intensity, it has the disadvantage of requiring 2 1/2 years for superior conjunction. It therefore, must be rejected from considerations of spacecraft deterioration.

Of the remaining candidates (2/3, 3/4 and 4/5) the 3/4-year orbit possesses a special advantage which is not apparent from the acompanying table: it carries the spacecraft through not one, but three superior conjunctions with the sun (Fig. 3-1). Furthermore, this orbit permits the vehicle to remain within a subtended angle of 3^{o} from the sun for more than six months, compared with less than one month for the 2/3- and 4/5-year orbits.

Sunblazer design work has determined that the 2/3-year orbit both reduces the permitted payload weight to marginal levels for a first mission, and creates cooling problems for this lightened vehicle at perihelion. Therefore, in order to achieve a balance between the conflicting requirements of low injection-velocity and a minimum time to superior conjunection, as well as to take advantage of its other special properties, the 3/4-year orbit has been selected.

3.4 The Generation of Three Superior Conjunctions

In order to understand why the selected orbit yields three superior conjunctions with the sun instead of just one, we need only call attention to three simple facts. First, any orbit which remains wholly inside the earth's orbit must have, on the average, an angular velocity greater than that of the earth. Second, because the vehicle is launched from the earth, that launch point is at the aphelion of the 3/4-year orbit where the angular velocity is actually less than that of the earth (recall that the injection direction is opposite to that of the earth's orbital velocity). Third, at superior conjunction 1 1/2 years after launch, the vehicle will be back at exactly the same point in its orbit from which it was launched (i.e., after having made exactly two revolutions about the sun, it is again at aphelion and has a smaller angular velocity than the earth).

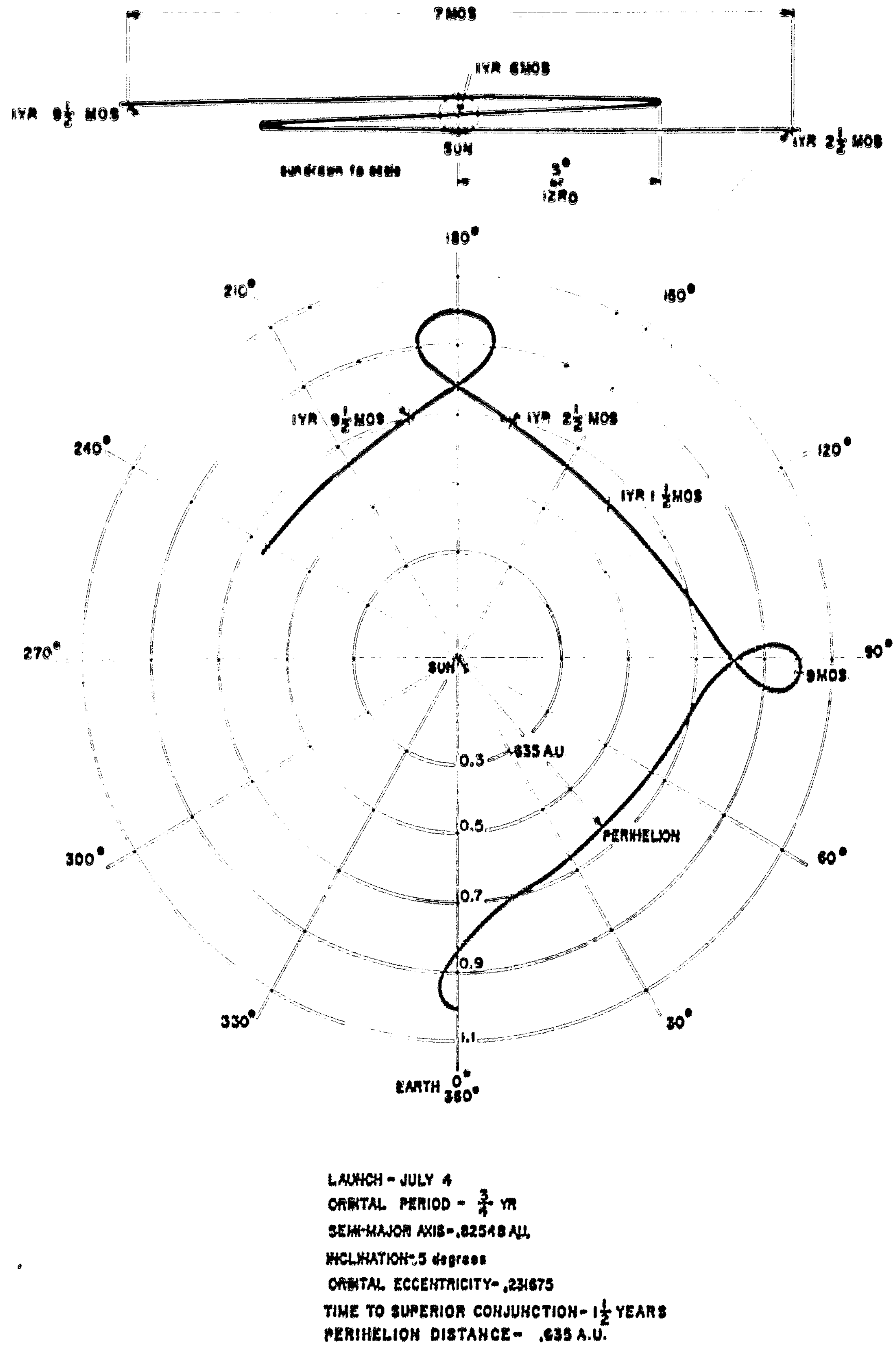

Fig. 3-1 Motion of Sunblazer relative to the earth.

We see from the first fact that the vehicle must, on the average, gain central angle on the earth; but from the second fact it appears that the earth will gain on the vehicle whenever the latter is near aphelion (including the launch point). Therefore, we see that the vehicle will make steady gains on the earth, interrupted periodically by small segments of apparent retrograde motion. Furthermore, from the third fact we note that one of these retrograde segments will occur "behind the sun" after 1 1/2 years, thus giving rise to a triple superior conjunction.

3.4.1 Influence of Launch Time on the Retrograde Motion Amplitude

During the first mission-planning studies of the 3/4-year orbit done at MIT, it was discovered that the amount of this apparent retrograde motion of the spacecraft about the triple superior conjunction was markedly influenced by the earth's orbital position at launch 1 1/2 years earlier (or equivalently, by the calendar date of the launch). It was subsequently concluded that the seemingly small eccentricity of the earth's orbit (0.016726) was responsible for this effect (Figs. 3-2 to 3-13) by means of the following mechanism.

If the vehicle is launched around July first, when the earth is near its own aphelion, then the aphelion of the 3/4-year orbit must be at least as great as that of the earth, or greater than 1 AU. Correspondingly, the perihelion must decrease in order to keep the major axis (and the orbital period) constant. This increase in aphelion and decrease in perihelion for a July first launch results in a slightly larger eccentricity for the vehicle's orbit, thus increasing the extremes of angular velocity at these points. In particular, the spacecraft's angular velocity at aphelion is even smaller than it would be if launched tangentially at exactly 1 astronomical unit. But 1 1/2 years from launch it will be January first, and the earth will be at perihelion where its angular velocity is greatest. Thus, the small change in conditions caused by launching on July first adds two independent inputs to the magnitude of the vehicle's apparent retrograde motion 1 1/2 years later, so that the subtended amplitude of this retrograde motion is 6° as seen from the earth. Similarly, the decrease in eccentricity of the vehicle's orbit for a January third launch has been found to decrease the amplitude of retrograde motion to only about 1°.

3.4.2 In-Plane Errors

Although the sensitivity of the 3/4-year orbit to out-of-plane launch error has been minimized, it is still necessary to consider the effect of the in-plane component of error. To do this, it was first determined that the sensitivity of the orbital period to a change from the nominal heliocentric velocity of the spacecraft was about 20 days/km/sec (e.g., if the nominal launch velocity were changed in magnitude only from 3.3 to 3.3 + 0.2 km/sec, then the orbital period would be changed from 3/4 of a year to about 274 + [0.2] [20], or 274 ± 4 days).

If we assume that the vehicle's launch velocity is 200 meters per second too high, then its orbital period will be shortened by four days so that 1 1/2 years later, after two revolutions, it will arrive at its aphelion point eight days sooner than nominal. Since the earth moves about 1^{o} per day, it will then be about 8^{o} from the spacecraft-sun line, and since the spacecraft will be about 2 AU from the earth, the subtended angle between the vehicle and the sun will be 4^{o} as seen from the earth. This means that, if the launch velocity is 200 meters per second too high, every point in the solar-encounter profile will be moved about 4^{o} to the left. This would be acceptable, at least for the first missions, since the spacecraft would still remain within a region of interest for more than half a year.

It should also be noticed here that all of the solar-encounter profiles could be centered by changing the initial velocity by less than 100 meters per second. The reason some of the profiles are not centered is that the period of the orbits has been fixed at 3/4-year, and the earth is in an orbit of finite eccentricity. Also, the nominal inclination to the ecliptic is zero, and the selection of $1/2^{o}$ inclination in the solar-encounter profiles is only to demonstrate the effect of a finite inclination.

3.4.3 Escape Velocity Error

It should be emphasized here that all of the previous figures ignore the hyperbolic escape trajectory from the earth or even the need for achieving escape velocity. They apply only at the earth's sphere of influence, which is at a radius of about 920,000 km. Unfortunately, the errors present at launch-vehicle burnout (without 300 km of the earth's surface) are magnified considerably at the sphere of influence. To see why, define v_b as the burnout velocity, v_∞ as the velocity at the sphere of influence, and v_e as the earth's escape velocity as the burnout altitude. Conversation of energy yields the equation $v_\infty = \sqrt{v_b^2 - v_e^2}$. If we take the derivative of v_∞ with respect to v_b, we will get:

$$\frac{d\,v_\infty}{d\,v_b} = \frac{v_b}{\sqrt{v_b^2 - v_e^2}} = \frac{v_b}{v_\infty} \simeq \frac{12}{3.3} \simeq 3\ 1/2 \qquad (3.1)$$

for the 3/4-year orbit. This means that, if the burnout velocity is in error by 1 meter per second, the error at the earth's sphere of influence will be about 3 1/2 meters per second. Consequently, the 200-meter-per-second error discussed previously reduces to about 60 meters per second, or about 180 feet per second for the launch vehicle at burnout.

3.5 Computer-Generated Numerical and Graphical Orbit Information

The position of the spacecraft during the 3/4-year orbit is graphically shown in 10-day increments in Fig. 3-2 through 3-13, and the angular displacement effect on the triple conjunction characteristics due to launch time is also shown in the same figures entitled "Solar Encounter Profile".

The numerical data which were utilized to generate these graphs are also presented.

SOLAR ENCOUNTER PROFILE

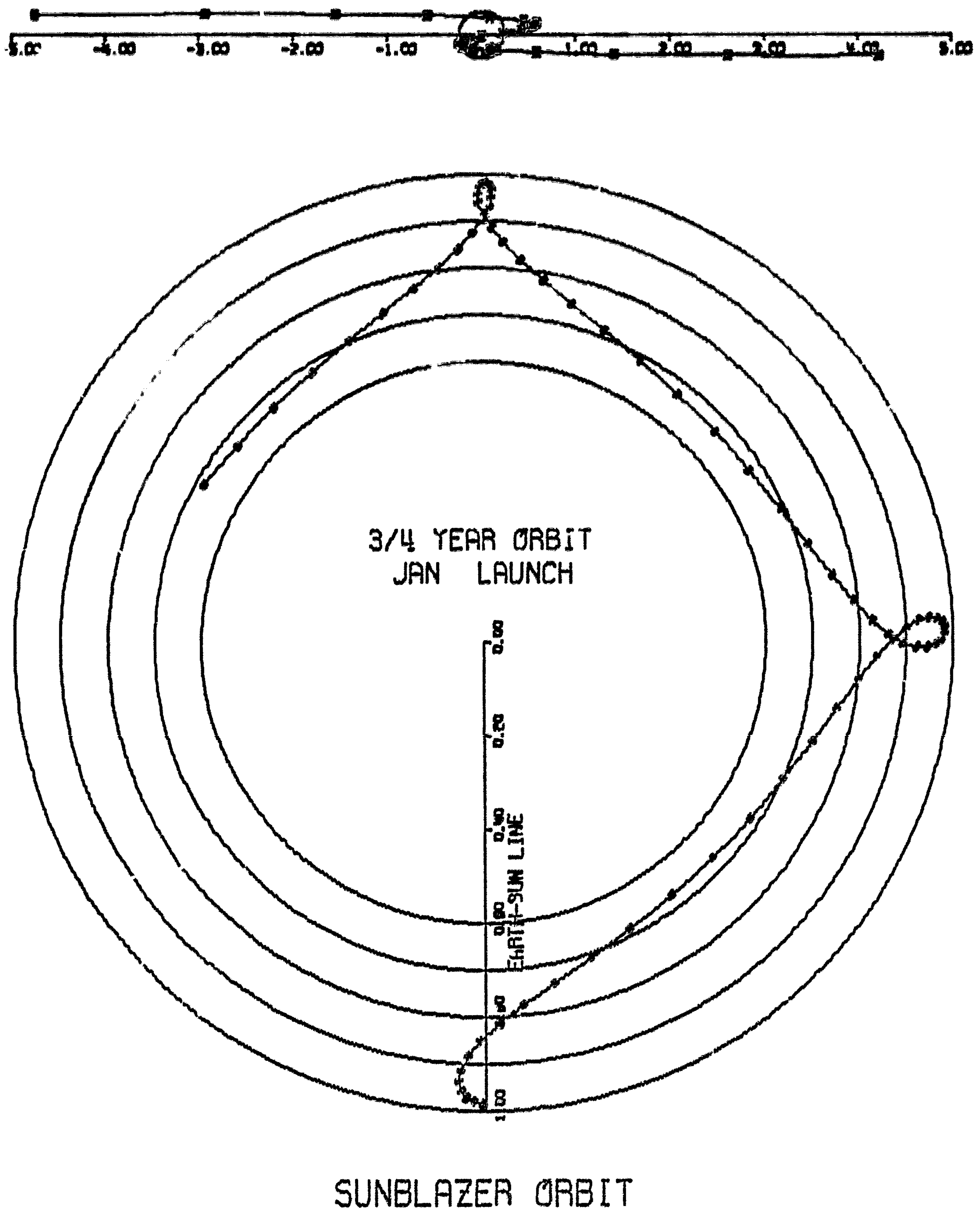

SUNBLAZER ORBIT

Fig. 3-2.

SOLAR ENCOUNTER PROFILE

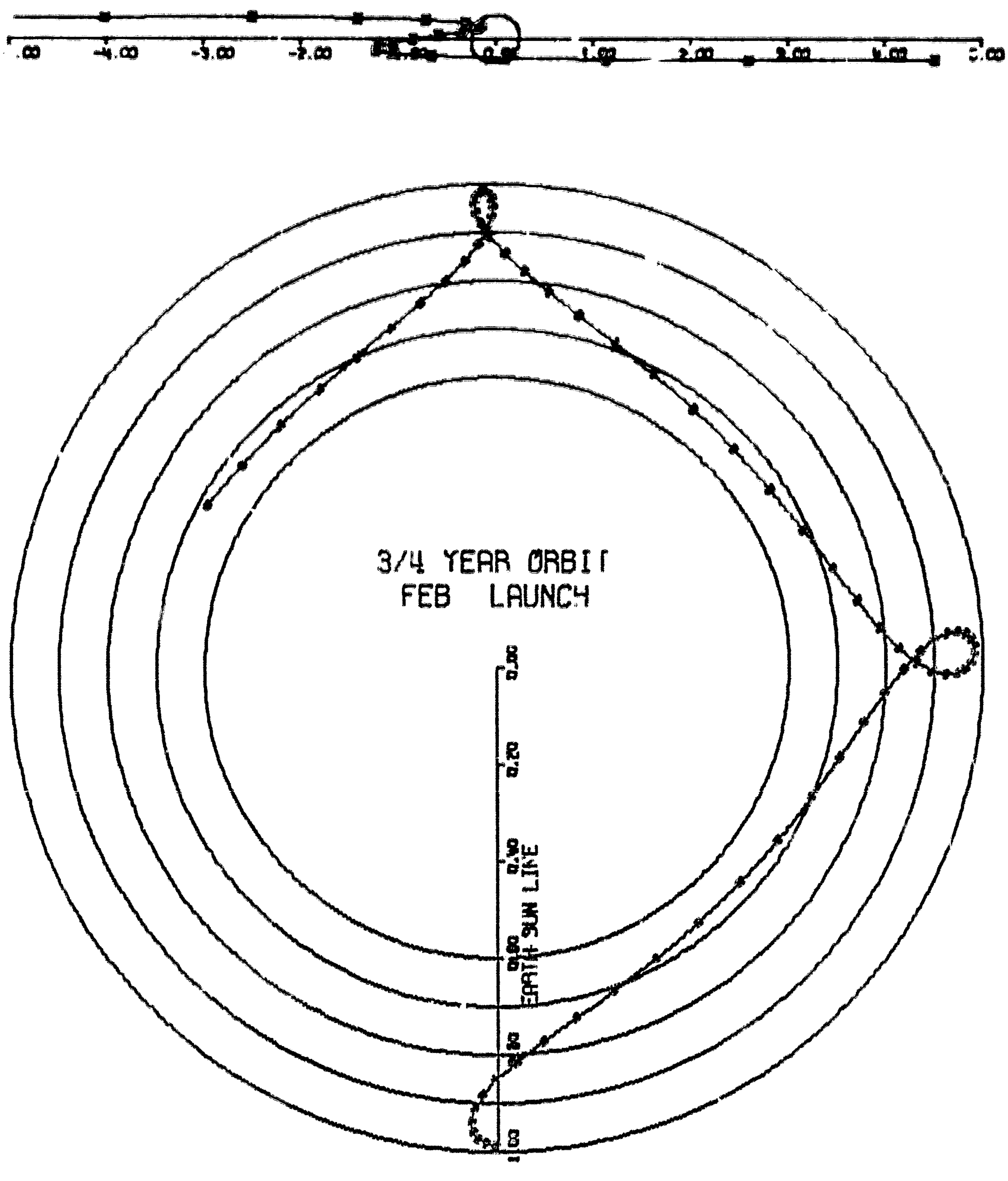

SUNBLAZER ORBIT

Fig. 3-3.

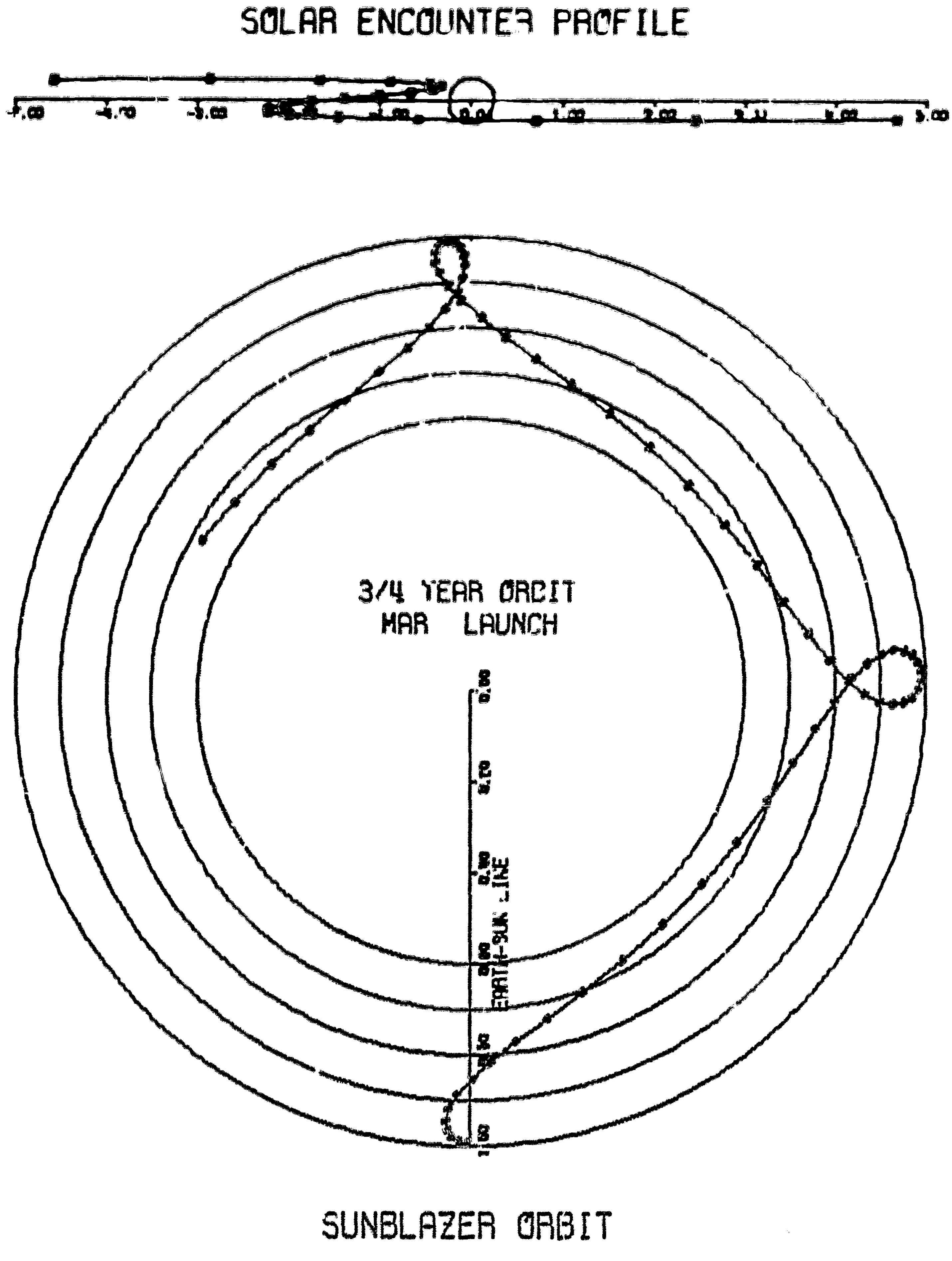
SOLAR ENCOUNTER PROFILE
3/4 YEAR ORBIT
MAR LAUNCH
EARTH-SUN LINE
SUNBLAZER ORBIT

Fig. 3-4.

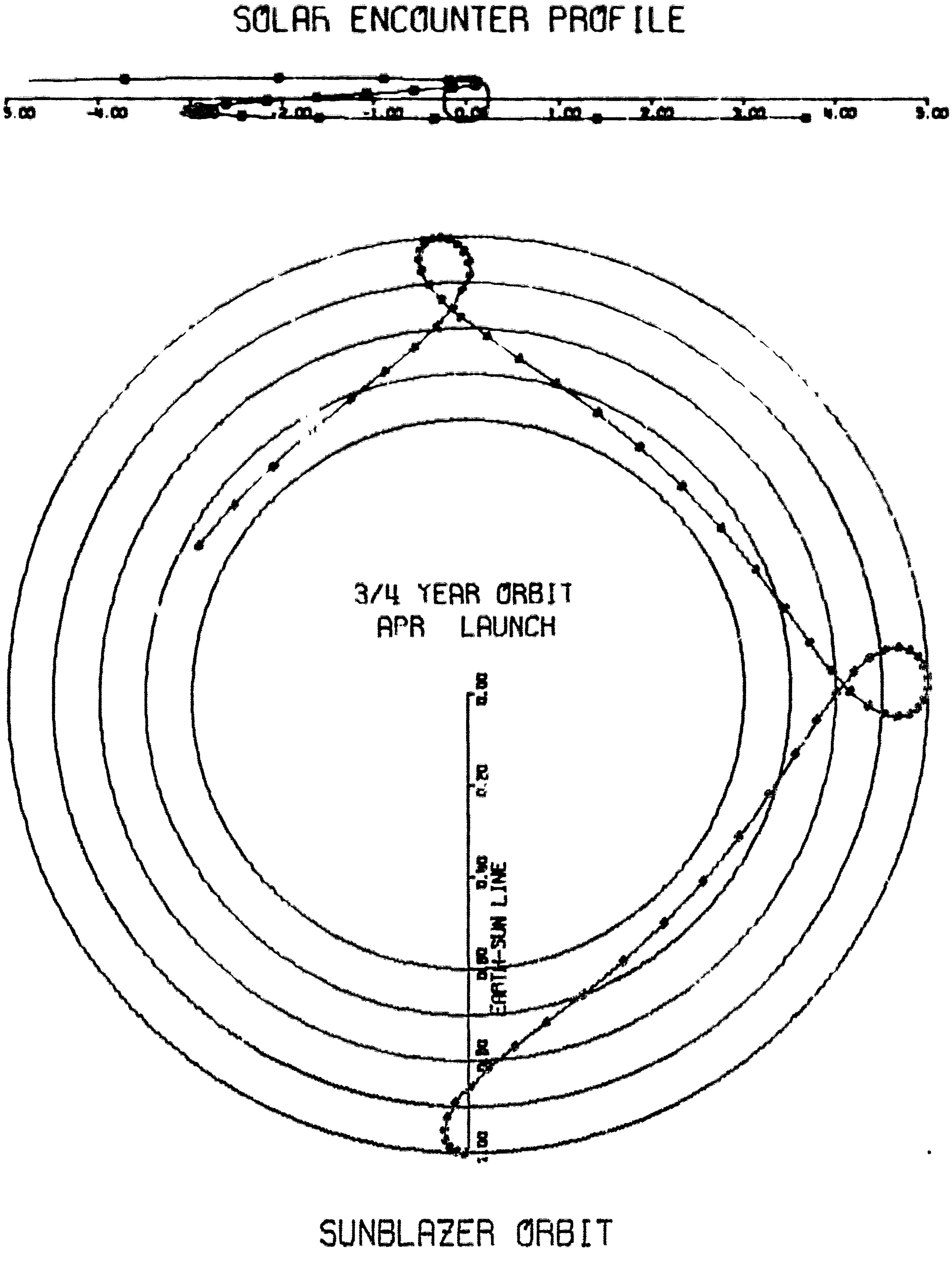
SOLAR ENCOUNTER PROFILE
-5.00
-4.00
-2.00
-1.00
0.00
1.00
2.00
3.00
4.00
5.00
3/4 YEAR ORBIT
APR LAUNCH
EARTH-SUN LINE
SUNBLAZER ORBIT

Fig. 3-5.

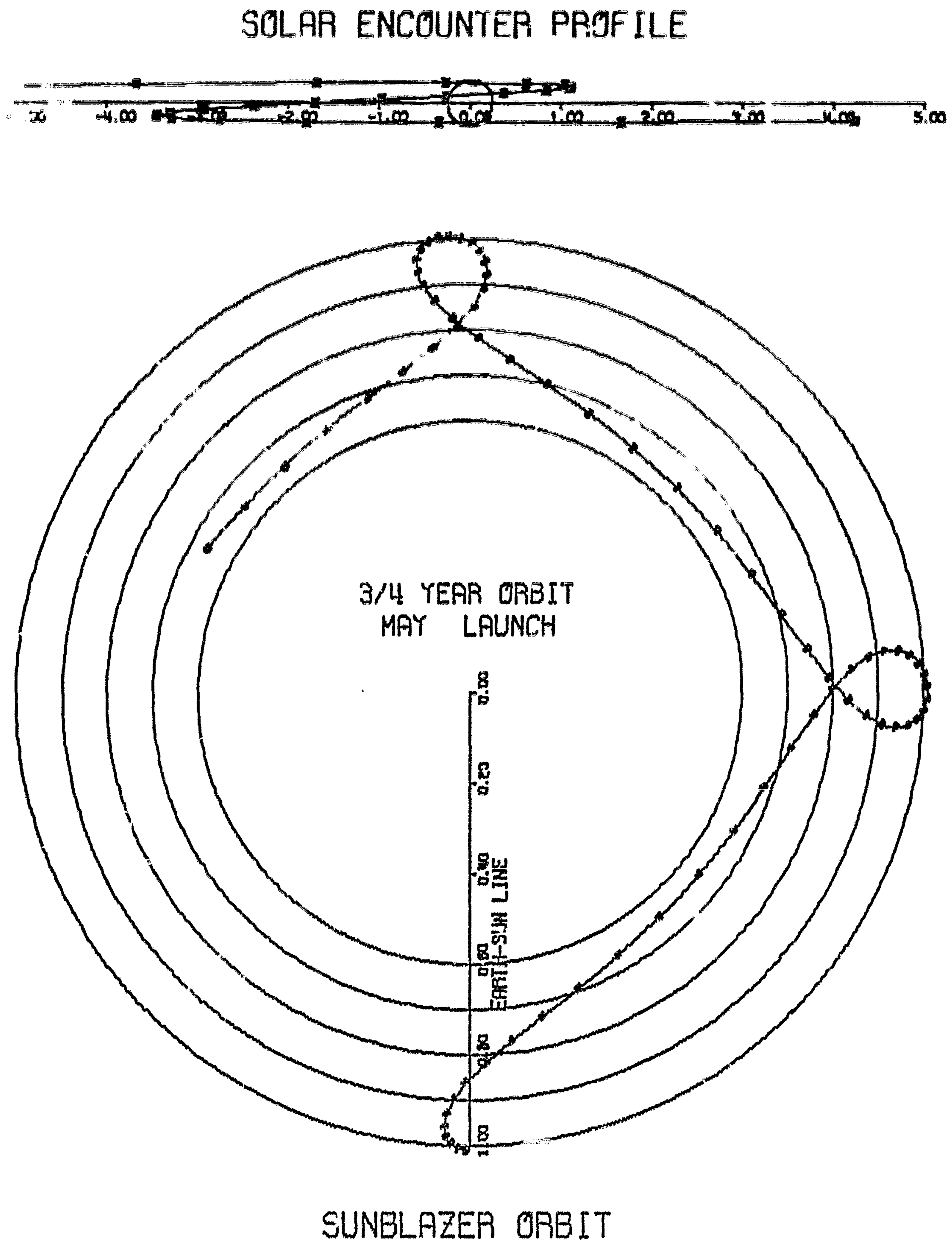
SOLAR ENCOUNTER PROFILE
-4.00
-2.00
-1.00
0.00
1.00
2.00
3.00
4.00
5.00
3/4 YEAR ORBIT
MAY LAUNCH
0.00
0.20
0.40
0.60
0.80
1.00
EARTH-SUN LINE
SUNBLAZER ORBIT

Fig. 3-6.

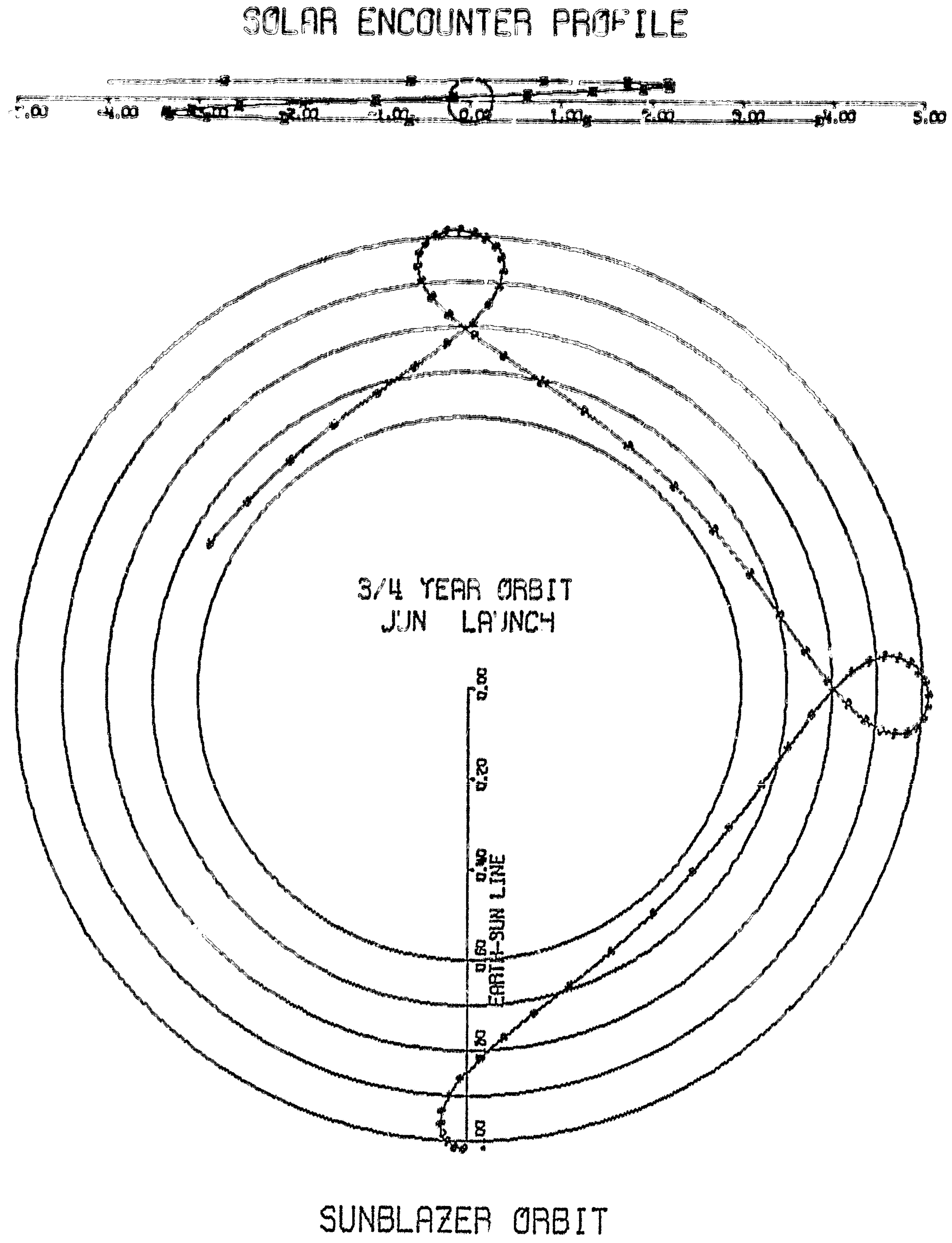
SOLAR ENCOUNTER PROFILE
0.00
1.00
2.00
4.00
5.00
3/4 YEAR ORBIT
JUN LAUNCH
EARTH-SUN LINE
0.20
0.80
SUNBLAZER ORBIT

Fig. 3-7.

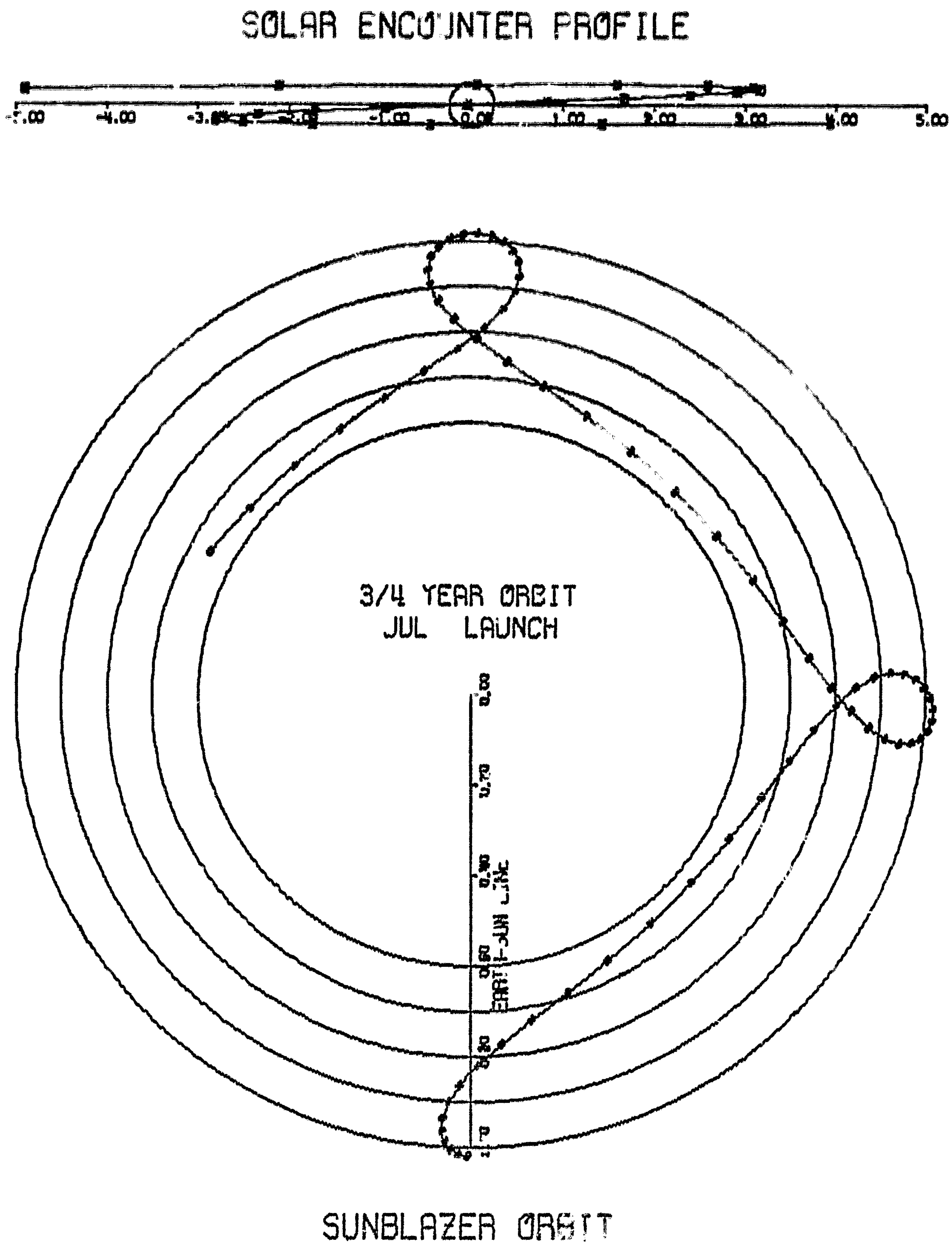
SOLAR ENCOUNTER PROFILE
-4.00
1.00
2.00
3.00
5.00
3/4 YEAR ORBIT
JUL LAUNCH
SUNBLAZER ORBIT

Fig. 3-3.

SØLAR ENCOUNTER PROFILE

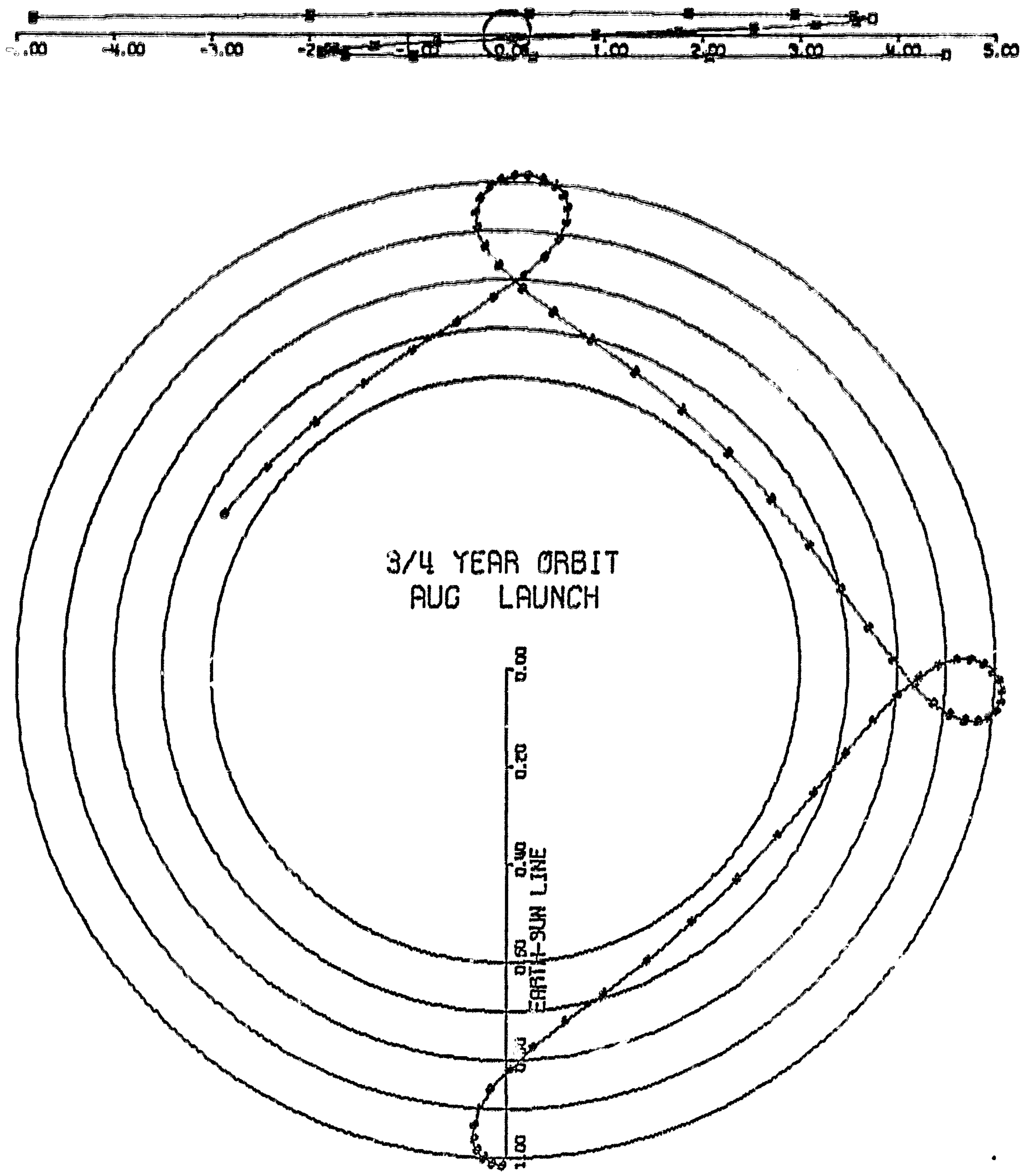

SUNBLAZER ØRBIT

Fig. 3-9.

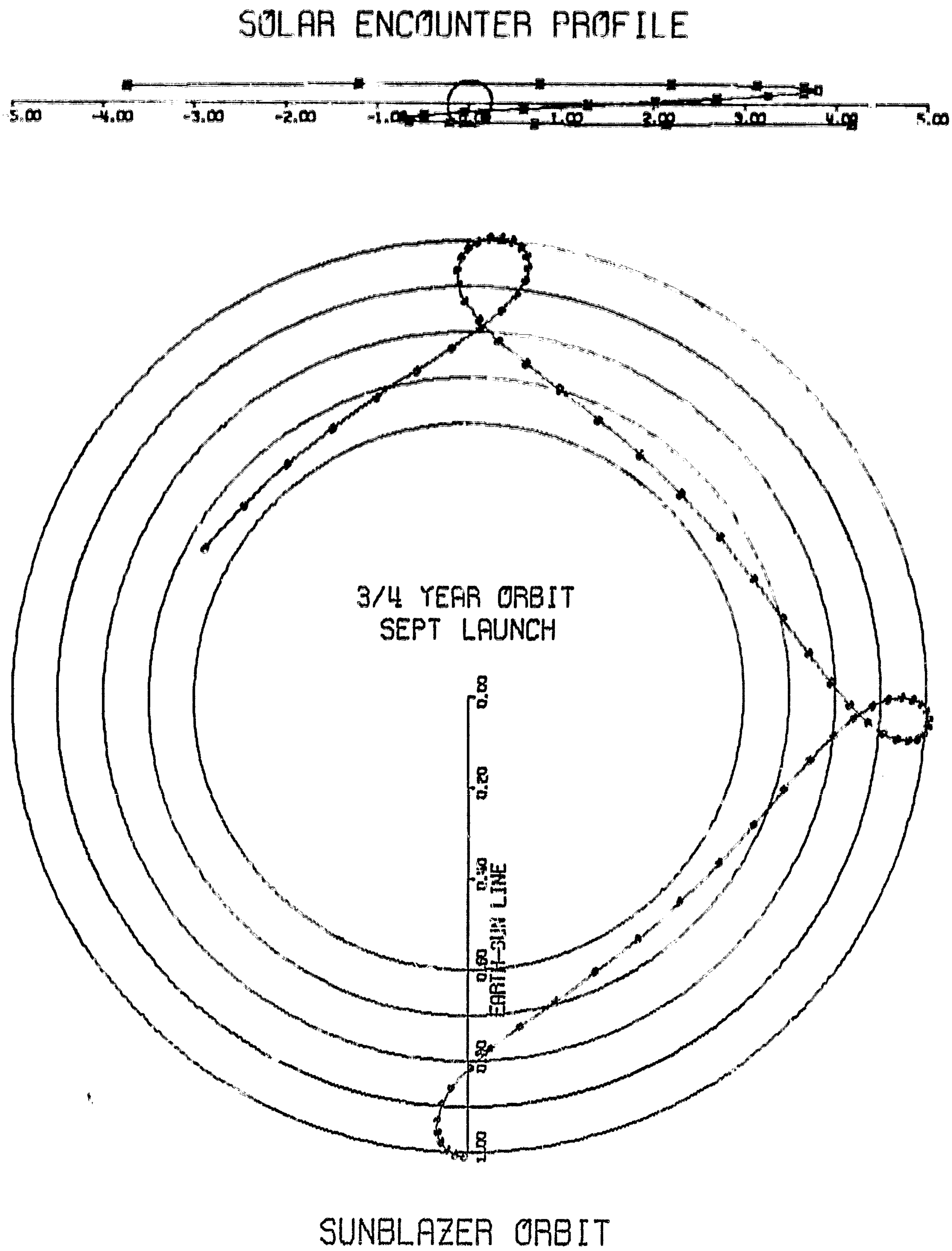
SOLAR ENCOUNTER PROFILE
-5.00
-4.00
-3.00
-2.00
2.00
5.00
3/4 YEAR ORBIT
SEPT LAUNCH
EARTH-SUN LINE
SUNBLAZER ORBIT

Fig. 3-10.

SOLAR ENCOUNTER PROFILE

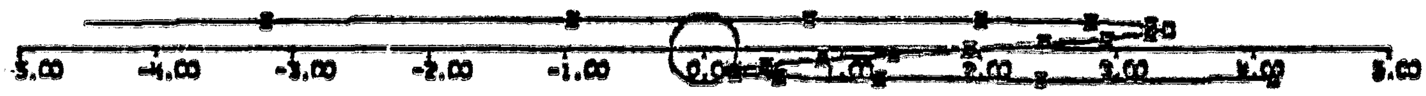

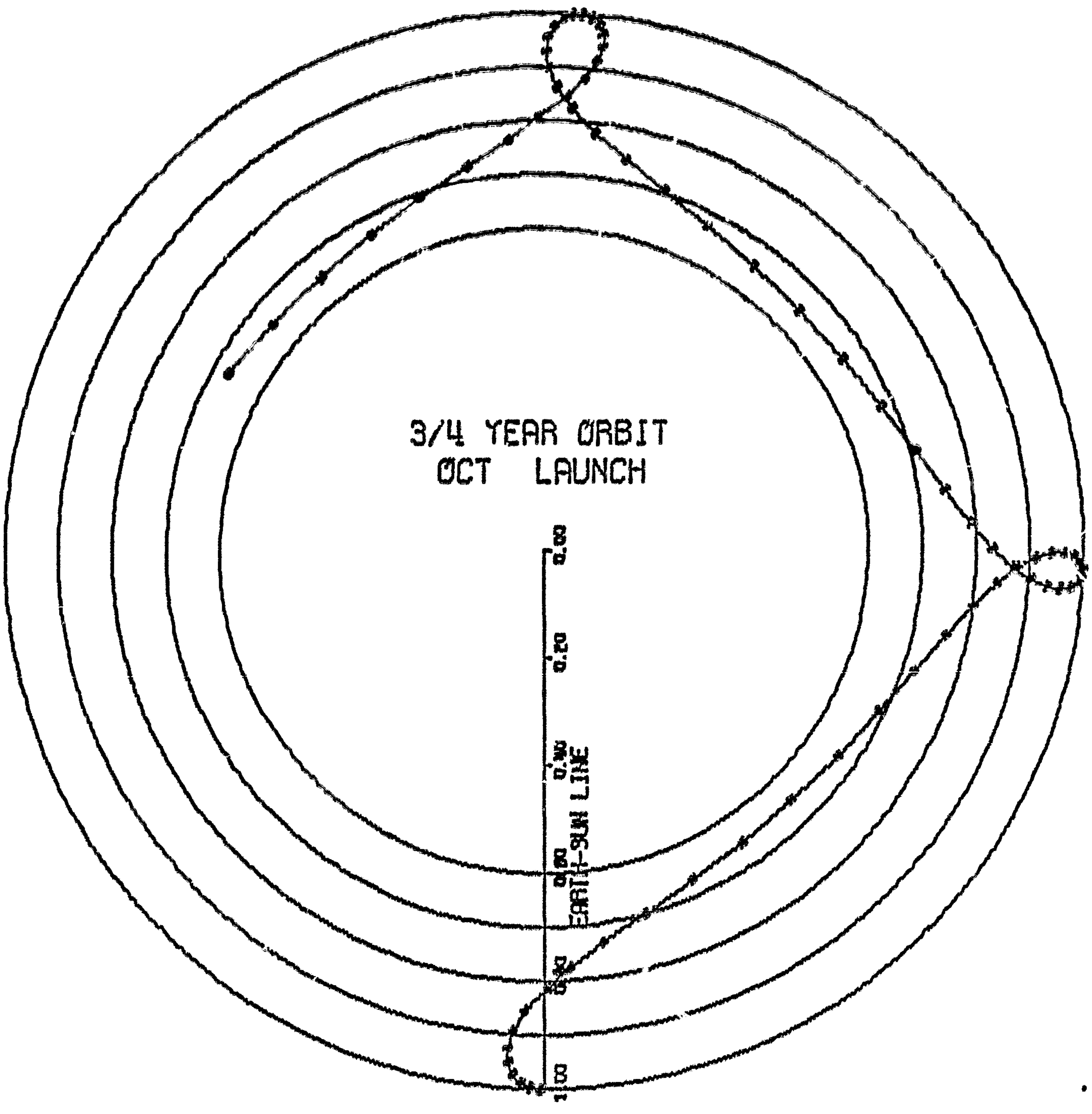

SUNBLAZER ORBIT

Fig. 2-11.

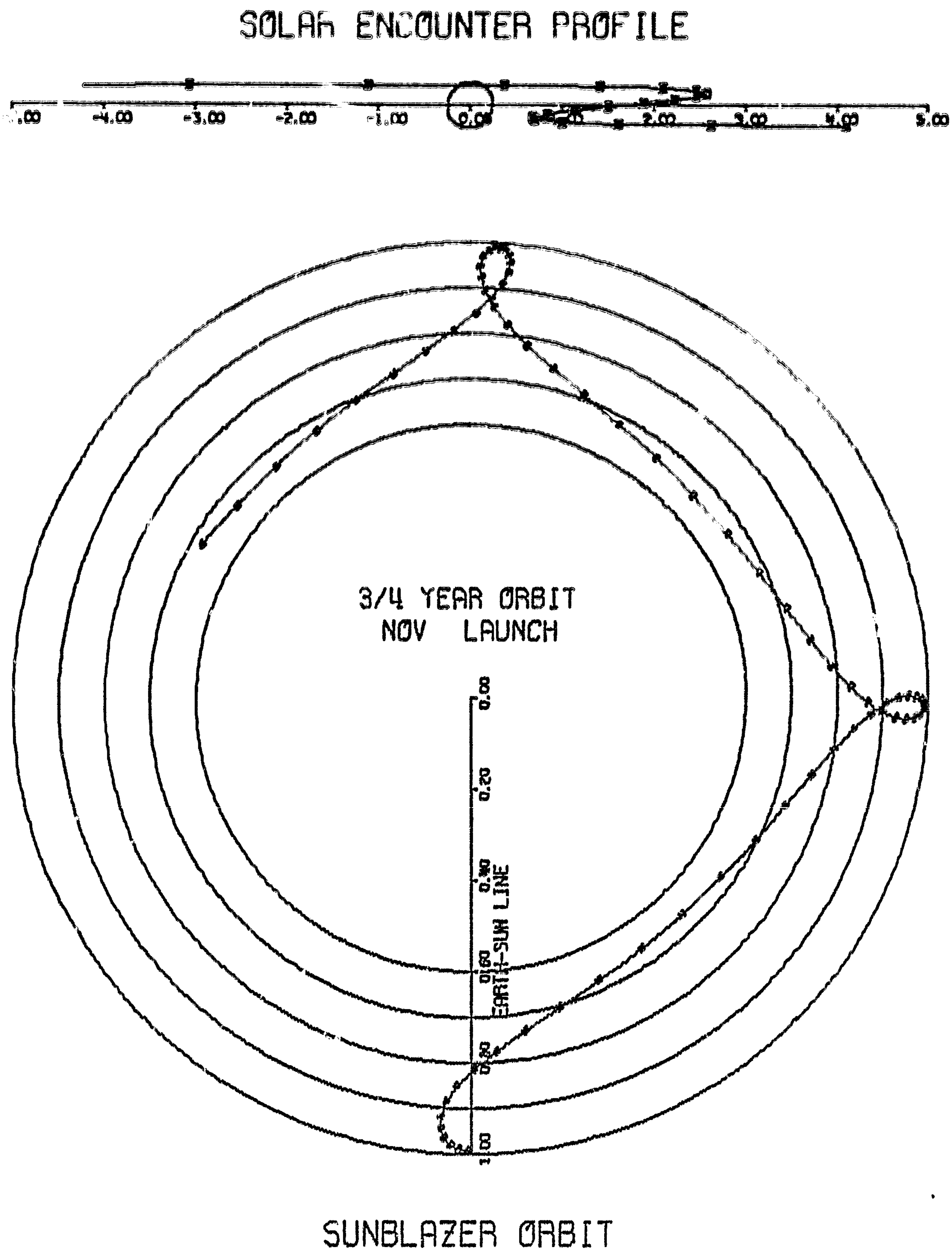
SOLAR ENCOUNTER PROFILE
-4.00
-3.00
-2.00
-1.00
0.00
2.00
3.00
4.00
5.00
3/4 YEAR ORBIT
NOV LAUNCH
0.00
0.20
0.40
0.60
0.80
1.00
EARTH-SUN LINE
SUNBLAZER ORBIT

Fig. 3-12.

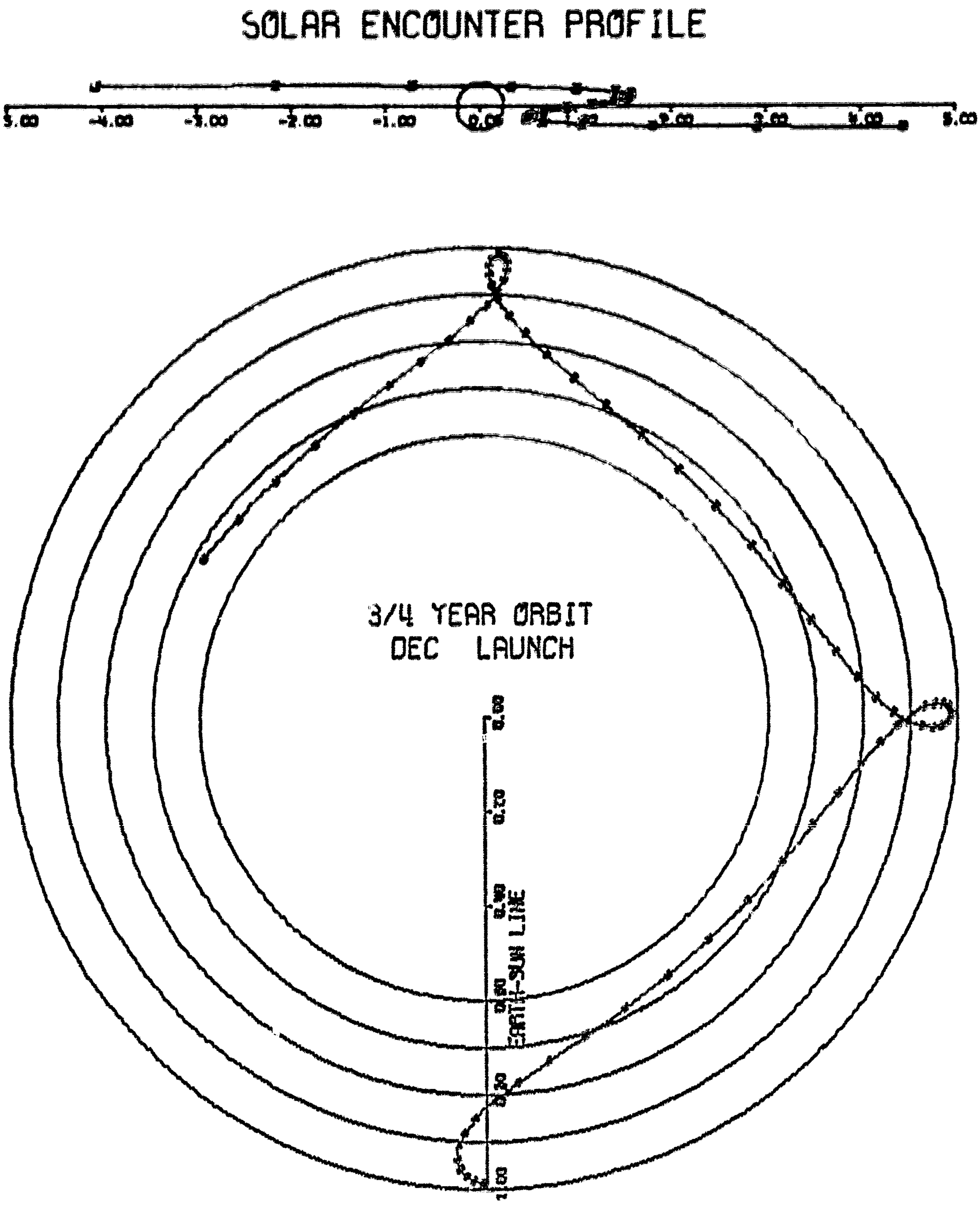

SUNBLAZER ORBIT

Fig. 3-13.

SUNBLAZER ORBIT

TINIT= 0.0 TDELT= 5.0 TFINL= 700.0 TBFS= 0.0 SEMI MAJOR AXIS=0.82548177

ECCENTRICITY=0.19115162 INCLINATION= 0.5000 SC INJECTION VELOCITY=0.90698

PERIOD SENS TO INJECT VEL= 20.65 DAYS PER/KM/SEC VSBSOI=0.11021 TPA= 0.0

TIME	REB	RSB	DIST	FEB	FSB	AZIMUTH	ELEVATION
0.0	0.98240	0.98327	0.00618	3.265	2.913	-97.934	4.048
5.0	0.98247	0.98254	0.01550	8.362	7.461	-89.810	4.118
10.0	0.98267	0.98035	0.02476	13.457	12.022	-83.885	4.127
15.0	0.98301	0.97671	0.03383	18.549	16.611	-78.268	4.130
20.0	0.98347	0.97162	0.04270	23.638	21.241	-72.650	4.125
25.0	0.98406	0.96512	0.05130	28.721	25.927	-66.878	4.116
30.0	0.98477	0.95722	0.05971	33.798	30.683	-60.886	4.094
35.0	0.98560	0.94795	0.06797	38.867	35.526	-54.609	4.055
40.0	0.98653	0.93736	0.07627	43.928	40.471	-48.015	3.992
45.0	0.98757	0.92549	0.08481	48.980	45.536	-41.097	3.897
50.0	0.98870	0.91241	0.09391	54.020	50.739	-33.879	3.764
55.0	0.98991	0.89819	0.10399	59.050	56.101	-26.445	3.587
60.0	0.99120	0.88293	0.11552	64.067	61.642	-18.915	3.365
65.0	0.99255	0.86672	0.12898	69.072	67.385	-11.436	3.103
70.0	0.99396	0.84970	0.14492	74.063	73.352	-4.197	2.810
75.0	0.99541	0.83203	0.16379	79.041	79.568	2.716	2.499
80.0	0.99689	0.81389	0.18599	84.005	86.057	9.023	2.183
85.0	0.99840	0.79550	0.21188	88.955	92.845	14.771	1.875
90.0	0.99991	0.77711	0.24166	93.890	99.955	19.871	1.584
95.0	1.00143	0.75901	0.27549	98.812	107.407	24.324	1.315
100.0	1.00293	0.74152	0.31342	103.719	115.218	28.147	1.070
105.0	1.00441	0.72502	0.35539	108.612	123.395	31.371	0.852
110.0	1.00585	0.70988	0.40124	113.493	131.937	34.043	0.658
115.0	1.00725	0.69651	0.45069	118.360	140.830	36.208	0.488
120.0	1.00859	0.68530	0.50334	123.214	150.043	37.917	0.340
125.0	1.00988	0.67661	0.55867	128.056	159.528	39.221	0.212
130.0	1.01108	0.67075	0.61605	132.887	169.220	40.171	0.102
135.0	1.01221	0.66794	0.67477	137.708	179.037	40.821	0.008
140.0	1.01325	0.66827	0.73407	142.519	188.891	41.220	-0.070
145.0	1.01419	0.67175	0.79320	147.321	198.689	41.419	-0.136
150.0	1.01503	0.67824	0.85141	152.114	208.342	41.466	-0.189
155.0	1.01576	0.68749	0.90807	156.901	217.774	41.402	-0.232
160.0	1.01638	0.69919	0.96262	161.682	226.923	41.267	-0.265
165.0	1.01688	0.71298	1.01462	166.458	235.743	41.091	-0.290
170.0	1.01726	0.72844	1.06376	171.230	244.208	40.902	-0.308
175.0	1.01751	0.74519	1.10980	175.999	252.307	40.720	-0.320
180.0	1.01764	0.76283	1.15262	180.766	260.039	40.560	-0.326
185.0	1.01764	0.78102	1.19213	[illegible]	267.417	40.434	-0.327
190.0	1.01752	0.79944	1.22833	190.300	274.456	40.349	-0.324

195.0	1.01727	0.81779	1.26124	195.067	281.178	40.308	-0.316
200.0	1.01690	0.83585	1.29092	199.841	287.607	40.314	-0.309
205.0	1.01641	0.85340	1.31746	204.617	293.768	40.367	-0.296
210.0	1.01579	0.87025	1.34072	209.397	299.685	40.464	-0.282
215.0	1.01507	0.88627	1.36143	214.184	305.382	40.604	-0.265
220.0	1.01424	0.90132	1.37909	218.977	310.883	40.783	-0.247
225.0	1.01330	0.91531	1.39401	223.779	316.210	40.995	-0.227
230.0	1.01226	0.92813	1.40631	228.589	321.382	41.238	-0.206
235.0	1.01114	0.93973	1.41611	233.409	326.420	41.505	-0.184
240.0	1.00994	0.95004	1.42353	238.240	331.342	41.790	-0.160
245.0	1.00866	0.95902	1.42870	243.082	336.164	42.089	-0.136
250.0	1.00732	0.96663	1.43176	247.935	340.904	42.394	-0.110
255.0	1.00592	0.97283	1.43284	252.802	345.577	42.699	-0.085
260.0	1.00448	0.97761	1.43210	257.681	350.197	42.999	-0.058
265.0	1.00300	0.98094	1.42967	262.574	354.773	43.285	-0.031
270.0	1.00150	0.98282	1.42573	267.481	359.337	43.550	-0.004
275.0	0.99999	0.98324	1.42042	272.401	363.884	43.788	0.023
280.0	0.99847	0.98220	1.41393	277.336	368.434	43.990	0.051
285.0	0.99697	0.97969	1.40644	282.285	373.006	44.149	0.078
290.0	0.99548	0.97574	1.39815	287.249	377.576	44.256	0.105
295.0	0.99403	0.97035	1.38926	292.226	382.237	44.304	0.132
300.0	0.99262	0.96355	1.37998	297.217	386.937	44.285	0.158
305.0	0.99126	0.95535	1.37054	302.221	391.710	44.189	0.183
310.0	0.98997	0.94580	1.36119	307.237	396.573	44.010	0.207
315.0	0.98875	0.93493	1.35215	312.266	401.542	43.739	0.229
320.0	0.98762	0.92280	1.34371	317.306	406.635	43.370	0.250
325.0	0.98658	0.90947	1.33611	322.357	411.871	42.894	0.268
330.0	0.98564	0.89502	1.32964	327.417	417.269	42.308	0.283
335.0	0.98481	0.87954	1.32455	332.487	422.851	41.606	0.295
340.0	0.98409	0.86314	1.32111	337.563	428.639	40.785	0.304
345.0	0.98350	0.84597	1.31959	342.646	434.658	39.843	0.309
350.0	0.98303	0.82819	1.32022	347.735	440.930	38.779	0.310
355.0	0.98269	0.80997	1.32322	352.827	447.481	37.596	0.306
360.0	0.98248	0.79156	1.32876	357.922	454.336	36.297	0.297
365.0	0.98240	0.77321	1.33698	363.018	461.517	34.887	0.283
370.0	0.98247	0.75521	1.34795	368.115	469.045	33.373	0.265
375.0	0.98266	0.73790	1.36168	373.210	476.933	31.764	0.242
380.0	0.98299	0.72166	1.37811	378.302	485.189	30.070	0.214
385.0	0.98344	0.70686	1.39709	383.391	493.808	28.304	0.183
390.0	0.98403	0.69392	1.41838	388.475	502.773	26.480	0.148
395.0	0.98473	0.68322	1.44169	393.552	512.049	24.612	0.111
400.0	0.98555	0.67511	1.46667	398.622	521.584	22.718	0.073
405.0	0.98648	0.66989	1.49291	403.683	531.309	20.817	0.034
410.0	0.98751	0.66774	1.52002	408.735	541.143	18.927	-0.004
415.0	0.98864	0.66876	1.54761	413.776	550.992	17.069	-0.041

420.0	0.98985	0.67280	1.57535	418.606	560.764	15.261	-0.076
425.0	0.99113	0.67999	1.60294	423.824	570.378	13.521	-0.107
430.0	0.99248	0.68980	1.63018	428.829	579.754	11.667	-0.135
435.0	0.99383	0.70138	1.65690	433.121	588.835	10.302	-0.157
440.0	0.99534	0.71615	1.68361	438.800	597.582	8.859	-0.180
445.0	0.99682	0.73192	1.70842	443.764	605.969	7.524	-0.196
450.0	0.99832	0.74869	1.73309	448.715	613.989	6.300	-0.208
455.0	0.99984	0.76662	1.75699	453.651	621.645	5.208	-0.216
460.0	1.00135	0.78495	1.78008	458.573	628.946	4.228	-0.220
465.0	1.00285	0.80337	1.80232	463.481	635.918	3.364	-0.222
470.0	1.00433	0.82168	1.82369	468.375	642.575	2.610	-0.220
475.0	1.00578	0.83985	1.84412	473.256	648.945	1.961	-0.215
480.0	1.00718	0.85706	1.86356	478.124	655.057	1.411	-0.208
485.0	1.00853	0.87375	1.88196	482.979	660.920	0.956	-0.199
490.0	1.00982	0.88957	1.89926	487.822	667.573	0.587	-0.188
495.0	1.01103	0.90446	1.91539	492.654	672.035	0.296	-0.175
500.0	1.01216	0.91815	1.93029	497.475	677.327	0.082	-0.161
505.0	1.01320	0.93072	1.94391	502.286	682.469	-0.107	-0.146
510.0	1.01415	0.94204	1.95617	507.088	687.480	-0.199	-0.127
515.0	1.01499	0.95207	1.96704	511.882	692.379	-0.245	-0.112
520.0	1.01573	0.96076	1.97647	516.669	697.183	-0.250	-0.094
525.0	1.01635	0.96807	1.98440	521.450	701.907	-0.223	-0.076
530.0	1.01686	0.97397	1.99082	526.225	706.568	-0.172	-0.057
535.0	1.01724	0.97844	1.99568	530.999	711.178	-0.097	-0.038
540.0	1.01750	0.98147	1.99897	535.768	715.754	0.0	-0.018
545.0	1.01764	0.98303	2.00067	540.535	720.308	0.112	0.001
550.0	1.01764	0.98314	2.00077	545.302	724.855	0.226	0.021
555.0	1.01753	0.98178	1.99926	550.069	729.407	0.329	0.040
560.0	1.01729	0.97897	1.99620	554.838	733.979	0.425	0.059
565.0	1.01692	0.97471	1.99155	559.610	738.583	0.505	0.078
570.0	1.01643	0.96902	1.98535	564.385	743.235	0.560	0.096
575.0	1.01583	0.96191	1.97762	569.165	747.949	0.593	0.114
580.0	1.01511	0.95343	1.96842	573.951	752.740	0.589	0.131
585.0	1.01428	0.94359	1.95776	578.745	757.624	0.543	0.147
590.0	1.01335	0.93245	1.94572	583.545	762.618	0.448	0.162
595.0	1.01232	0.92005	1.93233	588.355	767.740	0.297	0.176
600.0	1.01120	0.90648	1.91766	593.174	773.009	0.082	0.189
605.0	1.01000	0.89180	1.90176	598.005	778.444	-0.214	0.200
610.0	1.00872	0.87611	1.88471	602.846	784.069	-0.570	0.209
615.0	1.00738	0.85954	1.86655	607.699	789.905	-1.015	0.216
620.0	1.00599	0.84222	1.84738	612.565	795.974	-1.554	0.221
625.0	1.00455	0.82433	1.82723	617.444	802.304	-2.191	0.224
630.0	1.00307	0.80605	1.80616	622.336	808.918	-2.933	0.223
635.0	1.00157	0.78763	1.78422	627.242	815.841	-3.785	0.220
640.0	1.00006	0.76932	1.76145	632.162	823.095	-4.752	0.213
645.0	0.99854	0.75145	1.73791	637.096	830.698	-5.836	0.202
650.0	0.99704	0.73433	1.71360	642.045	838.665	-7.041	0.188

655.0	0.99555	0.71836	1.68857	647.007	846.9[illegible]	-8.363	0.170
660.0	0.99410	0.70323	1.66286	651.983	855.636	-9.801	0.148
665.0	0.99267	0.69143	1.63655	656.974	864.728	-11.347	0.122
670.0	0.99133	0.68126	1.60971	661.977	874.065	-12.993	0.093
675.0	0.99003	0.67374	1.58251	666.996	883.647	-14.724	0.060
680.0	0.98881	0.66917	1.55514	672.021	893.403	-16.526	0.025
685.0	0.98767	0.66769	1.52789	677.061	903.246	-18.381	-0.012
690.0	0.98663	0.66938	1.50106	682.111	913.088	-20.270	-0.050
695.0	0.98568	0.67416	1.47504	687.172	922.833	-22.172	-0.089
700.0	0.98484	0.68186	1.45022	692.240	932.400	-24.067	-0.126

SUNBLAZER ORBIT

TINIT= 0.0 TDELT= 5.0 TFINL= 700.0 TBEG= 30.0 SEMI MAJOR AXIS=0.82548177

ECCENTRICITY=0.19387531 INCLINATION= 0.5000 SB INJECTION VELOCITY=0.90441

PERIOD SENS TO INJECT VEL= 20.59 DAYS PER/KM/SEC VSBSOI=0.11078 TPA= 0.0

TIME	RER	RSB	DIST	FER	FSB	AZIMUTH	ELEVATION
0.0	0.98477	0.98552	0.00610	3.241	2.890	-96.929	4.077
5.0	0.98560	0.98478	0.01550	8.311	7.414	-86.540	4.102
10.0	0.98653	0.98257	0.02478	13.372	11.953	-80.071	4.109
15.0	0.98757	0.97889	0.03391	18.423	16.519	-74.186	4.107
20.0	0.98870	0.97376	0.04285	23.463	21.126	-68.372	4.093
25.0	0.98991	0.96719	0.05162	28.493	25.789	-62.463	4.079
30.0	C.99120	0.95921	0.06025	33.510	30.523	-56.347	4.046
35.0	0.99255	0.94985	0.06885	38.515	35.343	-49.971	3.994
40.0	0.99396	0.93914	0.07760	43.506	40.266	-43.315	3.914
45.0	0.99541	0.92715	0.08678	48.484	45.309	-36.391	3.801
50.0	0.99689	0.91393	0.09670	53.448	50.492	-29.249	3.648
55.0	0.99840	0.89954	0.10779	58.398	55.834	-21.974	3.455
60.0	0.99991	0.88410	0.12049	63.333	61.356	-14.696	3.221
65.0	1.00143	0.86769	0.13530	68.255	67.082	-7.571	2.955
70.0	1.00293	0.85046	0.15268	73.162	73.033	-0.677	2.665
75.0	1.00441	0.83255	0.17306	78.056	79.236	5.695	2.364
80.0	1.00585	0.81416	0.19681	82.936	85.716	11.584	2.063
85.0	1.00725	0.79551	0.22422	87.803	92.498	16.894	1.773
90.0	1.00859	0.77684	0.25550	92.657	99.606	21.593	1.499
95.0	1.00988	0.75845	0.29079	97.500	107.063	25.685	1.247
100.0	1.01108	0.74068	0.3301[illegible]	102.331	114.884	29.192	1.018
105.0	1.01221	0.72388	0.37341	107.151	123.078	32.144	0.812
110.0	1.01325	0.70847	0.42051	111.962	131.647	34.580	0.629
115.0	1.01419	0.69484	0.47114	116.764	140.574	36.543	0.468
120.0	1.01503	0.68341	0.52488	121.558	149.830	38.079	0.327
125.0	1.01576	0.67455	0.58119	126.344	159.365	39.233	0.205
130.0	1.01638	0.66856	0.63945	131.125	169.112	40.055	0.099
135.0	1.01688	0.66569	0.69891	135.901	178.990	40.592	0.008
140.0	1.01726	0.66604	0.75880	140.673	188.905	40.894	-0.068
145.0	1.01751	0.66959	0.81836	145.442	198.763	41.010	-0.132
150.0	1.01764	0.67621	0.87685	150.210	208.471	40.984	-0.184
155.0	1.01764	0.68565	0.93360	154.976	217.952	40.860	-0.226
160.0	1.01752	0.69758	0.98810	159.744	227.141	40.673	-0.259
165.0	1.01727	0.71162	1.03989	164.513	235.993	40.457	-0.284
170.0	1.01690	0.72737	1.08867	169.284	244.483	40.236	-0.301
175.0	1.01641	0.74440	1.13423	174.060	252.597	40.031	-0.313
180.0	1.01579	0.76234	1.17645	178.841	260.339	39.856	-0.319
185.0	1.01507	0.78081	1.21527	183.627	267.719	39.723	-0.321
190.0	1.01423	0.79950	1.25069	188.421	274.756	39.637	-0.319

195.0	1.01330	0.81812	1.28275	193.222	281.471	39.604	-0.313
200.0	1.01226	0.83643	1.31153	198.032	287.890	39.623	-0.303
205.0	1.01114	0.85420	1.33709	202.852	294.037	39.695	-0.292
210.0	1.00994	0.87127	1.35955	207.683	299.938	39.817	-0.278
215.0	1.00866	0.88748	1.37701	212.525	305.618	39.987	-0.262
220.0	1.00732	0.90271	1.39558	217.379	311.100	40.200	-0.244
225.0	1.00592	0.91685	1.40939	222.245	316.407	40.452	-0.224
230.0	1.00448	0.92982	1.42055	227.124	321.558	40.737	-0.203
235.0	1.00300	0.94154	1.42920	232.017	326.574	41.049	-0.181
240.0	1.00150	0.95196	1.43545	236.924	331.474	41.382	-0.158
245.0	0.99999	0.96103	1.43945	241.845	336.274	41.731	-0.134
250.0	0.99847	0.96871	1.44133	246.780	340.991	42.088	-0.109
255.0	0.99697	0.97498	1.44124	251.729	345.641	42.447	-0.084
260.0	0.99548	0.97980	1.43933	256.692	350.238	42.799	-0.058
265.0	0.99403	0.98317	1.43575	261.669	354.797	43.138	-0.031
270.0	0.99262	0.98507	1.43067	266.660	359.332	43.455	-0.004
275.0	0.99126	0.98549	1.42425	271.664	363.855	43.743	0.023
280.0	0.98997	0.98444	1.41669	276.680	368.382	43.993	0.051
285.0	0.98875	0.98191	1.40818	281.709	372.926	44.197	0.078
290.0	0.98762	0.97792	1.39891	286.750	377.499	44.346	0.105
295.0	0.98656	0.97248	1.38911	291.800	382.117	44.432	0.132
300.0	0.98564	0.96560	1.37899	296.861	386.793	44.445	0.158
305.0	0.98481	0.95732	1.36879	301.930	391.544	44.377	0.183
310.0	0.98409	0.94767	1.35877	307.006	396.385	44.219	0.207
315.0	0.98350	0.93669	1.34917	312.089	401.332	43.964	0.229
320.0	0.98303	0.92443	1.34027	317.176	406.404	43.603	0.250
325.0	0.98269	0.91095	1.33234	322.270	411.619	43.131	0.268
330.0	0.98248	0.89633	1.32565	327.365	416.998	42.541	0.284
335.0	0.98240	0.88067	1.32049	332.461	422.561	41.829	0.296
340.0	0.98247	0.86407	1.31712	337.558	428.333	40.992	0.305
345.0	0.98266	0.84668	1.31581	342.653	434.336	40.029	0.310
350.0	0.98299	0.82866	1.31680	347.745	440.596	38.940	0.310
355.0	0.98344	0.81019	1.32029	352.834	447.139	37.727	0.306
360.0	0.98403	0.79151	1.32648	357.918	453.989	36.394	0.298
365.0	0.98473	0.77288	1.33546	362.995	461.169	34.948	0.284
370.0	0.98555	0.75459	1.34732	368.065	468.702	33.396	0.265
375.0	0.98648	0.73699	1.36205	373.126	476.602	31.748	0.242
380.0	0.98751	0.72046	1.37954	378.178	484.877	30.014	0.214
385.0	0.98864	0.70539	1.39964	383.219	493.524	28.206	0.183
390.0	0.98985	0.69220	1.42209	388.249	502.525	26.340	0.148
395.0	0.99113	0.68129	1.44656	393.267	511.845	24.430	0.111
400.0	0.99248	0.67302	1.47265	398.272	521.432	22.494	0.073
405.0	0.99389	0.66768	1.49994	403.265	531.215	20.549	0.034
410.0	0.99534	0.66549	1.52801	408.243	541.109	18.616	-0.004
415.0	0.99682	0.66653	1.55643	413.208	551.019	16.714	-0.041

420.0	0.99832	0.67075	1.58486	418.158	560.852	14.863	-0.075
425.0	0.99984	0.67800	1.61301	423.094	570.518	13.080	-0.107
430.0	1.00135	0.68800	1.64065	428.016	579.941	11.383	-0.135
435.0	1.00285	0.70042	1.66743	432.925	589.061	9.783	-0.159
440.0	1.00433	0.71486	1.69385	437.819	597.838	8.292	-0.179
445.0	1.00578	0.73091	1.71926	442.699	606.248	6.915	-0.195
450.0	1.00718	0.74817	1.74381	447.567	614.282	5.658	-0.206
455.0	1.00853	0.76625	1.76749	452.422	621.946	4.521	-0.215
460.0	1.00982	0.78480	1.79028	457.265	629.250	3.504	-0.219
465.0	1.01103	0.80349	1.81215	462.097	636.217	2.604	-0.220
470.0	1.01216	0.82207	1.83308	466.918	642.866	1.816	-0.219
475.0	1.01320	0.84027	1.85302	471.729	649.225	1.136	-0.214
480.0	1.01415	0.85791	1.87194	476.531	655.318	0.560	-0.207
485.0	1.01499	0.87481	1.88979	481.325	661.169	0.101	-0.198
490.0	1.01573	0.89082	1.90650	486.113	666.805	-0.332	-0.187
495.0	1.01635	0.90582	1.92203	490.894	672.248	-0.642	-0.174
500.0	1.01686	0.91972	1.93632	495.670	677.520	-0.881	-0.160
505.0	1.01724	0.93243	1.94930	500.442	682.640	-1.054	-0.145
510.0	1.01750	0.94388	1.96094	505.211	687.630	-1.165	-0.129
515.0	1.01764	0.95401	1.97116	509.978	692.507	-1.224	-0.112
520.0	1.01764	0.96279	1.97994	514.745	697.288	-1.238	-0.094
525.0	1.01753	0.97017	1.98723	519.512	701.990	-1.210	-0.075
530.0	1.01729	0.97613	1.99300	524.281	706.627	-1.150	-0.057
535.0	1.01692	0.98064	1.99721	529.053	711.215	-1.062	-0.037
540.0	1.01643	0.98370	1.99984	533.828	715.767	-0.953	-0.018
545.0	1.01583	0.98528	2.00089	538.609	720.299	-0.834	0.001
550.0	1.01511	0.98539	2.00034	543.395	724.822	-0.704	0.021
555.0	1.01428	0.98402	1.99819	548.188	729.351	-0.575	0.040
560.0	1.01335	0.98118	1.99446	552.989	733.899	-0.451	0.059
565.0	1.01232	0.97688	1.98916	557.799	738.480	-0.333	0.078
570.0	1.01120	0.97113	1.98230	562.618	743.109	-0.244	0.096
575.0	1.01000	0.96395	1.97394	567.448	747.801	-0.174	0.114
580.0	1.00872	0.95538	1.96409	572.290	752.569	-0.149	0.131
585.0	1.00738	0.94544	1.95281	577.143	757.432	-0.144	0.147
590.0	1.00599	0.93418	1.94014	582.009	762.404	-0.201	0.162
595.0	1.00455	0.92165	1.92616	586.887	767.504	-0.301	0.176
600.0	1.00307	0.90792	1.91091	591.780	772.752	-0.464	0.189
605.0	1.00157	0.89307	1.89447	596.686	778.168	-0.701	0.200
610.0	1.00006	0.87720	1.87691	601.606	783.775	-1.013	0.210
615.0	0.99854	0.86042	1.85830	606.540	789.594	-1.412	0.217
620.0	0.99704	0.84288	1.83870	611.489	795.650	-1.906	0.222
625.0	0.99555	0.82475	1.81819	616.451	801.968	-2.500	0.225
630.0	0.99410	0.80621	1.79683	621.427	808.574	-3.200	0.224
635.0	0.99269	0.78752	1.77468	626.418	815.492	-4.013	0.221
640.0	0.99133	0.76893	1.75179	631.421	822.747	-4.945	0.214
645.0	0.99003	0.75076	1.72819	636.437	830.357	-5.999	0.204
650.0	0.98881	0.73336	1.70394	641.465	838.337	-7.176	0.189

655.0	0.98767	0.71711	1.67905	646.505	846.692	-8.476	0.171
660.0	0.98663	0.70241	1.65358	651.555	855.417	-9.895	0.149
665.0	0.98568	0.68967	1.62758	656.615	864.489	-11.426	0.123
670.0	0.98484	0.67929	1.60115	661.684	873.871	-13.062	0.093
675.0	0.98412	0.67162	1.57442	666.760	883.507	-14.786	0.061
680.0	0.98352	0.66695	1.54759	671.845	893.320	-16.585	0.025
685.0	0.98305	0.66544	1.52092	676.931	903.225	-18.438	-0.012
690.0	0.98270	0.66717	1.49471	682.023	913.127	-20.328	-0.051
695.0	0.98249	0.67205	1.46934	687.118	922.931	-22.231	-0.089
700.0	0.98241	0.67991	1.44518	692.214	932.551	-24.130	-0.127

SUNBLAZER ORBIT

TINIT= 0.0 TDELT= 5.0 TFINL= 700.0 TBEG= 61.0 SEMI MAJOR AXIS=0.62548177

ECCENTRICITY=0.20157915 INCLINATION= 0.5000 SB INJECTION VELOCITY=0.89719

PERIOD SENS TO INJECT VEL= 20.42 DAYS PER/KM/SEC VSBSOI=0.11213 TPA= 0.0

TIME	RER	RSB	DIST	FER	FSB	AZIMUTH	ELEVATION
0.0	0.99146	0.99188	0.00618	3.181	2.832	-93.711	3.970
5.0	0.99283	0.99112	0.01362	8.184	7.292	-83.273	4.029
10.0	0.99425	0.98885	0.02501	13.172	11.766	-76.812	4.034
15.0	0.99570	0.98508	0.03431	18.147	16.267	-70.963	4.025
20.0	0.99719	0.97980	0.04342	23.108	20.809	-65.180	4.011
25.0	0.99870	0.97306	0.05241	28.055	25.408	-59.302	3.986
30.0	1.00021	0.96485	0.06132	32.988	30.078	-53.235	3.946
35.0	1.00173	0.95523	0.07026	37.907	34.836	-46.912	3.866
40.0	1.00323	0.94422	0.07944	42.811	39.697	-40.337	3.799
45.0	1.00470	0.93187	0.08914	47.702	44.680	-33.536	3.678
50.0	1.00613	0.91824	0.09967	52.580	49.804	-26.553	3.521
55.0	1.00752	0.90341	0.11146	57.444	55.090	-19.485	3.325
60.0	1.00886	0.88746	0.12495	62.296	60.559	-12.456	3.094
65.0	1.01012	0.87050	0.14060	67.136	66.235	-5.596	2.834
70.0	1.01132	0.85266	0.15887	71.965	72.143	0.944	2.555
75.0	1.01243	0.83410	0.18016	76.783	78.309	7.081	2.267
80.0	1.01345	0.81501	0.20485	81.592	84.760	12.708	1.981
85.0	1.01437	0.79560	0.23321	86.392	91.523	17.772	1.705
90.0	1.01519	0.77615	0.26546	91.185	98.626	22.257	1.445
95.0	1.01589	0.75694	0.30173	95.970	106.091	26.164	1.205
100.0	1.01649	0.73834	0.34208	100.750	113.940	29.511	0.986
105.0	1.01696	0.72072	0.38643	105.525	122.184	32.326	0.789
110.0	1.01732	0.70452	0.43463	110.296	130.824	34.643	0.613
115.0	1.01755	0.69016	0.48639	115.065	139.849	36.502	0.457
120.0	1.01765	0.67810	0.54128	119.832	149.225	37.943	0.320
125.0	1.01763	0.66872	0.59875	124.599	158.904	39.012	0.201
130.0	1.01748	0.66239	0.65812	129.367	168.813	39.753	0.098
135.0	1.01721	0.65935	0.71864	134.136	178.863	40.216	0.009
140.0	1.01681	0.65971	0.77946	138.909	188.954	40.450	-0.066
145.0	1.01629	0.66347	0.83980	143.685	198.982	40.503	-0.128
150.0	1.01566	0.67048	0.89888	148.467	208.849	40.424	-0.180
155.0	1.01491	0.68046	0.95603	153.255	218.468	40.254	-0.221
160.0	1.01406	0.69305	1.01070	158.049	227.773	40.032	-0.254
165.0	1.01310	0.70784	1.06246	162.853	236.718	39.790	-0.278
170.0	1.01205	0.72438	1.11101	167.665	245.274	39.554	-0.296
175.0	1.01091	0.74224	1.15615	172.487	253.433	39.345	-0.308
180.0	1.00969	0.76101	1.19780	177.320	261.198	39.176	-0.314
185.0	1.00839	0.78029	1.23591	182.164	268.584	39.058	-0.316
190.0	1.00704	0.79976	1.27050	187.020	275.612	38.997	-0.313

195.0	1.00563	0.81912	1.30164	191.889	282.307	38.996	-0.307
200.0	1.00418	0.83812	1.32941	196.771	288.694	39.056	-0.293
205.0	1.00270	0.85654	1.35390	201.667	294.803	39.174	-0.287
210.0	1.00120	0.87420	1.37523	206.576	300.659	39.350	-0.273
215.0	0.99968	0.89095	1.39352	211.500	306.289	39.577	-0.258
220.0	0.99817	0.90667	1.40889	216.438	311.717	39.851	-0.240
225.0	0.99667	0.92125	1.42146	221.390	316.966	40.168	-0.221
230.0	0.99519	0.93461	1.43136	226.356	322.058	40.520	-0.201
235.0	0.99374	0.94668	1.43873	231.336	327.014	40.902	-0.179
240.0	0.99234	0.95740	1.44370	236.329	331.852	41.306	-0.156
245.0	0.99100	0.96673	1.44641	241.336	336.589	41.725	-0.133
250.0	0.98972	0.97462	1.44701	246.355	341.243	42.151	-0.108
255.0	0.98852	0.98105	1.44564	251.386	345.828	42.578	-0.083
260.0	0.98740	0.98601	1.44247	256.428	350.361	42.996	-0.057
265.0	0.98638	0.98946	1.43767	261.481	354.855	43.397	-0.031
270.0	0.98546	0.99141	1.43139	266.543	359.325	43.773	-0.004
275.0	0.98465	0.99185	1.42382	271.614	363.784	44.116	0.023
280.0	0.98396	0.99077	1.41515	276.692	368.246	44.415	0.050
285.0	0.98339	0.98817	1.40559	281.776	372.724	44.663	0.077
290.0	0.98295	0.98407	1.39534	286.865	377.233	44.849	0.104
295.0	0.98263	0.97849	1.38464	291.958	381.787	44.964	0.131
300.0	0.98245	0.97142	1.37370	297.053	386.399	45.000	0.157
305.0	0.98241	0.96291	1.36279	302.150	391.087	44.947	0.182
310.0	0.98249	0.95299	1.35215	307.246	395.865	44.796	0.206
315.0	0.98272	0.94169	1.34205	312.341	400.750	44.539	0.229
320.0	0.98307	0.92906	1.33277	317.433	405.762	44.170	0.250
325.0	0.98355	0.91517	1.32460	322.521	410.919	43.680	0.268
330.0	0.98416	0.90009	1.31781	327.603	416.242	43.064	0.284
335.0	0.98489	0.88392	1.31269	332.679	421.754	42.319	0.297
340.0	0.98573	0.86676	1.30952	337.747	427.477	41.442	0.306
345.0	0.98668	0.84875	1.30857	342.807	433.438	40.433	0.311
350.0	0.98773	0.83006	1.31006	347.856	439.662	39.292	0.312
355.0	0.98887	0.81088	1.31423	352.896	446.177	38.023	0.308
360.0	0.99010	0.79144	1.32123	357.923	453.011	36.630	0.299
365.0	0.99140	0.77201	1.33119	362.938	460.189	35.120	0.285
370.0	0.99276	0.75290	1.34415	367.941	467.735	33.501	0.267
375.0	0.99418	0.73448	1.36009	372.931	475.668	31.784	0.243
380.0	0.99563	0.71713	1.37889	377.906	483.996	29.980	0.216
385.0	0.99712	0.70128	1.40036	382.868	492.720	28.100	0.184
390.0	0.99863	0.68738	1.42419	387.816	501.823	26.160	0.149
395.0	1.00014	0.67585	1.45002	392.749	511.270	24.175	0.112
400.0	1.00165	0.66711	1.47742	397.668	521.004	22.163	0.073
405.0	1.00315	0.66146	1.50591	402.574	530.951	20.141	0.035
410.0	1.00463	0.65914	1.53501	407.465	541.019	18.132	-0.004
415.0	1.00606	0.66023	1.56430	412.343	551.105	16.154	-0.041

420.0	1.00746	0.66471	1.59340	417.208	561.106	14.229	-0.075
425.0	1.00879	0.67237	1.62200	422.061	570.927	12.376	-0.107
430.0	1.01006	0.68294	1.64990	426.902	580.484	10.613	-0.134
435.0	1.01126	0.69604	1.67696	431.741	589.715	8.951	-0.158
440.0	1.01237	0.71124	1.70310	436.550	598.578	7.404	-0.178
445.0	1.01340	0.72810	1.72829	441.359	607.050	5.977	-0.194
450.0	1.01433	0.74619	1.75253	446.160	615.124	4.675	-0.206
455.0	1.01515	0.76509	1.77582	450.953	622.807	3.500	-0.214
460.0	1.01586	0.78445	1.79816	455.739	630.115	2.450	-0.218
465.0	1.01646	0.80391	1.81954	460.519	637.070	1.524	-0.219
470.0	1.01694	0.82322	1.83997	465.294	643.696	0.715	-0.217
475.0	1.01730	0.84211	1.85939	470.065	650.022	0.059	-0.213
480.0	1.01754	0.86038	1.87779	474.834	656.074	-0.570	-0.206
485.0	1.01765	0.87786	1.89512	479.601	661.880	-1.056	-0.197
490.0	1.01763	0.89440	1.91133	484.368	667.464	-1.450	-0.186
495.0	1.01749	0.90989	1.92635	489.135	672.852	-1.756	-0.173
500.0	1.01722	0.92421	1.94015	493.905	678.066	-1.982	-0.159
505.0	1.01683	0.93730	1.95265	498.677	683.128	-2.136	-0.144
510.0	1.01632	0.94909	1.96382	503.453	688.057	-2.224	-0.128
515.0	1.01569	0.95951	1.97358	508.235	692.871	-2.253	-0.111
520.0	1.01495	0.96853	1.98190	513.022	697.590	-2.231	-0.093
525.0	1.01410	0.97612	1.98874	517.817	702.227	-2.164	-0.075
530.0	1.01315	0.98224	1.99406	522.620	706.801	-2.058	-0.056
535.0	1.01210	0.98687	1.99782	527.431	711.324	-1.923	-0.037
540.0	1.01096	0.99001	2.00001	532.253	715.811	-1.761	-0.018
545.0	1.00975	0.99163	2.00060	537.085	720.276	-1.583	0.001
550.0	1.00846	0.99174	1.99960	541.929	724.736	-1.392	0.020
555.0	1.00711	0.99034	1.99700	546.784	729.200	-1.200	0.040
560.0	1.00570	0.98742	1.99281	551.653	733.684	-1.006	0.059
565.0	1.00425	0.98301	1.98705	556.534	738.201	-0.826	0.077
570.0	1.00277	0.97710	1.97974	561.429	742.765	-0.659	0.095
575.0	1.00127	0.96973	1.97091	566.338	747.392	-0.520	0.113
580.0	0.99976	0.96091	1.96061	571.261	752.098	-0.414	0.130
585.0	0.99824	0.95069	1.94889	576.198	756.897	-0.343	0.146
590.0	0.99674	0.93910	1.93560	581.149	761.809	-0.323	0.162
595.0	0.99526	0.92620	1.92141	586.115	766.851	-0.356	0.176
600.0	0.99381	0.91205	1.90578	591.094	772.040	-0.453	0.189
605.0	0.99241	0.89673	1.88900	596.087	777.402	-0.625	0.200
610.0	0.99106	0.88033	1.87113	601.093	782.956	-0.878	0.210
615.0	0.98978	0.86298	1.85226	606.111	788.728	-1.218	0.217
620.0	0.98858	0.84481	1.83247	611.142	794.743	-1.660	0.222
625.0	0.98746	0.82600	1.81183	616.184	801.027	-2.206	0.225
630.0	0.98643	0.80674	1.79041	621.236	807.608	-2.867	0.225
635.0	0.98551	0.78728	1.76827	626.298	814.514	-3.648	0.222
640.0	0.98469	0.76790	1.74547	631.368	821.768	-4.555	0.215
645.0	0.98399	0.74890	1.72203	636.446	829.396	-5.593	0.205
650.0	0.98342	0.73067	1.69800	641.530	837.412	-6.763	0.191

655.0	0.98297	0.71361	1.67339	646.618	845.826	-8.065	0.173
660.0	0.98265	0.69814	1.64823	651.711	854.632	-9.495	0.151
665.0	0.98246	0.68471	1.62256	656.806	863.812	-11.047	0.1[illegible]
670.0	0.98241	0.67374	1.59645	661.903	873.326	-12.711	0.095
675.0	0.98249	0.66563	1.57002	666.999	883.112	-14.470	0.062
680.0	0.98270	0.66068	1.54344	672.094	893.094	-16.310	0.026
685.0	0.98305	0.65908	1.51695	677.186	903.174	-18.208	-0.012
690.0	0.98353	0.66091	1.49087	682.274	913.250	-20.145	-0.051
695.0	0.98413	0.66608	1.46557	687.357	923.219	-22.097	-0.090
700.0	0.98485	0.67440	1.44143	692.433	932.989	-24.043	-0.127

SUNBLAZER ORBIT

TINIT= 0.0 TDELT= 5.0 TFINL= 700.0 TBEG= 91.0 SEMI MAJOR AXIS=0.82548177

ECCENTRICITY=0.21164328 INCLINATION= 0.5000 SB INJECTION VELOCITY=0.80781

PERIOD SENS TO INJECT VEL= 20.21 DAYS PER/KM/SEC VSBSOI=0.11340 TPA= 0.0

TIME	RER	RSB	DIST	FER	FSB	AZIMUTH	ELEVATION
0.0	1.00021	1.00019	0.00618	3.120	2.771	-89.588	3.917
5.0	1.00173	0.99941	0.01578	8.038	7.148	-81.075	3.944
10.0	1.00323	0.99706	0.02532	12.943	11.538	-75.172	3.942
15.0	1.00470	0.99316	0.03479	17.834	15.956	-69.645	3.927
20.0	1.00613	0.98771	0.04408	22.711	20.416	-64.087	3.912
25.0	1.00752	0.98074	0.05324	27.576	24.933	-58.396	3.886
30.0	1.00886	0.97225	0.06231	32.428	29.521	-52.483	3.847
35.0	1.01012	0.96229	0.07144	37.268	34.197	-46.325	3.788
40.0	1.01132	0.95089	0.08080	42.096	38.978	-39.911	3.704
45.0	1.01243	0.93809	0.09067	46.915	43.883	-33.260	3.588
50.0	1.01345	0.92395	0.10137	51.724	48.931	-26.428	3.438
55.0	1.01437	0.90854	0.11330	56.524	54.143	-19.499	3.251
60.0	1.01519	0.89195	0.12692	61.316	59.542	-12.600	3.030
65.0	1.01589	0.87428	0.14266	66.102	65.153	-5.833	2.782
70.0	1.01649	0.85567	0.16101	70.882	71.001	0.658	2.513
75.0	1.01696	0.83626	0.18238	75.657	77.116	6.707	2.235
80.0	1.01732	0.81626	0.20716	80.428	83.526	12.301	1.958
85.0	1.01755	0.79588	0.23564	85.197	90.262	17.359	1.689
90.0	1.01765	0.77539	0.26806	89.964	97.354	21.850	1.435
95.0	1.01763	0.75512	0.30458	94.731	104.828	25.770	1.198
100.0	1.01748	0.73543	0.34528	99.498	112.710	29.136	0.982
105.0	1.01721	0.71672	0.39010	104.268	121.015	31.969	0.787
110.0	1.01681	0.69946	0.43891	109.040	129.747	34.302	0.613
115.0	1.01629	0.68413	0.49140	113.817	138.897	36.169	0.458
120.0	1.01566	0.67121	0.54716	118.598	148.434	37.613	0.321
125.0	1.01491	0.66115	0.60560	123.386	158.303	38.675	0.202
130.0	1.01406	0.65434	0.66600	128.181	168.427	39.403	0.099
135.0	1.01310	0.65106	0.72755	132.984	178.709	39.846	0.010
140.0	1.01205	0.65145	0.78936	137.796	189.036	40.056	-0.065
145.0	1.01091	0.65550	0.85054	142.619	199.293	40.085	-0.127
150.0	1.00969	0.66303	0.91040	147.451	209.371	39.982	-0.179
155.0	1.00839	0.67374	0.96809	152.296	219.175	39.794	-0.220
160.0	1.00704	0.68722	1.02311	157.152	228.632	39.561	-0.252
165.0	1.00563	0.70301	1.07501	162.021	237.695	39.317	-0.276
170.0	1.00418	0.72061	1.12351	166.903	246.337	39.088	-0.294
175.0	1.00270	0.73957	1.16843	171.798	254.550	38.894	-0.305
180.0	1.00120	0.75942	1.20970	176.708	262.343	38.751	-0.311
185.0	0.99968	0.77976	1.24730	181.631	269.734	38.668	-0.313
190.0	0.99817	0.80025	1.28129	186.569	276.747	38.649	-0.310

195.0	0.99667	0.82057	1.31172	191.521	284.410	38.698	-0.304
200.0	0.99510	0.84047	1.33872	196.467	289.755	38.813	-0.295
205.0	0.99374	0.85972	1.36238	201.467	295.811	38.992	-0.284
210.0	0.99234	0.87814	1.38283	206.461	301.606	39.232	-0.270
215.0	0.99100	0.89559	1.40020	211.467	307.169	39.527	-0.255
220.0	0.98972	0.91134	1.41462	216.486	312.527	39.871	-0.238
225.0	0.98852	0.92708	1.42623	221.518	317.701	40.258	-0.219
230.0	0.98740	0.94094	1.43515	226.560	322.717	40.681	-0.199
235.0	0.98638	0.95344	1.44154	231.613	327.594	41.132	-0.177
240.0	0.98546	0.96454	1.44552	236.675	332.351	41.605	-0.155
245.0	0.98465	0.97419	1.44726	241.746	337.007	42.089	-0.131
250.0	0.98396	0.98235	1.44689	246.826	341.579	42.579	-0.107
255.0	0.98339	0.98901	1.44457	251.908	346.082	43.064	-0.082
260.0	0.98295	0.99412	1.44048	256.997	350.531	43.537	-0.057
265.0	0.98263	0.99769	1.43477	262.090	354.943	43.988	-0.031
270.0	0.98245	0.99971	1.42763	267.185	359.329	44.408	-0.004
275.0	0.98241	1.00015	1.41924	272.281	363.705	44.789	0.023
280.0	0.98249	0.99904	1.40980	277.378	368.084	45.120	0.050
285.0	0.98272	0.99636	1.39952	282.473	372.479	45.392	0.077
290.0	0.98307	0.99213	1.38862	287.564	376.905	45.596	0.104
295.0	0.98355	0.98635	1.37732	292.652	381.376	45.722	0.131
300.0	0.98416	0.97905	1.36587	297.735	385.906	45.761	0.157
305.0	0.98489	0.97025	1.35451	302.811	390.512	45.703	0.182
310.0	0.98573	0.95998	1.34351	307.879	395.209	45.541	0.206
315.0	0.98668	0.94827	1.33315	312.938	400.015	45.265	0.229
320.0	0.98773	0.93518	1.32370	317.988	404.948	44.869	0.250
325.0	0.98887	0.92076	1.31545	323.027	410.030	44.346	0.268
330.0	0.99010	0.90510	1.30870	328.055	415.280	43.692	0.284
335.0	0.99140	0.88826	1.30372	333.070	420.722	42.902	0.297
340.0	0.99276	0.87038	1.30081	338.073	426.381	41.975	0.307
345.0	0.99418	0.85158	1.30022	343.062	432.284	40.911	0.312
350.0	0.99563	0.83203	1.30221	348.038	438.459	39.711	0.313
355.0	0.99712	0.81193	1.30698	353.000	444.937	38.378	0.309
360.0	0.99863	0.79150	1.31471	357.948	451.746	36.920	0.301
365.0	1.00014	0.77103	1.32551	362.881	458.917	35.342	0.287
370.0	1.00165	0.75085	1.33941	367.800	466.477	33.652	0.269
375.0	1.00315	0.73133	1.35659	372.705	474.448	31.862	0.245
380.0	1.00463	0.71290	1.37630	377.597	482.844	29.982	0.218
385.0	1.00606	0.69601	1.39843	382.475	491.667	28.026	0.186
390.0	1.00746	0.68115	1.42394	387.340	500.903	26.006	0.151
395.0	1.00879	0.66880	1.45093	392.192	510.516	23.938	0.113
400.0	1.01006	0.65941	1.47940	397.033	520.447	21.842	0.075
405.0	1.01126	0.65333	1.50884	401.863	530.614	19.736	0.035
410.0	1.01237	0.65083	1.53875	406.682	540.915	17.641	-0.003
415.0	1.01340	0.65202	1.56865	411.491	551.237	15.580	-0.040

420.0	1.01433	0.65683	1.59814	416.292	561.465	13.575	-0.075
425.0	1.01515	0.66507	1.62695	421.084	571.491	11.647	-0.107
430.0	1.01586	0.67640	1.65486	425.870	581.226	9.813	-0.135
435.0	1.01646	0.69041	1.68177	430.650	590.603	8.090	-0.159
440.0	1.01694	0.70663	1.70764	435.425	599.577	6.489	-0.178
445.0	1.01730	0.72456	1.73247	440.197	608.127	5.018	-0.194
450.0	1.01754	0.74374	1.75630	444.965	616.250	3.680	-0.206
455.0	1.01765	0.76373	1.77915	449.733	623.955	2.477	-0.213
460.0	1.01763	0.78414	1.80105	454.500	631.262	1.408	-0.218
465.0	1.01749	0.80461	1.82201	459.267	638.198	0.472	-0.219
470.0	1.01722	0.82487	1.84203	464.036	644.792	-0.342	-0.216
475.0	1.01683	0.84464	1.86110	468.809	651.072	-1.028	-0.212
480.0	1.01632	0.86373	1.87917	473.585	657.070	-1.601	-0.205
485.0	1.01569	0.88196	1.89621	478.366	662.813	-2.067	-0.195
490.0	1.01495	0.89918	1.91217	483.154	668.330	-2.433	-0.184
495.0	1.01410	0.91528	1.92698	487.948	673.646	-2.704	-0.172
500.0	1.01315	0.93015	1.94060	492.751	678.786	-2.889	-0.158
505.0	1.01210	0.94373	1.95295	497.563	683.770	-2.996	-0.143
510.0	1.01096	0.95594	1.96398	502.385	688.619	-3.031	-0.127
515.0	1.00975	0.96673	1.97364	507.217	693.354	-3.003	-0.110
520.0	1.00846	0.97606	1.98186	512.060	697.990	-2.917	-0.092
525.0	1.00711	0.98390	1.98860	516.916	702.546	-2.783	-0.074
530.0	1.00570	0.99023	1.99383	521.784	707.036	-2.606	-0.056
535.0	1.00425	0.99502	1.99751	526.666	711.477	-2.395	-0.037
540.0	1.00277	0.99825	1.99960	531.561	715.881	-2.156	-0.018
545.0	1.00127	0.99993	2.00010	536.469	720.265	-1.897	0.001
550.0	0.99976	1.00005	1.99900	541.393	724.639	-1.624	0.020
555.0	0.99824	0.99860	1.99629	546.329	729.021	-1.347	0.039
560.0	0.99674	0.99558	1.99197	551.281	733.421	-1.069	0.058
565.0	0.99526	0.99102	1.98608	556.246	737.855	-0.802	0.076
570.0	0.99381	0.98492	1.97863	561.225	742.337	-0.555	0.095
575.0	0.99241	0.97730	1.96967	566.218	746.863	-0.330	0.112
580.0	0.99106	0.96818	1.95923	571.224	751.506	-0.140	0.129
585.0	0.98978	0.95760	1.94737	576.243	756.225	0.059	0.145
590.0	0.98858	0.94559	1.93416	581.273	761.056	0.108	0.161
595.0	0.98746	0.93221	1.91965	586.315	766.020	0.153	0.175
600.0	0.98643	0.91752	1.90394	591.367	771.135	0.124	0.188
605.0	0.98551	0.90160	1.88709	596.429	776.424	0.071	0.199
610.0	0.98469	0.88453	1.86919	601.500	781.911	-0.190	0.209
615.0	0.98399	0.86644	1.85034	606.577	787.620	-0.487	0.216
620.0	0.98342	0.84747	1.83061	611.661	793.579	-0.887	0.222
625.0	0.98297	0.82778	1.81009	616.750	799.816	-1.401	0.225
630.0	0.98265	0.80759	1.78884	621.843	806.361	-2.038	0.225
635.0	0.98246	0.78713	1.76692	626.938	813.246	-2.805	0.222
640.0	0.98241	0.76669	1.74439	632.035	820.497	-3.709	0.216
645.0	0.98249	0.74662	1.72126	637.131	828.143	-4.753	0.206
650.0	0.98270	0.72729	1.69756	642.226	836.204	-5.940	0.192

655.0	0.98305	0.70915	1.67328	647.318	844.692	-7.271	0.174
660.0	0.98353	0.69265	1.64843	652.406	853.605	-8.740	0.152
665.0	0.98413	0.67829	1.62302	657.489	867.925	-10.341	0.126
670.0	0.98485	0.66653	1.59706	662.565	872.612	-12.062	0.096
675.0	0.98569	0.65782	1.57067	667.633	882.600	-13.888	0.063
680.0	0.98663	0.65249	1.54398	672.693	892.805	-15.800	0.026
685.0	0.98768	0.65078	1.51724	677.743	903.121	-17.775	-0.012
690.0	0.98882	0.65274	1.49076	682.783	913.432	-19.791	-0.051
695.0	0.99004	0.65831	1.46492	687.811	923.623	-21.822	-0.090
700.0	0.99133	0.66724	1.44015	692.827	933.594	-23.847	-0.128

SUNBLAZER ORBIT

TINIT= 0.0 TDELT= 5.0 TFINL= 700.0 TBEG=122.0 SEMI MAJOR AXIS=0.82548177

ECCENTRICITY=0.22186953 INCLINATION= 0.5000 SB INJECTION VELOCITY=0.87833

PERIOD SENS TO INJECT VEL= 19.99 DAYS PER/KM/SEC VSBSOI=0.11415 TPA= 0.0

TIME	RER	RSB	DIST	FER	FSB	AZIMUTH	ELEVATION
0.0	1.00912	1.00863	0.00625	3.073	2.723	-85.373	3.835
5.0	1.01037	1.00782	0.01599	7.911	7.017	-80.375	3.854
10.0	1.01155	1.00541	0.02567	12.738	11.325	-75.423	3.848
15.0	1.01264	1.00138	0.03524	17.554	15.660	-70.381	3.838
20.0	1.01364	0.99577	0.04461	22.361	20.037	-65.164	3.827
25.0	1.01454	0.98857	0.05383	27.160	24.471	-59.737	3.807
30.0	1.01534	0.97981	0.06292	31.951	28.978	-54.055	3.775
35.0	1.01602	0.96952	0.07202	36.735	33.573	-48.106	3.725
40.0	1.01659	0.95773	0.08129	41.514	38.274	-41.873	3.651
45.0	1.01704	0.94449	0.09097	46.288	43.099	-35.373	3.549
50.0	1.01737	0.92984	0.10138	51.059	48.069	-28.646	3.414
55.0	1.01758	0.91386	0.11291	55.827	53.206	-21.768	3.242
60.0	1.01766	0.89664	0.12601	60.594	58.533	-14.857	3.036
65.0	1.01761	0.87827	0.14115	65.361	64.076	-8.042	2.799
70.0	1.01744	0.85888	0.15880	70.129	69.863	-1.458	2.540
75.0	1.01714	0.83862	0.17944	74.899	75.924	4.792	2.267
80.0	1.01672	0.81770	0.20348	79.672	82.290	10.579	1.992
85.0	1.01617	0.79634	0.23126	84.449	88.994	15.843	1.722
90.0	1.01552	0.77481	0.26305	89.232	96.070	20.538	1.465
95.0	1.01475	0.75345	0.29905	94.021	103.550	24.655	1.225
100.0	1.01387	0.73263	0.33936	98.818	111.460	28.202	1.005
105.0	1.01290	0.71280	0.38398	103.623	119.823	31.197	0.805
110.0	1.01183	0.69445	0.43277	108.437	128.647	33.669	0.627
115.0	1.01067	0.67809	0.48546	113.261	137.924	35.654	0.468
120.0	1.00943	0.66427	0.54161	118.096	147.624	37.191	0.328
125.0	1.00813	0.65348	0.60062	122.943	157.690	38.325	0.207
130.0	1.00676	0.64516	0.66175	127.801	168.039	39.106	0.101
135.0	1.00535	0.64264	0.72411	132.673	178.564	39.586	0.011
140.0	1.00389	0.64306	0.78677	137.558	189.139	39.820	-0.065
145.0	1.00240	0.64742	0.84880	142.456	199.636	39.865	-0.128
150.0	1.00089	0.65550	0.90933	147.368	209.933	39.776	-0.180
155.0	0.99938	0.66698	0.96762	152.295	219.927	39.600	-0.221
160.0	0.99787	0.68139	1.02308	157.235	229.541	39.383	-0.253
165.0	0.99637	0.69822	1.07527	162.190	238.723	39.159	-0.277
170.0	0.99490	0.71693	1.12391	167.159	247.448	38.957	-0.295
175.0	0.99346	0.73701	1.16883	172.142	255.713	38.798	-0.306
180.0	0.99207	0.75798	1.20999	177.138	263.529	38.695	-0.311
185.0	0.99074	0.77941	1.24739	182.147	270.920	38.658	-0.312
190.0	0.98947	0.80092	1.28108	187.168	277.914	38.691	-0.310

195.0	0.98829	0.82222	1.31117	192.202	284.543	38.796	-0.303
200.0	0.98719	0.84301	1.33776	197.246	290.842	38.970	-0.294
205.0	0.98619	0.86309	1.36098	202.301	296.841	39.210	-0.283
210.0	0.98529	0.88228	1.38097	207.365	302.573	39.512	-0.269
215.0	0.98451	0.90042	1.39785	212.437	308.068	39.868	-0.254
220.0	0.98384	0.91738	1.41178	217.517	313.353	40.273	-0.236
225.0	0.98329	0.93308	1.42287	222.602	318.452	40.719	-0.217
230.0	0.98288	0.94743	1.43129	227.692	323.389	41.196	-0.197
235.0	0.98259	0.96037	1.43717	232.786	328.186	41.703	-0.176
240.0	0.98243	0.97184	1.44066	237.881	332.863	42.224	-0.154
245.0	0.98241	0.98181	1.44192	242.979	337.438	42.753	-0.131
250.0	0.98253	0.99024	1.44109	248.074	341.927	43.282	-0.107
255.0	0.98278	0.99710	1.43833	253.168	346.348	43.802	-0.082
260.0	0.98316	1.00238	1.43381	258.259	350.715	44.303	-0.056
265.0	0.98366	1.00606	1.42771	263.346	355.043	44.777	-0.030
270.0	0.98430	1.00813	1.42022	268.427	359.347	45.215	-0.004
275.0	0.98505	1.00859	1.41151	273.502	363.640	45.606	0.023
280.0	0.98591	1.00744	1.40179	278.568	367.936	45.942	0.050
285.0	0.98688	1.00468	1.39127	283.626	372.248	46.214	0.077
290.0	0.98795	1.00032	1.38016	288.673	376.591	46.411	0.103
295.0	0.98911	0.99436	1.36870	293.710	380.979	46.525	0.130
300.0	0.99035	0.98683	1.35713	298.736	385.427	46.546	0.156
305.0	0.99167	0.97774	1.34571	303.749	389.951	46.466	0.181
310.0	0.99304	0.96713	1.33468	308.749	394.567	46.276	0.206
315.0	0.99446	0.95502	1.32434	313.735	399.293	45.969	0.228
320.0	0.99593	0.94147	1.31495	318.708	404.148	45.537	0.249
325.0	0.99742	0.92654	1.30682	323.667	409.152	44.975	0.268
330.0	0.99893	0.91029	1.30021	328.612	414.327	44.278	0.284
335.0	1.00044	0.89280	1.29544	333.543	419.638	43.442	0.298
340.0	1.00196	0.87420	1.29279	338.459	425.291	42.467	0.307
345.0	1.00345	0.85462	1.29251	343.362	431.134	41.353	0.313
350.0	1.00492	0.83420	1.29486	348.250	437.257	40.101	0.314
355.0	1.00635	0.81317	1.30006	353.126	443.692	38.714	0.311
360.0	1.00773	0.79174	1.30827	357.988	450.473	37.200	0.303
365.0	1.00905	0.77022	1.31960	362.838	457.633	35.564	0.289
370.0	1.01031	0.74894	1.33411	367.677	465.202	33.816	0.271
375.0	1.01149	0.72830	1.35174	372.504	473.208	31.965	0.248
380.0	1.01259	0.70874	1.37235	377.321	481.669	30.021	0.220
385.0	1.01359	0.69077	1.39571	382.128	490.591	27.998	0.188
390.0	1.01450	0.67491	1.42146	386.927	499.962	25.909	0.153
395.0	1.01530	0.66169	1.44915	391.719	509.746	23.769	0.115
400.0	1.01599	0.65161	1.47827	396.503	519.880	21.598	0.076
405.0	1.01657	0.64509	1.50825	401.282	530.277	19.415	0.036
410.0	1.01702	0.64240	1.53857	406.057	540.823	17.244	-0.003
415.0	1.01736	0.64367	1.56871	410.827	551.392	15.108	-0.041

420.0	1.01757	0.64884	1.59828	415.596	561.856	13.031	-0.076
425.0	1.01766	0.65769	1.62700	420.363	572.097	11.037	-0.107
430.0	1.01761	0.66983	1.65469	425.130	582.015	9.144	-0.135
435.0	1.01745	0.68480	1.68128	429.898	591.540	7.371	-0.159
440.0	1.01715	0.70208	1.70676	434.667	600.625	5.729	-0.179
445.0	1.01674	0.72112	1.73118	439.440	609.252	4.226	-0.195
450.0	1.01620	0.74143	1.75460	444.218	617.419	2.868	-0.206
455.0	1.01555	0.76253	1.77708	449.000	625.143	1.654	-0.214
460.0	1.01479	0.78401	1.79866	453.789	632.447	0.586	-0.218
465.0	1.01372	0.80550	1.81936	458.585	639.360	-0.345	-0.218
470.0	1.01275	0.82671	1.83919	463.390	645.916	-1.136	-0.216
475.0	1.01188	0.84737	1.85814	468.203	652.147	-1.798	-0.211
480.0	1.01073	0.86727	1.87617	473.027	658.087	-2.338	-0.204
485.0	1.00949	0.88625	1.89322	477.861	663.766	-2.761	-0.195
490.0	1.00819	0.90414	1.90925	482.708	669.214	-3.077	-0.183
495.0	1.00683	0.92085	1.92419	487.565	674.457	-3.293	-0.171
500.0	1.00542	0.93627	1.93797	492.436	679.519	-3.416	-0.157
505.0	1.00396	0.95032	1.95052	497.321	684.425	-3.455	-0.142
510.0	1.00247	0.96295	1.96177	502.218	689.195	-3.419	-0.126
515.0	1.00097	0.97410	1.97167	507.130	693.848	-3.314	-0.109
520.0	0.99945	0.98374	1.98015	512.055	698.403	-3.150	-0.091
525.0	0.99794	0.99183	1.98715	516.995	702.877	-2.932	-0.073
530.0	0.99644	0.99836	1.99264	521.949	707.285	-2.670	-0.055
535.0	0.99497	1.00330	1.99656	526.918	711.642	-2.372	-0.037
540.0	0.99353	1.00664	1.99890	531.900	715.964	-2.046	-0.018
545.0	0.99213	1.00837	1.99963	536.895	720.264	-1.699	0.001
550.0	0.99080	1.00848	1.99875	541.904	724.556	-1.337	0.020
555.0	0.98953	1.00699	1.99624	546.925	728.855	-0.975	0.039
560.0	0.98834	1.00388	1.99211	551.958	733.173	-0.610	0.057
565.0	0.98724	0.99918	1.98640	557.002	737.523	-0.265	0.076
570.0	0.98624	0.99288	1.97911	562.056	741.924	0.071	0.094
575.0	0.98533	0.98502	1.97030	567.119	746.387	0.366	0.111
580.0	0.98454	0.97560	1.96002	572.191	750.928	0.628	0.128
585.0	0.98387	0.96467	1.94831	577.270	755.565	0.845	0.144
590.0	0.98332	0.95225	1.93525	582.355	760.318	1.002	0.159
595.0	0.98289	0.93840	1.92092	587.445	765.202	1.096	0.173
600.0	0.98260	0.92318	1.90538	592.539	770.241	1.115	0.186
605.0	0.98244	0.90665	1.88874	597.634	775.456	1.047	0.198
610.0	0.98241	0.88892	1.87108	602.731	780.872	0.884	0.208
615.0	0.98252	0.87010	1.85248	607.827	786.515	0.615	0.215
620.0	0.98276	0.85032	1.83305	612.921	792.416	0.237	0.221
625.0	0.98313	0.82976	1.81285	618.012	798.603	-0.269	0.224
630.0	0.98364	0.80862	1.79196	623.100	805.109	-0.907	0.225
635.0	0.98426	0.78715	1.77043	628.181	811.969	-1.683	0.222
640.0	0.98501	0.76565	1.74831	633.256	819.213	-2.605	0.216
645.0	0.98587	0.74447	1.72560	638.323	826.874	-3.678	0.206
650.0	0.98683	0.72401	1.70229	643.381	834.976	-4.904	0.193

655.0	0.98790	0.70475	1.67836	648.429	843.536	-6.233	0.175
660.0	0.98905	0.68719	1.65379	653.467	852.555	-7.810	0.153
665.0	0.99029	0.67185	1.62852	658.492	862.018	-9.478	0.127
670.0	0.99160	0.65926	1.60257	663.506	871.882	-11.275	0.097
675.0	0.99297	0.64971	1.57598	668.507	882.061	-13.183	0.063
680.0	0.99439	0.64418	1.54889	673.494	892.519	-15.182	0.027
685.0	0.99586	0.64234	1.52152	678.468	903.082	-17.247	-0.011
690.0	0.99735	0.64445	1.49421	683.427	913.639	-19.354	-0.051
695.0	0.99886	0.65043	1.46738	688.373	924.063	-21.477	-0.090
700.0	1.00037	0.66001	1.44146	693.304	934.242	-23.592	-0.129

SUNBLAZER ORBIT

TINIT= 0.0 TDELT= 5.0 TFINL= 700.0 TBEG=152.0 SEMI MAJOR AXIS=0.82548177

ECCENTRICITY=0.22901154 INCLINATION= 0.5000 SB INJECTION VELOCITY=0.87175

PERIOD SENS TO INJECT VEL= 19.84 DAYS PER/KM/SEC VSBSOI=0.11437 TPA= 0.0

TIME	RER	RSB	DIST	FER	FSB	AZIMUTH	ELEVATION
0.0	1.01534	1.01453	0.00625	3.049	2.697	-82.374	3.821
5.0	1.01602	1.01370	0.01614	7.834	6.934	-81.270	3.795
10.0	1.01659	1.01124	0.02587	12.612	11.185	-77.312	3.793
15.0	1.01704	1.00713	0.03547	17.386	15.464	-72.771	3.788
20.0	1.01737	1.00140	0.04487	22.157	19.784	-67.908	3.780
25.0	1.01758	0.99405	0.05404	26.925	24.102	-62.749	3.767
30.0	1.01766	0.98511	0.06306	31.692	28.611	-57.313	3.743
35.0	1.01761	0.97459	0.07199	36.459	33.150	-51.571	3.704
40.0	1.01744	0.96254	0.08097	41.227	37.795	-45.500	3.645
45.0	1.01714	0.94899	0.09022	45.997	42.566	-39.120	3.560
50.0	1.01672	0.93401	0.10004	50.770	47.482	-32.454	3.443
55.0	1.01617	0.91764	0.11082	55.548	52.566	-25.574	3.289
60.0	1.01552	0.89998	0.12298	60.331	57.842	-18.568	3.099
65.0	1.01475	0.88112	0.13702	65.120	63.337	-11.553	2.875
70.0	1.01387	0.86120	0.15347	69.916	69.080	-4.700	2.622
75.0	1.01290	0.84037	0.17281	74.721	75.102	1.854	2.350
80.0	1.01183	0.81881	0.19552	79.535	81.435	7.986	2.071
85.0	1.01067	0.79676	0.22198	84.359	88.115	13.606	1.794
90.0	1.00943	0.77451	0.25252	89.194	95.178	18.654	1.527
95.0	1.00813	0.75238	0.28738	94.041	102.659	23.104	1.277
100.0	1.00676	0.73078	0.32669	98.900	110.587	26.951	1.047
105.0	1.00535	0.71015	0.37047	103.771	118.988	30.212	0.838
110.0	1.00389	0.69102	0.41862	108.656	127.874	32.916	0.652
115.0	1.00240	0.67393	0.47087	113.555	137.239	35.097	0.486
120.0	1.00089	0.65946	0.52681	118.467	147.053	36.798	0.340
125.0	0.99938	0.64815	0.58581	123.393	157.259	38.066	0.214
130.0	0.99787	0.64046	0.64710	128.334	167.769	38.954	0.105
135.0	0.99637	0.63676	0.70978	133.288	178.468	39.520	0.012
140.0	0.99490	0.63721	0.77286	138.257	189.222	39.823	-0.066
145.0	0.99346	0.64178	0.83535	143.240	199.890	39.923	-0.131
150.0	0.99207	0.65027	0.89637	148.236	210.345	39.879	-0.183
155.0	0.99074	0.66230	0.95511	153.245	220.473	39.745	-0.225
160.0	0.98947	0.67738	1.01097	158.267	230.196	39.566	-0.257
165.0	0.98829	0.69495	1.06351	163.300	239.460	39.380	-0.281
170.0	0.98719	0.71445	1.11244	168.345	248.242	39.217	-0.298
175.0	0.98619	0.73533	1.15760	173.400	256.540	39.098	-0.309
180.0	0.98529	0.75708	1.19895	178.464	264.370	39.037	-0.314
185.0	0.98451	0.77927	1.23650	183.536	271.759	39.043	-0.315
190.0	0.98384	0.80150	1.27032	188.615	278.737	39.119	-0.312

195.0	0.98329	0.82346	1.30050	193.701	285.340	39.266	-0.305
200.0	0.98288	0.84486	1.32719	198.791	291.604	39.481	-0.296
205.0	0.98259	0.86554	1.35049	203.884	297.563	39.760	-0.284
210.0	0.98243	0.88525	1.37055	208.980	303.251	40.098	-0.270
215.0	0.98241	0.90385	1.38751	214.076	308.697	40.488	-0.254
220.0	0.98253	0.92125	1.40152	219.172	313.930	40.923	-0.237
225.0	0.98278	0.93732	1.41270	224.267	318.976	41.395	-0.218
230.0	0.98316	0.95201	1.42123	229.358	323.860	41.896	-0.198
235.0	0.98366	0.96524	1.42722	234.445	328.602	42.417	-0.176
240.0	0.98430	0.97697	1.43085	239.526	333.222	42.950	-0.154
245.0	0.98505	0.98715	1.43225	244.600	337.741	43.487	-0.131
250.0	0.98591	0.99575	1.43159	249.667	342.174	44.018	-0.106
255.0	0.98688	1.00276	1.42902	254.724	346.538	44.536	-0.082
260.0	0.98795	1.00815	1.42472	259.772	350.848	45.031	-0.056
265.0	0.98911	1.01190	1.41885	264.809	355.119	45.494	-0.030
270.0	0.99035	1.01402	1.41160	269.834	359.366	45.916	-0.004
275.0	0.99167	1.01449	1.40316	274.847	363.602	46.289	0.023
280.0	0.99304	1.01331	1.39372	279.847	367.841	46.603	0.050
285.0	0.99446	1.01050	1.38349	284.834	372.096	46.850	0.077
290.0	0.99593	1.00604	1.37269	289.807	376.382	47.020	0.103
295.0	0.99742	0.99996	1.36154	294.766	380.714	47.104	0.130
300.0	0.99893	0.99227	1.35028	299.710	385.105	47.095	0.156
305.0	1.00044	0.98299	1.33916	304.641	389.573	46.984	0.181
310.0	1.00196	0.97214	1.32845	309.557	394.133	46.761	0.205
315.0	1.00345	0.95977	1.31839	314.460	398.803	46.422	0.228
320.0	1.00492	0.94591	1.30929	319.349	403.603	45.958	0.249
325.0	1.00635	0.93062	1.30140	324.224	408.553	45.364	0.268
330.0	1.00773	0.91397	1.29504	329.087	413.676	44.635	0.284
335.0	1.00905	0.89605	1.29048	333.937	418.997	43.770	0.298
340.0	1.01031	0.87695	1.28800	338.775	424.542	42.765	0.307
345.0	1.01149	0.85682	1.28789	343.603	430.342	41.621	0.313
350.0	1.01259	0.83582	1.29037	348.419	436.427	40.340	0.315
355.0	1.01359	0.81413	1.29568	353.227	442.832	38.926	0.312
360.0	1.01450	0.79202	1.30399	358.026	449.591	37.383	0.304
365.0	1.01530	0.76976	1.31541	362.817	456.740	35.718	0.291
370.0	1.01599	0.74771	1.33000	367.602	464.314	33.940	0.272
375.0	1.01657	0.72627	1.34770	372.381	472.341	32.057	0.249
380.0	1.01702	0.70592	1.36840	377.155	480.845	30.080	0.221
385.0	1.01736	0.68718	1.39184	381.926	489.835	28.020	0.190
390.0	1.01757	0.67060	1.41765	386.696	499.299	25.893	0.154
395.0	1.01766	0.65676	1.44540	391.461	509.202	23.712	0.116
400.0	1.01761	0.64619	1.47454	396.228	519.482	21.498	0.077
405.0	1.01745	0.63933	1.50449	400.996	530.043	19.270	0.037
410.0	1.01715	0.63650	1.53471	405.766	540.765	17.054	-0.003
415.0	1.01674	0.63784	1.56467	410.539	551.512	14.874	-0.041

420.0	1.01620	0.64328	1.59394	415.316	562.146	12.756	-0.076
425.0	1.01555	0.65256	1.62240	420.098	572.539	10.725	-0.108
430.0	1.01479	0.66529	1.64973	424.887	582.587	8.803	-0.136
435.0	1.01392	0.68095	1.67596	429.684	592.214	7.006	-0.161
440.0	1.01295	0.69898	1.70109	434.488	601.376	5.349	-0.180
445.0	1.01198	0.71881	1.72521	439.302	610.054	3.840	-0.176
450.0	1.01073	0.73992	1.74838	444.125	618.251	2.483	-0.207
455.0	1.00949	0.76180	1.77069	448.960	625.985	1.280	-0.215
460.0	1.00819	0.78402	1.79218	453.806	633.283	0.236	-0.218
465.0	1.00683	0.80623	1.81288	458.664	640.178	-0.674	-0.217
470.0	1.00542	0.82809	1.83280	463.535	646.706	-1.433	-0.216
475.0	1.00396	0.84937	1.85190	468.419	652.902	-2.055	-0.211
480.0	1.00247	0.86983	1.87016	473.317	658.800	-2.548	-0.204
485.0	1.00097	0.88932	1.88751	478.228	664.433	-2.920	-0.194
490.0	0.99945	0.90768	1.90389	483.154	669.832	-3.179	-0.183
495.0	0.99794	0.92479	1.91922	488.094	675.023	-3.333	-0.170
500.0	0.99644	0.94058	1.93342	493.048	680.032	-3.392	-0.156
505.0	0.99497	0.95496	1.94642	498.016	684.884	-3.364	-0.141
510.0	0.99353	0.96787	1.95814	502.998	689.598	-3.257	-0.125
515.0	0.99213	0.97927	1.96852	507.994	694.196	-3.082	-0.108
520.0	0.99080	0.98912	1.97747	513.002	698.694	-2.844	-0.091
525.0	0.98953	0.99738	1.98496	518.023	703.111	-2.555	-0.073
530.0	0.98834	1.00405	1.99092	523.056	707.463	-2.221	-0.055
535.0	0.98724	1.00908	1.99531	528.100	711.763	-1.853	-0.036
540.0	0.98624	1.01249	1.99810	533.154	716.028	-1.455	-0.018
545.0	0.98533	1.01426	1.99927	538.218	720.271	-1.041	0.001
550.0	0.98454	1.01438	1.99880	543.290	724.507	-0.615	0.020
555.0	0.98387	1.01285	1.99671	548.369	728.748	-0.196	0.039
560.0	0.98332	1.00968	1.99298	553.454	733.009	0.219	0.057
565.0	0.98289	1.00488	1.98765	558.544	737.303	0.626	0.075
570.0	0.98260	0.99845	1.98075	563.637	741.646	1.006	0.093
575.0	0.98244	0.99042	1.97232	568.732	746.052	1.347	0.110
580.0	0.98241	0.98081	1.96240	573.829	750.537	1.646	0.127
585.0	0.98252	0.96963	1.95107	578.925	755.119	1.891	0.143
590.0	0.98276	0.95694	1.93838	584.020	759.815	2.076	0.158
595.0	0.98313	0.94276	1.92443	589.111	764.646	2.186	0.172
600.0	0.98364	0.92718	1.90929	594.198	769.631	2.217	0.185
605.0	0.98426	0.91025	1.89305	599.280	774.794	2.156	0.196
610.0	0.98501	0.89206	1.87580	604.354	780.161	1.994	0.206
615.0	0.98587	0.87274	1.85765	609.421	785.757	1.721	0.214
620.0	0.98683	0.85241	1.83865	614.479	791.615	1.328	0.220
625.0	0.98790	0.83124	1.81891	619.528	797.766	0.805	0.223
630.0	0.98905	0.80944	1.79847	624.565	804.243	0.145	0.224
635.0	0.99029	0.78727	1.77739	629.591	811.083	-0.660	0.221
640.0	0.99160	0.76502	1.75570	634.604	818.320	-1.618	0.216
645.0	0.99297	0.74306	1.73338	639.605	825.989	-2.733	0.206
650.0	0.99439	0.72182	1.71043	644.592	834.116	-4.004	0.193

655.0	0.99586	0.70177	1.68677	649.566	842.723	-5.434	0.175
~~660.0~~	~~0.99735~~	~~0.68366~~	~~1.66235~~	~~654.526~~	~~851.816~~	~~-7.01[illegible]~~	~~0.153~~
665.0	0.99886	0.66740	1.63710	659.471	861.377	-8.749	0.127
670.0	1.00037	0.65421	1.61100	664.402	871.368	-10.611	0.097
675.0	1.00188	0.64440	1.58406	669.320	881.717	-12.589	0.064
680.0	1.00338	0.63838	1.55641	674.223	892.323	-14.660	0.027
685.0	1.00485	0.63644	1.52827	679.112	903.062	-16.779	-0.011
690.0	1.00628	0.63866	1.50000	683.988	913.797	-18.980	-0.051
695.0	1.00766	0.64495	1.47203	688.851	924.387	-21.176	-0.090
700.0	1.00899	0.65500	1.44487	693.702	934.715	-23.362	-0.129

SUNBLAZER ORBIT

TINIT= 0.0 TDELT= 5.0 TFINL= 700.0 TDEG=183.0 SEMI MAJOR AXIS=0.82548177

ECCENTRICITY=0.23167515 INCLINATION= 0.5000 SB INJECTION VELOCITY=0.86930

PERIOD SENS TO INJECT VEL= 19.79 DAYS PER/KM/SEC VSBSOI=0.11439 TPA= 0.0

TIME	RER	RSB	DIST	EER	ESB	AZIMUTH	ELEVATION
0.0	1.01766	1.01672	0.00633	3.042	2.689	-81.346	3.772
5.0	1.01758	1.01590	0.01614	7.809	6.905	-83.529	3.788
10.0	1.01739	1.01341	0.02593	12.577	11.135	-80.442	3.777
15.0	1.01706	1.00928	0.03555	17.348	15.392	-76.338	3.771
20.0	1.01662	1.00350	0.04490	22.122	19.692	-71.758	3.768
25.0	1.01605	0.99610	0.05404	26.900	24.048	-66.852	3.758
30.0	1.01537	0.98708	0.06291	31.684	28.477	-61.616	3.743
35.0	1.01458	0.97649	0.07161	36.475	32.995	-56.053	3.715
40.0	1.01369	0.96434	0.08024	41.273	37.620	-50.142	3.671
45.0	1.01269	0.95068	0.08896	46.080	42.369	-43.866	3.603
50.0	1.01160	0.93557	0.09808	50.896	47.266	-37.247	3.505
55.0	1.01043	0.91906	0.10793	55.722	52.330	-30.323	3.372
60.0	1.00918	0.90124	0.11894	60.559	57.587	-23.176	3.200
65.0	1.00786	0.88221	0.13165	65.408	63.065	-15.933	2.988
70.0	1.00648	0.86209	0.14658	70.269	68.791	-8.746	2.742
75.0	1.00506	0.84104	0.16429	75.143	74.797	-1.764	2.471
80.0	1.00359	0.81925	0.18531	80.031	81.118	4.813	2.184
85.0	1.00210	0.79695	0.21008	84.932	87.789	10.907	1.876
90.0	1.00059	0.77442	0.23897	89.847	94.847	16.410	1.615
95.0	0.99708	0.75201	0.27226	94.777	102.327	21.286	1.349
100.0	0.99757	0.73011	0.31011	99.720	110.261	25.519	1.104
105.0	0.99607	0.70919	0.35257	104.678	118.676	29.120	0.882
110.0	0.99460	0.68976	0.39956	109.649	127.584	32.118	0.684
115.0	0.99318	0.67239	0.45082	114.634	136.982	34.550	0.509
120.0	0.99180	0.65768	0.50594	119.633	146.839	36.464	0.356
125.0	0.99048	0.64616	0.56432	124.645	157.097	37.911	0.223
130.0	0.98923	0.63834	0.62518	129.669	167.669	38.948	0.109
135.0	0.98806	0.63457	0.68760	134.705	178.434	39.638	0.013
140.0	0.98698	0.63502	0.75056	139.751	189.254	40.044	-0.068
145.0	0.98600	0.63968	0.81308	144.808	199.988	40.231	-0.134
150.0	0.98513	0.64833	0.87423	149.874	210.502	40.260	-0.188
155.0	0.98436	0.66057	0.93319	154.948	220.682	40.189	-0.231
160.0	0.98372	0.67590	0.98934	160.028	230.444	40.064	-0.263
165.0	0.98320	0.69375	1.04223	165.115	239.738	39.927	-0.287
170.0	0.98281	0.71355	1.09155	170.205	248.541	39.806	-0.304
175.0	0.98255	0.73472	1.13715	175.299	256.852	39.724	-0.315
180.0	0.98242	0.75677	1.17896	180.395	264.687	39.695	-0.320
185.0	0.98243	0.77924	1.21700	185.492	272.073	39.728	-0.320
190.0	0.98257	0.80174	1.25133	190.588	279.045	39.826	-0.316

195.0	0.98284	0.82395	1.28206	195.681	285.638	39.921	-0.309
200.0	0.98325	0.84560	1.30930	200.772	291.839	40.219	-0.300
205.0	0.98378	0.86647	1.33319	205.858	297.833	40.500	-0.287
210.0	0.98444	0.88637	1.35336	210.938	303.504	40.840	-0.273
215.0	0.98521	0.90515	1.37144	216.011	308.932	41.234	-0.257
220.0	0.98610	0.92270	1.38610	221.075	314.146	41.661	-0.239
225.0	0.98709	0.93892	1.39796	226.131	319.172	42.120	-0.220
230.0	0.98818	0.95373	1.40717	231.177	324.035	42.603	-0.199
235.0	0.98936	0.96706	1.41368	236.211	328.756	43.102	-0.177
240.0	0.99061	0.97888	1.41823	241.234	333.357	43.609	-0.155
245.0	0.99194	0.98914	1.42038	246.244	337.854	44.116	-0.131
250.0	0.99332	0.99781	1.42049	251.242	342.266	44.614	-0.107
255.0	0.99475	1.00467	1.41869	256.226	346.609	45.096	-0.082
260.0	0.99622	1.01030	1.41517	261.196	350.898	45.552	-0.056
265.0	0.99772	1.01408	1.41010	266.152	355.148	45.976	-0.030
270.0	0.99923	1.01621	1.40364	271.094	359.374	46.357	-0.004
275.0	1.00075	1.01669	1.39598	276.022	363.589	46.689	0.023
280.0	1.00226	1.01550	1.38732	280.936	367.807	46.962	0.050
285.0	1.00375	1.01267	1.37785	285.835	372.042	47.168	0.077
290.0	1.00521	1.00818	1.36778	290.721	376.307	47.299	0.103
295.0	1.00663	1.00205	1.35734	295.594	380.617	47.346	0.130
300.0	1.00800	0.99431	1.34674	300.454	384.986	47.302	0.156
305.0	1.00931	0.98495	1.33624	305.302	389.434	47.159	0.181
310.0	1.01055	0.97402	1.32608	310.138	393.973	46.908	0.205
315.0	1.01172	0.96155	1.31653	314.963	398.623	46.543	0.228
320.0	1.01280	0.94758	1.30785	319.778	403.402	46.058	0.249
325.0	1.01378	0.93216	1.30032	324.584	408.332	45.447	0.268
330.0	1.01467	0.91536	1.29422	329.381	413.436	44.705	0.284
335.0	1.01545	0.89727	1.28983	334.171	418.738	43.829	0.297
340.0	1.01612	0.87799	1.28744	338.954	424.266	42.818	0.307
345.0	1.01667	0.85766	1.28730	343.732	430.049	41.671	0.313
350.0	1.01710	0.83644	1.28968	348.506	436.120	40.390	0.315
355.0	1.01741	0.81452	1.29479	353.276	442.512	38.977	0.312
360.0	1.01760	0.79214	1.30280	358.044	449.263	37.436	0.304
365.0	1.01766	0.76961	1.31385	362.811	456.408	35.775	0.291
370.0	1.01759	0.74727	1.32799	367.578	463.982	33.999	0.273
375.0	1.01740	0.72554	1.34519	372.346	472.018	32.119	0.250
380.0	1.01708	0.70489	1.36534	377.116	480.537	30.143	0.222
385.0	1.01664	0.68586	1.38818	381.890	489.551	28.084	0.190
390.0	1.01608	0.66901	1.41340	386.668	499.050	25.955	0.155
395.0	1.01541	0.65493	1.44052	391.452	508.999	23.772	0.117
400.0	1.01462	0.64417	1.46905	396.242	519.333	21.553	0.077
405.0	1.01373	0.63719	1.49840	401.040	529.956	19.321	0.037
410.0	1.01274	0.63431	1.52802	405.846	540.745	17.100	-0.003
415.0	1.01166	0.63567	1.55743	410.662	551.559	14.918	-0.041

420.0	1.01049	0.64120	1.58624	415.488	562.257	12.799	-0.077
425.0	1.00924	0.65066	1.61419	420.324	572.708	10.769	-0.109
430.0	1.00793	0.66360	1.64113	425.173	582.804	8.852	-0.137
435.0	1.00655	0.67952	1.66704	430.033	592.470	7.066	-0.162
440.0	1.00513	0.69784	1.69196	434.907	601.660	5.423	-0.182
445.0	1.00366	0.71797	1.71595	439.794	610.357	3.934	-0.197
450.0	1.00217	0.73937	1.73910	444.694	618.564	2.603	-0.208
455.0	1.00066	0.76155	1.76147	449.609	626.301	1.429	-0.216
460.0	0.99915	0.78405	1.78312	454.537	633.596	0.420	-0.219
465.0	0.99764	0.80652	1.80407	459.480	640.484	-0.448	-0.220
470.0	0.99614	0.82863	1.82430	464.437	647.001	-1.165	-0.217
475.0	0.99467	0.85013	1.84380	469.408	653.184	-1.740	-0.212
480.0	0.99324	0.87081	1.86249	474.393	659.066	-2.184	-0.204
485.0	0.99186	0.89048	1.88033	479.391	664.682	-2.505	-0.195
490.0	0.99054	0.90901	1.89722	484.402	670.063	-2.710	-0.183
495.0	0.98929	0.92628	1.91310	489.425	675.234	-2.809	-0.170
500.0	0.98812	0.94220	1.92787	494.460	680.224	-2.814	-0.156
505.0	0.98703	0.95670	1.94145	499.506	685.055	-2.742	-0.141
510.0	0.98605	0.96972	1.95376	504.563	689.749	-2.573	-0.125
515.0	0.98517	0.98121	1.96472	509.628	694.325	-2.345	-0.108
520.0	0.98440	0.99113	1.97426	514.701	698.803	-2.059	-0.091
525.0	0.98375	0.99946	1.98232	519.782	703.199	-1.724	-0.073
530.0	0.98322	1.00617	1.98885	524.868	707.530	-1.346	-0.055
535.0	0.98282	1.01124	1.99380	529.958	711.809	-0.939	-0.036
540.0	0.98256	1.01468	1.99715	535.052	716.053	-0.509	-0.017
545.0	0.98242	1.01645	1.99887	540.148	720.275	-0.044	0.001
550.0	0.98242	1.01657	1.99895	545.245	724.490	0.381	0.020
555.0	0.98256	1.01504	1.99739	550.341	728.710	0.830	0.038
560.0	0.98282	1.01185	1.99420	555.435	732.949	1.261	0.057
565.0	0.98322	1.00701	1.98940	560.525	737.222	1.671	0.075
570.0	0.98375	1.00054	1.98303	565.611	741.544	2.051	0.093
575.0	0.98440	0.99244	1.97513	570.691	745.930	2.392	0.110
580.0	0.98517	0.98275	1.96576	575.765	750.395	2.682	0.126
585.0	0.98605	0.97149	1.95496	580.830	754.956	2.916	0.142
590.0	0.98704	0.95869	1.94282	585.886	759.631	3.083	0.157
595.0	0.98812	0.94440	1.92942	590.932	764.441	3.172	0.171
600.0	0.98930	0.92868	1.91483	595.967	769.406	3.177	0.184
605.0	0.99055	0.91161	1.89914	600.991	774.550	3.087	0.196
610.0	0.99187	0.89325	1.88244	606.002	779.898	2.893	0.205
615.0	0.99325	0.87374	1.86482	611.000	785.478	2.585	0.213
620.0	0.99468	0.85320	1.84635	615.985	791.320	2.154	0.219
625.0	0.99615	0.83181	1.82710	620.955	797.456	1.593	0.222
630.0	0.99765	0.80977	1.80713	625.912	803.922	0.892	0.223
635.0	0.99916	0.78734	1.78648	630.855	810.754	0.059	0.220
640.0	1.00067	0.76481	1.76515	635.783	817.987	-0.956	0.215
645.0	1.00218	0.74257	1.74313	640.698	825.658	-2.112	0.205
650.0	1.00367	0.72102	1.72039	645.598	833.796	-3.426	0.192

655.0	1.00514	0.70067	1.69685	650.485	842.420	-4.899	0.174
660.0	1.00656	0.68206	1.67242	655.358	851.539	-6.526	0.153
665.0	1.00793	0.66575	1.64704	660.219	861.137	-8.298	0.127
670.0	1.00925	0.65234	1.62064	665.067	871.175	-10.203	0.097
675.0	1.01049	0.64235	1.59326	669.904	881.581	-12.223	0.064
680.0	1.01166	0.63622	1.56500	674.729	892.249	-14.335	0.027
685.0	1.01275	0.63424	1.53610	679.545	903.056	-16.515	-0.011
690.0	1.01374	0.63651	1.50692	684.351	913.857	-18.736	-0.051
695.0	1.01463	0.64290	1.47794	689.149	924.511	-20.971	-0.090
700.0	1.01541	0.65314	1.44970	693.939	934.894	-23.195	-0.129

SUNBLAZER ORBIT

TINIT= 0.0 TDELT= 5.0 TFINL= 700.0 TBEG=213.0 SEMI MAJOR AXIS=0.82548177

ECCENTRICITY=0.22905254 INCLINATION= 0.5000 SB INJECTION VELOCITY=0.87171

PERIOD SENS TO INJECT VEL= 19.84 DAYS PER/KM/SEC VSHSOI=0.11437 TPA= 0.0

TIME	RER	RSB	DIST	FER	FSB	AZIMUTH	ELEVATION
0.0	1.01537	1.01456	0.00625	3.049	2.697	-82.348	3.821
5.0	1.01458	1.01374	0.01605	7.840	6.934	-86.523	3.816
10.0	1.01369	1.01127	0.02587	12.638	11.184	-83.902	3.793
15.0	1.01269	1.00716	0.03545	17.445	15.462	-80.022	3.790
20.0	1.01160	1.00143	0.04482	22.261	19.783	-75.612	3.784
25.0	1.01043	0.99408	0.05388	27.087	24.160	-70.834	3.778
30.0	1.00918	0.98514	0.06264	31.924	28.609	-65.724	3.768
35.0	1.00786	0.97462	0.07114	36.773	33.148	-60.273	3.748
40.0	1.00648	0.96257	0.07946	41.634	37.792	-54.456	3.714
45.0	1.00506	0.94902	0.08774	46.509	42.563	-48.250	3.661
50.0	1.00359	0.93403	0.09623	51.396	47.478	-41.652	3.579
55.0	1.00210	0.91766	0.10527	56.297	52.562	-34.680	3.463
60.0	1.00059	0.90000	0.11529	61.212	57.836	-27.410	3.306
65.0	0.99908	0.88114	0.12680	66.142	63.333	-19.944	3.106
70.0	0.99757	0.86121	0.14038	71.085	69.076	-12.441	2.866
75.0	0.99607	0.84038	0.15662	76.043	75.097	-5.088	2.594
80.0	0.99460	0.81882	0.17608	81.014	81.430	1.959	2.300
85.0	0.99318	0.79677	0.19928	85.999	88.111	8.479	1.998
90.0	0.99180	0.77451	0.22660	90.998	95.173	14.415	1.702
95.0	0.99048	0.75238	0.25837	96.010	102.654	19.695	1.421
100.0	0.98923	0.73077	0.29476	101.034	110.582	24.290	1.161
105.0	0.98806	0.71014	0.33583	106.070	118.983	28.207	0.925
110.0	0.98698	0.69100	0.38149	111.116	127.869	31.478	0.715
115.0	0.98600	0.67391	0.43153	116.173	137.235	34.144	0.530
120.0	0.98513	0.65943	0.48[illegible]1	121.239	147.050	36.257	0.369
125.0	0.98436	0.64812	0.54285	126.313	157.257	37.874	0.231
130.0	0.98372	0.64043	0.60279	131.392	167.768	39.058	0.113
135.0	0.98320	0.63673	0.66443	136.480	178.468	39.873	0.013
140.0	0.98281	0.63717	0.72678	141.570	189.222	40.386	-0.070
145.0	0.98255	0.64175	0.78885	146.664	199.892	40.665	-0.138
150.0	0.98242	0.65024	0.84973	151.760	210.347	40.773	-0.193
155.0	0.98243	0.66228	0.90861	156.857	220.477	40.766	-0.237
160.0	0.98257	0.67736	0.96484	161.953	230.199	40.695	-0.270
165.0	0.98284	0.69494	1.01796	167.046	239.464	40.599	-0.294
170.0	0.98325	0.71444	1.06766	172.137	248.246	40.510	-0.311
175.0	0.98378	0.73532	1.11375	177.223	256.545	40.449	-0.321
180.0	0.98444	0.75707	1.15616	182.303	264.375	40.432	-0.326
185.0	0.98521	0.77926	1.19488	187.376	271.764	40.468	-0.326
190.0	0.98610	0.80150	1.22997	192.440	278.742	40.562	-0.322

195.0	0.98709	0.82347	1.26153	197.496	285.345	40.714	-0.315
200.0	0.98818	0.84490	1.28964	202.542	291.609	40.923	-0.305
205.0	0.98936	0.86555	1.31445	207.576	297.567	41.184	-0.292
210.0	0.99061	0.88526	1.33608	212.599	303.255	41.493	-0.277
215.0	0.99194	0.90387	1.35466	217.609	308.701	41.844	-0.260
220.0	0.99332	0.92127	1.37034	222.607	313.934	42.230	-0.242
225.0	0.99475	0.93735	1.38326	227.591	318.974	42.644	-0.222
230.0	0.99622	0.95204	1.39354	232.561	323.862	43.078	-0.201
235.0	0.99772	0.96527	1.40134	237.517	328.604	43.526	-0.179
240.0	0.99923	0.97700	1.40681	24[illegible].459	333.225	43.980	-0.156
245.0	1.00075	0.98718	1.41007	247.387	337.742	44.433	-0.133
250.0	1.00226	0.99578	1.41130	252.301	342.175	44.876	-0.108
255.0	1.00375	1.00279	1.41063	257.200	346.539	45.303	-0.083
260.0	1.00521	1.00818	1.40823	262.086	350.849	45.705	-0.057
265.0	1.00663	1.01193	1.40425	266.959	355.120	46.075	-0.031
270.0	1.00800	1.01405	1.39888	271.819	359.366	46.405	-0.004
275.0	1.00931	1.01452	1.39228	276.667	363.602	46.688	0.023
280.0	1.01055	1.01335	1.38465	281.503	367.840	46.916	0.050
285.0	1.01172	1.01053	1.37616	286.328	372.095	47.080	0.077
290.0	1.01280	1.00608	1.36702	291.143	376.381	47.174	0.104
295.0	1.01378	0.99999	1.35745	295.949	380.712	47.189	0.130
300.0	1.01467	0.99230	1.34766	300.746	385.104	47.117	0.156
305.0	1.01545	0.98302	1.33789	305.536	389.571	46.951	0.181
310.0	1.01612	0.97217	1.32838	310.319	394.130	46.684	0.205
315.0	1.01667	0.95980	1.31937	315.097	398.800	46.309	0.228
320.0	1.01710	0.94594	1.31113	319.871	403.600	45.819	0.249
325.0	1.01741	0.93065	1.30393	324.641	408.549	45.209	0.267
330.0	1.01760	0.91399	1.29804	329.409	413.672	44.475	0.284
335.0	1.01766	0.89607	1.29374	334.176	418.993	43.612	0.297
340.0	1.01759	0.87697	1.29130	338.943	424.538	42.619	0.307
345.0	1.01740	0.85683	1.29099	343.711	430.337	41.494	0.312
350.0	1.01708	0.83582	1.29304	348.481	436.422	40.239	0.314
355.0	1.01664	0.81414	1.29769	353.255	442.827	38.854	0.311
360.0	1.01608	0.79202	1.30511	358.033	449.586	37.346	0.303
365.0	1.01541	0.76976	1.31544	362.817	456.735	35.717	0.291
370.0	1.01462	0.74770	1.32875	367.607	464.309	33.976	0.273
375.0	1.01373	0.72626	1.34502	372.405	472.336	32.131	0.250
380.0	1.01274	0.70591	1.36414	377.211	480.841	30.191	0.222
385.0	1.01166	0.68716	1.38591	382.027	489.830	28.168	0.190
390.0	1.01049	0.67058	1.41001	386.853	499.295	26.076	0.155
395.0	1.00924	0.65673	1.43603	391.689	509.199	23.929	0.117
400.0	1.00793	0.64616	1.46348	396.538	519.480	21.748	0.077
405.0	1.00655	0.63930	1.49182	401.398	530.042	19.555	0.037
410.0	1.00513	0.63647	1.52054	406.272	540.765	17.373	-0.003
415.0	1.00366	0.63781	1.54918	411.159	551.513	15.230	-0.041

420.0	1.00217	0.64324	1.57736	416.059	567.147	13.151	-0.077
425.0	1.00066	0.65253	1.60484	420.974	572.542	11.163	-0.109
430.0	0.99915	0.66526	1.63147	425.902	582.590	9.287	-0.138
435.0	0.99764	0.68092	1.65722	430.845	592.218	7.541	-0.162
440.0	0.99614	0.69896	1.68210	435.802	601.381	5.940	-0.182
445.0	0.99467	0.71880	1.70617	440.773	610.054	4.492	-0.198
450.0	0.99324	0.73991	1.72950	445.758	618.256	3.202	-0.209
455.0	0.99186	0.76179	1.75215	450.756	625.990	2.070	-0.217
460.0	0.99054	0.78402	1.77414	455.767	633.288	1.096	-0.221
465.0	0.98929	0.80623	1.79548	460.790	640.183	0.273	-0.221
470.0	0.98812	0.82810	1.81615	465.825	646.710	-0.401	-0.218
475.0	0.98703	0.84938	1.83611	470.871	652.906	-0.942	-0.213
480.0	0.98605	0.86985	1.85530	475.928	658.804	-1.349	-0.205
485.0	0.98517	0.88933	1.87364	480.993	664.437	-1.635	-0.196
490.0	0.98440	0.90770	1.89106	486.066	669.835	-1.809	-0.184
495.0	0.98375	0.92482	1.90746	491.147	675.026	-1.880	-0.171
500.0	0.98322	0.94061	1.92276	496.233	680.035	-1.859	-0.157
505.0	0.98282	0.95499	1.93687	501.323	684.886	-1.757	-0.142
510.0	0.98256	0.96790	1.94970	506.417	689.600	-1.580	-0.126
515.0	0.98242	0.97930	1.96118	511.513	694.198	-1.341	-0.109
520.0	0.98242	0.98915	1.97124	516.610	698.696	-1.049	-0.091
525.0	0.98256	0.99742	1.97982	521.706	703.113	-0.709	-0.073
530.0	0.98282	1.00408	1.98687	526.800	707.464	-0.337	-0.055
535.0	0.98322	1.00912	1.99234	531.890	711.764	0.071	-0.036
540.0	0.98375	1.01252	1.99621	536.976	716.028	0.481	-0.018
545.0	0.98440	1.01429	1.99845	542.056	720.271	0.905	0.001
550.0	0.98517	1.01441	1.99906	547.130	724.507	1.331	0.020
555.0	0.98605	1.01288	1.99803	552.195	728.748	1.747	0.039
560.0	0.98704	1.00972	1.99538	557.251	733.008	2.146	0.057
565.0	0.98812	1.00491	1.99114	562.297	737.302	2.519	0.075
570.0	0.98930	0.99849	1.98533	567.332	741.644	2.858	0.093
575.0	0.99055	0.99045	1.97800	572.356	746.051	3.153	0.110
580.0	0.99187	0.98084	1.96920	577.367	750.535	3.397	0.127
585.0	0.99325	0.96966	1.95898	582.365	755.117	3.581	0.142
590.0	0.99468	0.95696	1.94742	587.350	759.813	3.696	0.157
595.0	0.99615	0.94279	1.93459	592.320	764.643	3.734	0.171
600.0	0.99765	0.92720	1.92056	597.277	769.628	3.685	0.184
605.0	0.99916	0.91027	1.90541	602.220	774.790	3.543	0.195
610.0	1.00067	0.89208	1.88923	607.148	780.156	3.296	0.205
615.0	1.00218	0.87275	1.87209	612.063	785.753	2.938	0.213
620.0	1.00367	0.85242	1.85406	616.963	791.611	2.459	0.218
625.0	1.00514	0.83125	1.83521	621.850	797.761	1.851	0.221
630.0	1.00656	0.80945	1.81557	626.723	804.238	1.108	0.222
635.0	1.00793	0.78727	1.79517	631.584	811.077	0.225	0.219
640.0	1.00925	0.76502	1.77401	636.432	818.315	-0.813	0.213
645.0	1.01049	0.74306	1.75209	641.269	825.984	-1.998	0.204
650.0	1.01166	0.72181	1.72934	646.094	834.111	-3.337	0.190

655.0	1.01275	0.70175	1.70569	650.910	842.719	-4.830	0.173
660.0	1.01374	0.68342	1.68106	655.716	851.812	-6.472	0.152
665.0	1.01463	0.66737	1.65540	660.514	861.373	-8.254	0.126
670.0	1.01541	0.65418	1.62863	665.304	871.365	-10.164	0.096
675.0	1.01609	0.64437	1.60081	670.088	881.715	-12.186	0.063
680.0	1.01664	0.63835	1.57207	674.866	892.321	-14.297	0.027
685.0	1.01708	0.63641	1.54263	679.639	903.062	-16.473	-0.011
690.0	1.01740	0.63863	1.51290	684.410	913.796	-18.690	-0.050
695.0	1.01759	0.64492	1.48333	689.178	924.390	-20.920	-0.090
700.0	1.01766	0.65497	1.45449	693.945	934.717	-23.139	-0.128

SUNBLAZER ORBIT

TINIT= 0.0 TDELT= 5.0 TFINL= 700.0 THEC=244.0 SEMI MAJOR AXIS=0.82548177

ECCENTRICITY=0.22164446 INCLINATION= 0.5000 SB INJECTION VELOCITY=0.87854

PERIOD SENS TO INJECT VEL= 20.00 DAYS PER/KM/SEC VSBSOI=0.11414 TPA= 0.0

TIME	RER	RSB	DIST	FER	FSB	AZIMUTH	ELEVATION
0.0	1.00892	1.00844	0.00618	3.074	2.724	-85.407	3.883
5.0	1.00759	1.00764	0.01599	7.926	7.020	-89.725	3.854
10.0	1.00620	1.00522	0.02571	12.789	11.329	-87.079	3.844
15.0	1.00477	1.00120	0.03526	17.666	15.666	-83.183	3.836
20.0	1.00330	0.99559	0.04458	22.556	20.046	-78.762	3.830
25.0	1.00180	0.98839	0.05357	27.460	24.481	-73.983	3.826
30.0	1.00029	0.97964	0.06223	32.378	28.989	-68.886	3.817
35.0	0.99877	0.96936	0.07056	37.310	33.586	-63.448	3.802
40.0	0.99727	0.95758	0.07864	42.256	38.289	-57.641	3.775
45.0	0.99578	0.94434	0.08658	47.217	43.116	-51.431	3.730
50.0	0.99432	0.92971	0.09464	52.191	48.088	-44.805	3.658
55.0	0.99290	0.91375	0.10310	57.179	53.226	-37.761	3.552
60.0	0.99153	0.89653	0.11240	62.181	58.555	-30.361	3.404
65.0	0.99022	0.87816	0.12308	67.195	64.099	-22.711	3.211
70.0	0.98899	0.85880	0.13570	72.221	69.888	-14.958	2.973
75.0	0.98784	0.83857	0.15091	77.259	75.950	-7.315	2.696
80.0	0.98678	0.81767	0.16929	82.308	82.317	0.305	2.394
85.0	0.98582	0.79633	0.19137	87.367	89.022	6.911	2.081
90.0	0.98496	0.77482	0.21757	92.434	96.098	13.163	1.771
95.0	0.98423	0.75348	0.24821	97.509	103.578	18.727	1.476
100.0	0.98360	0.73269	0.28346	102.591	111.488	23.571	1.203
105.0	0.98311	0.71289	0.32338	107.678	119.850	27.702	0.956
110.0	0.98274	0.69456	0.36787	112.770	128.671	31.156	0.737
115.0	0.98251	0.67822	0.41670	117.865	137.945	33.978	0.545
120.0	0.98241	0.66442	0.46946	122.961	147.641	36.228	0.379
125.0	0.98244	0.65365	0.52559	128.057	157.703	37.965	0.236
130.0	0.98261	0.64634	0.58435	133.153	168.048	39.255	0.115
135.0	0.98291	0.64283	0.64488	138.246	178.567	40.166	0.012
140.0	0.98334	0.64325	0.70625	143.335	189.137	40.766	-0.072
145.0	0.98390	0.64760	0.76751	148.420	199.628	41.120	-0.142
150.0	0.98458	0.65567	0.82777	153.499	209.921	41.293	-0.198
155.0	0.98538	0.66713	0.88626	158.570	219.911	41.339	-0.241
160.0	0.98629	0.68152	0.94234	163.633	229.520	41.307	-0.275
165.0	0.98730	0.69832	0.99553	168.687	238.699	41.239	-0.300
170.0	0.98841	0.71701	1.04549	173.730	247.423	41.163	-0.317
175.0	0.98960	0.73706	1.09203	178.763	255.687	41.104	-0.327
180.0	0.99087	0.75801	1.13504	183.783	263.503	41.078	-0.332
185.0	0.99221	0.77941	1.17450	188.791	270.894	41.094	-0.332
190.0	0.99360	0.80091	1.21045	193.786	277.888	41.159	-0.328

195.0	0.99505	0.82218	1.24294	198.767	284.513	41.279	-0.320
200.0	0.99652	0.84295	1.27207	203.734	290.818	41.437	-0.310
205.0	0.99802	0.86302	1.29795	208.688	296.818	41.647	-0.297
210.0	0.99954	0.88219	1.32071	213.627	302.552	41.900	-0.282
215.0	1.00105	0.90031	1.34047	218.552	308.048	42.191	-0.264
220.0	1.00256	0.91726	1.35736	223.463	313.334	42.513	-0.246
225.0	1.00404	0.93295	1.37150	228.360	318.435	42.862	-0.226
230.0	1.00549	0.94729	1.38303	233.243	323.375	43.230	-0.204
235.0	1.00691	0.96022	1.39210	238.113	328.173	43.611	-0.182
240.0	1.00827	0.97168	1.39883	242.971	332.852	43.998	-0.158
245.0	1.00956	0.98164	1.40337	247.816	337.428	44.384	-0.134
250.0	1.01079	0.99006	1.40586	252.650	341.919	44.764	-0.109
255.0	1.01194	0.99692	1.40644	257.473	346.342	45.128	-0.084
260.0	1.01300	1.00220	1.40526	262.286	350.711	45.472	-0.058
265.0	1.01397	1.00587	1.40249	267.090	355.041	45.786	-0.031
270.0	1.01483	1.00795	1.39828	271.885	359.346	46.066	-0.004
275.0	1.01559	1.00841	1.39281	276.674	363.641	46.302	0.023
280.0	1.01624	1.00726	1.38625	281.456	367.939	46.489	0.050
285.0	1.01676	1.00450	1.37877	286.233	372.253	46.618	0.077
290.0	1.01717	1.00014	1.37058	291.006	376.598	46.682	0.104
295.0	1.01746	0.99418	1.36188	295.776	380.988	46.673	0.131
300.0	1.01762	0.98666	1.35288	300.543	385.438	46.585	0.157
305.0	1.01765	0.97757	1.34381	305.310	389.964	46.410	0.182
310.0	1.01756	0.96697	1.33489	310.077	394.581	46.141	0.206
315.0	1.01734	0.95487	1.32637	314.846	399.309	45.770	0.228
320.0	1.01700	0.94133	1.31850	319.617	404.165	45.292	0.249
325.0	1.01654	0.92641	1.31155	324.392	409.171	44.701	0.267
330.0	1.01596	0.91017	1.30577	329.171	414.348	43.992	0.283
335.0	1.01526	0.89270	1.30145	333.956	419.720	43.161	0.296
340.0	1.01445	0.87412	1.29884	338.747	425.315	42.205	0.306
345.0	1.01354	0.85455	1.29820	343.547	431.159	41.123	0.311
350.0	1.01253	0.83415	1.29978	348.355	437.283	39.914	0.313
355.0	1.01143	0.81314	1.30379	353.172	443.719	38.581	0.310
360.0	1.01024	0.79173	1.31044	358.000	450.501	37.127	0.302
365.0	1.00898	0.77024	1.31984	362.839	457.661	35.556	0.289
370.0	1.00766	0.74898	1.33208	367.690	465.230	33.875	0.271
375.0	1.00627	0.72836	1.34715	372.553	473.236	32.092	0.248
380.0	1.00484	0.70883	1.36499	377.429	481.695	30.216	0.221
385.0	1.00337	0.69088	1.38540	382.319	490.615	28.260	0.189
390.0	1.00187	0.67504	1.40810	387.222	499.983	26.235	0.154
395.0	1.00036	0.66185	1.43274	392.139	509.763	24.160	0.116
400.0	0.99885	0.65178	1.45887	397.071	519.893	22.052	0.077
405.0	0.99734	0.64527	1.48600	402.016	530.284	19.933	0.037
410.0	0.99585	0.64258	1.51368	406.976	540.825	17.827	-0.003
415.0	0.99438	0.64385	1.54147	411.950	551.389	15.760	-0.041

420.0	0.99296	0.64902	1.56902	416.937	561.848	13.756	-0.077
425.0	0.99159	0.65785	1.59609	421.938	572.083	11.840	-0.109
430.0	0.99028	0.66497	1.62251	426.951	561.998	10.033	-0.138
435.0	0.98905	0.68492	1.64823	431.977	591.519	8.352	-0.163
440.0	0.98769	0.70217	1.67324	437.015	600.602	6.810	-0.183
445.0	0.98643	0.72120	1.69756	442.063	604.227	5.417	-0.199
450.0	0.98586	0.74148	1.72123	447.121	617.394	4.174	-0.210
455.0	0.98500	0.76255	1.74427	452.188	625.117	3.086	-0.218
460.0	0.98426	0.78401	1.76669	457.263	632.420	2.147	-0.222
465.0	0.98363	0.80548	1.78848	462.344	639.314	1.353	-0.222
470.0	0.98313	0.82667	1.80962	467.432	645.891	0.705	-0.220
475.0	0.98276	0.84731	1.83004	472.523	652.123	0.192	-0.214
480.0	0.98252	0.86719	1.84968	477.617	658.065	-0.216	-0.207
485.0	0.98241	0.88615	1.86847	482.714	663.745	-0.494	-0.197
490.0	0.98244	0.90403	1.88632	487.810	669.194	-0.667	-0.186
495.0	0.98260	0.92072	1.90314	492.906	674.439	-0.742	-0.173
500.0	0.98289	0.93613	1.91885	497.999	679.503	-0.736	-0.158
505.0	0.98332	0.95017	1.93336	503.089	684.411	-0.650	-0.143
510.0	0.98387	0.96279	1.94658	508.174	689.182	-0.500	-0.127
515.0	0.98455	0.97394	1.95346	513.253	693.837	-0.288	-0.110
520.0	0.98534	0.98357	1.96891	518.325	698.394	-0.059	-0.092
525.0	0.98624	0.99166	1.97788	523.388	702.870	0.263	-0.074
530.0	0.98725	0.99818	1.98533	528.442	707.279	0.583	-0.055
535.0	0.98835	1.00311	1.99121	533.486	711.638	0.931	-0.037
540.0	0.98954	1.00645	1.99549	538.519	715.962	1.288	-0.018
545.0	0.99081	1.00818	1.99817	543.540	720.264	1.652	0.001
550.0	0.99214	1.00830	1.99923	548.548	724.558	2.011	0.020
555.0	0.99354	1.00680	1.99867	553.544	728.858	2.359	0.039
560.0	0.99497	1.00370	1.99650	558.526	733.178	2.685	0.057
565.0	0.99645	0.99900	1.99274	563.494	737.530	2.986	0.076
570.0	0.99795	0.99271	1.98744	568.448	741.932	3.250	0.093
575.0	0.99946	0.98485	1.98061	573.388	746.397	3.470	0.111
580.0	1.00098	0.97544	1.97232	578.313	750.941	3.639	0.127
585.0	1.00248	0.96451	1.96261	583.225	755.580	3.749	0.143
590.0	1.00397	0.95210	1.95155	588.123	760.334	3.792	0.158
595.0	1.00542	0.93826	1.93920	593.007	765.220	3.760	0.172
600.0	1.00684	0.92305	1.92562	597.877	770.261	3.643	0.184
605.0	1.00820	0.90654	1.91090	602.735	775.477	3.437	0.195
610.0	1.00950	0.88883	1.89509	607.581	780.895	3.131	0.205
615.0	1.01073	0.87002	1.87828	612.416	786.540	2.719	0.212
620.0	1.01189	0.85026	1.86051	617.239	792.441	2.191	0.218
625.0	1.01295	0.82971	1.84183	622.053	798.630	1.543	0.221
630.0	1.01392	0.80859	1.82229	626.857	805.137	0.764	0.221
635.0	1.01479	0.78714	1.80191	631.653	811.997	-0.156	0.218
640.0	1.01556	0.76567	1.78068	636.442	819.242	-1.205	0.212
645.0	1.01621	0.74451	1.75859	641.225	826.902	-2.401	0.203
650.0	1.01674	0.72408	1.73560	646.002	835.003	-3.743	0.189

655.0	1.01716	0.70485	1.71164	650.775	843.561	-5.229	0.172
660.0	1.01765	0.68741	1.68665	655.545	852.578	-6.856	0.150
665.0	1.01761	0.67199	1.66060	660.313	862.038	-8.615	0.124
670.0	1.01765	0.65942	1.63346	665.079	871.898	-10.494	0.095
675.0	1.01757	0.65008	1.60530	669.846	882.093	-12.479	0.062
680.0	1.01736	0.64437	1.57627	674.615	892.525	-14.547	0.027
685.0	1.01702	0.64252	1.54663	679.385	903.082	-16.678	-0.011
690.0	1.01656	0.64463	1.51676	684.158	913.633	-18.848	-0.050
695.0	1.01599	0.65060	1.48714	688.937	924.053	-21.031	-0.089
700.0	1.01530	0.66017	1.45831	693.722	934.228	-23.205	-0.127

SUNBLAZER ORBIT

TINIT= 0.0 TDELT= 5.0 TFINL= 700.0 TDEG=274.0 SEMI MAJOR AXIS=0.82548177

ECCENTRICITY=0.21172720 INCLINATION= 0.5000 SB INJECTION VELOCITY=0.88773

PERIOD SENS TO INJECT VEL= 20.21 DAYS PER/KM/SEC VSBSOI=0.11341 IPA= 0.0

TIME	RER	RSB	DIST	FER	FSB	AZIMUTH	ELEVATION
0.0	1.00029	1.00026	0.00610	3.119	2.770	-89.542	3.967
5.0	0.99877	0.99948	0.01587	8.051	7.146	-92.089	3.921
10.0	0.99727	0.99713	0.02550	12.998	11.536	-88.961	3.913
15.0	0.99578	0.99323	0.03498	17.958	15.954	-84.807	3.905
20.0	0.99432	0.98778	0.04418	22.932	20.413	-80.209	3.902
25.0	0.99290	0.98080	0.05307	27.921	24.929	-75.296	3.898
30.0	0.99153	0.97232	0.06160	32.922	29.517	-70.080	3.891
35.0	0.99022	0.96235	0.06979	37.936	34.192	-64.535	3.878
40.0	0.98899	0.95095	0.07770	42.963	38.973	-58.624	3.851
45.0	0.98784	0.93814	0.08548	48.001	43.877	-52.312	3.806
50.0	0.98678	0.92400	0.09332	53.049	48.924	-45.566	3.735
55.0	0.98582	0.90859	0.10157	58.108	54.135	-38.402	3.627
60.0	0.98496	0.89199	0.11066	63.175	59.534	-30.875	3.476
65.0	0.98423	0.87432	0.12111	68.250	65.144	-23.089	3.277
70.0	0.98360	0.85570	0.13350	73.332	70.992	-15.196	3.031
75.0	0.98311	0.83628	0.14850	78.420	77.106	-7.435	2.746
80.0	0.98274	0.81627	0.16666	83.511	83.516	0.237	2.434
85.0	0.98251	0.79588	0.18851	88.606	90.252	6.975	2.111
90.0	0.98241	0.77539	0.21445	93.702	97.343	13.281	1.793
95.0	0.98244	0.75511	0.24478	98.798	104.818	18.883	1.491
100.0	0.98261	0.73540	0.27964	103.894	112.700	23.748	1.213
105.0	0.98291	0.71669	0.31906	108.987	121.005	27.892	0.963
110.0	0.98334	0.69942	0.36293	114.077	129.738	31.353	0.741
115.0	0.98390	0.68408	0.41102	119.161	138.889	34.185	0.547
120.0	0.98458	0.67115	0.46291	124.240	148.427	36.446	0.380
125.0	0.98538	0.66108	0.51806	129.312	158.298	38.200	0.236
130.0	0.98629	0.65427	0.57577	134.375	168.424	39.513	0.114
135.0	0.98730	0.65099	0.63524	139.428	178.708	40.451	0.012
140.0	0.98841	0.65139	0.69559	144.472	189.037	41.081	-0.074
145.0	0.98960	0.65544	0.75594	149.504	199.296	41.465	-0.143
150.0	0.99087	0.66297	0.81545	154.524	209.375	41.663	-0.199
155.0	0.99221	0.67368	0.87338	159.532	219.181	41.730	-0.244
160.0	0.99360	0.68717	0.92911	164.527	228.640	41.711	-0.278
165.0	0.99505	0.70297	0.98215	169.508	237.703	41.645	-0.303
170.0	0.99652	0.72058	1.03218	174.476	246.346	41.563	-0.320
175.0	0.99802	0.73954	1.07896	179.429	254.559	41.487	-0.330
180.0	0.99954	0.75940	1.12238	184.368	262.353	41.434	-0.335
185.0	1.00105	0.77976	1.16238	189.293	269.743	41.416	-0.335
190.0	1.00256	0.80025	1.19898	194.204	276.756	41.438	-0.331

195.0	1.00404	0.82058	1.23221	199.101	283.420	41.503	-0.324
200.0	1.00569	0.84049	1.26217	203.984	289.764	41.612	-0.313
205.0	1.00691	0.85974	1.28894	208.854	295.819	41.764	-0.300
210.0	1.00827	0.87818	1.31263	213.712	301.614	41.956	-0.285
215.0	1.00956	0.89563	1.33336	218.557	307.177	42.183	-0.268
220.0	1.01079	0.91198	1.35124	223.391	312.533	42.442	-0.249
225.0	1.01194	0.92713	1.36640	228.214	317.708	42.726	-0.228
230.0	1.01300	0.94099	1.37896	233.027	322.722	43.030	-0.207
235.0	1.01397	0.95350	1.38906	237.831	327.599	43.348	-0.184
240.0	1.01483	0.96460	1.39682	242.627	332.355	43.675	-0.160
245.0	1.01559	0.97425	1.40237	247.415	337.010	44.003	-0.136
250.0	1.01624	0.98242	1.40586	252.198	341.581	44.328	-0.110
255.0	1.01676	0.98907	1.40742	256.974	346.084	44.642	-0.085
260.0	1.01717	0.99419	1.40720	261.747	350.533	44.938	-0.058
265.0	1.01746	0.99776	1.40535	266.517	354.944	45.211	-0.031
270.0	1.01762	0.99977	1.40202	271.285	359.329	45.453	-0.004
275.0	1.01765	1.00022	1.39738	276.052	363.704	45.658	0.023
280.0	1.01756	0.99911	1.39160	280.819	368.063	45.818	0.050
285.0	1.01734	0.99643	1.38486	285.587	372.477	45.927	0.078
290.0	1.01700	0.99219	1.37734	290.358	376.902	45.977	0.105
295.0	1.01654	0.98642	1.36924	295.133	381.372	45.960	0.131
300.0	1.01596	0.97912	1.36077	299.912	385.902	45.870	0.157
305.0	1.01526	0.97031	1.35214	304.697	390.507	45.700	0.182
310.0	1.01445	0.96004	1.34358	309.489	395.204	45.441	0.206
315.0	1.01354	0.94833	1.33534	314.288	400.009	45.086	0.228
320.0	1.01253	0.93523	1.32765	319.096	404.942	44.633	0.249
325.0	1.01143	0.92081	1.32077	323.914	410.022	44.072	0.267
330.0	1.01024	0.90514	1.31497	328.741	415.271	43.398	0.283
335.0	1.00898	0.88830	1.31051	333.580	420.713	42.607	0.296
340.0	1.00766	0.87041	1.30764	338.431	426.372	41.697	0.305
345.0	1.00627	0.85161	1.30664	343.294	432.275	40.665	0.310
350.0	1.00484	0.83205	1.30772	348.170	438.450	39.512	0.312
355.0	1.00337	0.81194	1.31113	353.060	444.927	38.238	0.308
360.0	1.00187	0.79150	1.31703	357.963	451.736	36.845	0.300
365.0	1.00036	0.77103	1.32558	362.880	458.907	35.340	0.287
370.0	0.99885	0.75084	1.33685	367.812	466.467	33.727	0.269
375.0	0.99734	0.73131	1.35086	372.757	474.438	32.015	0.246
380.0	0.99585	0.71286	1.36755	377.717	482.834	30.213	0.219
385.0	0.99438	0.69597	1.38675	382.691	491.659	28.334	0.187
390.0	0.99296	0.68110	1.40823	387.678	500.896	26.390	0.153
395.0	0.99159	0.66874	1.43166	392.679	510.510	24.398	0.115
400.0	0.99028	0.65934	1.45666	397.693	520.442	22.376	0.076
405.0	0.98905	0.65327	1.48278	402.719	530.611	20.345	0.036
410.0	0.98789	0.65076	1.50961	407.756	540.915	18.328	-0.003
415.0	0.98683	0.65195	1.53674	412.804	551.239	16.348	-0.041

420.0	0.98586	0.65676	1.56385	417.862	561.468	14.429	-0.077
425.0	0.98500	0.66501	1.59067	422.929	571.496	12.593	-0.109
430.0	0.98476	0.67635	1.61705	428.004	581.232	10.860	-0.138
435.0	0.98363	0.69037	1.64289	433.086	590.610	9.245	-0.162
440.0	0.98313	0.70659	1.66813	438.173	599.585	7.760	-0.183
445.0	0.[illegible]76	0.72454	1.69276	443.264	608.136	6.414	-0.199
450.0	0.98252	0.74472	1.71680	448.359	616.259	5.210	-0.210
455.0	0.98241	0.76372	1.74023	453.455	623.964	4.150	-0.218
460.0	0.98244	0.78414	1.76304	458.551	631.272	3.231	-0.222
465.0	0.98260	0.80462	1.78521	463.647	638.208	2.448	-0.223
470.0	0.98289	0.82488	1.80670	468.740	644.801	1.797	-0.221
475.0	0.98332	0.84466	1.82744	473.830	651.081	1.271	-0.216
480.0	0.98387	0.86376	1.84738	478.915	657.078	0.859	-0.208
485.0	0.98455	0.88199	1.86643	483.994	662.821	0.555	-0.199
490.0	0.98534	0.89922	1.88451	489.066	668.338	0.346	-0.187
495.0	0.98624	0.91532	1.90154	494.129	673.653	0.232	-0.174
500.0	0.98725	0.93020	1.91743	499.184	678.792	0.187	-0.160
505.0	0.98835	0.94378	1.93211	504.228	683.775	0.222	-0.144
510.0	0.98954	0.95599	1.94550	509.260	688.624	0.313	-0.128
515.0	0.99081	0.96679	1.95753	514.281	693.358	0.457	-0.111
520.0	0.99214	0.97612	1.96814	519.290	697.994	0.645	-0.093
525.0	0.99354	0.98397	1.97727	524.285	702.548	0.865	-0.075
530.0	0.99497	0.99030	1.98489	529.267	707.038	1.112	-0.056
535.0	0.99645	0.99508	1.99096	534.235	711.478	1.379	-0.037
540.0	0.99795	0.99832	1.99544	539.189	715.882	1.654	-0.018
545.0	0.99946	1.00000	1.99833	544.129	720.265	1.932	0.001
550.0	1.00098	1.00012	1.99461	549.054	724.639	2.207	0.020
555.0	1.00248	0.99866	1.99928	553.966	729.019	2.470	0.039
560.0	1.00397	0.99565	1.99736	558.864	733.419	2.711	0.058
565.0	1.00542	0.99109	1.99387	563.748	737.852	2.927	0.076
570.0	1.00684	0.98499	1.98883	568.619	742.333	3.108	0.094
575.0	1.00820	0.97736	1.98227	573.477	746.878	3.249	0.111
580.0	1.00950	0.96824	1.97423	578.323	751.501	3.340	0.128
585.0	1.01073	0.95766	1.96478	583.157	756.219	3.376	0.144
590.0	1.01189	0.94565	1.95395	587.980	761.051	3.348	0.159
595.0	1.01295	0.93226	1.94180	592.794	766.014	3.250	0.173
600.0	1.01392	0.91757	1.92841	597.598	771.127	3.075	0.185
605.0	1.01479	0.90164	1.91382	602.395	776.416	2.814	0.196
610.0	1.01[illegible]	0.88457	1.89810	607.183	781.902	2.460	0.206
615.0	1.01621	0.86647	1.88131	611.966	787.611	2.005	0.213
620.0	1.01674	0.84749	1.86351	616.743	793.568	1.444	0.218
625.0	1.01716	0.82780	1.84473	621.516	799.806	0.768	0.221
630.0	1.01745	0.80759	1.82502	626.286	806.352	-0.044	0.221
635.0	1.01761	0.78713	1.80440	631.054	813.235	-0.952	0.218
640.0	1.01765	0.76668	1.78287	635.821	820.487	-2.005	0.211
645.0	1.01757	0.74660	1.76042	640.587	828.133	-3.193	0.202
650.0	1.01736	0.72727	1.73703	645.356	836.194	-4.516	0.188

655.0	1.01702	0.70911	1.71266	650.127	844.683	-5.973	0.170
660.0	1.01656	0.69261	1.68728	654.899	853.597	-7.562	0.149
665.0	1.01599	0.67823	1.66088	659.678	862.918	-9.273	0.123
670.0	1.01530	0.66647	1.63350	664.463	872.606	-11.096	0.094
675.0	1.01449	0.65776	1.60522	669.254	882.597	-13.016	0.061
680.0	1.01359	0.65243	1.57622	674.054	892.803	-15.015	0.026
685.0	1.01258	0.65071	1.54678	678.861	903.121	-17.074	-0.011
690.0	1.01148	0.65267	1.51727	683.678	913.434	-19.168	-0.050
695.0	1.01030	0.65824	1.48814	688.505	923.627	-21.276	-0.089
700.0	1.00905	0.66718	1.45991	693.344	933.599	-23.377	-0.126

SUNBLAZER ORBIT

TINIT= 0.0 TDELT= 5.0 TFINL= 700.0 TREG=305.0 SEMI [illegible]OR AXIS=0.82548177

ECCENTRICITY=0.20134747 INCLINATION= 0.5000 SB INJECTION VELOCITY=0.89741

PERIOD SENS TO INJECT VEL= 20.43 DAYS PER/KM/SEC VSBSUI=0.11210 TPA= 0.0

TIME	RER	RSB	DIST	FER	FSB	AZIMUTH	ELEVATION
0.0	0.99126	0.99169	0.00618	3.183	2.833	-93.808	3.971
5.0	0.98997	0.99093	0.01572	8.200	7.295	-93.066	4.006
10.0	0.98875	0.98866	0.02522	13.229	11.771	-89.065	4.002
15.0	0.98762	0.98489	0.03454	18.269	16.274	-84.455	3.998
20.0	0.98658	0.97962	0.04359	23.320	20.819	-79.539	3.997
25.0	0.98564	0.97288	0.05233	28.380	25.420	-74.367	3.994
30.0	0.98481	0.96468	0.06072	33.449	30.092	-68.915	3.966
35.0	0.98409	0.95506	0.06880	38.526	34.851	-63.147	3.969
40.0	0.98350	0.94406	0.07665	43.609	39.714	-57.017	3.938
45.0	0.98303	0.93172	0.08442	48.697	44.699	-50.488	3.884
50.0	0.98269	0.91811	0.09236	53.789	49.825	-43.549	3.800
55.0	0.98248	0.90329	0.10081	58.884	55.112	-36.214	3.677
60.0	0.98240	0.88736	0.11023	63.980	60.583	-28.561	3.508
65.0	0.98247	0.87041	0.12116	69.077	66.261	-20.722	3.290
70.0	0.98266	0.85259	0.13416	74.172	72.170	-12.851	3.026
75.0	0.98299	0.83405	0.14986	79.265	78.337	-5.188	2.726
80.0	0.98344	0.81498	0.16878	84.353	84.788	2.110	2.405
85.0	0.98403	0.79560	0.19140	89.437	91.552	8.834	2.078
90.0	0.98473	0.77616	0.21806	94.514	98.655	14.903	1.760
95.0	0.98555	0.75699	0.24899	99.584	106.120	20.257	1.460
100.0	0.98648	0.73841	0.28432	104.645	113.968	24.889	1.187
105.0	0.98751	0.72082	0.32402	109.697	122.211	28.823	0.941
110.0	0.98864	0.70464	0.36798	114.738	130.849	32.102	0.724
115.0	0.98985	0.69030	0.41594	119.768	139.870	34.781	0.535
120.0	0.99113	0.67825	0.46750	124.786	149.244	36.919	0.371
125.0	0.99248	0.66890	0.52213	129.792	158.918	38.578	0.230
130.0	0.99389	0.66258	0.57916	134.784	168.822	39.819	0.111
135.0	0.99534	0.65954	0.63786	139.762	178.867	40.706	0.010
140.0	0.99682	0.65990	0.69739	144.727	188.952	41.299	-0.074
145.0	0.99832	0.66366	0.75694	149.677	198.975	41.658	-0.143
150.0	0.99984	0.67065	0.81573	154.613	208.837	41.836	-0.198
155.0	1.00135	0.68062	0.87304	159.536	218.452	41.886	-0.242
160.0	1.00285	0.69319	0.92830	164.444	227.754	41.848	-0.276
165.0	1.00433	0.70795	0.98103	169.338	236.695	41.760	-0.302
170.0	1.00578	0.72447	1.03089	174.218	245.250	41.650	-0.319
175.0	1.00718	0.74231	1.07766	179.086	253.407	41.54[illegible]	-0.330
180.0	1.00853	0.76104	1.12118	183.941	261.172	4[illegible].45[illegible]	-0.335
185.0	1.00982	0.78031	1.16140	188.784	268.558	4[illegible].3[illegible]	-0.336
190.0	1.01103	0.79975	1.19829	193.616	275.586	41.3[illegible]	-0.332

195.0	1.01216	0.81909	1.23171	198.437	282.281	41.380	-0.325
200.0	1.01320	0.83807	1.26230	203.248	288.670	41.436	-0.314
205.0	1.01415	0.85647	1.28956	208.050	294.780	41.544	-0.301
210.0	1.01499	0.87411	1.31376	212.844	300.637	41.671	-0.286
215.0	1.01573	0.89085	1.33502	217.632	306.268	41.843	-0.269
220.0	1.01635	0.90655	1.35346	222.413	311.698	42.047	-0.250
225.0	1.01686	0.92112	1.36919	227.189	316.949	42.279	-0.230
230.0	1.01724	0.93667	1.38231	231.961	322.063	42.533	-0.208
235.0	1.01750	0.94653	1.39297	236.730	327.001	42.804	-0.185
240.0	1.01764	0.95724	1.40128	241.497	331.840	43.087	-0.161
245.0	1.01764	0.96655	1.40737	246.264	336.579	43.375	-0.136
250.0	1.01753	0.97444	1.41137	251.042	341.235	43.663	-0.111
255.0	1.01729	0.98087	1.41342	255.801	345.823	43.945	-0.085
260.0	1.01692	0.98582	1.41367	260.572	350.357	44.214	-0.058
265.0	1.01643	0.98928	1.41225	265.347	354.853	44.465	-0.031
270.0	1.01583	0.99122	1.40933	270.128	359.325	44.689	-0.004
275.0	1.01511	0.99166	1.40505	274.914	363.786	44.881	0.023
280.0	1.01428	0.99058	1.39960	279.707	368.250	45.034	0.051
285.0	1.01335	0.98798	1.39314	284.508	372.730	45.140	0.078
290.0	1.01232	0.98389	1.38586	289.318	377.241	45.193	0.105
295.0	1.01120	0.97830	1.37795	294.137	381.796	45.184	0.132
300.0	1.01000	0.97125	1.36963	298.968	386.411	45.107	0.158
305.0	1.00872	0.96275	1.36110	303.809	391.100	44.954	0.183
310.0	1.00738	0.95283	1.35259	308.662	395.880	44.717	0.206
315.0	1.00599	0.94154	1.34434	313.528	400.768	44.391	0.229
320.0	1.00455	0.92892	1.33660	318.406	405.781	43.968	0.249
325.0	1.00307	0.91504	1.32961	323.299	410.940	43.441	0.267
330.0	1.00157	0.89998	1.32365	328.205	416.265	42.806	0.283
335.0	1.00006	0.88382	1.31896	333.125	421.778	42.058	0.295
340.0	0.99854	0.86668	1.31582	338.059	427.502	41.194	0.304
345.0	0.99704	0.84869	1.31447	343.008	433.464	40.212	0.309
350.0	0.99555	0.83002	1.31516	347.970	439.690	39.110	0.310
355.0	0.99410	0.81086	1.31810	352.947	446.206	37.891	0.307
360.0	0.99269	0.79144	1.32347	357.937	453.040	36.557	0.299
365.0	0.99133	0.77204	1.33142	362.940	460.219	35.111	0.285
370.0	0.99003	0.75295	1.34204	367.956	467.764	33.562	0.267
375.0	0.98881	0.73455	1.35535	372.984	475.696	31.916	0.244
380.0	0.98767	0.71723	1.37128	378.024	484.023	30.183	0.217
385.0	0.98663	0.70141	1.38971	383.074	492.745	28.376	0.185
390.0	0.98568	0.68752	1.41042	388.134	501.844	26.507	0.151
395.0	0.98484	0.67602	1.43310	393.203	511.287	24.593	0.113
400.0	0.98412	0.66728	1.45741	398.279	521.017	22.651	0.074
405.0	0.98352	0.66165	1.48295	403.362	530.959	20.702	0.035
410.0	0.98305	0.65933	1.50932	408.450	541.021	18.766	-0.004
415.0	0.98270	0.66042	1.53615	413.542	551.102	16.865	-0.041

420.0	0.98249	0.66489	1.56311	418.637	561.099	15.021	-0.077
425.0	0.98241	0.67254	1.58994	423.733	570.914	13.254	-0.109
430.0	0.98246	0.68310	1.61645	428.830	580.468	11.581	-0.137
435.0	0.98265	0.69617	1.64252	433.925	589.695	10.017	-0.162
440.0	0.98297	0.71135	1.66806	439.018	598.556	8.574	-0.182
445.0	0.98342	0.72819	1.69304	444.107	607.026	7.258	-0.198
450.0	0.98400	0.74625	1.71741	449.191	615.099	6.073	-0.210
455.0	0.98470	0.76513	1.74116	454.268	622.781	5.020	-0.218
460.0	0.98551	0.78445	1.76426	459.338	630.089	4.098	-0.222
465.0	0.98644	0.80390	1.78667	464.400	637.044	3.303	-0.223
470.0	0.98746	0.82318	1.80834	469.452	643.671	2.628	-0.221
475.0	0.98858	0.84205	1.82922	474.494	649.998	2.068	-0.216
480.0	0.98979	0.86030	1.84923	479.525	656.051	1.615	-0.209
485.0	0.99107	0.87777	1.86831	484.543	661.858	1.259	-0.200
490.0	0.99242	0.89429	1.88638	489.549	667.444	0.998	-0.188
495.0	0.99382	0.90976	1.90336	494.542	672.834	0.817	-0.175
500.0	0.99527	0.92408	1.91918	499.521	678.050	0.709	-0.161
505.0	0.99675	0.93716	1.93376	504.486	683.113	0.665	-0.145
510.0	0.99825	0.94893	1.94703	509.438	688.044	0.680	-0.129
515.0	0.99977	0.95934	1.95893	514.375	692.860	0.742	-0.112
520.0	1.00128	0.96836	1.96941	519.297	697.580	0.843	-0.094
525.0	1.00278	0.97594	1.97842	524.206	702.220	0.979	-0.075
530.0	1.00426	0.98205	1.98591	529.101	706.795	1.140	-0.056
535.0	1.00571	0.98669	1.99186	533.982	711.320	1.319	-0.037
540.0	1.00712	0.98982	1.99623	538.851	715.810	1.507	-0.018
545.0	1.00847	0.99144	1.99901	543.706	720.278	1.700	0.001
550.0	1.00976	0.99155	2.00020	548.550	724.739	1.889	0.020
555.0	1.01097	0.99015	1.99979	553.382	729.205	2.067	0.040
560.0	1.01211	0.98724	1.99779	558.203	733.691	2.229	0.058
565.0	1.01315	0.98282	1.99422	563.015	738.209	2.367	0.077
570.0	1.01410	0.97692	1.98910	567.818	742.776	2.474	0.095
575.0	1.01495	0.96955	1.98246	572.612	747.405	2.544	0.113
580.0	1.01570	0.96075	1.97433	577.400	752.112	2.571	0.129
585.0	1.01632	0.95053	1.96477	582.181	756.914	2.546	0.145
590.0	1.01683	0.93895	1.95382	586.957	761.827	2.464	0.160
595.0	1.01722	0.92606	1.94153	591.729	766.869	2.317	0.174
600.0	1.01749	0.91192	1.92796	596.499	772.062	2.097	0.187
605.0	1.01763	0.89662	1.91316	601.266	777.425	1.800	0.197
610.0	1.01765	0.88023	1.89720	606.033	782.982	1.415	0.207
615.0	1.01754	0.86290	1.88013	610.800	788.754	0.940	0.214
620.0	1.01730	0.84475	1.86199	615.569	794.770	0.369	0.219
625.0	1.01694	0.82596	1.84285	620.340	801.055	-0.324	0.221
630.0	1.01646	0.80673	1.82273	625.114	807.637	-1.117	0.221
635.0	1.01586	0.78729	1.80167	629.895	814.542	-2.029	0.218
640.0	1.01514	0.76792	1.77968	634.680	821.798	-3.065	0.211
645.0	1.01432	0.74896	1.75677	639.472	829.424	-4.226	0.201
650.0	1.01339	0.73075	1.73293	644.273	837.439	-5.512	0.187

660.0	1.01125	0.69826	1.68264	653.902	854.656	-8.457	0.148
665.0	1.01006	0.68485	1.65591	658.731	863.843	-10.105	0.122
670.0	1.00879	0.67391	1.62850	663.572	873.342	-11.857	0.093
675.0	1.00745	0.66581	1.60038	668.426	883.123	-13.699	0.060
680.0	1.00606	0.66087	1.57174	673.291	893.100	-15.617	0.025
685.0	1.00462	0.65928	1.54287	678.168	903.176	-17.589	-0.012
690.0	1.00314	0.66110	1.51414	683.061	913.247	-19.595	-0.050
695.0	1.00165	0.66626	1.48596	687.965	923.211	-21.616	-0.088
700.0	1.00013	0.67456	1.45880	692.885	932.976	-23.629	-0.126

SUNBLAZER ORBIT

TINIT= 0.0 TDELT= 5.0 TFINL= 700.0 TBEG=335.0 SEMI MAJOR AXIS=0.82546177

ECCENTRICITY=0.19391727 INCLINATION= 0.5000 SB INJECTION VELOCITY=0.90437

PERIOD SENS TO INJECT VEL= 20.59 DAYS PER/KM/SEC VSBSOI=0.11078 TPA= 0.0

TIME	RER	RSB	DIST	FER	FSB	AZIMUTH	ELEVATION
0.0	0.98481	0.98556	0.00618	3.241	2.889	-96.806	4.025
5.0	0.98409	0.98482	0.01566	8.318	7.414	-92.213	4.062
10.0	0.98350	0.98261	0.02495	13.401	11.952	-87.223	4.081
15.0	0.98303	0.97893	0.03411	18.489	16.517	-82.088	4.083
20.0	0.98269	0.97379	0.04301	23.581	21.124	-76.803	4.083
25.0	0.98248	0.96722	0.05163	28.676	25.787	-71.319	4.078
30.0	0.98240	0.95924	0.05995	33.772	30.520	-65.579	4.067
35.0	0.98247	0.94988	0.06804	38.869	35.340	-59.541	4.041
40.0	0.98266	0.93917	0.07599	43.964	40.262	-53.148	3.997
45.0	0.98299	0.92718	0.08400	49.057	45.306	-46.378	3.926
50.0	0.98344	0.91395	0.09238	54.145	50.488	-39.249	3.819
55.0	0.98403	0.89957	0.10147	59.229	55.830	-31.791	3.670
60.0	0.98473	0.88412	0.11176	64.306	61.352	-24.119	3.473
65.0	0.98555	0.86771	0.12378	69.376	67.077	-16.370	3.230
70.0	0.98648	0.85047	0.13808	74.437	73.028	-8.729	2.947
75.0	0.98751	0.83256	0.15520	79.489	79.231	-1.414	2.636
80.0	0.98864	0.81417	0.17562	84.530	85.711	5.495	2.312
85.0	0.98985	0.79551	0.19973	89.560	92.493	11.768	1.990
90.0	0.99113	0.77683	0.22781	94.578	99.601	17.382	1.681
95.0	0.99248	0.75844	0.26004	99.584	107.057	22.303	1.394
100.0	0.99389	0.74066	0.29650	104.576	114.878	26.544	1.133
105.0	0.99534	0.72387	0.33715	109.554	123.073	30.133	0.900
110.0	0.99682	0.70845	0.38184	114.519	131.642	33.116	0.693
115.0	0.99832	0.69482	0.43031	119.469	140.570	35.545	0.513
120.0	0.99984	0.68338	0.48216	124.405	149.826	37.477	0.356
125.0	1.00135	0.67451	0.53687	129.328	159.362	38.967	0.221
130.0	1.00285	0.66853	0.59380	134.236	169.111	40.072	0.106
135.0	1.00433	0.66566	0.65224	139.130	178.989	40.851	0.009
140.0	1.00578	0.66600	0.71140	144.011	188.905	41.358	-0.072
145.0	1.00718	0.66955	0.77052	148.878	198.764	41.647	-0.140
150.0	1.00853	0.67617	0.82884	153.733	208.473	41.769	-0.194
155.0	1.00982	0.68562	0.88570	158.576	217.954	41.770	-0.238
160.0	1.01103	0.69756	0.94053	163.408	227.144	41.689	-0.272
165.0	1.01216	0.71160	0.99288	168.229	235.997	41.561	-0.297
170.0	1.01320	0.72735	1.04242	173.040	244.487	41.413	-0.315
175.0	1.01415	0.74439	1.08891	177.842	252.602	41.266	-0.326
180.0	1.01499	0.76233	1.13220	182.637	260.344	41.137	-0.332
185.0	1.01573	0.78081	1.17223	187.424	267.724	41.037	-0.333
190.0	1.01635	0.79950	1.20898	192.205	274.760	40.974	-0.330

195.0	1.01686	0.81813	1.24247	196.981	281.476	40.951	-0.323
200.0	1.01724	0.83643	1.27276	201.753	287.894	40.971	-0.313
205.0	1.01750	0.85421	1.29991	206.522	294.041	41.034	-0.300
210.0	1.01764	0.87128	1.32603	211.290	299.942	41.137	-0.285
215.0	1.01764	0.88750	1.34521	216.056	305.622	41.278	-0.268
220.0	1.01753	0.90273	1.36356	220.824	311.104	41.454	-0.249
225.0	1.01729	0.91687	1.37919	225.593	316.410	41.661	-0.229
230.0	1.01692	0.92986	1.39221	230.366	321.561	41.893	-0.208
235.0	1.01643	0.94157	1.40276	235.140	326.577	42.145	-0.185
240.0	1.01583	0.95199	1.41094	239.920	331.476	42.413	-0.161
245.0	1.01511	0.96106	1.41688	244.706	336.276	42.690	-0.136
250.0	1.01428	0.96874	1.42073	249.499	340.993	42.971	-0.111
255.0	1.01335	0.97501	1.42261	254.300	345.642	43.250	-0.085
260.0	1.01232	0.97983	1.42266	259.110	350.239	43.519	-0.058
265.0	1.01120	0.98320	1.42103	263.929	354.797	43.774	-0.031
270.0	1.01000	0.98510	1.41788	268.760	359.332	44.006	-0.004
275.0	1.00872	0.98552	1.41336	273.601	363.855	44.209	0.023
280.0	1.00738	0.98447	1.40765	278.454	368.381	44.377	0.051
285.0	1.00599	0.98194	1.40092	283.320	372.924	44.500	0.078
290.0	1.00455	0.97795	1.39335	288.198	377.497	44.573	0.106
295.0	1.00307	0.97251	1.38516	293.091	382.115	44.587	0.132
300.0	1.00157	0.96563	1.37654	297.997	386.791	44.534	0.158
305.0	1.00006	0.95735	1.36772	302.917	391.542	44.408	0.183
310.0	0.99854	0.94770	1.35892	307.851	396.382	44.199	0.207
315.0	0.99704	0.93672	1.35039	312.800	401.329	43.902	0.229
320.0	0.99555	0.92445	1.34237	317.762	406.400	43.509	0.249
325.0	0.99410	0.91097	1.33512	322.739	411.615	43.014	0.267
330.0	0.99269	0.89635	1.32891	327.729	416.994	42.410	0.283
335.0	0.99133	0.88069	1.32400	332.732	422.557	41.694	0.295
340.0	0.99003	0.86409	1.32065	337.748	428.328	40.862	0.304
345.0	0.98881	0.84669	1.31911	342.776	434.331	39.913	0.309
350.0	0.98767	0.82867	1.31963	347.816	440.591	38.844	0.310
355.0	0.98663	0.81020	1.32242	352.866	447.134	37.658	0.306
360.0	0.98568	0.79151	1.32766	357.926	453.983	36.358	0.297
365.0	0.98484	0.77287	1.33550	362.995	461.164	34.947	0.284
370.0	0.98412	0.75458	1.34601	368.071	468.697	33.434	0.266
375.0	0.98352	0.73698	1.35922	373.154	476.597	31.826	0.242
380.0	0.98305	0.72044	1.37507	378.242	484.873	30.133	0.215
385.0	0.98270	0.70537	1.39342	383.334	493.520	28.367	0.184
390.0	0.98249	0.69217	1.41407	388.429	502.521	26.541	0.149
395.0	0.98241	0.68126	1.43672	393.525	511.842	24.672	0.112
400.0	0.98246	0.67298	1.46104	398.622	521.430	22.777	0.073
405.0	0.98265	0.66765	1.48663	403.717	531.213	20.874	0.034
410.0	0.98297	0.66546	1.51311	408.810	541.108	18.983	-0.004
415.0	0.98342	0.66649	1.54010	413.899	551.019	17.126	-0.041

420.0	0.98400	0.67072	1.56729	418.983	560.853	15.322	-0.076
425.0	0.98470	0.67796	1.59440	424.060	570.520	13.588	-0.108
430.0	0.98551	0.68797	1.62122	429.130	579.944	11.943	-0.136
435.0	0.98644	0.70039	1.64760	434.192	589.065	10.400	-0.161
440.0	0.98746	0.71484	1.67345	439.244	597.842	8.968	-0.181
445.0	0.98858	0.73090	1.69869	444.286	606.252	7.655	-0.197
450.0	0.98979	0.74816	1.72329	449.317	614.287	6.464	-0.209
455.0	0.99107	0.76624	1.74721	454.335	621.950	5.397	-0.217
460.0	0.99242	0.78480	1.77041	459.341	629.255	4.452	-0.222
465.0	0.99382	0.80350	1.79285	464.334	636.221	3.626	-0.223
470.0	0.99527	0.82207	1.81448	469.313	642.871	2.914	-0.221
475.0	0.99675	0.84028	1.83525	474.278	649.229	2.309	-0.216
480.0	0.99825	0.85793	1.85509	479.229	655.322	1.806	-0.209
485.0	0.99977	0.87483	1.87394	484.167	661.173	1.397	-0.200
490.0	1.00128	0.89084	1.89173	489.089	666.809	1.075	-0.189
495.0	1.00278	0.90585	1.90840	493.998	672.231	0.829	-0.176
500.0	1.00426	0.91975	1.92386	498.893	677.522	0.654	-0.161
505.0	1.00571	0.93246	1.93806	503.774	682.643	0.548	-0.146
510.0	1.00712	0.94391	1.95094	508.643	687.632	0.487	-0.130
515.0	1.00847	0.95404	1.96243	513.498	692.509	0.481	-0.112
520.0	1.00976	0.96282	1.97249	518.342	697.290	0.517	-0.094
525.0	1.01097	0.97020	1.98107	523.174	701.991	0.581	-0.076
530.0	1.01211	0.97616	1.98813	527.995	706.628	0.672	-0.057
535.0	1.01315	0.98068	1.99364	532.807	711.215	0.784	-0.038
540.0	1.01410	0.98373	1.99758	537.610	715.768	0.908	-0.018
545.0	1.01495	0.98531	1.99993	542.404	720.298	1.038	0.001
550.0	1.01570	0.98542	2.00069	547.192	724.821	1.168	0.021
555.0	1.01632	0.98405	1.99985	551.973	729.350	1.290	0.040
560.0	1.01683	0.98121	1.99743	556.749	733.898	1.401	0.059
565.0	1.01722	0.97691	1.99343	561.521	738.479	1.491	0.078
570.0	1.01749	0.97116	1.98788	566.291	743.107	1.556	0.096
575.0	1.01763	0.96398	1.98081	571.058	747.799	1.587	0.113
580.0	1.01765	0.95541	1.97225	575.825	752.567	1.579	0.130
585.0	1.01754	0.94547	1.96225	580.592	757.428	1.525	0.146
590.0	1.01730	0.93420	1.95084	585.361	762.400	1.419	0.161
595.0	1.01694	0.92168	1.93809	590.133	767.500	1.254	0.175
600.0	1.01646	0.90794	1.92405	594.906	772.749	1.018	0.188
605.0	1.01586	0.89309	1.90877	599.687	778.164	0.714	0.199
610.0	1.01514	0.87722	1.89231	604.473	783.770	0.328	0.208
615.0	1.01432	0.86044	1.87473	609.264	789.589	-0.147	0.215
620.0	1.01339	0.84290	1.85610	614.065	795.644	-0.718	0.220
625.0	1.01237	0.82476	1.83645	618.874	801.963	-1.387	0.222
630.0	1.01125	0.80622	1.81583	623.694	808.569	-2.163	0.222
635.0	1.01006	0.78752	1.79429	628.523	815.488	-3.051	0.218
640.0	1.00879	0.76893	1.77185	633.364	822.742	-4.055	0.212
645.0	1.00745	0.75075	1.74855	638.218	830.352	-5.178	0.201
650.0	1.00606	0.73335	1.72439	643.083	838.332	-6.423	0.187

655.0	1.00462	0.71709	1.69940	647.960	846.648	-7.787	0.169
660.0	1.00314	0.70238	1.67360	652.853	855.414	-9.266	0.147
665.0	1.00165	0.68964	1.64706	657.757	864.486	-10.855	0.122
670.0	1.00013	0.67926	1.61986	662.677	873.867	-12.543	0.092
675.0	0.99862	0.67159	1.59213	667.611	883.504	-14.318	0.060
680.0	0.99711	0.66691	1.56409	672.558	893.319	-16.164	0.025
685.0	0.99562	0.66541	1.53602	677.520	903.224	-18.063	-0.012
690.0	0.99417	0.66713	1.50826	682.496	913.127	-19.945	-0.050
695.0	0.99275	0.67202	1.48120	687.486	922.932	-21.941	-0.088
700.0	0.99139	0.67988	1.45527	692.488	932.553	-23.882	-0.126

PRECEDING PAGE BLANK NOT FILMED.

CHAPTER 4

4.0 COMMUNICATION SYSTEM

This chapter provides an overall description of the communication system requirements and constraints, and the functional design of each of the major elements of the system. Topics covered include the signal design, the anticipated signal-to-noise ratios, analysis of the expected system performance, and the hardware implementation of the spacecraft equipment.

4.1 System Requirements and Constraints

The purpose of the communication system is to satisfy the mission objectives described in Chapter 1 of this report. Within this general framework there are two notable subdivisions.

The propagation experiment of immediate interest requires the transmission of accurately timed pulses of coherent RF energy at two different frequencies, and the precise measurement of relative transmission time delays, and frequency and delay perturbations induced by the transmission medium. As described fully in Chapter 1, these measurements are expected to yield unique data describing the electron density surrounding the sun, and the nature of the turbulence.

Another important communication system requirement is to provide engineering data confirming the viability of the small, inexpensive, solar stabilized, spacecraft as a vehicle for the propagation experiment and for possible subsequent particle and fields experiments in the 0.5 AU region of interplanetary space. Primarily, this requires a reliable acquisition and tracking capability and the provision of a telemetry data link for evaluation of the spacecraft behavior and for the return of data from experimental packages carried on the spacecraft.

Principal communication system constraints are imposed by the expected perturbations in the channel that is to be investigated, and by the very low signal-to-noise ratio. The latter is limited severely by the very long range over which communication must be maintained. Additionally, the spacecraft size and weight restrictions conspire to limit both the average power available to the spacecraft transmitter and the peak power that can be realized with available space-quality components.

4.2 Functional Description of the Communication System

Seven major system elements are relevant directly to a discussion of the total system function and performance:

1. the spacecraft programmer, which generates all the timing pulses and reference frequencies required in the spacecraft;
2. the main transmitter, concerned primarily with the short pulses required by the propagation experiment;
3. the beacon transmitter, used primarily to provide a spacecraft tracking signal and a telemetry link for spacecraft engineering evaluation data;
4. the communication channel, which also is the medium that is to be investigated;
5. the receiving antenna, a large phased array;
6. the receiver RF section, which provides power gain with the least possible additive noise; and
7. the data evaluation section of the receiver, which is concerned with the accurate measurement of time and frequency perturbations.

Functional diagram, D-106-400000, shows the relation between these various elements.

In the spacecraft a stable, crystal-controlled, oscillator, operating at a frequency close to 5 MHz, provides a basic timing reference signal. Output of this oscillator is frequency multiplied to define the required RF carrier frequencies of 70, 75, and 80 MHz. Output of the oscillator is also counted down in the programer to define the time intervals during which the transmitters are turned on. Derivation of the timing pulses and carrier frequencies from the same source ensures that the transmitted pulses are completely coherent and, as will be discussed later, makes it possible to phase code the pulse in a manner which enhances substantially the time measurement capability of the system.

The main transmitter emits pulses with a duration of 3 ms, internally phase coded with a baud time of 25 μs. Peak power output of this transmitter is 2 kW. The pulse repetition rate varies, in sympathy with the actual power available from the solar cell array, from a minimum of one pulse in 120 s to a maximum of one pulse in 0.8 s. Eighty percent of the total energy output of this transmitter is used to emit pulses alternately at the two extreme carrier frequencies of 70 and 80 MHz. These are the pulses used in the relative delay time measurement. Twenty percent of the energy output is transmitted in the form of similar short pulses at a carrier frequency of 75 MHz. These pulses serve an important function during the signal acquisition and receiver synchronization process, and, also, permit some of the freqency spreading effects of the channel to be measured.

The beacon transmitter emits pulses with a peak power of 50 watts at a carrier frequency of 75 MHz. This transmitter operates in two modes. In the first few days of flight, before the spacecraft solar-cell array is oriented properly towards the sun, the beacon transmitter operates from a battery power supply and transmits pulses with a duration ranging from 50 to 150 ms at a repetition rate of one pulse in 120 seconds. These pulses provide an immediate spacecraft tracking signal, while the pulse duration is used to convey telemetry data describing the behavior of the spacecraft during the initial solar-acquisition and spacecraft-stabilization phase. After the spacecraft has been oriented, and sufficient power is available from the solar cell array, the main transmitter is activated. In this mode, the beacon pulse duration is increased to range from 5 to 7 seconds. These longer pulses are interleaved infrequently with the main transmitter output. This permits some additional frequency-spreading data to be measured, and also provides a continuing, redundant telemetry link.

Pulses transmitted from the spacecraft must pass through the communication channel, which is the physical entity that is to be investigated. It is expected that the channel will introduce significant frequency dependent time delays and apparent frequency and time perturbations. These effects are described fully in Chapter 2 of this report. Here we note only that the anticipated relative time delays are expected to range from a few μs up to the order of 1 ms, and that the probable frequency perturbations range up to a few hundred Hz at the carrier frequencies used by Sunblazer. As will be seen, these parameter ranges affect importantly the optimum signal design.

The phased array receiving antenna and associated RF amplifiers also are described fully in Chapter 12 of this report. Here we note only that the measurement precision required when the communication line of sight passes close to the sun dictates a combination of high gain antenna and low noise amplifier with an effective signal-to-noise ratio of the order of 50 dB. Later sections of this chapter will show this in detail.

The data evaluation sections of the receiver include a 5-MHz oscillator that is slaved to the oscillator in the spacecraft. Three separate control loops are used in different combinations. For initial acquisition, the oscillator is tuned manually by an operator referring to a display of the received signal. The oscillator then is tuned more finely by a pulsed frequency discriminator that is used to examine the 75-MHz pulses emanating from the main spacecraft transmitter. And, finally, the oscillator is tuned precisely by measuring the time interval between received pulses; that is, by measuring the pulse repetition rate which is known to be integrally related to the transmitted carrier frequency. In a manner analogous to that used in the spacecraft, the oscillator output is counted down to provide accurate timing pulses, and is frequency multiplied to provide coherent RF reference signals. These RF signals are used as reference inputs to the mixers in the front end of the receiver.

Prime measurements are conducted by banks of correlators in the receiver. By reference to the basic oscillator, these correlators compare the signal actually received with a multiplicity of postulated signals generated in the receiver. The actual time of signal arrival is obtained by a maximum likelihood choice based on the outputs of the correlator banks. This subject is discussed in later sections of this chapter. Here we note only that the required system precision necessitates the use of a few hundred correlators for the examination of each of the two extreme carrier frequencies of 70 and 80 MHz.

Other sections of the spacecraft and receiver complex are concerned with the conversion, coding, decoding, and display of telemetered data. This is superposed on the beacon link by pulse duration modulation, and on the main link by pulse position modulation. The rationale for this is discussed in later sections of this chapter. Here we note only that the format is designed so that the prime propagation experiments are not degraded by this piggyback data.

4.3 Signal Design

Two separate but related communication links are included in the Sunblazer system. For maximum reliability, these two links are used redundantly as much as possible. Both links offer a capability for the measurement of frequency broadening induced by the transmission medium, and both provide a capacity for the superposition of telemetry data. Each link, however, has a difference prime function that dictates a different optimum form for the signal coding. This optimum signal design is the subject of this section of the report.

4.3.1 Main Transmitter

The signal coding used in the main transmitter is designed to optimize the prime propagation experiment. This experiment requires that the spacecraft emit pulses of relatively short duration with large peak power at each of two different carrier frequencies, so that the relative transmission delay imposed by the medium can be measured accurately.

Practically, there is a fairly broad range of acceptable values for the duration and peak power of the transmitted pulse. A somewhat arbitrary 'optimum' combination of these parameters has to be chosen on the basis of a tradeoff among several conflicting system constraints. This compromise leads to the selection of a pulse with an envelope duration of the order of 3 ms, a peak power of the order of 2 kW, and an internal phase coded structure with a baud time of the order of 25 μs. Telemetry is best superposed on this structure by pulse-position modulation. The rationale for these choices is discussed below.

4.3.1.1 Pulse Envelope Duration

Consider first the most desirable duration for a single transmitted pulse. In order to enhance the time resolution capability of the system, and to minimize the effective sample aperture time for the experiment, the pulse duration should be as short as possible. But, in order to minimize both the transmitter peak power requirement and the receiving antenna gain requirement, the pulse duration should be as long as possible. A compromise between these two conflicting requirements can be effected by considering the limitations of the receiving antenna and the postulated behavior of the medium when the spacecraft is close to superior conjunction.

A practical lower limit for the beamwidth of the receiving antenna is of the order of 0.5 degrees. This minimum beamwidth is primarily constrained by the necessity for tolerating angular scintillations which cause an apparent random motion of the signal source.

This finite antenna beamwidth will prohibit reception when the angular offset between the solar disc and the line of sight from spacecraft to earth is less than about one degree. In this condition a portion of the solar disc will intercept the antenna beam. And since the sun has an effective noise temperature of a few million degrees at the frequencies of interest, the total background noise picked up by the receiving antenna will increase prohibitively.

Now, as the spacecraft approaches superior conjunction the range over which communication has to be maintained is 2 AU, or 3×10^{11} meters. This causes a path loss of:

$$\frac{1}{4\pi R^2} = \frac{1}{4\pi(3 \times 10^{11})^2} \approx -240 \text{ dB.} \tag{4.1}$$

Because of this very substantial signal attenuation it is necessary to design the receiver to detect the presence of a pulse by coherent integration of the total energy in the pulse. But for this to be possible, each pulse must be individually coherent. That is, the RF carrier phase must remain essentially undisturbed for the duration of a single pulse.

Some quantitative speculation relevant to this requirement is provided by Chapter 2 of this report. There it is shown that the average channel coherence time is likely to be related to the offset of the line of sight from the solar disc in the following manner:

Offset (Degrees)	Coherence time (milliseconds)
0.5	0.3
1.0	3.0
1.5	10.0

It is apparent from these figures that the "optimum" pulse duration is of the order of 3 ms.

A pulse significantly shorter than 3 ms would require either the transmitter peak power or the receiving antenna gain, or both, to be increased to maintain the same collected signal energy per pulse. But these rather difficult and expensive changes would not improve the experiment significantly. Since the channel coherence time reduces very rapidly for offset angles less than about one degree, and the solar noise contribution increases very rapidly at the same time, the possible decrease in minimum observable angular offset is very limited.

At the expense of a rather significant increase in the minimum observable offset angle, a pulse longer than 3 ms could be used to justify a reduction in the transmitter peak power or receiving antenna gain. However, this increase in minimum observable angular offset would materially degrade the experiment in a region of particular interest.

Further, if the increased pulse duration were used to justify a reduction in the transmitter peak power, then the total radiated energy per pulse would be unchanged and no other system constraints would be relieved. The only effect of this change, therefore, would be to reduce slightly the difficulty involved in the design of the transmitter at the expense of a degradation in the experiment.

On the other hand, if the transmitter peak power is assumed to be a constant, a longer pulse duration could be used to justify a reduction in the required receiving antenna gain. But this is not an unalloyed blessing. Since the energy per transmitted pulse is increased by this change, while the average power collected by the spacecraft solar cell array remains constant, the pulse repetition rate would have to be reduced proportionately. Thus the sample data points obtained at the two different carrier frequencies would be more widely separated in time and the total sampling rate would be reduced. Both of these changes represent a further degradation of the experiment.

4.3.1.2 Peak Power

The most desirable transmitter peak power also has to be chosen as a compromise between two conflicting sets of constraints. It is desirable that this be as low as possible, both in order to permit the maximum possible pulse-repetition rate compatible with the limited average power available in the spacecraft, and also in order to simplify the design of the transmitter. But the peak power should be as high as possible to provide a maximum overall signal-to-noise ratio so as to achieve a maximum precision in the time of arrival measurement for a given receiving antenna gain, or, equivalently, to minimize the required receiving antenna gain for a specified measurement accuracy. The compromise here is settled largely on the basis of the transmitter design difficulty and the achieved pulse-repetition rate.

Available transistors permit a single power amplifier stage to generate about 70 W at the frequencies of interest. As described elsewhere in this report, a larger total RF output is created by using many such stages in parallel. In principle, this procedure can be extended as far as necessary. Practically, however, the inputs and outputs of the paralleled stages must be isolated by lossy power dividers and combiners to prevent destructive interference between the parallel stages. As the number of stages is increased, the losses introduced in the combining process tend to increase progressively due to the increasing difficulty of maintaining a precise phase match between the various parallel paths.

Extensive design and experimentation have shown that a few tens of stages may be connected in parallel with a consequent total peak-power output of the order of a few kW. At the present time, this represents a practical upper limit for this procedure. And, in turn, this sets one rough bound on the choice of peak-power level.

One of the physical parameters of interest in the propagation experiment is the scale size of the turbulence in the electron density. Currently, it is believed that the plasma will contain 'blobs' with a diameter of the order of 200 to 300 km moving radially outward from the sun, with an initial velocity of the order of 200 to 300 km per second. These 'blobs', then, may be expected to traverse the communication line of sight in a time of one to ten seconds.

It follows that the propagation experiment must achieve a sampling rate of the order of one sample per second. This will, at least, permit the observation of large inhomogeneities moving diagonally across the line of sight.

The average power output of the solar cell array is of the order of 18 W when the spacecraft approaches superior conjunction. After allowing for some inefficiencies in the energy conversion processes, and for the fixed overhead drain of the spacecraft timing and control circuits, this allows an average RF output power of the order of 6 W at the two extreme carrier frequencies involved in the propagation experiment.

The required combination of one pulse per second and an average output power of 6 W requires the energy of a single transmitted pulse to be 6 joules. And since the pulse duration has already fixed as 3 ms, this requires that the peak power be 2 kW.

As shown earlier, this requirement for 2-kW peak power is compatible with the capability that can be achieved in the transmitter. It will be shown later, also, that a 6-joule pulse permits the required measurement precision to be obtained with a receiving antenna gain of the order of 50 dB.

4.3.1.3 Intrapulse Coding

The 3-ms-duration pulses are internally coded to improve the time of arrival measurement precision that can be attained. This internal coding (modulation) increases the effective bandwidth of the signal and, in combination with a matched filter receiver, permits a measurement precision equivalent to that which could be obtained with a much shorter duration but equal energy pulse.

Since the pulse envelope duration has been chosen so that the received pulse is coherent, in the sense that the carrier phase remains correlated for the total duration of the pulse, the required coding can be superposed by phase modulation of the transmitted signal. That is, the total pulse is divided into a number of discrete but contiguous segments distinguished by the phase of the RF carrier.

Selection of an optimum segment duration, or baud time, requires some consideration of the effective bandwidth of the channel. It will be shown later that the error in the estimation of pulse arrival time is related directly to the baud duration. Ideally, therefore, the baud duration should be very short. Practically, the usable duration is determined by the necessarily finite bandwidth of the channel. This bandwidth imposes a minimum limit below which the signal will be severely attenuated, with a consequent serious waste of signal energy.

In the Sunblazer system the frequency selective nature of the channel imposes the most stringent limitation on the minimum usable baud duration. Note that the spectrum of the transmitted signal will include numerous sidebands with a total frequency extent that is inversely proportional to the chosen baud time. Since the channel is frequency selective, these sidebands will be delayed selectively in a manner that causes the envelope of the received pulse to be different from the envelope of the transmitted pulse. This effect can cause a significant reduction in the output of the receiver matched filter which, in the absence of prior knowledge of the channel characteristics, is optimally matched to the transmitted signal.

As noted in Chapter 2 of this report, this effect has been studied in detail. It transpires that the channel can be characterized by a 'dispersion time', and that the effective system signal-to-noise ratio is related to the channel dispersion time, T_c, and the selected baud duration, T_b, by the factor:

$$G = \frac{1}{1 + \frac{T_c}{T_b}} \qquad (4.2)$$

Also shown in Chapter 2 is some quantitative speculation relating the channel 'dispersion time' to the angular offset of the communication line of sight from the solar disc. Using these data, it is postulated that the signal attenuation will be related to the angular offset and the chosen baud duration in the following manner:

Baud duration (microseconds)	Angular offset (degrees) 0.5	1.0	1.5
35	-3.3dB	-1.5dB	-1.2dB
25	-4.2	-2.0	-1.7
15	-5.6	-3.0	-2.6

From this tabulation it is seen that a baud duration of 25 to 30 μs will permit continued observation to an angular offset of about one degree without intolerable signal degradation. This choice is consistent with the receiving antenna beamwidth and channel coherence time limitations discussed previously. Thus we have the desirable situation that no individual system parameter is unduly restrictive.

Now, since the best pulse envelope duration is of the order of 3 ms, and the best baud duration is of the order of 25 μs, it follows that the intrapulse coding should be chosen to yield about 120 segments. Two important additional restrictions are that the code should have a good aperiodic autocorrelation function with a strong central peak and minimum sidelobes, and that it should be easy to generate with a minimum amount of hardware in the spacecraft. A less important, but not negligible, restriction is that the baud duration chosen should be a binary multiple of the period of the basic 5-MHz oscillator in the spacecraft. This, also, will tend to minimize the complexity of spacecraft hardware.

One class of codes satisfying these requirements is the set of 127-bit pseudonoise sequences that can be generated readily with a seven stage shift register using linear feedback. Several hundred possible sequences are available within this class. The particular sequence chosen, on the basis of minimum hardware complexity, is such that:

$$Bit_1 = Bit_2 = \ldots\ldots\ldots = Bit_7$$

$$Bit_{(i+7)} = Bit_{(i)} \oplus Bit_{(i+6)} \qquad \left[1 \le i \le 120\right]$$

The particular baud-duration chosen, again on the basis of minimum hardware complexity, is 25.6 μs. Thus the exact pulse envelope duration is:

$$127 \times 25.6 \times 10^{-3} = 3.2512 \text{ ms}$$

4.3.1.4 Telemetry Modulation

There are two ways in which telemetry data may be superposed on the main communication channel without materially affecting the prime propagation experiment: either by choosing a different intrapulse coding sequence to represent different telemetry data bits or combinations of bits, or by using pulse position modulation in which the telemetry data bit is represented by the relation between the actual pulse transmission time and an arbitrarily defined time reference. These two approaches differ mainly in the achievable telemetry data rates and the amount of hardware required in the receiver.

The telemetry data rate that can be achieved using pulse position modulation is limited by the number of different time slots that can be recognized unambiguously. In the Sunblazer system the relative transmission delay may be as large as a few tens of milliseconds. The time separation between pulses transmitted at the two extreme carrier frequencies may, in some circumstances, be as small as 0.4 s. In this context the choice is restricted to, say, four different time slots. Correspondingly, each transmitted pulse may represent one of four different quantized levels with a consequent data rate of two bits per pulse.

By contrast, there are several hundred distinctive, nearly orthogonal, intrapulse code sequences that may be used. With this system, therefore, each transmitted pulse may be used to represent one of several hundred different quantized levels, with a consequent data rate of the order of eight to ten data bits per pulse.

The amount of receiver hardware required to detect telemetry data superposed by pulse position modulation is much less than that required to detect a multiplicity of different codes. In each case, the pulse time of arrival has to be estimated for the purpose of the propagation experiment. This requires a bank of filters matched to the expected pulse. If the data are superposed by pulse position modulation, the same bank of filters may be used repeatedly at times corresponding to the possible data time slots. But if the data are superposed by the use of unique codes, a separate bank of filters must be provided to match each possible code.

Another distinction may be made on the basis of the probable error rate. For a particular signal-to-noise ratio and data rate in a given channel, there is a corresponding theoretic bound on the bit error rate. This error rate increases rather rapidly as the data rate is pushed toward the limiting channel capacity. Physically, we may note that, since the pulse rate is fixed by the requirements of the propagation experiment, an increase in telemetry data rate requires that the receiver be presented with a larger number of distinctive signals. This, in turn, increases the probability that the receiver will incorrectly identify the received signal.

Since the telemetry data rate required in the initial Sunblazer flight is quite low, we elect to use the simplest possible system in which each transmitted pulse is used to represent one data bit, and the bit is identified by transmitting the pulse at either one of two predefined times. For subsequent flights, additional hardware can be added to the receiver to increase the system capability without in any way inhibiting continued reception from the first spacecraft.

4.3.2 Beacon Transmitter

Signal coding for the beacon transmitter is designed primarily to enhance the performance of this communication link during the critical first few days of the spacecraft flight. In this time era, while the spacecraft is orienting the solar cell array toward the sun, the beacon must provide accurate spacecraft tracking data and engineering telemetry describing the behavior of the spacecraft.

These functions are performed by transmitting a pulse with a peak power of 50 W at a constant carrier frequency of 75MHz. Telemetry is superposed by analog modulation of the pulse duration from 50 to 150 ms. The rationale for this choice is discussed below.

4.3.2.1 Pulse Envelope

Accurate tracking of the spacecraft and prediction of its orbit require measure of two important parameters: the spacecraft direction with respect to earth at the time of observation, and its relative motion. A determination of the current spacecraft direction requires mainly an ability to point the receiving antenna beam so as to maximize the received signal amplitude. A determination of relative motion can be made by measuring the Doppler shift induced in the known carrier frequency.

The signal coding used in the beacon is designed to ensure that these measurements can be made with adequate precision. Primarily, the signal power is chosen to yield a received signal-to-noise ratio sufficient to permit the antenna to be pointed accurately. The minimum pulse duration is chosen to permit an adequate measure of the received frequency and, correspondingly, the Doppler shift.

At any instant, the received signal-to-noise (power) ratio is:

$$\frac{S}{N} = \frac{P_t A_e}{4\pi R^2 \, k \, T \, \Delta f} \qquad (4.3)$$

where P_t is the peak power of the transmitter,

R is the spacecraft-to-earth range,

k is Boltzmann's constant,

T is the combined effective noise temperature of the observed background and the receiver front end, and

Δf is the receiver bandwidth;

and A_e, the effective area of the receiving antenna, is given by:

$$A_e = \frac{\lambda^2 G_r}{4\pi} \quad (4.4)$$

where G_r is the directional gain of the receiving antenna.

Analysis of the spacecraft dynamics, described elsewhere in this report, indicates that the initial stabilization phase, during which the beacon may be the only communication link, will continue for a period of about ten days. Orbit calculations, also described elsewhere in this report, show that in this period the maximum range achieved will be 3.9×10^9 meters, and that the maximum Doppler frequency will be 800 Hz. The average galactic background noise temperature at 75 MHz is 1800° K, and the receiver front-end equivalent-noise temperature is 850° K. Assuming a receiving antenna gain of 30 dB, which present schedule and funding limitations indicate is all that may be available at the time of the first engineering test launch, and assuming a receiver bandwidth equal to the maximum expected Doppler frequency, we have:

$$\frac{S}{N} = \frac{P_t \times 4^2 \times 10^3}{(4\pi \times 3.9 \times 10^9)^2 \times 1.38 \times 10^{-23} \times (1800 + 850) \times 800}$$

$$\approx 0.23\ P_t. \quad (4.5)$$

However, a proper receiving antenna beam pointing capability requires a reasonable signal-to-noise ratio of, say, 10 dB. This, then, requires the peak power of the transmitted pulse to be on the order of:

$$P_t \approx \frac{10}{0.23} \approx 44 \text{ W} \quad .$$

Available transistors permit use of a single stage to generate a fairly long pulse with a peak power of 50 W. This, therefore, is selected as the best peak power to use for the beacon transmitter.

To permit adequate accuracy in the prediction of the spacecraft orbit, the rms error in the measurement of Doppler frequency must be held to about 1 Hz. In terms of the pulse duration and the signal-to-noise (power) ratio, this measurement error is:

$$\sigma = \frac{1}{T_p \times 2\pi\sqrt{\frac{S}{N}}} \quad (4.6)$$

We therefore require:

$$T_p = \frac{1}{\sigma \times 2\pi\sqrt{\frac{S}{N}}}$$

$$T_p \approx \frac{1}{1 \times 2\pi\sqrt{10}} \approx \frac{1}{19.8} \approx 50 \text{ ms} . \qquad (4.7)$$

Fifty milliseconds, therefore, is selected as the best minimum pulse duration for the beacon transmitter.

4.3.2.2 Telemetry Modulation

A prime requirement for the telemetry superposed on the beacon transmitter in the early phase of the flight is that the data rate be reasonably high in order to provide a comprehensive description of the initial behavior of the spacecraft. For maximum reliability it is desirable, also, that the hardware be as simple as possible. And it is necessary that each transmitted pulse convey as much information as possible so that the number of pulses and the consequent drain on the battery power supply may be restricted.

For these reasons the beacon telemetry is implemented as an analog system in which the magnitude of the data point is represented by the duration of the transmitted pulse. Since the minimum pulse duration has already been fixed for other reasons, it is only necessary now to choose the maximum duration so that the available range will permit a tolerable data measurement accuracy.

In terms of the receiver bandwidth and the received signal-to-noise (power) ratio, the rms error associated with the measurement of a pulse duration is:

$$\sigma = \frac{1}{B\sqrt{2\frac{S}{N}}} \qquad (4.8)$$

or, with the assumptions used previously, is:

$$\sigma = \frac{1}{800\sqrt{20}}$$

$$\approx \frac{1}{3580} \approx 280\ \mu s. \qquad (4.9)$$

The full-scale data range is chosen as 100 ms in order to limit the contribution of this error source to a tolerably small 0.25%. That is, the beacon pulse is designed to be modulated from a minimum of 50 ms to a maximum of 150 ms.

4.4 Signal-to-Noise Ratio

In this section we discuss and evaluate the nature and magnitude of the various signal-to-noise ratios that are of interest. It is shown that the ratio of interest in the main communication link is the energy ratio and that the minimum value of this ratio is 16 dB. For the beacon link the parameter of interest is the power ratio which has a minimum value of 13 dB.

4.4.1 Main Communication Link

The prime purpose of the main communication link is to permit the accurate measurement of pulse arrival time that is required by the propagation experiment. This measurement is best accomplished by the use of a bank of matched filters in the receiver. This matched filter reception procedure performs coherent detection such that the receiver output signal-to-noise ratio is related to the input signal-to-noise energy ratio. That is, the critical ratio determining system performance is the ratio between the total energy in each received pulse and the total system-noise energy or spectral density.

The signal-to-noise (energy) ratio is:

$$\frac{E}{N_o} = \frac{E_t\, G_t\, A_e}{4\,\pi\, R^2\, k\, T} \qquad (4.10)$$

or, substituting:

$$A_e = \frac{\lambda^2\, G_r}{4\,\pi} \qquad (4.11)$$

$$\frac{E}{N_o} = \frac{E_t\, G_t\, \lambda^2\, G_r}{(4\,\pi\, R)^2\, k\, T} \qquad (4.12)$$

where E_t is the energy of the transmitted pulse, in joules,

G_t is the gain of the spacecraft antenna in the direction of earth,

λ is the wavelength of the RF carrier, in meters,

G_r is the directional gain of the receiving antenna,

R is the range from spacecraft to earth, in meters,

k is Boltzmann's constant, in joules per degree K,

T is the total equivalent noise temperature of the galactic background and the receiver front end, in degrees K.

The transmitted pulse energy is:

$$E_t = 3.25 \times 10^{-3} \times 2 \times 10^3 = 6.5 \text{ joules.}$$

The main spacecraft antenna provides a directional gain of 3 dB in the galactic plane, and the receiving antenna is assumed to have a directional gain of 50 dB. The average galactic background noise temperature at 75 MHz is 1800° K, and the equivalent noise temperature of the receiver front end is 850° K.

Substituting these values:

$$\frac{E}{N_o} = \frac{6.5 \times 2 \times 4^2 \times 10^5}{(4 \pi R)^2 \, 1.38 \times 10^{-23} \times 2.65 \times 10^3}$$

$$\approx \frac{3.6 \times 10^{24}}{R^2} \qquad (4.13)$$

Evaluation of this ratio yields Fig. 4-1 which shows the energy ratio as a function of the angle between the communication line of sight and the solar disc throughout the spacecraft flight. It is seen that the energy ratio remains above 16 dB up to the time at which the receiving antenna beam intercepts part of the solar disc and the direct solar noise contribution becomes prohibitive. As will be shown later, this energy ratio is sufficient to yield the required measurement accuracy.

4.4.2 Beacon Communication Link

One prime purpose of the beacon communication link in the early phase of the flight is to permit rapid signal acquisition using non-coherent detection to minimize the search difficulties. In the later phase of the flight, the beacon transmitter is used to emit a relatively long pulse designed to permit a direct measurement of the frequency spreading induced by the medium: the nature of the disturbance which is to be measured will make the received signal incoherent, again necessitating non-coherent detection. The critical system parameter for this link, therefore, is the ratio between the received peak signal-power and the total system noise-power within a defined bandwidth.

The signal-to-noise (power) ratio is:

$$\frac{S}{N} = \frac{P_t \, G_t \, \lambda^2 \, G_r}{(4 \pi R)^2 \, k \, T \, \Delta f} \qquad (4.14)$$

where P_t is the peak power of the transmitted pulse, in watts,

Δf is the receiver bandwidth, in Hz,

and all other terms are as previously defined.

The beacon transmitter peak power is 50 W. Substituting this and other previously defined values yields:

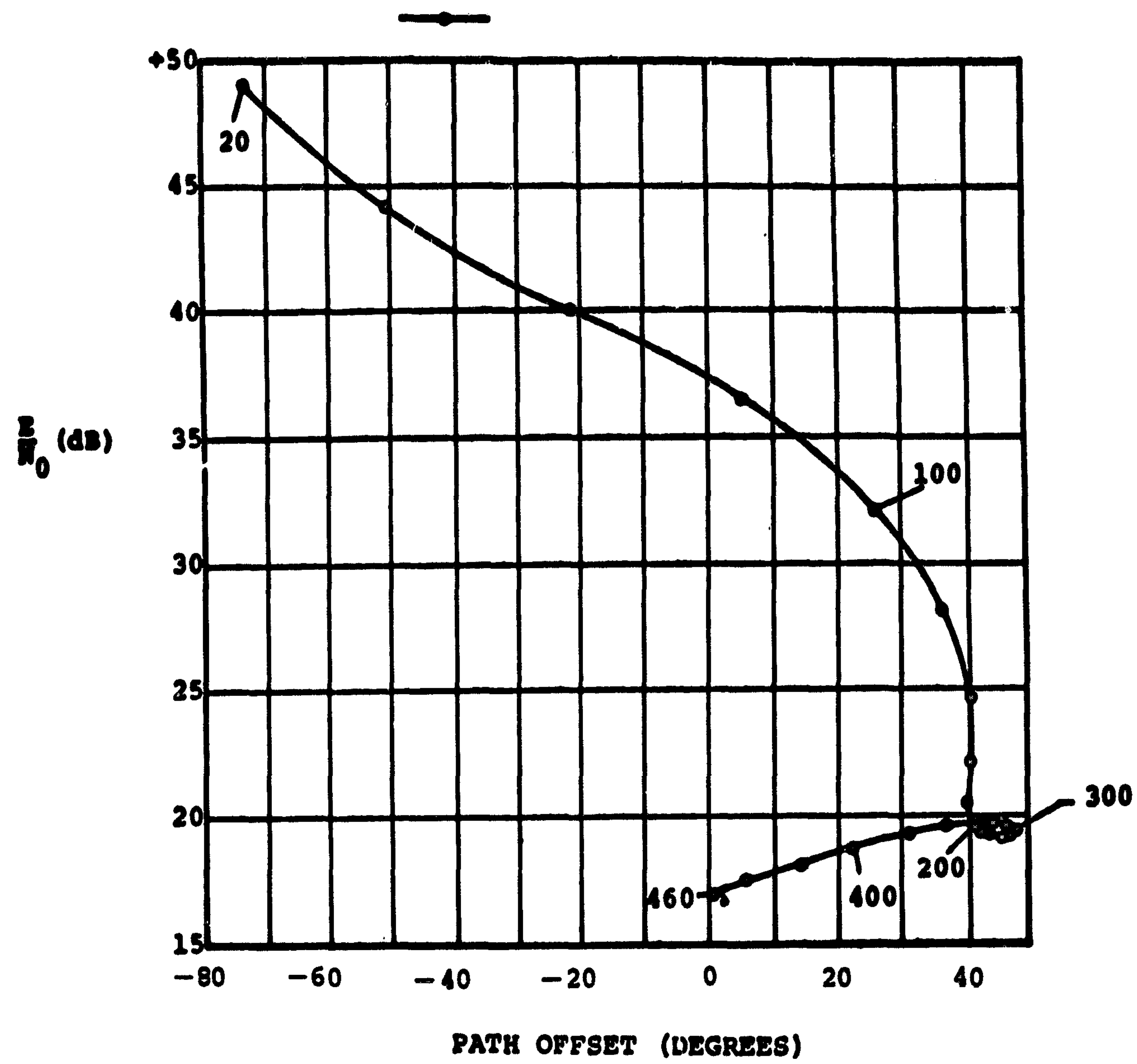

Fig. 4-1 Energy ratio at 75 MHz (neglecting solar noise).

$$\frac{S}{N} = \frac{50 \times 2 \times 4^2 \times G_r}{(4 \pi R)^2 \times 1.38 \times 10^{-23} \times 2.65 \times 10^3 \Delta f}$$

$$\approx \frac{2.8 \times 10^{20} G_r}{R^2 \Delta f} \qquad (4.15)$$

There are three different time regimes, and corresponding sets of system parameters, for which this must be evaluated.

For the first ten days of the flight, a prime task is to acquire the signal rapidly without requiring an accurate knowledge of the Doppler shift. To permit this, the receiver bandwidth must be of the order of 800 Hz, which is the maximum frequency shift expected in the first few days. Another constraint is set by current funding and schedule limitations which indicate that, for the first engineering test launch, the receiving antenna gain will be limited to 30 dB.

After these first few days it is expected that the spacecraft will orient the solar cell array toward the sun, permitting the main transmitter to be activated. In this mode the beacon pulse duration is increased to five seconds. This long pulse, coupled with the fact that prior measurements will than permit a fairly accurate prediction of spacecraft position and motion, will allow the receiver bandwidth to be reduced to, say, 100 Hz.

The third era of interest commences about six months after launch, when a measurement of the medium induced frequency spreading starts to become interesting. For this experiment the receiver bandwidth must be maintained in the order of 20 Hz to accommodate the expected perturbations, and the full receiving antenna gain of 50 dB is required. For the three different eras, then, we have:

$$\frac{S}{N} = \frac{2.8 \times 10^{20} \times 10^3}{R^2 \times 8 \times 10^2} = \frac{3.5 \times 10^{20}}{R^2} \qquad \left[0 \le \text{Days} \le 10\right]$$

$$\frac{S}{N} = \frac{2.8 \times 10^{20} \times 10^3}{R^2 \times 1 \times 10^2} \approx \frac{2.8 \times 10^{21}}{R^2} \qquad \left[10 \le \text{Days} \le 40\right]$$

$$\frac{S}{N} = \frac{2.8 \times 10^{20} \times 10^5}{R^2 \times 20} \approx \frac{1.4 \times 10^{24}}{R^2} \qquad \left[200 \le \text{Days}\right] . \qquad (4.16)$$

Evaluation of these ratios yields Fig. 4-2, which shows the beacon link signal-to-noise (power) ratio throughout the three interesting segments of the spacecraft flight. It will be shown later that the achieved ratios are sufficient to permit the required measurement accuracies to be obtained.

4.5 System Performance and Measurement Accuracy

This section demonstrates the validity of the communication system design by showing that it is possible to obtain detection probabilities and measurement accuracies that are consistent with the aims of the experiment. Clearly, the system performance will depend not only on the signal design described previously, but also on the efficiency with which the received signal is processed. For this reason we start with a description of some of the important characteristics of the receiver and the manner in which it operates.

4.5.1 The Correlation Receiver

In the ground receiver we are confronted by the classic radar problem: a noisy input must be processed to detect the presence of a signal of known form; and the time of arrival of that signal must then be estimated. In the Sunblazer system the problems are particularly challenging for two reasons. First, as a consequence of the wide bandwidth signal that must be employed, the peak power signal-to-noise ratio is very low. Second, the received signal will be subject to substantial pulse to pulse time perturbations of a pseudo-random nature due to the turbulence of the medium. These problems, however, are a matter of degree affecting the detail and complexity rather than the form of the solution.

An optimum detection procedure for this situation involves the calculation of the cross correlation between a postulated signal of the known form and the actual signal received, and the subsequent comparison of the correlator output with a predetermined threshold. A decision "signal present" or "signal absent" is made, depending on whether or not the correlator output exceeds the threshold. The arrangement may be said to test the hypothesis that a signal of the postulated form exists as one component of the noisy input.

Two kinds of error can occur. A 'false alarm' occurs if the receiver decides that a signal is present when it is truly absent, and a 'miss' occurs if the receiver decides that a signal is absent when it is truly present. A tradeoff between these two kinds of errors may be made by adjustment of the threshold. A low threshold setting will decrease the probability of a miss, but increase the probability of a false alarm, and vice versa.

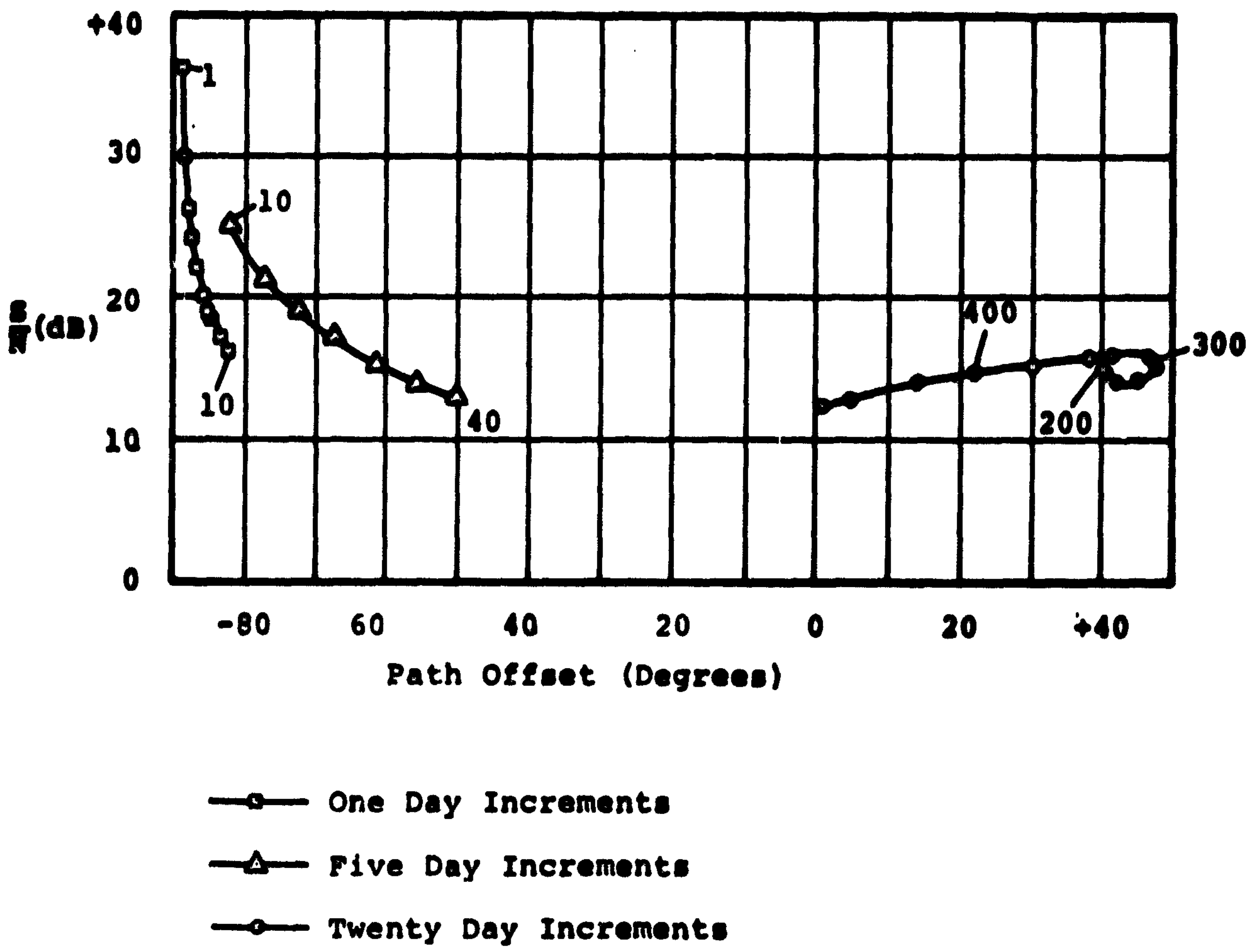

Fig. 4-2 Signal/noise (power) ratio for beacon link.

Simultaneous minimization of both kinds of error can only be accomplished by increasing the signal-to-noise (energy) ratio. We are not concerned here with a detailed examination of the receiver performance in this respect. We note only that it is possible to achieve both a miss probability and a false alarm probability of 0.002 if the energy ratio is of the order of 13 dB, and a simultaneous miss probability and false alarm probability of 0.00001 if the energy ratio is of the order of 16 dB. As shown previously, the minimum expected energy ratio in the Sunblazer system is, indeed, 16dB. Since the pulse repetition rate is in the order of one pulse per second we may therefore expect a maximum combined statistical detection error rate of the order of two events in 28 hours of observation time. Evidently, this is not the most critical problem that has to be solved.

Since the energy ratio is sufficient to provide a high level of confidence in the detection procedure, we may now turn our attention to the next problem of defining the time of arrival of the signal. This is an extension of the detection problem: we now wish to know not only that a signal is present but, also, that it is present at a particular time.

By analogy, an optimum procedure for this time estimation involves the calculation of the cross correlation between the noisy input and a signal of the known form occurring at a known time. Subsequent comparison of the correlator output with a known threshold will then permit a decision "signal present at this time" or "signal absent at this time" to be made.

But a further improvement in detection strategy can be effected by calculating simultaneously the cross correlation between the noisy input and a multiplicity of signals of the known form occurring at different times. An estimate of signal arrival time is then made by noting the correlator which provides the maximum output; or, equivalently, by noting a pair of correlators which bracket the maximum and provide equal outputs.

This is the 'maximum likelihood' detection strategy. In detection parlance, the arrangement may be said to yield the aposteriori probability that the signal arrived at time t, given the reception of the signal.

This arrangement is commonly implemented with a parallel group of matched filters, exemplified by the tapped delay line. This implementation, however, is less than optimum for the Sunblazer system for several reasons. First, the time-bandwidth products involved make a tapped delay line prohibitively expensive. Second, analog signal processing tends to require frequent and critical calibration. Third, it is not clear that an analog system could be adjusted readily to accommodate the expected signal perturbations. Fourth, a hard wired system lacks the flexibility required to cope with the sequential observation of several spacecraft transmitting different signals.

We elect, therefore, to use an implementation that is largely digital in nature. This is shown as Fig. 4-3. In a synchronous demodulator the received signal is multiplied by a reference carrier to effect a frequency translation. The resultant video is processed in several parallel paths. In each path it is multiplied by a version of the expected modulation. These various locally generated signals are displaced successively in time by a small increment, t. Outputs of these multipliers are integrated separately. The integrator outputs are then compared in order to select that path in which the signal is most closely aligned with the locally generated expected signal.

Most of the hardware is concerned with the code multiplication process. This is inherently a simple, inexpensive procedure, making it practical to replicate the parallel processing paths in large numbers. Typically, we envision several hundred individual correlators making it possible to use a small separation time increment for adequate measurement resolution with a large total time span coverage for adequate capture range.

The foregoing description has glossed over many of the practical difficulties involved in the implementation; a full discussion is provided by the reporting of the associated contract for the development of the phased array and receiver complex. One point worth noting here is that the lack of a stable phase lock between the received carrier and the local reference used in the "synchronous" demodulator makes it necessary to calculate not the cross correlation function itself, but the square of this function. This affects the system performance analysis, but does not affect the validity of the comparison procedure used in the maximum likelihood estimation strategy.

4.5.2 Time of Arrival Measurement Accuracy

One criterion in the signal design is the use of an intrapulse code having a 'good' autocorrelation function with a strong central peak and minimum sidelobes. The maximum likelihood, multiple correlation, procedure yields a set of sample points tracing out this autocorrelation function in terms of the time displacement between the received signal and the locally generated postulated signals. The form of this output is shown as Fig. 4-4.

Evidently, the measurement precision cannot be better than the resolution that is determined by the time displacement between successive correlators. To permit an analysis of the system accuracy, therefore, we assume that, at least in the vicinity of the central peak, there are enough correlators

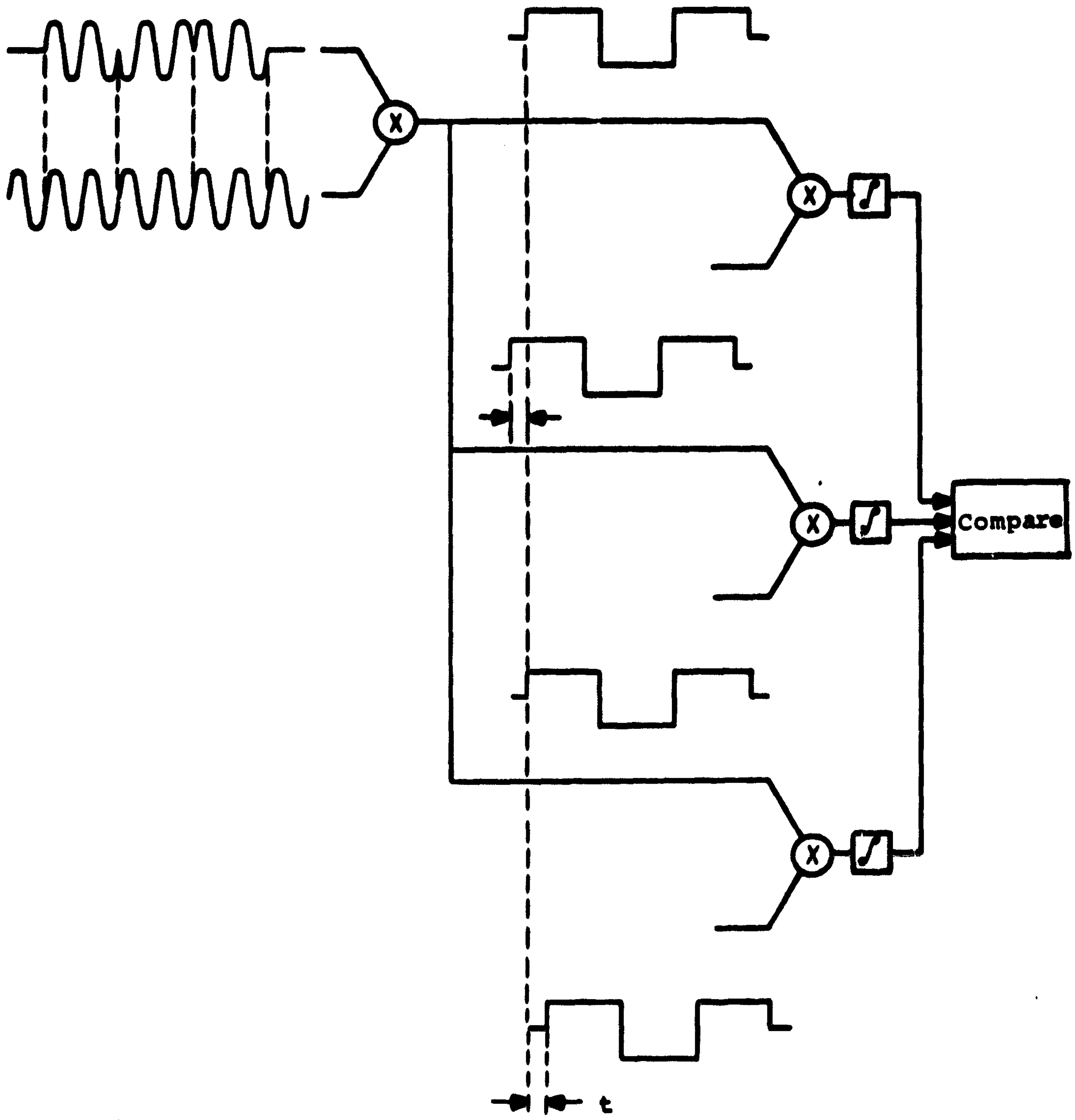

Fig. 4-3 Maximum likelihood correlation receiver.

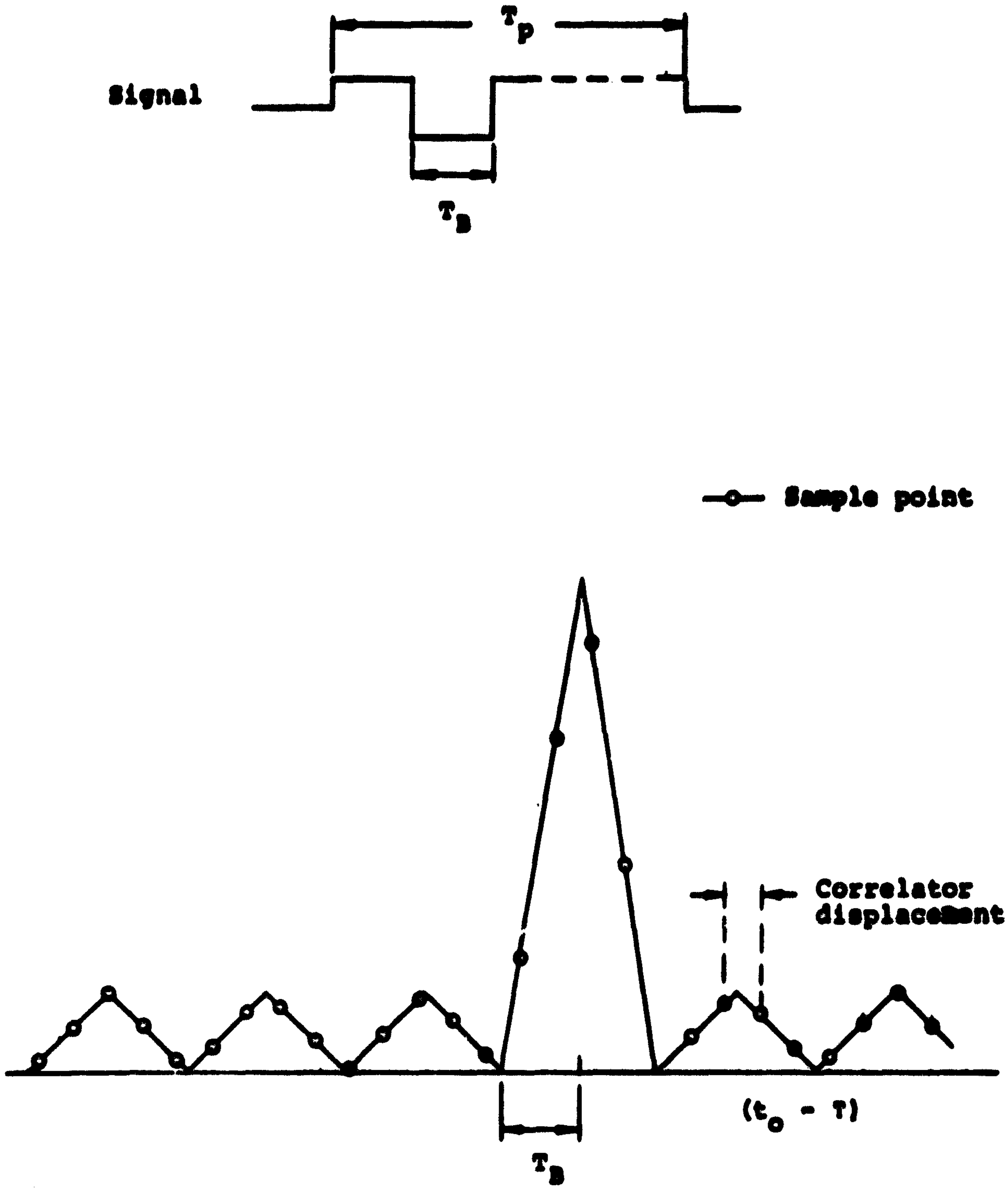

Fig. 4-4 Form of sampled correlation function.

separated by a sufficiently small increment that the output is a virtually continuous tracing of the autocorrelation function.

It is also evident that a discussion of system accuracy is meaningless if the receiver mistakenly selects a sidelobe rather than the central peak. We also assume, therefore, that the form of the autocorrelation function and the system signal-to-noise ratio are adequate to avoid this ambiguity.

With these assumptions, the interesting portion of the sampled function is as shown by Fig. 4-5. The ideal central peak is a triangle with amplitude A determined by the energy of the received signal pulse, and base width $2T_B$ determined by the baud time of the intrapulse code. Noise is superposed on this peak with a relative magnitude determined by the system signal-to-noise ratio.

Consider, then, a time estimate made by noting which correlator output sample first exceeds 50% of the maximum output; or, equivalently, the time at which the "leading edge" of the function crosses a threshold set at A/2. The error in this time estimate will be proportional to n(t), and inversely proportional to the slope of the function. But this slope is A/T_B so:

$$\Delta T = \frac{n(t)}{A/T_B}$$

$$= \frac{T_B}{A/n(t)} \qquad (4.17)$$

and for repeated measurements, the variance will be:

$$\sigma^2 = \overline{\Delta T^2} = \frac{T_B^2}{[A^2/n^2]} \qquad (4.18)$$

Now, the IF energy ratio may be shown as:

$$\left(\frac{E}{N}\right)_{IF} = \frac{E_r}{k\,T} \qquad (4.19)$$

where E_r is the signal energy at the output of the receiver RF preamplifier and mixer,

k is Boltzmann's constant,

T is the effective system noise temperature, including the contribution of the RF section of the receiver.

Synchronous demodulation doubles the signal-to-noise ratio. This is a consequence of the fact that the frequency translated signal sidebands add coherently, while the noise components add incoherently. So, following synchronous demodulation, the energy ratio is:

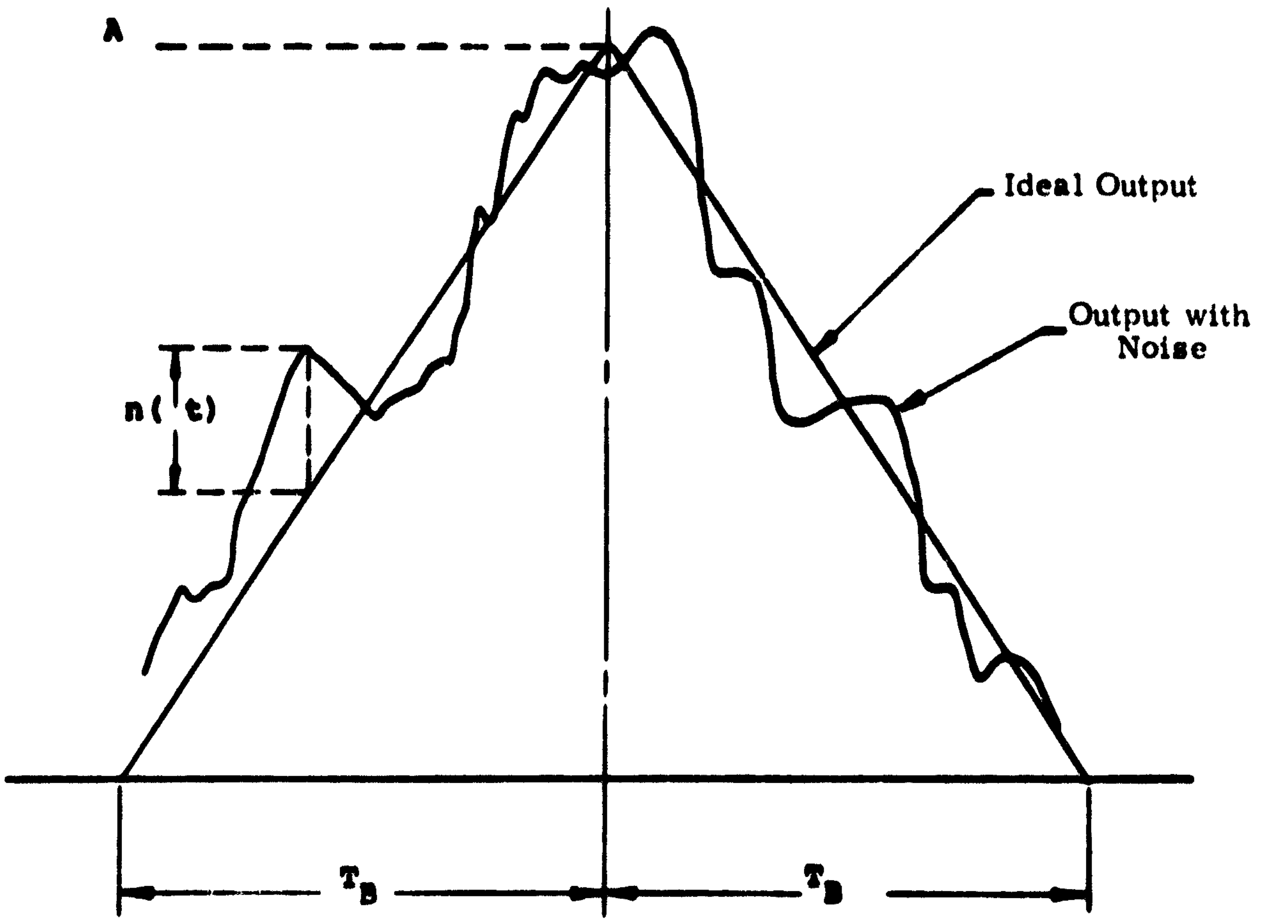

Fig. 4-5 Central peak of autocorrelation function.

$$\left(\frac{E}{N}\right)_{VIDEO} = 2\left(\frac{E}{N}\right)_{IF} = \frac{E_r}{kT/2} \tag{4.20}$$

Then after the matched filter and integrator, we have:

$$A = \int_o^{T_p} \sqrt{\frac{E_r}{T_p}} \frac{1}{\sqrt{T_p}} dt = \sqrt{E_r} \tag{4.21}$$

and

$$\sqrt{\overline{n^2}} = \sqrt{\frac{kT}{2}} \tag{4.22}$$

Hence the measurement variance is:

$$\sigma^2 = \frac{T_B^2}{\left[A^2/\overline{n^2}\right]} = \frac{T_B^2}{2\left[\frac{E_r}{kT}\right]}. \tag{4.23}$$

But the form of the autocorrelation function is such that the output noise is uncorrelated at sample times separated by intervals of T_B. We can, therefore, make a similar, independent measurement on the "trailing edge" of the function at the same threshold level of A/2. Averaging these measurements will improve the overall measurement by a factor of 2. Hence the total rms error in the measurement of pulse arrival time will be:

$$\sigma = \sqrt{\frac{T_B^2}{4\left[\frac{E_r}{kT}\right]}} = \frac{T_B}{2\sqrt{\frac{E_r}{kT}}} \tag{4.24}$$

Then, setting T_B, the code baud time, equal to 25 μs, and using the data of Fig. 4-1 which shows the signal-to-noise (energy) ratio throughout the spacecraft flight, and the data of Fig. 2-1, which shows the predicted magnitude of the relative delay that is to be measured, we obtain Fig. 4-6 which shows the rms error as a percentage of the measured quantity. It is evident that the measurement accuracy is consistent with the aims of the experiment.

4.5.3 Main Telemetry

As described previously, data are superposed on the main communication link by pulse position modulation such that each transmitted pulse has only two possible positions in time. These times are chosen to be far enough apart that there is no possibility of a reception ambiguity caused by a sudden fluctuation of the total signal propagation time.

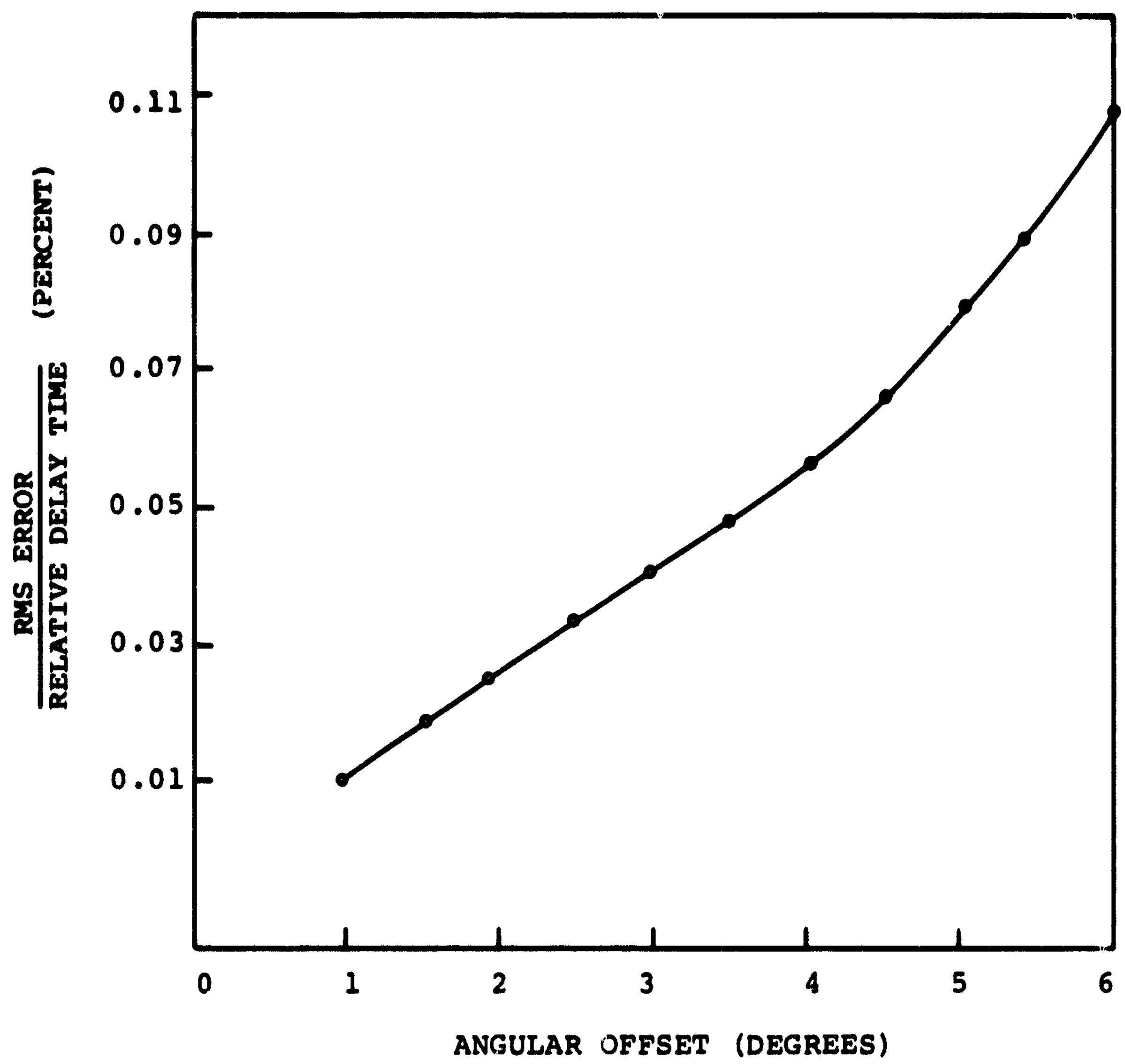

Fig. 4-6 RMS measurement error as percentage of measured quantity.

An undetected data bit error, therefore, requires the receiver to "miss" a pulse by indicating that a signal is absent when it is truly present at one time; and, for the other one of the pair of possible time slots, to cause a "false alarm" by deciding that a signal is present when it is truly absent. We require to know, therefore, the probability that these two different kinds of error will occur jointly.

The probability of a "miss" and the probability of a "false alarm" are both related to the threshold used in the detection procedure and the effective system signal-to-noise (energy) ratio. These probabilities are tabulated in the literature. A convenient description is given by Barton[(1)].

Using these data, and setting the threshold so that the probability of a "miss" is equal to the probability of a "false alarm", we find that the joint probability of an undetected error is related to the energy ratio in the following manner:

Energy Ratio dB	"Miss" probability	"False Alarm" probability	Joint Error probability
10	0.03	0.03	9×10^{-4}
12	0.005	0.005	2.5×10^{-5}
14	0.0007	0.0007	5×10^{-7}
16	0.00001	0.00001	1×10^{-10}

It is instructive to compare this with the number of telemetry data bits received during the spacecraft flight. The pulse repetition rate is of the order of one pulse per second and an average of four hours observation time is expected each day. Hence the number of data bits received per day is 1.4×10^4, and in 400 days the total is 5.6×10^6. The error rate associated with an energy ratio of 16 dB indicates a loss of one bit in about 2000 spacecraft flights. If the energy ratio decreases to about 12 dB, a statistical undetected error rate of one data bit in each spacecraft flight can be expected.

Of course, these extrapolations are not very significant because the number of data bits involved is not large enough to make the statistical error rate meaningful. Most likely, errors will occur in bursts when detection is less than optimum for some reason, such as a gross mispointing of the receiver antenna. However, the calculated data reliability shows, at least, that no serious problem is involved.

4.5.4 Beacon Telemetry

In the first few days of the flight the beacon transmitter provides the only communication link. Telemetry is superposed on this link by pulse duration modulation to describe the initial behavior of the spacecraft. In this time era the power signal-to-noise ratio is amply large to ensure reliable detection of the signal. We are principally concerned, therefore, with the precision with which the duration of a received pulse can be measured.

Consider the possible error in the measurement of a single pulse of the form shown as Fig. 4-7. An estimate of the time of occurrence of the leading edge can be made by noting the time at which the pulse amplitude first exceeds a threshold set at, say, 50% of the maximum amplitude. For reasonably large signal-to-noise ratios, the error in this measurement will be:

$$\Delta T_r = \frac{n(t)}{A/t_r} \qquad (4.25)$$

A similar, independent error will occur in the measurement of the time of occurrence of the trailing edge of the pulse, so the combined error in the estimate of pulse duration will be:

$$\Delta T = \sqrt{2}\, \Delta T_r = \frac{\sqrt{2}\, n(t)}{A/t_r} = \frac{\sqrt{2}\, t_r}{A/n(t)} \qquad (4.26)$$

Then the measurement variance will be:

$$\sigma^2 = \frac{2\, t_r^2}{\left[A^2/n^2\right]} = \frac{2\, t_r^2}{[S/N]} \qquad (4.27)$$

where S/N is the video signal-to-noise (power) ratio. But the pulse rise time will be limited primarily by the receiver bandwidth so:

$$t_r \approx \frac{1}{2F} \qquad (4.28)$$

where F is the effective bandwidth, in hertz. Further, the signal-to-noise ratio may be written as:

$$\frac{S}{N} = \frac{S_r}{k\,T\,F} \qquad (4.29)$$

where S_r is the received signal power,
- k is Boltzmann's constant,
- T is the total effective system noise temperature, and
- F is the receiver bandwidth.

So:

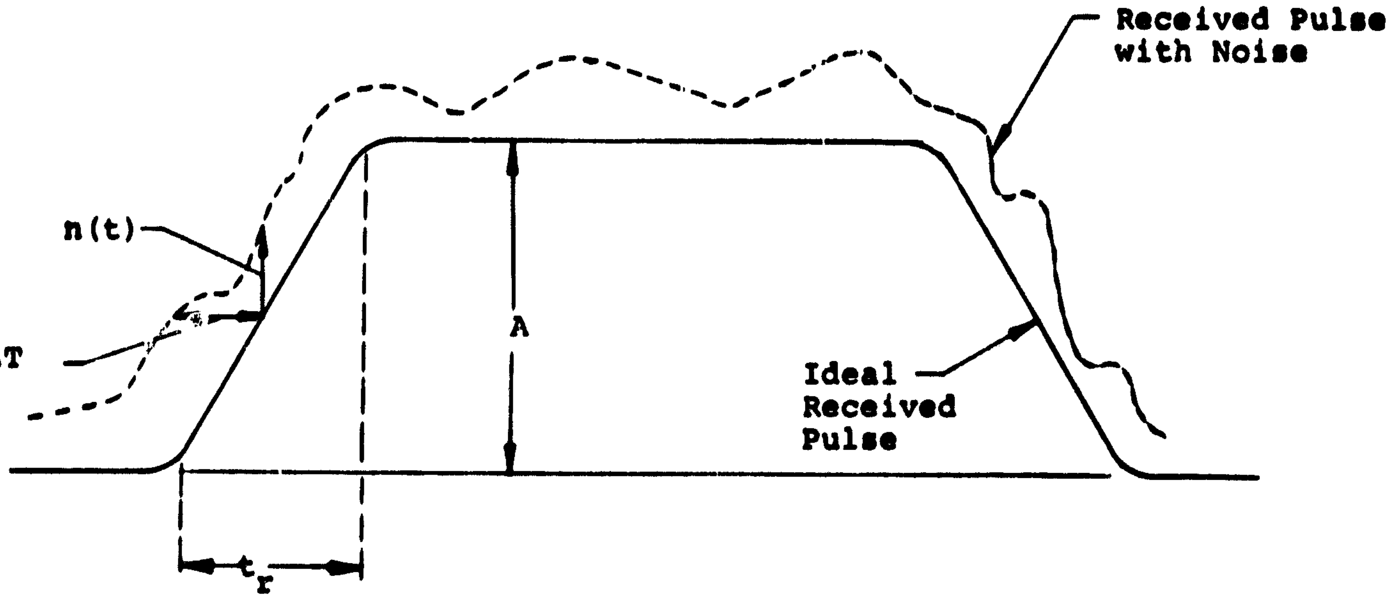

Fig. 4-7 Error in measurement of pulse duration.

$$\sigma = \sqrt{\frac{2\,k\,T\,F}{(2F)^2\,S_r}} = \sqrt{\frac{k\,T}{2\,F\,S_r}} \tag{4.30}$$

Note that the receiver bandwidth appears in the denominator of this expression. This is a consequence of the fact that the pulse rise time is limited primarily by the receiver bandwidth. In practice, little will be gained by making this bandwidth greater than, say, 50 times the reciprocal of the pulse duration. Since, as shown previously, the bandwidth required to accommodate the Doppler shift is of the order of 800 Hz, this can be used as the receiver bandwidth.

Now, the received signal power level is:

$$S_r = \frac{P_T \times G_T \times \lambda^2 \times G_R}{(4 \times \pi \times R)^2} \tag{4.31}$$

where P_T is the transmitted power, in watts,

G_T is the directional gain of the spacecraft antenna,

λ is the wavelength, in meters,

G_R is the directional gain of the receiving antenna, and

R is the range, in meters.

So, for a 30-dB receiving antenna, which may be all that is available for the first engineering test flight, we have:

$$S_r = \frac{50 \times 1 \times 4^2 \times 1000}{(4 \times \pi \times 3 \times 10^9)^2}$$

$$\approx 5 \times 10^{-16} \text{ watts} \tag{4.32}$$

And, typically:

$$kT = 1.38 \times 10^{-23} \times 2.5 \times 10^3 \approx 3.5 \times 10^{-20} \text{ W/Hz} \tag{4.33}$$

Substituting these values yields:

$$\sigma = \sqrt{\frac{3.5 \times 10^{-20}}{2 \times 800 \times 5 \times 10^{-16}}}$$

$$\approx 2 \times 10^{-4} = 200\ \mu s \tag{4.34}$$

Since the full scale range of the analog data representation is from 50 to 150 ms, the rms measurement error is:

$$\epsilon = \frac{200 \times 10^{-6} \times 10^2}{(150-50) \times 10^{-3}} = 0.2\% \tag{4.35}$$

This is acceptably small, both in comparison with the probable data conversion errors in the spacecraft and in terms of the function required of this telemetry link.

4.6 Spacecraft Programer

This section of the report describes the hardware implementation of the spacecraft programer and telemetry subsystem. Topics covered include the functional operation of the subsystem, detail of the hardware implementation, and the telemetry format. This format is consistent with the signal design criteria discussed earlier.

4.6.1 Functional Description

Drawing No. D-106-400000 shows a functional diagram of the total Sunblazer system. The spacecraft equipment includes a programer that is responsible for timing all the activities on the spacecraft, a beacon transmitter and its associated telemetry encoding equipment, a main transmitter and its associated telemetry encoding equipment, the aspect sensor and sail controller, and a power subsystem. In this section of the report, we are concerned primarily with the programer and telemetry encoding subsystems.

A more detailed functional diagram of the spacecraft is shown by Drawing No. D-106-400001. All timing pulses and RF carriers used in the spacecraft are developed from a basic 5-MHz oscillator. Output of this oscillator is counted down by the pulse duration counter and the pulse spacing counter to generate "transmit" controls for both the beacon and main transmitters. Other outputs of the countdown chain are used to control the operation of the telemetry encoders so that appropriate data modulation can be added to the transmitted pulses. Output of the oscillator is also frequency multiplied to generate the required RF carrier frequencies.

4.6.2 Logic Design

Logic diagram E-106-400017 and timing diagram E-106-400018 show the detailed implementation of the spacecraft programer and the resultant pulse and telemetry formats. The logic symbology used is chosen to maintain a one-to-one correspondence between the logic elements and the actual hardware elements. This symbology is explained as a part of the logic diagram.

The pulse duration and pulse spacing counters together form a 29-stage binary counter. Principal outputs of this counter chain are: a square wave with a period of 25.6 μs, used to define the baud duration for the phase coded main transmitter pulses; a square wave with a period of 3.2 ms, used to define the envelope duration for the main transmitter pulse; and a square wave with a period ranging from 0.8 to 107 seconds, used to define the pulse repetition rate for the transmitters. Other outputs of the counter chain are available to control the remainder of the timing and encoding hardware.

A mode control section (flip-flops 30 and 31) define which one of the two operating modes is in effect. In the "beacon only" mode, the spacecraft operates from a battery power supply, and the main transmitter and all its associated control hardware are inactive. In the "main" mode, both the main transmitter and the beacon transmitter are used, with power being derived from the spacecraft solar cell array.

The pulse duration modulator (flip-flops 32 through 38) controls the duration of the pulse that is emitted by the beacon transmitter. In the "beacon only" mode, the minimum pulse duration is fixed as 50 ms by the control gates associated with flip-flop 33. The maximum duration of the pulse is 150 ms. This is controlled by the element shown in the logic diagram as flip-flop 38. This element has the form of an astable multivibrator in which the pulse recovery time is controlled by an analog input.

The controlling analog input is obtained from the output of the beacon data multiplexer. This is a set of 16 gates activated sequentially to select one of 15 possible data inputs. One position is left blank to provide a beacon telemetry synchronization signal. At present, we envision seven of the data inputs to be digital in nature, and eight of them to be analog. However, the instrumentation is such that this grouping can be changed readily to accord with the final definition of the data points that are required to be handled by this telemetry data link. The multiplexer is controlled by the beacon word counter which simply counts sequentially through all possible positions of the multiplexer in synchronization with the beacon transmitter output.

The pulse interval controller (flip-flops 55 through 57) is activated only in the "main" mode. It controls the operation of the last seven stages of the basic countdown chain (flip-flops 23 through 29) so as to determine the actual transmitted pulse rate for the main transmitter. The pulse interval controller is a reversible counter permitting eight possible output states with a consequent eight possible pulse repetition rates. Modification of the content of this counter can occur only at the end of a complete data frame.

The pulse position modulator (flip-flops 43 through 46) determines which one of two possible time slots shall be used for the main transmitter pulse. In this way the telemetry data is superposed on the main transmitter by pulse position modulation. A data bit of zero is distinguished by transmitting the main transmitter pulse in the first of two possible time slots. A data bit of one is distinguished by transmitting the main pulse in a time slot that is 200 ms later.

The sequence generator (flip-flops 47 through 54) is responsible for the phase modulation of the main transmitter pulse. The group of seven flip-flops, 48 through 54, form a seven-stage shift register with linear feedback used to generate a 127-bit maximal length pseudo-noise code.

The bit counter and parallel-to-serial converter, (flip-flops 58 through 64) is responsible for converting the quantized data representation to a serial form and assembling this with word synchronizing pulses into the required output telemetry data format. Flip-flops 59 through 63 form the equivalent of a ten-stage shift register which sequentially selects one of the quantized data input bits or word synchronizing bits.

The quantized data bits may be obtained directly from an eight-bit digital input, or from the output of an eight-bit analog-to-digital converter. This quantized data is stored in flip-flops 70 through 77. The data are quantized in this register by allowing this group of flip-flops to act as a counter for a time interval that is proportional to the magnitude of the analog data.

Selection of the main input data is controlled by the main data multiplexer, which is a group of 32 gates activated sequentially under control of the main word counter. At present, we envision two digital input channels, one of which will be used to transmit the status of the beacon word counter as an additional synchronizing signal, and one of which accepts an eight-bit digital word from an external source. The other main data inputs are analog in nature. Again, this grouping of digital and analog data sources can be changed readily to accord with the final selection of telemetry data inputs.

4.6.3 Pulse Format

The pulse format is shown by sheet 1 of Drawing No. E-106-400018. In the "beacon only" mode, pulses are transmitted at a fixed repetition interval of 107 seconds. A group of 16 sequential pulses forms a data frame. One pulse in each frame is deleted to provide telemetry synchronization. Each of the other 15 pulses is used to represent one data point by pulse duration modulation. The duration is related linearly to the magnitude of the analog data point such that 0 volts is represented by a 50-ms pulse, and 5 volts is represented by a 150-ms pulse. Digital data are represented by a pulse with a duration of either 60 or 120 ms.

In the "main" mode, the beacon pulse duration is increased to range from 5 to 7 seconds, again proportional to the magnitude of the data point that is to be transmitted. These pulses are interleaved relatively infrequently with the main transmitter pulses. The longest frame duration is controlled by the time required to cycle completely through the sixteen beacon pulses.

The sixteen segments corresponding to the beacon words are defined as "major frames". Each major frame is divided into two "minor frames" distinguished only by word zero. In one minor frame the beacon transmitter is activated in this time interval; in the other minor frame word zero is left blank. This provides telemetry frame synchronization for the main communication channel.

The remainder of each minor frame comprises 31 data words. Each word is formed by ten bits. Two of these are transmitted at 75 MHz. The remaining eight are transmitted alternately at the two extreme carrier frequencies of 70 and 80 MHz. The uncoded 75-MHz pulses are used in the initial acquisition of frequency synchronization in the receiver, to permit a direct measure of the frequency perturbations induced by the medium, and to serve the function of telemetry data word synchronizing pulses. The coded pulses transmitted at 70 and 80 MHz form the backbone of the experiment. These are the pulses that permit the relative delay time experiment to be conducted. Additionally the pulses are coded by pulse position modulation to form the main telemetry data link.

Ordinarily, the pulse repetition interval for the main transmitter pulses is 1.6 seconds. Thus, the word duration is 16 s, the minor frame duration is 514 s, the major frame duration is 1024 s or 17 minutes, and the beacon frame duration is 272 minutes or 4 1/2 hours.

These "normal" rates are chosen so as to utilize fully the average power available from the solar cell array when the spacecraft is 1 astronomical units distant from the sun. As the spacecraft approaches closer to the sun, however, the average available power also increases. The pulse interval controller then moves to double the pulse rate so as to take full advantage of the extra power.

As a safety precaution, the pulse interval controller also can reduce the average pulse repetition rate by successive factors of two. If, for example, 50% of the solar cell array should fail, the rate would be reduced from one pulse every 1.6 s to one pulse every 3.2 s; the experiments and the reception of telemetry data could thus continue, although at a lower data rate. In this mode, the beacon frame duration would extend to nine hours. This may be longer than the observation period available in one day, so it may not be possible to see a complete frame of beacon telemetry data. To circumvent this problem, the content of the beacon word counter is transmitted as one word of the main telemetry frame so that beacon telemetry synchronization still can be achieved.

The pulse interval controller is actually implemented to make possible increase of the pulse repetition interval by successive factors of two, up to as much as 107 seconds. This emergency backup mode requires very little extra hardware and permits at least some experimental data to be obtained even if the power source degrades to about 5% of the nominal value.

4.6.4 Hardware Implementation

The spacecraft programer uses the Fairchild 9040 series of low power diode-transistor logic integrated circuits. This series provides the best combination of low power, logic flexibility, and space-qualified reliability that is available today. This integrated circuit family is being used extensively in many other NASA oriented equipments and is the subject of continuing and close scrutiny by NASA Goddard Quality Assurance.

Recent production runs have shown serious reliability problems. However, the production process responsible for this has been identified by NASA Goddard Quality Assurance and by Fairchild. Our information is that Fairchild is now modifying the production process and that qualified units will be available again in early 1969. Since this matter is of considerable moment to many NASA programs, it is attracting a great deal of attention and we are confident that the problems will be solved completely long before the Sunblazer flight hardware has to be committed.

Should this hope not be realized, however, there is a recourse available. Amelco is now starting production of a second source copy of the Fairchild units. On the basis of contacts with NASA Goddard Quality Assurance, it is understood that the Amelco units avoid the questionable production process and are, therefore, likely to be qualified in the very near future. If even this recourse should fail, the next alternative would be to redesign the programer to use the nearly equivalent Texas Instrument family of low power TTL circuits. The modifications required would not be extensive. The major problem would be a slight increase in total subsystem power consumption.

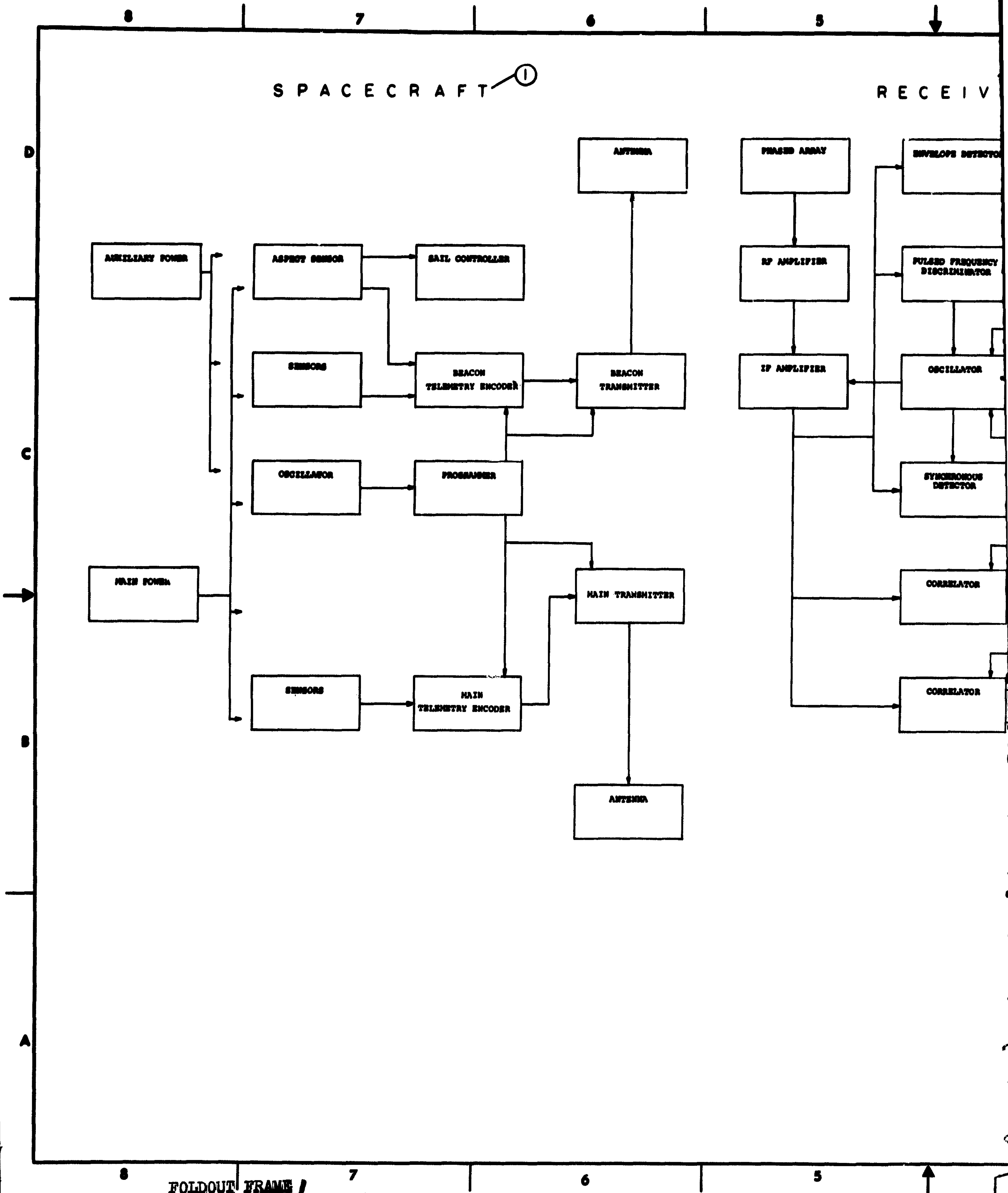

FOLDOUT FRAME 1

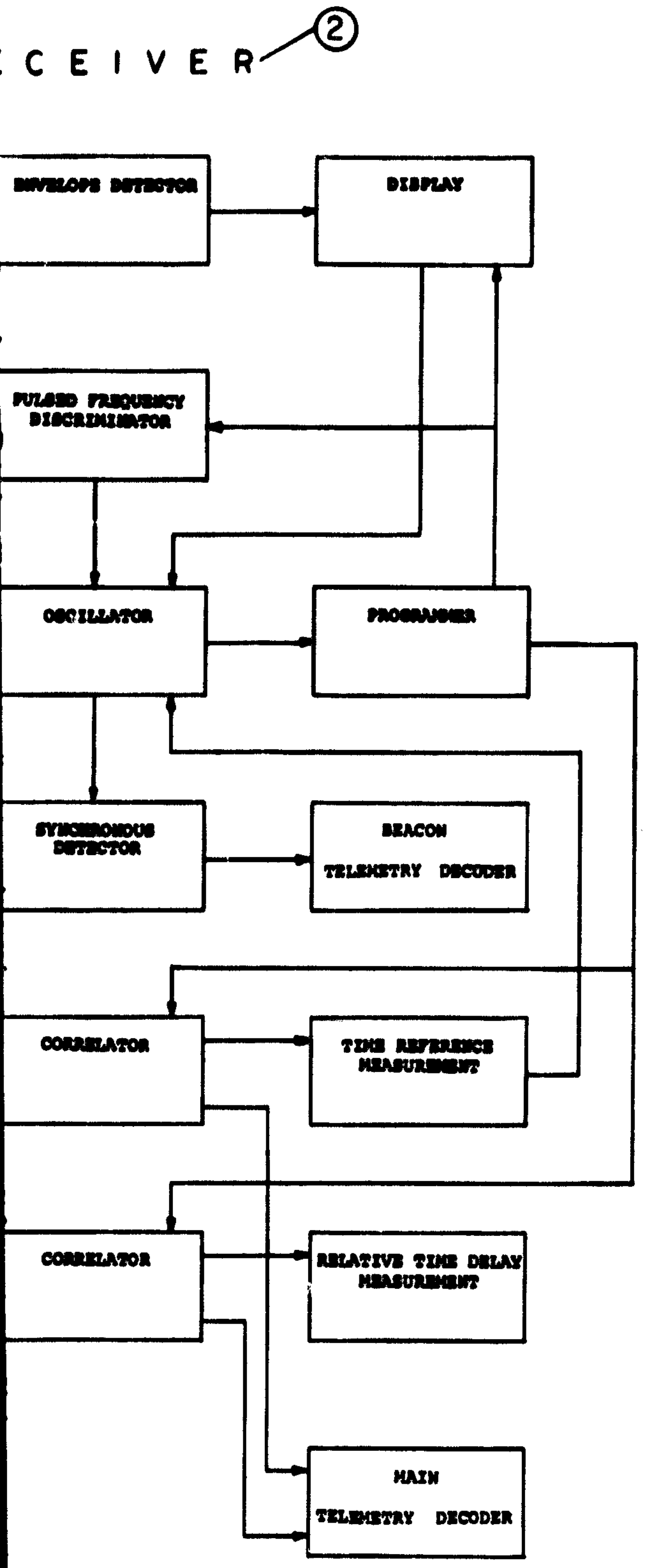

REVISIONS

ZONE	LTR	DESCRIPTION	DR	CHK	DATE	APPROVED

FIND NO.	QTY REQD	PART OR IDENT. NO.	NOMENCLATURE OR DESCRIPTION	MATERIAL OR SPECIFICATION
	REF	E-106-800006	DRAWING TREE	
2	REF	D-106-400002	FUNCTIONAL DIAGRAM, RECEIVER	
1	REF	D-106-400001	FUNCTIONAL DIAGRAM, SPACECRAFT	

LIST OF MATERIALS

UNLESS OTHERWISE SPECIFIED
CAPACITOR VALUES ARE IN μf
RESISTOR VALUES ARE IN OHMS
ELECTRICAL TOLERANCES = ±5%

DIMENSIONS ARE IN INCHES
TOLERANCES ON
FRACTIONS DECIMALS ANGLES
± ± ±
DO NOT SCALE THIS DRAWING

MATERIAL

NEXT ASSY | USED ON
APPLICATION

DRAWN
CHECKED
APPROVED Bennett 7-22-68
APPROVED

MIT APPROVED DATE

CENTER FOR SPACE RESEARCH
MASSACHUSETTS INSTITUTE OF TECHNOLOGY
CAMBRIDGE, MASS.

FUNCTIONAL DIAGRAM SUNBLAZER

SIZE D | CODE IDENT NO. | DRAWING NO. 106-400000

SCALE | SHEET 1 OF 1

106-400000 | 8

FOLDOUT FRAME 2

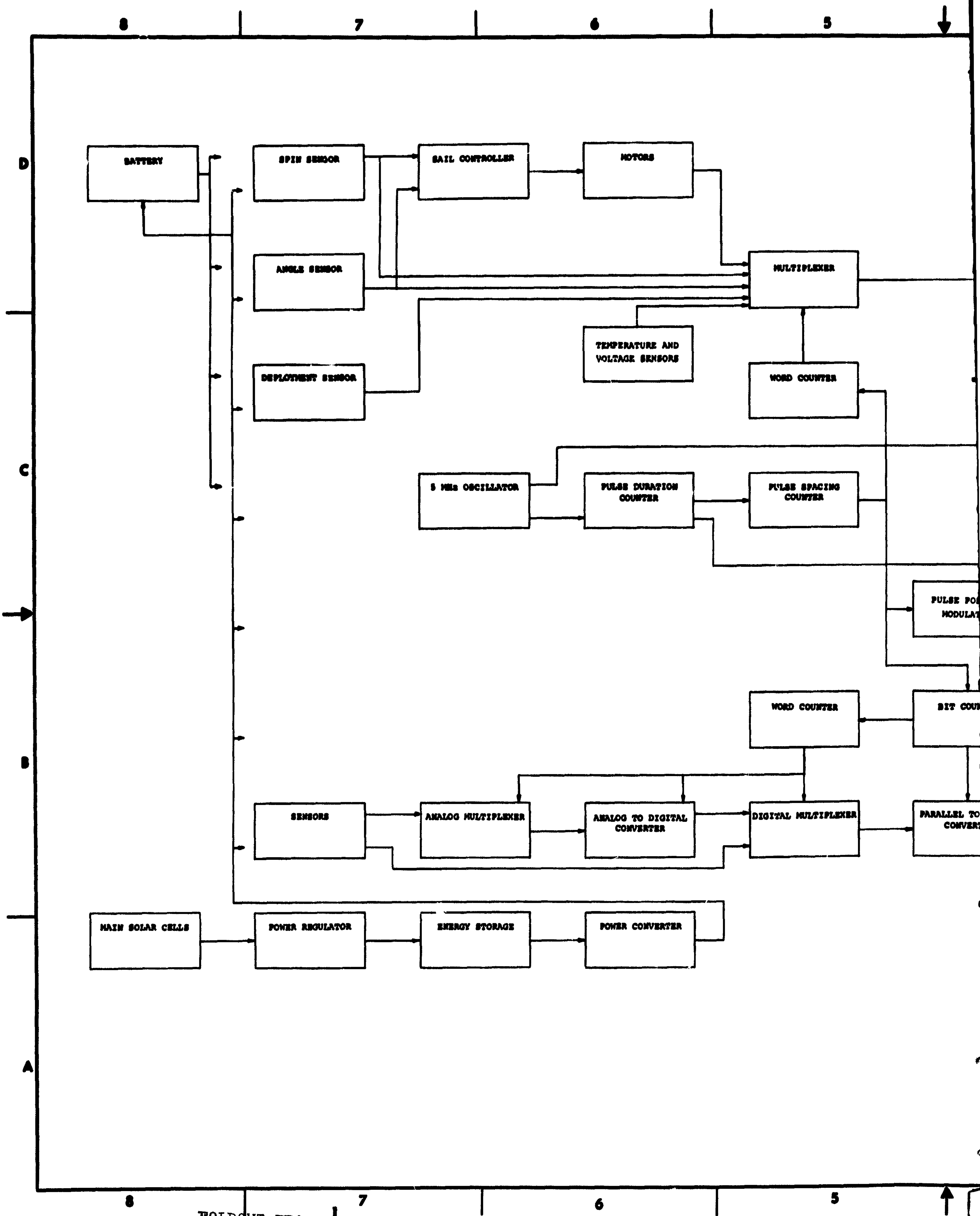

FOLDOUT FRAME

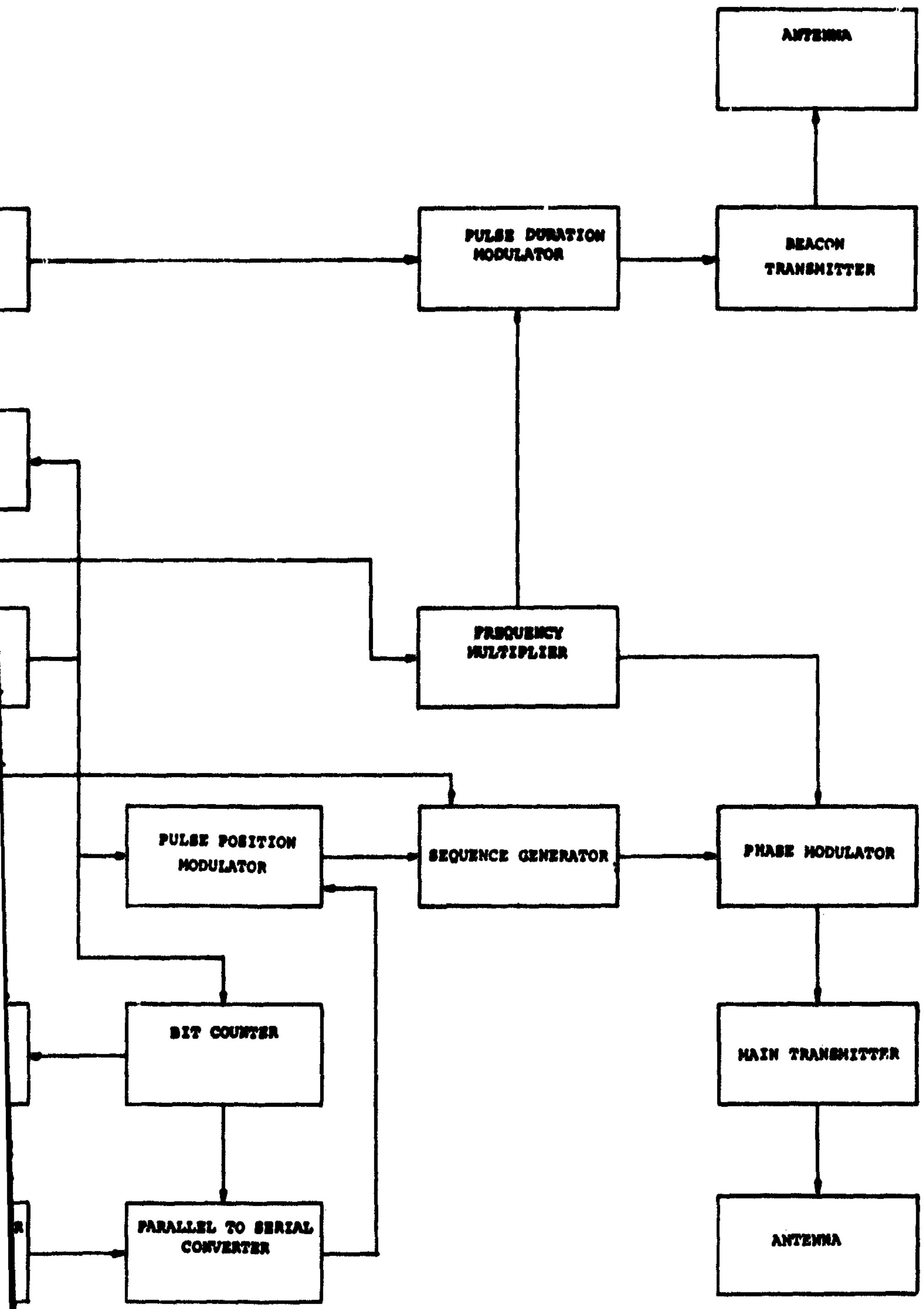

FIND NO.	QTY REQD	PART OR IDENT. NO.	NOMENCLATURE OR DESCRIPTION	MATERIAL OR SPECIFICATION
	REF	E-106-400017	LOGIC DIAGRAM, SPACECRAFT PROGRAMMER	
	REF		SPACECRAFT	

LIST OF MATERIALS

UNLESS OTHERWISE SPECIFIED
CAPACITOR VALUES ARE IN μf
RESISTOR VALUES ARE IN OHMS
ELECTRICAL TOLERANCES = ±5%

DIMENSIONS ARE IN INCHES
TOLERANCES ON
FRACTIONS DECIMALS ANGLES
± ± ±
DO NOT SCALE THIS DRAWING

MATERIAL

NEXT ASSY	USED ON
D-106-400000	

APPLICATION

DRAWN
CHECKED
APPROVED Bennett 7-22-68
APPROVED
MIT APPROVED DATE

CENTER FOR SPACE RESEARCH
MASSACHUSETTS INSTITUTE OF TECHNOLOGY
CAMBRIDGE, MASS.

FUNCTIONAL DIAGRAM SPACECRAFT

SIZE D | CODE IDENT NO. | DRAWING NO. 106-400001
SCALE | SHEET 1 OF 1

FOLDOUT FRAME 2

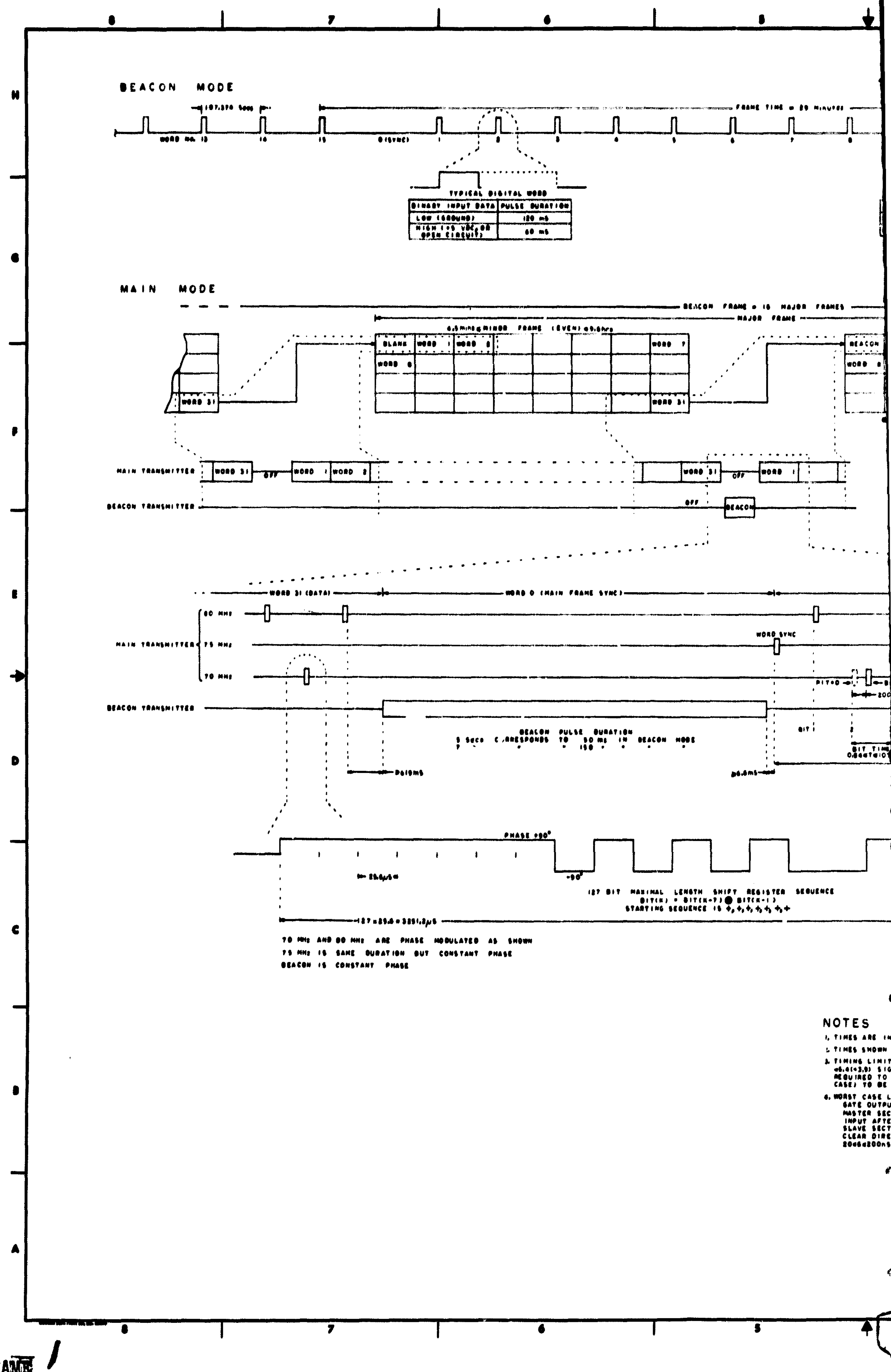

FOLDOUT FRAME 1

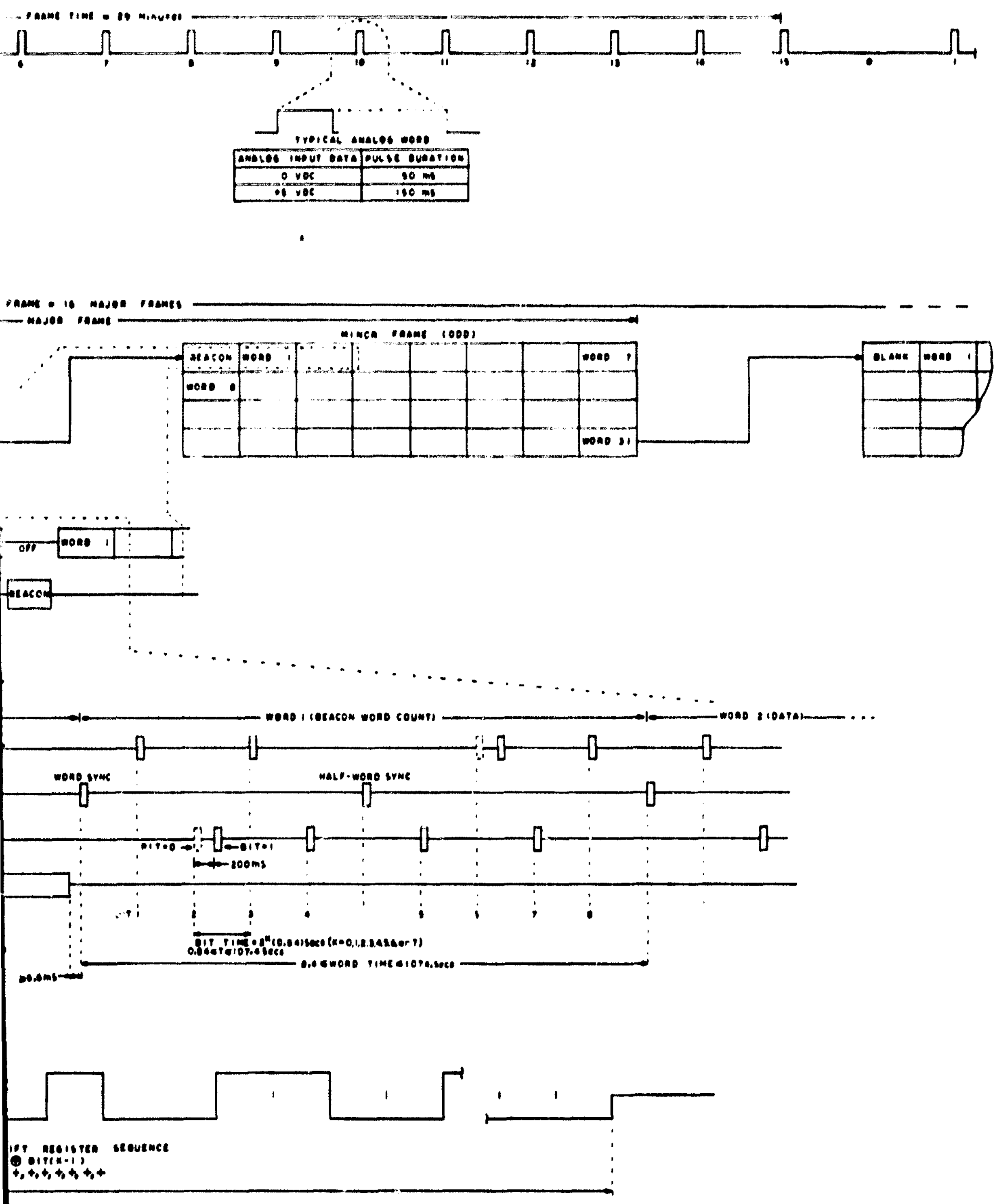

NOTES

1. TIMES ARE IN MICROSECONDS UNLESS OTHERWISE NOTED
2. TIMES SHOWN ARE BASED ON 5 MHz CRYSTAL.
3. TIMING LIMIT NOTATION:
   <6.4(<3.9) SIGNIFIES THAT MARKED TIME INTERVAL IS REQUIRED TO BE LESS THAN 6.4µS AND EXPECTED (WORST CASE) TO BE LESS THAN 3.9µS
4. WORST CASE LIMITS FOR CIRCUIT ELEMENTS:
   GATE OUTPUT CORRESPONDS TO INPUT AFTER DELAY G;
   MASTER SECTION OF FLIP-FLOP CORRESPONDS TO DATA INPUT AFTER DELAY M;
   SLAVE SECTION OF FLIP-FLOP FOLLOWS CLOCK PULSE, CLEAR DIRECT, OR SET DIRECT INPUT AFTER DELAY S;
   20<G<200ns   0<M<120ns   20<S<300ns

E-106-400028
E-106-400017
NEXT ASSY

TIMING DIAGRAM
SPACECRAFT PROGRAMMER

E

106-400018

SHEET 1 OF 4

106-400018 3

FOLDOUT FRAME 2

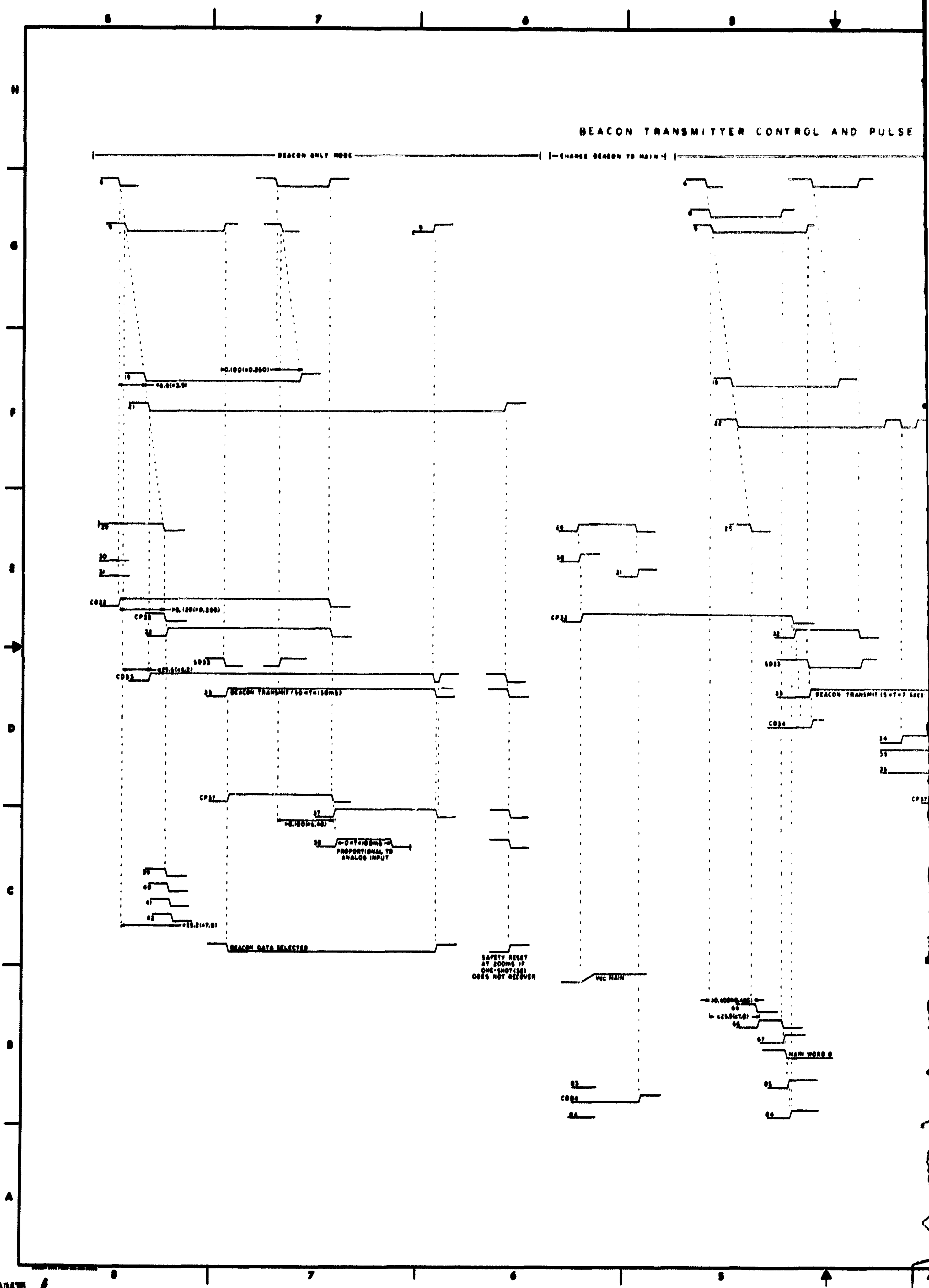

FOLDOUT FRAME 1

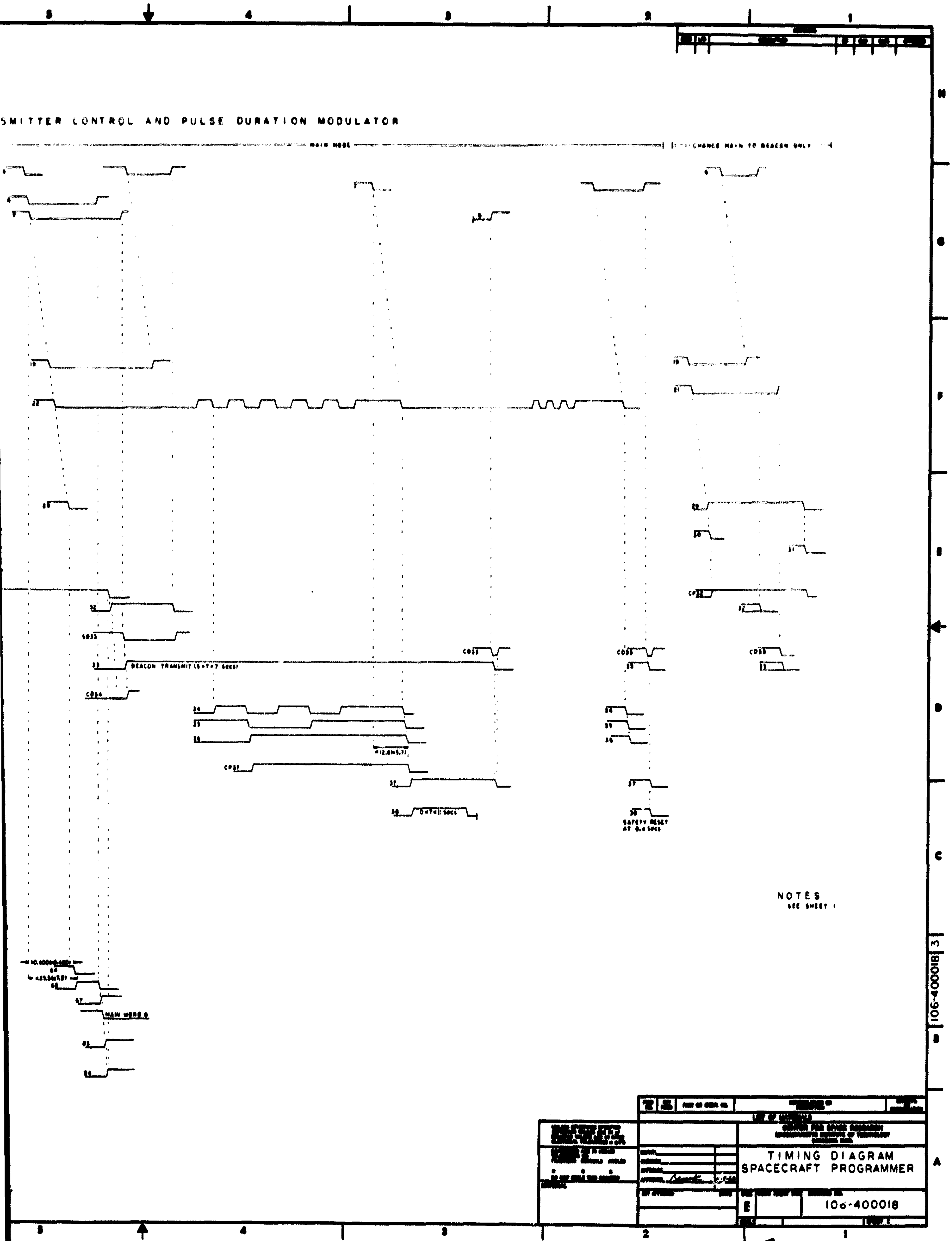

FOLDOUT FRAME 2

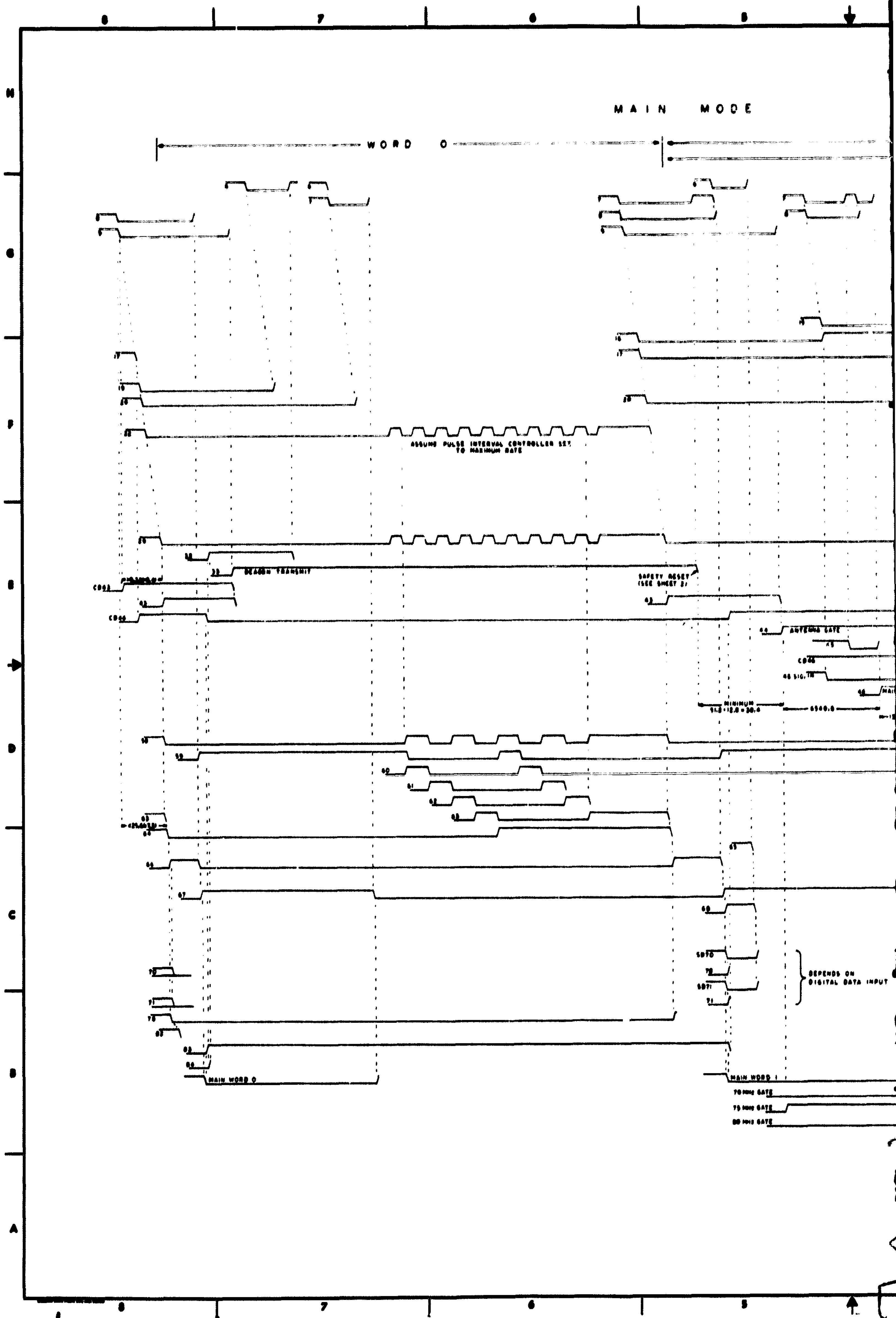

FOLDOUT FRAME 1

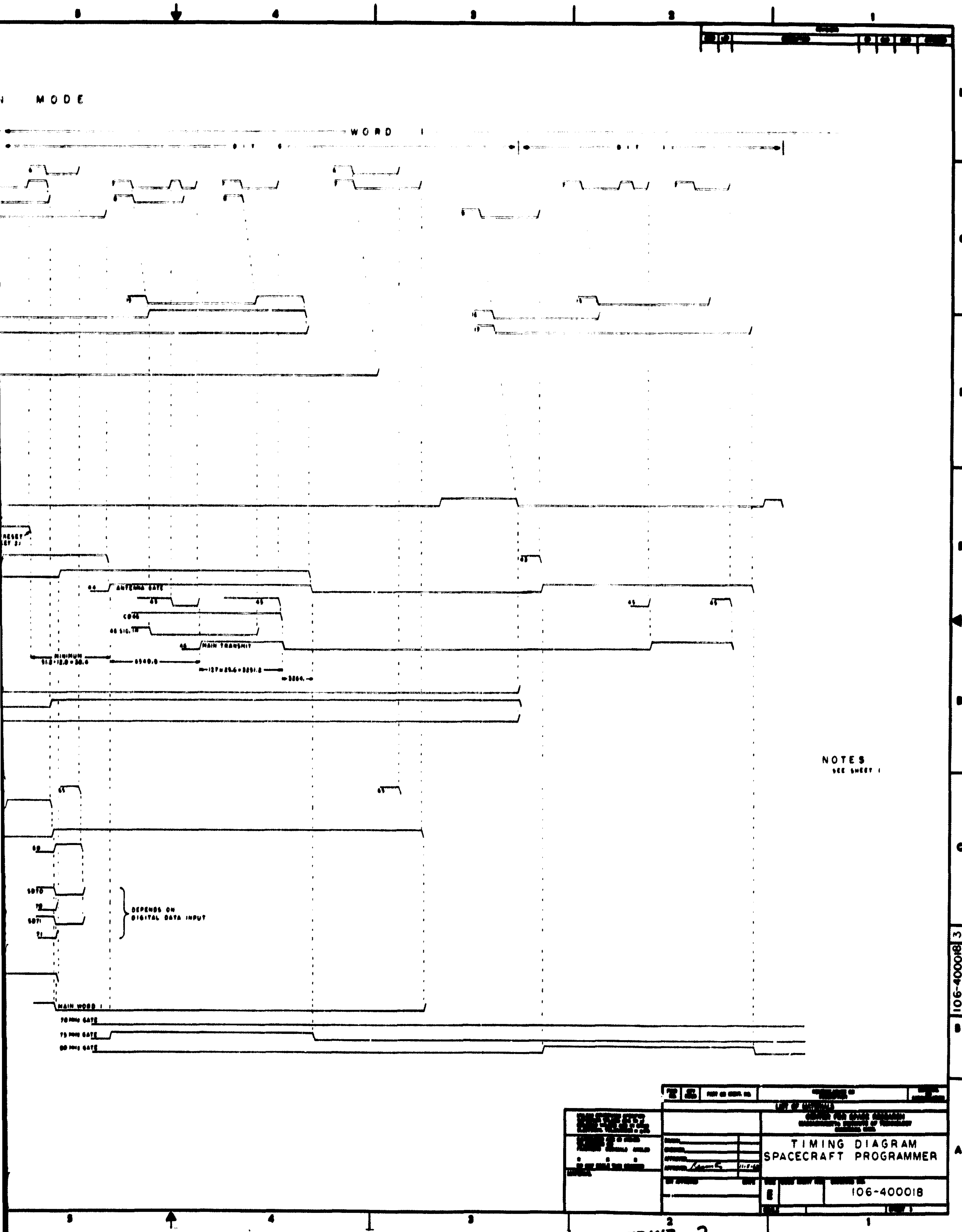

FOLDOUT FRAME 2

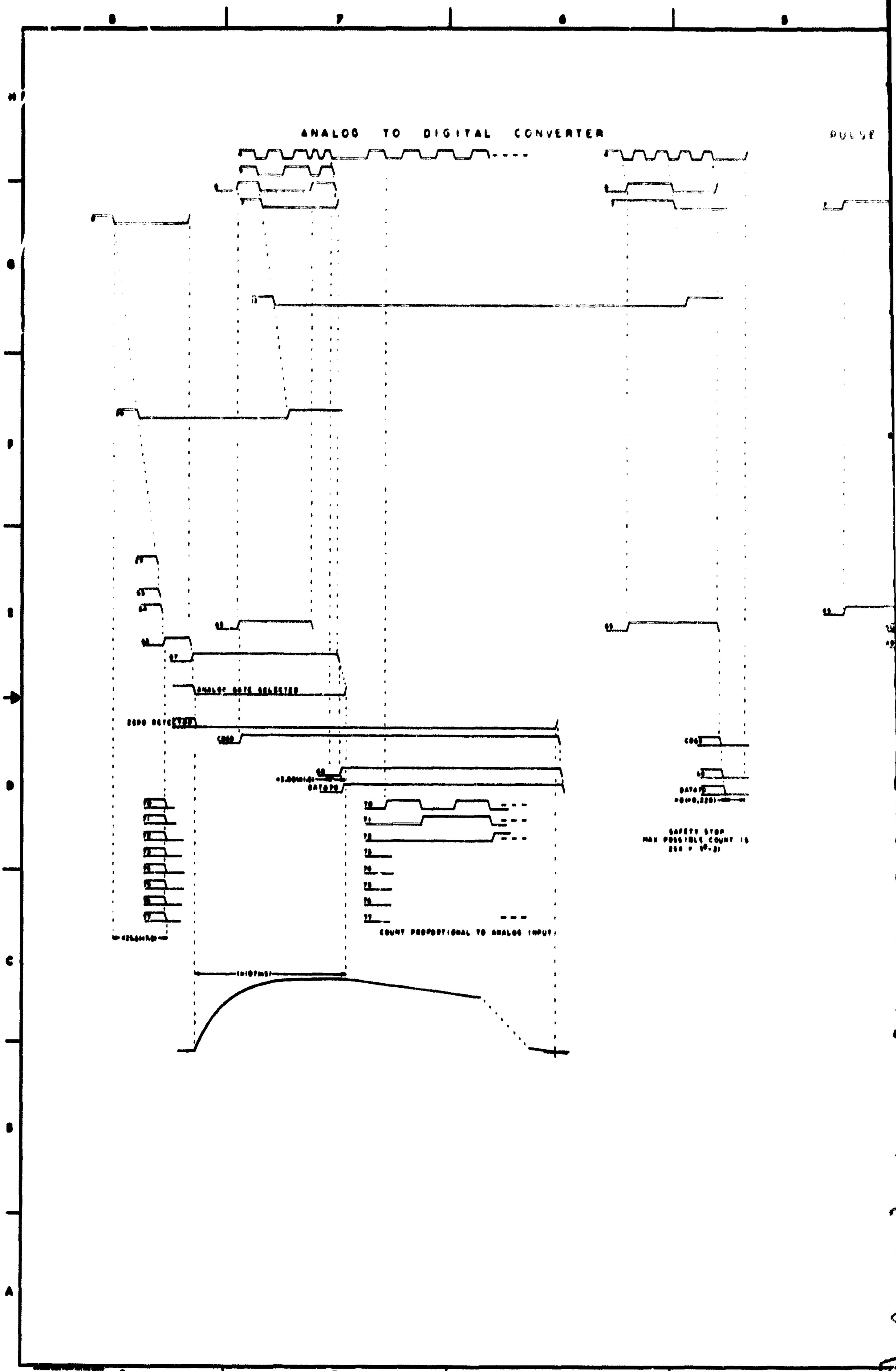

FOLDOUT FRAME

PULSE INTERVAL CONTROLLER AND PULSE SPACING COUNTER

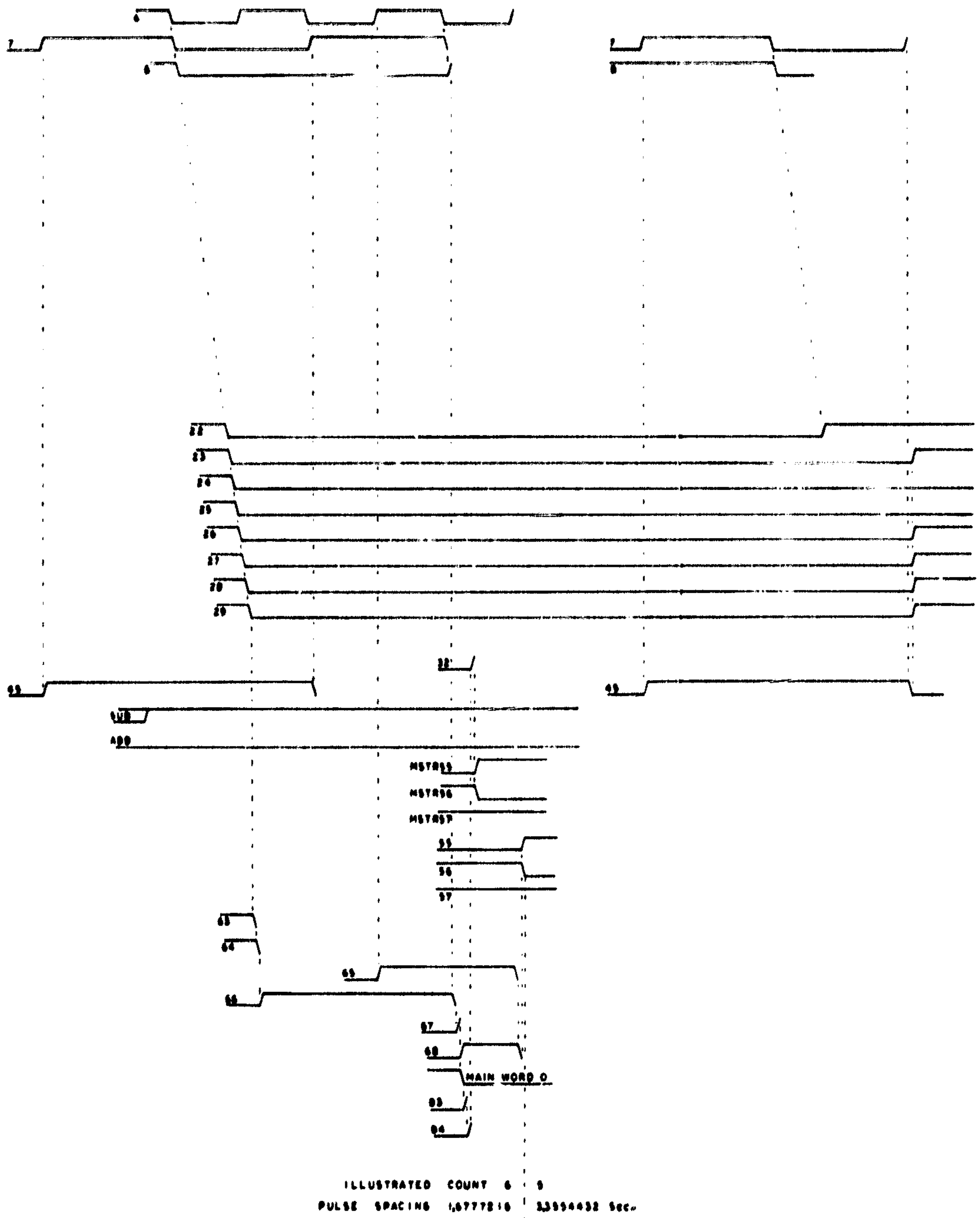

NOTES
SEE SHEET 1

LIST OF MATERIALS

CENTER FOR SPACE RESEARCH
MASSACHUSETTS INSTITUTE OF TECHNOLOGY
CAMBRIDGE, MASS.

TIMING DIAGRAM
SPACECRAFT PROGRAMMER

E

106-400018

SHEET 4 OF 4

106-400018 3

FOLDOUT FRAME 2

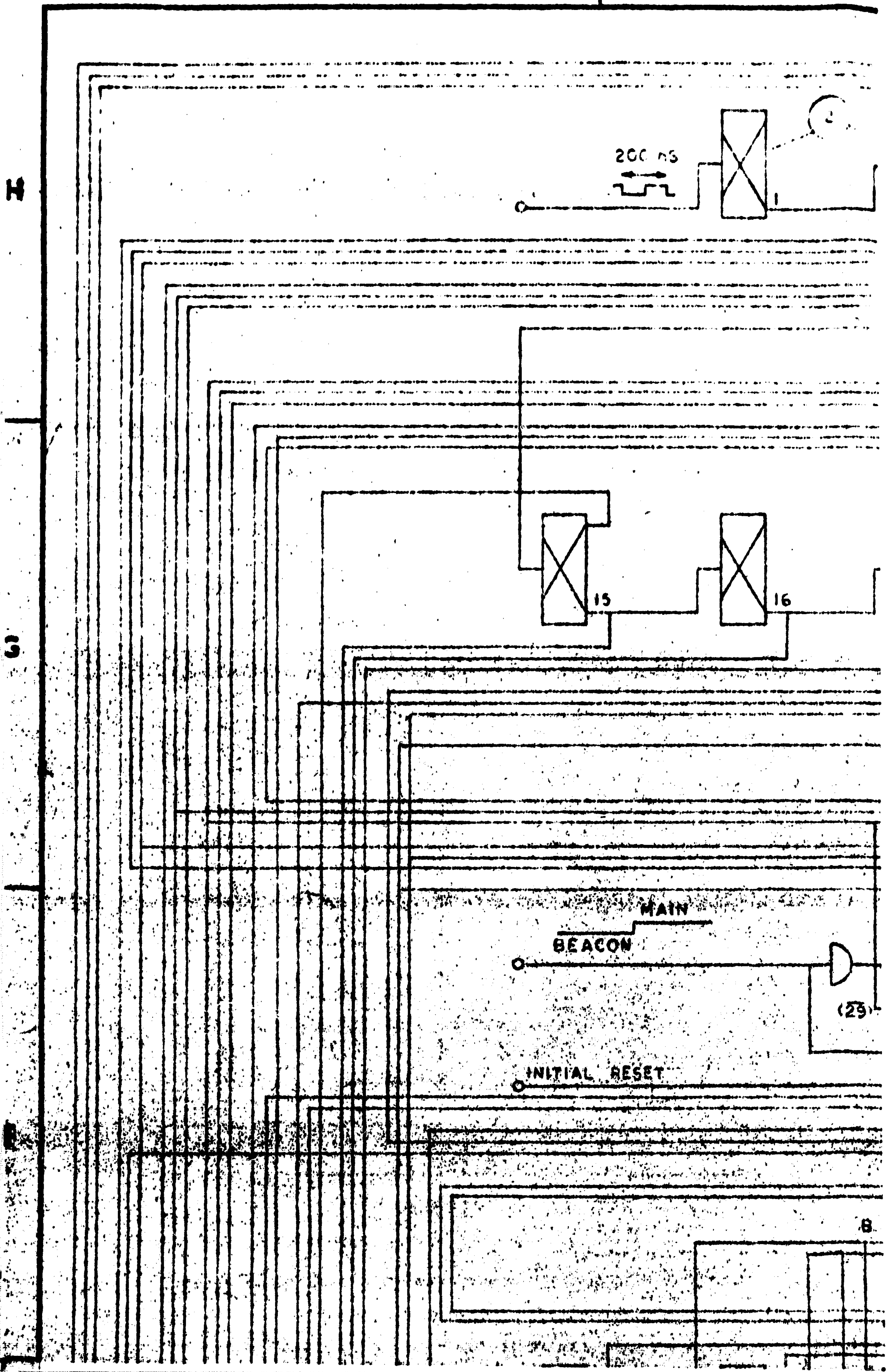
H
200 nS
1
15
16
G
MAIN
BEACON
(25)
INITIAL RESET
B

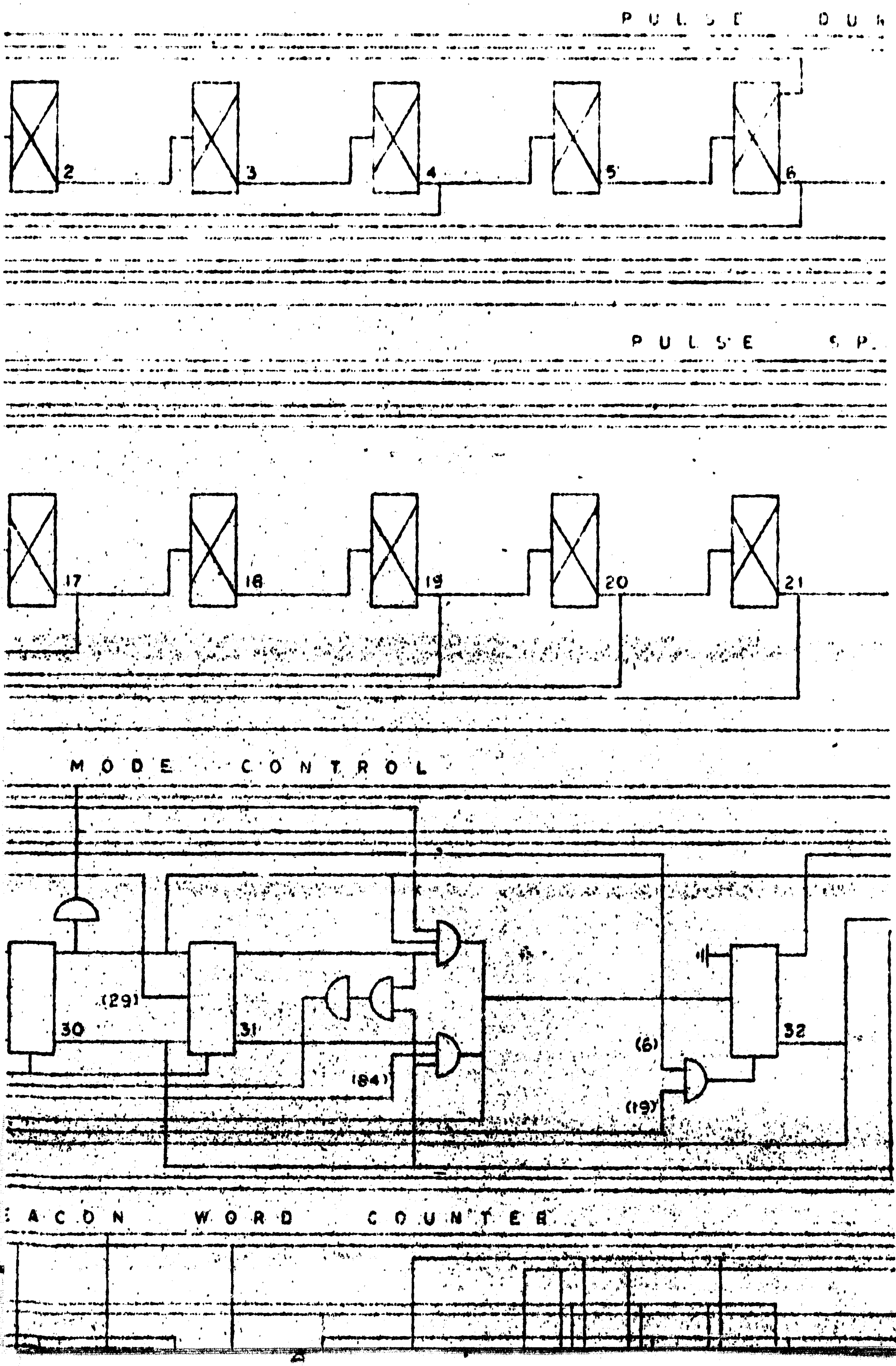
PULSE SP.
2
3
4
5
6
17
18
19
20
21
MODE CONTROL
(29)
30
31
32
(6)
(19)
(84)
ACON WORD COUNTER

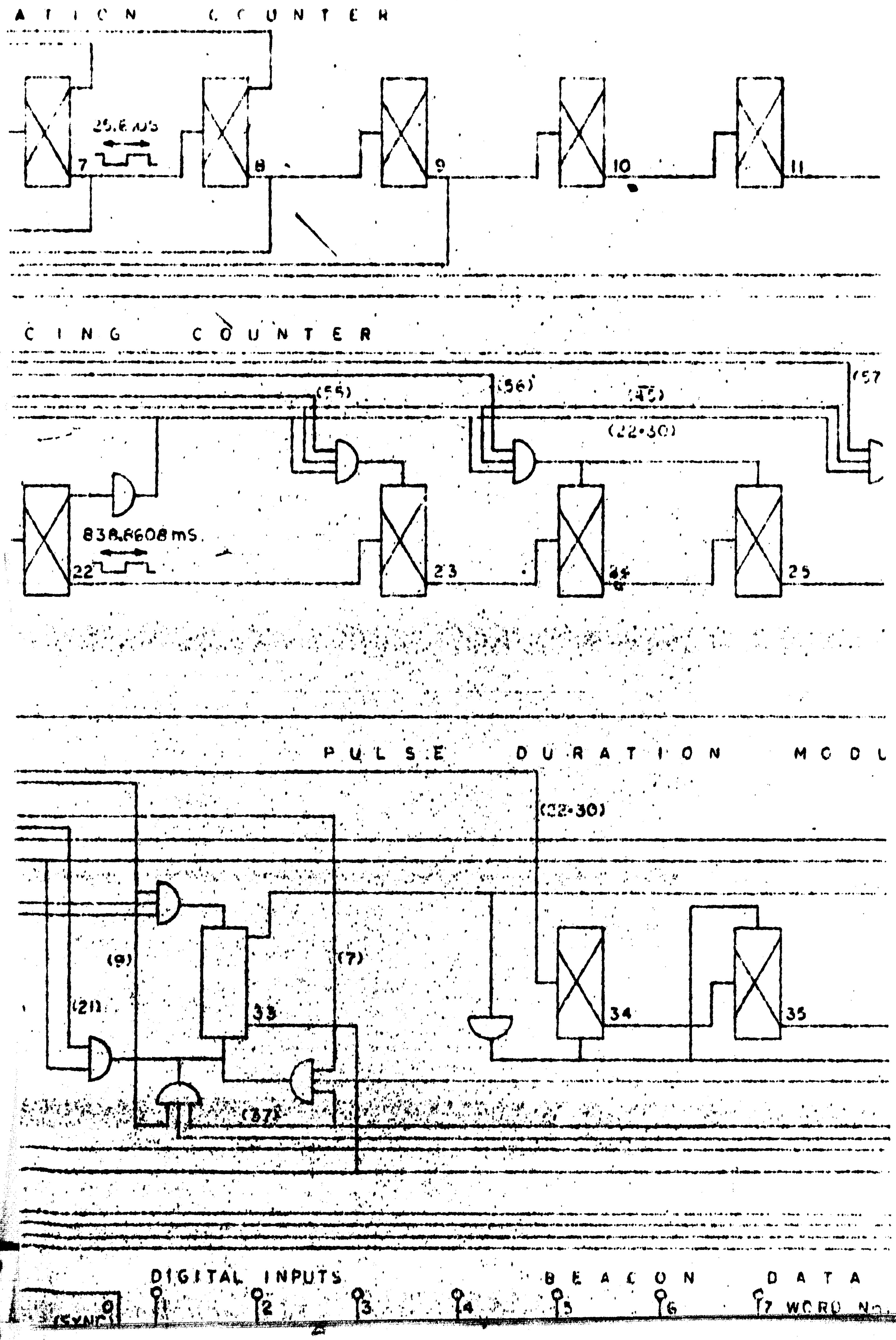
ATION COUNTER
25.6 µs
7
8
9
10
11
CING COUNTER
(55)
(56)
(45)
(22·30)
838.8608 ms
22
23
24
25
PULSE DURATION MODU
(22·30)
(9)
(21)
33
(7)
34
35
(37)
DIGITAL INPUTS
BEACON DATA
(SYNC) 0
1
2
3
4
5
6
7 WORD No.

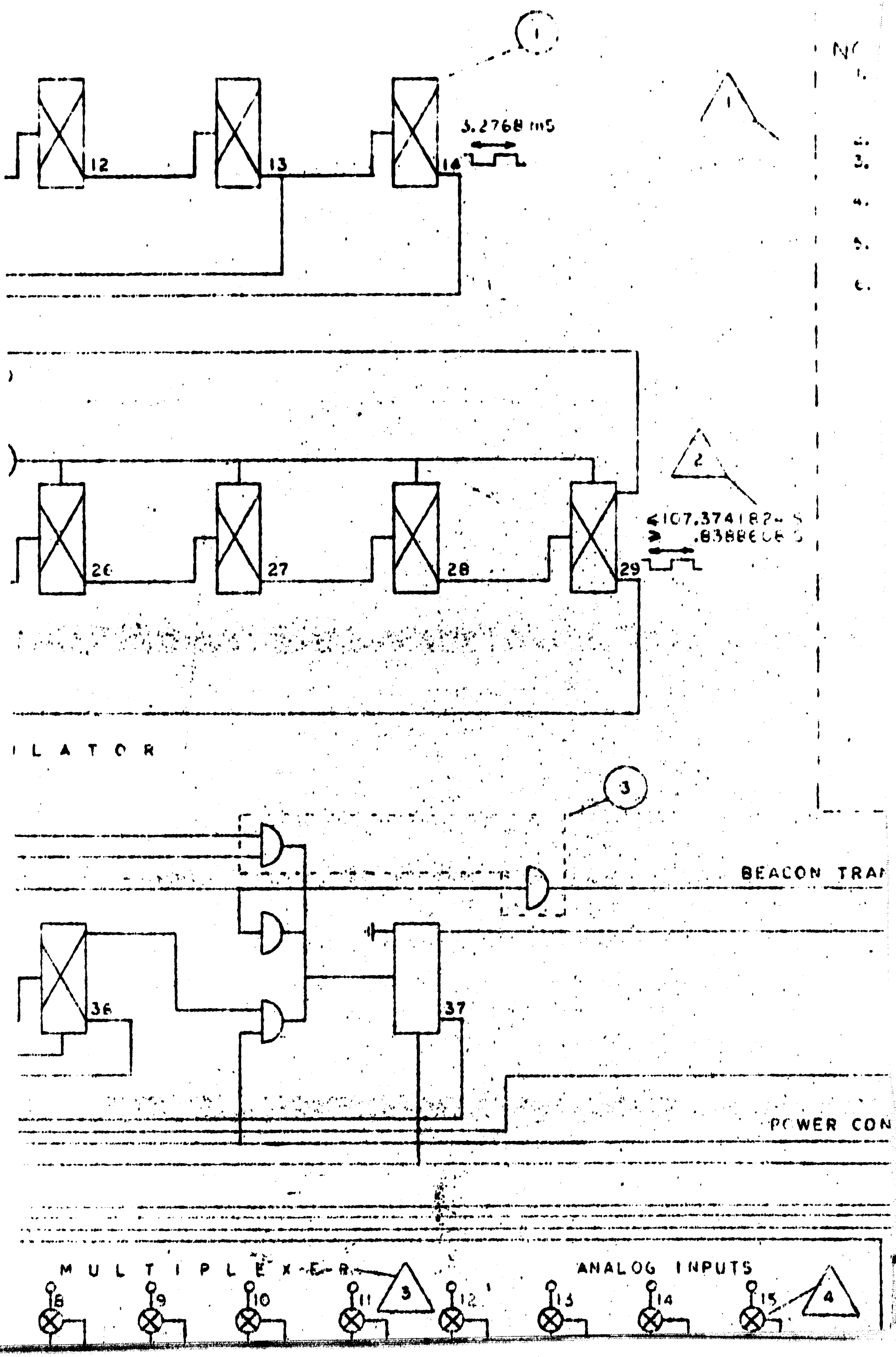
3.2768 mS
12
13
14
26
27
28
29
107.374182 S
.8388608 S
ILATOR
BEACON TRAN
36
37
POWER CON
MULTIPLEXER
ANALOG INPUTS
8
9
10
11
12
13
14
15

2

ZONE	LTR	DESCRIPTION

ES
LIST OF MATERIALS REFERS ONLY TO ITEMS TO LEFT OF THIS LINE
TIMES SHOWN ARE BASED ON 5 MHZ
PROPORTION OF ANALOG AND DIGITAL INPUTS MAY CHANGE
DISCRETE COMPONENT ANALOG GATE, MAY BE LOCATED REMOTELY
UNUSED PINS ON ITEMS 1,2 AND 3 MUST BE LEFT BLANK
ABOVE THIS LINE USE Vcc(BATTERY)
BELOW THIS LINE USE Vcc(MAIN)

FOLDOUT FRAME 5

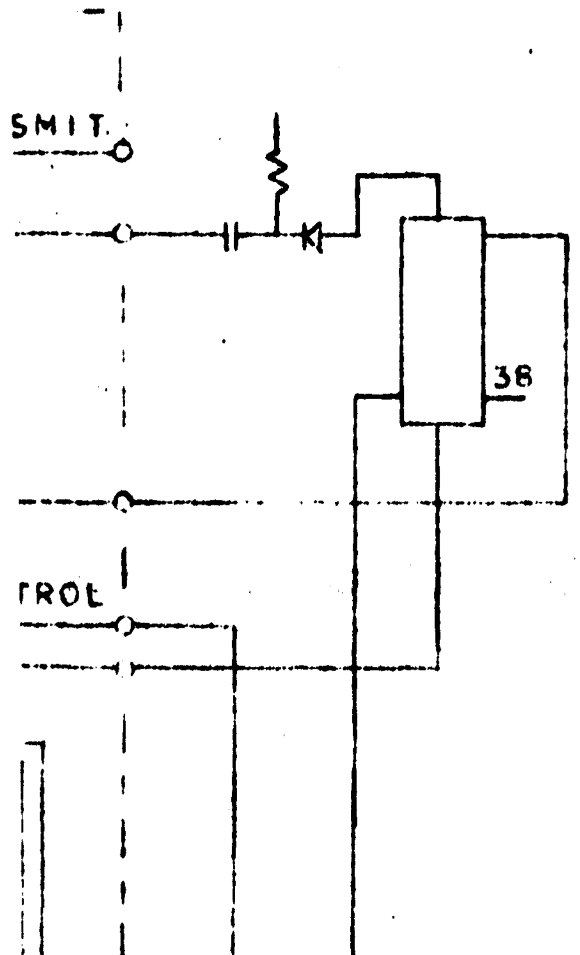

1

REVISIONS				
	DR	CHK	DATE	APPROVED

FOLDOUT FRAME 6

H

G

F

FOLDOUT FRAME 7

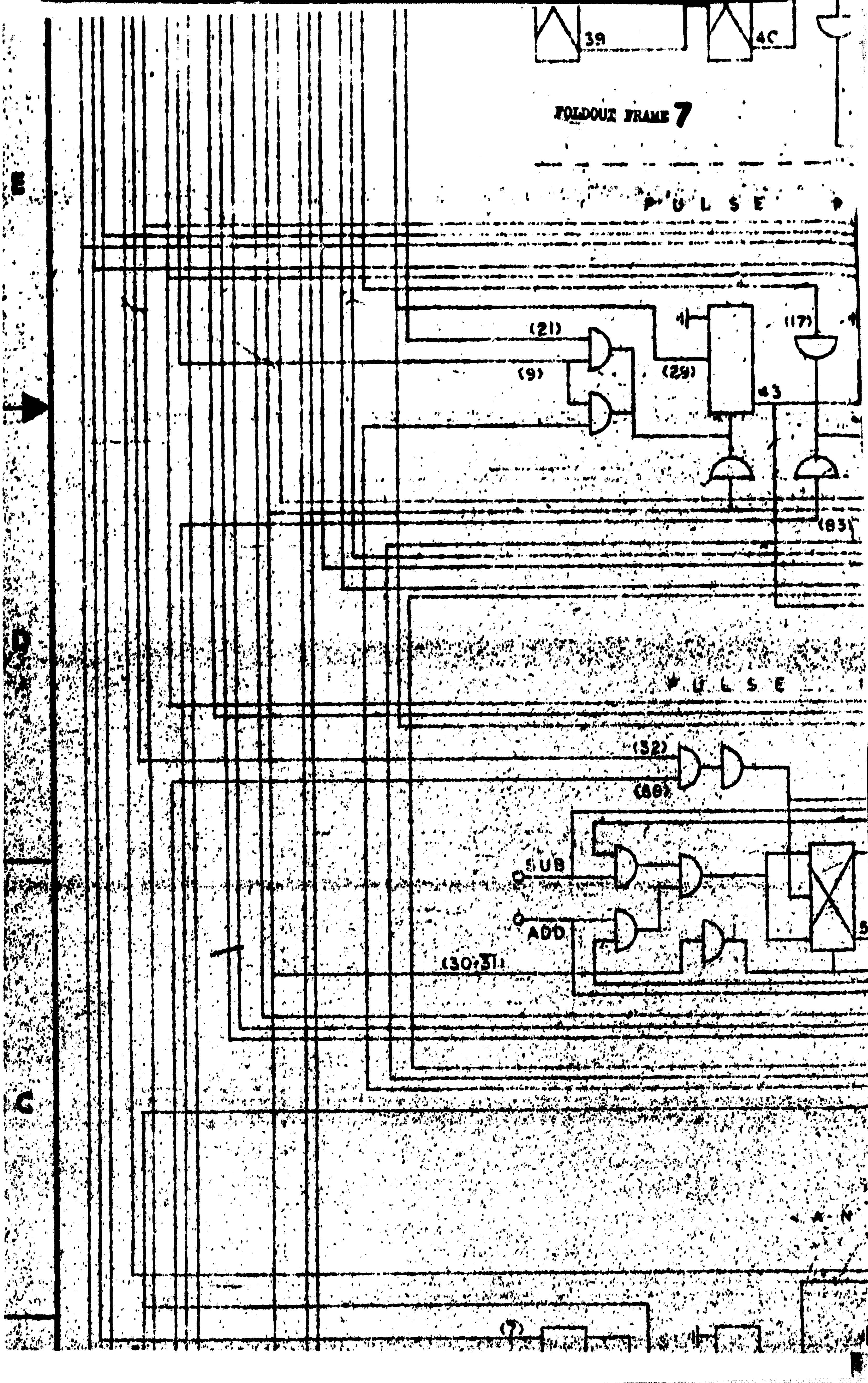

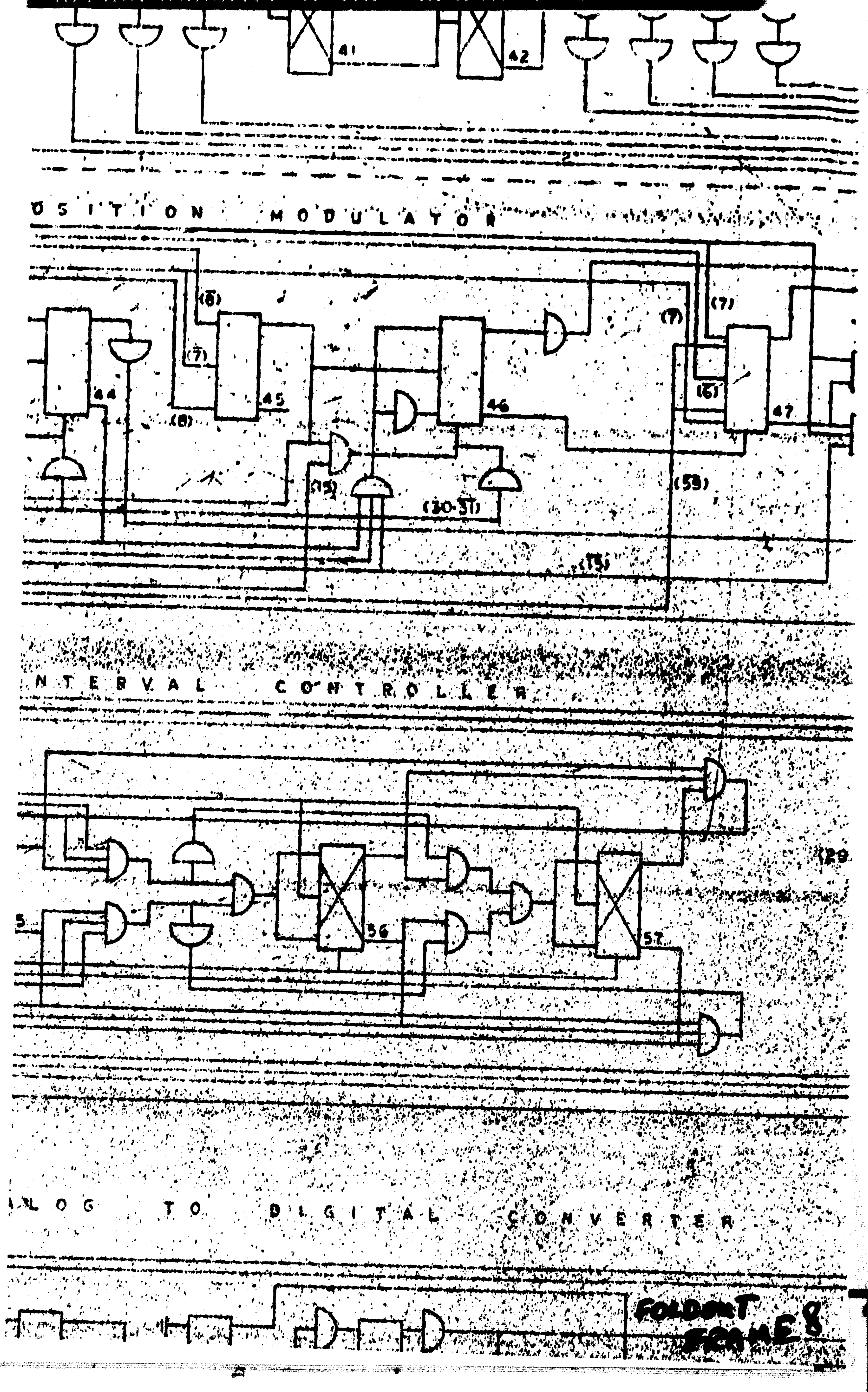
41
42
OSITION MODULATOR
44
45
46
47
(8)
(7)
(6)
(15)
(30-31)
(55)
NTERVAL CONTROLLER
56
57
(29
LOG TO DIGITAL CONVERTER
FOLDOUT FRAME 8

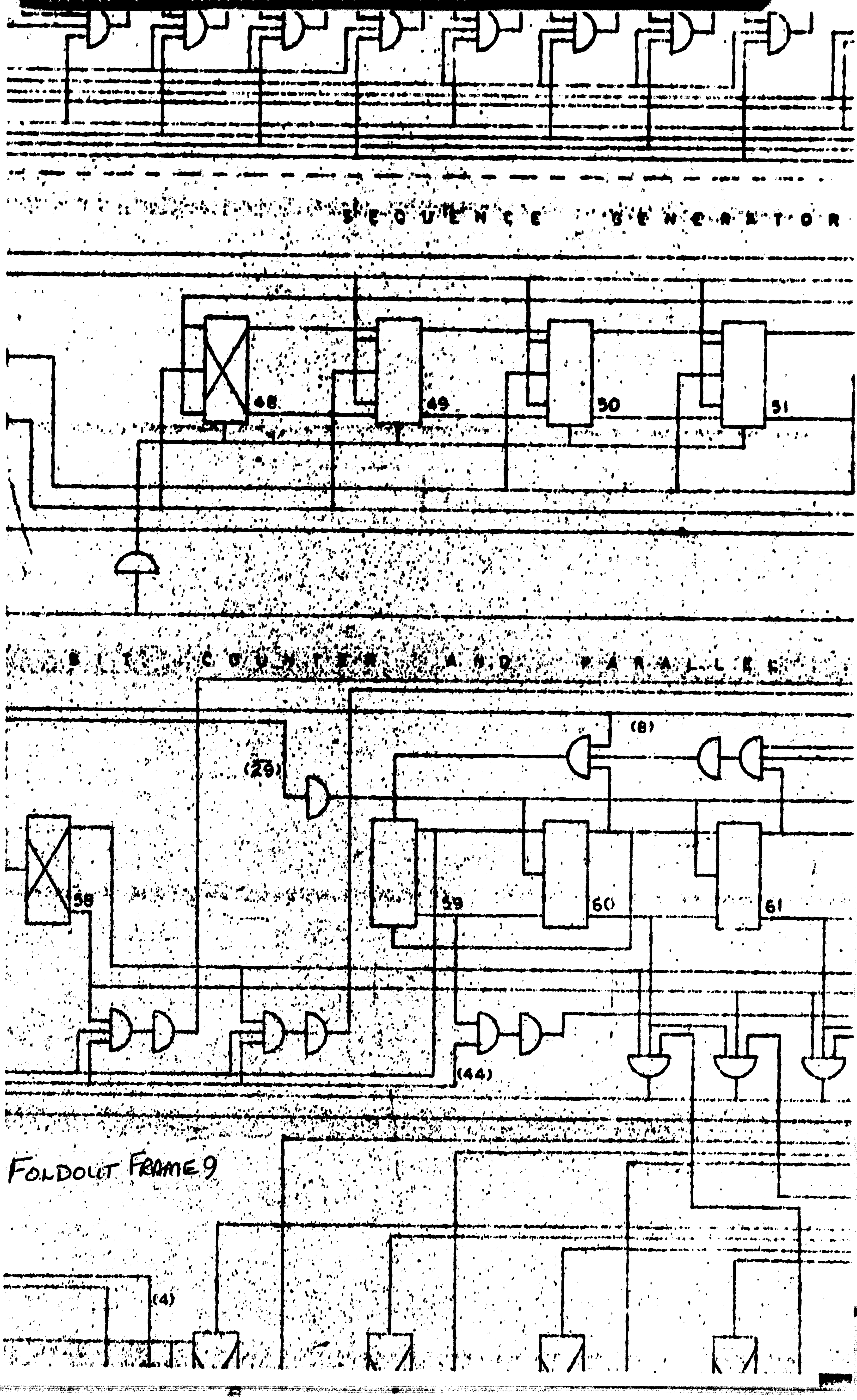
SEQUENCE GENERATOR
48
49
50
51
BIT COUNTER AND PARALLEL
(8)
(29)
58
59
60
61
(44)
FOLDOUT FRAME 9
(4)

FOLDOUT FRAME 10

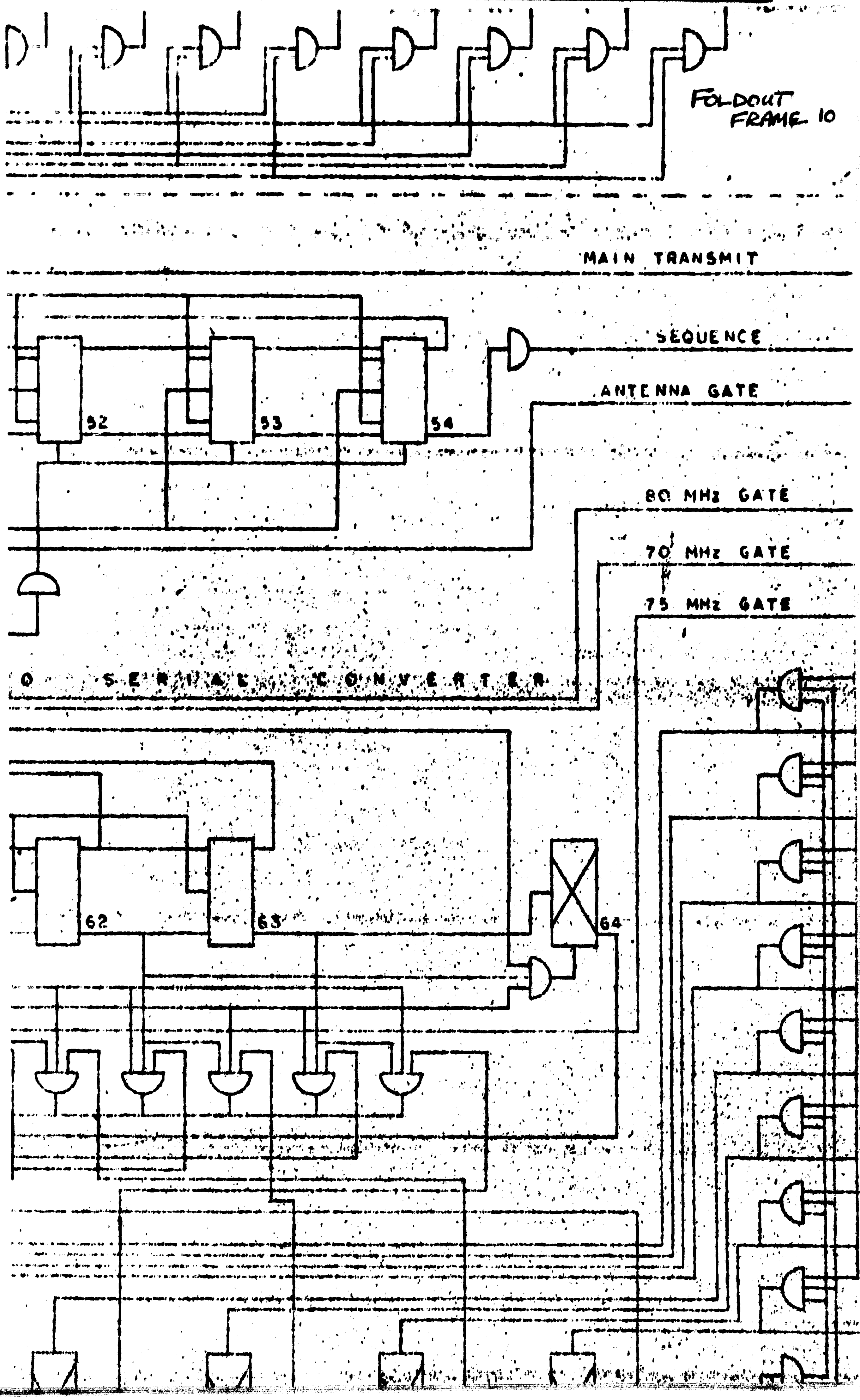

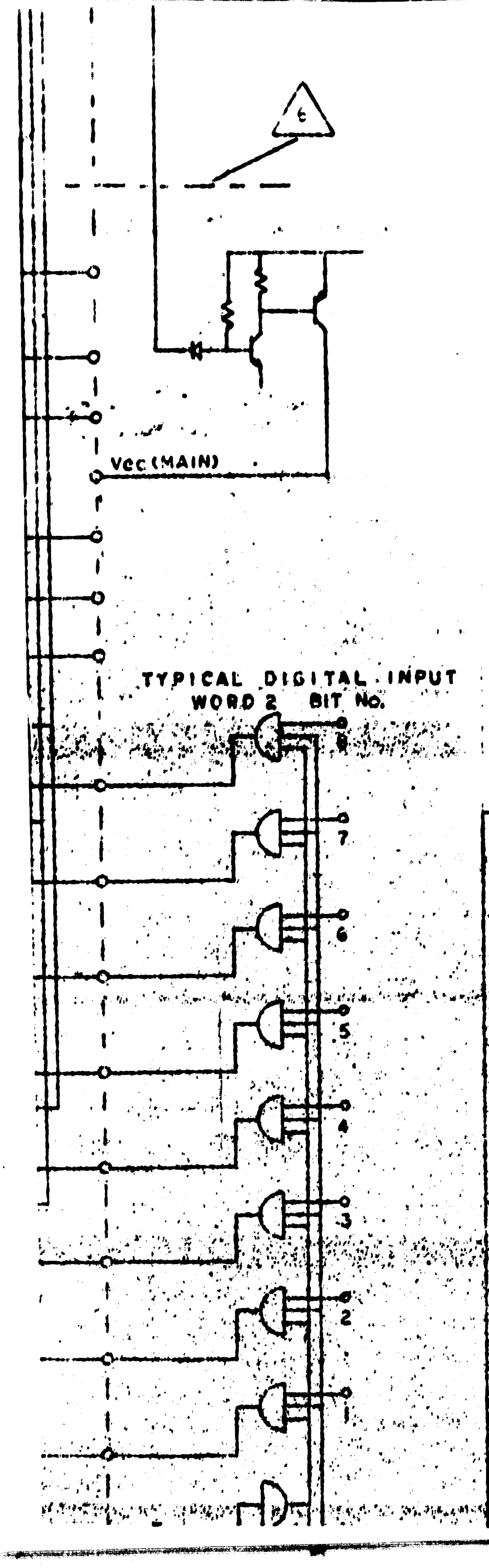

3	87	ALL GATES	FAIRCHILD L PIN CONNECTI PINS 4, 5 AND PINS 11, 12 A BOTH SECTION INTERCHANGEA AFTER WIRING ADDITIONAL C MADE AS FOLL PIN 2 MAY BE PIN 9 MAY BE
2	2	FLIP FLOPS 1, 2	DTL945 PIN CONNECTI

FOLDOUT FRAME 12

E

PDTμL9041 OR AMELCO 6041BH
ONS:

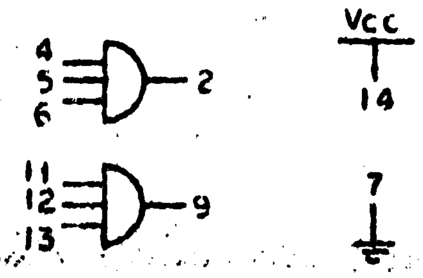

6 ARE INTERCHANGEABLE
ND 13 ARE INTERCHANGEABLE
S ARE IDENTICAL AND
BLE
LAYOUT IS COMPLETED,
ONNECTIONS WILL
OWS:
STRAPPED TO PIN 1 OR 3
STRAPPED TO PIN 8 OR 10

C

INS:

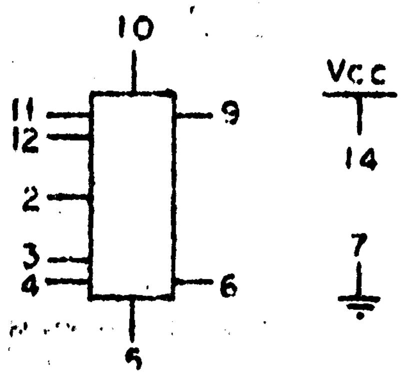

4

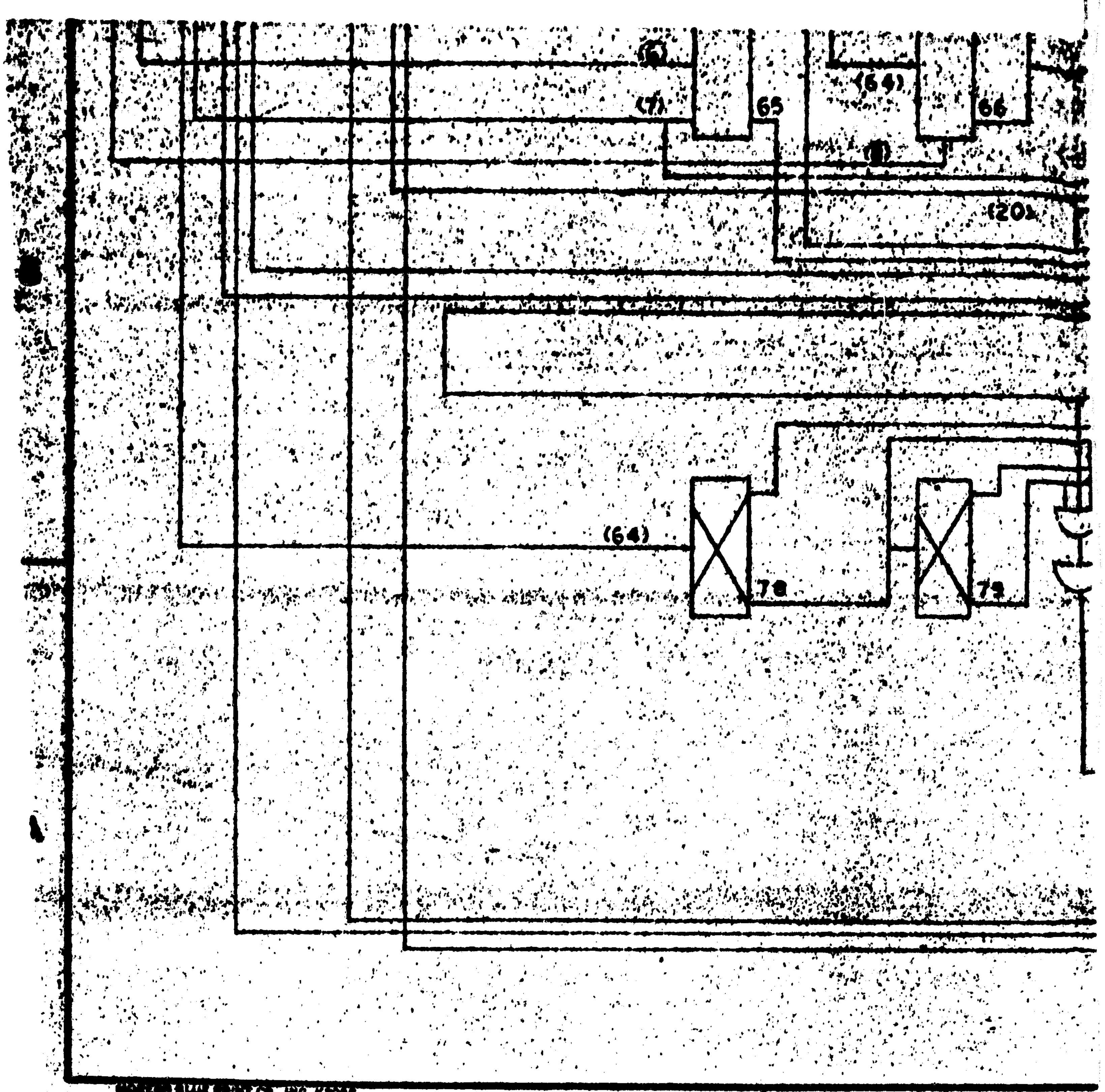
(6)
(64)
(7)
65
66
(8)
(20)
(64)
78
79

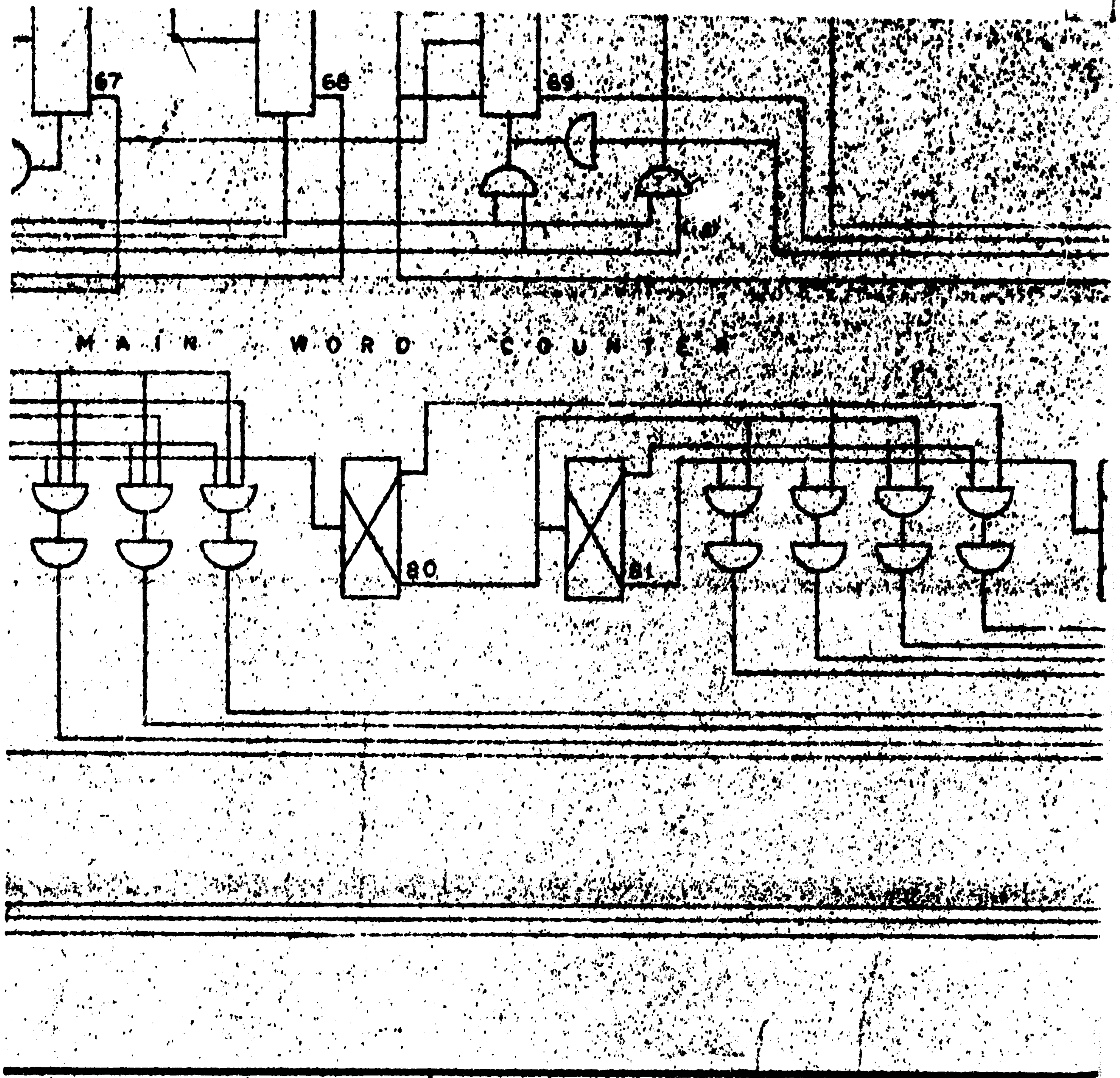
67
68
69
MAIN WORD COUNTER
80
81

FOLDOUT FRAME 15

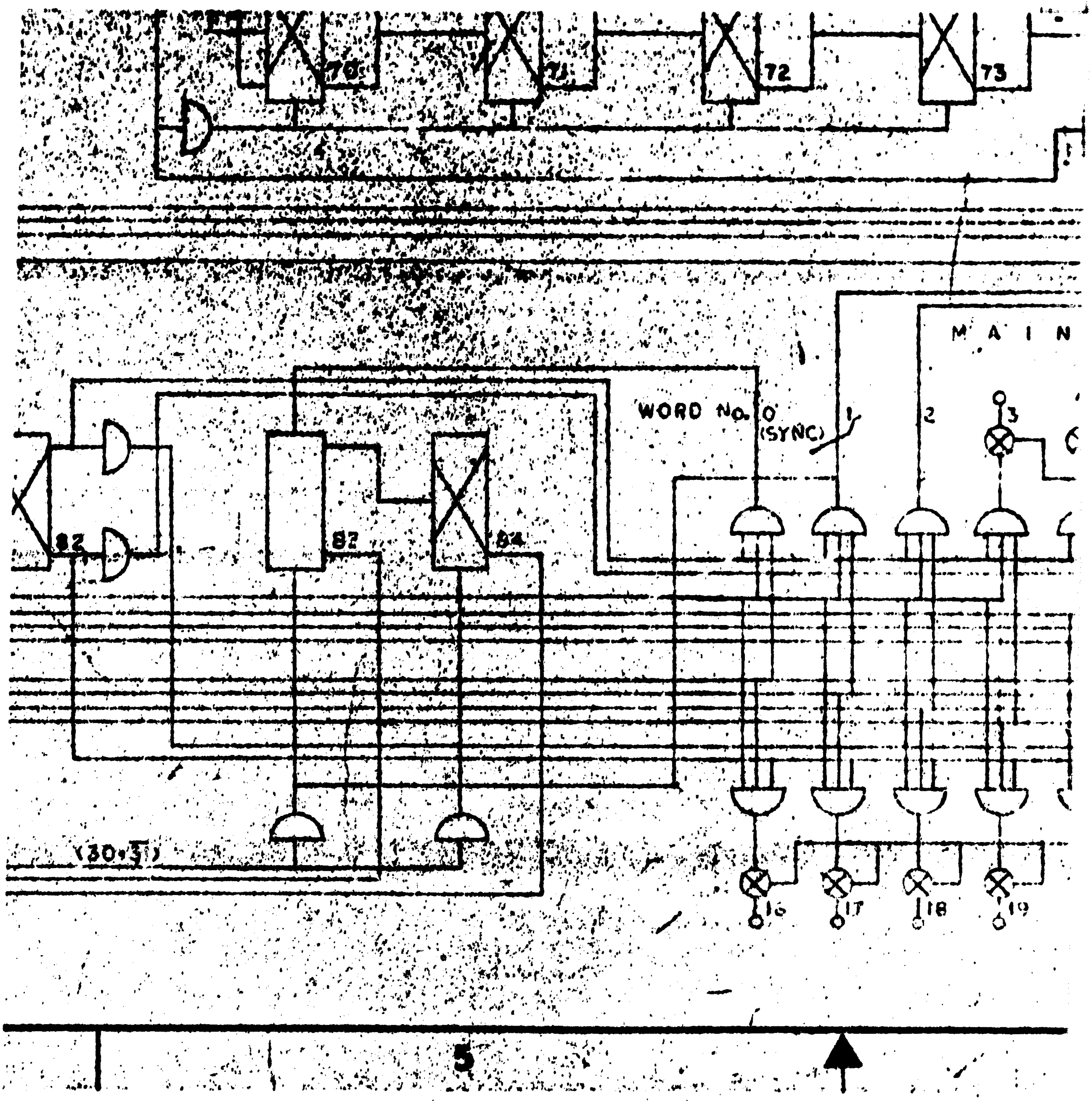

FOLDOUT FRAME 16

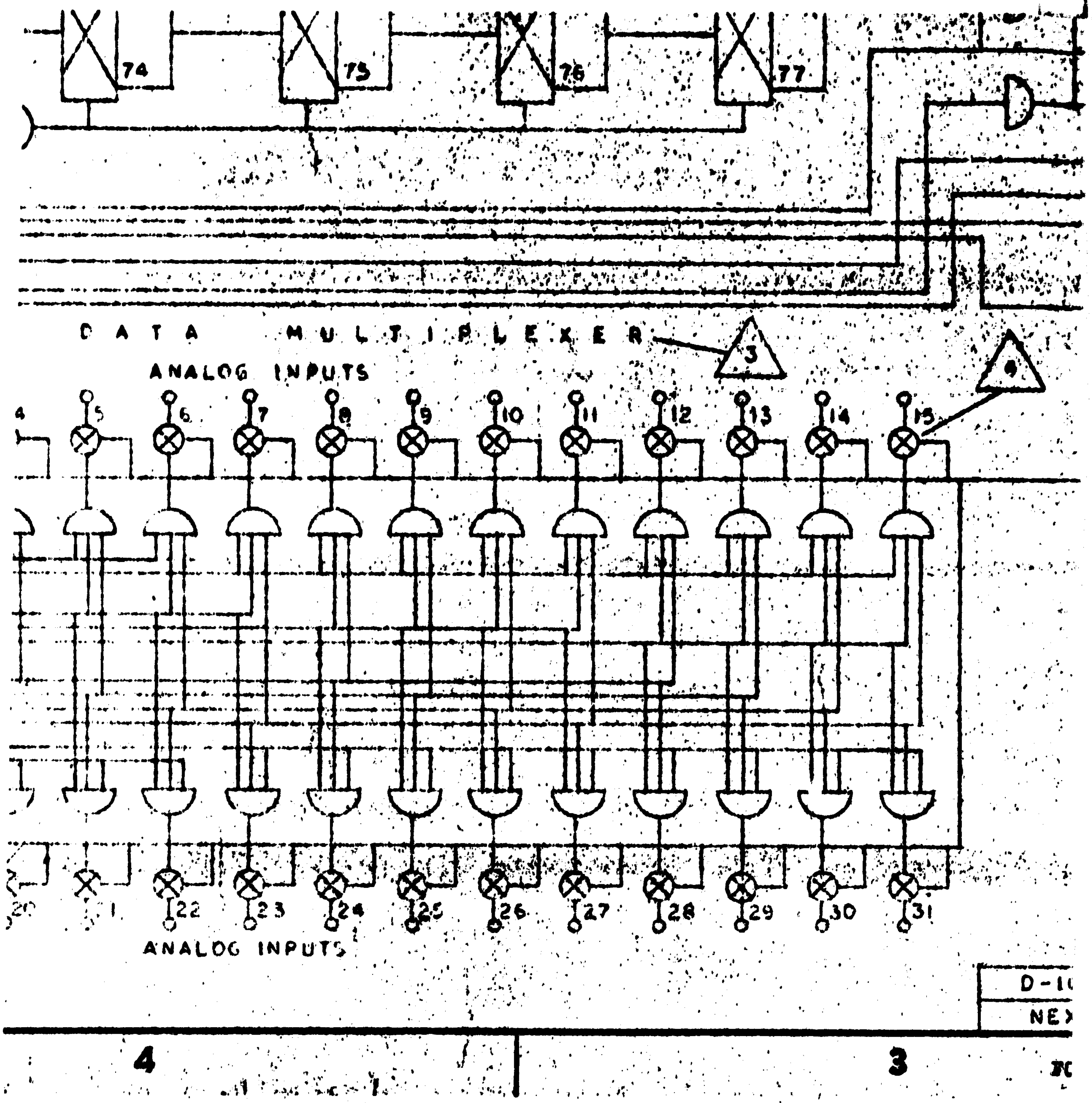

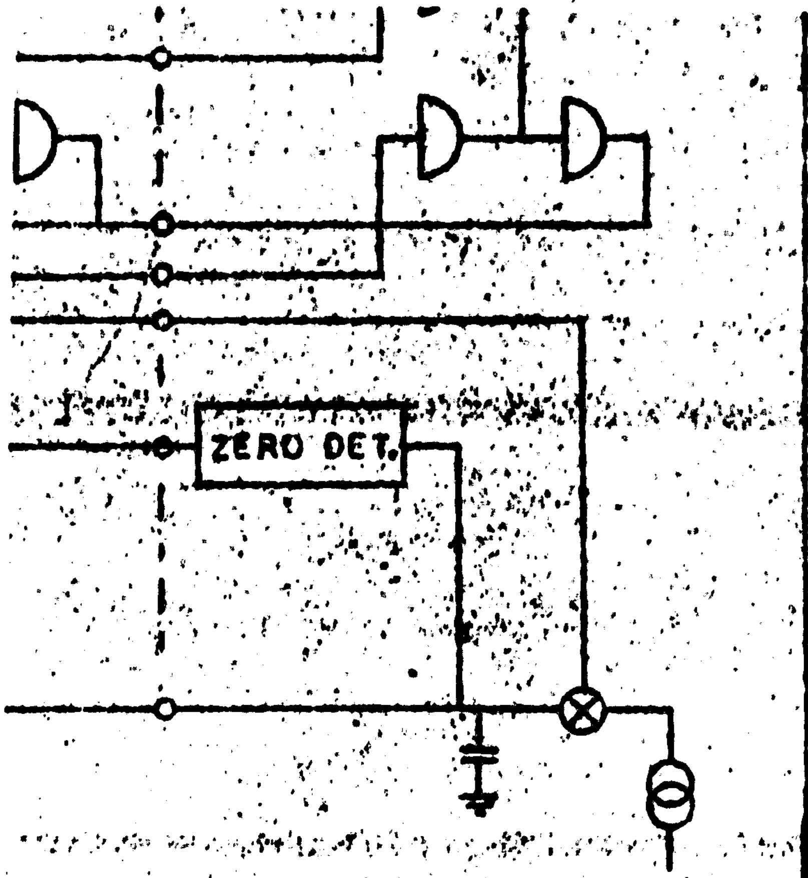

			PINS 3 AND PINS 11 AN
1	81	ALL FLIP FLOPS EXCEPT 1, 2	FAIRCHILD PIN CONNECT PINS 2 AND PINS 12 AND
	REF	E-106-400018	TIMING DGRM
FIND NO.	QTY REQD	PART OR IDENT. NO.	

LIST OF M

UNLESS OTHERWISE SPECIFIED
CAPACITOR VALUES ARE IN μf
RESISTOR VALUES ARE IN OHMS
ELECTRICAL TOLERANCES = ±5%

DIMENSIONS ARE IN INCHES
TOLERANCES ON
FRACTIONS DECIMALS ANGLES
± ± ±
DO NOT SCALE THIS DRAWING

MATERIAL

DRAWN
CHECKED
APPROVED
APPROVED Bennett 11-5-68

MIT APPROVED DATE

MA

L
SPACEC

SIZE E
CODE IDEN
SCALE

6-400001
T ASSY

I ARE INTERCHANGEABLE
12 ARE INTERCHANGEABLE

FDTµL9040 OR AMELCO 6040BH
IONS:

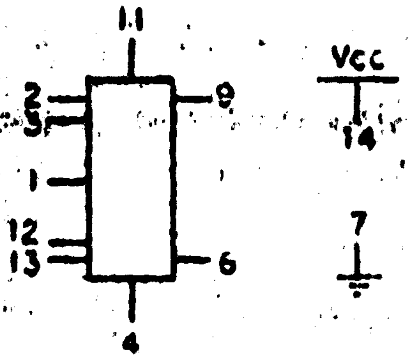

5 ARE INTERCHANGEABLE
13 ARE INTERCHANGEABLE

, SPACECRAFT PROGRAMMER

NOMENCLATURE OR DESCRIPTION	MATERIAL OR SPECIFICATION

TERIALS

ENTER FOR SPACE RESEARCH
ACHUSETTS INSTITUTE OF TECHNOLOGY
CAMBRIDGE, MASS.

OGIC DIAGRAM
RAFT PROGRAMMER

NO.	DRAWING NO.
	106-400017

SHEET 1 OF 1

106-400017

B

A

CHAPTER 5

5.0 GROUND ARRAY

5.1 Function of the Ground Array

From a systems point of view, the Sunblazer ground array may be considered a linear-active transducer. Regarded as such, the array provides coupling between an incident radiation field, originating from the spacecraft, and earth-station data-processing equipment. Thus the array must interface with the on-board electronics system and the correlation receiver, both of which are described in other sections of this document. The antenna itself is characterized by its effective area or gain, frequency response, polarization, noise characteristics and tracking capability. The interrelationship of these quantities with the on-board electronics and the correlation receiver is given below, followed by a brief description of additional uses and capabilities of the array system. Section 5.2 presents a systems analysis of the array; Sec. 5.3 is a detailed description of the Sunblazer array electronic organization and hardware.

5.1.1 Relationship to the Sunblazer Spacecraft

To be compatible with the Sunblazer communications system, antenna characteristics such as gain and noise figure must be maintained at the frequencies radiated by the on-board transmitter, plus an allowance for modulation bandwidths and dispersion due to Doppler, attenuation and plasma effects. Three specific frequency bands are of primary interest:

Table 5-I

Signal frequency bands.

69.72 MHz ± 500 KHz
74.70 MHz ± 500 KHz
79.68 MHz ± 500 KHz

Since it is impractical to provide separate band-tuning networks for each of the frequency bands, the array system is being designed to operate over the range 69.2 MHz to 80.2 MHz.

In addition to bandwidth considerations, the polarization of the transmitted signal from the spacecraft is of some importance. The on-board antenna is linearly polarized, but the radiating elements rotate at a mean angular velocity of about 1 rpm with respect to a fixed direction in the plane of the receiving array. The resulting polarization of the received energy varies with time. In addition, expected Faraday rotation effects will cause displacement of the received electric field vector. Therefore, to insure a maximum received signal and to estimate the effects of Faraday rotation, the ground array must be capable of receiving two orthogonally polarized waves. For the remainder of this paper, a dual cross-polarized array is assumed unless explicitly stated otherwise.

5.1.2 Relationship to the Correlation Receiver

The output of the array must interface with the correlation receiver. This interface may be considered a low noise mixer which coherently translates the received and amplified RF signals to video. At this point the signal is again amplified and made available to the correlation receiver. In order to preserve the accuracy of the propagation experiment data, the energy-signal-to-noise ratio of the signal supplied to the correlation receiver must be maintained as high as possible. This requirement implies the following constraints upon the array for all frequencies and view-times of interest.

1. The array gain must be maintained as high as possible (50 dB).
2. The overall noise figure must be as low as possible (approximately 5 dB).
3. Intermodulation and cross-modulation products must be held to a minimum, and system dynamic range must be high.
4. All losses, regardless of origin, e.g., mutual coupling, mismatch or attenuation, must be held to a minimum.
5. Pattern grating lobes and side lobes must be held to a minimum.

More quantitative values will be given in Sec. 5.2 and 5.3 for these system parameters. For the present, it should be noted that every design compromise which reduces the array gain or increases its system noise contribution reduces the accuracy of the data output of the correlation receiver.

5.1.3 Other Uses for the Ground Array

Because of the stringent requirements imposed upon the array by the propagation experiment, the antenna system is not limited to data acquisition and tracking of the Sunblazer, but is a sensitive radio telescope in its own right. The additional advantages of the array have been detailed elsewhere [1]. The following is a summary of the additional array uses:

1. It can serve as radiometer for the observation of the newly-discovered pulsars.
2. By the addition of power amplifiers at each element the array would become a radar telescope for a future uplink station to Sunblazer.
3. As a solar radar, improved sensitivity and resolution would make it possible to resolve quadrants of the solar disk in Doppler and Doppler broading radar observations.
4. As a planetary radar, this instrument could detect the planet Jupiter, and could make observations of venus and Mars at a much lower frequency than has been used in the past [1].

5.2 System Considerations

5.2.1 Antenna Gain and Number of Elements

An overall antenna gain (G) of 50 dB (resulting from communication system considerations such as "free-space-attenuation loss" and propagation-delay measurement accuracy) is the primary design goal of the Sunblazer ground array This specification implies an effective collecting aperture, A_{eff}, of greater than 10^5 square meters ($A_{eff} = G \frac{\lambda_0^2}{4\pi}$, $\lambda_0 = 4$ meters). The beam width, which depends upon element spacing, is less than 0.6^o. An aperture having these characteristics obviously implies the use of an array of elements. The exact array dimensions and beam characteristics are dependent on the latitude of the site selected for the final array. The system outlined in this paper will be suitable for either El Campo, Texas site (latitude 29^o N) or Saint Croix, V.I. (latitude 17.5^o N).

In considering the problem of synthesizing a phased array to satisfy the conflicting requirements of high gain, wide bandwidth and low noise, two concepts are of fundamental importance: 1) the superposition principle, and 2) the pattern-multiplication rule. The superposition principle requires that, in the far field of an array of elements, the resulting field at a point is the vector sum of the fields due to the individual elements. The pattern-multiplication rule, as applied to an array of identical elements, states that the resulting antenna pattern of an array is the product of the element pattern and a polynomial characteristic of the array. The polynomial is commonly referred to as the array factor. In general terms the beam-pattern function $E(\theta, \phi)$ may be expressed as a product of the form:

$$E(\theta, \phi) = E_e A(\theta, \phi) \qquad (5.1)$$

where E_e is the element factor, and A is the array factor. When the array geometry is symmetric, Eq (5.1) may be used in simplified form, and permits a straightforward presentation of the salient features of the array.

However, the pattern-multiplication rule must be applied with caution since its use includes the implicit assumption that mutual coupling between elements may be neglected. The pattern of an element, in general, will change when it is brought in close proximity to other elements. "The fact that all elements are physically identical does not insure that all elements of the array have the same pattern."[2] When the array elements are spaced "far enough" apart and are highly directive, the superposition principle requires that the resultant array power-gain is merely the product of the number of elements in the array and the gain per element. In general, however, the array gain is a function of the element factor, the number of elements and the element spacing, as has been shown by several authors.[3, 4]

To a first-order approximation then, the gain of the proposed array is:

$$NG_E = 10^5 \qquad (5.2)$$

where N is the number of elements in the array and G_E is the power gain per element. If N is now restricted to values of the form 2^q where q is an integer, the element gain is also specified. Table 5-II gives the values of the total number of elements N as a function of the gain per element.

Table 5-II

Gain per element.

G_E (dB)	N
23	512
20	1024
17	2048
14	4096
11	8192

The value N = 4096 and G_E = 14 dB have been selected as a compromise between a very large number of elements and high gain per element. (In the final array N is made somewhat larger than 4096.)

The selection of the 14-dB element is of primary importance to the array design since it determines the general level of complexity of the electronics system. The actual description of array electronics is given in Sec. 5.3. However, there is a fundamental question of the physical realization of the 14-dB element: "Of the many types of element available in this frequency range, which element exhibits the desirable properties of low cost, wide bandwidth and high gain?" During the course of this program many antenna types were evaluated, and each was found to have limitations for array use. A detailed description of the evolution of the element design and selection is given in Sec. 1.3 of this report and in the document entitled "History and Design Summary, Sunblazer Phased Array".[5] In summary, a system parametric study was made for each of the element types, including a cost evaluation of mechanical and electrical array components. These cost-performance studies led to the following fundamental conclusion concerning the element:

> "The best method, in terms of satisfying the Sunblazer tracking requirements (both engineering and science) at minimum overall cost (initial installation, operation and maintenance) is to construct a cross-polarized wideband dipole array at El Campo, Texas."[5]

Details of the various costs are given in Ref. 5. Basically, it has beeen determined that a 14-dB antenna element arrayed through electronic means is less expensive and has better performance when constructed by connecting 6 dipole elements, as opposed to employing single or multiple backfire, yagis or helices. A detailed description of the 14-dB dipole element is given in Sec. 5.3.2. Figure 5-4 shows the physical layout of the 6-dipole (double tee) 14-dB element.

5.2.2 Frequency Sensitivity

Because of the relatively wide bandwidth of the array, system performance will, in general, exhibit frequency-dependent effects. Both the dipole elements and the overall array dimensions (as measured in wavelengths) are frequency-sensitive. However, both these frequency variations are of a second-order nature and will not be discussed in detail. There is a first-order frequency-sensitive effect associated with the beam steering that requires additional discussion since it is of fundamental importance to the method by which the electronic-phasing system is organized.

The general method of beam scanning is obtained as shown in Fig. 5-1. This figure indicates that properly chosen phase delays located at each 14-dB element will permit beam scanning to some desired angle. Consider now only the array elements along the x-axis with an energy incident at some

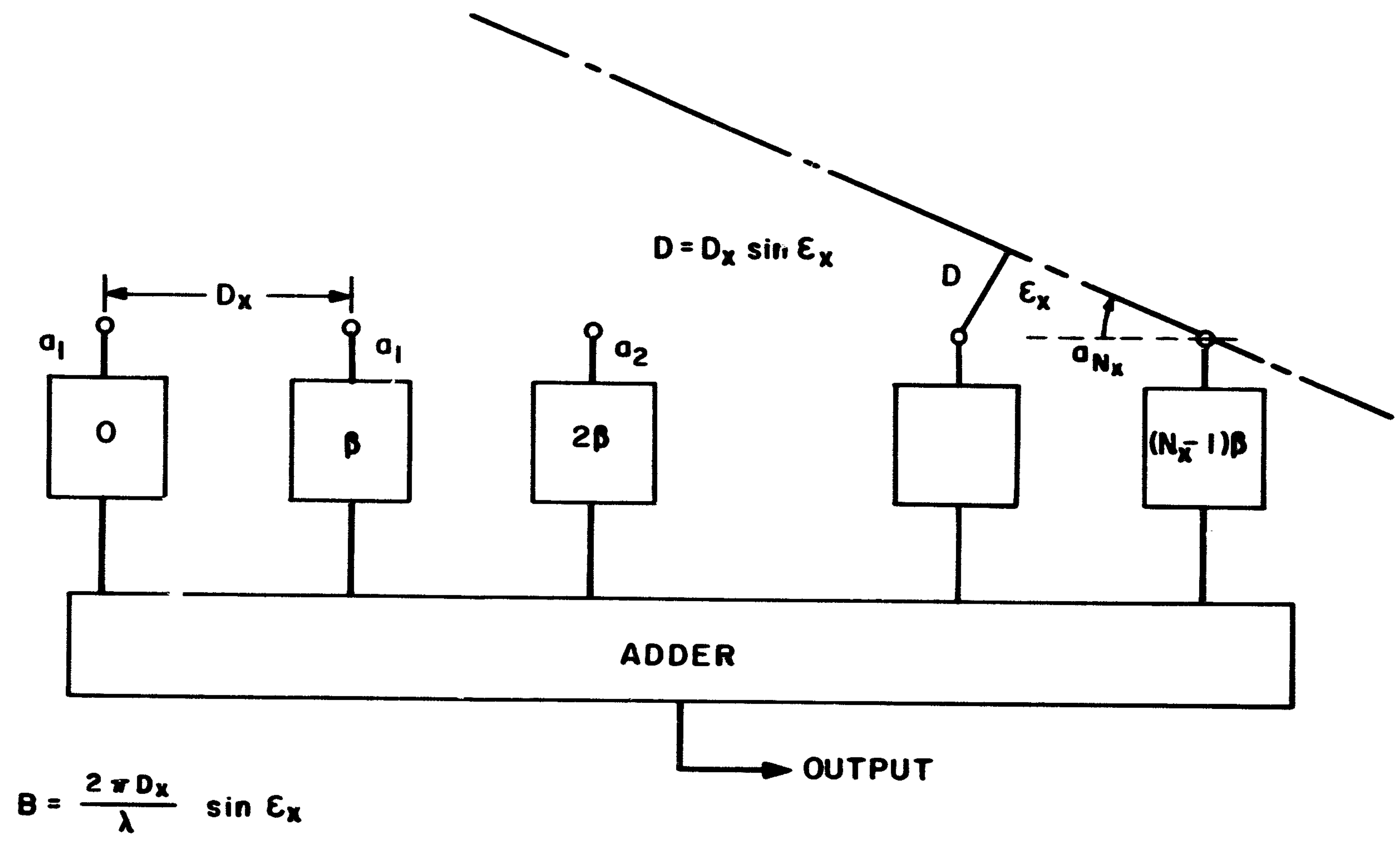

Fig. 5-1 Beam steering by progressive phase shifts.

angle ϵ_x. If it is desired to steer the beam in the direction ϵ_x, then a phase-delay taper, β, from element to element (progressive phase), must be supplied to each element where:

$$\beta = \frac{2\pi D_x}{\lambda} \sin \epsilon_x = \frac{2\pi D_x f}{c} \sin \epsilon_x \quad . \tag{5.3}$$

If the first element is the reference, the phase delay required at the second element is β, at the third element 2β, etc. Therefore, the required phase term at each element is linearly dependent upon frequency. To accomplish this frequency dependence, the device used to affect the phase change must have a linear phase-frequency characteristic over the frequency band of interest. A non-dispersive delay line exhibits this property, and its use as a phasing element will insure that the array beam will point in the same direction for all frequencies. The resultant system configuration is termed a delayed array as distinguished from a phased array in which frequency sensitivity is not important.[6] The Sunblazer ground array is a delayed array, and details of its electronic system organization are given in Sec. 5.3.

5.2.3 Noise Considerations

The concept of total system gain was of fundamental importance in the array aperture design since it set limits on the array electronics, dimensions, number of elements and element type. In an almost completely analogous way, the concepts of receiver noise temperature, T_r, and sky brightness temperature, T_B, are characteristic of the array system noise performance. There are several factors which contribute to these temperatures. Some of these, such as amplifier noise figure, are under the control of the system designer; while others, such as external man-made interference are not. This section will define some of the factors which contribute to the total system noise.

In the final array each 14-dB element will have its own amplifier. However, for noise-analysis purposes, it is sufficient to consider the entire array as one antenna followed by a single amplifier (as shown in the array system noise model of Fig. 5-2). Noise may enter the system or be generated by each of the components, the antenna, connecting cables and receiver. The major contributions to the system noise follow:

1. Background sky noise, characterized by the brightness temperature T_B. The intensity of this quantity is primarily a function of the system operating frequency. For the Sunblazer ground array an average value of 1850° is characteristic.

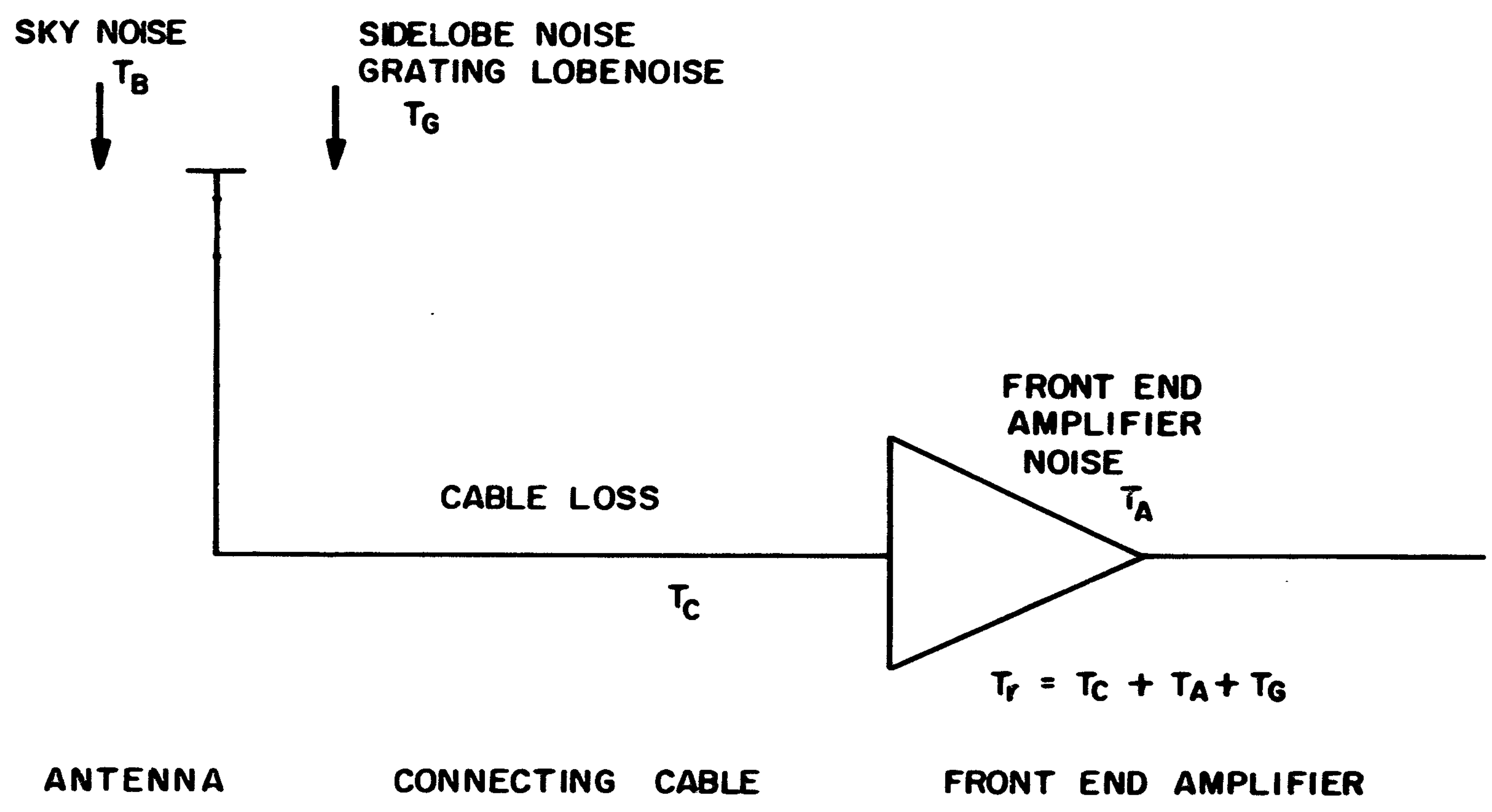

Fig. 5-2 Noise model.

2. Noise due to antenna side lobes and grating lobes pointing at galactic hot spots. An estimated value of this quantity is 200°.

3. Noise due to antenna element losses, cable losses, impedance mismatches and mutual coupling. These have been estimated as 1 dB or 75°.

4. Front-end amplifier noise. For the design under consideration a value of 3 dB or 290° is typical.

5. Spurious man-made noise entering the antenna at and near the desired signal frequencies. Additional noise may be added by intermodulation products due to high-level signals entering the amplifier. The exact specification of intermodulation depends upon local conditions, but as an example: for competing TV signals of the order 50μV, intermodulation products should be down by 80 dB for satisfactory system performance. It is clear that system dynamic range and low intermodulation distortion are related, and both are required for system linearity.

Neglecting the noise contribution due to intermodulation, the total receiver noise temperature is 565°. Therefore, the total equivalent system noise temperature is $T_r + T_B \simeq 2400° = T_s$. Because T_B is relatively large compared to T_r, improvements in T_r will have only second-order effects upon T_s. System noise performance will not substantially be improved by a reduction of T_r, but rather by the selection of a site in which local RFI is at a minimum.

Although discrete sky-noise sources may contribute to total system noise, they are useful in a practical way for antenna-calibration purposes. In the 50-dB array, the near field of the antenna $\left(\frac{2D^2}{\lambda}\right)$ extends to an altitude of approximately 100 kilometers above the surface of the earth. This distance is so large that only a system utilizing a satellite could be expected to perform conventional far-field pattern measurements. However, a radio star such as Cassiopeia A provides a solution for this measurement problem. The measurement is performed by directing the beam of the array toward a source of known intensity and spectral distribution. As the beam is allowed to pass through the source, the output of the array is a measure of the gain of the antenna elements, the electronics and the beamwidth of the antenna. This test is also an indication of the accuracy with which the beam may be steered. A similar method was used to test an experimental dipole receiving-array constructed at El Campo.

5.3 Description of the Proposed Arrays

In this section, the individual dipole design is shown. Following this description, there is a discussion of the element and how it is constructed, mounted in the ground, connected with its five neighbors to form a 14-dB antenna element, etc. Then, an outline of the electronics system necessary to form these individual 14-dB element into a 29-dB pilot array is presented. Section 5.3.4 indicates how the 29-dB pilot arrays are electronically joined to form an expanded 43-dB array. Section 5.3.5 briefly describes the final 50-dB antenna system concept.

5.3.1 The Individual Dipole Element

The individual dipole element is to be constructed from 3/4-inch OD aluminum tube, mounted on a treated wooden post by wax-impregnated wooden dowels. The wooden post is suitably held in the clay ground of El Campo, without the necessity for a concrete footing, by using sand poured around the post as shown in Fig. 5-3.

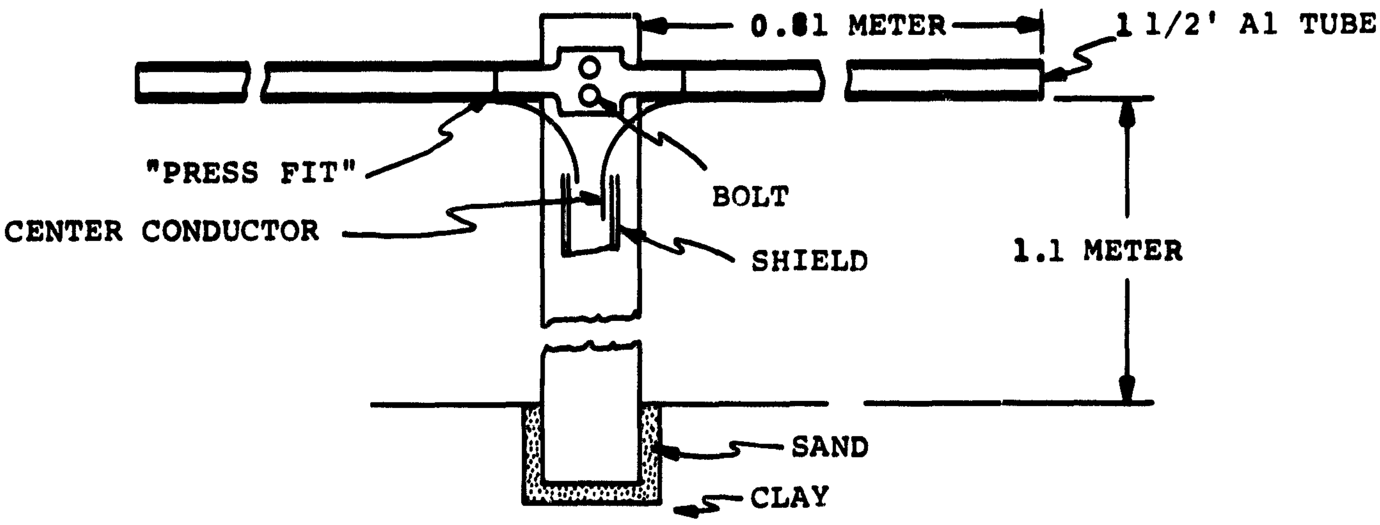

Fig. 5-3 Individual dipole element.

From the experience with the 38 MHz solar-radar dipole array, as well as the Sunblazer 75 MHz (narrowband) dipole array at El Campo, it has been demonstrated that the feed cable may be connected to the dipole without the use of a balanced-to-unbalanced matching network (balun) as shown.

5.3.2 The Six-Dipole, 14-dB Antenna Element

Figure 5-4 shows some details of the proposed connection pattern of six dipoles to form a 14-dB antenna element. Dipoles 1, 2, and 3 are connected

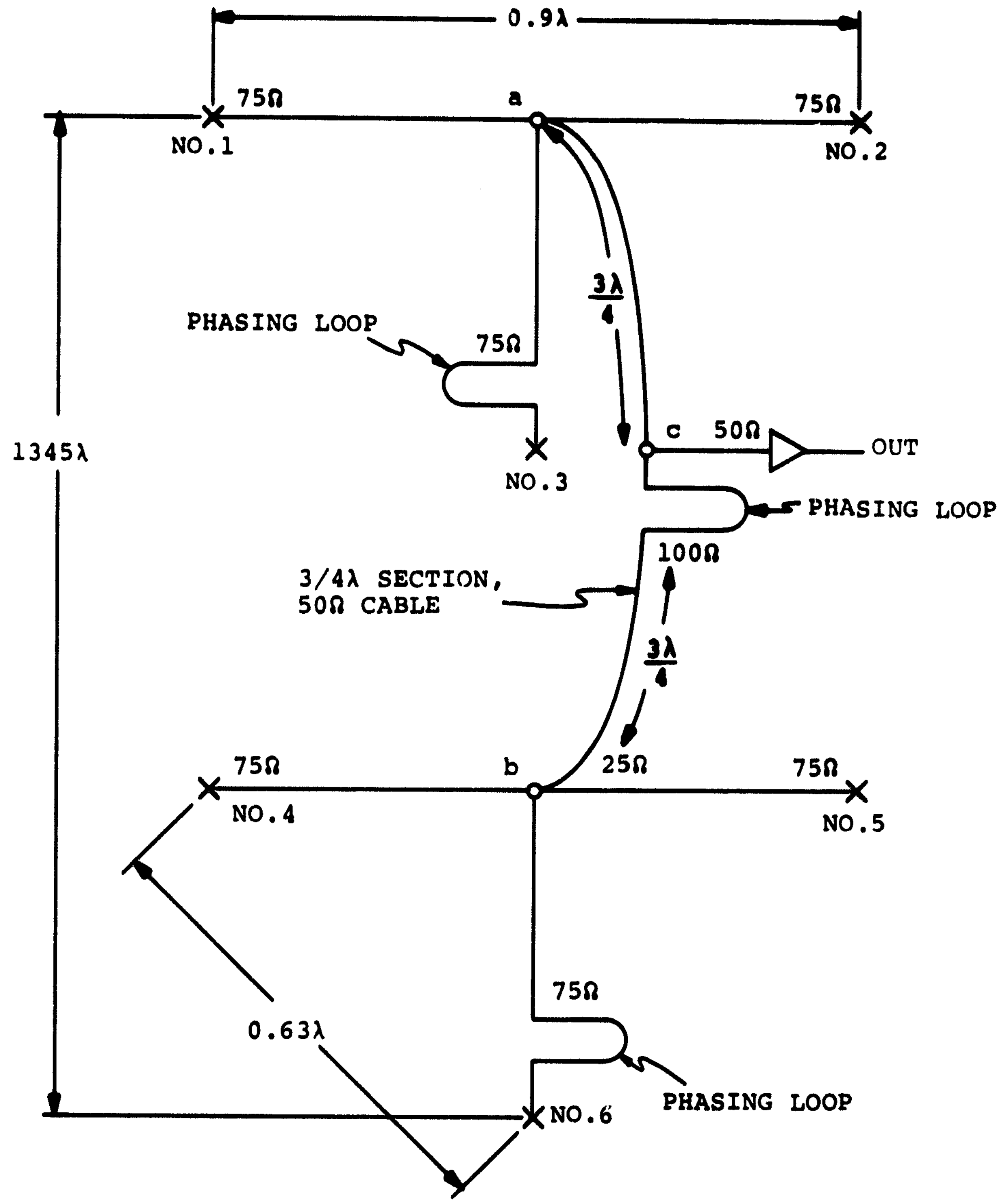

Fig. 5-4 Six-dipole configuration.

by 75Ω cables at point a, as are dipoles 4, 5, and 6 at point b. Summing points a and b, therefore, have a 25Ω impedance which is transformed to 100Ω levels by a 3/4 wavelength 50Ω cables to summing point c. Point c, consequently, may be properly terminated with a 50Ω cable.

The six-dipole configuration of Fig. 5-4 yields a gain of approximately 14 dB with an EW beamwidth (3 dB) of 40° and a NS beamwidth of 28°. This "double T" interconnection pattern was selected over several possibilities, namely "four-dipole square", "four-dipole line element", and "four-dipole zizgag", because it results in relatively high gain, and requires that only two of the six dipoles be manually phased about four times per year in declination, yet affords about two hours of daily viewing time. Also, this configuration is easy to match, utilizing our standard cables, and the RF power-summing is accomplished without electronic components.

The manual phasing for a six-dipole set can be accomplished by utilizing switched delay lines, physically located on posts 3 and 6. The necessary time delay (phasing loops) can be switched with mercury switches connected as shown in Fig. 5-5.

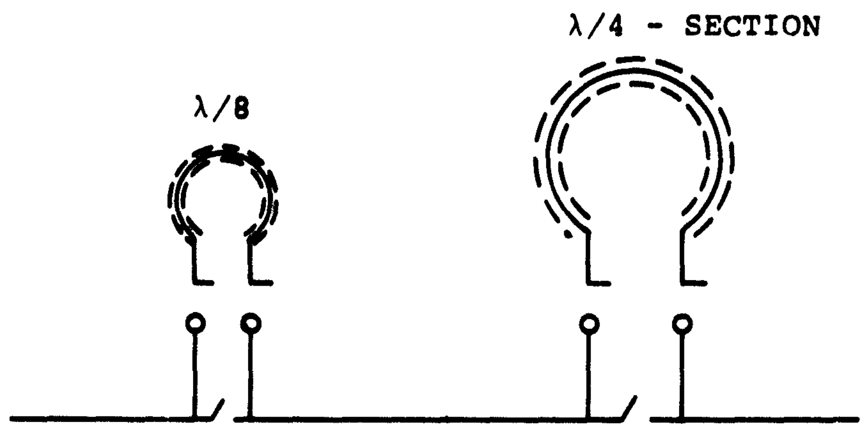

Fig. 5-5 Mercury-switched phased loops (schematic).

Based on several years experience with manually-phased 1000-dipole, 38 MHz El Campo solar radar, the estimated phasing time with this concept is about 0.005 hours/switch location. For a 40-dB array (3072 dipoles with 1024 phasing locations) the array can be phased in 8 man hours.

The mercury switches are inexpensive, exhibit excellent RF performance (insertion loss 0.04 dB, isolation 30 dB), and are judged to be more reliable than connectors which must be plugged and unplugged. Also, these switched delay line systems may in the future be made fully automatic by replacing the manual switches with mercury relays.

5.3.3 The Pilot Array

5.3.3.1 General Description

Thirty-two of the 14-dB dipole subsets of Fig. 5-4 combine to form a 192-dipole array as shown in Fig. 5-6. This pilot array measures 142 x 100 feet.

Each of the six-dipole subsets is connected to an electronic phase-shifter box located at the geometric center of the pilot. The function of the central electronic box is to shift the phase of the signals from each of the six-dipole subsets so that the RF signals may be summed to form one output per polarization. To interconnect the pilot array requires about 8300 feet of cable (including both polarizations), of which 3000 feet are used in the subset and 5300 feet to connect the subsets to the central electronics. To insure relatively-constant operating temperature and a resulting phase stability, all cables are buried in shallow trenches.

Table 5-III summarizes the characteristics of the pilot antenna.

Table 5-III

Design summary 29-dB pilot array.

Operating Frequencies	69.72 MHz, 74.7 MHz, 79.68 MHz
Total Array Gain	28.9 dB
Element Type	$\lambda/2$ dipole, $\lambda/4$ above a ground plane
Realized Gain Per Dipole	6 dB
Number of Dipoles	192
Dipole Grouping	6 per group in double T interconnection
Dipole Spacing	0.63 λ echelon
Array Area	10.68 λ by 7.65 λ (142' by 100')
Grating Lobes	None in Zenith pointing array
Polarization	Two independent polarizations NS and EW
Beamwidth	$6^{o} \times 8^{o}$
Phasing	Hybrid system: rapid electronic scan for short-term tracking, manual phasing using mercury switches for long-term (declination) scans.

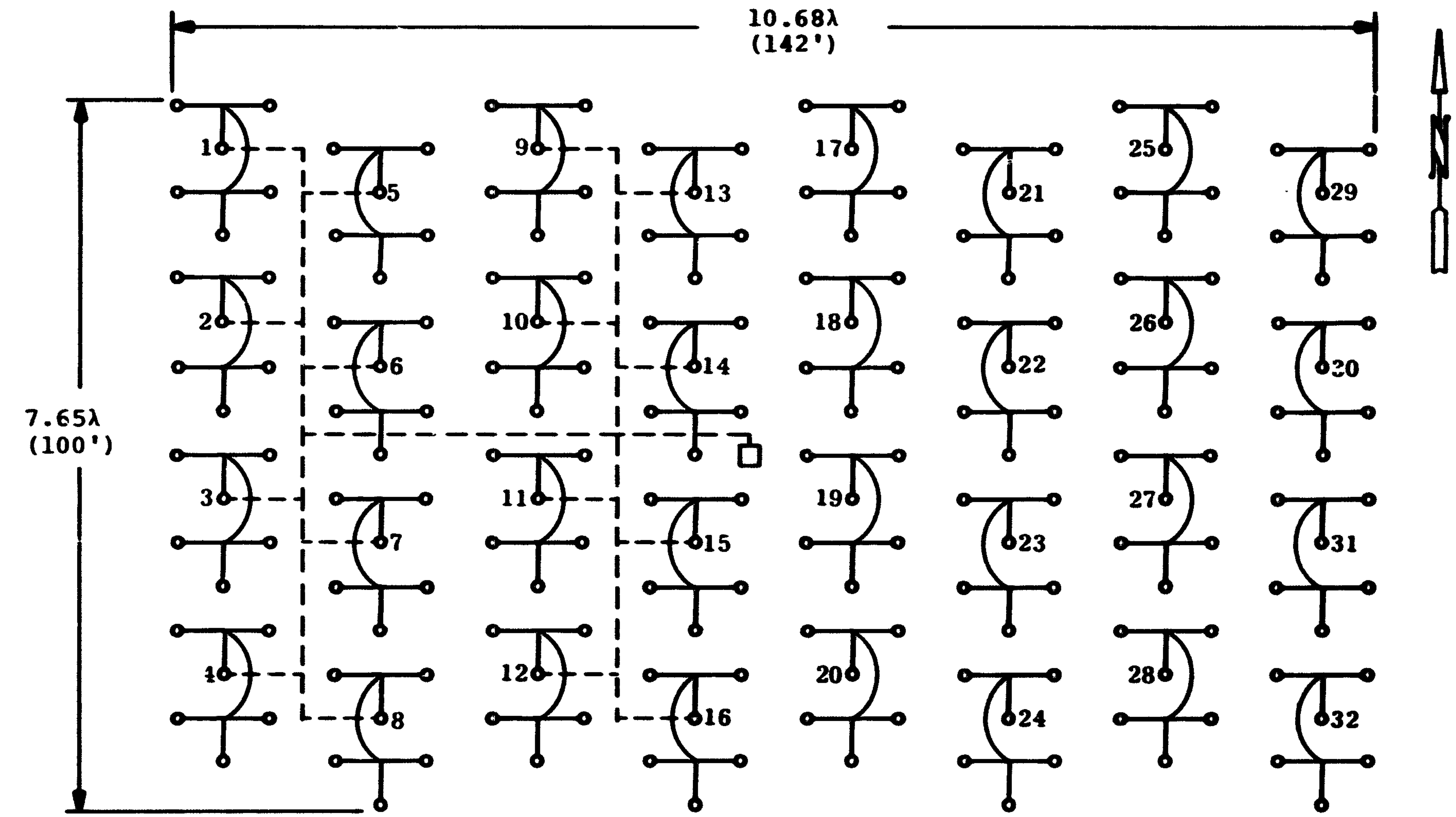

GAIN ≈ 29db, BW ≈ 6°×8°

Fig. 5-6 192-dipole array.

5.3.3.2 Electronics for Pilot Array

The governing design philosophy for a 50-dB array has been to design a pilot-array module which contains all of the system compromises and trade-offs regarding performance and cost, and then to construct a large array by joining these self-contained pilots to obtain the required overall antenna aperture.

There are several feasible organizations of a pilot model. For example, the RF outputs of individual dipoles could be returned to a central point at which all time-delay and control circuits are located; however, this would be prohibitively expensive. On the other extreme, the electronics could be more or less evenly distributed over the array aperture and the combining and control performed at many points in the pilot array. The solution of providing phasing by manually-switched delay lines at the 14-dB element level, and connecting these points directly to a centrally located electronic control point as outlined by Fig. 5-4, 5-5, 5-6 yielded good performance and reduced both cable and electronic cost.

The block diagram of Fig. 5-7 shows the centrally located electronics required to combine the signals from each of the 32 six-dipole elements. To trace a signal path, consider, for example, the energy arriving from the 14-dB element designated as point 1. The signal is first amplified in a low-noise broadband amplifier, and then supplied to network W. The signal from point 2, which is adjacent to point 1 in the first column, is also amplified and supplied to network W. In this circuit the amount of signal delay is dependent upon the desired array look-angle, and then summed. A second level of combining is performed by network X, which delays and sums the output from two adjacent W networks. The output of network X is a complete column output of the pilot array. There are eight such column outputs in the array. These outputs are delayed and combined in a way similar to the above by the operation networks Y, Z, and T. The RF output of network T represents the sum of all 192 dipoles. All of the combining networks are of the same design, and there are only two types of RF circuits used in the entire system: 1) a broadband amplifier, and 2) a time-delay summation network. There is only one amplifier per 14-dB element per polarization. The noise figure of the amplifier is an important design consideration; for an overall pilot system noise-figure of 5 dB, the front-end noise figure must be about 3 dB. This in turn requires a transistor with a noise figure of somewhat less than 3 dB to allow for some mismatch and attenuation losses in the coupling circuit between the RF input and the device. Fortunately, however, the gain required in the front end is relatively low. The

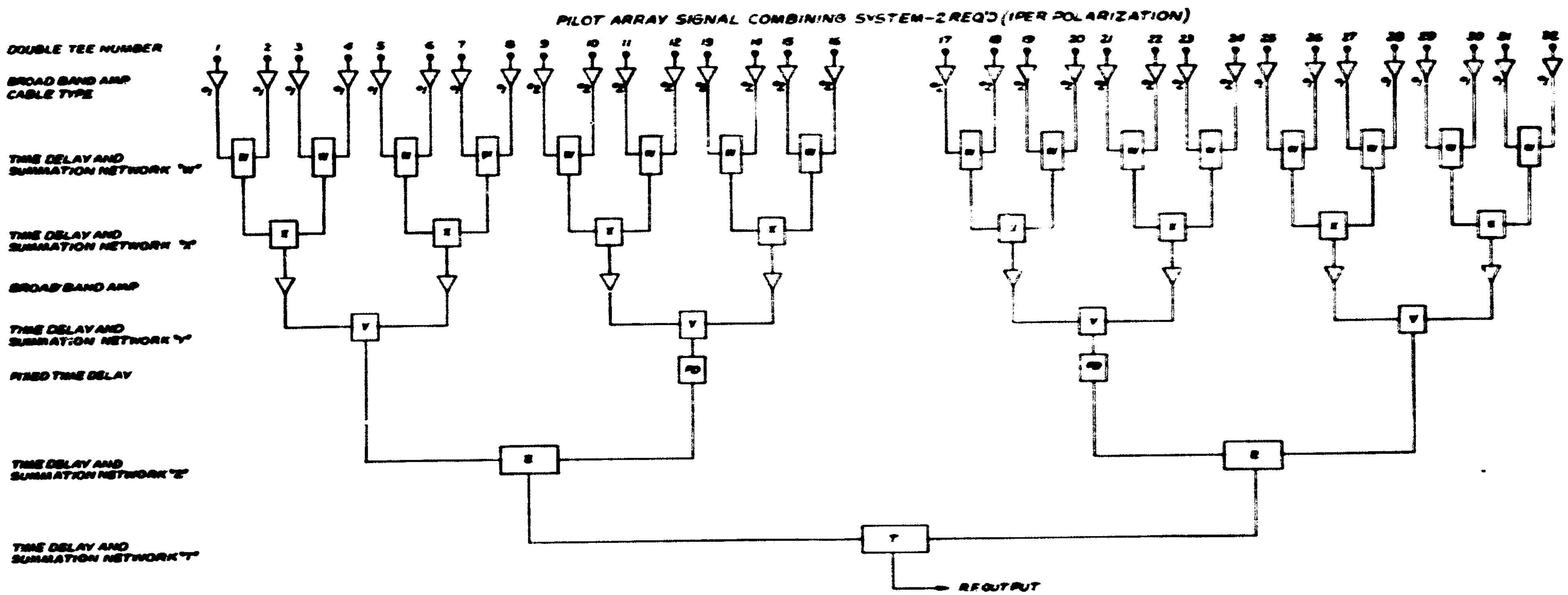

Fig. 5-7 Electronics system block diagram.

amplifier can then be designed with a minimum-noise, rather than a maximum-gain criterior, and is therefore readily realizable.

The amplifier frequency response and linearity have also been carefully considered, for it is somewhat impractical in a low-cost, high-volume production to provide independent RF pass bands for each of the design frequencies. Accordingly, the amplifier has been designed with a 3-dB bandwidth covering the frequency range from 60 MHz to 90 MHz. But since this frequency band is a region of high RF interference, due to local TV and other commercial services, the linearity, dynamic range, crossmodulation and intermodulation of the amplifier are of prime importance and have been carefully considered in the design.

The time-delay circuit for shifting the RF signal phase (for example network W) shown in simplified form in Fig. 5-8, is composed of sections of RF cables which are switched in and out of the circuit via diodes to obtain the required time delay. At each level, in both the intracolumn and inter-column combining, the time-delay function is performed in a similar way with the exception that the dealy lines are made longer as the summation progresses toward the system output.

Table 5-IV gives a summary of the total number of circuits for the pilot along with pertinent characteristics.

5.3.3.3 Testing Considerations

The primary reason for the construction of a pilot array is to obtain engineering data on design and performance problems such as amplifier and phaser uniformity, mutual coupling effects, precise antenna gain, losses, etc. that cannot be accurately anticipated. A search for such effects will be made as the array is constructed and tested. The theoretical performance including gain and effect of grating lobes and mutual coupling will be experimentally verified. The reliability of the field electronics will be determined under actual weather and working conditions. Accurate cost and construction techniques for the final array will also be determined.

After the array is constructed, an overall evaluation will be made by using known celestial sources. Cassiopeia, Cygnus, and the Sun may be used for the pilot array; Virgo, Taurus, and several others, including pulsating sources, may be used to test the 40-dB array.

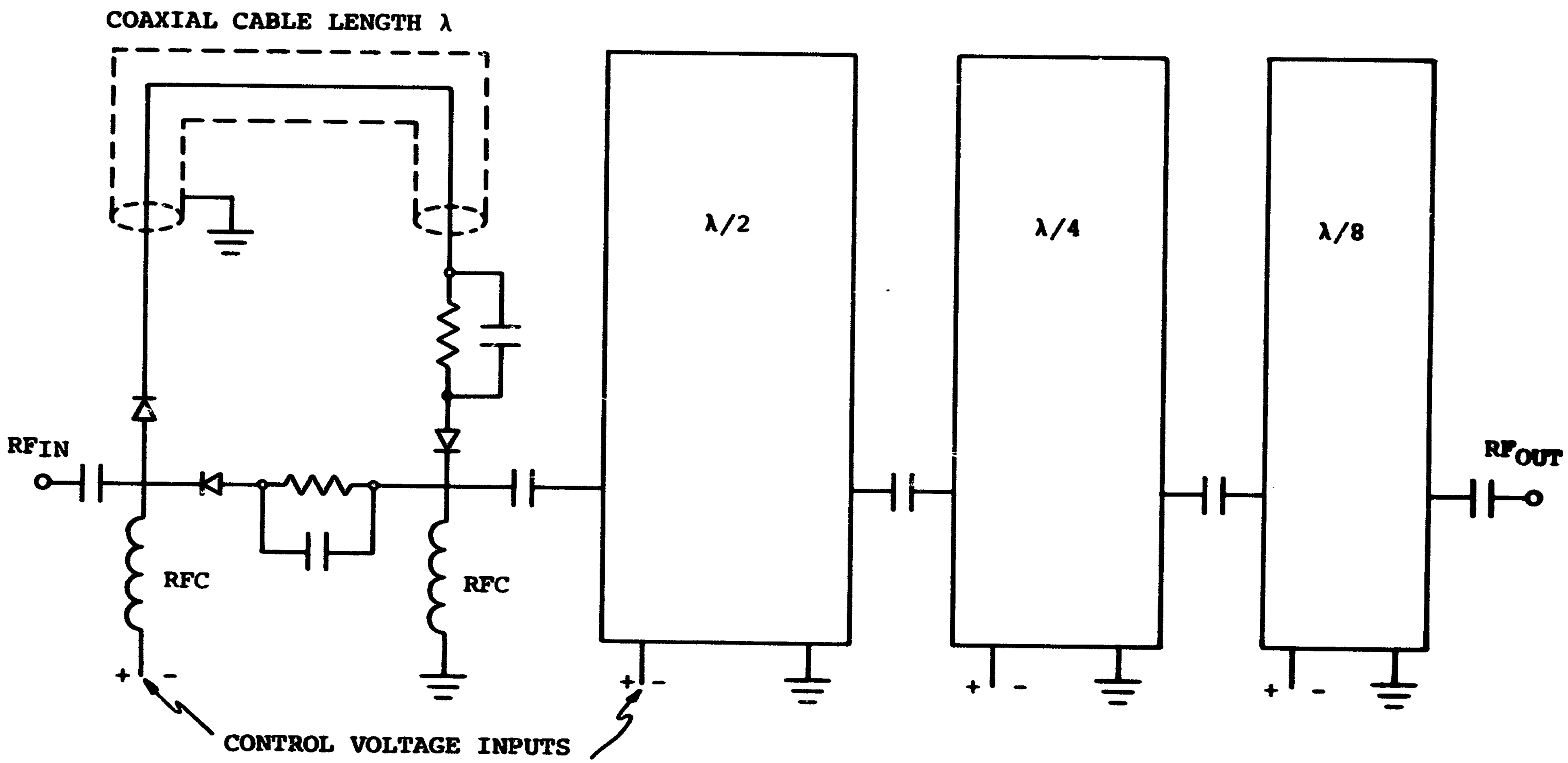

Fig. 5-8 Time delay circuit.

Table 5-IV

Pilot array electronics.

Circuit Type	Number Required	Description and/or Major Specifications
Broadband Amplifier	80	Noise Figure = 3 dB 3 dB Bandwidth = 30 mc Gain = 17.5 dB average
Time Delay and Summation Network "W"	32	Maximum Delay = 1 7/8 λ_o in λ_o/8 steps Insertion Loss = 6 dB max. Amplitude Variation = 1 dB Coherently combines two signals from 14 dB elements
Time Delay and Summation Network "X"	16	Maximum Delay = 3 7/8 λ_o in λ_o/8 steps Insertion Loss = 6 dB max. Amplitude Variation = 1 dB Coherently combines two signals from network "W"
Time Delay and Summation Network "Y"	8	Maximum Delay = 1 7/8 λ_o in λ_o/8 steps Insertion Loss = 6 dB max. Amplitude Variation = 1 dB Coherently combines two signals from network "X"
Time Delay and Summation Network "Z"	4	Maximum Delay = 3 7/8 λ_o in λ_o/8 steps Insertion Loss = 6 dB max. Amplitude Variation = 1 dB Coherently combines two signals from network "Y"
Time Delay and Summation Network "T"	2	Maximum Delay = 7 7/8 λ_o in λ_o/8 steps Insertion Loss = 7 dB max. Amplitude Variation = 1 dB Coherently combines two signals from Network "Z"
Fixed Delay	4	2.67λ_o phase-equalizing cable
Power Supply	1	120 V ac @ 1.1 amp 130.0 watts input 3.6 V dc @ 1.2 amp 3.6 watts 12 V dc @ 10.0 amp 80.0 watts 15 V dc @ 0.4 amp 6.0 watts
Logic	4	4-, 5-, and 6-bit counters with SCR drivers for beam pointing control

5.3.4 The Expanded Array

5.3.4.1 General Comments

Since the pilot array is completely self-contained, i.e. it is designed as a "module", an increase in array-effective aperture may be obtained by adding pilot array modules to realize the desired gain. Two pilot modules will yield a gain improvement of 3 dB, four modules will result in 6 dB improvement, etc. For the Sunblazer engineering payload, the required minimum receiving system gain which will provide satisfactory telemetry and tracking data is judged to be about 40 dB, which may be realized by expanding or adding the 15 pilot arrays as indicated in Fig. 5-9. A summary of the antenna system characteristics for the expanded array is given in Table 5-V.

Table 5-V

Design summary of 40-dB array.

Operating Frequency	69.72 MHz, 74.7 MHz, 79.68 MHz
Total Array Gain	40.9 dB
Gain Per Dipole	6 dB
Total Number Dipoles	3072
Dipole Grouping	Double T
Dipole Spacing	0.63 λ
Array Area	568' x 400'
Beamwidth	$1.3^{\circ} \times 1.9^{\circ}$

5.3.4.2 Expanded 40-dB Array Electronics

Each of the pilot array outputs is returned to a central building. The electronic circuits for each of the 16 proposed pilot arrays are identical to the system described above; but, of course, electronics must be constructed to shift the phase of the RF signal from each pilot and sum the results.

Figure 5-10 shows a block diagram of the electronic system to shift the phase and sum the signals. As for the pilot, the signal energy from adjacent segments is summed in pairs, the two pairs are then summed, and finally the columns are treed together to form one output per polarization.

The time-delay network W', X', Y', and Z' is identical in design to that of the pilot array (W, X, Y, and Z), except that extra stages of cable loops are added to accommodate increased delay resulting from the fact that the

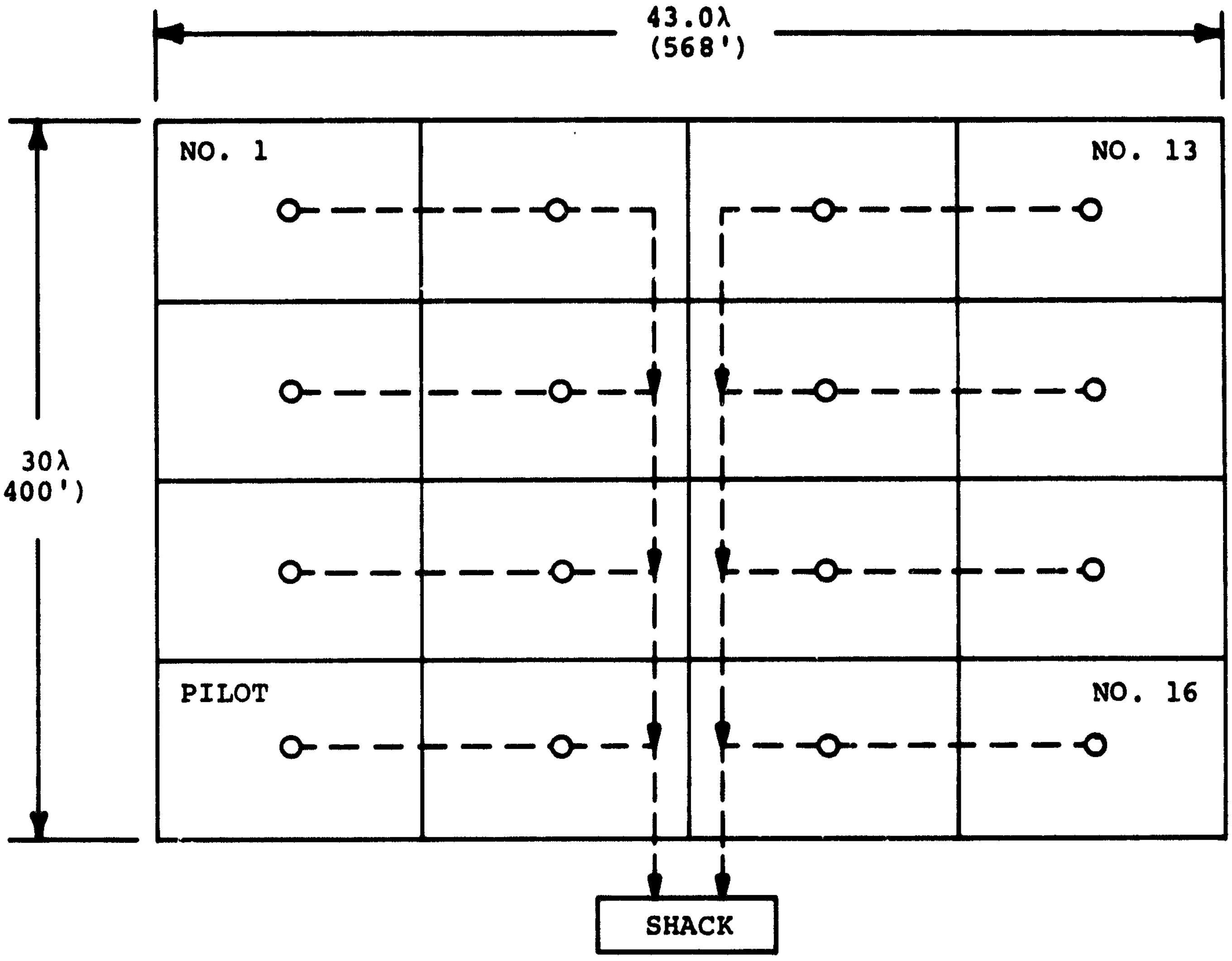

Fig. 5-9 Expanded 40-dB array.

signals come from phase centers which are more widely separated in physical distance.

5.3.4.3 Testing

Each segment of the expanded array will be tested individually as an antenna in a manner similar to the original pilot section. The resulting sum will then be characterized for gain, noise figure, beamwidth, bandwidth, etc. The central building (control center) for the array will contain the necessary equipment to operate, i.e. steer the array, receive and record signals, etc. from the Sunblazer engineering spacecraft.

5.3.5 The 50-dB Array

A 50-dB array may be realized by continuing the expansion philosophy outlined in the discussion of the pilot and 40-dB arrays. Essentially, a 50-dB array results from adding the signals from 140 pilot arrays. The electronics, construction techniques, trenches, cables, etc. are all the same type.

Technical difficulties encountered in expanding the 40-dB array into a 50-dB array should be virtually non-existent. In fact, one may realistically view the modular and orderly growth procedure outlined here as minimizing the likelihood of any fumdamental problem remaining undiscovered prior to construction of the final antenna.

Figure 5-11 shows the proposed plan for the 50-dB array, and Table 5-VI gives some characteristics.

Table 5-VI

Design summary of 50-dB array.

Operating Frequencies	69.72 MHz, 74.7 MHz, 79.68 MHz
Total Array Gain	50.4 dB
Gain Per Dipole	6 dB
Total Number of Dipoles	26880
Dipole Grouping	Double T
Dipole Spacing	0.63 λ
Array Area	1400' x 1400'
Beamwidth	$0.5^{\circ} \times 0.5^{\circ}$ (Zenith)

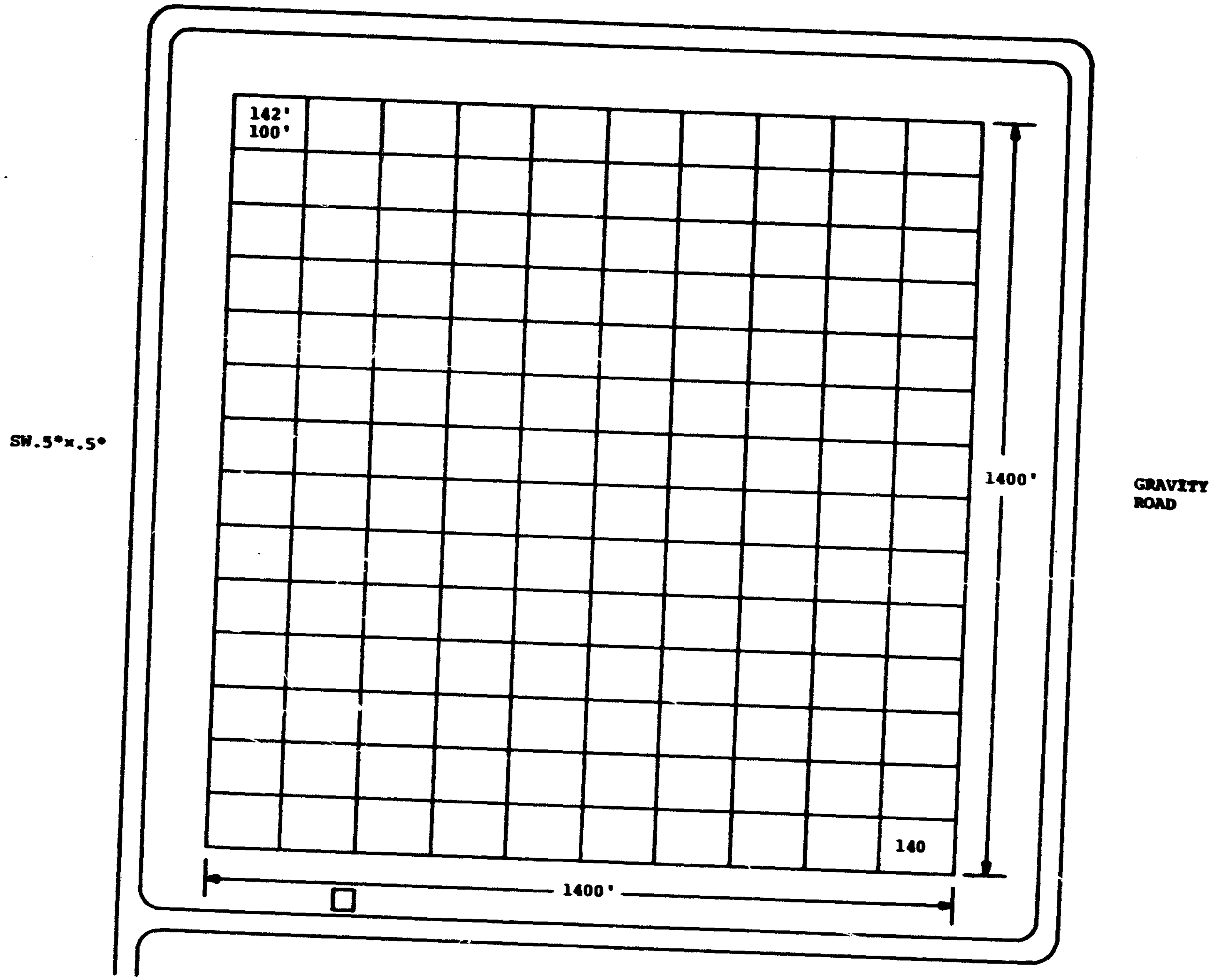

Fig. 5-11 Proposed plan for 50-dB array.

PAGE 148 ~~BLANK~~ MISSING FROM ORIGINAL DOCUMENT

CHAPTER 6

6.0 SPACECRAFT CONSTRAINTS

The concept of using a relatively small, unguided launch vehicle to provide the escape velocity required for a solar-orbiting scientific experiment implies the use of a very small spacecraft as the payload. The standard four-stage Scout vehicle has been selected to launch the Sunblazer spacecraft; and to provide the escape velocity required, a BE-3 motor has been added to the vehicle as the fifth stage.

6.1 Distribution of the Payload Weight

The Scout User's Manual Fig.5-43, reproduced here as Fig.6-1, shows a performance curve of a five-stage Scout, which indicates the capability of placing a 57-pound payload into 0.65 astronomical unit inferior solar orbit. The approximate distribution of this payload weight for the initial Sunblazer experiments is:

Table 6-I

Distribution of Payload Weight		
Spacecraft	28.00 lbs	58.5%
Sunblazer Adapter	5.41	
Upper F Structure	3.25	41.5%
Ignition Timer	4.13	
Balance Weights	1.00	
Despin System	0.95	
Telesponder System	8.37	
Performance T/M	5.89	
Total	57.00 lbs	

The initial system engineering launches, which will monitor the performance of the modified Scout vehicle and the Sunblazer spacecraft, limit the engineering model spacecraft's weight to 28 pounds.

SOLAR PROBE MISSIONS

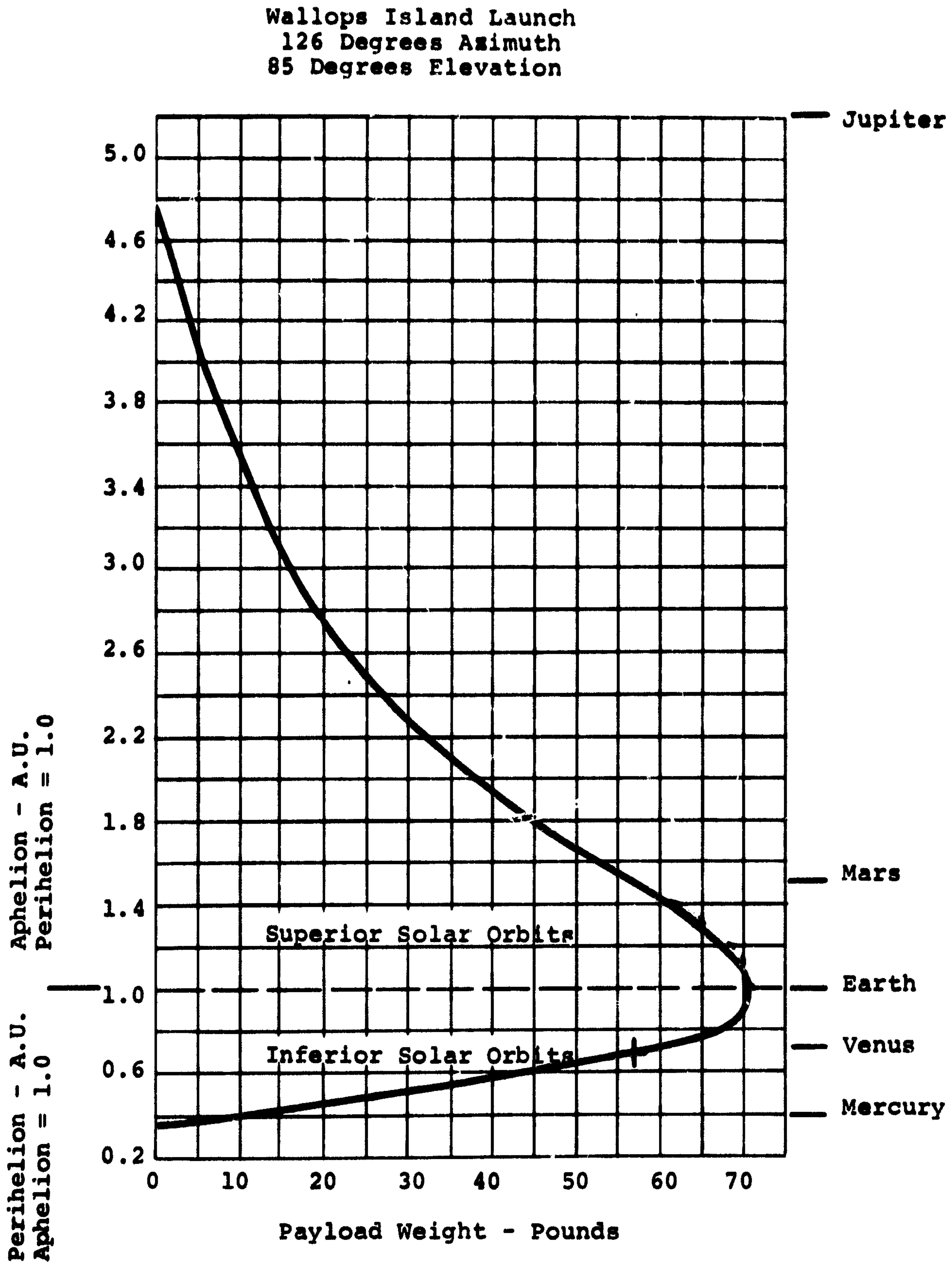

Fig. 6-1 Solar probe performance using Scout fifth stage — Wallops Station.

6.2 Dimensional Limitations

The standard Scout heat shield for the payload has been increased in length by 15 inches to accommodate the addition of the fifth stage and the spacecraft. In Fig. 6-2 the relative positions of the payload configuration and the envelope of this extended heat shield are shown. The adapter (transtage) used to position the spacecraft derives its height from a spacecraft sail configuration option, which allows a geometric flexibility in the design of these devices.

One of the basic requirements of the spacecraft design is to provide a solar cell-mounting area which is capable of delivering about 18 watts of power at 1 astronomical unit. This requirement establishes the initial dimension of the spacecraft at about 20 inches diameter. Since the volume in which the spacecraft is placed is a truncated cone, the upper positional limit of the 20-inch diameter has been calculated to be Station -21.94.

The separation plane of the spacecraft and adapter is located at Station -15.00, and the total height of the spacecraft is 6.501 inches, which locates the solar cell platform flanges at Station -21.50.

The cylindrical launch geometry of the spacecraft is, therefore, approximately defined by a 20-inch diameter and a 6.5-inch height, or a total of 2042 cubic inches, with a maximum weight of 28 pounds.

6.3 Spacecraft - Adapter Interface

The orientation of the spacecraft to the yaw and pitch axes of the launch vehicle is generally predetermined by the interfacing bolt pattern provided by the design of the LTV Sunblazer Adapter.

The LTV drawing of this assembly, J23-003691 (View A-A) shows two of the interface bolt holes diametrically aligned in the launch vehicle yaw axis. Since these holes are displaced from the geometric centerlines of the spacecraft by 22.5 degrees, the resultant orientation of the spacecraft to the launch vehicle is shown in Fig. 6-3.

The spacecraft is mounted to the adapter so that Energy Storage Capacitors 1 and 5 lie in the yaw axis, with Capacitor 1 located on the range side and Capacitor 5 on the tower side.

6.3.1 Attachment Method

To permit the attachment of the spacecraft to the adapter without requiring a disassembly of a portion of the spacecraft, the following procedure is proposed.

The separation springs of the adapter are compressed and secured by the mounting plate and pyrotechnic bolt.

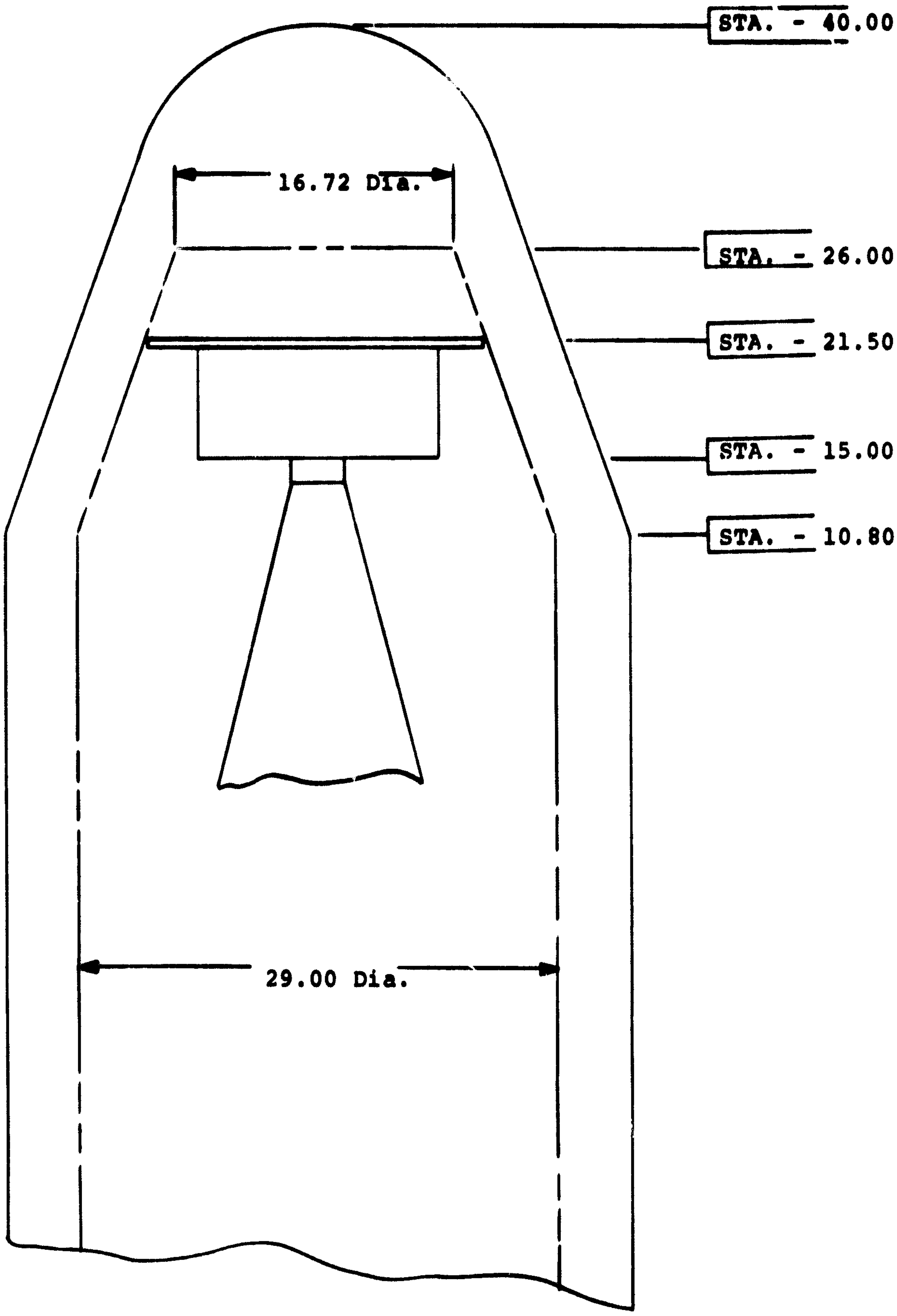

Fig. 6-2 Location of spacecraft in -40 heat shield.

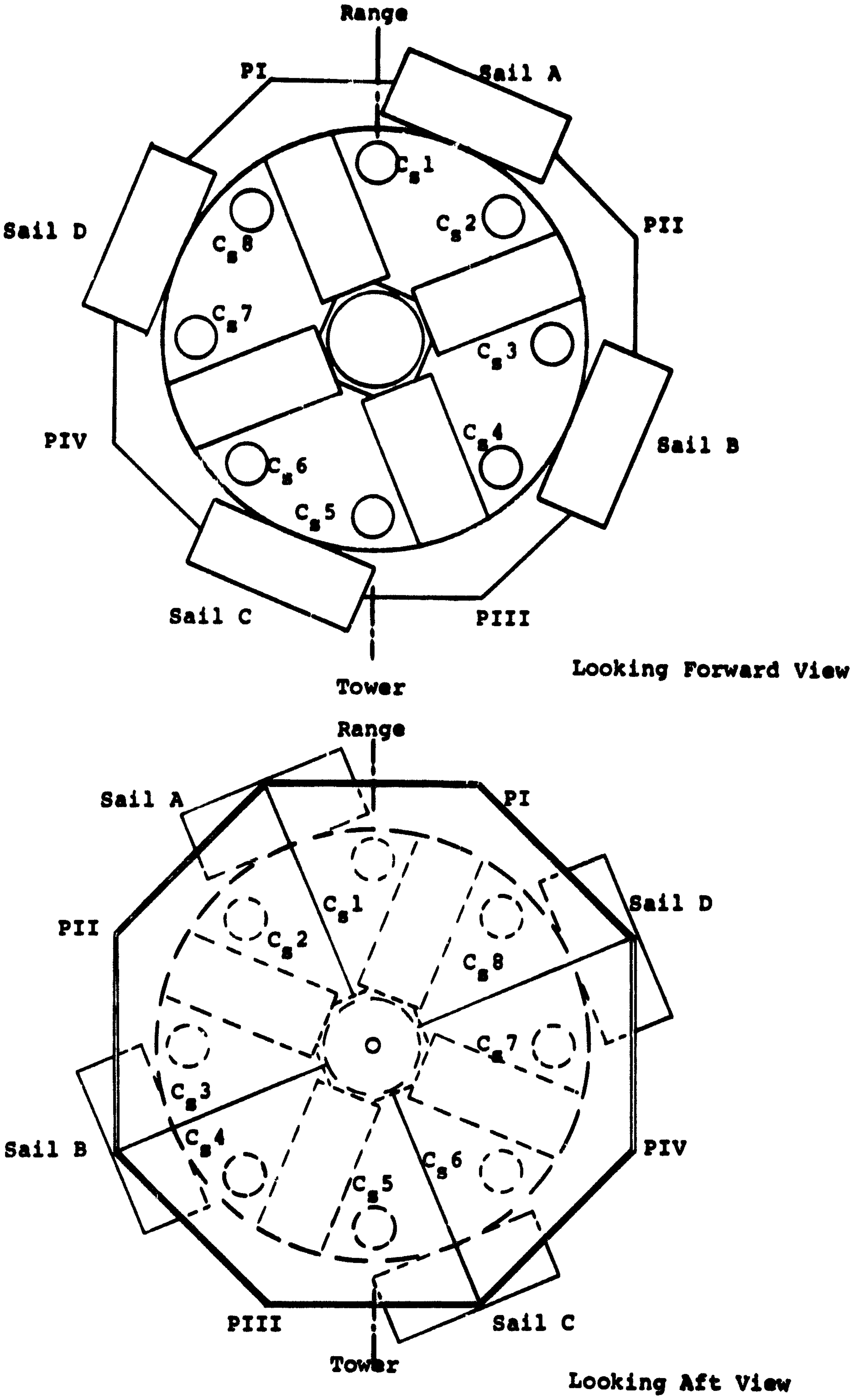

Fig. 6-3 Axial alignment of spacecraft.

The spacecraft has the sails and antennas in the stored (launch) position. The separation trigger mechanism, which initiates despin, is retained by a temporarily installed inhibitor device.

The spacecraft is axially oriented to the vehicle. The mounting screws are inserted through clearance holes in the upper ring flange, and seated on the mounting plate by screwing into the hub of the spacecraft. Due to the close proximity of upper-ring sidewall stiffeners in this area, Allen-head screws will most likely be used in association with a specially-designed right-angle ratchet wrench.

When the eight interface screws are properly torqued, the inhibiting devices on the separation trigger will be removed. The mechanical interface will then be complete.

6.3.2 Despin-Deployment Actuator

Mechanical separation sensors are mounted on the exposed portion of two vertical members of the electronic compartment, and are referenced to a small pad which is mounted on the sides of the upper ring-assembly of the adapter.

The two separation sensors used are basically push-rods which will have a radial force of five pounds or less acting upon each of them.

6.4 Environmental Testing Prior to June 1968

6.4.1 Vibration

The first vibration testing of the Sunblazer vehicle took place February 3, 1966. It was foreseen then that the vehicle would be changed, but it was desirable to test the principle of a spacecraft made of aluminum sheet metal. The results were extremely satisfactory. Brittle shellac was used in order to have an idea of the magnitude of the safety factor. The stress level never went above 4,000 psi on any part. Since the vehicle interface had not been specified at that time, the vehicle was hard-mounted to the vibrator, with the solar cell panel facing the vibrator.
The test program was:

Thrust Axis

Run 1-4.5g sinusoidal for 120 seconds, 40 to 80 cps
2-6.0g sinusoidal for 144 seconds, 20 to 2000 cps
3-3.0g random for 284 seconds, 20 to 2000 cps
4-9.0g sinusoidal for 120 seconds, 40 to 80 cps
5-12.0g sinusoidal for 120 seconds, 20 to 80 cps

Transverse Axes

(along the compartment and between the compartments 45° away)

Run 1-6.0g sinusoidal for 144 seconds, 20 to 2000 cps
2-3 0g random for 284 seconds, 20 to 2000 cps
3-12.0g sinusoidal for 120 seconds, 20 to 80 cps

On March 10, 1967, a test was run with the first transtage. Three sets of electronic sections were aboard; the solar cell panel faced away from the vibrator. There was a new input on the test levels (described below).
A sinusoidal sweep in the thrust axis was made at 2 octaves per minute for four minutes. The level of vibration was:

20 to 50 cps	1 g
50 to 500 cps	4 g
500 to 2000 cps	8 g

The random vibration in the thrust axis lasted 2 1/2 minutes under the following conditions:

20 to 2000 cps, 7.7 g rms, and 0.03 g^2/cps power spectral density, (This is a flight acceptance level.)

The sinusoidal sweep in the transverse axis (only one transverse axis was vibrated because of symmetry and time) was made twice at two different levels:

(Sweep speed 2 octaves per minute)

20 to 50 cps	0.6 g
5[illegible] to 500 cps	0 [illegible] g
500 to 2000 cps	1.6 g

(This is a flight acceptance level)

5 to 10 cps	0.2 in.
10 to 50 cps	1.0 g
50 to 500 cps	1.5 g
500 to 2000 cps	2.5 g

(This is a qualification level)

The random test in the thrust axis was also made at two levels, and in only one transverse axis.

20 to 2000 cps, 4.4 g rms, 0.01 g^2/cps power spectral density

(This is a flight acceptance level) time 4 minutes

20 to 2000 cps, 6.3 g rms, 0.02 g^2/cps power spectral density

(This is a qualification level) time 4 minutes

The test with brittle shellac showed that the transtage had a safety factor of two, and that the sail, as then designed, was sound. Following is a summary of the effect of vibration on the electronics that were aboard:

1. 270-Watt Amplifier
   Evaluation after shake revealed the presence of a nondestructive, low-frequency oscillation. This was traced to a repositioning of amplifier input circuit inductors during shake. Restoring these components to their original positions resulted in normal operation. No other failures were observed. The inductors will be replaced by a more rigid type in future amplifiers.

2. 28-Volt, 5-Watt Beacon
   The beacon was inoperative after shake. Loss of output was traced to two open component leads which resulted from poor soldering practice. The beacon operated after these leads were restored, but a tendency toward low-frequency oscillation was noted. This oscillation was traced to the pre-driver stage, and the apparent cause isolated to coil deformation. An epoxy base for these coils would seem to be called for. In the future, breadboard circuits will not be expected to undergo shake.

3. Low Level Stages
   Operation after shake was essentially the same as before, with slight detuning of output circuits noted.

6.5 Structural Analysis

6.5.1 Introduction

Weight saving is of prime importance in spacecraft structure design, and structures with maximum stiffness-to-weight ratio are employed. However, Sunblazer's special features (oriented during flight), and their implications, have to some extent dictated the basic configuration of the spacecraft. Maximizing the stiffness-to-weight ratio is thus restricted to the selection of optimum material dimensions and placing of required stiffeners.

It is, therefore, sufficient for this analysis to verify that the selected structure design will withstand the expected loadings. This is done by computing the stresses in models of those parts of Sunblazer expected to experience critical loadings. By choosing a conservative (weaker than reality) model, acceptable computation results will assume a safe structure.

A more detailed analysis is planned, applying the stiffness or flexibility method to the entire structure along with a vibration analysis.

6.5.2 Calculations

The structure should withstand acceleration forces of 100 g. With the spacecraft mounted as shown in Fig. 6-4, the critical stresses are expected to appear . the compartment side walls and covers, parts of the platform, and in the vertical member supporting the electronics. A primary structure model, Fig. 6-5 is used to represent the entire structure, except for the electronics. In this model the weights of the platform-radiator, capacitors, sails, etc., are assumed to be concentrated along a ring of diameter D = 15 inches. These weights are supported by four box beams mounted to the hub which is assumed to be rigid. The assumed weights W are

$$W = 6150 \text{ gm}$$

or per beam

$$\frac{W}{4} = 1537 \text{ gm} = 3.38 \text{ lbs.}$$

From beam theory the stress due to bending is

$$S = \frac{MI}{C} \tag{6-1}$$

where S = normal stress,
M = bending moment,
I = moment of inertia, and
C = distance from neutral layer to outer fiber.

Thus (see Fig. 6-6 for I and C of box beam) for 100 g loading,

$$S = \frac{338 \times 4.5 \times 1.85}{3} = 940 \text{ psi.}$$

The load gives rise to a shear stress of (see Fig. 6-6 for A)

$$T = \frac{100 \frac{W}{4}}{A} = \frac{338}{0.365} = 930 \text{ psi.}$$

The other critical part of the structure is the vertical member in the electronics compartments. Each typically supports eight printed-circuit boards weighing 100 gm each. Under an acceleration load of 100 g the compression stress will be

$$S = \frac{177}{0.150} = 1180 \text{ psi}$$

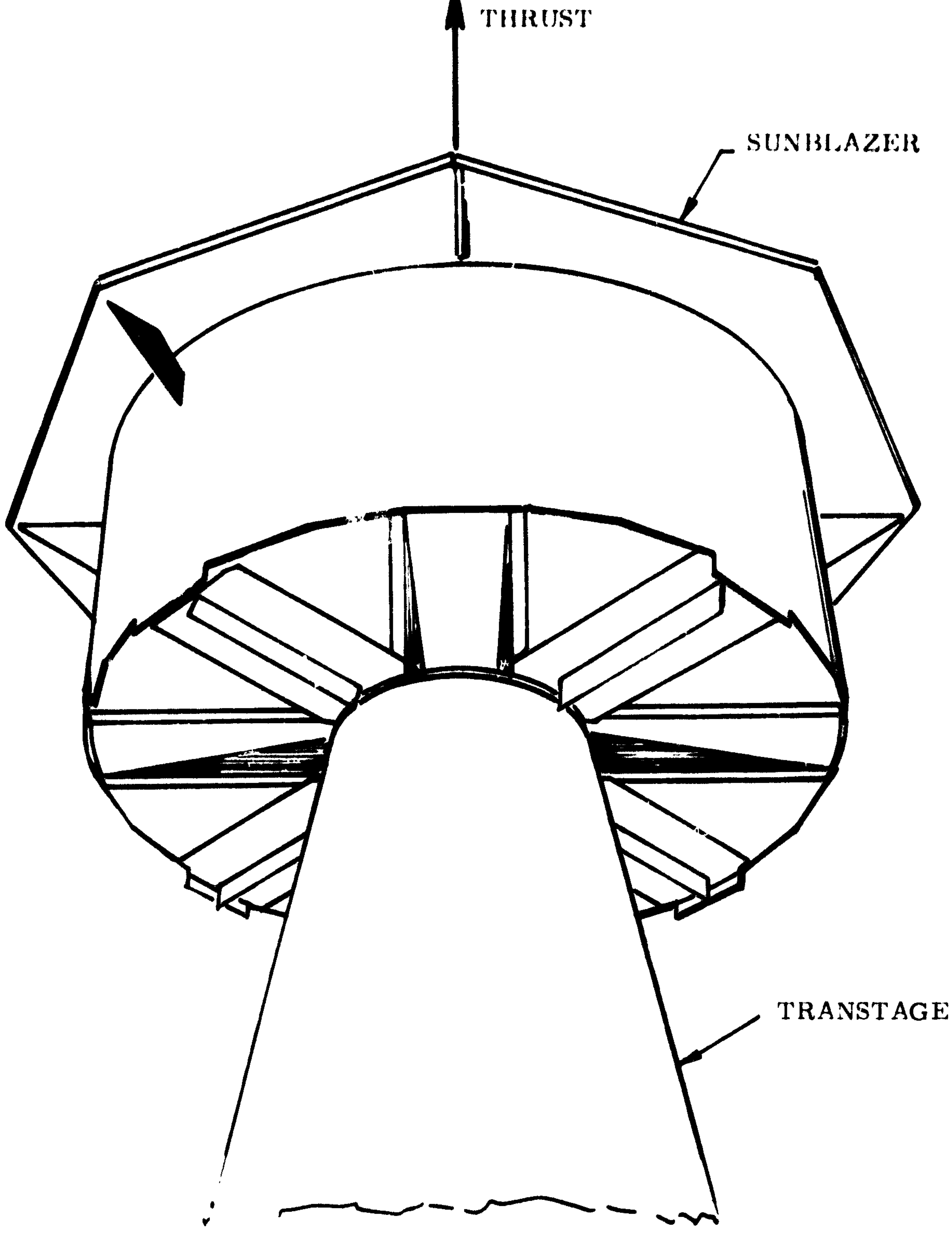

Fig. 6-4 Spacecraft mounting.

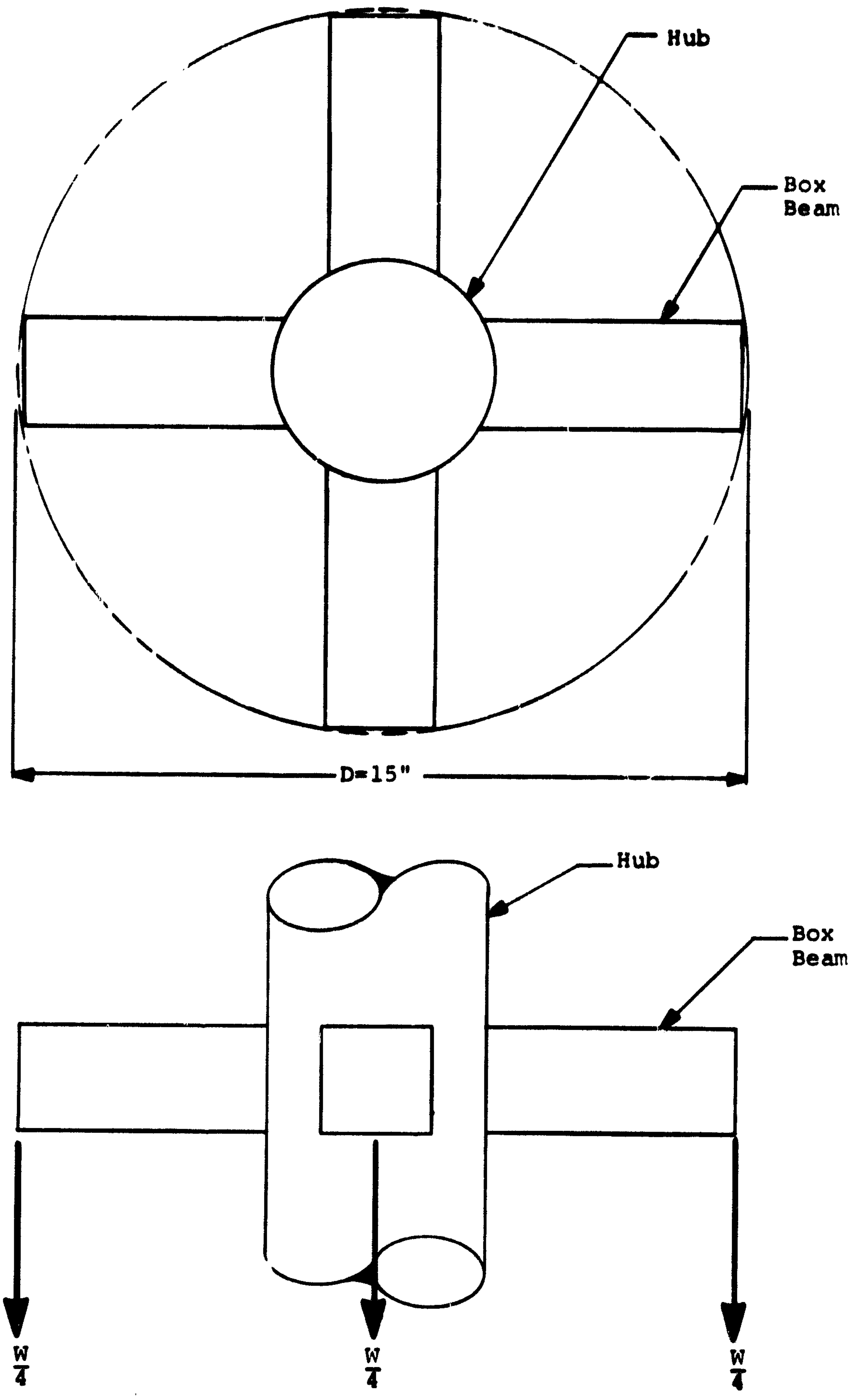

Fig. 6-5 Primary structure model (box beam).

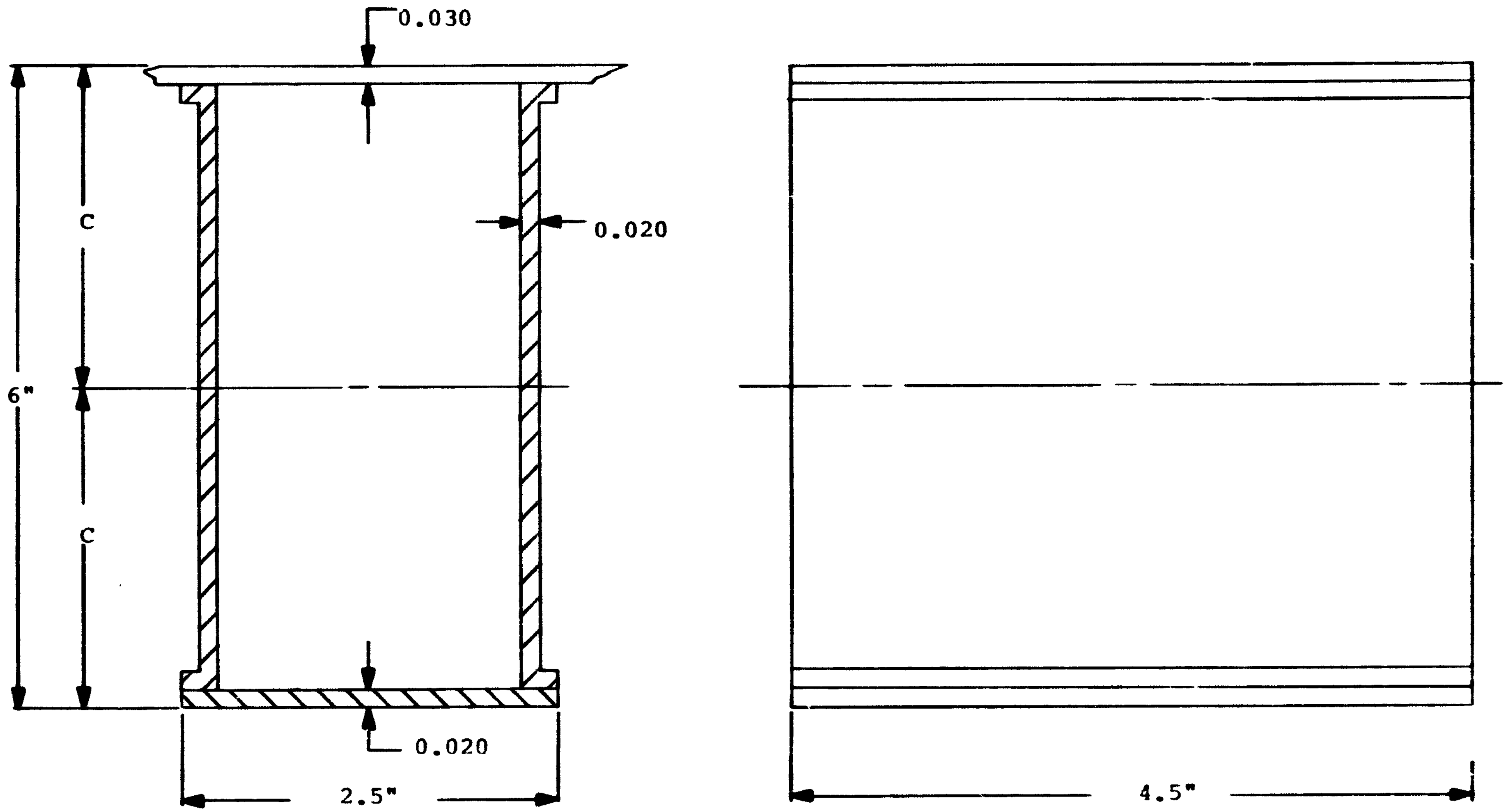

moment of inertia $I = 1.85 \text{ in}^4$
$C = 3 \text{ in}$
cross section area $A = 0.365 \text{ in}^2$

Fig. 6-6 Box beam section.

and the shearing stress at the connection to the compartment shield will be

$$T = \frac{177}{0.180} = 985 \text{ psi}.$$

6.5.3 Discussion

Although the above computations oversimplify the real situation, they fulfill the requirements set up in the introduction (6.5.1). The model employed for the calculations of the primary structure is certainly conservative in the sense that it is much weaker than the real structure. Also, by lumping all the weights (excluding electronics) at the ends of the box beams, the situation depicted for the model is worse than the actual. With acceptable values for the model, it must be concluded that the actual structure is safe. The same arguments apply to vertical members. Buckling has not been mentioned at all since buckling, in those parts where it can be expected, can be prevented by adding stiffeners which do not change the basic structure or significantly increase the weight.

PRECEDING PAGE BLANK NOT FILMED

CHAPTER 7

7.0 DESCRIPTION OF THE SPACECRAFT

The spacecraft consists of six principal sub-assemblies:

1. Platform-Radiator
2. Electronics and Power
3. Aspect Sensor
4. Sails
5. Antennas
6. Despin - Deployment

7.1 Platform-Radiator Sub-Assembly

The platform-radiator sub-assembly is an aluminum sheet metal structure, which is thermo-mechanically designed to be a mount for solar cells, sails, and antennas, and to provide a passively-controlled thermal housing for the electronics, energy storage, aspect sensor and sail-drive mechanism.

7.1.1 Fabrication

The platform-radiator sub-assembly is developed from four symmetrical segments, (Fig. 7-1), each of which consists of the following parts: segment, radiator, left- and right-hand compartment sidewalls and gussets. These parts are cut and bent by use of guides and stops on the shear and break, with tolerances being held to 0.005 inch.

An assembly jig (Fig. 7-2) is used to position the parts properly with respect to dimensions, parallelism and/or perpendicularity. The pre-cleaned parts are fastened by rivets, while in the assembly jig, and after post-assembly inspection, each segment is dip-brazed.

The dip-brazing unitization of the platform-radiator segments is used to provide a maximum thermal conductivity between parts by filling junction voids with metal. This process has the secondary effect of increasing the mechanical strength of the entire sub-assembly.

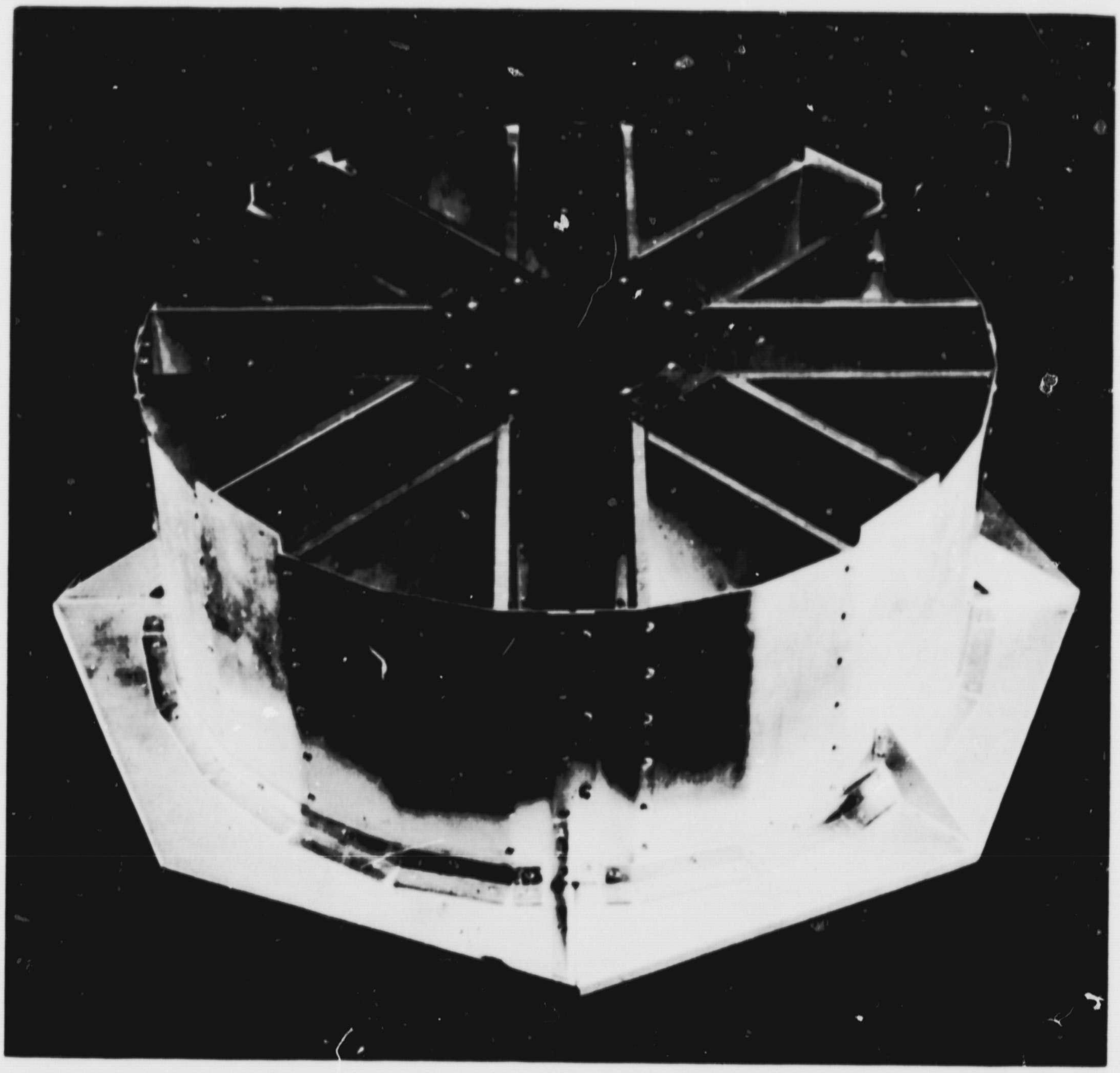

Fig. 7-1 Platform-radiator sub-assembly segment.

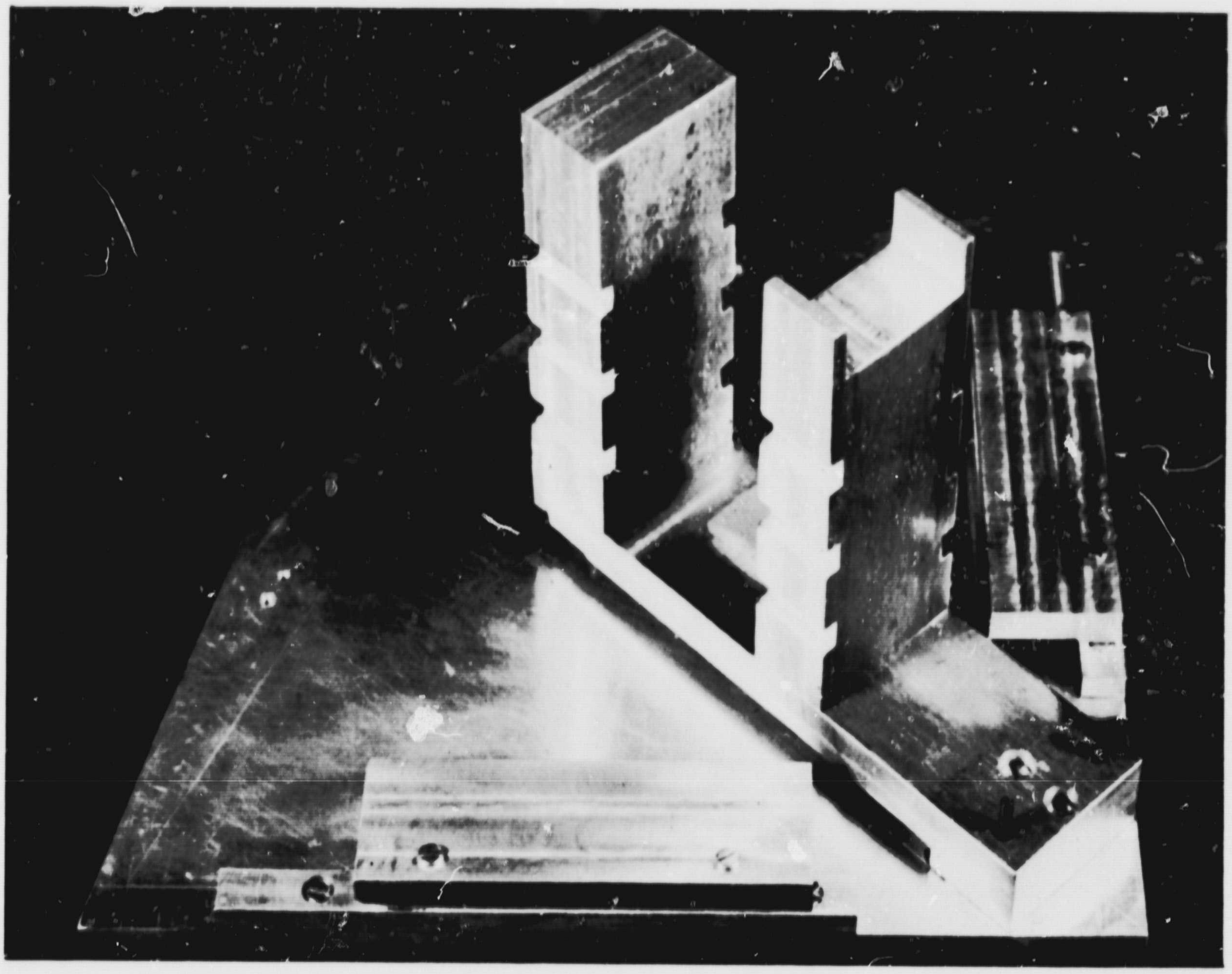

Fig. 7-2 Assembly jig.

7.1.2 Area Available for Solar Cells

The total area of one 90-degree segment is 70.71 $in.^2$, or a total platform area of 282.84 $in.^2$

The front area of the aspect sensor is 23.76 $in.^2$ Area for the main solar cell array is:

$$282.84\ in.^2 - 23.76\ in.^2 = 259.08\ in.^2$$

Converted to metric, the area equals $259.08\ in.^2 \times 6.452\ \frac{cm^2}{in.^2} = 1671.58\ cm^2$.

The number of solar cells are: 4 sets of 40 series-connected cells per segment: or 160 cells per segment times 4 segments: or 640 cells total. Basic area of the cells is $2cm^2 \times 640 = 1280cm^2$. Area required for interconnections of the cells $= 1280cm^2 \times 1.09 = 1395.2cm^2$.

Total mounting area	=	$1671.58cm^2$
Total area of the cells	=	$\underline{1395.20cm^2}$
Non-cell area	=	$276.38cm^2$

The non-cell area of the platform will have thin second-surface mirrors mounted as an aid in passive thermal control of the spacecraft.

Area distribution is:

$$\frac{\text{cells}}{\text{platform}} = \frac{1395.20cm^2}{1671.58cm^2} \simeq 84\%$$

Solar cells = 84% of available area for power.
Mirrors = 16% used for thermal control.

7.1.3 Platform-Radiator Drawings

MIT-CSR drawings used for the construction of the platform-radiator are:

D-106-001	Segment Assembly
D-106-202-B	Segment
D-106-203-B	Radiator
D-106-217	Compartment Wall, Left
D-106-218	Compartment Wall, Right

7.2 The Electronics Sub-Assembly

The electronics sub-assembly consists of five components, the central Hub and four electronic modules positioned at 90-degree intervals around the Hub

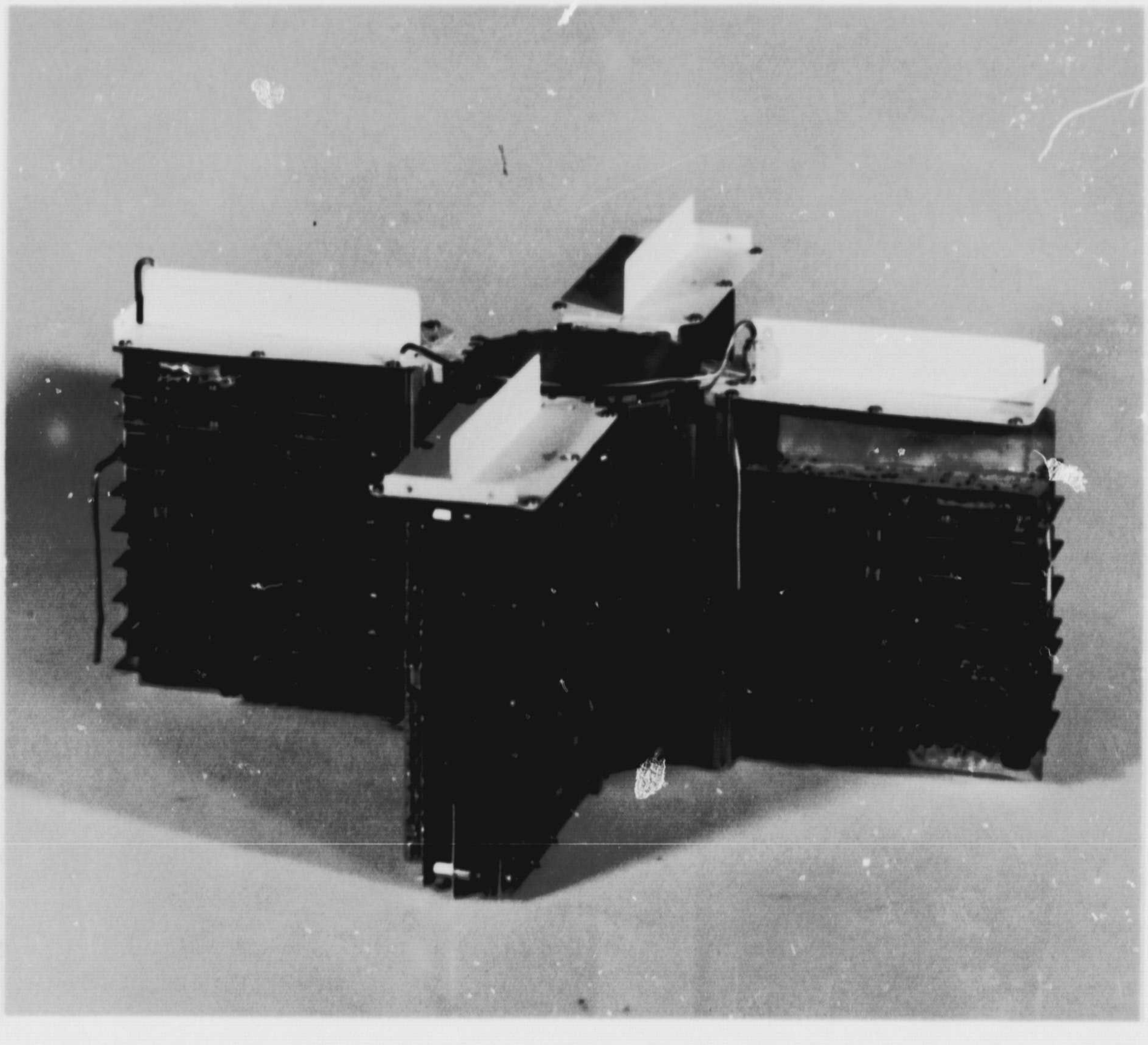

Fig. 7-3 Electronics sub-assembly.

PRECEDING PAGE BLANK NOT FILMED.

as shown in Fig. 7-3.

This packaging configuration was selected to establish thermal and RFI control and to provide for the elimination of standard connectors and epoxy foam encapsulants, while maintaining mechanical and electrical integrity.

7.2.1 The Hub

The Hub is machined from a section of tubular NEMA LE(N), retaining the tubular form over most of its length, with the exception of the front and rear octagonal flanges which are used for hard-mounting the electronic components. The Hub functions as the central mechanical stiffener of the spacecraft; as the housing for the aspect sensor; as the support for intraconnecting wiring; as the initial support of the electronic components; and as the principal launch vehicle-spacecraft mechanical interface member.

The intraconnections of the electrical system are accomplished by placing eight epoxy-Fiberglas boards (G-10, 1/16 in. thick) around the periphery of the Hub; these are used as mounting plates for the receptacles and their associated flexible printed-circuit wiring. Low-level electrical power and control signals are transferred from the electronic modules to the intraconnect wiring through RF filters, which mate with the receptacles due to a compatible hard-mount of the filters in an associated Compartment Shield.

Figure 7-4 shows a sectional view of the electrical intraconnection scheme. The module (PI, PII, PIII, or PIV) may be inserted or removed from the intrawiring around the Hub during system checkout, due to the electromechanical connections provided by the receptacle and RF filter. Prior to flight, all of these connections are to be soldered to provide a parallel current path through the junction and, by so doing, eliminate the necessity of relying on a failure-prone connector in flight.

7.2.2 Hub and Module Drawings

Parts and drawings associated with the Hub are:

MIT-CSR Drawing, D-106-201-B
Amp Receptacle, part no. 380598-1
Erie Filtercon, part no. 1250-003

<u>The Electronic Modules</u> (Components) PI, PII, PIII, PIV

The electronic module consists of four basic mechanical parts:

1.	Compartment Shield	D-106-200-C
2.	Vertical Member	C-106-207-B
3.	Cover	B-106-206
4.	Printed Circuit Board (Master)	D-106-901

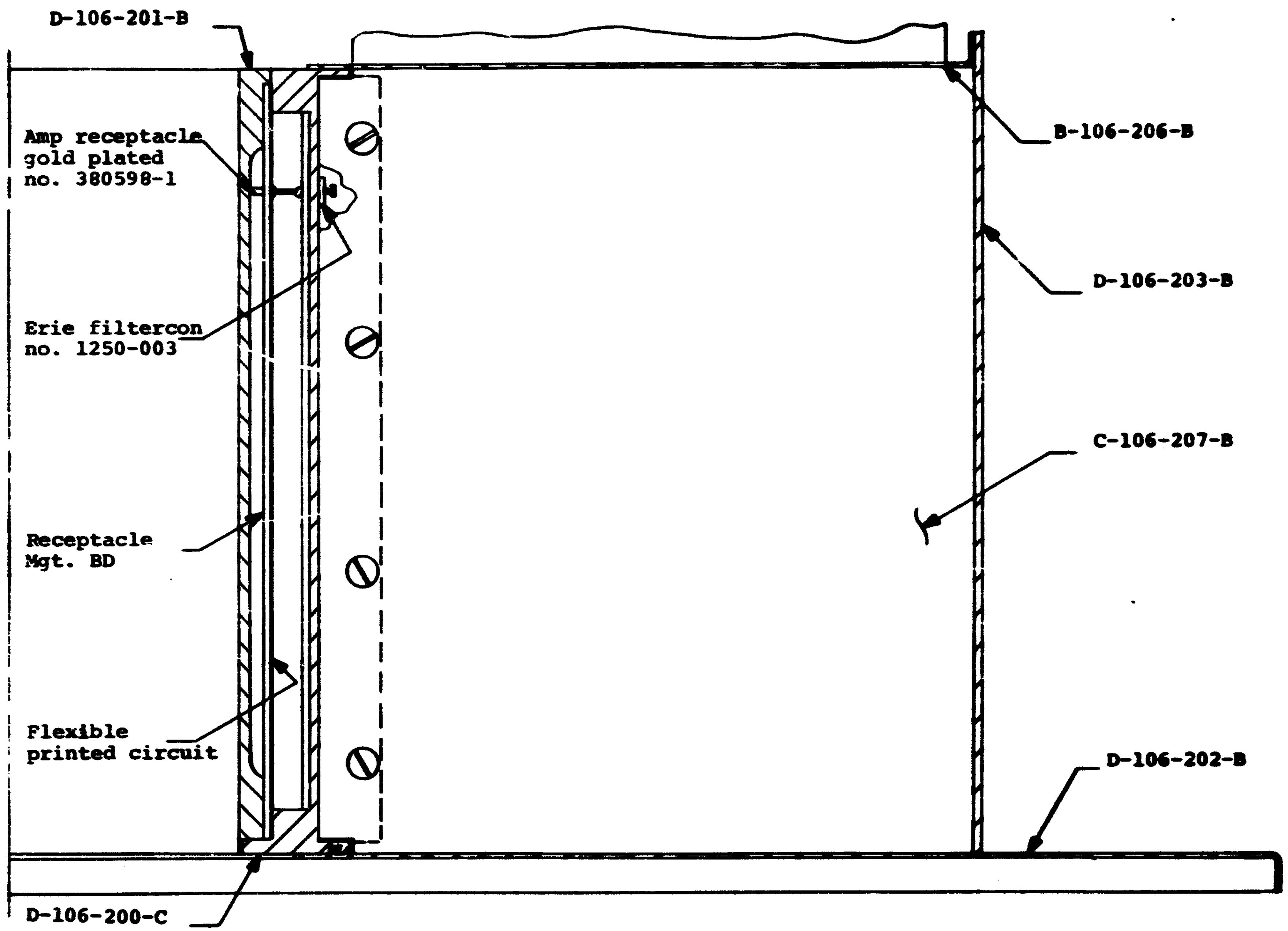

Fig. 7-4 Section view intraconnect.

7.2.3 The Compartment Shield

The Compartment Shield is machined aluminum alloy (2024) and features two parallel flanges (front and rear) which are used for mounting to the Hub; a longitudinal, off-center flange on the opposite side to mount the Vertical Member; and a groove on three sides to accept Metex RFI shielding (Part No. 10-309). The fourth side of the Compartment Shield has the cover permanently attached. Erie RF Filtercons (Part No. 1250-003) are thread-mounted into the two long edges of the Compartment Shield in Specified locations to transfer electrical functions in and out of the electronic compartment.

7.2.4 The Vertical Member

The Vertical Member is a 0.032-in. piece of sheet aluminum (6061). It is used to support printed-circuit boards and to function as a thermal sink for the electronics located in its particular compartment. RF circuit boards are slotted one-half of their length, and are inserted into the Vertical Member by mating with similar slots contained by that part. The aluminum parts and the printed-circuit boards of the electronic module are unitized by soldering, in order to establish an electrical ground return and a thermally-conductive path from the printed-circuit boards. To make practicable the soldered interface within the electronic module, all aluminum parts are copper-plated (0.0005), and then tin-lead plated (0.0005).

The Vertical Member is preheated by an induction method to eliminate its heat-sinking capability. The printed-circuit boards are then fillet-soldered to the Vertical Member with a standard soldering iron.

7.2.5 Cover

The Cover is 0.032 in. sheet aluminum (6061) and is centrally slotted within its length to accommodate the passage of a portion of the Vertical Member through it. The Cover's functions are: to form the sixth side of the electronic compartment (4 fixed, 2 moveable); to heat-sink and provide thermal radiation; to develop mechanical stiffening for the compartment sidewalls and RFI shielding to the compartment. The cover compartment sidewall-closure shielding is accomplished by a strip of RF gasketing, 0.020 in. thick, Eccoshield SV-R.

7.2.6 Plating Specifications and Process

Platings of the Compartment Shield, Vertical Member, and Cover are performed to the following specifications:

Copper - MIL-C-14550 Class 2

Tin-lead (solder) - MIL-F-14072-M222

The total cleaning and plating of these parts is as follows:

Caustic etch
Nitric hydrofloric pickling
Rezincating
Nitric hydrofloric pickling
Rezincating
Copper flash
Copper plate (0.0005 inch)

Bake for 1/2 hour at 375°F; if no blisters, then electrochemically solder plate: (0.005 in.).

7.2.7 Electronics Sub-Assembly Critical Parts Tests

<u>Braid Shielding (RFI)</u>

In order to evaluate the RFI shielding capability of various braid and mounting groove configurations, a mock-up compartment shield was mounted centrally in a box which provided a variable braid compression (gap adjustment). A 75-MHz source was located in one side of the shield and a receiver on the opposite side. In this manner the relative attenuation of the mechanical configuration could be observed.

Table 7-I

Results of RFI shielding tests.

Test No.	Braid Size	Groove Size	Average Gap	Attenuation
1	1/8" Diam.	0.125" × 0.093"	0.012	~ 60dB
2	1/8" Diam.	0.125" × 0.093"	0.016	~ 60dB
3	1/8" Diam.	0.125" × 0.040"	0.060	~ 62dB
4	1/16" × 1/8" flat	0.125" × 0.055"	0.018	~ 23dB
5	1/16" × 1/8" flat	NONE	0.052	~ 11dB
6	1/16" × 1/8" flat	NONE	0.045	~ 37dB
7	1/8" Diam.	0.125" × 0.055"	0.045	~ 43dB

Tests 5 and 6 indicate that a flat braid, when reasonably compressed 0.018 in., does not provide the shielding capability of a round braid seated in a groove, as shown in test 3 which had a compression of 0.025 in.

It can be seen from Tests 1 and 2 that a similarity in the cross-sectional area of the groove and the cross-sectional area of the braid provides an attenuation capability which is not appreciably affected by the amount of compression provided.

Tests 1 and 2: Groove cross-sectional area $= 0.125 \times 0.093 = 0.012$ in.^{2}

1/8" diameter braid cross sectional area $= \pi \times 0.0625^2$
$= 0.0123$ in.^{2}

Projection of braid from groove $= 0.125 - 0.093 = 0.032$ in.

Test 1: Compression $= 0.032 - 0.012 = 0.020$ in.
Test 2: Compression $= 0.032 - 0.016 = 0.016$ in.

Compartment shield drawing D-106-200 shows the braid mounting groove $= 0.93$ in. $\times$ 0.075 in.
Groove C.S. area $= 0.093 \times 0.075 = 0.006975$ in.^{2}
Braid selected is Metex Part No. 10-309 (3/32 in. diam.)
Braid C.S. area $= \pi\ (0.046875)^2 = 0.006902$ in.^{2}
Basic mounting dimension (width) of the braid = 1.830 in.
Total Width $= 1.830 + 2(0.09375) = 2.0175$ in.

Compression $= \frac{0.0175}{2} = 0.00875$ in.

Gap $= \frac{2.00 - 1.98}{2} = 0.010$ in.

RFI Filters

All wiring external to the electronics compartments is exposed to the 2 kilowatts of radiated RF. Leads entering or leaving the electronics compartments are therefore filtered to attenuate this induced signal.

This RF filtering will be provided by Erie Filtercons (Part No. 1250-003). Manufacturer's specifications include the following:

Weight = 1.3 grams

Minimum Insertion Loss over temp. range per MIL-STD-220 = { 2 Amp DC load 45dB; 200 MHz to 10 GHz no load 50dB }

Capacitance = 1500 pF

Working voltage = 100 WV dc @ +125°C
200 WV dc @ +85°C

Operating temp. = -55°C to +125°C

Max dc and low freq current = 10 amperes

Samples of this part were subjected to high-current pulses to monitor possible changes in waveforms, the voltage drop across the device, and their high-current capability. The test pulse format was two 100 ms pulses separated by 100 ms repeated at 52-second intervals.

Table 7-II
Test results on filtercons.

	Risetime ±0.04 μsec		Falltime ±0.04 μsec			
Pulse Current	With Filter	Without Filter	With Filter	Without Filter	Pulse Voltage	Load
4.5A	0.20μs	0.20μs	0.16μs	0.16μs	34V	7.6Ω
8.5A	0.20μs	0.20μs	0.20μs	0.20μs	34V	4.0Ω
13.2A	0.20μs	0.20μs	0.25μs	0.25μs	33V	2.5Ω
20.6A	0.20μs	0.20μs	0.30μs	0.30μs	31V	1.5Ω
43.4A	0.20μs	0.20μs	0.30μs	0.30μs	26V	0.6Ω
Maximum voltage drop across the filter is 0.04 volts at 43.4 amperes.						

Hub Material NEMA-LE

A comparison test of the tapped screw-thread strength of NEMA-LE was made with aluminum and magnesium, using standard tapped holes and Heli-coil inserts.

A stainless steel 4-40 screw was inserted in the thread to be tested, leaving sufficient clearance under the screw head to mount the sensor of a dial-indicator micrometer. Compression force was applied to the screw through a Dillon force gauge.

Table 7-III
Thread strength test results (averaged).

STD. Thread	NEMA-LE	Magnesium	Aluminum
Force	725 lb	900 lb	1600 lb
Deflection	0.017 in.	0.014 in.	0.026 in.
Heli-coil insert			
Force	600 lb	1000 lb	1500 lb
Deflection	0.016 in.	0.020 in.	0.029 in.

Part of the deflection indicated was, of course, due to compression of the test screw. Most of the tests terminated in a shearing of the top two threads of the various materials. These forces represent the thread failure of the material, and not the maximum allowable force.

7.3 Sails

Four triangular-shaped sails are used for orientation and stabilization of the spacecraft. Each of these has its vertex located between the electronic compartments, where it is attached to its associated pitch-drive mechanism. The presently-considered sail is fabricated with aluminized mylar which is stretched between two longerons of prestressed spring-steel tape and stiffened by a cross-frame rod at the extremity (base).

Each sail has a vertex angle of 14^{o} and an area of about $0.14\ m^2$, for a total sail area of $0.56\ m^2$. With the flight position of the sails determined by a rearward (aft) canting of 26^{o}, (from the perpendicular to the spacecraft's spin axis), the total projected zero-sun-angle area would be about $0.47\ m^2$.

During the launch phase, each of the sails is stored in a tubular configuration adjacent to the rear of the radiator. The storage of the sails during launch is provided to insure against physical damage from centrifugal loading caused by spinup and despin of the launch vehicle and the spacecraft. Thermal protection from aerodynamically-generated heat is provided, since all exposed aluminized mylar is attached to the helixed longeron which will act as a heat sink.

Sail storage is accomplished by winding the sail from the base toward the vertex on a 1 1/4 in. diameter pipe in the rearward (aft) direction. This action causes the longerons to form an overlapping, bifilar helix spring, which has sufficient stored energy to deploy a test sail to the flight position against against a 1 g load.

The aspect sensor control logic will provide a negative pitch command to the sails when the spacecraft's spin axis approaches a small angle to the sun line, an action that is principally provided to prevent the spacecraft's spin rate from approaching too close to zero. The secondary benefits from the negative pitch control are: the obviation of design concern in establishing an absolute mechanical zero sail-pitch angle, and the necessity of maintaining a wrinkle-free sail surface, either of which could cause residual torque errors if the sails were to be positioned in a supposed zero-torque situation.

7.3.1 Sail Drive Mechanism

The design problems associated with the sail drive mechanism are centered about its control system and the sail-pitch drive motor. Three types of control candidates are possible: one is a proportional system which provides sail-pitch corrections in proportion to the pointing and/or spin error. A second type is the bang-bang approach, a system which delays sail motion until a pre-set minimum or maximum angle or rate is detected, and then applies maximum pitch movement. The third system is a combination of the two, in which bang-bang methods are used when large angle or rate errors are involved, and proportional control is applied when small errors are to be corrected.

In the engineering models of the spacecraft, the design concern for control-system reliability places a priority emphasis on the simple approach, which would be an "on-off" concept, or the bang-bang system.

Once the spacecraft has accomplished its initial sun orientation, torques caused by minor geometric unsymmetries could still spin-up (or spin-down) the craft, with a resultant pointing error being induced. Rather than wait for the pointing error to reach some pre-set maximum angle before applying a corrective pitch to the sail, an immediate small pitch could be applied, which indeed, might have the effect of generating an exact counter-torque (or nearly so) that would have the general tendency of minimizing the total number of sail-pitch adjustments required during the mission.

The combination of a bang-bang control, which is designed to override the proportional control, seems to provide a system that is reasonably simple, a redundancy for insurance, and has a built-in capability of autogenerating a near-equaliberatory spacecraft geometry.

<u>Stepping Motor</u>

Possible design candidates for the stepping motor which will be used for sail-pitch motion are divided into two categories, both of which have been successfully utilized in space application.

The first is the type which is constructed with a permanent-magnet armature, and has a sequentially-coded pulse format applied to the field, which incrementally causes a rotation of the field, with the resultant rotation of the magnetic armature. These motors are available in a variety of physical sizes and output torques, but require an electronic system to provide the various pulse-code formats for stepping the motors in either direction.

A second type of stepping motor is the solenoid-activated device which has a mechanical linear-to-rotary converter. Two types of converters are used, one of which is ratchet and pawl, the other a ball and wedge-shaped detent design. These motors have a high torque-to-weight parameter, but are limited to a monodirectional rotation. To compensate for this restriction, the ball converter can use two motors in a back-to-back configuration to provide the bi-directional capability, but the ratchet-and-pawl type requires an auxiliary solenoid to provide a direct-gear transfer in the driven gear train to accomplish a rotational direction change.

A consideration of the advantages and disadvantages of all these motor types makes the back-to-back, solenoid-activated ball and detent converter to be most favorable for selection. Typical of these motors is the Ledex Size 11, which was redesigned for space and used on Surveyor to drive the solar panel arrays and the earth-pointing antenna.

Although the gearing and bearings on the sail-drive mechanism are designed to help prevent an accumulation of friction and space-induced cold welding, the design simplicity of a high-torque output solenoid appears to have a greater, more prolonged capability of overcoming vacuum-induced stiction.

The proposed sail drive is shown in Fig. 7-5. A commercial version of the stepper motor is shown (Ledex 213227-029), which drives a 12.44-to-1 reduction gear assembly through two non-slip, low-friction belts.

7.4 The Spacecraft's Mechanical Sequence at Injection

Timing apparatus associated with the Scout's fifth stage provides the electrical ignition of the BE-3, which has a 10-second burn time; and after an appropriate delay (possibly several minutes) the central explosive bolt is fired and sheared, causing a spring-forced separation of about 3 ft/s velocity between the spacecraft and the adapter-motor assembly.

The spin rate of the total assembly up to this point is in the approximate range of 180 to 200 rpm. In order to help minimize spacecraft tip-off during separation and to despin known moments of inertia, this spin rate is maintained until after separation, when the mechanical sequence of despinning and deployment will take place.

Design calculation and demonstrative models of the separation sensors, despin and deployment hardware places the initial weight of these devices in the 500 to 600 gm range. Of this total weight, about 68.2% is associated with sail and antenna restrainers and release hardware, 22.7% with the despin assembly, and 9.1% with the separation detectors.

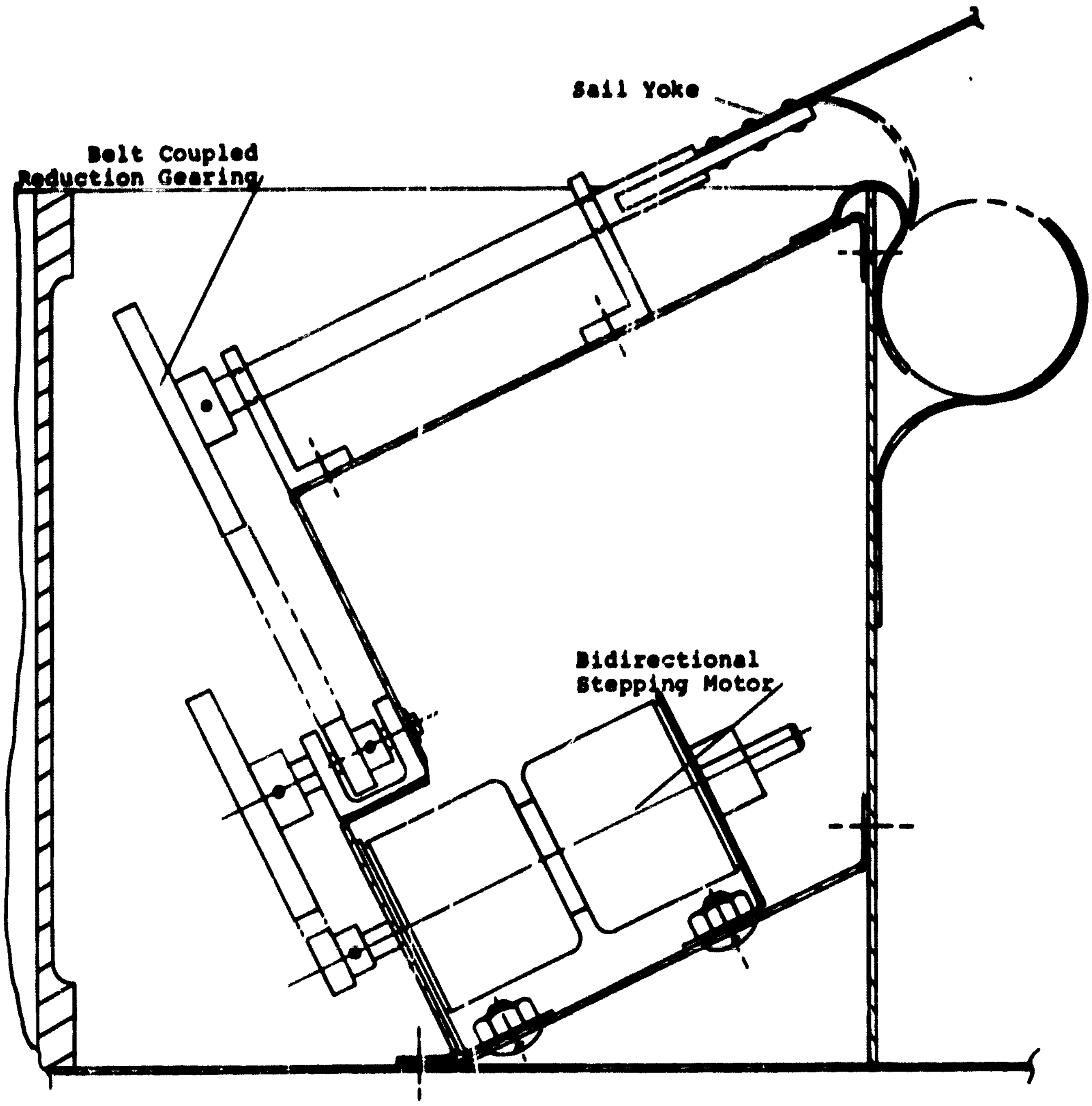

Fig. 7-5 Sail drive mechanism.

Figure 7-6 shows a schematic representation of the separation sensors (see 6.3.2.), which are spring-loaded pin-pullers whose linear motion upon separation releases the despin masses. When the despin masses have moved from a tangential to a radial position (end of despin), their release is accomplished by a combination of their outward radial force and the now-unrestrained despin anchor.

The departure of the despinner is followed by the activation of the two sail pin-pullers, which unlock the sail-restraining cables and covers, allowing deployment of the sails to occur.

The antennas which are displaced from the sail axes by 45° are restrained from deploying by a wedge of material on the despin wire. The wedge is held in position during despin by the tangential force on that wire, which is removed by the despinner moving radially about 45° before final spacecraft despin has occurred. The time difference between the deployment of the antennas and the sails will be small, due to the fact that, although the spacecraft at this time moves through 45° at a low angular rate, the despin wire moves from the tangent to the radial position (90°) with a significantly higher angular rate.

7.4.1 Possible Separation Dynamics Compensation Requirements

The mechanical sequence outlined in Sec. 7.4 is based on the premise that the booster motor-spacecraft assembly has a slow rate of cone angle buildup during the long coast period (delay time to separation).

If the cone-angle buildup is rapid and approaches 30° during the coasting period after the fifth-stage burnout, the mechanical sequence of initiating despin upon separation becomes a marginal safety situation. For the danger of collision between the deploying spacecraft sails and the coning adapter (transtage) is increased, due to the tangential separation velocity (caused by the coning), on the spacecraft approaches its axial separation velocity. This action would produce a separation angle approaching 45°, and with despin and deployment occurring in 0.5 to 0.7 second after separation, the sail tips could be below or in the plane of the coning transtage.

Similarly, the long-coast phase from burnout of the fifth stage to spacecraft separation appears to be capable of causing a large deviation in the nominal spacecraft spin axis-sunline angle.

Tentative solutions to these dynamically-produced problems include:

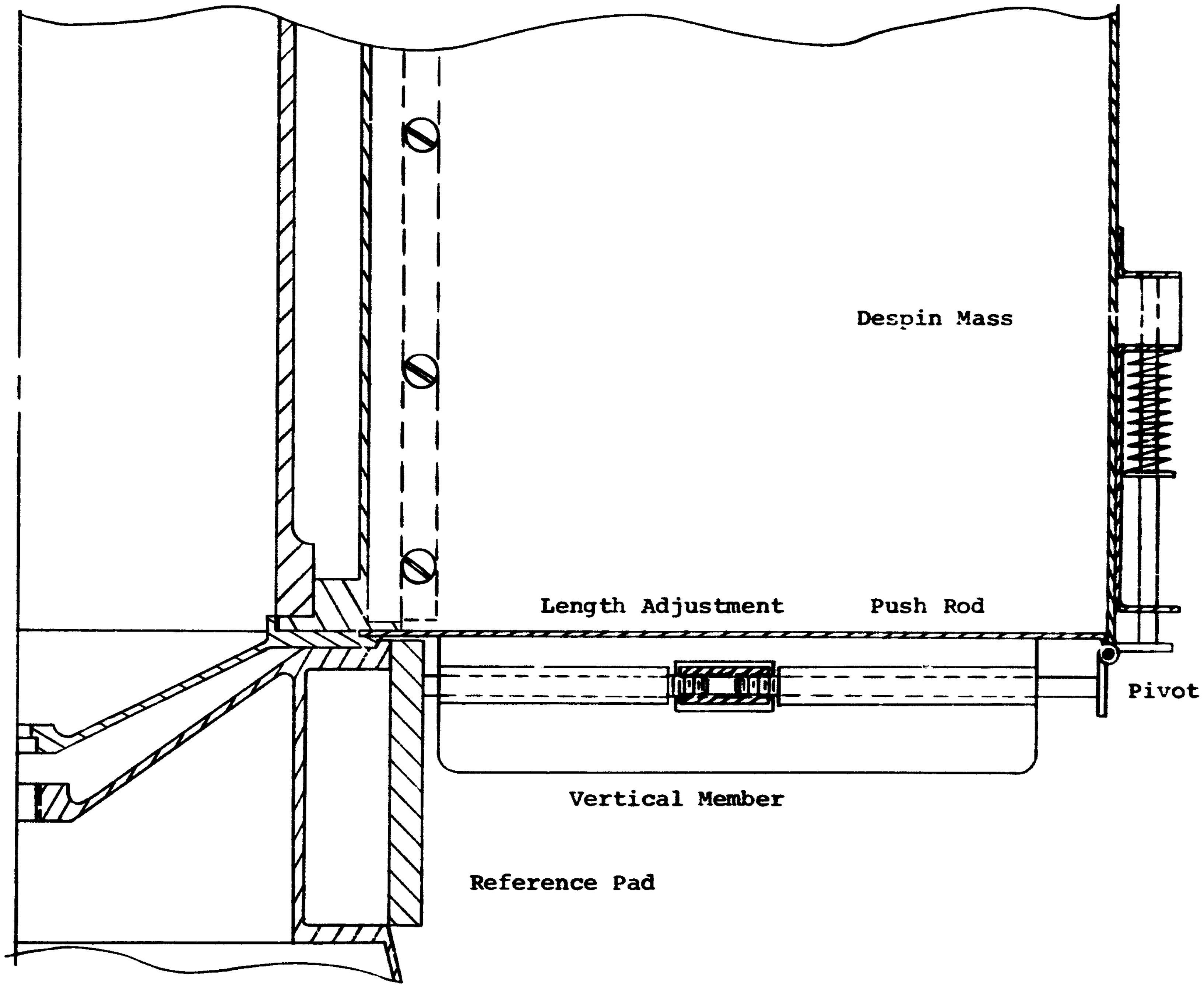

Fig. 7-6 Schematic separation sensor.

More rigid control of cone-generating parameters.

Shorter coast period.

Increased separation-spring energy.

Sun-sensed activation of separation.

An immediate transfer of spin to the major moments axis of the booster-adapter assembly after separation occurs.

A delay in activating despin of the spacecraft.

If engineering tolerances preclude a reasonable tightening of alignment parameters which are involved with generating an excessive coning angle of the final launch vehicle assembly, the sun-sensed activation of separation may be utilized. This would be simply the logically ANDED separation signal from the timer and the amplified output of a photoelectric device to cause separation to occur in the most favorable sector of the cone.

The transfer of spin to the major moment axis of the booster-adapter assembly may be accomplished by providing a despin system which has one-half of the despin device mounted on each side of the center of mass of the assembly.

The separation-to-despin delay can be accomplished for about the same weight (50 gm) as the direct-acting mechanical system. Power would be supplied to an E-cell timing circuit by a separation-activated switch, with the amplified output of this circuit providing the ignition energy to a pair of pyrotechnic dimple-moter activated pin-pullers which would release the despin weights.

Initial tests of hardware built to this design concept indicate a total energy requirement of about 0.2 joule to provide a five-minute delay, plus the pyrotechnic release which demonstrate load-release capability in excess of twenty pounds.

7.5 Weight Distribution of the Spacecraft

Many of the spacecraft parts are multi-functional, therefore could be listed in any one of several categories. But in this distribution analysis, each part was included in an area considered representative of its primary function:

Sub-Assembly	Weight (gm)	Percentage
Main Electronics	3995.8 gm	31.2
Power	2636.0 gm	20.6
Thermal and/or Mechanical	3259.8 gm	25.5
Orientation	2904.6 gm	22.7
TOTAL	12,796.2 gm	100.0

In the derivation of these weights, the following contingencies were used:

Sub-assemblies considered frozen	= 3%
Sub-assemblies partially completed	= 10%
Sub-assemblies in design	= 25%

The breakdown of the sub-assembly weight is as follows:

Main Electronics

RF Sub-system	1880.0 gm + 10% =	2068.0 gm
Digital Sub-system	383.1 gm + 10% =	421.4 gm
Intraconnections	351.2 gm + 3% =	361.7 gm
Chassis	897.8 gm + 3% =	924.7 gm
Antennas	200.0 gm + 10% =	220.0 gm
TOTAL		3995.8 gm

Power

Solar Cells	(calculated)	516.0 gm
Converters	347.6 + 25%	434.5 gm
Storage Capacitors	1636.0 + 3%	1685.5 gm
TOTAL		2636.0 gm

Thermal and/or Mechanical

Platform-Radiator	(weighed)	2034.8 gm
Sail Release	373.5 + 3%	384.7 gm
Despin	175.0 + 3%	180.3 gm
Balance Weights	600.0 + 10%	660.0 gm
TOTAL		3259.8 gm

Orientation

Aspect Sensor	755.4 + 25%	944.3 gm
Sails and Drive	1903.2 + 3%	1960.3 gm
TOTAL		2904.6 gm

These listed weights are shown graphically in Fig. 7-7.

7.6 Moments of Inertia

The moments of inertia of the spacecraft have been calculated for the spin and yaw-pitch axes for both the deployed and undeployed states. The numerical values obtained from the use of weights given in Sec 7.5 are listed in the table below.

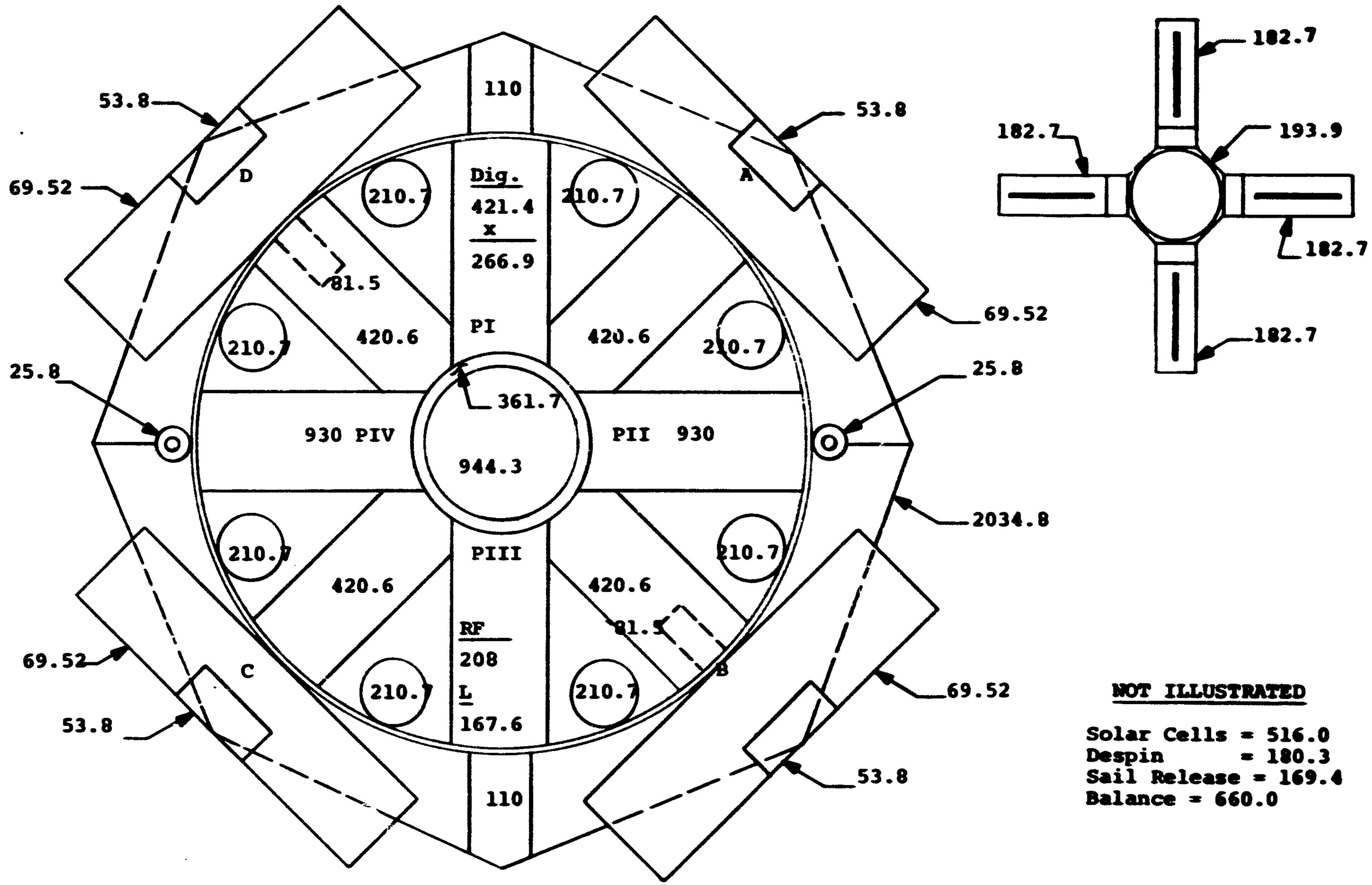

Fig. 7-7 Weight distribution.

Table 7-IV

Results: moments of inertia.

Part	Spin ($\times 10^{-6}$ gm-cm^2) Deploy.	Not Deploy.	Pitch, Yaw ($\times 10^{-6}$ gm-cm^2) Deploy.	Not Deploy.
Platform	0.25190	see deploy.	0.19600	see deploy.
Radiator	0.39100	"	0.32050	"
Compart. Walls	0.09398	"	0.05485	"
Compart. Covers	0.01379	"	0.01334	"
Electronics	0.64170	"	0.39146	"
Hub	0.01321	see deploy.	0.01579	see deploy.
Contents of Hub	0.01250	"	0.02651	"
Damper	0.00292	"	0.00786	"
Capacitors	0.52036	"	0.30015	"
Antennas	0.23963	0.12696	0.09537	0.07950
Sail Drive	0.28084	see deploy.	0.15737	see deploy.
Sail	2.02748	0.32293	1.38889	0.18257
Despin Mech.	0.08000	see deploy.	0.03920	see deploy.
Sail Depl. Mech.	0.07220	"	0.00320	"
TOTAL	4.642	2.824	3.011	1.789

CHAPTER 8

8.0 ATTITUDE CONTROL SYSTEM

8.1 Introduction

The Sunblazer is a spinning, oriented spacecraft which faces the sun for the purpose of transmitting a radio wave through the corona.

Orientation of the spacecraft is desirable for several reasons:

1a. Solar cell power is maximized when all the cells are in a plane facing the sun. Solar cell impedance matching and thermal variations are also minimized when the solar input is nearly static, as it would be for an oriented spacecraft.

1b. Thermal design of spacecraft experiment and electronics packages is simplified when their thermal surroundings are not subjected to pseudo-random solar inputs.

1c. Antenna patterns can be maximized for a spacecraft with an axis oriented toward the sun. For transmission through the solar corona between two points in the ecliptic plane (spacecraft to earth), system performance can be improved by maximizing the antenna pattern in the direction of the sun. With a spinning spacecraft, the antenna pattern would ideally by symmetric about the spin axis, with gain versus θ roughly inversely proportional to distance-squared (as a function of θ).

A <u>spinning</u> spacecraft is desirable for several reasons:

2a. A reliable passive mechanism which would despin the spacecraft down to a spin rate on the order of one revolution per hour is not known. However, spin rates on the on the order of 1-10 r/min are believed feasible.

2b. Disturbances of micrometeorites, or of other momentum impulses to the spacecraft spinning at 1 r/min, will be hundreds of times smaller than to a static spacecraft. For the Sunblazer, based on Pegasus data (NASA-TM-X-1316), the probability of a disturbance greater that 2^{O} to the spinning spacecraft is on the order of 1% (in one year).

2c. Motion of spacecraft simplifies to precessional mode for spin rates on the order of 1 r/min, making control simpler to achieve than for a slower spacecraft requiring description of motion by complete equations of motion. For the spacecraft ($\omega \sim$ 1 r/min), nutational motion also simplifies (to the force-free approximation).

2d. Rotation of the spacecraft makes possible a limited scan of a sensor, or some other device, in a circle about the spin axis. This rotation, and the fact that the spin axis is not pointed exactly at the sun in the normal mode of motion, allow measurement of the angular velocity by an on-board sensor.

Considering the preceding reasons for having an oriented, spinning spacecraft, a list of tentative design objectives for the Sunblazer attitude-control system will be discussed in sections 8.1.1 and 8.1.2.

8.1.1 Orientation of Spacecraft within 10^{O} of Sun

Twenty-five degrees would be sufficient to ensure roughly 90% of maximum solar-cell power, but 10^{O} is desirable to avoid losses in antenna pattern when spacecraft-sun-earth angle is greater than, say, 30^{O} from conjunction.

8.1.2 Spin Rate of Spacecraft Between Two Limits

A lower limit of about 0.1 r/min, which would make the spin rate at least five times larger than the libration rate (as discussed below under the equations of motion), would ensure that the motion is a reasonable approximation to the precessional mode. A high spin rate would be desirable for reasons 2a - 2d above, in addition to the increased sensitivity of the motion to torque imbalances at low spin rates. An upper limit of about 19 r/min would ensure that the pseudo-equilibrim orientation of the spin axis will not exceed roughly 5^{O} from the sun. These limits assume a precession-torque coefficient of about 0.2 dyn-cm/deg, which would apply to the vane system described below[1].

Spin rates near the lower limit of 0.1 r/min should occur after the initial phase of acquisition, as illustrated in the solutions below. Spin rates near the upper limit can occur as a result of four causes:

1. Momentum buildup as a result of solar-pressure torque imbalances on the sail structure (described below). For the typical crude design considered, such motion is likely to build to an asymptotic maximum spin rate of roughly 10 r/min within about a year.

2. Mechanical failure of the control system, with the vanes stuck in one position, resulting in a large spin torque. In this case, the whole spacecraft will probably fail.

3. Failure of a despin mechanism. This could be caused by tumbling of the rocket-payload prior to separation and/or a faulty separation mechanism.

4. Impact of a particle with the spacecraft, followed by conversion of axes (assuming an internal damping mechanism), resulting in a relatively high spin rate about the spacecraft axis of maximum moment of inertia (and axis of symmetry), with the spin axis, in general, not directed at the sun.

In cases 3 and 4, the vehicle would probably stabilize (assuming that the control system were properly activated), but stabilization could take a long time, depending on the residual spin rate.

Generally speaking, spin control is not so critical as θ-control. That is why spin rate is allowed to vary within such wide limits. In fact, for the system described below, it is not felt necessary to control the spin rate actively because 1)the probability of a disturbance may not be great enough to justify the complexity of an independent, active spin-control sub-system, and 2) some disturbances can be corrected for the proposed system, with the help of a passive mechanism, thermal damping[2]. Thermal damping should help stabilize the system at very low spin rates, and the vanes should work at very high spin rates. These cases have been studied on a computer to see how wide a margin of stability exists (as a function of system parameters, error conditions, etc). (See Section 8.9)

8.1.3 Simplicity of Control System

Simplicity of the control system is desirable for the reliability of a spacecraft which is to maintain its stability for a period on the order of one year.

Ideally, the control system would be completely passive (no moving parts and no expenditure of material), and would control both θ and spin rate to desired values. The control system which is described below is semi-passive (no expenditure of material) and can only be said to control θ within limits (it provides practically no control of spin rate).

8.2 Solar Pressure Stabilization

The use of solar pressure as a means for stabilizing a solar-oriented satellite has definite advantages:

1. The solar radiation flux has an inherent reference direction, toward which the satellite is to be directed.

2. Solar radiation provides a practically unlimited source of momentum. Completely passive stabilization systems based on solar pressure have been studied before[(1), (3)]. (See Section 8.3 for systems based on solar momentum.)

Solar radiation is considered to be a flux of energy parallel to the line from the spacecraft to the sun. (The finite angular size of the sun, and the slight convergence of the solar rays, will not be considered here.) Solar radiation can be considered a flux of momentum, which is absorbed and reflected according to the laws of geometrical optics[(4)]. Given a flux of energy of I watts/m^2 in a given direction, the flux of momentum is

$$p = \frac{I}{c} \qquad \text{(MKS)} \qquad (8.1)$$

across a surface perpendicular to the given direction, where c = velocity of light (MKS). If the flux of energy is reflected from a surface perpendicular to the given direction, then the radiation pressure on the surface is

$$p_o = \frac{2I}{c} \qquad \text{(MKS)} \qquad (8.2)$$

If the flux of energy is reflected from a surface with a normal making an angle θ with the flux direction, then the radiation pressure on the surface is (see Fig. 8-1)

$$p_r(\theta) = \frac{2I}{c} \cos^2\theta \qquad \text{(MKS)} \qquad (8.3)$$

(This expression is derived by reflecting the component of momentum perpendicular to the surface.)

Assuming a numerical value for I = 1380 watt/m^2, [(5)] a numerical value for p_o can be calculated as

$$p_o = 0.92 \text{ dyn/m}^2 \qquad (8.4)$$

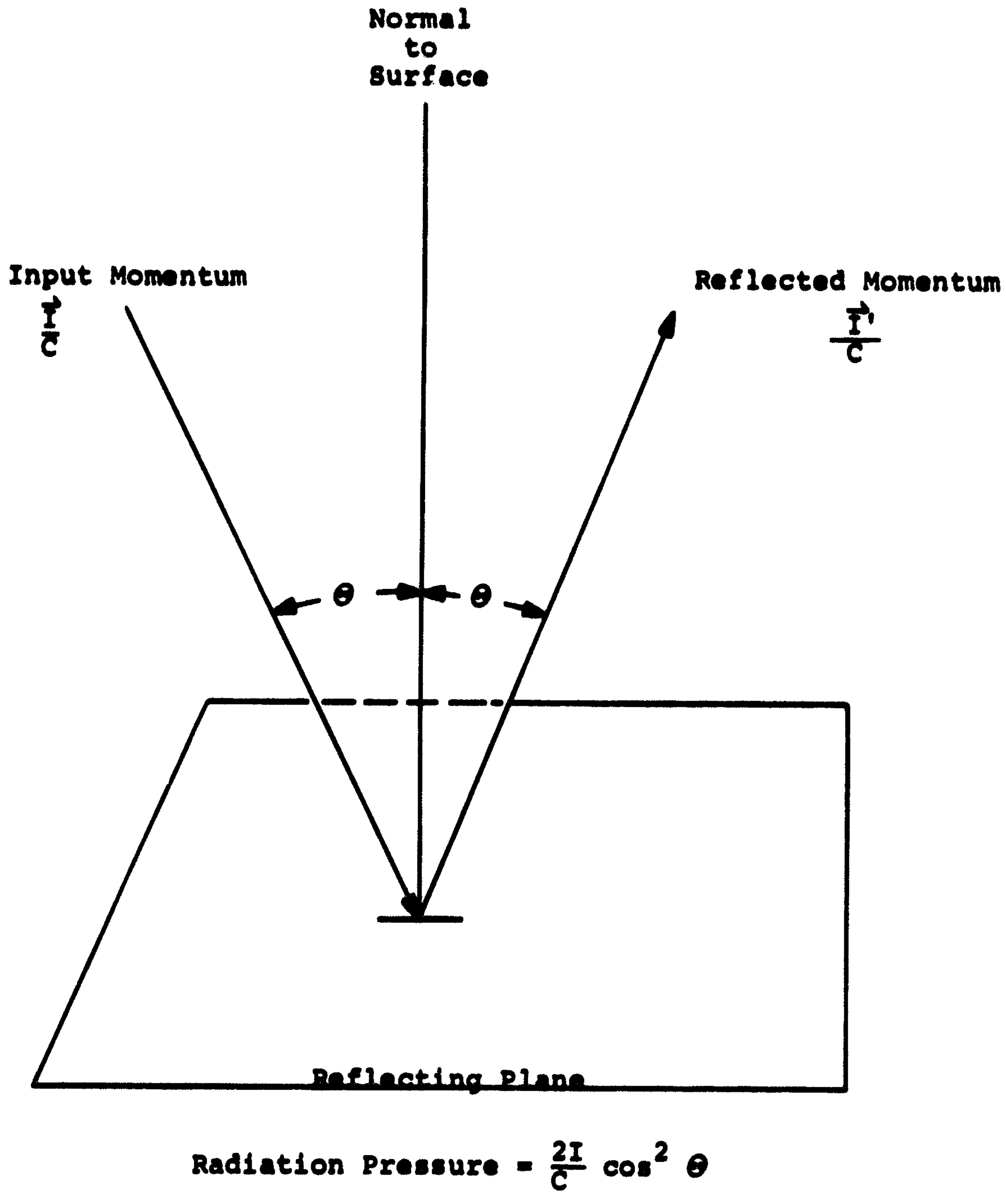

Fig. 8-1 Radiation pressure geometry.

By reflecting and absorbing this momentum at surfaces which are geometrically asymmetrical with respect to a plane made by the sun line and an axis of the spacecraft, it is possible to produce torques which act in that plane perpendicular to that axis and along that axis. These torques can be used to act on a spacecraft which is spinning about an axis, respectively to precess that axis toward the sun and to change the angular velocity about that axis.

These torque components exist in all the systems which have been studied and are described below. Incidently, the force components have been worked out for the vane system described below, and the effect on the orbital parameters of the satellite can easily be estimated.

8.3 Basic Stabilization Systems

Several stabilization systems utilizing solar pressure have been studied, and are mentioned in the following:

1. Totally passive, librating system with weathercock sail, using a thermal damper and/or a mechanical damper. Problems of total despin and of sensitivity to disturbances eliminated this system.

2. Semi-passive, librating system with movable sail. Problems of control-system requirements and of sensitivity to disturbances eliminated this system.

3. Totally passive, spinning system with reradiative damper[2] Problems of despin to a low rate and of long-term spin control eliminated this system.

4. Totally passive, spinning system with simple, asymmetrical sail and no spin control[1]. Longterm spin control is a problem with this system.

5. Totally passive, spinning system with a compound, asymmetrical sail providing angle and spin control. Difficulty of constructing this sail and instability of system for angles greater than 90° eliminated this system[3].

6. Totally passive, spinning system with a compound, asymmetrical providing angle and spin control, and an improved, ring-type, reradiative damper providing additional angle stability. Difficulty of construction, instability for angles greater than 90°, and the relatively low absolute efficiency of such a system

have eliminated this system in favor of the semi-passive vane-type system. (At this point, absolute efficiency can be defined as maximum erecting torque/total sail area, although it should be realized that a final evaluation of performance should involve total erecting time, which is a complicated function of erecting and spin torques, moments of inertia, and initial and final conditions).

7. Semi-passive, spinning system with movable vanes providing angle control. Spin is not controlled, but is expected to stay within reasonable limits. This system has the big advantages of being much faster than the passive systems and of providing stability out to large angles, near 180°. This system has the disadvantages of requiring a mechanical device to rotate the vanes, which will probably have to be activated twice (one cycle, on-off) in a period of several weeks. It also lacks a spin-control subsystem, which would be desirable in the improbable occurrence of a momentum disturbance caused by a micrometeorite or by outgassing of a component, etc.

All of these systems have been investigated. However, only the Falcovitz sail (5,6) and the vane-type sail (7) have been studied in sufficient detail to show feasibility for the Sunblazer application. The Falcovitz sail has been referenced, and the vane system is presented below[3].

8.4 Special Sunblazer Conditions

Special conditions peculiar to the Sunblazer spacecraft place special constraints on the design of the attitude-control system. Such conditions are initial conditions, tracking requirements, orbit conditions, and weight and volume requirements.

8.4.1 Initial Conditions

Initial conditions are determined by the launch trajectory and spin history of the rocket. In the absence of more accurate information, it is assumed that the initial angle and spin rate are respectively 60° from the sun and 200 r/min (referred to the major axis of the spacecraft), and that the initial angle between the spacecraft axis and the sun line may vary between 45° and 90°. Another initial condition which is assumed is that the spacecraft is also nutating with a half-cone angle of 10°. However, it is realized that, because of an attempt to coast after burnout with the last-stage rocket motor attached to the spacecraft, this angle could increase to near 90° as the spin of the motor-spacecraft converts to tumble; in this case, a despin mechanism on the spacecraft would almost certainly fail (if the spacecraft were tumbling). Another uncertainty in the initial conditions could be caused by an attempt to despin the motor-spacecraft prior to separation; because of uncertainty in the burnout moment of inertia, a sizable error could be caused by a yo-yo type of despin mechanism. Repeating, the nominal conditions are assumed to be an angle of 60° from the sun, nutations with a half-cone angle of 10°, a spin rate of 200 r/min.

The inital conditions are important to the initial phase of stabilization because, for the vanes system: 1) stabilization time increases very rapidly as the initial angle increases; 2) stabilization time, to a first approximation, varies linearly with the initial spin rate; and 3) nutations, or more seriously, tumbling, can confuse a sun sensor or foul up a despin mechanism.

8.4.2 Tracking Requirements

Tracking requirements make it desirable that the Sunblazer orient toward the sun and start transmitting as soon as possible, in order to make an estimate of the orbital parameters as accurately as possible while the signal-to-noise ratio is still relatively high. Tracking requirements should not be very critical for the experiment, because the beamwidth of the proposed antenna should be wide enough that the angles from the orbit to the earth should not need to be known to better than about 0.1°. However, accurate tracking may be desirable to evaluate the performance of the launch vehicle.

8.4.3 Orbit Conditions

Orbit conditions do not significantly affect the dynamical motion of the spacecraft. It can be shown that the dynamical trajectories of the spacecraft's rigid-body motion are relatively invariant to motion around the orbit. Assuming that the spacecraft is launched at 1 AU, we can neglect the variation in initial solar intensity caused by the slight eccentricity of the earth's orbit. The most significant effect on orbit conditions is the change in spacecraft temperature distribution, which will not significantly affect the spacecraft rigid-body dynamics.

8.4.4 Weight and Volume Requirements

Weight and volume requirements place an upper limit on the size of the attitude-control system. For the vanes system, it is felt that the whole system could be built at less than 200 g and could be stowed within the available nosecone space without too much loss in performance. For the Falcovitz system (mentioned above), there are critical tolera... on the design of the sail, possibly requiring a more rigid structure weighing around 500 g, probably requiring storage of the whole sail without folding and deployment. But for the vanes system, weight and volume requirements are not felt to be critical.

8.5 Basic Description of Vanes System

The vanes system is a semi-passive attitude-control system utilizing the effect of solar pressure on the vanes to produce torques which will align the spacecraft spin axis toward the sun. The system is called semi-passive because 1) it does not expend any material, but 2) it does require the mechanical motion of the vanes to change the torques as the angle between the spacecraft spin axis and the sun exceeds certain limits.

As presently conceived, the vanes system (shown in Fig. 8.2 below) consists of several parts:

1. Four triangular vanes, attached to the spacecraft at points spaced 90^{o} around the rear of the spacecraft cylindrical radiator. The vanes are to be made of mylar, attached to a furlable structure.

2. Four stepping motors, to rotate the vanes about their longitudinal axis. For the following anglysis, the vanes are assumed to have three positions: $+35.26^{o}$, 0^{o} ($\pm 1^{o}$), -35.26^{o}. The position 35.26^{o} was found to maximize the spin and erecting torques. The 0^{o} position is considered to have some error because of imperfect design and construction of the vane and stepping mechanism.

3. A control sub-system, to tell the vanes when to switch between the three positions. The vanes are assumed to work synchronously, because, for a fast-spinning spacecraft, the advantages of switching them asynchronoulsy would require switching each vane twice for each revolution of the spacecraft (on the order of twice per minute) instead of once every few days, which could make the mechanical system less reliable, in addition to requiring a more complex control logic than for the proposed system. Such asynchronous switching would have very definite advantages if the spacecraft were trapped in a very low-spin mode, but the probability of this occurring is not felt to be high

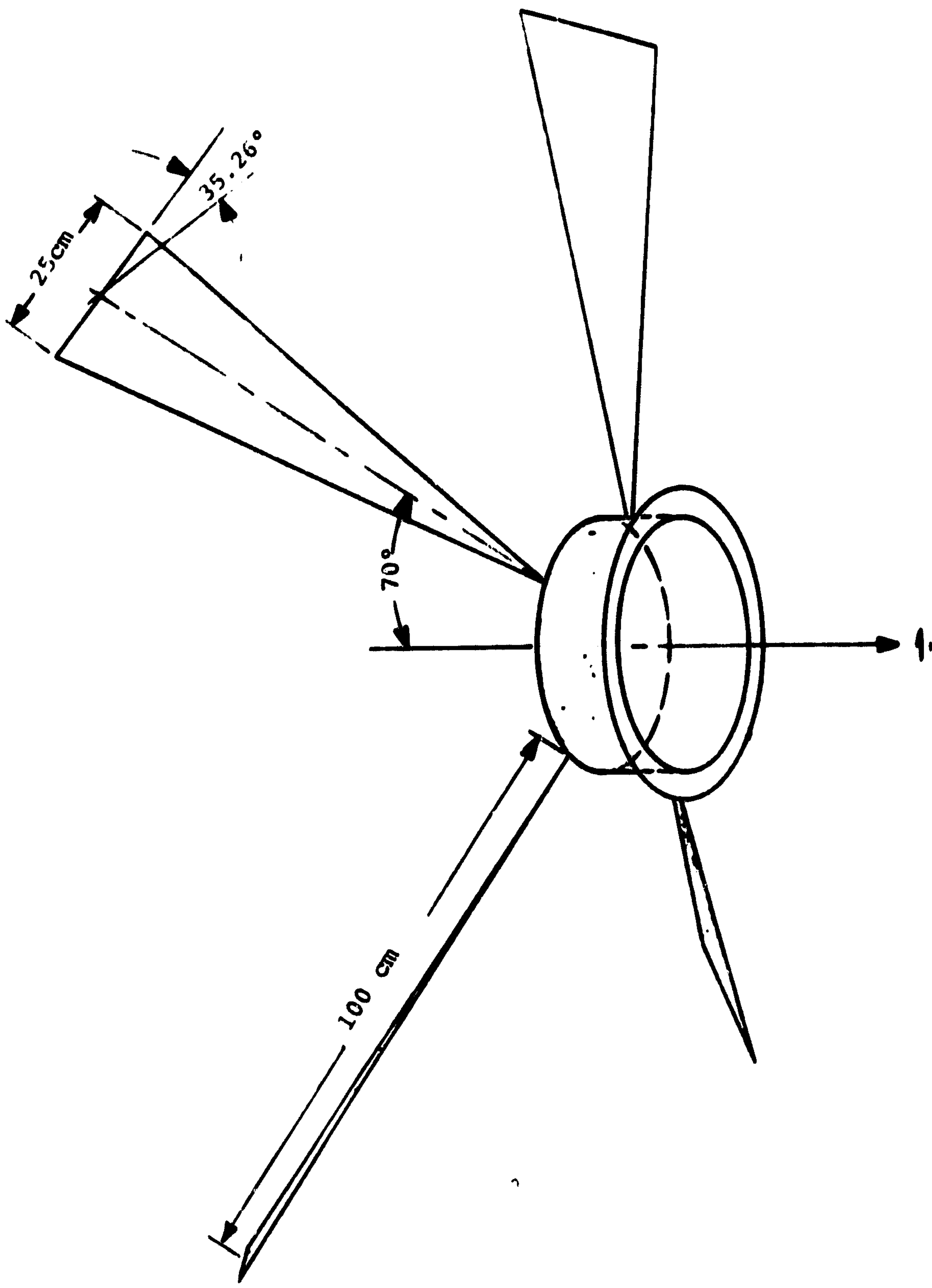

Fig. 8-2 Configuration of stabilizing vanes.

enough to justify the additional complexity.

4. A sensor, to measure the angle between the spacecraft axis of symmetry and the sun line, and a sensor to measure the spin rate of the spacecraft. These measurements are used as inputs to the control circuits which decide when to switch the vanes.

The vanes are controlled as a function of angle, not as a function of spin rate, with one exception: if the spin rate decreases, heading toward the danger zone near 0 r/min, it would be desriable to trim the vanes. Trimming by increments on the order of a fraction of a degree to provide a positive spin torque and an increasing spin rate, will insure the normal mode of motion discussed below and in Section 8.9.

Normal operations of the attitude-control system can be divided into two modes: initial and long term. Both modes can be controlled by the same logic. The common logic, which controls the vanes of the proposed system for all modes, is very simple: If the spacecraft-sun angle is greater than an upper limit, say 10°, then the vanes turn to ±35.26 (depending on the spin direction). If the spacecraft-sun angle is less than a lower limit, say 2°, then the vanes go to 0°. However, if the spacecraft spin rate starts to decrease, then the vanes should be trimmed to provide a positive spin torque.

Given this logic, the typical motion of the spacecraft is summarized as follows: Initially, the spacecraft is at a large angle (assumed $\sim 60^{\circ}$), spinning fast (it is assumed that after despin by the MIT mechanism, the spin rate would be about 20 r/min) therefore, the vanes would be pitched to a full -35.26°. It can be shown that the initial motion can be approximated by a functional relationship between θ and ω (angle and spin rate). This relationship neglects angular velocity of the spacecraft in its orbit. With the vanes on, θ and ω will both decrease approximately along this curve until θ is less than a lower limit (2°). Then the vanes would be nulled (pitched to $\sim 0^{\circ}$). For the initial conditions given, with four vanes each 25 cm × 100 cm canted at 70° to the spin axis, this initial phase is estimated to take about 13.7 days. After "nulling" the vanes, some slight error in the vanes' twist angle is assumed, resulting in error torques in the erecting and spin directions. To simplify matters, so that the spin rate does not go through zero, it is assumed that the "null" error is opposite in sense to that of the initial pitch of the vanes. In this case, the spin rate and angle of the spacecraft will start to increase and will continue to increase until the angle exceeds the upper limit (10°). For a pitch error of 1°, the time required for this process will initially be several weeks; however, as a result of long term stabilizing effects, which tend to increase the average spin rate, the spin-up period will increase to several months by the end of a year.

Another effect which has not been mentioned above is the change in the nutation cone angle. Nutations can increase as a result of radiation torques, and can decrease as a result of thermal damping and of internal dissipation, possibly by an onboard damper (assuming a nutation about the axis of maximum moment of inertia). The effect of a static torque on nutations has been investigated by Peterson (Section 8.11). The effects of reradiative torques and of mechanical damping have also been investigated (8.11.5, 8.12).

This description of the predicted performance of the attitude-control system is derived in part by analytical methods, in part by numerical methods, based on the equations of motion for a rigid body, which are derived in the following sections.

8.6 Elementary Dynamics

A most elementary understanding of the precessional motion of a spinning, rigid body can be obtained from the treatment given in a basic physics book.[6] (See Fig. 8-3) A force couple acting on a given axis produces a torque which tends to precess the axis about which the body is spinning in the direction given by the torque.

For the Sunblazer vanes system, when the vanes are pitched to $\sim 0^{\circ}$, as shown in Fig. 8-4, the effect of solar radiation pressure is shown as a force acting on the vane in the plane defined by the sun line and the spin axis of the spacecraft. The force is perpendicular to the vane, which is assumed to be pitched at 0°, such that the force is also in the plane of the sun and the spin axis. As is well known from elementary statics, a force acting on a body can be resolved into a force acting at the center of mass of the body (which we can neglect at the present time, since it accelerates the body linearly) and a torque acting about the center of mass. For the picture of the vane, the torque is acting about an axis perpendicular to the plane of the sun and the spin axis, with the magnitude of the torque given by the product of an effective moment arm (not exactly the same as a moment arm which could be derived by a geometric construction on the picture, which is only schematic) times the magnitude of the force, such that the spin axis of the spacecraft would tend to precess in a direction perpendicular to the plane of the sun and the spin axis. The rate of precession is derived[6] to be

$$\text{Precession rate} = \frac{\text{torque}}{\begin{matrix}\text{spin}\\ \text{rate}\end{matrix} \times \begin{matrix}\text{moment of}\\ \text{inertia}\end{matrix}} \qquad (8.5)$$

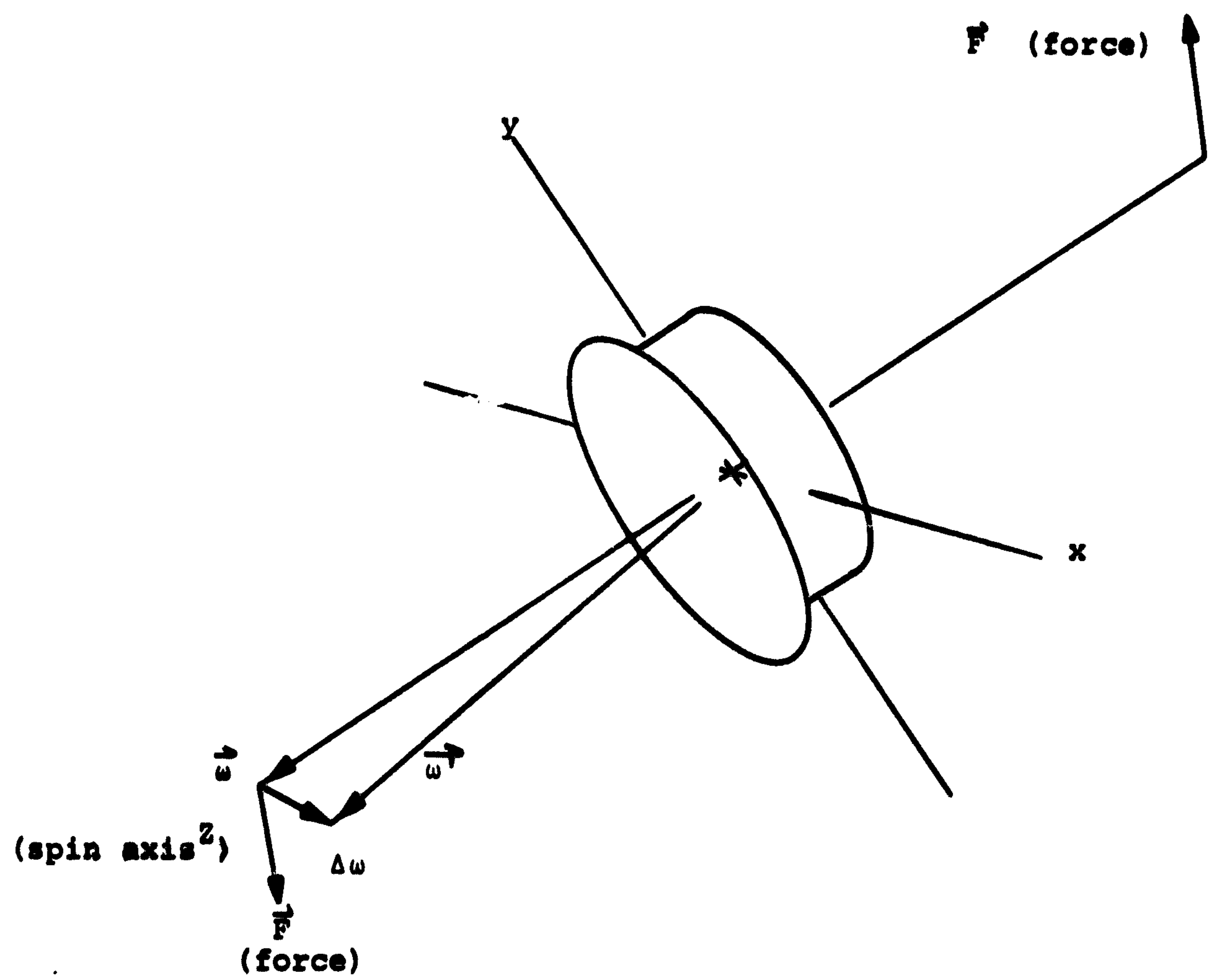

Fig. 8-3 Simple precession.

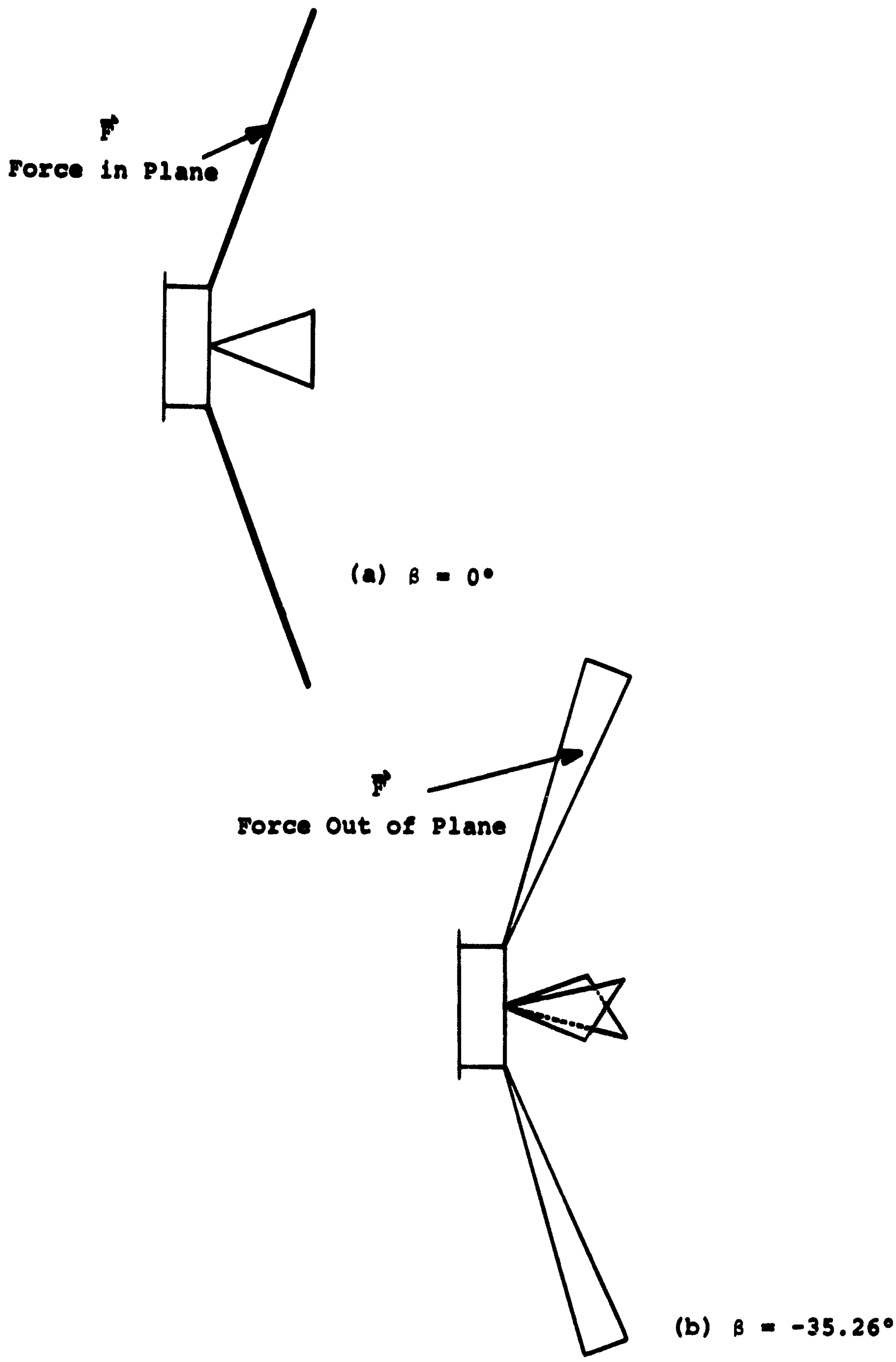

Fig. 8-4 Force on vanes.

In the absence of any other torques, the spin axis would simply precess uniformly forever about the sun line. Because the torque is perpendicular to both the spin axis and the sun line, the angle between the spin axis and the sun line would never change, so that the spin axis would always lie in the surface of a cone centered on the sun line. Thus this motion is sometimes described as "coning".

For the Sunblazer vanes, when the vanes are pitched to -35.26^{o}, as shown in Fig. 8-4, the effective force on the vane (assumed perpendicular to the vane due to reflected solar radiation) is no longer in the plane of the spin axis and the sun line, so that there are components of force (force is considered as a vector) which produce torques acting in the plane of the spin axis and the sun line. The component of torque acting along the spin axis will tend to change the magnitude of the angular velocity, while the component of torque acting in the plane perpendicular to the spin axis will tend to precess the spin axis toward (or away from) the sun. The precession rate, or erection rate is given by Eq (8.5).

These two components of torque are very useful in controlling the attitude and the spin rate of the spacecraft. These torque components are present, to some degree, in all the control systems which have been studied and are mentioned above. The torque components for the vanes system will be derived below.

8.7 Vector Dynamics

A second, more satisfactory description of the precessional motion of a spinning, rigid spacecraft, is given in terms of the vector equation of motion,

$$\dot{\vec{L}} = \vec{N} \tag{8.6}$$

where $\vec{L}$ = angular momentum vector, $\vec{N}$ = torque vector, and

$$\vec{L} = \tilde{I}\vec{\omega} \tag{8.7}$$

$\tilde{I}$ is the inertia tensor. However, if the body is spinning about its axis of maximum moment of inertia, I_3, then $\tilde{I}\vec{\omega}$ is simply a vector of magnitude $I_3\,\omega$ in the direction of the spin axis.(7) The equation of motion holds in any inertial frame; for a rotating frame, an additional term will be added later.

Keeping in mind the vector angular momentum $\vec{L}$, as shown in Fig. 8-5, the effect of the torque vector $\vec{N}$ acting according to Eq (8.6) is to cause $\vec{L}$ to move along a curve whose tangent is always in the direction of $\vec{N}$. The effect

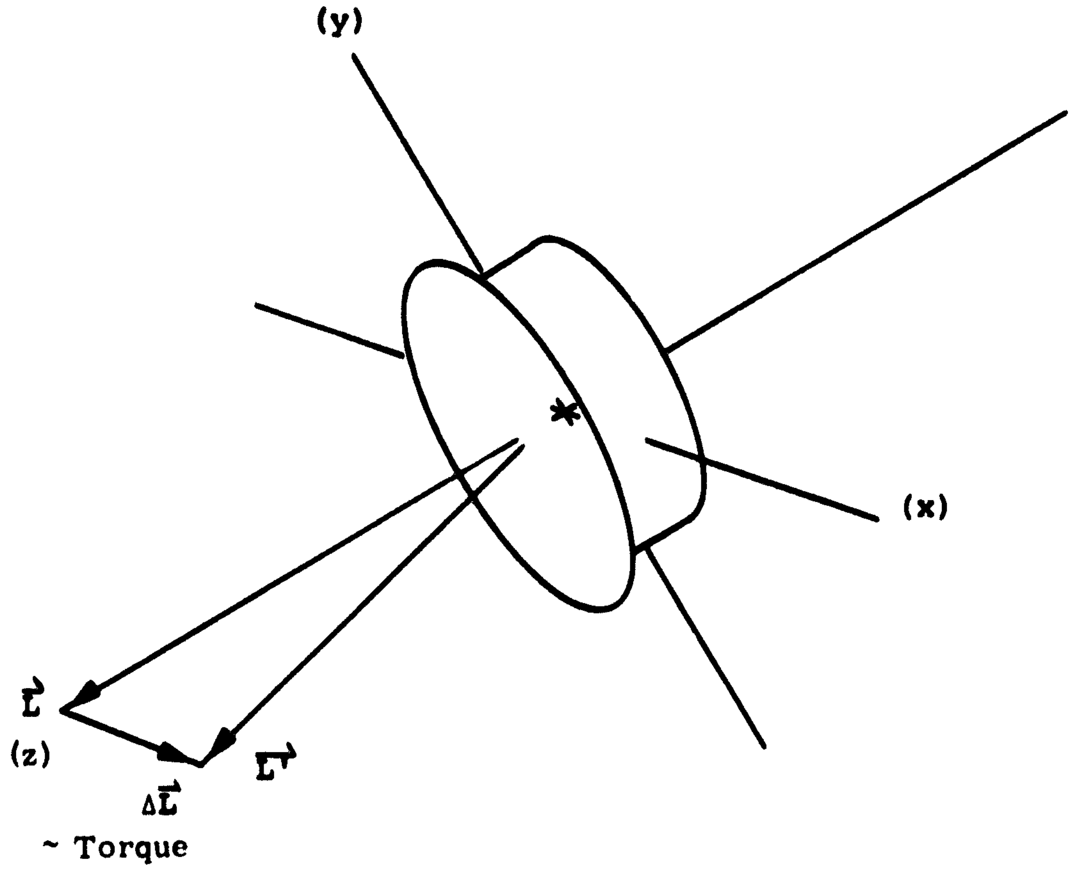

Fig. 8-5 Angular momentum.

of the component of $\vec{N}$ in the direction of $\vec{L}$ is to change the magnitude of $\vec{L}$, while the components of $\vec{N}$ perpendicular to $\vec{L}$ will tend to precess $\vec{L}$ toward (or away from) and around the sun. The component of $\vec{N}$ in the direction of $\vec{L}$ will be called the spin component; the component of $\vec{N}$ perpendicular to $\vec{L}$, and in the plane of the sun and $\vec{L}$, will be called the erecting component; and the component perpenducular to the plane of the sun and $\vec{L}$ will be called the precession component. The qualitative effect of these torques has been explained in Section 8.6 in reference to Fig. 8-3. One fact which will be obvious, once the average torques $\vec{N}$ have been derived as a function of θ for the vanes, is the fact that since the erecting component of $\vec{N}(\theta)$ will be shown to be positive for all θ, the spacecraft will always erect toward the sun (showing stability for this mode of motion).

For the purpose of obtaining a more exact description of the motion, we will describe the motion in terms of Euler angles[8], (see Fig 8-6), which are basically three angles specifying: 1) the angle, θ, between the spin axis (or $\vec{L}$) and the sun line; 2) a precession angle, ϕ, around the sun line (for our purposes, the reference zero for ϕ will be defined to be in the plane of the spacecraft orbit); and 3) a rotation angle, ψ, about the spin axis (this angle we will ignore, but its derivative $\dot{\psi}$ will be equated to ω, the spin rate). We should like to transform the vector equations of motion for ϕ, θ, $\dot{\psi}$, so that these quanities can be solved for as a function of time on a digital computer.

Before deriving the individual equations of motion, it will be desirable to add a term to the right hand side of Eq (8.6), representing the effect of a rotating frame of coordinates (such as the rotation of the sun line during the orbit and, more importantly, the rotation of coordinates which will be necessary to refer our equations to body-centered coordinates, since our torques $\vec{N}$ will be derived in body coordinates); and to put the equations in a completely rigorous form, so that the subsequent derivation will at least have a firm reference set of equations as a basis.

Equation (8.6) referred to a coordinate system rotating at a vector velocity $\vec{\Gamma}_o$ is changed to [9]

$$\dot{\vec{L}} = \vec{N} - \vec{\Gamma}_o \times \vec{L} \qquad (8.8)$$

Now given this equation, we would like to put

$$\vec{\Gamma}_o = \vec{\Gamma}_1 + \vec{\Omega} \qquad (8.9)$$

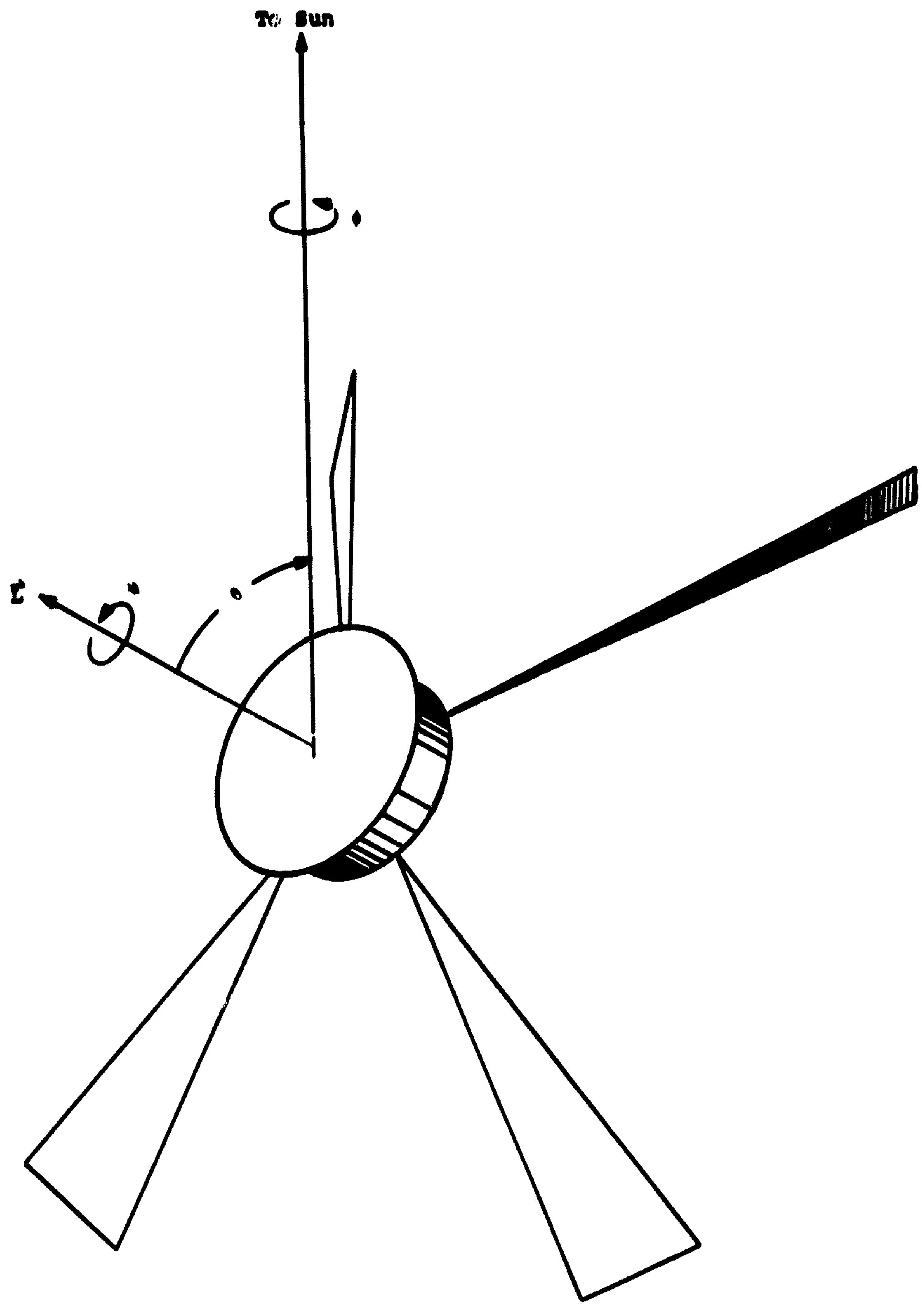

Fig. 8-6 Euler angles.

where $\vec{\Gamma}_1$ refers the equations to body coordinates, where θ and ϕ are not varying, and $\vec{\Omega}$ is the angular velocity of the spacecraft in its orbit. These rotations essentially refer the equations back to an inertial frame of coordinates. In terms of Euler angles, these vectors are given by [10]

$$\vec{L} = \vec{i}I_1 \dot{\theta} + \vec{j} I_1\dot{\phi} \sin \theta + \vec{k}I_3 (\dot{\psi} + \dot{\phi} \cos \theta) \tag{8.10}$$

$$\vec{\Gamma}_1 = \vec{i}\dot{\theta} + \vec{j}\dot{\phi} \sin \theta + \vec{k}\dot{\phi} \cos \theta \tag{8.11}$$

$$\vec{\Omega} = \Omega(\vec{i} \cos \phi - \vec{j} \cos \theta \sin \phi + \vec{k} \sin \theta \sin \phi) \tag{8.12}$$

where 1) $\vec{i}$, $\vec{j}$, and $\vec{k}$ are unit vectors respectively in the precession, erecting, and spin directions. These vectors are in the body; however, they do not rotate with ψ, as shown by $\vec{\Gamma}_1$; and 2) we have also assumed that the body is inertially axi-symmetric (i.e. $I_1 = I_2$); this will simplify our equations (and the solution for nutations). Performing the operations indicated by Eq (8.8) leads to the results given below:

$$\dot{\vec{L}} = \vec{i}I_1 \ddot{\theta} + \vec{j}I_1 (\ddot{\phi} \sin \theta + \dot{\phi} \dot{\theta} \cos \theta) + \vec{k}I_3 \frac{d}{dt} (\dot{\psi} + \dot{\phi} \cos \theta) \tag{8.13}$$

$$\vec{\Gamma}_1 \times \vec{L} = \vec{i} [I_3\dot{\phi} \sin \theta (\dot{\psi} + \dot{\phi} \cos \theta) - I_1\dot{\phi}^2 \sin \theta \cos \theta] + \vec{j}[I_1\dot{\phi} \dot{\theta} \cos \theta - I_3 \dot{\theta}(\dot{\psi} + \dot{\phi} \cos \theta)] \tag{8.14}$$

$$\begin{aligned}\vec{\Omega} \times \vec{L} = \Omega \Big[&-\vec{i} (I_3 \sin \phi \cos \theta (\dot{\psi} + \dot{\phi} \cos \theta) + I_1\dot{\phi} \sin^2 \theta \sin \phi) \\ &- \vec{j} (I_3 \cos \phi (\dot{\psi} + \dot{\phi} \cos \theta) - I_1\dot{\theta} \sin \theta \sin \phi) \\ &+ \vec{k}(I_1 \dot{\phi} \sin \theta \cos \phi + I_1\dot{\theta} \cos \theta \sin \phi) \Big]\end{aligned} \tag{8.15}$$

The important equations of motion, which we wanted to derive, are now obtained from the $\vec{i}$, $\vec{j}$, $\vec{k}$ components of Eq (8.8) after substituting Eq (8.13), (8.14), (8.15):

$$I_1\ddot{\theta} - I_1\dot{\phi}^2 \sin \theta \cos \theta + I_3\dot{\phi}\omega \sin \theta = N_1(\theta) - (\vec{\Omega} \times \vec{L})_1 \tag{8.16}$$

$$I_1(\ddot{\phi} \sin \theta + 2\dot{\phi} \dot{\theta} \cos \theta) - I_3\dot{\theta}\omega = N_2(\theta) - (\vec{\Omega} \times \vec{L})_2 \tag{8.17}$$

$$I_3 \frac{d\omega}{dt} = N_3 (\theta) - (\vec{\Omega} \times \vec{L})_3 \tag{8.18}$$

where $\omega = \dot{\psi} + \dot{\phi} \cos \theta$ (8.19)

and $(\vec{\Omega} \times \vec{L})$ is not transcribed, pending the following simplifications.

There are two cases in which $\dot{\phi}, \dot{\psi}, \dot{\theta}$ are of comparable magnitude: 1) when we are studying high-frequency nutations (as studied by Peterson, see Sec. 8.11), the nutational period is so short that any coupling with $\vec{\Omega}$ can be neglected; and 2) when $\dot{\psi}$ is very low. If either of these situations exists we have a near-librational situation, and the librational period is also short enough to decouple $\vec{\Omega}$ so that in both cases we will assume (low spin rate and nutations)

$$\vec{\Omega} \times \vec{L} = 0 \quad . \tag{8.20}$$

In a case when $\dot{\psi} >> \dot{\phi}, \dot{\theta}$ (precessional mode), we can assume $\Omega << \dot{\psi}, \dot{\phi}, \dot{\theta}$, resulting in the following simplification (high spin rates):

$$\vec{\Omega} \times \vec{L} = \Omega \left[-\vec{i} I_3 \; \dot{\psi} \; \cos\theta \; \sin\phi - \vec{j} I_3 \; \dot{\psi} \; \cos\phi \right] \tag{8.21}$$

For the case of high $\dot{\psi}$, further simplifications will be made, to Eq (8.16), (8.17), (8.18), (8.21). In order to derive the precessional equations of motion, which hold for high $\dot{\psi}$, we shall be able to neglect $\ddot{\phi}, \ddot{\theta}$ so that we have the following assumptions:

$$\ddot{\phi} = 0 \tag{8.22}$$

$$\ddot{\theta} = 0 \tag{8.23}$$

$$\dot{\phi} << \omega \tag{8.24}$$

$$\dot{\theta} << \omega \tag{8.25}$$

which, when applied to Eq (8.16), (8.17), (8.18), lead to the precessional equations of motion for high spin rate:

$$I_3 \omega \dot{\phi} \sin \theta = N_1 (\theta) + I_3 \Omega \omega \cos \theta \sin \phi \tag{8.26}$$

$$I_3 \omega \dot{\theta} = -N_2 (\theta) - I_3 \Omega \omega \cos \phi \tag{8.27}$$

$$I_3 \dot{\omega} = N_3(\theta) \tag{8.28}$$

These equations have been solved (integrated) on a digital computer, and the solution which has been obtained so far will be described below, after deriving the vane torques in the next section.

8.8 Vane Torques

The vanes system has four triangular vanes, assumed to be 100 cm long x 25 cm base, attached to the rear of the spacecraft radiator at four points spaced by 90°, (See Fig. 8.7). The vanes are assumed to be canted 70° up from the spin axis, and to be pitched -35.26° (measured about the longitudinal axis of the vane, with pitch = 0° when the vane is tangent to a 70° cone containing the longitudinal axes of the vanes). The vanes are further assumed to be made of mylar, aluminized on the front with absorptivity = 0.2 and emissivity = 0.05, black on the back with absorptivity = emissivity = 0.9. The spacecraft radiator is assumed to be black with absorptivity = emissivity = 1. (This part is not too important because it is near the spacecraft center of mass and is relatively symmetrical).

A most elementary estimate of the torques on this model is made by assumin that 1) there will be no shadowing of vanes, 2) no radiation will fall on rear of vanes, and 3) torques on the central spacecraft radiator section can be ignored. These assumptions are good for small θ ($\theta < 50^\circ$). In this case, we shall first derive the torques as a function of ψ; and then average the torques for $0 < \psi < 2\pi$ (which will give us the average torques, independent of ψ), applied to the vanes when the spacecraft is rotating uniformly and fast enough that variation in ψ can be ignored.

With the assumptions above (primarily, no shadowing), the force on a vane can be represented as a vector acting at a point 2/3 of the distance along the longitudinal axis of the triangular vane; this is the effective center of pressure, given by

$$\ell_0 = \frac{\int_0^{\ell} f\lambda^2 d\lambda}{\int_0^{\ell} f\lambda d\lambda} = \frac{2}{3}\ell \tag{8.29}$$

The force vector has three physically-distinct components: 1) an absorbed momentum component, in the direction of the incident radiation $\vec{I}$; 2) a reflected momentum component, normal to the vane $\vec{P}$; and 3) a reradiated momentum component, also normal to the vane $\vec{P}$. The following definitions will be made; and, in the following derivation, because the algebraic expressions are quite lengthy, sin and cos will be represented simply as s and c.

$\vec{P}$ = unit normal vector to vane (8.30)

$\vec{I}_0$ = unit vector to sun (8.31)

I = solar radiation intensity (watts/m^2) (8.32)

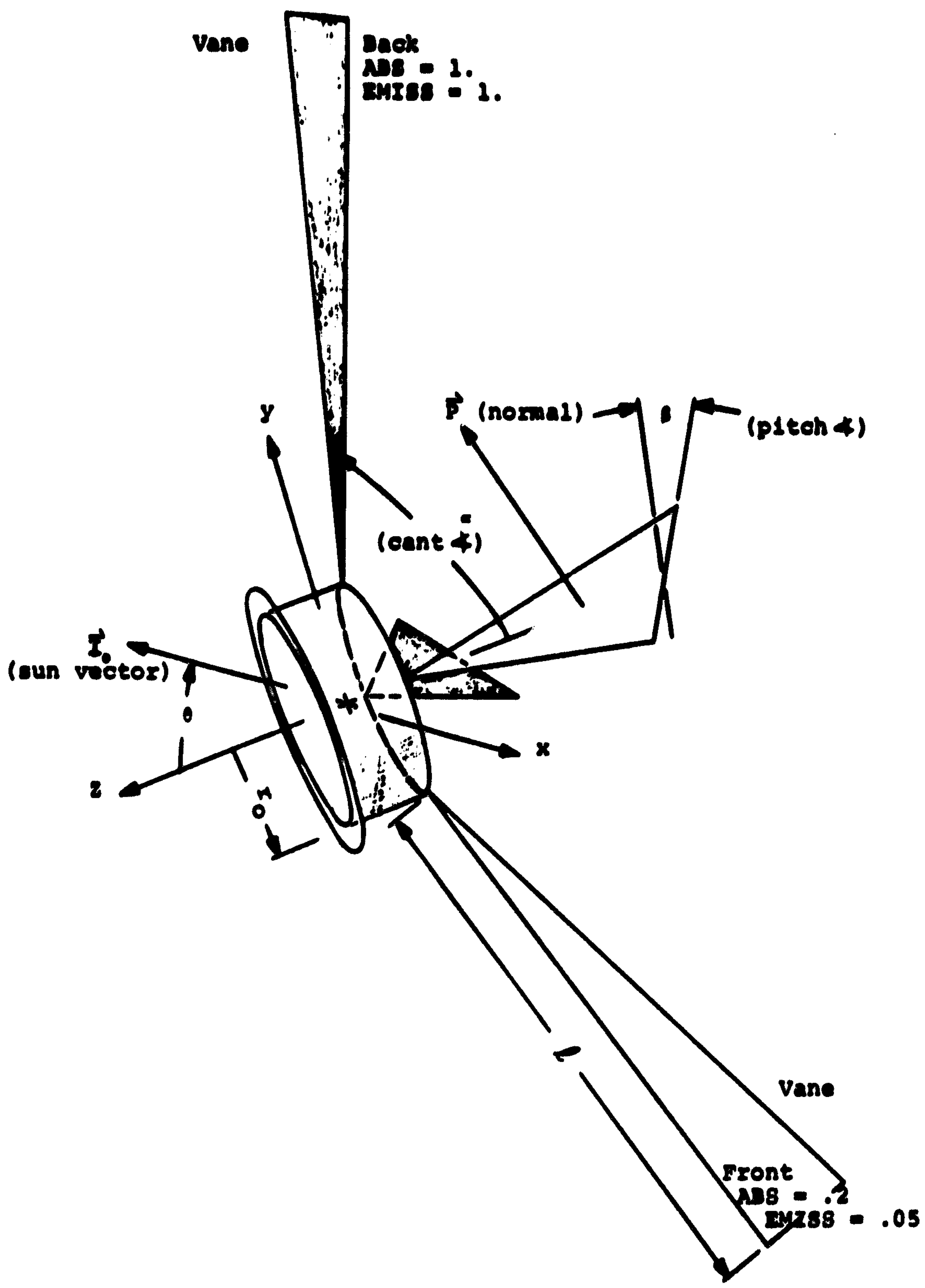

Fig. 8-7 Vanes system.

c = velocity of light (MKS) (8.33)

abs = absorptivity of vane (8.34)

emiss = emissivity of vane (8.35)

α = cant angle of vane (8.36)

β = pitch angle of vane (8.37)

With these definitions, and with reference to Fig. 8-7,

$$\vec{P} = \vec{i}(c\alpha\ c\beta\ c\psi + s\beta\ s\psi) + \vec{j}(c\alpha\ c\beta\ s\psi - s\beta\ c\psi) + \vec{k}\,(s\alpha\ c\beta) \tag{8.38}$$

or

$$\vec{P} = \vec{i}a\ c\psi' + \vec{j}a\ s\,\psi' + \vec{k}b \tag{8.39}$$

$$a = \sqrt{1 - s^2\alpha\ c^2\beta} = \sqrt{1-b^2} \tag{8.40}$$

$$b = s\alpha\ c\beta \tag{8.41}$$

$$\psi' = \psi - A \tag{8.42}$$

$$A = \tan^{-1}\left(\frac{s\beta}{c\alpha\quad c\beta}\right) \tag{8.43}$$

$$\vec{I}_o = \vec{j}\,s\theta + \vec{k}\,c\,\theta \tag{8.44}$$

Using these expressions, we can find the cosine of the angle between the normal to the vane and the incident radiation to be(See Eq 8.3):

$$c(\theta) = \vec{P}\cdot\vec{I}_o = a\ s\theta\ \ s\psi' + b\ c\theta\,. \tag{8.45}$$

Using this cosine, the absorbed and reflected radiation pressure components are given by:

$$\vec{F}_{\text{absorbed}}(\psi') = \text{Area}\cdot\text{abs}\cdot\frac{I}{C}\cdot(\vec{P}\cdot\vec{I}_o)\cdot(-\vec{I}_o) \tag{8.46}$$

$$\vec{F}_{\text{reflected}}(\psi') = \text{Area}\cdot(1-\text{emiss})\cdot\frac{2I}{C}\cdot(\vec{P}\cdot\vec{I}_o)^2\cdot(-\vec{P}) \tag{8.47}$$

For a <u>reradiative force</u>, resulting from a reradiated intensity I_R, assuming isotropic radiation, according to Lambert's law, the effective normal component of the intensity and the force are given by:

$$I_N = I_R \frac{\int_0^{\frac{\pi}{2}} \sin\theta \cos^2\theta \, d\theta}{\int_0^{\frac{\pi}{2}} \sin\theta \cos\theta \, d\theta} = \frac{2}{3} I_R \qquad (8.48)$$

$$\vec{F}(\psi')_{\text{reradiated}} = \text{Area} \cdot \frac{I_N}{C} \cdot (-\vec{P}) \qquad (8.49)$$

I_R can be separated into two parts: 1) a part which varies with ψ' (this leads to an erecting torque, as first investigated by Peterson[2] (CSR-T-66-3)); and 2) an average value which produces a spin torque. These are relatively small for the most important stabilization conditions ($\beta = -35.26^o, \theta < 50^o$), and therefore will be derived later.

The major torque component for these primary conditions ($\beta = -35.26$, $\theta < 50^o$) is the reflective torque, obtained from the force by taking $\vec{r} \times \vec{F}$ in Eq (8.47), leading to:

$$\vec{N}(\psi')_{\text{reflected}} = \text{Area} \cdot (1 - \text{emiss}) \cdot \frac{2I}{C} \cdot (\vec{P} \cdot \vec{I}_o)^2 \cdot (\vec{P} \times \vec{r}) \qquad (8.50)$$

where we will take

$$\vec{r} = \text{center of pressure of vane} \qquad (8.51)$$

$$\vec{r} = \vec{i} r_1 \, c\psi + \vec{j} r_1 \, s\psi - \vec{k} z_1 \qquad (8.52)$$

$$r_1 = r_o + \ell_o \, s\alpha \qquad (8.53)$$

$$z_1 = \ell_o \, c\alpha . \qquad (8.54)$$

ℓ_o is given by Eq (8.29) and, for approximate results, numerical values can be assigned to: $\ell = 100$ cm, $r_o = 20$ cm, Area $= 0.125$ m^2 and, as before, abs $= 0.2$, emiss $= 0.05$. So we have:

$$\vec{P} \times \vec{r} = \vec{i}\left[-(az_1 + br_1 cA)\, s\psi' - br_1 sA\, c\psi'\right]$$
$$+ \vec{j}\left[(az_1 + br_1 cA)\, c\psi' - br_1 sA\, s\psi'\right]$$
$$+ \vec{k} r_1\, s\beta \ . \qquad (8.55)$$

From Eq (8.45),

$$(\vec{P}\cdot\vec{I}_0)^2 = s^2\theta\,(a^2 s^2\psi' - b^2) + 2ba\, s\theta\, c\theta\, s\psi' + b^2 \ . \qquad (8.56)$$

Now, using Eq (8.50), (8.55), and (8.56), we are in a position to average the reflected torque for $0 \le \psi' \le 2\pi$:

$$\vec{N}_{reflected} = \frac{1}{2\pi}\int_0^{2\pi} \vec{N}_{reflected}(\psi')\, d\psi' \qquad (8.57)$$

giving

$$\vec{N}_{reflected} = \text{Area}\cdot(1 - \text{emiss})\cdot\frac{2I}{C}\times$$
$$\Big[-\vec{i}\left(s^2\alpha\, c\alpha\, c^3\beta\, r_1 + s\alpha\, c\beta\,(1 - s^2\alpha\, c^2\beta)\, z_1\right)s\theta\, c\theta$$
$$-\vec{j}\left(s^2\alpha\, s\beta\ c^2\beta\, r_1\right)s\theta\, c\theta$$
$$+\vec{k}\left(s^2\alpha\, s\beta\, c^2\beta + s\beta\left[\tfrac{1}{2} - \tfrac{3}{2}s^2\alpha\, c^2\beta\right]s^2\theta\right)r_1\Big] \ . \qquad (8.58)$$

This torque is the major torque acting for $\beta = \pm 35.26^\circ$, $\theta < 50^\circ$ and could be used in Eq (8.26), (8.27), (8.28) to give a description of the initial stabilization. Two points should be noted in Eq (8.58): 1) the sign of $N_2(\theta)$ always remains the same for $\theta < 90^\circ$; and 2) for small angles, $-N_2(\theta)/\theta \cong N_3(\theta)$. Point 1) indicates stability for $\theta < 90^\circ$, and point 2) will be shown to result in a simplified description of the motion, based on these torque components, at small angles.

The second most important torque is the <u>absorbed torque</u>, obtained from the absorbed force in Eq (8.46) by taking $\vec{r} \times \vec{F}$ absorbed and averaging for $0 < \psi' < 2\pi$ as outlined by the following equations:

$$\vec{N}_{absorbed} = \frac{1}{2\pi}\int_0^{2\pi} \vec{N}_{absorbed}(\psi')\, d\psi' \qquad (8.59)$$

$$\vec{N}_{\text{absorbed}}(\psi') = \text{Area} \cdot \text{abs} \cdot \frac{I}{C} \cdot (\vec{P} \cdot \vec{I}_o) \cdot (\vec{I}_o \times \vec{r}) \quad . \tag{8.60}$$

From Eq. (8.38), (8.44), and (8.52):

$$\vec{I}_o \times \vec{r} = \vec{i}\,(-z_1 s\theta - r_1 c\theta s\psi) + \vec{j} r_1 c\theta c\psi - \vec{k} r_1 s\theta c\psi \tag{8.61}$$

$$\vec{P} \cdot \vec{I}_o = s\theta\,(c\alpha\, c\beta\, s\psi - s\beta\, c\psi) + c\theta\,(s\alpha\, c\beta) \tag{8.62}$$

so after averaging:

$$\vec{N}_{\text{absorbed}} = \text{Area} \cdot \text{abs} \cdot \frac{I}{C} \left\{ \vec{i} \left[-z_1 s\alpha c\beta - \frac{r_1}{2} c\alpha c\beta \right] s\theta c\theta + \vec{j} \left[-\frac{r_1}{2} s\beta\ s\theta\ c\theta \right] + \vec{k} \left[\frac{r_1}{2} s\beta\ s^2\theta \right] \right\} . \tag{8.63}$$

The third most important torque is the reradiative torque, mentioned briefly above (see Eq (8.49)), which can be differentiated into: 1) a small erecting component, and 2) an average spin component. These will be derived below.

The erecting component will be derived only for $\beta = 0$ because only near $\beta = 0$ is the erecting component large enough to be comparable to the reflecting component of torque. In the interest of obtaining an analytical solution, we shall also assume $\theta \sim 0$, minimizing the temperature variations on the vanes. Assuming that the body is spinning uniformly at an angle θ to the sun, as usual, the input radiation intensity into a vane is proportional to $\vec{P} \cdot \vec{I}_0$, which is periodic in ψ', as given by Eq (8.45). Given this periodic input intensity, the temperature on the vane (assumed constant over the vane) satisfies a differential equation similar to that studied by Peterson[2] which is:

$$C_P^* \frac{dT}{dt} + \epsilon\sigma T^4 = \text{abs} \cdot I \cdot (bc\theta + as\theta s\psi') \quad . \tag{8.64}$$

Linearizing the equation, and assuming that:

$$T = T_0(1 + a_1 s\psi' + b_1 c\psi') \tag{8.65}$$

leads to the solution:

$$a_1 = \frac{\left(\frac{as\theta}{4s\alpha}\right)}{1 + \left(\frac{\omega}{\omega_{opt}}\right)^2} \tag{8.66}$$

$$b_1 = \frac{\left(\frac{as\theta}{4s\alpha}\right)}{\frac{\omega}{\omega_{opt}} + \frac{\omega_{opt}}{\omega}} \tag{8.67}$$

$$\omega_{opt} = \frac{4}{C_P^*} (abs \cdot I \cdot s\alpha)^{3/4} \cdot (\epsilon\sigma)^{1/4} \quad . \tag{8.68}$$

For aluminum with a thickness of 0.1 mm,

$$C_P^* = C_P \Delta t = 0.0246 \frac{\text{Joule}}{\text{cm}^2} \tag{8.69}$$

Assuming $I = 1380$ watt/m^2, abs $= 0.2$, $\alpha = 70^\circ$, $\epsilon = 0.95$, $\sigma = 5.672 \times 10^{-8}$ watt/m^2 - $^\circ K^4$, we get:

$$\omega_{opt} = \frac{3.95}{C_P^*} \frac{\text{watt}}{m^2 - {}^\circ K} = 0.016 \frac{\text{rad}}{\text{sec}} \tag{8.70}$$

and

$$T_o = \left[\frac{abs\ I\ s}{\epsilon \cdot \sigma}\right]^{1/4} = 263\tfrac{1}{2}\ {}^\circ K \tag{8.71}$$

This implies a reradiated intensity distribution of approximately:

$$I_R = abs \cdot I \cdot \left[bc\theta + \frac{as\theta\ s\psi'}{1 + \left(\frac{\omega}{\omega_{opt}}\right)^2} - \frac{as\theta\ c\psi'}{\left(\frac{\omega}{\omega_{opt}}\right) + \left(\frac{\omega_{opt}}{\omega}\right)} \right] \tag{8.72}$$

Using this expression for the intensity of I_R and averaging the torque given by $\vec{r} \times \vec{F}(\psi')$, with $\vec{F}(\psi')$ from Eq (8.49), we get:

$$N_{\substack{\text{reradiative} \\ \text{erecting}}} \simeq C_r\ \frac{1}{2}(az_1 + br_1 cA) \frac{as\theta}{\left(\frac{\omega}{\omega_{opt}} + \frac{\omega_{opt}}{\omega}\right)} \tag{8.73}$$

and

$$N_{\substack{\text{reradiative} \\ \text{spin}}} \approx C_r \cdot r_1 s\beta \cdot c\theta \tag{8.73}$$

with

$$C_r = \frac{2}{3} \frac{I_o}{C} \text{Area} \cdot abs \cdot \frac{(\text{emiss 1} - \text{emiss 2})}{(\text{emiss 2} + \text{emiss 1})} \tag{8.75}$$

where pertinent quantities appear in Eq (8.4), (8.40), (8.41), (8.43), (8.53), and (8.54).

The erecting component of the reradiative torque (Eq (8.73)) is only significant near $\beta = 0$ (relative to reflective torque) <u>and</u> near $\omega = \omega_{opt}$, where we are studying error torques in the coast phase (see Sec 8.9). The spin component of the reradiative torque (Eq (8.75)) is proportional to and a fraction of ($\sim$ 0.08 for abs = 0.2) the spin component of the reflected torque, for small θ. For very large θ, when the absorptive rear of the vanes is exposed, this component will be a major factor in causing a reversal of the spin torque.

For the initial performance, when $\beta = -35.26^\circ$ and $\theta < 60^\circ$, the torque can be mainly represented by the reflective torque, Eq (8.58). When $\theta < 10^\circ$, this torque can be simplified by letting $\cos\theta \to 1$, $\sin^2\theta \to 0$, leaving approximately linear terms in θ for the precession and erecting components of torque, and a constant for the spin component, the constant being equal to the coefficient of the erecting torque (see discussion of Eq (8.79)).

After the initial stabilization, the vanes are "nulled" to $\beta \simeq 0$; however, the error in β will result in error torques in the spin and erecting directions which will be added to the reradiative torques, causing motion of the spacecraft which, over a relatively long period, will be unstable. The reflective error torque can be linearized for $\beta \sim 0^\circ$, changing Eq (8.58) to:

$$\vec{N}_{\substack{\text{reflected}\\ \beta\sim 0\\ \theta\sim 0}} \simeq -\vec{i}s\alpha c\alpha\,(r_o s\alpha + \ell_o)s\theta \\ -\vec{j}\,s^2\alpha\, s\beta\, r_1\, s\theta \\ +\vec{k}\,s^2\alpha\, s\beta\, r_1 \,. \tag{8.76}$$

The reradiative torque component we are primarily interested in is the erecting component, Eq (8.73), which reduces to:

$$N_{\substack{\text{reradiative}\\ \text{erecting}\\ \sim 0}} = C_r\,\frac{1}{2}(\ell_o + r_o s\alpha)\,\frac{c\alpha s\theta}{\left(\frac{\omega}{\omega_{opt}} + \frac{\omega_{opt}}{\omega}\right)} \tag{8.77}$$

With such torques derived for $\beta \sim 0$, $\theta \sim 0$, we shall be able to get some estimate of the long-term behavior of the spacecraft.

The simplified torques derived above are derived for the purpose of demonstrating some more general features. The actual torques have been calculated as a part of a relatively complex computer program, which includes the effect of reflective and absorptive forces and shadowing by a geometrical structure such as is illustrated in the figures. Such an analysis will not be presented here, but the results are shown in Fig. 8-8.

8.9 Dynamical Motion of Spacecraft

Given the vector torques as shown in the preceding section, it is possible to determine the motion of the spacecraft, both short-term and long-term, from the equations of motion derived in Sec 8.7. In order to get an idea of what should happen in the initial phase of stabilization, before discussing the exact solution as integrated on a digital computer, one can take Eq (8.27), (8.28) and, neglecting terms involving Ω, obtain the result

$$\frac{d\omega}{\omega d\theta} = \frac{-N_3(\theta)}{N_2(\theta)} \qquad (8.78)$$

or

$$\ln\left(\frac{\omega}{\omega_0}\right) = -\int_{\theta_0}^{\theta} \frac{N_3(\xi)}{N_2(\xi)}\, d\xi \qquad (8.79)$$

which gives an approximate relationship between ω/ω_0 and θ, neglecting certain terms involving Ω and ω. For small θ, the integrand $\sim d\xi/\xi$, as discussed in reference to Eq (8.58) so that θ and ω are related by a power relationship (approximately linear), as shown in Fig. 8-9.

In addition, since the spin torque is roughly constant for small θ, as evidenced by Fig. 8-8 and Eq (8.58) for the major component, one would expect that $\dot{\omega} \approx$ const, from Eq (8.28); so that $\omega \approx \omega_0 - K_1 t$ and $\theta/\theta_0 \approx (\omega/\omega_0)^{K_2}$, $K_2 \approx 1$. Actual results do not fit this explanation too well because of deviation of the torques for large θ and because of rotation of sun line (at rate Ω). (Compare Fig. 8-9 and 8-11.)

8.9.1 Actual Results

The actual results of integrating the precessional equations of motion, Eq (8.26), (8.27), and (8.28), for the initial stabilization period of ~13.7 days when the spacecraft is erecting and despinning from its initial conditions of $\theta = 60^\circ$ and $\omega = 20$ r/min to its final orientation of $\theta = 2^\circ$ and $\omega \approx 1.1$ r/min, are shown in Fig. 8-10 and 8-11. Figure 8-10 plots the initial spiral (motion of figure axis) in terms of θ and ϕ (Euler angles, as shown in Fig. 8-6. Fig. 8-11 plots θ and ω vs time for the initial stabilization period. As seen from

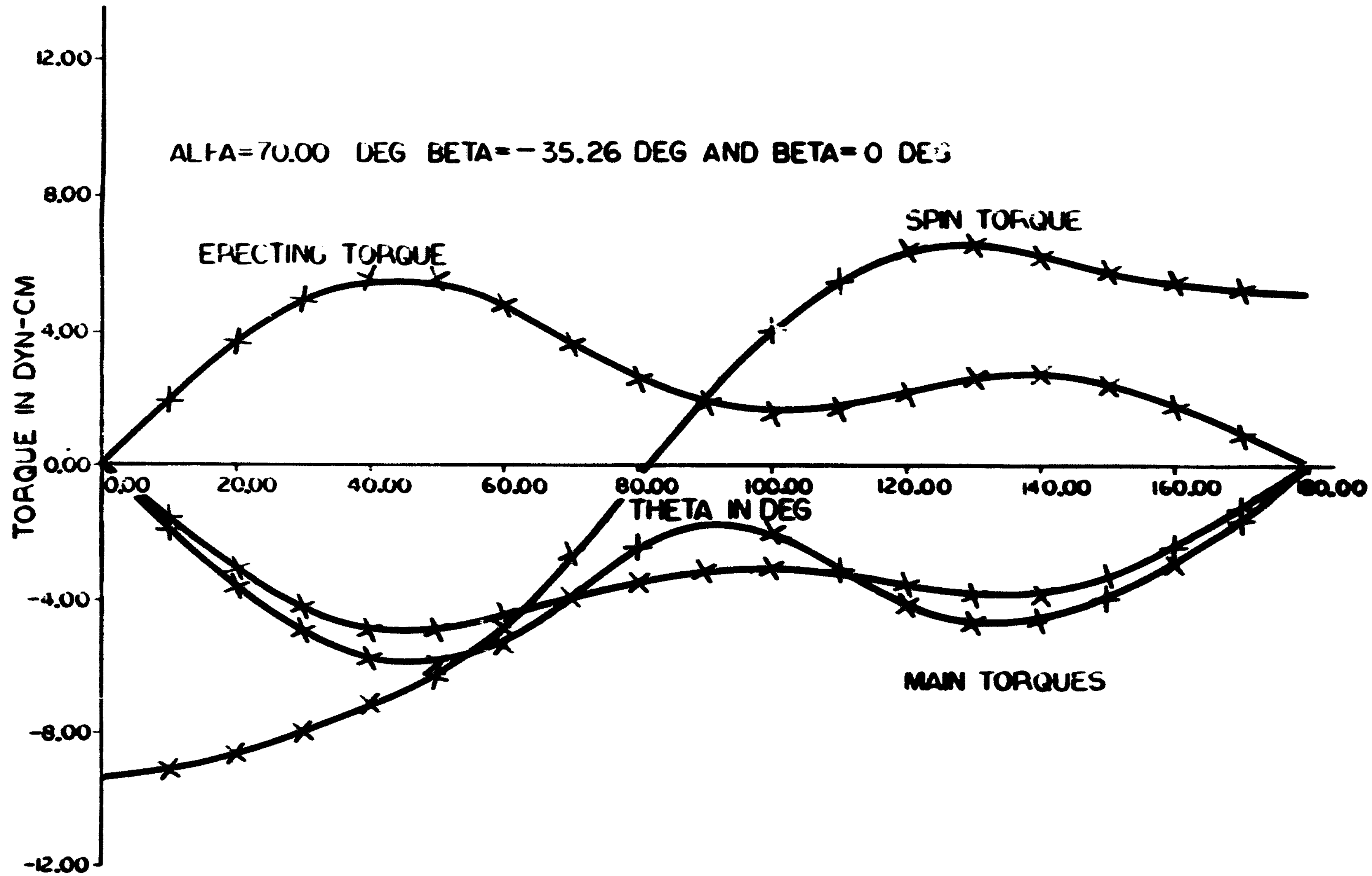

Fig. 8-8 Torques calculated for Sunblazer vanes.

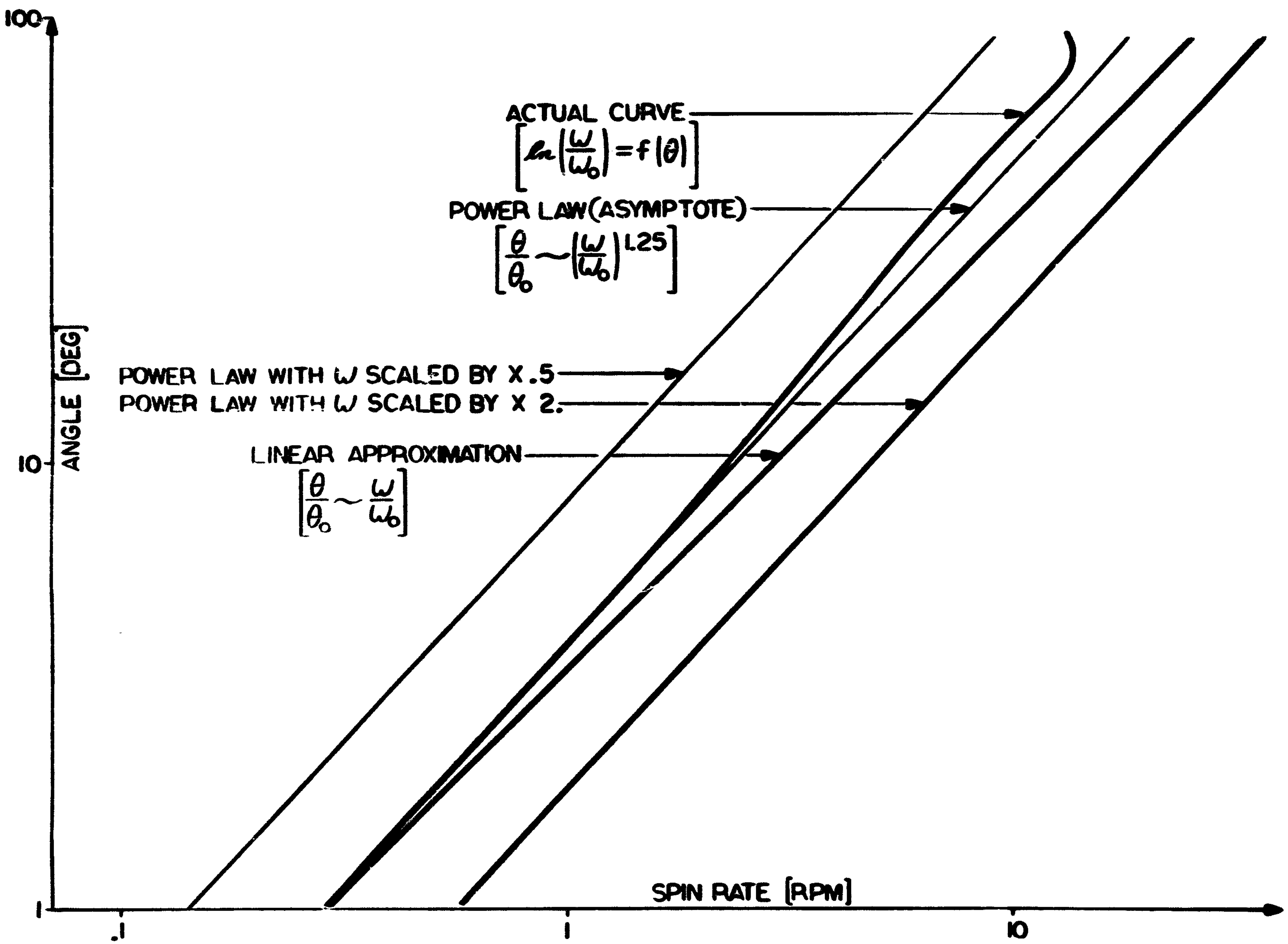

Fig. 8-9 Universal angle vs spin rate.

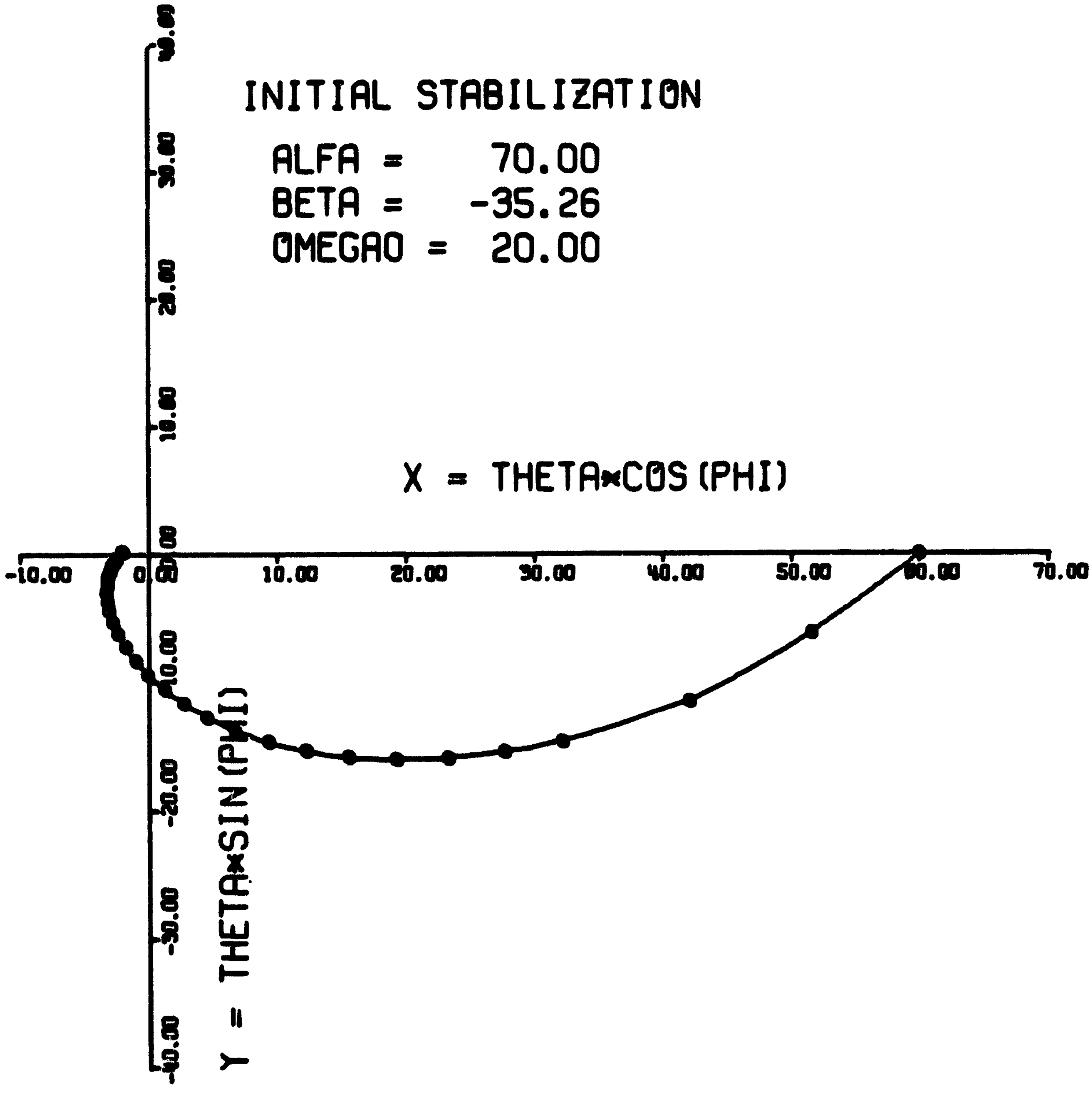

Fig. 8-10 Initial spiral — 60°, 20 r/min.

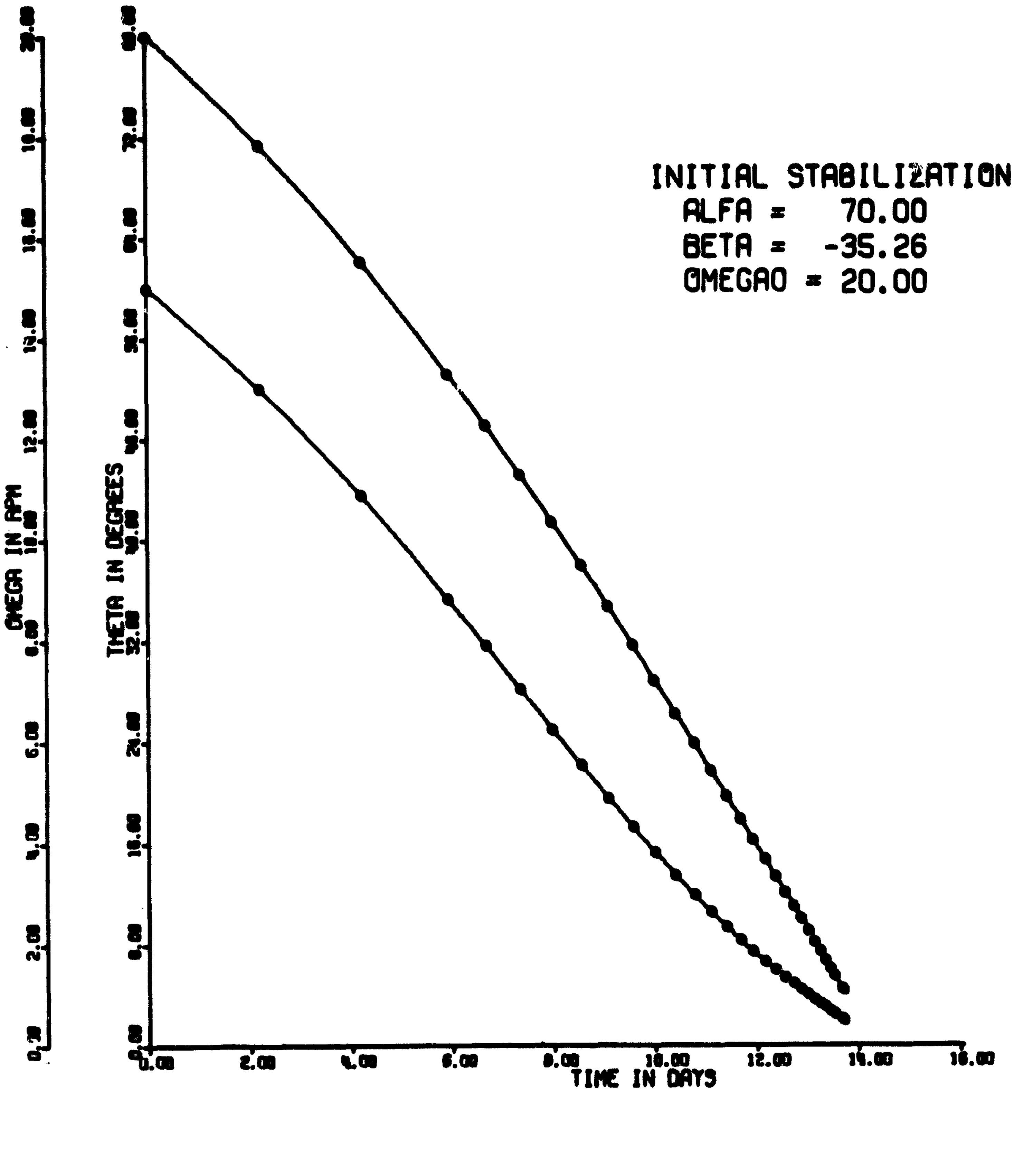

Fig. 8-11 Initial θ and ω vs time.

this plot, $\dot{\omega}$ is not constant, nor does $\theta/\theta_0 = (\omega/\omega_0)^{K_2}$. After this period, the investigation moves to the long-term stabilization.

Long-term motion of the spacecraft is characterized by cycles during which the spacecraft drifts out to $\theta = 10^\circ$ (as a result of spin-up and negative erecting torques), at which point the vanes are to be actively switched to a pitch angle of $\beta \cong -35^\circ$. This will bring the spacecraft axis back to within 2° of the sun in a short period. These cases have also been investigated on a digital computer, integrating the precessional equations of motion (Eq (8.26), (8.27), and (8.28)) as before, but switching the vanes' pitch angle between $\beta = +1^\circ$ and $\beta = -35.26^\circ$ when θ exceeds the limits 2° and 10° respectively. (In the computer program, θ is never allowed to exceed the limits by more than 0.001° before switching occurs.) The long-term behavior of θ and ω vs time is plotted in Fig. 8-12, showing approximately 6 cycles of θ from 2° to 10° and back again. On this plot, an asymptotic increase in average spin rate is also evident. In addition, each individual cycle from 2° to 10° and back has been plotted to show the spiraling motion of the spacecraft axis of symmetry in θ-ϕ coordinates. Typical spirals are shown in Fig. 8-13. For the later spirals, when the average spin rate is approaching its asymptote, the motion is slower, and the center of the spiral moves higher above the ecliptic plane ($\phi = 0^\circ$), consistent with Colombo's derivation[1]. In addition, the spirals are unstable, of increasing amplitude. This is consistant with the torques derived in Eq (8.55), (8.63), (8.73), and (8.74) above.

Furthermore, a closer inspection of Fig. 8-12 indicates that $\dot{\omega}$ is not constant during the drift periods (pitch angle $\beta = +1^\circ$), as might be expected by the unsuspecting observer. This fact is simply explained by the variation in solar intensity during the 3/4-year orbit. The final phase of the investigation involves optimization of the vanes' constants, and sensitivity of the system to initial conditions and error conditions. Results of this investigation are summarized in Fig. 8-14 to 8-21 below.

8.9.2 Optimization of Vanes' Cant Angle

The vanes' cant angle has been varied from 45° to 75°, and the initial stabilization time and long-term number of limit cycles has been plotted (Fig. 8-14, 8-15). These results vary significantly with the cant angle, but 70° was chosen to give nearly the minimum initial stabilization time without hurting the long-term stabilization too much.

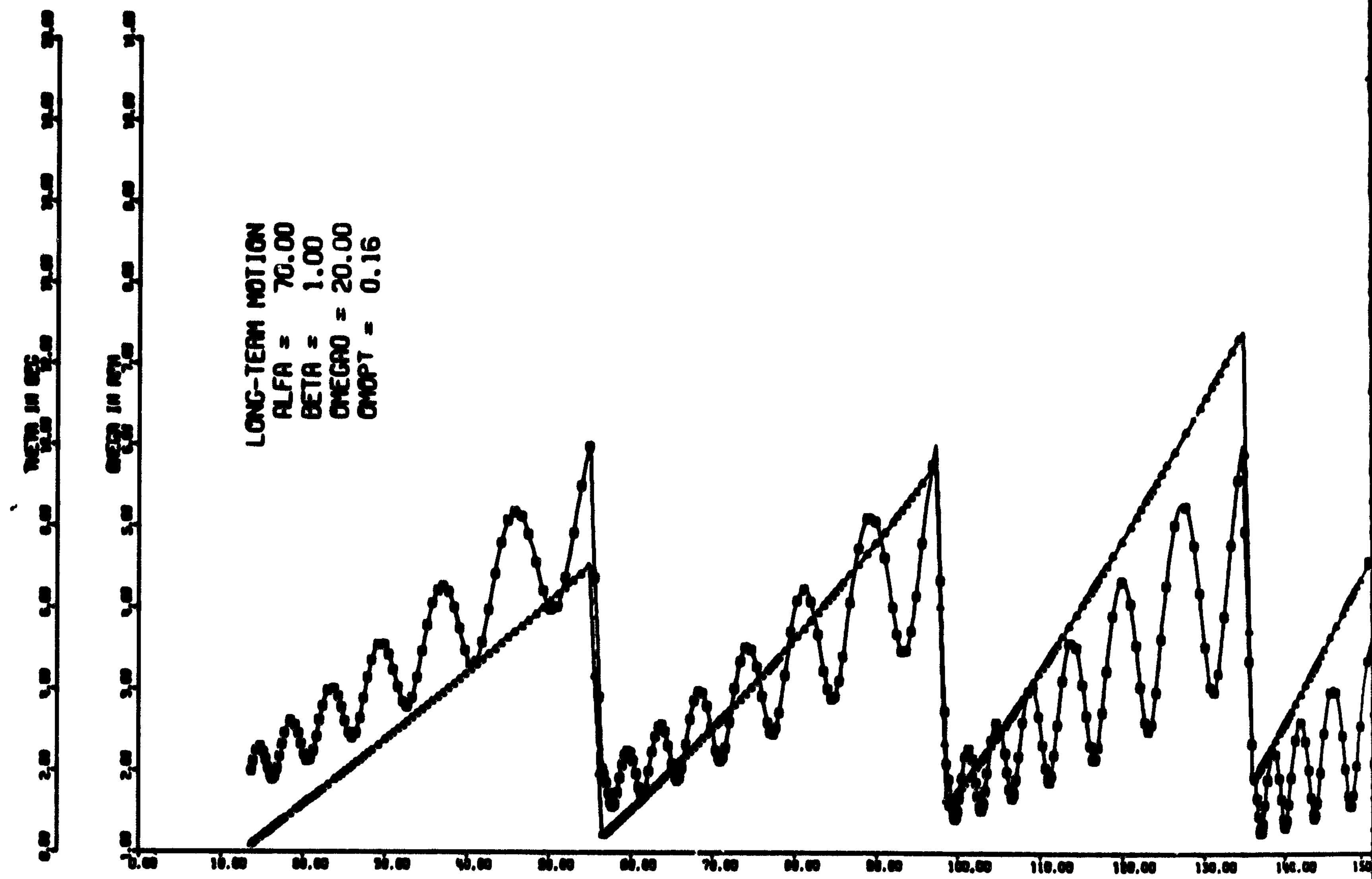

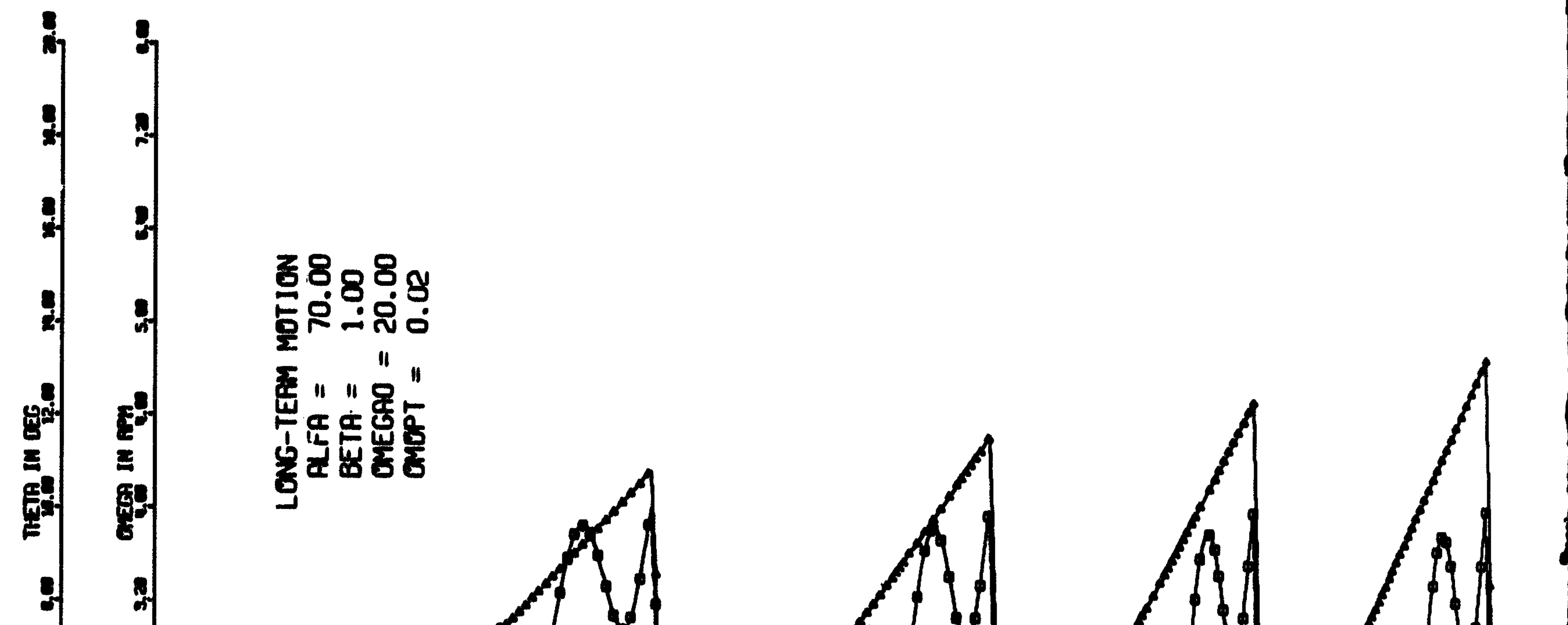

FOLDOUT FRAME 1

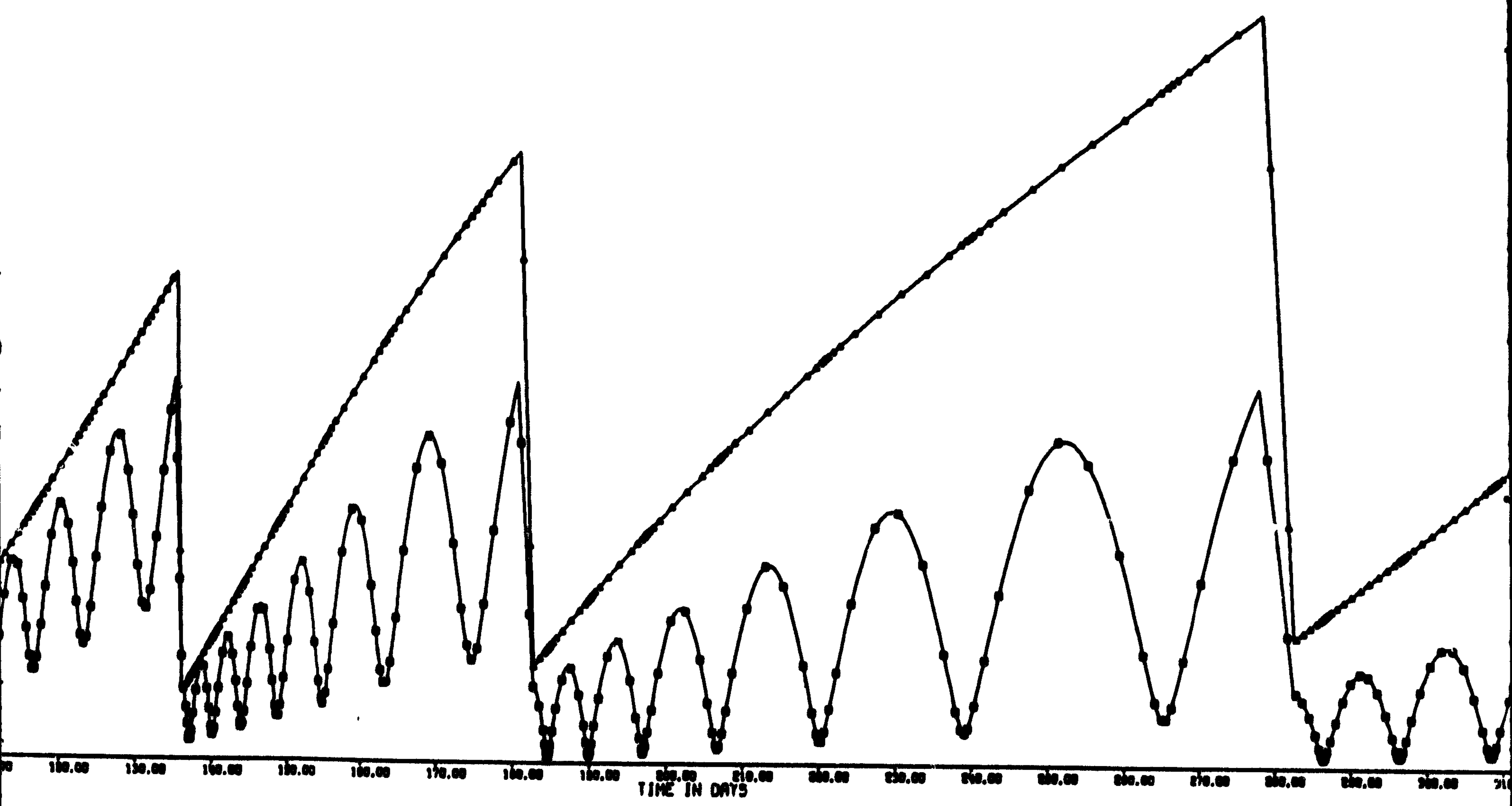

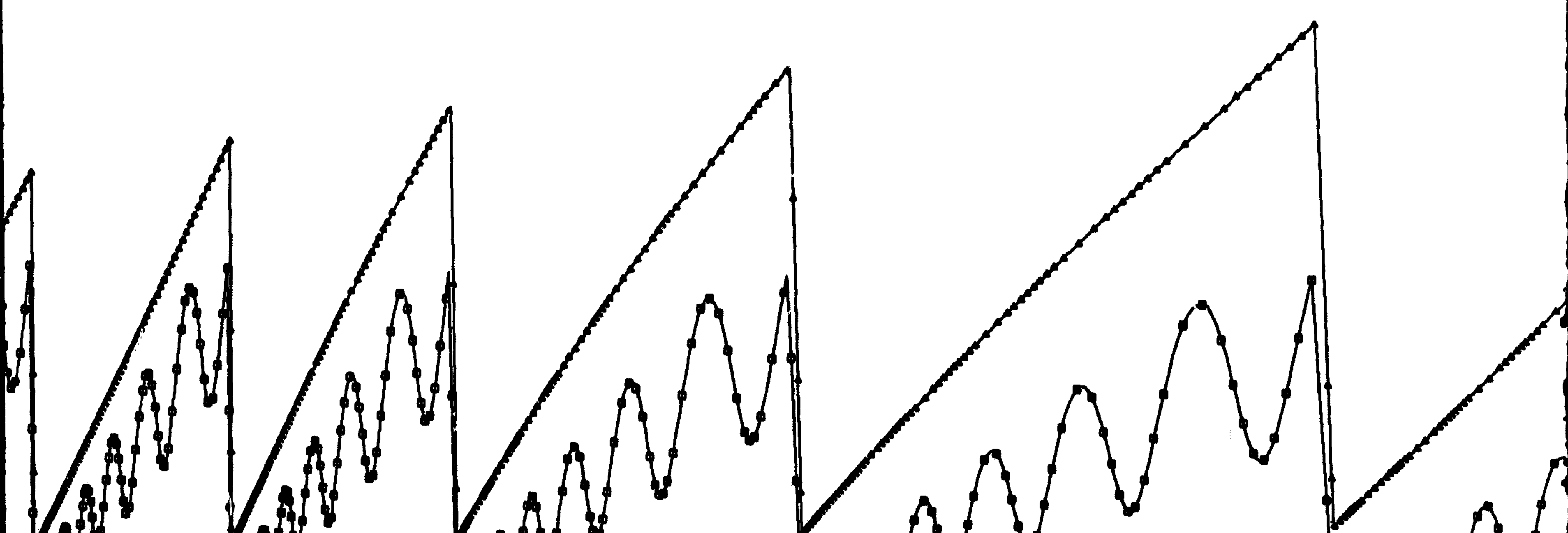

Foldout FRAME 2

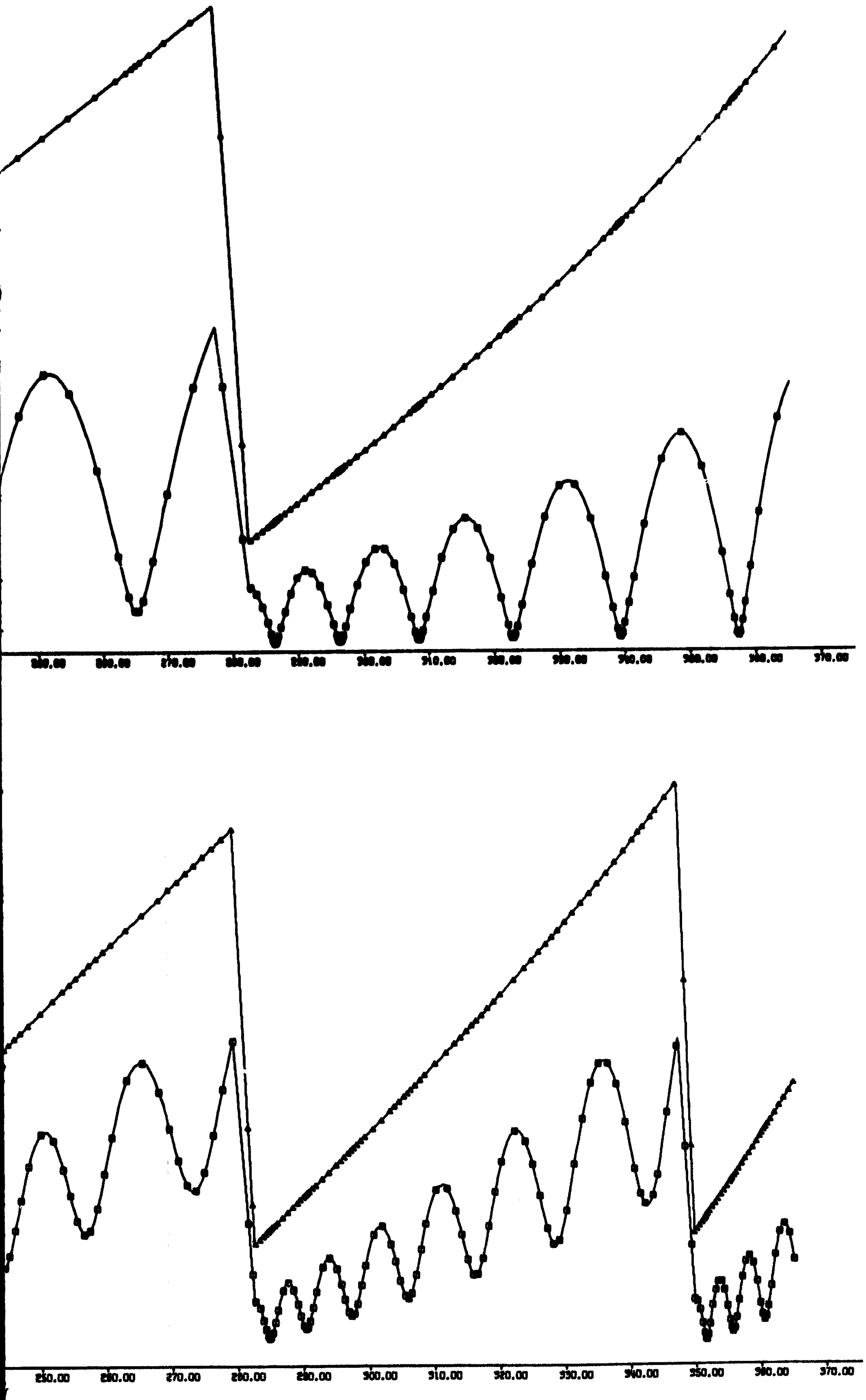

Fig. 8-12 Long-term θ and ω vs time.

FOLDOUT FRAME 3

PRECEDING PAGE BLANK NOT FILMED.

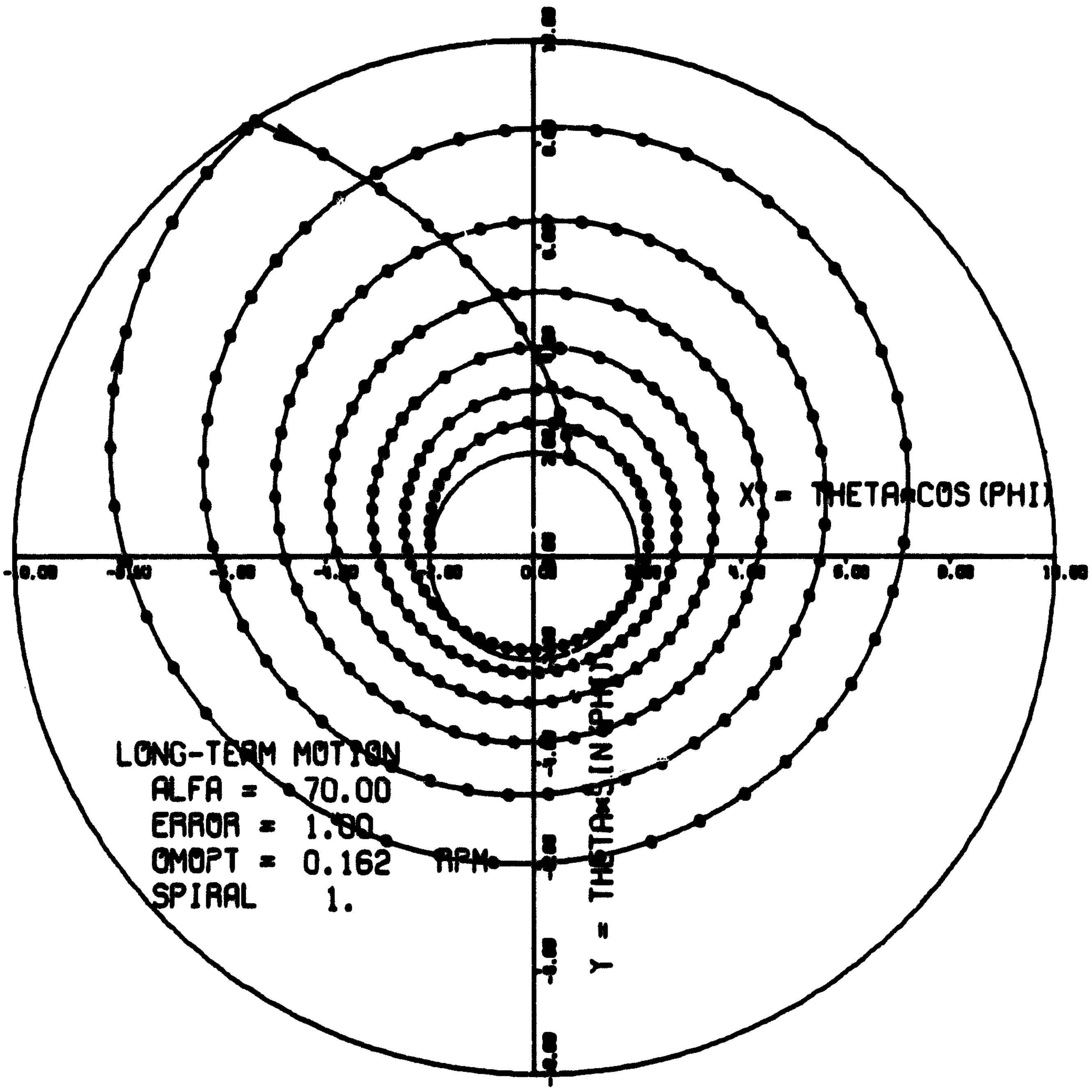

Fig. 8-13a Long-term spirals (1).

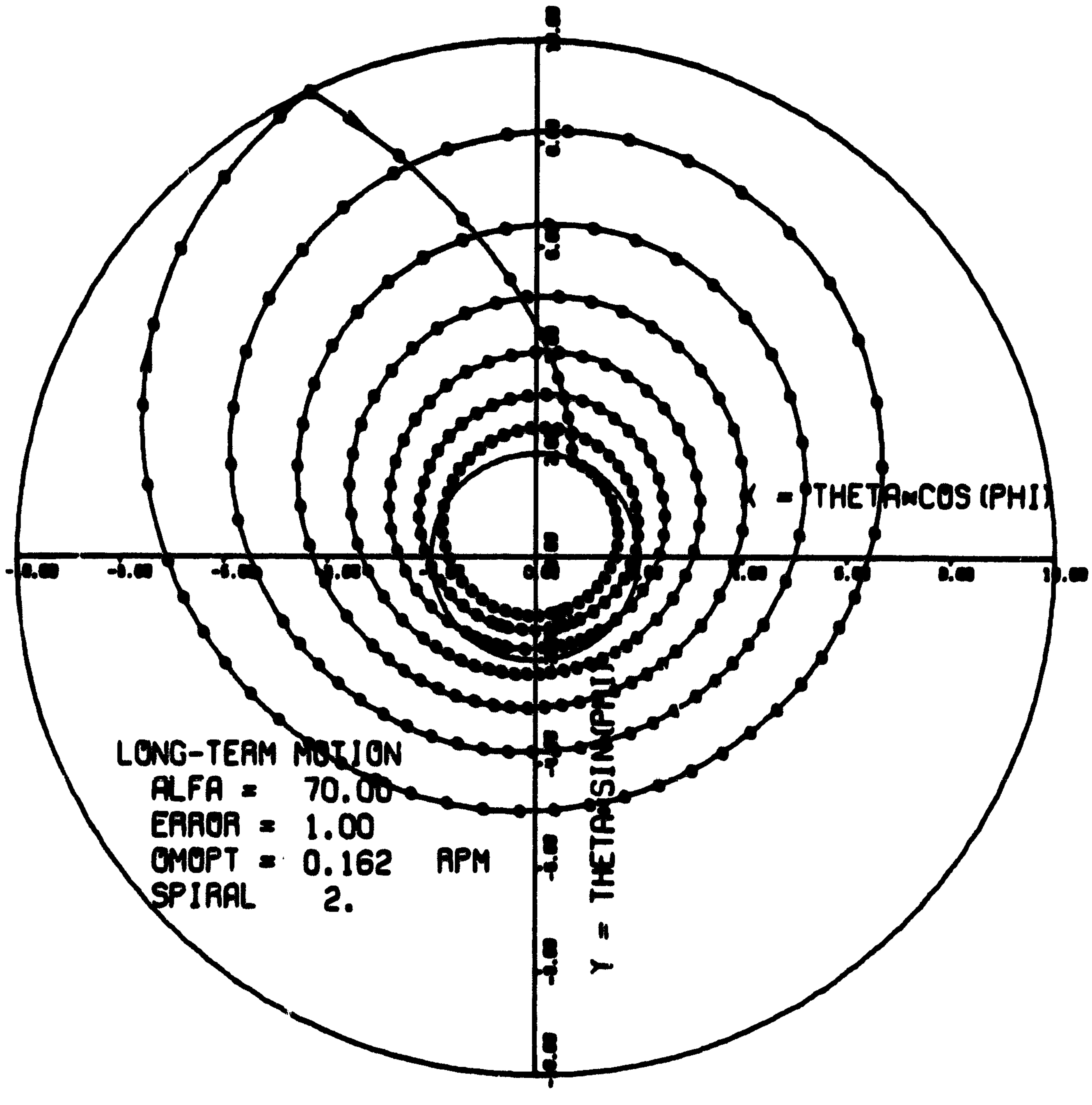

Fig. 8-13b Long-term spirals (2).

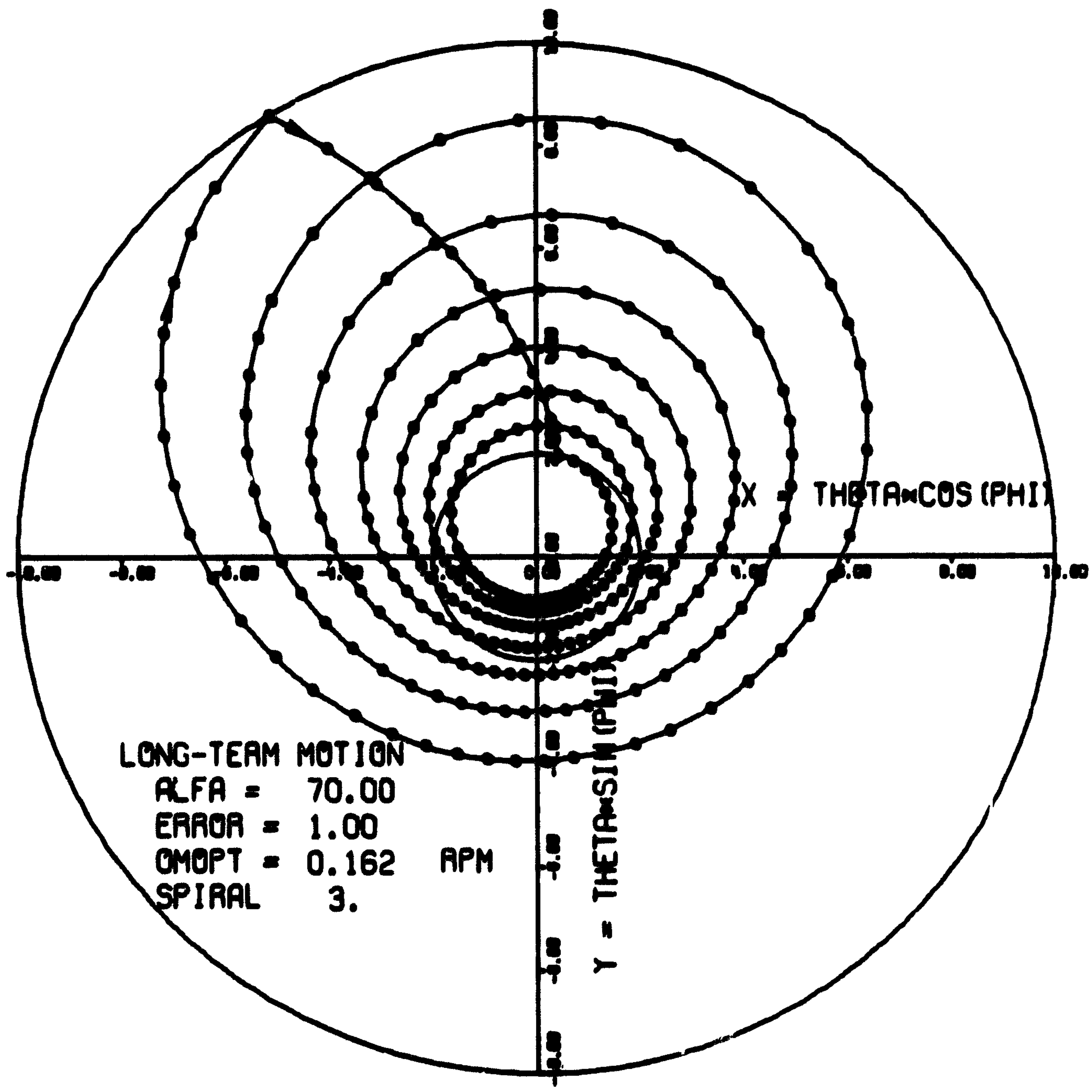

Fig. 8-13c Long-term spirals (3).

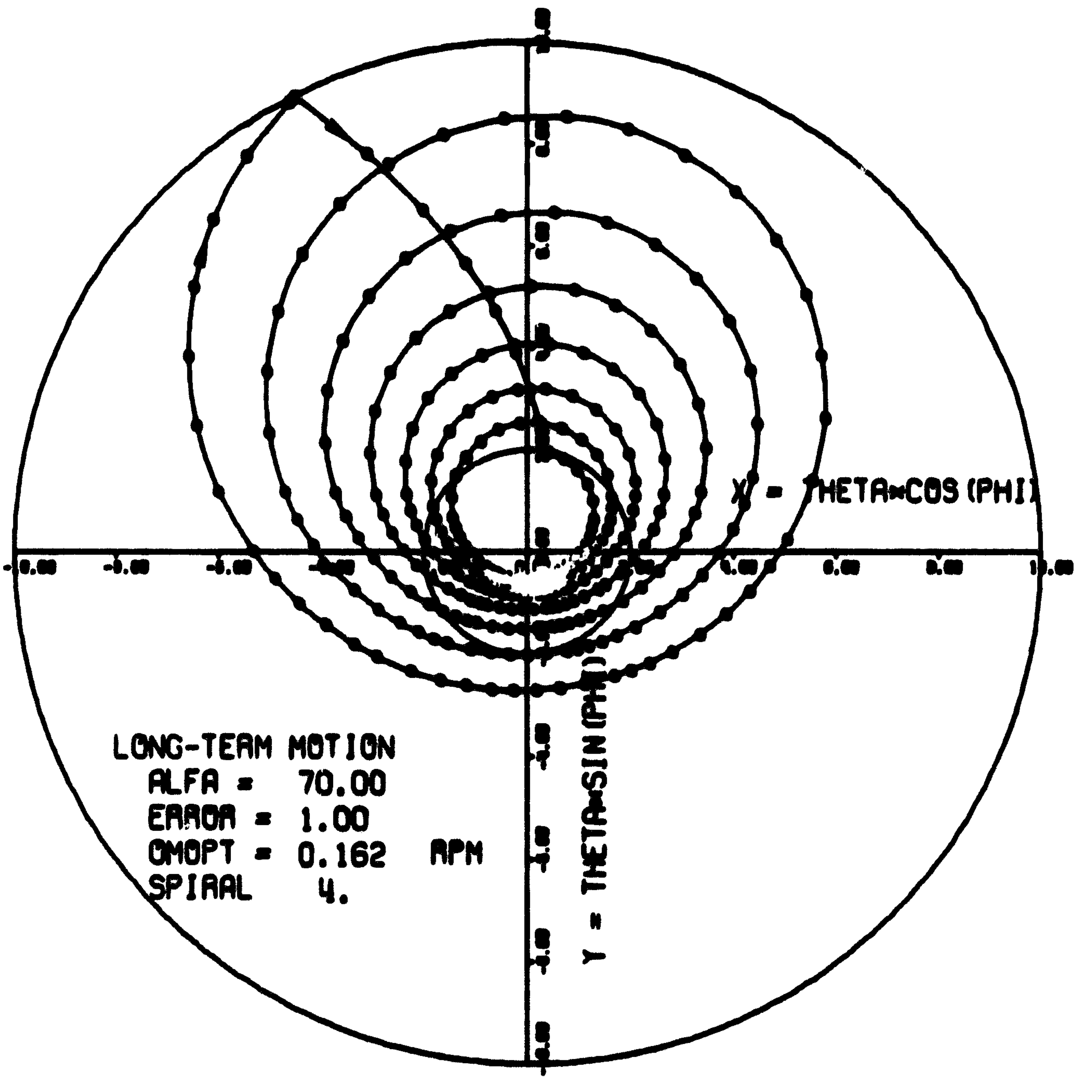

Fig. 8-13d Long-term spirals (4).

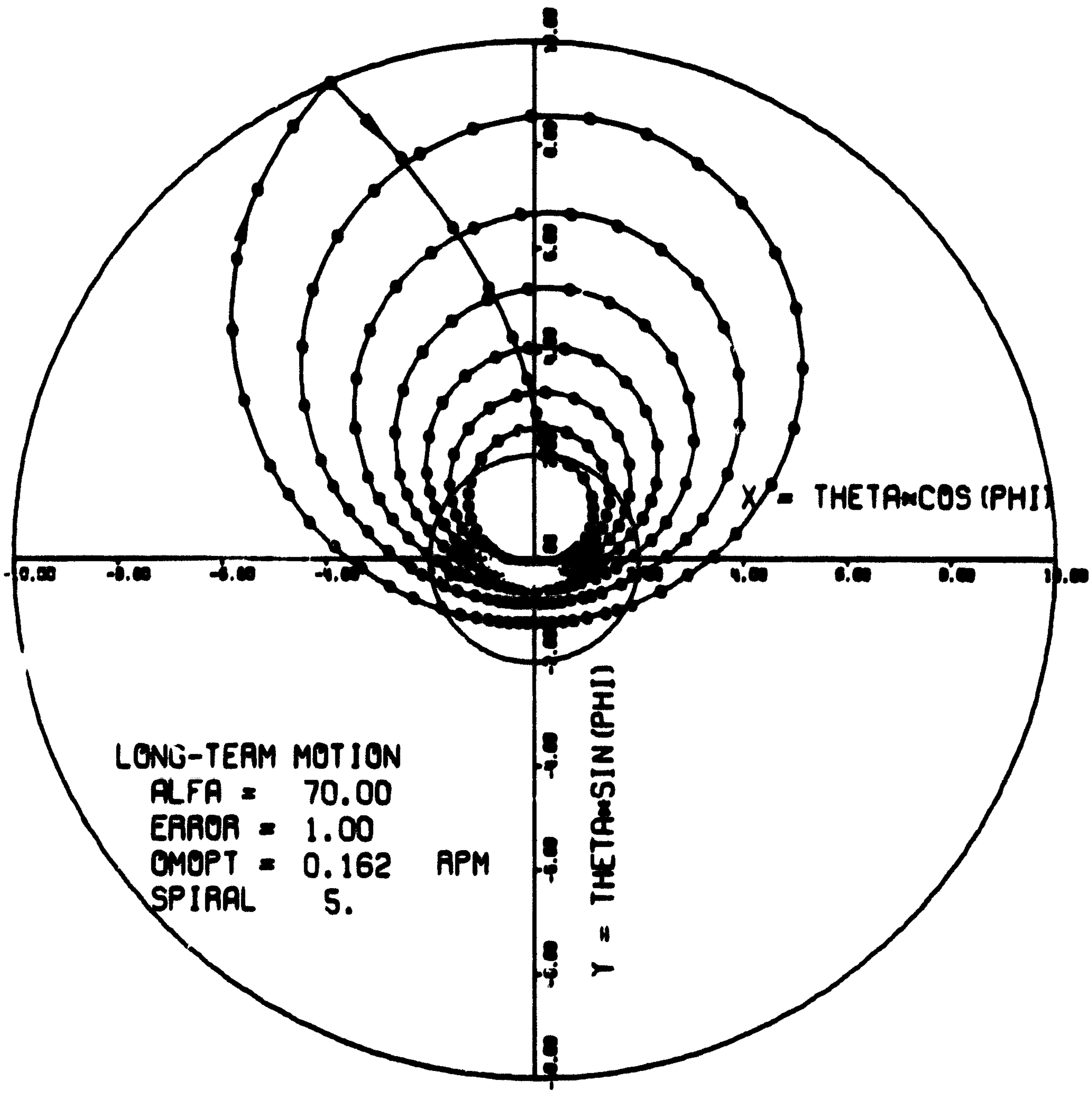

Fig. 8-13e Long-term spirals (5).

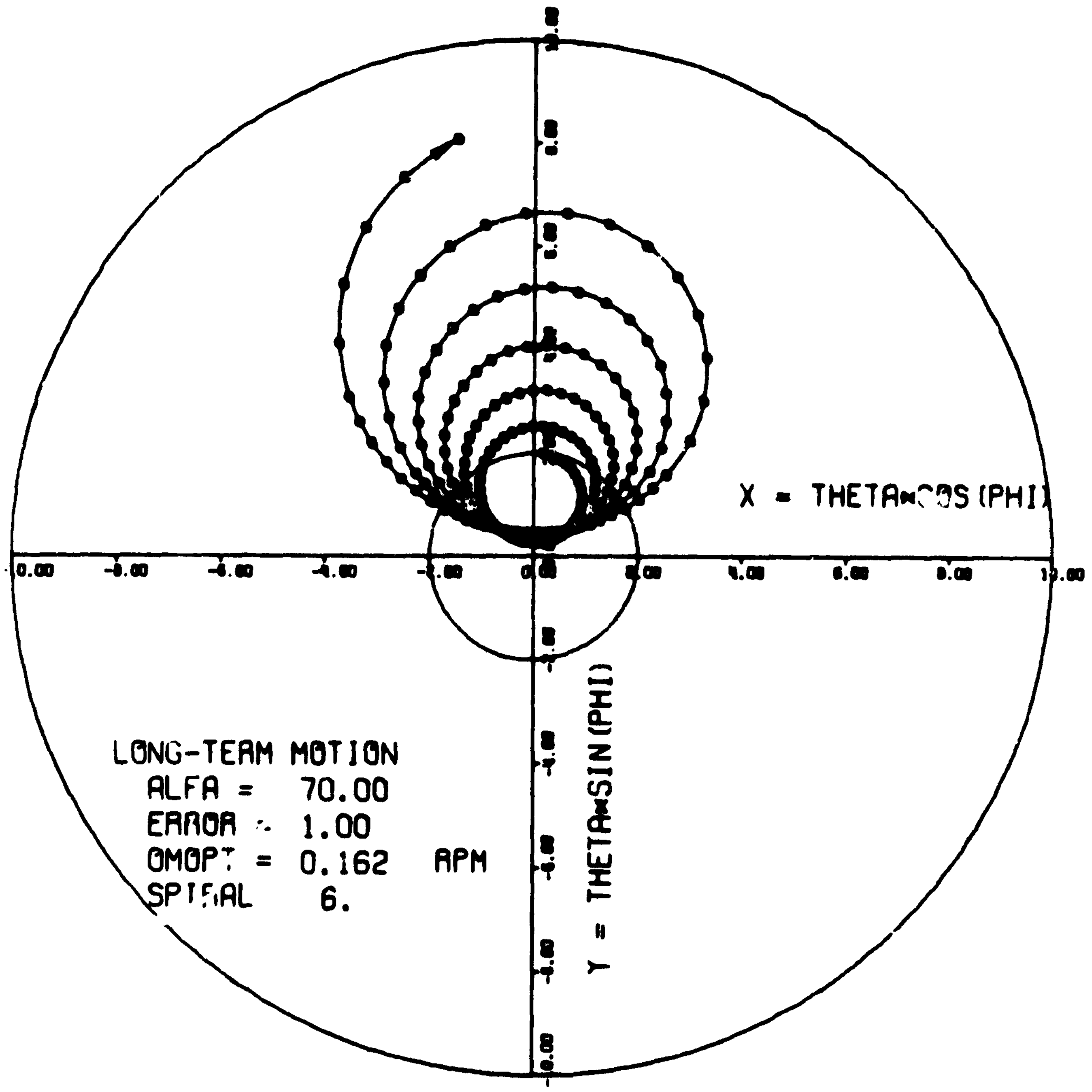

Fig. 8-13f Lcng-term spirals (6).

8.9.3 Sensitivity to Initial Conditions

Comprehensive plots of initial stabilization time and initial spirals (motion of figure axis) have been plotted vs initial theta and vs initial omega (in r/min). (See Fig. 8-16, 8-17, 8-18). As expected, initial stabilization time is approximately linear with initial spin rate; and initial stabilization time is relatively constant for 10° < initial theta < 70°, but changes very rapidly below 5° and above 75°.

8.9.4 Parametric Investigation of Long-Term Motion

The number of long-term limit cycles of the vanes has been taken as an index of the long-term performance. New results in this area indicate that the primary characteristics of the long-term motion are relatively independent of some of the conditions investigated here.

The vanes' cant angle affects the number of limit cycles, with the results shown in Fig. 8-15. If the area of each vane were trimmed to give the same initial stabilization time for each cant angle, then the number of long-term limit cycles would be nearly constant for cant angles between 45° and 70°.

The vanes' pitch error angle is roughly linear with the number of limit cycles, as expected. (See Fig 8-19).

The vanes' reradiation damping-time constant is not critical. Here a change in time constant by 3 orders of magnitude changes the number of limit cycles by a factor of 3.6, from 2.5 to 8.8, as shown in Fig. 8-20. In addition, analysis of torques shows that the system with damping is unstable for pitch angles greater than a fraction of a degree.

Initial conditions do not significantly affect the long-term performance, as shown in Fig. 8-21. Two extreme cases (initial omega of 5 r/min and 80 r/min) show the conversion of the system (over a period of one year) from its initial low spin state to a pseudo-equilibrium high spin state. Initial theta affects only the long-term performance as it affects the despin ratio from initial theta to 2°.

8.9.5 Nominal Conditions

All the preceding cases were run for fixed conditions, except for the condition of parameter which was varied:

Spacecraft moment of inertia	4.64×10^6 gm-cm^2
Vanes' cant angle	70°
Vanes' pitch error angle	1°

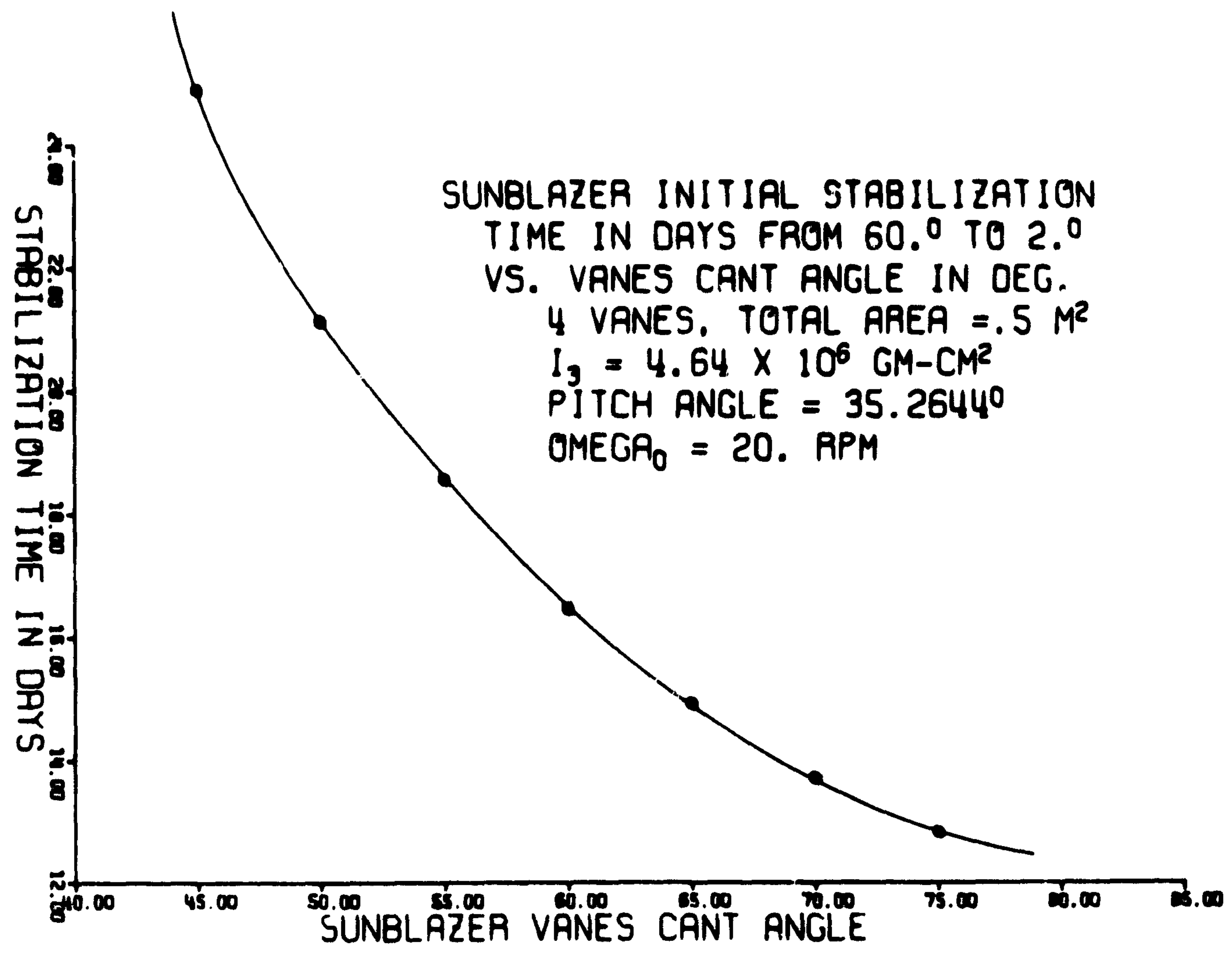

Fig. 8-14 Optimization of cant angle - stabilization time.

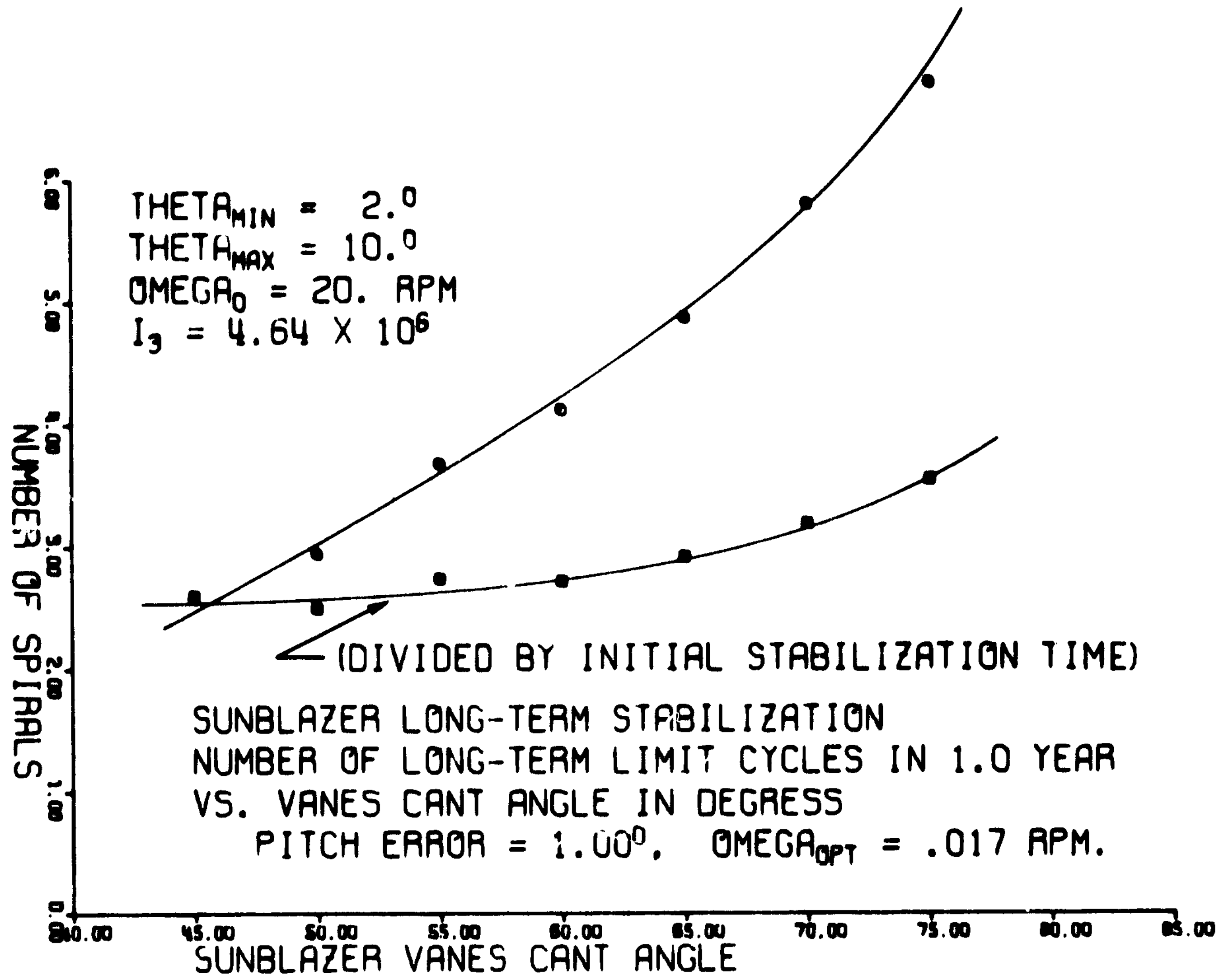

Fig. 8-15 Optimization of cant angle - long-term cycles.

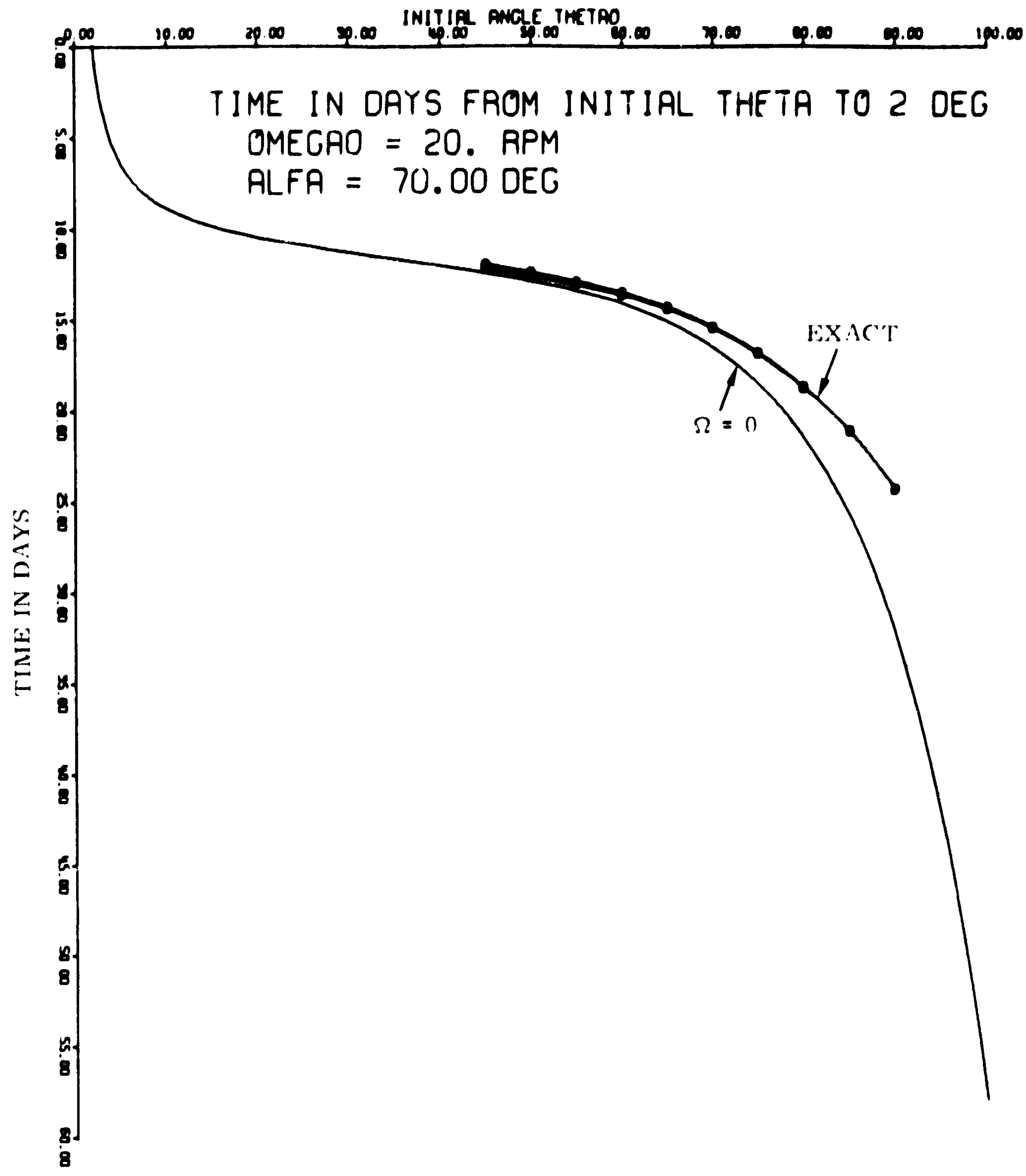

Fig. 8-16 Stabilization time vs initial θ.

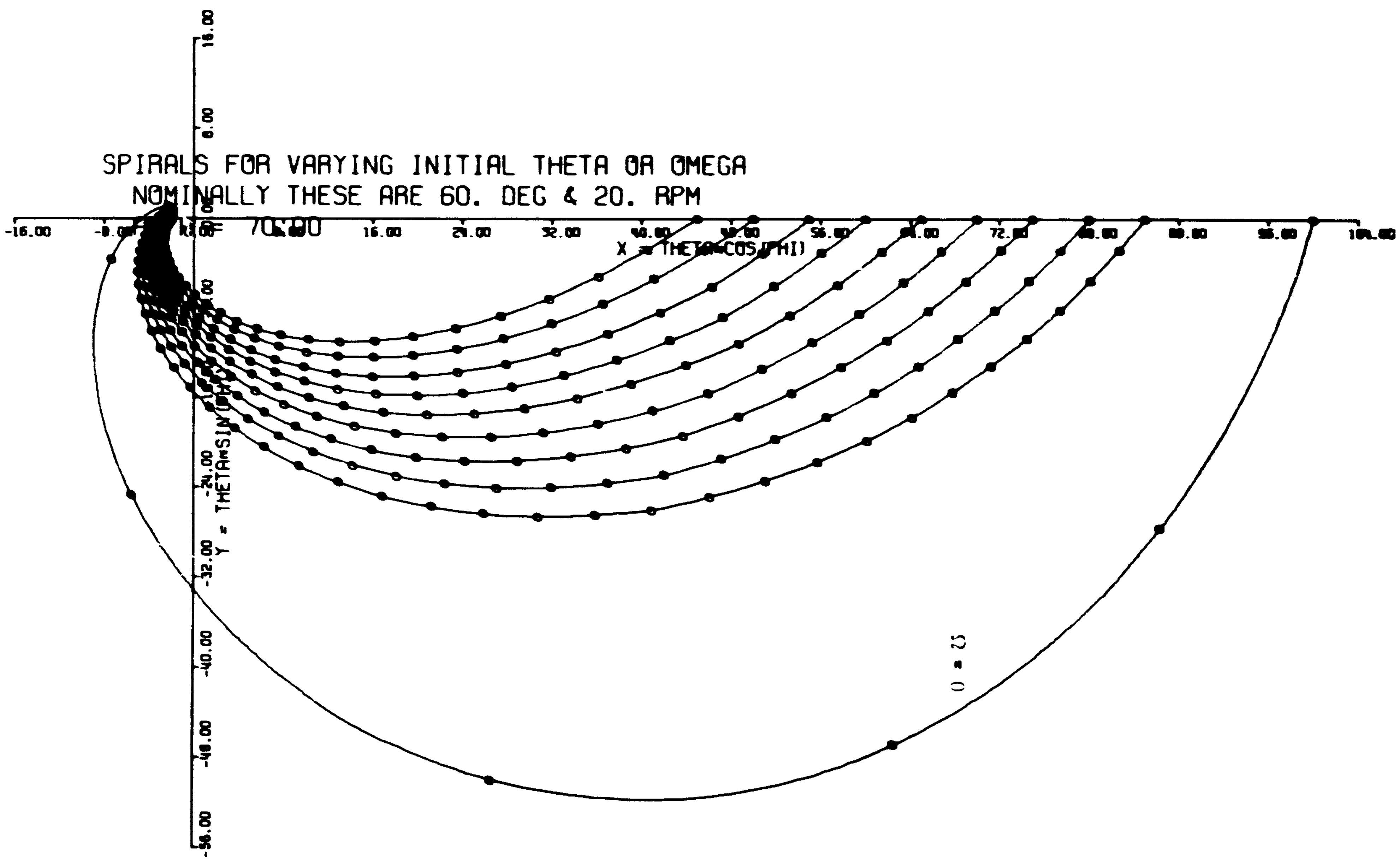

Fig. 8-17 Initial stabilization spirals - different initial conditions.

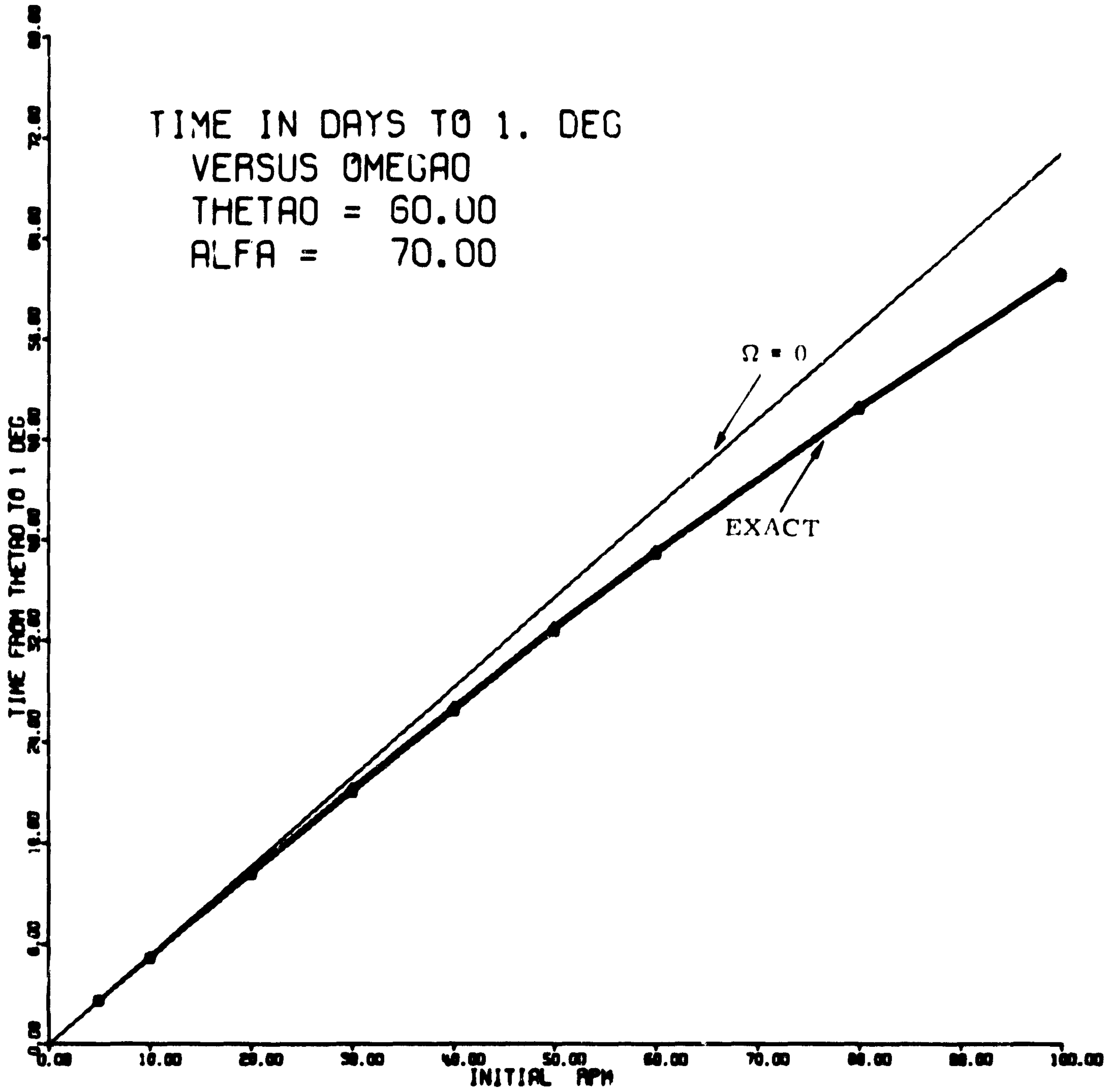

Fig. 8-18 Stabilization time vs initial ω.

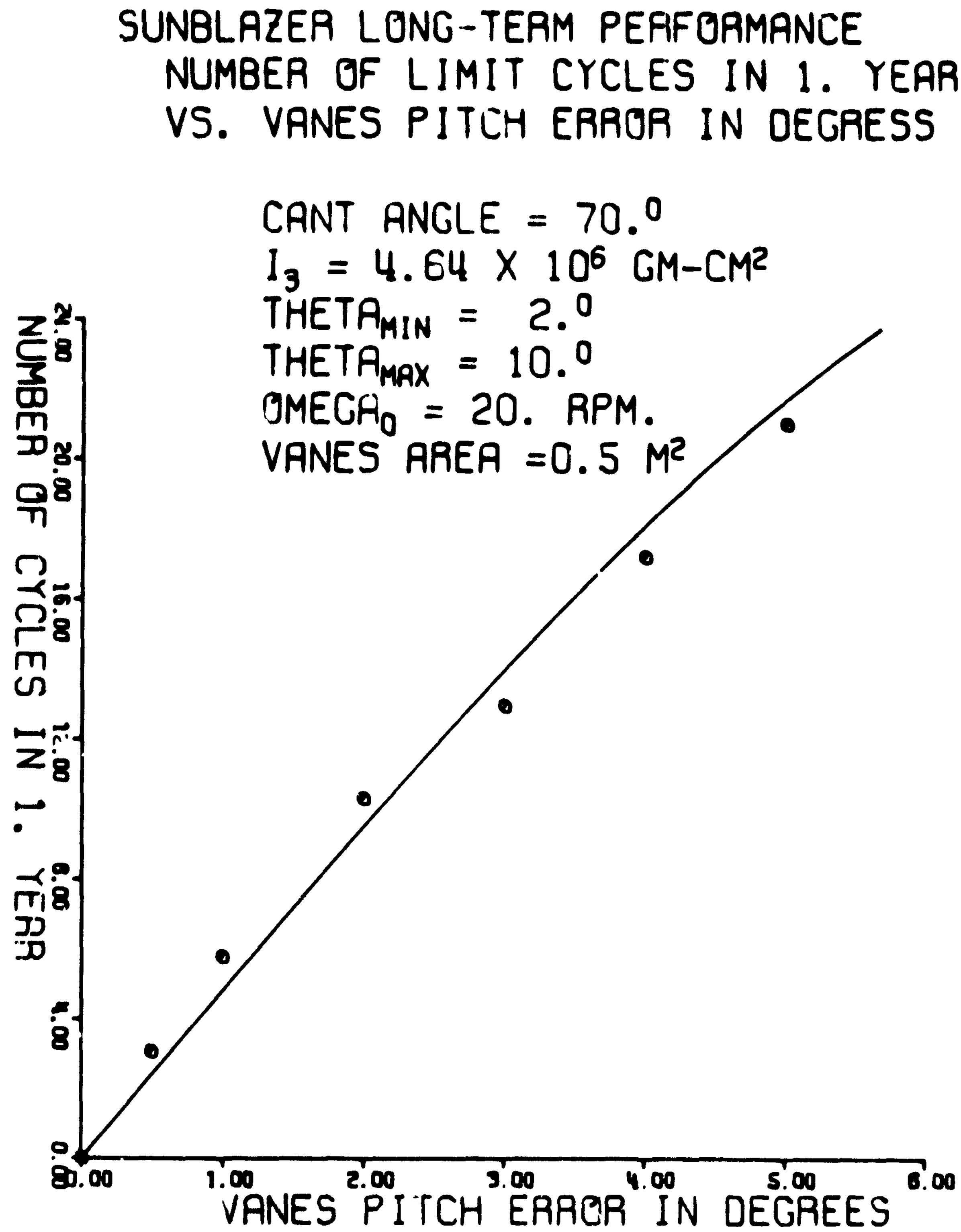

Fig. 8-19 Long-term number of cycles vs pitch error.

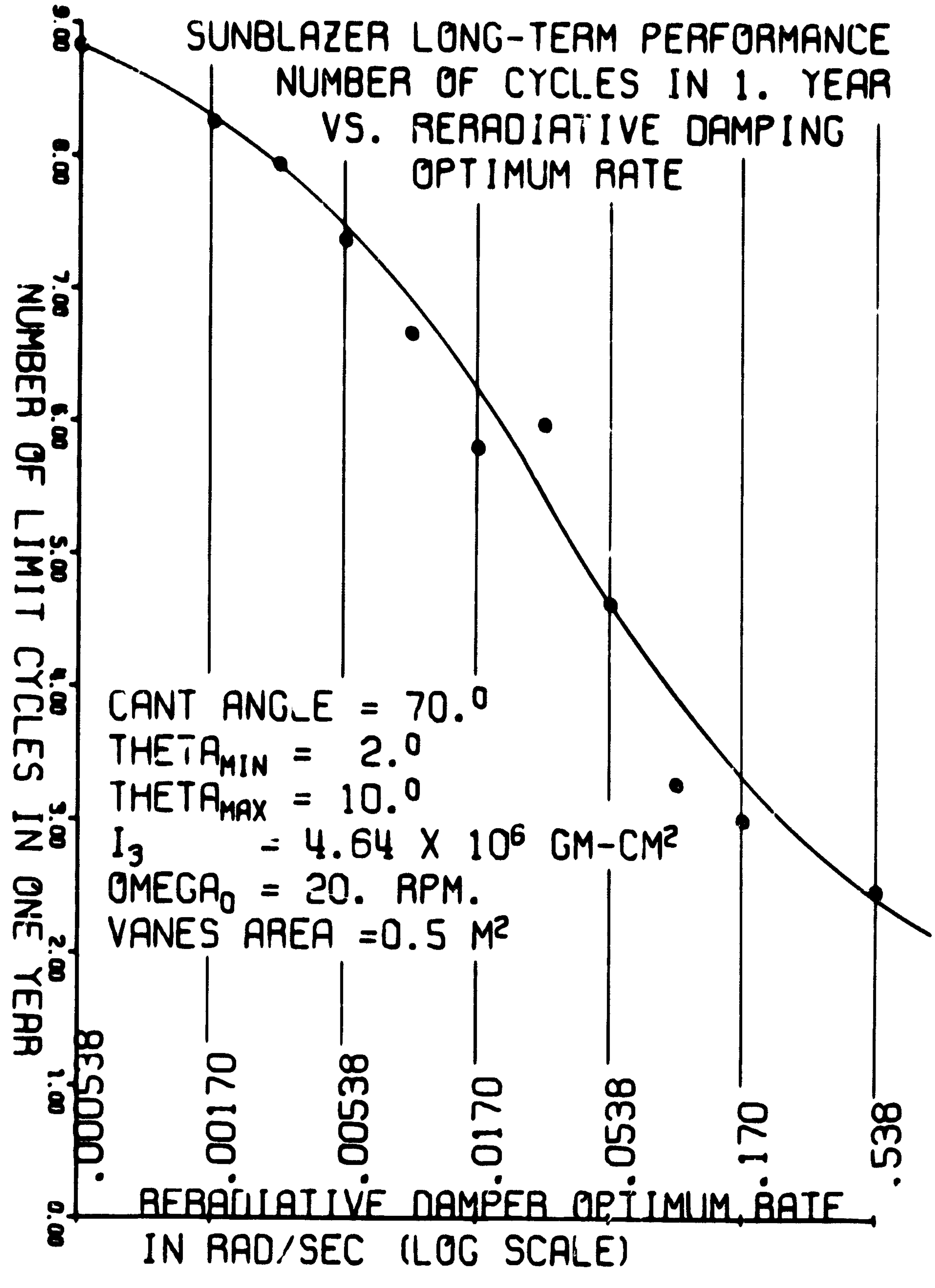

Fig. 8-20 Long-term cycles vs reradiation damping constant.

Reradiation damper rate	0.017 rad/sec
Initial spacecraft-sun angle	60^{o}
Initial spin rate	20. r/min

8.9.6 Possible Pitfalls in Motion

A major dynamics program has been run which integrates the complete equations of motion for a rigid body and includes the following variables:

1. Temperature on all four vanes
2. Three different moments of inertia
3. Arbitrary misalignment between torque axis (where erecting torque → 0) and principal axes
4. Arbitrary initial conditions
5. Arbitrary absorptivities and emissivities for vanes.

The results have shown that an incredibly small nutation amplitude (0.001 to 0.01 fractional amplitude) can result in extremely large libration-oscillation amplitudes (20^{o} to 70^{o}) if the error torque of the vanes results form a -1^{o} error in the pitch angle, in the same sense as the initial -35.26^{o} pitch, so that the spin rate goes through 0. A further integration of the equations of motion has shown that, with modified logic of the vanes control system, the motion might eventually stabilize to a small angle after a number of wild oscillations, but it is felt that the simulation of a few special cases does not give enough information to guarantee the stability of the system in general. It is felt, at the present stage of development, that special precautions should be taken to prevent the spin rate from going through 0.

A second major pitfall could result from an attempt to reverse the vanes (to $+35.26^{o}$) when the initial theta is large (120^{o}), hoping that the spacecraft would despin and go to 180^{o}, because of the reversal in spin torque of the vanes above 80^{o}. Hopefully, the spacecraft would then flip around and wind up at some small angle where the conventional control system would stabilize it. A promising fact is that it takes about as long in this mode to go from 120^{o} to 178^{o} as it does in the normal mode from 60^{o} to 2^{o}. However, the problem of going from 178^{o} hopefully to a small angle through 0 spin rate is not understood in sufficient detail to design a predictable control system.

A third major pitfall would result from an attempt to null the vanes after separation (at 60^{o}), and hopefully wait for the sun line to rotate into the axis of symmetry of the spacecraft. Here, the precession of the spacecraft would have to be taken into account; and initial results indicate that, even at an

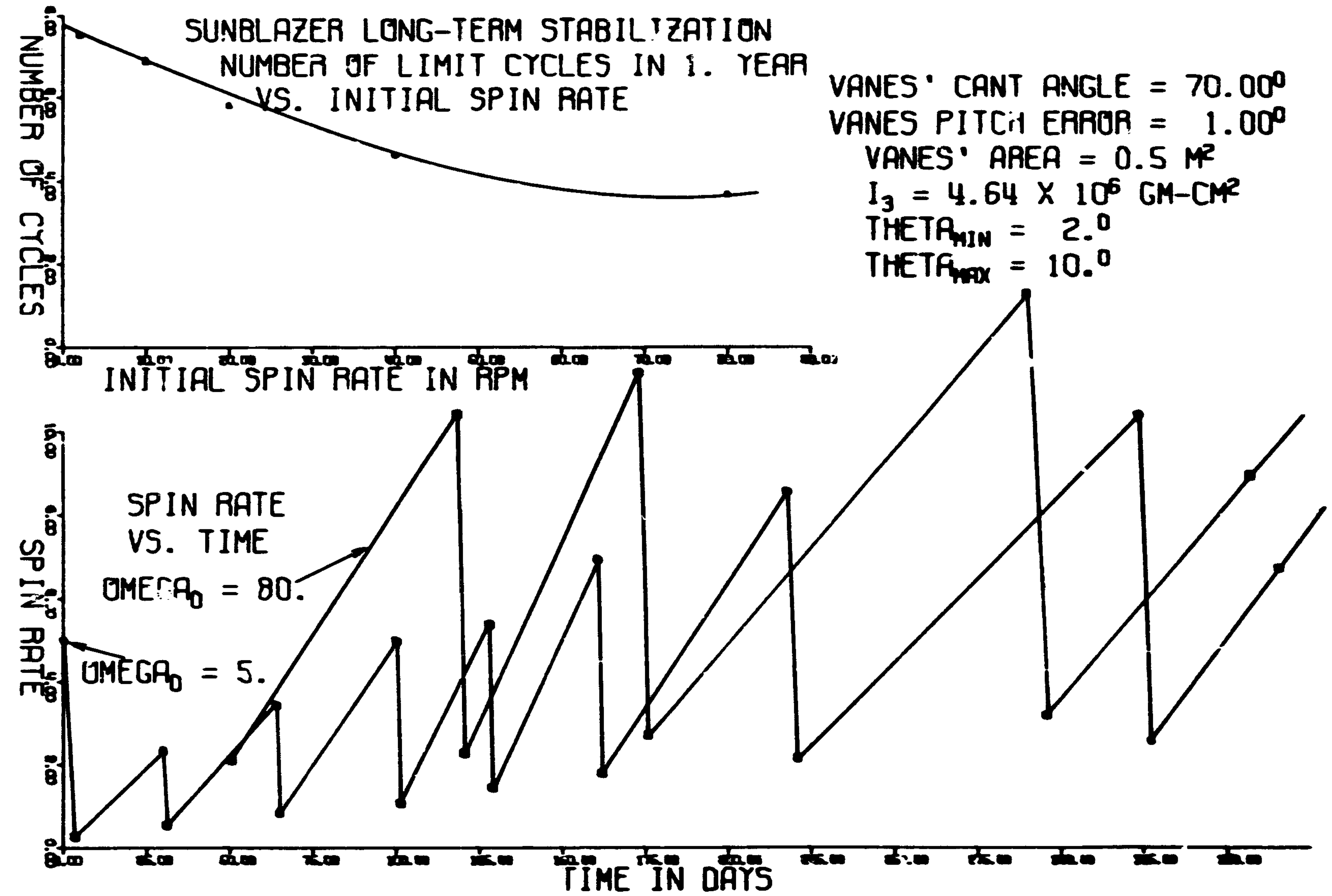

Fig. 8-21 Long term cycles vs initial spin rate.

initial rate of 160 r/min, the angle between the spacecraft axis and the sun would oscillate between 17° (which it would reach at 57.1 days) and 155° (at 158.2 days).

Nutation motion of the spacecraft (see Sec 8.11) can be derived very simply from the complete equations of motion Eq (8.16) and (8.17), by assuming $\ddot{\phi} = 0 = \ddot{\theta} = \dot{\omega}$, leading to

$$\dot{\phi} = \frac{I_3}{I_1} \frac{\omega}{\cos \theta_0} \qquad (8.80)$$

which is basically the formula for force-free precession(11), and:

$$\dot{\theta}_0 = \frac{N_2(\theta_0)}{I_3 \omega} \qquad (8.81)$$

The amplitude of the nutation circle, θ_0, can increase (or decrease) as a result of direct or reradiative torques and of internal dissipation. See Sec 8.11 for a more detailed discussion of radiative torques. Internal dissipation has not been determined; however, if sufficient dissipation is not available in the structure, it may be necessary to design an internal damper.

8.10 Ancillary Problems

Some ancillary problems might be mentioned

Surfaces for the spacecraft and vanes have not been investigated in sufficient detail. Although literature exists which indicated that the assumed surface characteristics are not unreasonable, the problem still remains of fabricating a structure and measuring the surfaces.

An aspect sensor, probably based on the technique successfully developed by the Goddard Space Center, of using multiple sensors and a mask to provide the maximum information with the minimum electrical hardware, does not seem to be a real problem.

Control logic consisting of a few AND and OR gates to switch the vanes, depending on the angle, is not felt to be a real problem either.

Micrometeorites are not felt to be a real threat to the spacecraft, either as momentum disturbance, or by erosion of the surfaces. (See Sec 8.1).

A practical test of the vane torques and the effect of the control system should definitely be made in vacuum.

8.11 Nutations

8.11.1 Convention Used to Distinguish Nutational From Precessional Modes

There are three main types of dynamical instabilities which are of concern in orienting the Sunblazer vehicle:

1. Librational instability for very low spin rates;
2. Precessional instability (increasing cone angle);
3. Nutational instability for moderate and high spin rates.

Because the nominal precession rate is always more than two orders of magnitude below the nominal spin rate, nutations can be analyzed dynamically as a "torque free" precession superposed upon a very slow and steady torqued precession. The convention to be followed here in distinguishing a nutational mode from a precessional mode is that the former causes the vehicle's spin axis to oscillate at an angular frequency comparable to that of the spin rate, while leaving both the direction and magnitude of the angular momentum vector essentially unchanged during a cycle. A precessional mode, on the other hand, causes the vehicle's axis to oscillate at an angular frequency much lower than the spin rate (in fact, about inversely proportional to the spin rate), and actually changes the direction of the angular momentum during a cycle. In general, both modes will be simultaneously present to some extent. The problem here will be to determine whether or not the amplitude of the nutational mode will increase or decrease with time under the various sets of circumstances Sunblazer might be expected to encounter.

Before proceeding to a more mathematical description of this problem, it should be stated that, although the actual derivation to be given here differs from others in this report, both the basic equations and the final notation are identical to the previous treatments (see Sec 8.7). Since the unsimplified basic equations themselves cannot be handled analytically, an approximation will be made which can adequately account for at least the nominal operating conditions of Sunblazer. In a few special cases, where insufficient confidence could be expected from purely analytical techniques, an analog computer has been used, which employs no approximations whatever.

Basic to the mathematical description will be a cascading of two uniformly-rotating coordinate systems. The uniform rotations rates will comprise one of the approximations, (see Fig. 8-13). For the first, system, we will temporarily use the same notation as Halfman[12], and then convert this to our standard notation. However, the definitions of θ, ϕ, and μ for the cone angle, precession angle and spin angle respectively will be the same in both notations.

8.11.2 General Dynamical Equations for an Axisymmetric Body and Conversion into the Standard Notation

Proceeding then to page 220 of Halfman, and also referring to the labeling in parentheses of Fig. 8-22, we find that the most general dynamical equations for an axisymmetric body are:

$$* \; M_X = I_X \frac{d\omega_x}{dt}$$

$$* \; M_y = I_T \frac{d\Omega_y}{dt} - \Omega_x I_T \Omega_z + \Omega_z I_x \omega_x \qquad (8.82)$$

$$* \; M_z = I_T \frac{d\Omega_z}{dt} - \Omega_y I_x \omega_x + \Omega_x I_T \Omega_y$$

where in this particular case

$$* \; \omega_x = \dot{\psi} + \dot{\phi} \cos\theta$$
$$* \; \Omega_x = \dot{\phi} \cos\theta \qquad (8.83)$$

$$* \; \Omega_y = \omega_y = \dot{\theta}$$
$$* \; \Omega_z = \omega_z = \dot{\phi} \sin\theta \qquad (8.84)$$

Substituting these last three relations into Eq (8.82) one obtains:

$$* \; M_x = I_x \frac{d\omega_x}{dt}$$

$$* \; M_y = I_T \ddot{\theta} - I_T \dot{\phi}^2 \sin\theta \cos\theta + I_x \dot{\phi} \omega_x \sin\theta \qquad (8.85)$$

$$* \; M_z = I_T \ddot{\phi} \sin\theta + 2 I_T \dot{\phi} \dot{\theta} \cos\theta - I_x \omega_x \dot{\theta} \; .$$

Converting these equations into the standard notation so that

$M_x \to N_z$, $M_y \to N_x$, $M_z \to N_y$, $I_x \to I_3$, $I_T \to I_1$, $\omega_x \to \omega_z$, $\omega_z \to \dot{\psi} + \dot{\phi} \cos\theta$,

* Not standard notation.

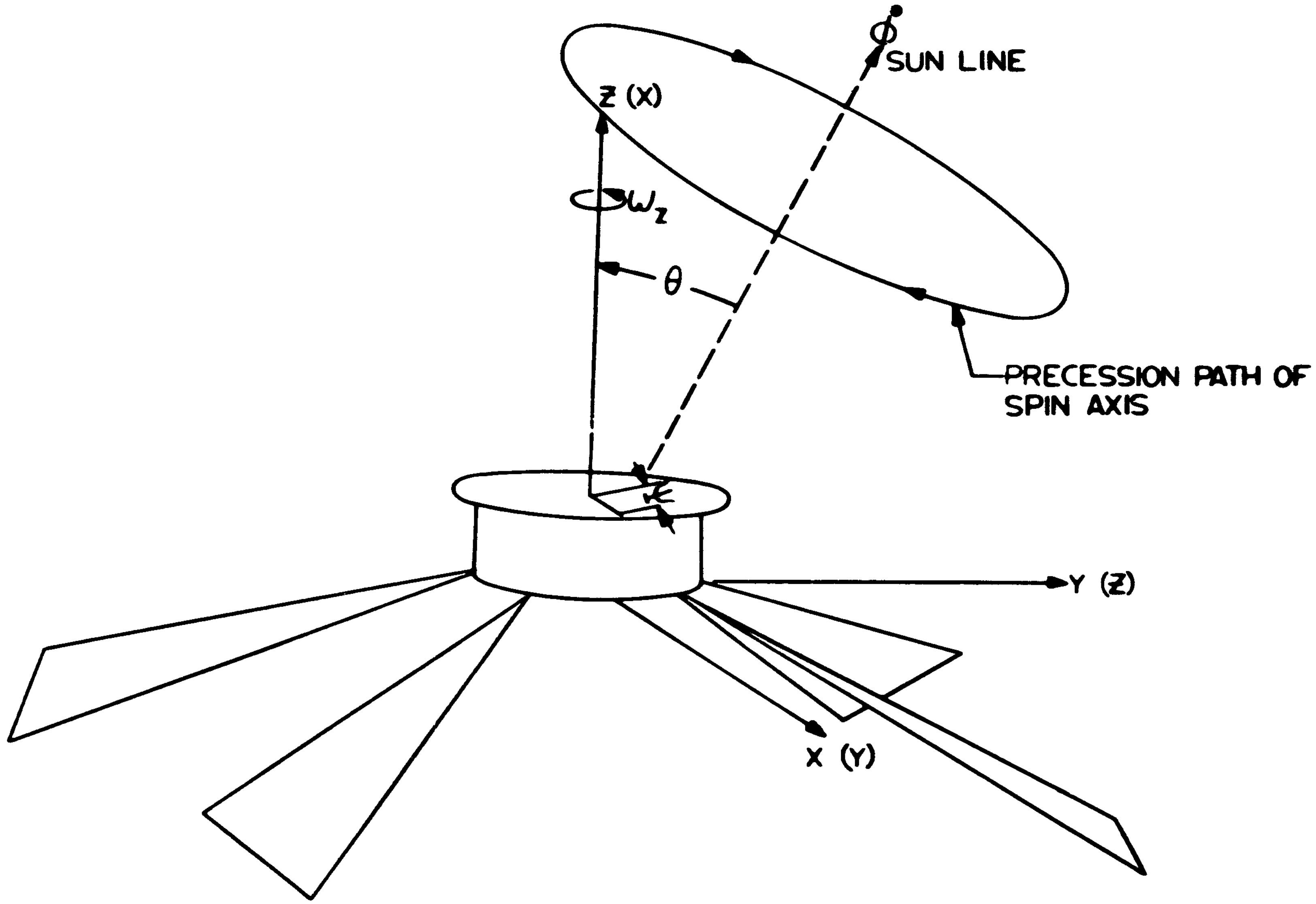

Fig. 8-22 Halfman's coordinates.

we will eventually get [c.f. Eq. (8.16), (8.17), (8.18)]

$$(N_p) \qquad N_x = I_1 \ddot{\theta} - I_1 \dot{\phi}^2 \sin\theta \cos\theta + I_3 \dot{\phi} \omega_z \sin\theta \qquad (8.86)$$

$$(N_e) \qquad N_y = I_1 \ddot{\phi} \sin\theta + 2I_1 \dot{\phi} \dot{\theta} \cos\theta - I_3 \omega_z \dot{\theta} \qquad (8.87)$$

$$(N_s) \qquad N_z = I_3 \frac{d\omega_z}{dt} \qquad (8.88)$$

Note that now the z-axis is along the axis of symmetry (instead of the x-axis as before) and the x-axis is perpendicular to the vehicle-sun line (instead of the previous y-axis). Because torques about certain coordinate axes are closely associated with definite motions of the spacecraft, N_x, N_y and N_z are commonly referred to as the "precession torque", "erecting torque", and "spin torque" respectively (N_p, N_e, and N_s). These torques are usually a function of θ only. It is also important to notice that, until now, no approximations have been made, and the only assumption used has been that of axial symmetry (about the z-axis) for the spacecraft.

In order to determine the steady rotation rates of each of the two cascaded systems, we first must require that $\dot{\theta} = \ddot{\theta} = \ddot{\phi} = \dot{\omega}_z = 0$. Then if we solve Eq (8.86) for $\dot{\phi}$ using the quadratic formula, we get

$$\dot{\phi} = \frac{I_3 \omega_z}{2I_1 \cos\theta} \left[1 \pm \sqrt{\left(1 - \frac{4I_1 \cos\theta \, N_x}{I_3^2 \omega_z^2 \sin\theta} \right)} \right] \qquad (8.89)$$

where the assumption of steady precession has been introduced. As usual in such situations, the minus sign corresponds to the slower mode of precession in which we are interested, and as long as N_x, the precession torque, is sufficiently small (i.e.,

$$N_x << \frac{I_3^2 \omega_z^2 \sin\theta}{4I_1 \cos\theta})$$

we may write

$$\dot{\phi} \cong \frac{N_x}{I_3 \omega_z \sin\theta} \qquad (8.90)$$

This approximation corresponds to the case when the direction of angular momentum and the z-axis nearly coincide. One now requires that the first of the two cascaded systems rotate at the constant rate given by Eq (8.89), as well as that its z-axis be aligned with the angular momentum of the vehicle (instead of the figure axis as before). This should work out all right, even relaxing the requirement that $\ddot{\theta}$, $\dot{\theta}$, and $\dot{\phi}$ be zero as long as the absolute value of N_x does not change much with a given range of θ so that the angular momentum vector will precess at a nearly constant rate (recall that the angular momentum does not change much in a nutation cycle).

The second rotating coordinate system of x', y', and z' (see Fig. 8-23) will rotate about the (slowly) precessing z-azis of the first system, will have its z'-axis always aligned with the vehicle's axis of symmetry, and its x'-axis perpendicular to the z-axis. If N_x is small or does not change appreciably within the range of any given θ oscillation (nutation), then for this θ the net effect of N_x on the nutation amplitude will be negligible, at least in one cycle. Also, because the nutational angular rates are much, much faster than the precessional rates, we may solve approximately for the motion in the second system by writing down the same equations as before but with $N_x = 0$. Solving for $\dot{\phi}'$ (with no further approximations):

$$\dot{\phi}' = \frac{I_3}{I_1} \frac{\omega_z}{\cos \theta'} \qquad (8.91)$$

which corresponds to the "torque-free" or "wobble" mode. Also, $\dot{\phi}'$ will be the constant rate at which the x', y', z' system precesses about the more slowly precessing z-axis.

8.11.3 Spacecraft Motion in Terms of Energy

Two very important points can now be made. First, suppose that there are absolutely no torques on the spacecraft and that it is both spinning at ω_z and "wobbling" at $\dot{\phi}'$. Given the fact that some of the mechanical energy of such a system can be converted into heat by non-elastic structural damping aboard the spacecraft (such as loose mylar in the vanes), this motion will not necessarily be stable. In the absence of external torques, the angular momentum of the spacecraft must remain constant, but its kinetic energy can change subject to this constraint and in general will tend towards a minimum. If we consider the two possible extremes of the spacecraft's motion in terms of energy, we find that it might be spinning steadily about its axis of symmetry on one hand or a transverse axis on the other. In both cases the angular momentum, L, will be the same so we may write

$$L = I_1 \omega_1 = I_3 \omega_3 \qquad (8.92)$$

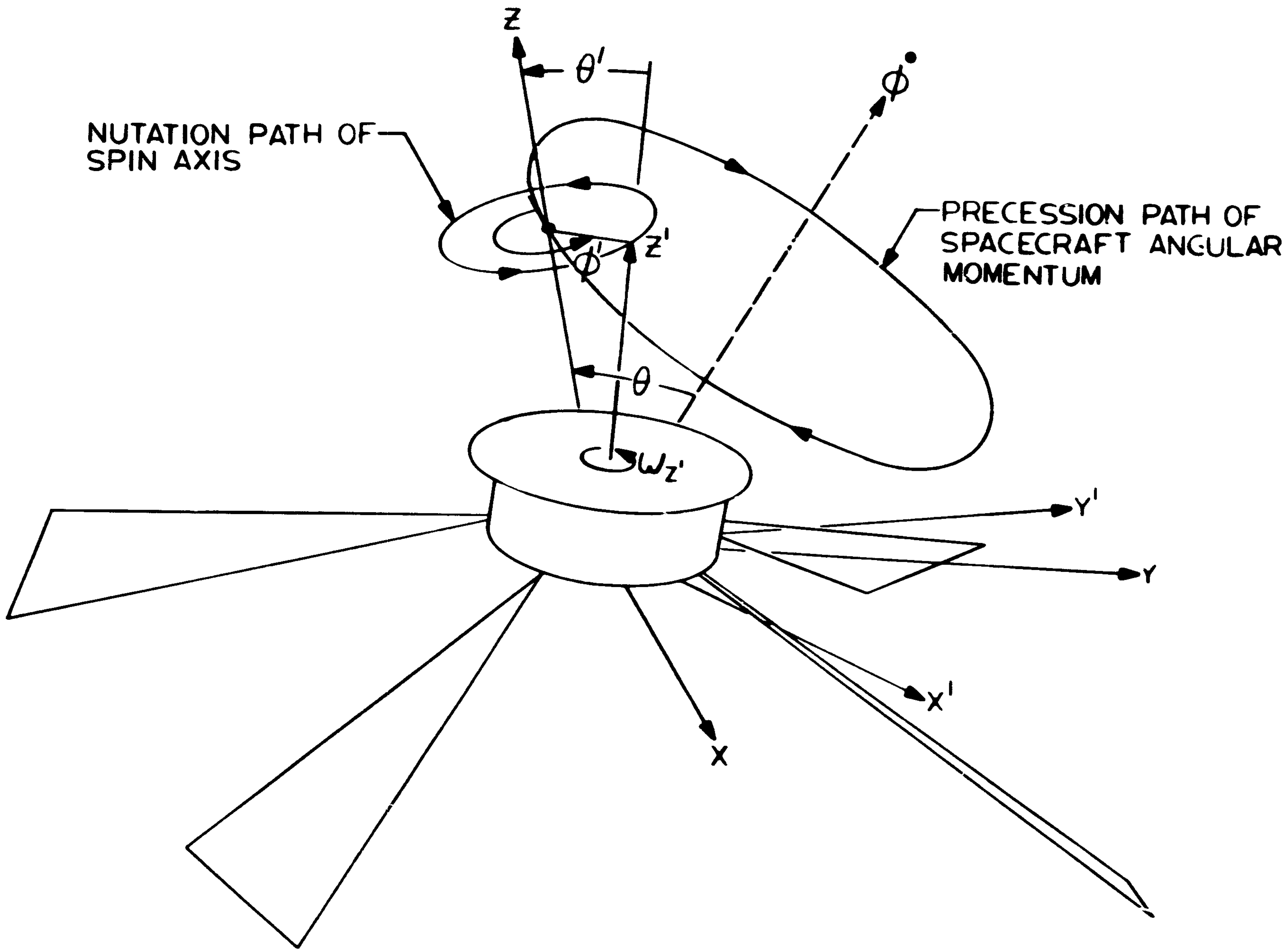

Fig. 8-23 Nutation coordinates.

However, the kinetic energy, T, will be different in each case so that

$$T_1 = 1/2 I_1 \omega_1^2 = 1/2 I_1 \left(\frac{I_3}{I_1}\omega_3\right)^2 = \frac{I_3}{I_1} T_3 \tag{8.93}$$

$$T_3 = 1/2\, I_3 \omega_3 \tag{8.94}$$

if we substitute for ω_1 from above. Thus it is readily seen from Eq (8.93) that the spin axis of smallest kinetic energy depends entirely upon the ratio of the moments of inertia. In particular, if $I_3 > I_1$, $T_1 > T_3$ and a steady spin about the axis of symmetry has the smaller kinetic energy and hence is the stable motion.

To illustrate this result in a more rigorous manner, we find that the angular momentum and kinetic energy of a body "wobbling" with a cone angle of θ' are respectively:

$$L^2 = I_1^2 \phi'^2 \sin^2 \theta' + I_3^2 \omega_{z'}^2, \tag{8.95}$$

$$T = 1/2 \left(I_1 \phi'^2 \sin^2 \theta' + I_3 \omega_{z'}^2\right) \tag{8.96}$$

Eliminating ω_z:

$$T = \frac{L^2}{2I_3} + \frac{I_1}{2}\left(1 - \frac{I_1}{I_3}\right)\dot{\phi}'^2 \sin^2 \theta' = \frac{L^2}{2I_3}\left[1 + \left(\frac{I_3}{I_1} - 1\right)\sin^2\theta\right] \tag{8.97}$$

It is clear from this last equation that if $I_3 > I_1$, then T monotonically decreases with decreasing θ', reaching a minimum at $\theta' = 0$. Therefore as before, the case where $\theta' = 0$ (or a pure spin about the z'-axis) will be the only stable dynamical mode. For this reason, the Sunblazer spacecraft has been designed to have $I_3 > I_1$ so that rotation about the axis of symmetry will be stable. If $I_1 > I_3$, then it would be energetically possible for the properly-spinning spacecraft to convert axes and end up tumbling instead.

The second important point to be noticed here is a possible confusion of the aspect sensor on the front of the spacecraft. Because as we have just shown, the spacecraft must be designed so the $I_3 > I_1$, it can be seen from Eq (8.91) that the vehicle actually precesses faster than it spins! If nutations or "wobbling" of the spacecraft were not damped out, and if the amplitude were large enough so that the nutational mode caused the axis of symmetry to encircle the sun, then the aspect sensor would record the spacecraft as spinning opposite to its true spin sense; this could badly affect the attitude-control system logic. In order to fix this idea a little more rigorously, if ω_z', is the actual sidereal spin rate, then it can be seen from Fig. 8-23 that the aspect sensor actually measures $\dot{\psi}' = \omega_z' - \dot{\phi}'$. In the nominal operating mode $\omega_z' \gg \dot{\zeta}$ so that $\dot{\psi}' \cong \omega_z'$. However, since for the torque-free mode $\dot{\phi}' > \omega_z'$ whenever $I_3 > I_1$ (see Eq (8.91)), it is apparent that if the sun is ever encircled by the axial projection of the nutational mode, $\dot{\psi}'$ will be negative even though both ω_z' and $\dot{\phi}'$ are positive. Therefore, it is most fortunate that, because of its rather large induced angular accelerations, the nutational mode is readily dissipated by small, passive mechanical devices; in fact, it has been demonstrated through many hours of experience in U.S. space programs (e.g. O.S.O.) that such devices can be both lightweight and mechanically simple.

8.11.4 Nutational Amplitude

Even though existing and space-tested hardware can effectively eliminate the nutational mode, it is still desirable for the sake of completeness to determine how its amplitude will be affected by the known external torques on the spacecraft. In order to do this, we now return to the two cascaded coordinate systems used to derive Eq (8.91). Recall that we had synthesized a combination of steady precession and steady torque-free modes to approximate a real nutation caused by very weak external torques. In order to determine the behavior of θ' under the influence of these torques, we now write Eq (8.86) - (8.88) in the x', y', z' system, and in each substitute Eq (8.91) for ϕ' to get:

$$N_{x'} = I_1 \ddot{\theta}' \qquad (8.98)$$

$$N_{y'} = I_1 \ddot{\phi}' \sin \theta' + \dot{\theta}' I_3 \omega_z' \qquad (8.99)$$

$$N_{z'} = \dot{\omega}_{z'} \qquad (8.100)$$

where it must be kept in mind that the N_x', N_y', and N_z' are the result of time averaging a combination of N_x, N_y, and N_z resolved into the x', y', z' system. For a more mathematical description of this, expand $N_x(\theta)$, $N_y(\theta)$, and $N_z(\theta)$ in a first-order Taylor series about θ_o (assuming that these torques are a function of θ only) so that:

$$N_x(\theta) \approx x_o + x_1(\theta - \theta_o) \qquad (8.101)$$

$$N_y(\theta) \approx y_o + y_1(\theta - \theta_o) \qquad (8.102)$$

$$N_z(\theta) \approx z_o + z_1(\theta - \theta_o) \qquad (8.103)$$

Then if the nutation amplitude is small (a justifiable assumption for a stability analysis) we find that, as a direct consequence of the dynamical geometry and definitions (see Fig. 8-13):

$$\theta(\phi') \cong \theta_o - \theta' \sin \phi' \tag{8.104}$$

and so:

$$N_x(\phi') = x_o - x_1 \theta' \sin \phi' \tag{8.105}$$

$$N_y(\phi') = y_o - y_1 \theta' \sin \phi' \tag{8.106}$$

$$N_z(\phi') = z_o - z_1 \theta' \sin \phi' \tag{8.107}$$

Notice further that the resolved components of N_x, N_y, and N_z onto $N_{x'}$, $N_{y'}$, and $N_{z'}$ are such that:

$$N_{x'} = -\sin\phi' N_x + \cos\phi' N_y \tag{8.108}$$

$$N_{y'} = -\cos\phi' N_x - \sin\phi' N_y \tag{8.109}$$

$$N_{z'} = N_z \tag{8.110}$$

replacing N_x, N_y, and N_z through Eq (8.105) - (8.107):

$$N_{x'}(\phi') = -\sin\phi' (x_o - x_1\theta' \sin\phi') + \cos\phi' (y_o - y_1\theta' \sin\phi') \tag{8.111}$$

$$N_{y'}(\phi') = -\cos\phi' (x_o - x_1\theta' \sin\phi') - \sin\phi' (y_o - y_1\theta' \sin\phi') \tag{8.112}$$

$$N_{z'}(\phi') = z_o - z_1\theta' \sin\phi' \tag{8.113}$$

Averaging these equations over one complete nutation cycle or for $0 < \phi' < 2\pi$:

$$\overline{N}_{x'} = 1/2\ x_1\theta' \tag{8.114}$$

$$\overline{N}_{y'} = 1/2\ y_1\theta' \tag{8.115}$$

$$\overline{N}_{z'} = z_o \tag{8.116}$$

Recalling that $x_1 = \left.\frac{dN_x(\theta)}{d\theta}\right|_{\theta_o}$, $y_1 = \left.\frac{dN_y(\theta)}{d\theta}\right|_{\theta_o}$, $z_o = N_z(\theta_o)$

substitute Eq. (8.114) - (8.116) into Eq. (8.98) - (8.100) to get:

$$1/2\theta' \left.\frac{dN_x(\theta)}{d\theta}\right|_{\theta_o} = I_1\ddot{\theta}' \tag{8.117}$$

$$1/2\theta' \left.\frac{dN_y(\theta)}{d\theta}\right|_{\theta_o} = I_1\ddot{\phi}' \sin\theta' + \dot{\theta}' I_3\omega_z' \tag{8.118}$$

$$N_z(\theta_o) = \dot{\omega}_z' \tag{8.119}$$

If θ' is small then, consistent with the first-order analysis, $\ddot{\theta}'$ can surely be neglected, thus eliminating Eq (8.117). Likewise for a stability analysis, neglect the product, $\ddot{\phi}' \sin\theta'$, compared to $\dot{\theta}'\omega_x'$ and get:

$$1/2\theta' \left.\frac{dN_y(\theta)}{d\theta}\right|_{\theta_o} = I_3\omega_z'\dot{\theta}' \tag{8.120}$$

$$N_z(\theta_o) = \dot{\omega}_z'$$

or, solving Eq (8.120) for θ :

$$\dot{\theta}' = \frac{\theta'}{2I_3\omega_z'} \left.\frac{dN_y(\theta)}{d\theta}\right|_{\theta_o} \tag{8.121}$$

Notice that $\ddot{\theta}'$ has the same sign at a given θ as does $\frac{dN_y(\theta)}{d\theta}$ (if we take ω_z' to be positive).

In order to estimate further the effects that $N_y(\theta)$ will have on an initial θ', recall that $N_y(\theta) \approx k \sin 2\theta$ for $\theta < 60^o$. Solve Eq (8.87) approximately for $\dot{\theta}$, using this value for $N_y(\theta)$, and including Eq (8.125):

$$\dot{\theta} \cong - \frac{k \sin 2\theta}{I_3\omega_z} \tag{8.122}$$

$$\dot{\theta}' = \frac{k \cos 2\theta}{I_3\omega_z'} \theta' \tag{8.123}$$

Dividing Eq (8.123) by Eq (8.122) and integrating:

$$\frac{d\theta'}{d\theta} = -(\cot 2\theta)\cdot\theta' \tag{8.124}$$

$$\frac{\theta'_1}{\theta'_2} = \sqrt{\frac{\sin 2\theta_2}{\sin 2\theta_1}} \tag{8.125}$$

Thus as θ decreases from 60^o to 10^o, θ' will increase by about a factor of 1.6 (this large value may invalidate the first-order analysis). However, this is actually not a serious problem to cope with, especially since this increase would occur over a period of several days, during which time existing mechanical nutation dampers, which have time-constants that are typically less than one hour, would effectively eliminate this mode. The preceding analysis has been at least qualitatively verified by an analog computer, and more exploration is currently being conducted in this particular area. It is hoped that future results can confirm the conclusions of the preceding treatment, as well as provide a more detailed discussion of mechanical dampers.

8.11.5 Reradiative Damping

In addition to the effect of a direct or static torque on a nutation amplitude, there is the damping effect of energy reradiated from the vanes with a lag relative to the input solar intensity. Using a method similar to the method which was originally suggested for Peterson's thesis and which was used to derive Eq (8.66) - (8.75), it is possible to show that the reradiative torques stabilize nutations of the vanes system (derivation is again for small nutational amplitude and high ω).

Starting with Eq. (8.64), linearizing the equation, and assuming that:

$$\theta \approx \theta_o + \theta_1 \sin\Omega t \tag{8.126}$$

$$\psi' \approx \omega_\psi t \tag{8.127}$$

$$\omega_\psi = \omega(1 - I_3/I_1) \tag{8.128}$$

and

$$\Omega \approx \omega I_3/I_1 \tag{8.129}$$

as in Eq (8.91) one is led to the following expression:

$$C_p^* \frac{dT}{dt} + 4\epsilon\sigma T_o^3 (T - T) \approx$$

$$abs \cdot I \cdot [bc\,\theta_o + as\theta_o s\psi' - bs\theta_o \cdot \theta_1 \sin \Omega t$$

$$- a \frac{c\theta_o}{2} \cdot \theta_1 \cos(\Omega t + \psi') + a \frac{c\theta_o}{2} \cdot \theta_1 \cos(\Omega t - \psi')] \qquad (8.130)$$

Expanding T in the appropriate harmonics, one can solve for the term in $\sin(\Omega - \omega_\psi)t$ which directly affects the nutation amplitude:

$$t_9 = \frac{\left[\dfrac{abs \cdot I \cdot ac\theta_o \cdot \theta_1}{8\epsilon\sigma T_o^3}\right]}{\left\{\dfrac{(\Omega - \omega_\psi) C_p^*}{4\epsilon\sigma T_o^3} + \dfrac{4\epsilon\sigma T_o^3}{(\Omega - \omega_\psi) C_p^*}\right\}} \qquad (8.131)$$

giving an effective "nutational" torque, as in Eq (8.121):

$$I_3 \omega \dot{\theta}_1 \approx T_{nut} \qquad (8.132)$$

$$T_{nut} = \frac{\left[\dfrac{abs \cdot I \cdot ac\theta \cdot \theta_1}{4}\right]}{\left\{\dfrac{\Omega - \omega_\psi}{\omega_{opt}} + \dfrac{\omega_{opt}}{\Omega - \omega_\psi}\right\}} \qquad (8.133)$$

where ω_{opt} is given by Eq (8.68) or Eq (8.70). From this equation it appears that this "torque" is on the same order of magnitude as the direct destabilizing "torque" which could be extracted from the similar Eq (8.121), when $\Omega - \omega_\psi \approx \omega_{opt}$. For higher ω in the normal range, say two orders of magnitude above ω_{opt}, the reradiative "torque" becomes much smaller than the direct destabilizing "torque" acting in Eq (8.125). This is another reason why a mechanical damper may be important for the spacecraft.

8.12 Heading and Cone Angle Change (Launch Through Deployment)

8.12.1 Introduction

In order to predict the time necessary to orient the spacecraft utilizing the radiation pressure, knowledge of the initial angle between the spin axis of the spacecraft and the sunline is of great importance, especially if this angle should approach 90°. In this case, the time for orientation increases rapidly.

After burn-out of the last stage of the rocket, the assembly will be in a force-free precessional mode, i.e., the spin axis will precess about the angular momentum vector at an angle θ. Events during injection (separation, despin, etc.) will change the angular momentum in both magnitude and direction (heading). The change in heading is proportional to the cone angle before the event, and will either increase or decrease the angle between the original heading and the sunline, according to where on the precessional cone the event occurs.

It is obvious, if the events occur successively at disadvantageous locations on large precession cones, that the angle between heading and sunline can increase to an undesirable (if not unacceptable) value.

Thus, to avoid large heading changes with each event, it is paramount to reduce the cone angle preceding that event.

8.12.2 Analysis

The launch sequence during which the heading may change is as follows (Fig. 8-24): After the successive burn-out of all five stages, it has been recommended that the assembly of the fifth stage and Sunblazer coast for five minutes, during which residual thrust is allowed to tail off. Separation of the payload, occuring next, will initiate the yo-yo despin. In separating from the spacecraft, after completed despin, the yo-yos will trigger the deployment of sails and antennas. A damper will then act to decrease the cone angle to zero.

The contribution of each event to the final heading change will now be analyzed separately.

1. Rocket Performance

Due to misalignment of the separation mechanism, unbalanced mass, etc, the cone angle after fourth-stage burn-out is expected to be 1.5° (3σ value)[13]. This has been substantiated by measurements during previous flights. No measurements exist for the new fifth stage. Separation of the fifth stage from the fourth will not appreciably change the cone angle. However, it is expected

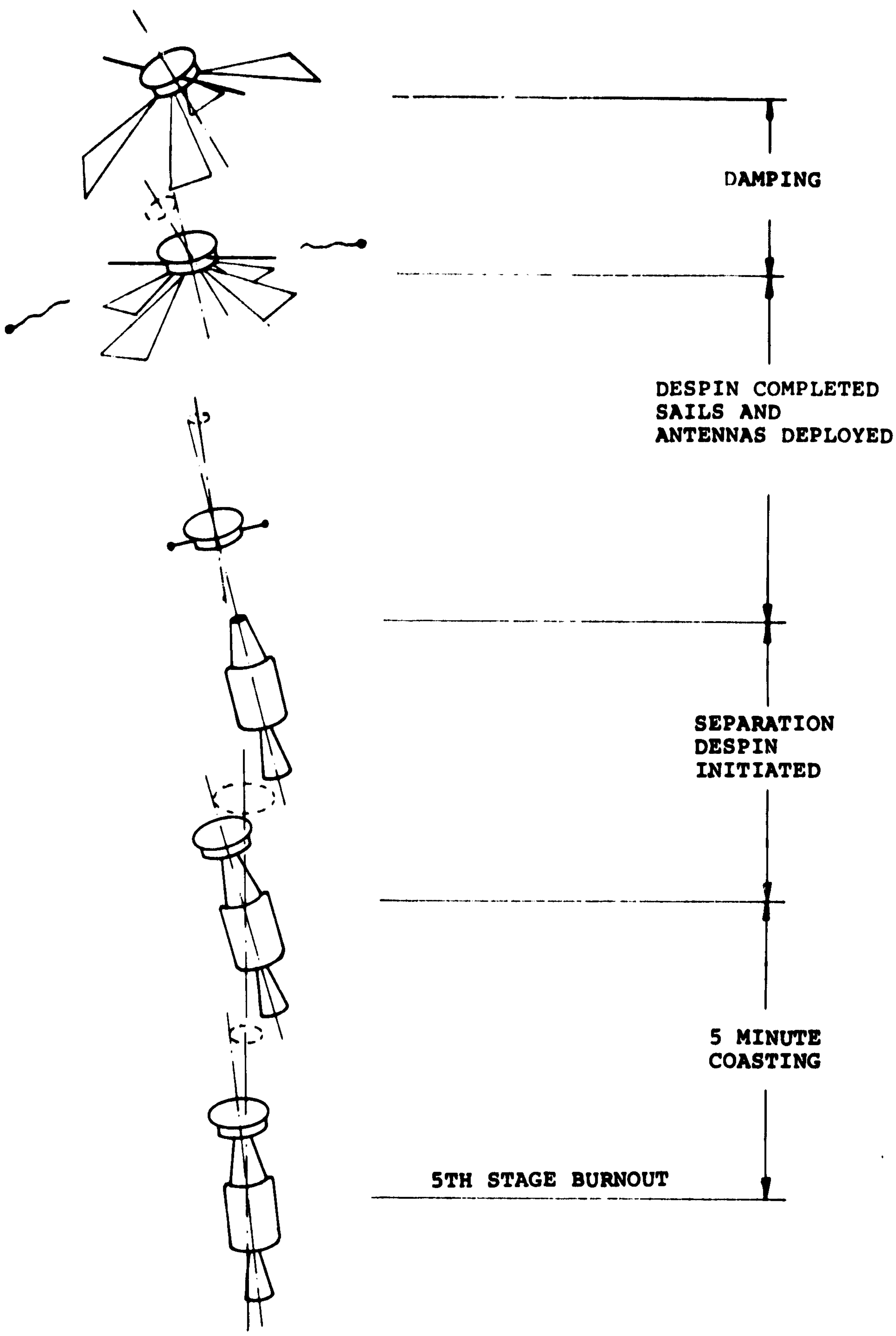

Fig. 8-24 Sunblazer deployment.

that thrust misalignment in the fifth stage will increase the angle by 4.5° for a spin rate of 180 r/min [13]. It is not obvious from the cited reference whether the above 4.5° is a 1σ or 3σ value, such that two 3σ values should be considered for the cone angle at fifth-stage burn-out:

$$\begin{aligned} &\text{a.} \quad \theta = 1.5^{\circ} + 4.5^{\circ} = 6^{\circ} \\ &\text{b.} \quad \theta = 3 \times (0.5 + 4.5) = 15^{\circ} . \end{aligned} \tag{8.134}$$

2. Coasting Period

If a body is in a force-free precessional mode and dissipates energy it will change to a configuration of least kinetic energy. The kinetic energy T can be expressed in terms of the cone angle θ, or θ as a function of T, as follows (for an axisymmetric body)[14]:

$$\sin^2\theta = \frac{I_1}{(I_3 - I_1)\, L^2}(2I_3T - L^2) \tag{8.135}$$

where I_1 = moment of inertia about transverse axis

I_3 = moment of inertia about spin axis

L = angular momentum .

If the energy loss is so small that the rigid body motion is not affected, the rate of change in θ with T is obtained by differentiating Eq (8.135) with respect to time:

$$2\sin\theta\cos\theta\ \dot{\theta} = \frac{2I_1I_3}{(I_3 - I_1)}\ \frac{\dot{T}}{L^2} \tag{8.136}$$

or, for small θ:

$$\theta\ \dot{\theta} = \frac{I_1I_3}{(I_3 - I_1)}\ \frac{\dot{T}}{L^2} . \tag{8.137}$$

Since $\dot{T}$ is negative, θ will increase if $I_1 > I_3$, which is the case for the assembly of the fifth stage and payload.

The dissipation of energy is due to the damped motion of the structural particles relative to each other. The motion can be represented by the equation for forced vibration with damping:

$$m\ddot{x} + \frac{Kg}{\omega}\dot{x} + kx = F_o \cos\omega t \tag{8.138}$$

where m = mass

k = spring constant

g = structural damping coefficient

$\left[\frac{Kg}{\omega}\right.$ is called the equivalent viscous damping coefficient for structural damping$\left.\right]$

ω = frequency of forcing function

F_o = amplitude of forcing function .

Solving Eq (8.138) gives:

$$x = \frac{F_o}{k} n \cos(\omega t - \eta)$$

where $\eta = \eta(\omega)$

$n = n(\omega) \cong$ constant for ω range considered.

The energy dissipated by the damping force is:

$$E = \int_{\text{cycle}} \frac{Kg}{\omega} \dot{x} \, dx = \pi Kg \left(\frac{F_o}{k} n\right)^2$$

or per unit time

$$\dot{T} = \frac{1}{2} Kg\omega \left(\frac{F_o}{k} n\right)^2 \quad . \tag{8.139}$$

The forcing function in this case is the inertial force (mass × acceleration) acting on each point of the structure. The acceleration can be expressed as:

$$\ddot{x} = \omega_z^2 \left| \left(\frac{I_3}{I_1}\right)^2 z\tan\theta \sin\left[\omega_z \left(1-\frac{I_3}{I_1}\right)t\right] + \left(\frac{I_3}{I_1}\right)^2 \tan^2\theta \cos^2\left[\omega_z \left(1-\frac{I_3}{I_1}\right)t\right] - x \right| . \tag{8.140}$$

This is for a point with coordinates (x, o, z), z being along the spin axis. The angular velocity about the spin axis is ω_z.

For small θ, neglecting higher orders of θ, and considering only the oscillatory part:

$$\ddot{x} \sim \omega_z^2 \theta z \left(\frac{I_3}{I_1}\right)^2 \sin\left[\omega_z \left(1-\frac{I_3}{I_1}\right)t\right] \quad . \tag{8.141}$$

The most important feature in Eq (8.141) is the relation:

$$\ddot{x} = \ddot{x}(\theta)$$

consequently

$$F_o \sim F_o(\theta)$$

and using Eq (8.139)

$$\dot{T} \sim \dot{T}(\theta^2) \quad .$$

Upon substitution of Eq (8.139) into Eq (8.137) and introduction of τ, the equation for θ will be

$$\theta \, \dot{\theta} = \frac{\theta^2}{\tau} \quad .$$

Integrating gives

$$\theta = \theta_o e^{t/\tau} \quad . \tag{8.142}$$

Thus, the cone angle increases exponentially with the dimensionless time t/τ. τ has the following expression:

$$\tau = \frac{2KL^2}{I_3 g \omega_z^5 \left(\frac{I_3}{I_1}\right)^4 n^2 f^2(m, l)} \tag{8.143}$$

$f(m, l)$ is a function of mass and size. To evaluate τ analytically would be impossible; however, Eq (8.143) can be used to scale τ from one configuration to another.

This was done[14] for Sunblazer, using information transmitted by LRC. However, this information was so sparse that the deduced τ values for Sunblazer must still be regarded as guesses. This does not mean that nothing was gained by performing the analysis. It is felt that a range of likely τ values was established. The corresponding θ values after five minutes coasting are shown in Fig. 8-25.

$$\left(\frac{\theta}{\theta_o}\right)_I = 2.7$$

$$\left(\frac{\theta}{\theta_o}\right)_{II} = 1.055 \tag{8.144}$$

3. Sunblazer Separation from Fifth Stage

In separating Sunblazer from the rocket, the springs will ideally impart a linear momentum to the vehicle, leaving the angular velocities about the spin axis and the transverse axis, ω_z and ω_t respectively, unchanged. From geometric considerations:

$$\tan\theta = \frac{I_1 \omega_t}{I_3 \omega_z} \tag{8.145}$$

Applying Eq (8.145) to the configuration, before separation and after, with ω_z and ω_t constant, gives

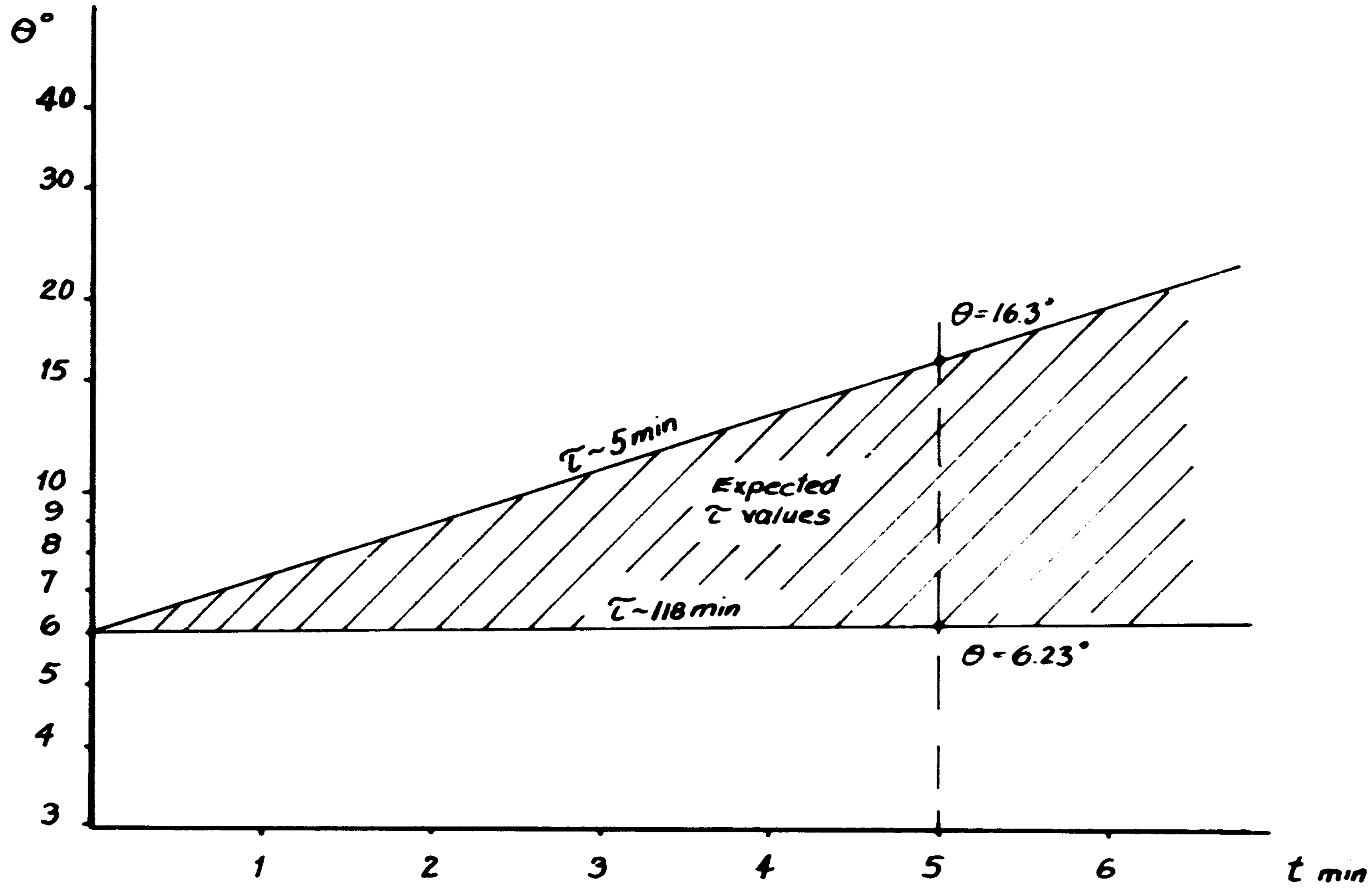

Fig. 8-25 Angular deviation during coasting period.

$$\tan \theta_1 = \frac{\left(\frac{I_1}{I_3}\right)_1}{\left(\frac{I_1}{I_3}\right)_o} \tan \theta_o \qquad (8.146)$$

where $\left(\frac{I_1}{I_3}\right)_o$ is the moment ratio for the combined Sunblazer and rocket configuration, and $\left(\frac{I_1}{I_3}\right)_1$ for Sunblazer alone.

$$\left(\frac{I_1}{I_3}\right)_o = 10.8$$

$$\left(\frac{I_1}{I_3}\right)_1 = 0.635$$

Thus for small θ

$$\theta_1 = \frac{1}{17} \theta_o \qquad (8.147)$$

As mentioned above, this would be true for the ideal release. However, design tolerances in mass unbalance, plunger cant angle, etc., will introduce torque impulses into the system, thus changing the angular velocities. These were shown to be negligible[13]. Another deviation from the ideal separation is introduced by a spring force unbalance.

In order to analyze this this effect, consider a symmetric disc spinning steadily about its figure axis at a rate, ω, which has an impulse delivered to it of magnitude J, directed parallel to the figure axis. If the disc has a mass m, and undergoes a velocity change, Δu, then the magnitude of the impulse must have been $m\Delta u$. However, suppose this impulse acted on the disc at a distance r from the axis of symmetry. Then if the disc has a moment of inertia I, the original angular momentum was $I\omega$ directed along the figure axis. Meanwhile, the impulse has instantaneously introduced angular momentum perpendicular to this axis of magnitude $Jr = m\Delta ur$. Therefore, the angle between the original and final angular momentum vectors, θ, is given by

$$\tan \theta = \frac{mr\Delta u}{I\omega} \qquad (8.148)$$

If the spacecraft is not coning initially, then this angle θ will represent the heading error as well as the coning angle. In the more general case when the vehicle is already coning at separation, θ represents the maximum change in the existing coning angle. In this connection, r is to be computed by finding the location of the center of force of the springs relative to the vehicle's axis of symmetry. Suppose m = 10,000 gm, Δv = 100 cm/s, r = ' cm, I = 3×10^6 gm-cm^2 and ω = 20 rad/s, then from Eq (8.148):

$$\tan\theta = \frac{1}{60}, \text{ or } \theta \sim 1^\circ \quad . \tag{8.149}$$

Since the displacement of the force center is of the order of 1 mm the contribution due to the above effect is negligible, and Eq (8.147) is assumed to be valid.

During this instantaneous change of cone angle the spacecraft remains fixed in space, thus the angular momentum (i.e., heading) must have changed by an amount

$$\theta_o - \theta_1 \quad . \tag{8.150}$$

4. Yo-Yo Despin

An extensive yo-yo despin analysis is given in ref 15. However, no mention is made of the heading change. An indication of the maximum heading change for certain despin parameters is given by idealizing the despin process. Consider an instantaneous despin, Fig. 8-26a, where only the angular velocity, ω_z, about the spin axis is decreased. The angular velocity ω_t is assumed to remain constant. Thus, the angular momentum vector $\vec{L}_o$ before despin is decreased by an amount $\Delta\vec{L}$, which is parallel to the spacecraft-spin axis, resulting in $\vec{L}_1$. After the despin process the spin axis then precesses about $\vec{L}_1$. The cone angle is increased to θ_1, where:

$$\tan\theta_1 = \frac{I_1\omega_t}{I_3\omega_{z1}} \tag{8.151}$$

or in terms of the cone angle θ_o before despin:

$$\tan\theta_1 = \frac{\omega_{zo}}{\omega_{z1}}\tan\theta_o \quad .$$

With appropriate values for Sunblazer (ω_{zo} = 200r/min, ω_{z1} = 33r/min) this leads to

$$\tan\theta_1 = 6.06\tan\theta_o \quad . \tag{8.152}$$

From Fig. 8-26 it is seen that the heading has changed from the original (before despin) by an amount

$$\theta_1 - \theta_o \tag{8.153}$$

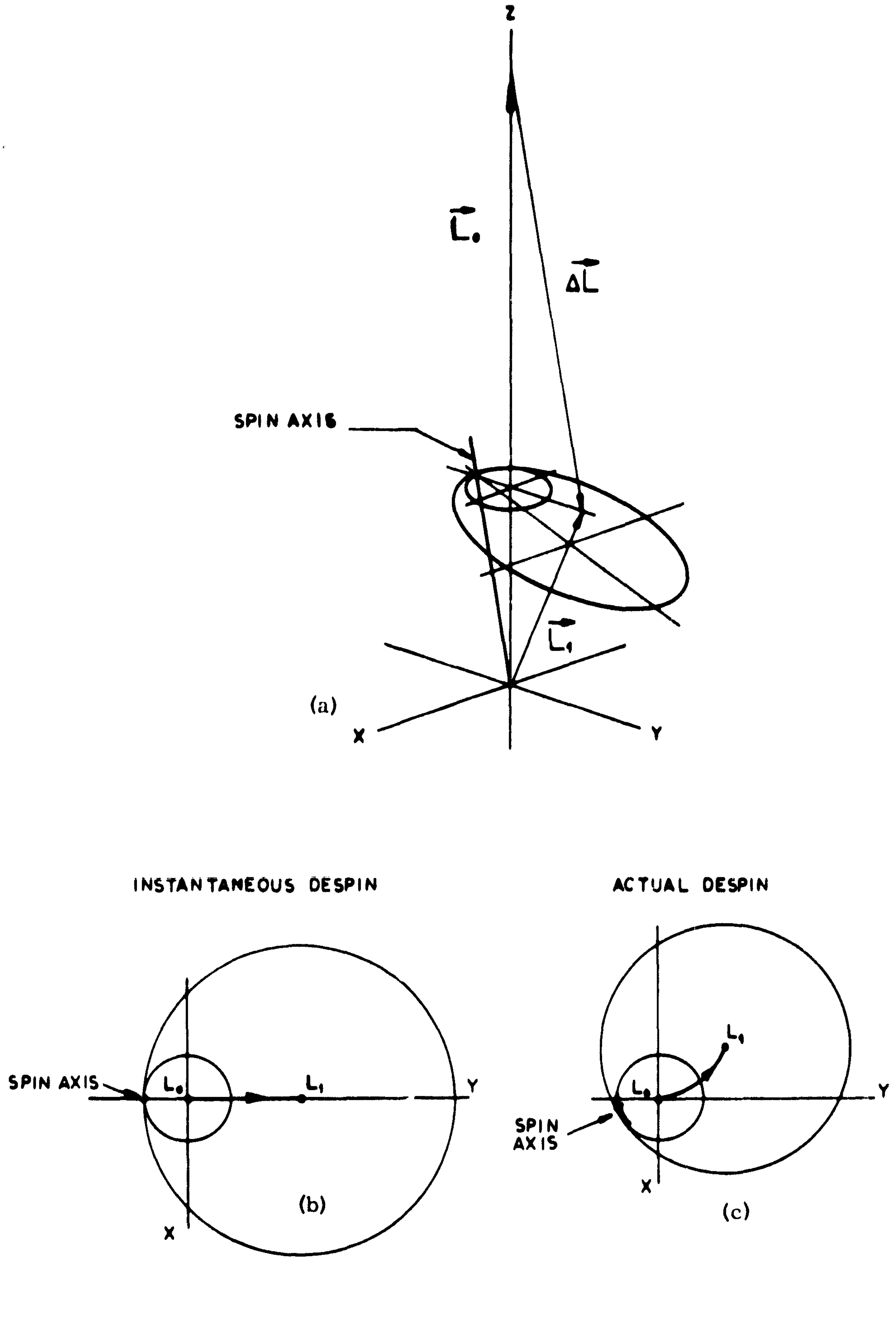

Fig. 8-26 Angular variations during despin.

in the plane formed by $\vec{L}_o$ and the instantaneous position of the spin axis at despin. Figure 8-26b is a top view of Fig. 8-26a showing the angular momentum shift.

However, the actual despin process is not instantaneous since the precession rate is of the order of 20 rad/s prior to despin, and the despin takes place in about one second. Thus, instead of tracing a straight line on a plane parallel to the x-y plane as in Fig. 8-26b $\vec{L}$ will be displaced along a curved line in that plane (Fig. 8-26c). Since Sunblazer's spin axis will precess about $\vec{L}$ fastest in the beginning of the despin process and slower towards the [illegible] when the spin is greatly reduced, the line from L_o to L_1 will have a small radius of curvature in the beginning and approach a straight line close to L_1. Clearly, the length of the line between L_o and L_1 is a measure of the angular momentum reduction; therefore, if this is the same amount for both cases (instantaneous and actual) the distance between L_o and L_1 is less in the actual case, i.e., smaller coning angle and heading change. If, in addition, the transverse angular velocity ω_t is reduced, this will reduce the cone angle and heading change even more.

Thus, the instantaneous analysis will give the maximum heading change and cone angle for a particular despin process. It will be used as an approximation to the actual process, bearing in mind that the increases in cone angle and heading are larger than the real changes.

Curves for θ in ref 15 show values less than the idealized values and also indicate that ω_t is reduced, confirming the above.

5. Deployment of Sails and Antennas

The primary effect of the deployment on the dynamics of motion is a reduction in spin. This is due to the increased moment of inertia about that axis. Since the angular momentum is constant during this process

$$(I_z \omega_z)_o = (I_z \omega_z)_1 \quad . \tag{8.154}$$

With $I_{zo} = 2.8\times10^6$ gm-cm^2, $I_{z1} = 4.6\times10^6$ gm-cm^2 and $\omega_{zo} = 33$ r/min, Eq (8.154) gives

$$\omega_{z1} = 20 \text{ r/min} \quad .$$

In the ideal deployment the cone angle and heading will not change (angular momenta constant). In case the sails do not deploy at the same time, the following can happen:

Consider Fig. 8-27a. The case of one sail deploying at a time is investigated. The rolled-up sail (m_2) is idealized as a mass, and the potential energy E is assumed to be stored in the bent rod connecting it to the vehicle (m_1). When the sail is released, part of that energy will be converted, through the action of the bending moment M, into rotational energy of the vehicle, and similarly for the sail. However, since no net torque is applied to the combined body, the angular momentum about the combined C. M. has to be constant. (For convenience, it is taken to be zero.) If both bodies are acted upon only by moments, the angular momentum of each is due to rotation about their own C. M.

Thus,

$$I_1\omega_1 + I_2\omega_2 = 0 \tag{8.155}$$

$$E = \frac{1}{2}I_1\omega_1^2 + \frac{1}{2}I_2\omega_2^2 \; . \tag{8.156}$$

Eq (8. 155) and (8. 156) give solutions for ω_1 and ω_2

$$\omega_1 = \sqrt{\frac{2E}{I_1\left(1 + \frac{I_2}{I_1}\right)}}$$

$$\omega_2 = \sqrt{\frac{2E}{I_2\left(1 + \frac{I_2}{I_1}\right)}} \; . \tag{8.157}$$

The angular momentum given to the vehicle (or sail) is

$$I_1\omega_1 = \sqrt{\frac{2EI_1}{\left(1 + \frac{I_1}{I_2}\right)}} \sim \sqrt{2EI_2} = I_2\omega_2 \tag{8.158}$$

since $I_1 = 0(10^6)$ and $I_2 = 0(10^2)$. For a spinning vehicle this would result in a cone angle θ

$$\tan\theta = \frac{I_1\omega_1}{I_z\omega_z} \tag{8.159}$$

which for Sunblazer gives $\theta \sim 1^{\circ}$. However, since the sail will remain attached to the vehicle, they both cannot keep rotating indefinitely. Due to the opposite rotations of sail and vehicle, the sail will bend the other way after being stretched out, and accumulate potential energy until the motion is stopped. Thus, an oscillatory motion will result which in time will be

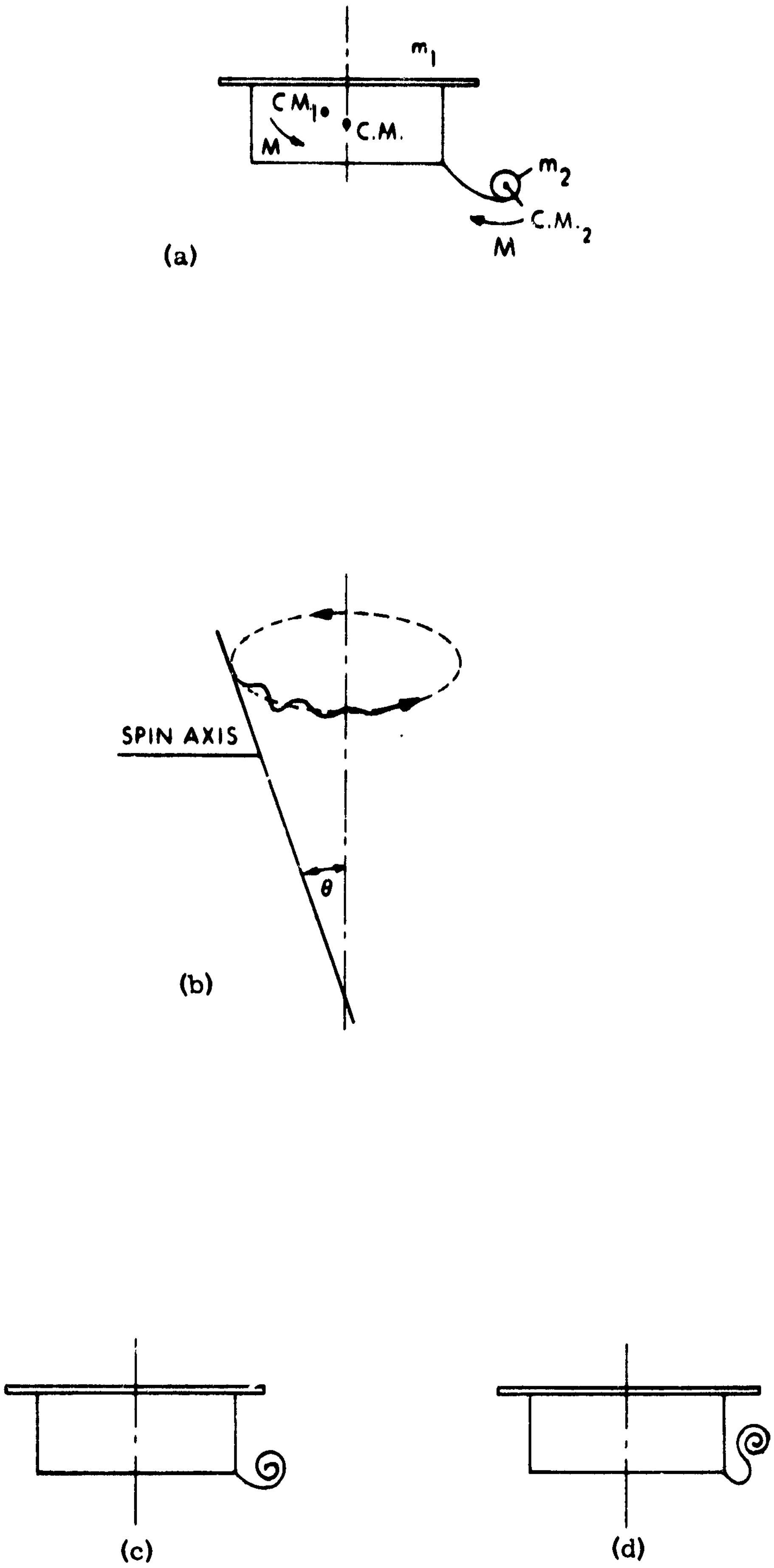

Fig. 8-27 Effects of sail deployment on spacecraft dynamics.

damped out by internal friction. This induced motion should not affect the force-free precession at some cone angle (angular moments have not changed), but can be regarded as a nutation (Fig. 8-27b).

The above analysis is true if energy is stored by rolling the sails as in Fig. 8-27c. This way, the potential energy has the same sign and the resulting moment the same direction. If the sail is rolled as in Fig. 8-27d, the spring constant can be adjusted so that each bend contains the same energy in magnitude, but with reversed signs. The total stored energy is zero and no motion can result after deployment.

8.12.3 Results

The analysis gave the quantitative effect of each step in the launch sequence. Depending on the position in which, relative to a fixed coordinate system in space, these steps happen, different headings can result. The best and worst positions are shown graphically in Fig. 8-28. Although both the worst and best cases are shown for the positions at which these steps occur only the worst case expected for each event is shown; i.e., the smallest τ value (Fig. 8-25) was applied to Eq (8.134) (3σ values) resulting in cone angles after coasting of 16° and 32° respectively. In despinning the vehicle, the ideal conditions are shown (Eq (8.152)) rather than the lesser cone angle for the actual despin.

This way, the heading can make an angle with the sunline of 100° and 80° in the worst case (position-wise) (corresponding to 15° and 6° in Eq (8.134), respectively) and 20° and 40° in the best case.

The most optimistic result would be to take 1σ values after rocket performance, i.e., 2° instead of 6° in Eq (8.134). Then assume the largest τ expected, which gives a cone angle of 3.16° after coasting. The effect of separation is fixed, i.e., reduction of cone angle by a factor of 17, giving a cone angle before despin of 0.186°. Without numerically solving the problem, only an estimate can be made for the angle increase due to despin. If it is estimated that this increase will be a factor of 3, the final heading in the best and worst positions will be 56.6° and 63.4°, respectively.

8.12.4 Discussion

As stated in the introduction, the concern is about the largest possible angle between heading and sunline. The results show that this angle can be expected to lie between 63.4° and 100° -- a wide range. From Fig. 8-28 it is seen that the largest contribution is due to the cone angle after coasting; subsequent events only increase the heading error by minor amounts (i.e., from 76° after

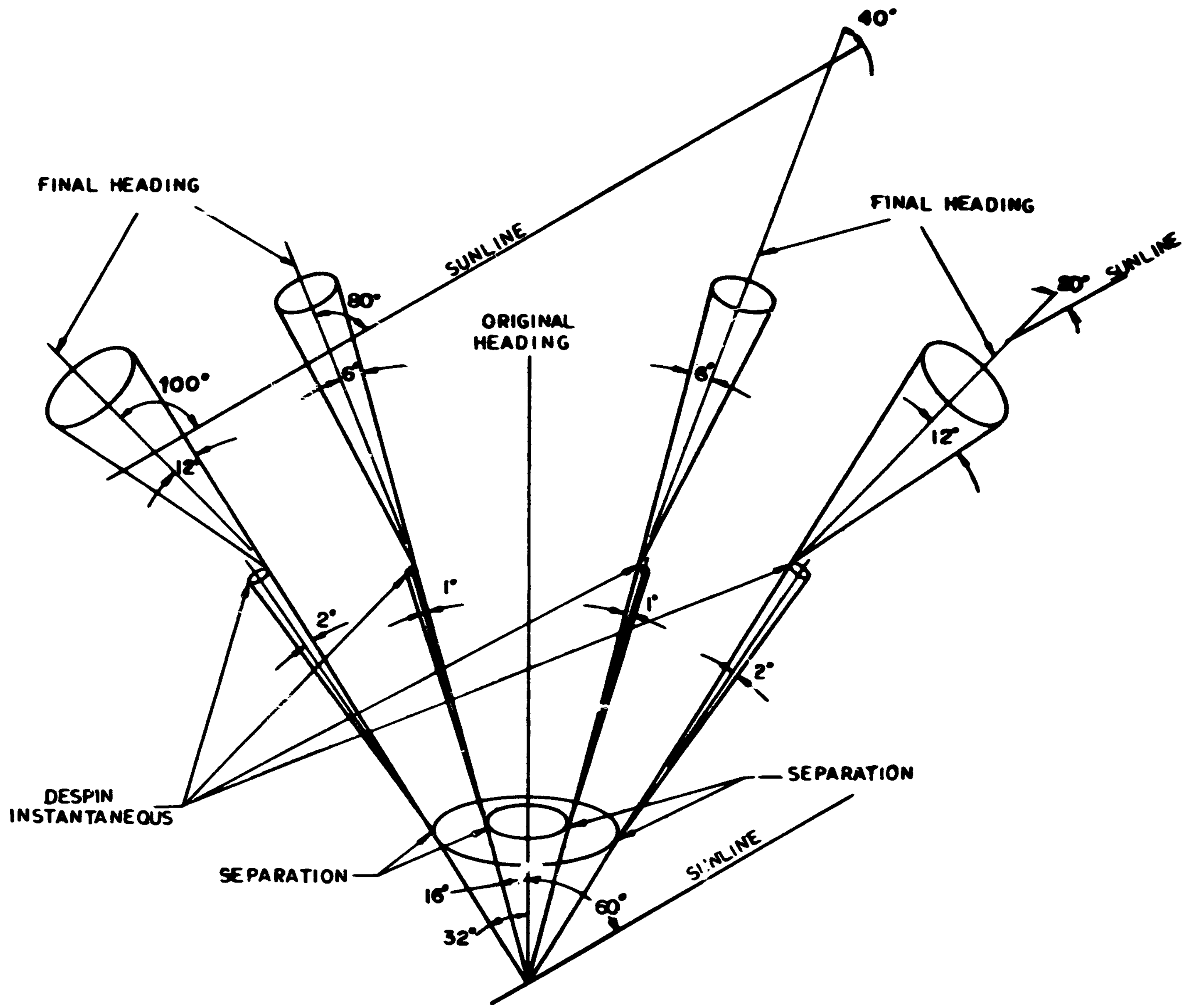

Fig. 8-28 Resulting headings from separation, despin and deployment.

coasting to 80° after deployment; or 92° to 100°). Of course, the cone angle after coasting is dependent on the angle after rocket performance.

Unfortunately, the information received from LRC on both these events is not adequate to predict a narrow range of cones angles after coasting. However, it is felt that a 15° cone angle after rocket performance is quite unlikely; this would eliminate the 32° cone in Fig. 8-28 and the final heading angle of 100°, and leave the range of heading between 63.4° and 80°.

If it is felt that this range is too close to the 90° mark, and unless future information about rocket performance and coasting effects reduce the maximum expected angle, there are two ways of avoiding the large heading angles:

1. Reduce the coasting period to a minimum.
2. Or, constantly monitor the attitude of Sunblazer relative to the sunline, so that the events can be initiated at favorable positions on the precession cones. In this case, large cone angles are desirable.

However, before these steps are employed, the heading change due to the present sequence has to be established more firmly.

CHAPTER 9

9.0 THERMAL BALANCE

9.1 Discussion

This discussion of the thermal balance for the Sunblazer spacecraft system is divided into three sections. The first section describes the overall system requirements, the second relates the problems that must be solved in order to satisfy these requirements, while the third section describes the general solutions to these problems.

The Sunblazer spacecraft is to have a retrograde launch into a heliocentric solar orbit. Consequently, the spacecraft will experience a time-varying solar flux which is, on the average, equal to about 1.5 equivalent suns. It varies in magnitude from about 0.96 suns (July launch) to about 2.44 suns. This relatively large average solar flux, coupled with the long duration of the flight, complicates the spacecraft thermal design in that the thermal-control surfaces must be stable for an extended period (1.5 to 3 years) in a harsh solar environment (1.5 suns). Early in the program it was recognized that, to obtain spacecraft surfaces whose parameters would remain relatively stable for 4.5 equivalent sun years (1.5 suns times 3 years), was a significant problem. Indeed, when this problem was first studied in 1964, these requirements were considered to be beyond the state of the art. This is probably not true in 1968; there have been significant advances regarding surface materials in the past four years. Nevertheless, surface stability was/is a formidable problem which has heavily influenced many of the spacecraft design concepts such as solar orientation, disc-cylinder (platform-radiator) construction, wide temperature range electric design, etc.

9.2 Requirements of Spacecraft Thermal Design

General requirements of the spacecraft thermal design can be described as follows. The spacecraft electro-mechanical configuration and thermal design must be such that the utilization of currently-existing chemical and mechanical space components and technologies will result in a thermal system that yields spacecraft operational-temperature extremes and gradients compatible with engineering concepts to satisfy the experimental physics goals. This general statement can in turn be translated into the following spacecraft system constants which are listed in Table 9-I. A few comments are important in order to interpret meaningfully the data of that table.

1. The results of Table 9-I were derived from "gross or first-order" calculations, and are to be considered accurate to ±5%. Considerably more accurate calculations are possible because the Sunblazer vehicle is a small (low thermal impedance) symmetrical vehicle without complicated error inducing shapes and booms.

2. Detailed thermal calculations are not deemed important (particularly at this time) as all of the expected operating temperatures are considerably within allowable operating limits of the various electrical, mechanical, and electro-mechanical components, subsystems and systems.

3. The center of the temperature (hence, the limits) range for each individual electronic item, with the possible exception of the solar-cell panels, can be scaled up or down if need be, by adjusting the size and/or the surface coating ($\frac{\alpha}{\epsilon}$ ratio) of the radiating areas.

4. The solar-cell panel will be set to operate at a minimum temperature in order to maximize energy-conversion efficiency.

5. Inasmuch as the present spacecraft is not intended to carry onboard any sensitive (hence, usually highly temperature-dependent) scientific instruments, the actual spacecraft operating temperatures are not critical. The general desire, therefore, is to operate at a low temperature in order to maximize available power and extend component life. It is especially important to start at as low an operating temperature as feasible, in that degradation of the thermal-control surface will ultimately bias the thermal balance constants toward higher values.

9.3 Problems

There are two fundamental problems associated with Sunblazer thermal balance. The first is a large variation in solar flux, which accounts for the rather large temperature ranges shown in Table 9-I. Second is the long operating life required of the spacecraft. This second requirement is a

Table 9-I

Sunblazer spacecraft thermal constants.

ITEM	DESIGN GOALS				OPERATING LIMITS
	Temp 1 AU	Range 0.6 AU	Thermal 1 AU	Gradients 0.6 AU	
Solar Cells	$7^\circ C$	$85^\circ C$	$1^\circ C$ -	$3^\circ C$	$-50^\circ C$ - $100^\circ C$
Front Plate (Platform) (center)	$5^\circ C$	$82^\circ C$	NONE		-
Front Plate (Platform) (rim)	$3^\circ C$	$80^\circ C$	NONE		-
Front Half Cylinder (Radiator)	$-5^\circ C$	$+55^\circ C$	$8^\circ C$ -	$16^\circ C$	-
Rear Half Cylinder (Radiator)	$-13^\circ C$	$+39^\circ C$			-
Gussets	$-3^\circ C$	$+54^\circ C$	NONE		-
Center Tube (Hub) Batteries	0	$5^\circ C$	$1^\circ C$ -	$2^\circ C$	$-20^\circ C$ to $40^\circ C$
Electronics	0	$5^\circ C$	$10^\circ C$ -	$2^\circ C$	$-50^\circ C$ - $80^\circ C$
Electronic Components Transmitter	0	$10^\circ C$	$3^\circ C$	$5^\circ C$	$-50^\circ C$ - $80^\circ C$
P & T	0	$5^\circ C$	$1^\circ C$	$2^\circ C$	$-50^\circ C$ - $80^\circ C$
Low Level RF	0	$5^\circ C$	$1^\circ C$	$2^\circ C$	$-30^\circ C$ to $80^\circ C$
Converters	0	$10^\circ C$	$2^\circ C$ -	$3^\circ C$	$-50^\circ C$ to $+80^\circ C$
Electronic Radiators (average of all four)	$-15^\circ C$	$0^\circ C$	$1^\circ C$	$3^\circ C$	-
Storage Capacitors	$-5^\circ C$	$0^\circ C$	NONE		$-40^\circ C$ to $85^\circ C$
Sails	$-20^\circ C$	$+50^\circ C$	NONE		-
Aspect Sensor	$-0^\circ C$	$+30^\circ C$	NONE		
Motors					
Antennas	$-10^\circ C$	$+60^\circ C$	$0^\circ C$ -	$12^\circ C$	-

*Program and Telemetery (Low power digital and analog circuits) problem because the relatively high average of solar flux (about 12, 700 equivalent sun hours per year) generally affects the thermal-control surfaces so as to reduce their effectiveness, i.e., long-term drift of $\frac{\alpha}{\epsilon}$ (the absorptivity, α, increases, and the emittance, ϵ, decreases with time).[1, 2, 3, 4]

The Sunblazer design concept minimizes these long-term effects because the spacecraft is oriented toward the sun. This consequently allows the use of high-performance (low absorptivity), highly-stable (low drift) second-surface mirrors on the sunlit portion; while on the shaded (dark) side of the spacecraft the surface which is made highly emissive and is unaffected by the sun's ultraviolet, since it is in perpetual darkness. Unfortunately, the surface properties of the solar cell areas, which necessarily represent a large fraction of the sunlit side, will degrade in time (principally through ultraviolet darking of the cover shields). However, the design attempts to minimize this degradation by utilizing annealed sapphire covers instead of quartz.[5, 6]

A third problem affecting thermal balance concerns control of thermal gradients by adjusting the various thermal impedances. The conceptual design calls for minimizing the thermal impedances between the solar cells and the platform, as well as between the platform and the radiator. Additionally, the design should maximize the thermal impedance (minimize thermal leakage) between the platform-radiator assembly and the electronic compartments. Low-impedance joints are to be constructed by brazing the platform-radiator assembly. The high-impedance joints (shields) can be constructed by inserting several layers of highly-reflective material between the electronics and compartment walls.[7, 8]

9.4 Solutions

The Sunblazer thermal balance concepts, along with the solutions to the system problems, are described by the following analyses.

9.4.1 Thermal Analysis

Referring to Fig. 9-1 and 9-2, Eq (1) represents the thermal balance condition. From Eq (1) the temperature may be expressed in terms of the solar input, as shown in Eq (2). The results of Eq (2) are plotted in the upper right-hand corner of Fig. 9-2, and we conclude that if the Sunblazer spacecraft were an isothermal body in thermal equilibrium, the temperature range of the spacecraft for 1 AU and 0.635 AU would be 7° C to 77° C.

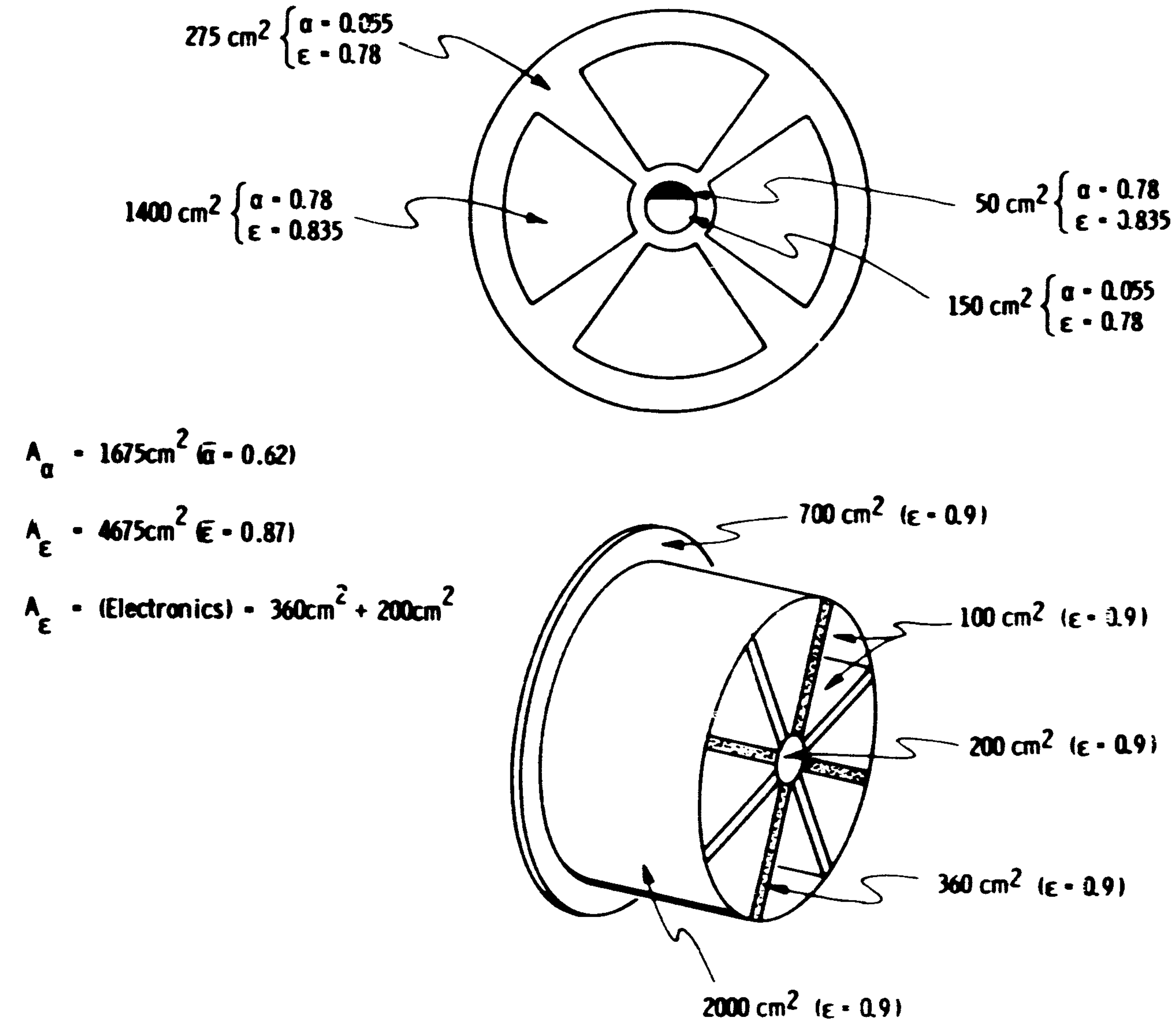

Fig. 9-1 Sunblazer surface properties.

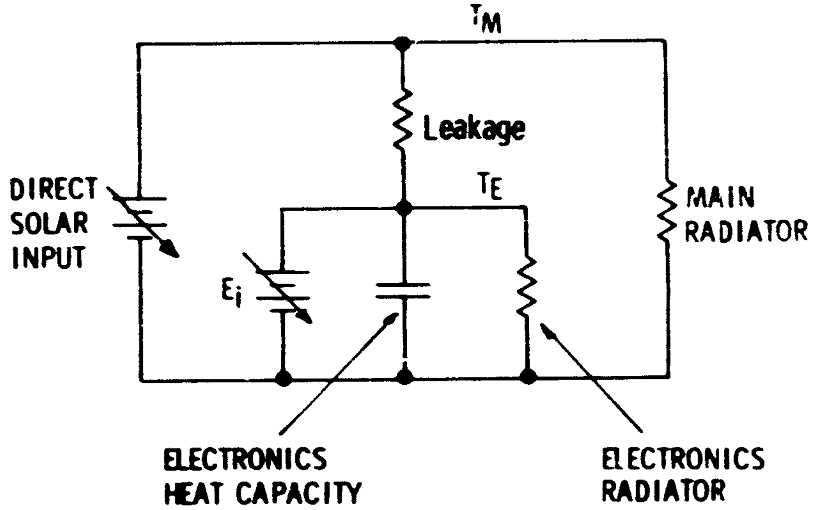

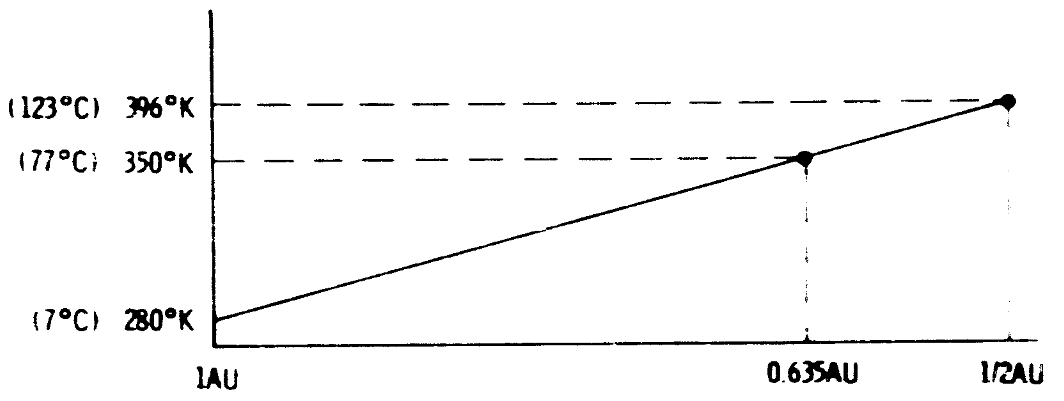

$\sqrt[4]{1} = 1$ $\qquad$ $\sqrt[4]{2.5} = 1.25$ $\qquad$ $\sqrt[4]{4} = 1.416$

$E_I \equiv$ Internal Power Dissipation

$$\varepsilon A_\varepsilon \sigma T^4 = \alpha A_\alpha S \qquad (1)$$

Therefore

$$T = \sqrt[4]{\frac{S}{\sigma}\frac{A_\alpha}{A_\varepsilon}\frac{\alpha}{\varepsilon}} = \sqrt[4]{\frac{S_0}{\sigma}\cdot\frac{S}{S_0}\frac{A_\alpha}{A_\varepsilon}\cdot\frac{\alpha}{\varepsilon}} \qquad (2)$$

Or

$$T = \sqrt[4]{\frac{S_0}{\sigma}}\sqrt[4]{\frac{S}{S_0}\frac{A_\alpha}{A_\varepsilon}\cdot\frac{\alpha}{\varepsilon}} = 395°K\left(\frac{A_\alpha}{A_\varepsilon}\right)^{1/4}\left(\frac{S}{S_0}\right)^{1/4}\left(\frac{\alpha}{\varepsilon}\right)^{1/4}$$

$$= 395°K(0.358)^{1/4}\left(\frac{S}{S_0}\right)^{1/4}\left(\frac{0.62}{0.87}\right)^{1/4}$$

$$= 395°K(0.775)\sqrt[4]{\frac{S}{S_0}}(0.915) = 280°K\sqrt[4]{\frac{S}{S_0}} \qquad (3)$$

Fig. 9-2 Sunblazer equivalent thermal circuit.

A simplified calculation for the electronic compartment temperature is shown in Fig. 9-3. The values used for the solar-cell power, RF power output, and radiator surface areas are representative of the actual spacecraft, and we calculate that the variation in the ambient temperature for the electronics, neglecting leakage from the compartment walls, is from $-10^{\circ}C$ to $+38^{\circ}C$.

Figure 9-4 shows[9] that the thermal leakage (worst case that is evaluated at the maximum temperature) is about 1/2 W per compartment, this when compared to the 21 W of internal dissipation, is essentially negligible.

9.4.2 Sail Temperature

The values used for the computation of the sail equilibrium temperature shown in Fig. 9-5 are indicative of the actual sail configuration constructed with aluminum-coated mylar. The computation neglects leakage from the spacecraft, which conceptually may be made equal to zero (the sails operate at the same temperature as the spacecraft radiator) or larger if the sails are utilized as additional radiation surfaces. (This technique could be used to reduce the spacecraft temperature.)

Although the variation in sail temperature for a 0.635 orbit is $70^{\circ}C$, a salient feature regarding this parameter is the design ability to set this temperature to cover almost any desired range by varying the $\frac{\alpha}{\epsilon}$ ratio of the front and back surfaces of the sail. The range from $-30^{\circ}C$ to $+40^{\circ}C$ seems to be a reasonable choice when utilizing aluminum-coated mylar.

9.4.3 Materials

9.4.3.1 Surfaces

The sunlit surface of the spacecraft is entirely covered (99%) with 1400 cm^2 of solar cells and 425 cm^2 of second-surface mirrors (silver-fused silica). Although second-surface mirrors are extremely resistant to ultraviolet and other radiation damage[10], the solar cell covers are subjected to "ultraviolet darkening" (browning) from prolonged exposure to space environment.

Annealed sapphire is more resistant to radiation damage than are fused quartz, synthetic fused silica, or the non-browning lead glasses, therefore will yield superior performance in the Sunblazer orbit. The threshold-integrated flux for low-energy proton damage in fused-silica material is apparently between 5×10^{16} and 1×10^{17} protons/cm^2. A total integrated dosage of 1.3×10^{17} 10-keV-protons/cm^2 at $298^{\circ}K$ results in a measurable increase in absorptivity. The above numbers indicate that radiation damage due to the solar wind is probably not a problem. However, little useful data

Solar Cells Output (19 ~ 33) watts

Dissipation = (19 ~ 33) w - (6 ~ 12) w (Rf) = (13 ~ 21) w

Radiator Surface 360 cm^2

$$T_{max} = \sqrt[4]{\frac{21\,w}{A_r \varepsilon \sigma}} = \left(\frac{21}{360\,(0.9)\,5.67 \times 10^{-12}}\right)^{1/4} = 338°K\ (65°C)$$

$$T_{min} = \sqrt[4]{\frac{13}{A_r \varepsilon \sigma}} = \left(\frac{13}{360\,(0.9)\,5.67 \times 10^{-12}}\right)^{1/4} = 290°K\ (17°C)$$

$$\Delta T = 48°K \quad (-10°C \sim 38°C)$$

Fig. 9-3 Electronic compartment temperature.

$$\underset{\varepsilon_1}{|}\ \underset{\varepsilon_2}{|} \quad q_r/A = \frac{1}{\frac{1}{\varepsilon_1}+\frac{1}{\varepsilon_2}-1}\,\sigma(T_1^4 - T_2^4) \qquad (1)$$

$$(q_r/A)_{\varepsilon_1 = \varepsilon_2 = 1} = 20\,\text{mw/cm}^2 \equiv (q_r/A)_0 \qquad (2)$$

$$T_1 = 350^0\text{K}$$

$$T_2 = 325^0\text{K}$$

$$\underset{\varepsilon_1}{|} = \underset{\varepsilon_2}{|} \ldots \underset{\varepsilon_n}{|} \quad (q_r/A)_n = (q_r/A)_0 \frac{1}{1+N} \qquad (3)$$

$$\underset{\varepsilon = 0.09,}{|\,|}\ \underset{\varepsilon = 0.5}{|} \quad q/A = 20 \frac{1}{\frac{1}{0.09}+\frac{1}{0.05}+\frac{1}{0.5}-1} = \frac{20}{21} \approx 1\,\text{mw/cm}^2 \qquad (4)$$

Where: $(g_r / A)_0$ = Net Radiation Exchange Without Shield

Compartment Polished Al $\varepsilon = 0.09$ $\varepsilon_{\text{Electronics Board}} = 0.5$

$A = 450\,\text{cm}^2$ $H_T \approx 0.45$ w/Compartment

Fig. 9-4 Thermal isolation.

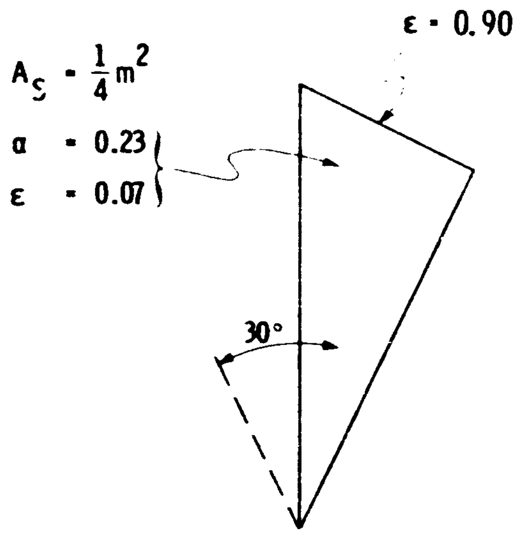

$H_{in} = \cos\theta \; A \, \alpha \, S$

$H_{in} = 0.9 \left(\frac{1}{4}\right) (0.27)\, 1300 \approx 30 \text{ watts}$

$H_o = \sigma \varepsilon A T^4 = H_{in}$

$T = \left(\frac{H_{in}}{\sigma \varepsilon A}\right)^{1/4} = 276°K \; (3°C)$ (Temperature at 1 AU)

$\Delta T = 70°$ (1 AU to 0.635 AU)

Fig. 9-5 Sail.

are available regarding solar flares. Estimates indicate that the solar-flare proton (greater than 5 MeV) flux that the spacecraft might experience is on the order of 1×10^6 protons/cm^2-sec-sr.[11] The characteristics of flare electron flux are unknown. In any event, use of annealed sapphire and the low-resistance (1Ω cm material) n on p solar cells yields a design with the least amount of time degradation. Beyond this, as a safety factor, the spacecraft power system and electronics will be designed to operate with a greatly reduced power level. This is done by relating the average pulse rate to the solar-cell power available.

The coating material for a dark (sun-shadowed surface) presents no problem. Several surface materials are acceptable. Tentatively, subject to further and more detailed investigation with surface finish, experts on such matters as ease of application, susceptibility to handling damage, i.e., fingerprints, etc., cost, etc., the coatings such as S-13G-type coating based on silicate-treated zinc oxide* or IIT's Z93 (emittance greater than 0.9) are acceptable.

The sail surfaces merit special consideration; fundamentally, from the thermal balance and control viewpoint, the sail surface is straightforward. As indicated in the simplified analysis, an aluminum-coated mylar with polished front (sun-lit) side has low absorptivity, and a high-emittance dark side (painted with zinc oxide) will yield an acceptable temperature range ($7^{\circ}C$ to $77^{\circ}C$) over the entire orbit. Also, if a lower α material such as polished silver ($\alpha = 0.07$) were used on the front side, or any other material with a low $\frac{\alpha}{\epsilon}$ ratio, the sail temperature can be reduced to a very low value. However, the problem which must be solved is to maintain the integrity (performance) of the surfaces when the sail has been deployed after having been stored for launch in a compact configuration. Additionally, a surface material must be chosen with regard to the stabilization torques, as discussed in Chapter 8. Aluminum-coated mylar appears to satisfy all the requirements and is presently being used; however, we are considering other materials.

9.4.4 Other Considerations

There do not appear to be any fundamental problems connected with the thermal isolation of the electronics. Indeed, as the analyses indicate even without any intention of thermally isolating the electronics, the operating temperatures are acceptable. The problem of maintaining an acceptably low thermal impedance, as determined from a number of tests reported in the past, has been solved by dip-brazing the structure.

*Developed under JPL Contract NASA-100, Sub-Contract 951737 and NASA MSFC Contract NAS8-5379.

9.4.5 Results

Table 9-II gives the expected temperatures of the various parts of the spacecraft at 1 AU and 0.635 AU.

Table 9-II

Expected spacecraft temperatures for 3/4-year orbit.

	1 AU	0.635 AU
Solar Cells	7° C	77° C
Front Plate	0° C	65° C
Front Half Cylinder	-5° C	55° C
Back Half Cylinder	-15° C	38° C
Center Tube	0° C	5° C
Electronics	0° C	10° C
Sails	-20° C	50° C
Aspect Sensors	0° C	30° C
Motors	0° C	20° C
Antenna	-10° C	60° C

9.5 Summary

The Sunblazer thermal-balance and control problem has been greatly simplified by designing a sun-oriented spacecraft with eternally sunlit and dark surfaces, maintaining relatively short thermal paths, optimizing the thermal radiator dimensions (see Appendix 3), and thermally isolating the electronics and electronic radiators from the main body of the spacecraft. Additionally, the various electronics have been designed for wide-temperature operation; and the use of highly temperature-sensitive components has been kept to a minimum. There is much detailed work to be accomplished; but conceptually, the overall design and analysis show that contemporary spacecraft-design techniques, materials, and components are available to accomplish readily the proposed scientific and engineering goals.

9.6 Spacecraft Thermal Test

A study made in June 1967 determined that, if the spacecraft did not orientate into position within a day, the total temperature balance could be below -7° C. This was corrected by increasing the radiator's length, which then gave the spacecraft an average temperature above -7° C no matter what its orientation.

A test chamber then was built using infrared radiation as an energy source. The cold wall reached -313° F and the vacuum was 10^{-5} torr. Although the source did not match the solar spectrum, it did match its energy flux and was a good "in-house" test chamber. There is only one chamber that will give a true picture of what the vehicle will see, and that is outerspace. Every earth-bound chamber has its shortcomings. The information obtained from the test chamber was correlated with that which had been calculated. The information received from the test, which would have been very difficult to calculate was:

1. The electronic side wall runs, on the average, 6° C higher than the radiator.
2. The electronic radiator, with a simple rubber insulator will produce a 25° C gradient with the electronics side wall at 0.63 AU.

Calculations were made to determine the size of the electronic radiators once it was known how much heat energy had to be dissipated from each section.

PRECEDING PAGE BLANK NOT FILMED

CHAPTER 10

10.0 ASPECT SENSOR AND CONTROL

The use of an active solar pressure orientation and stabilization system on the spacecraft requires a device which is capable of measuring the angle formed between the sun line and the spacecraft's major (spin) axis. A sub-system capable of performing this function, which is independent of the space-craft's main electrical system, consists of a detector, signal-processing electronics, photo-electric transducers, energy storage and an RF trans-mitter. This sub-system is called the Aspect Sensor.

The Aspect Sensor has two principal functions, which are of about equal importance. The first is to process information concerning spin rate and sense with respect to sun angle, and to provide electrical pulses to the sail-drive stepping motors to cause a properly sensed pitch of the sails to occur.

The second function of the Aspect Sensor is to provide basic engineering telemetry data during the time interval between launch and initial spacecraft sun aquisition.

10.1 The Detector Mechanical Configuration

The detector design consists of photo-electric diodes which have their light source interrupted (chopped) by means of mechanical apertures which are sequentially exposed to sunlight due to the spacecraft' s rotation and sun-alignment error.

The detector is mounted on the spacecraft's spin axis at the forward end of the Hub, and projects beyond the main solar-cell array by about 1.5 inches. In Fig. 10-1 the detector configuration is shown. It is essentially a truncated cone which has a central tubular compartment surrounded by six radially isolated compartments. A photodiode is positioned in each of the seven compartments, and is thereby provided with an individual view angle deter-mined by an aperture which ranges from a pin hole to a nearly full-length slot.

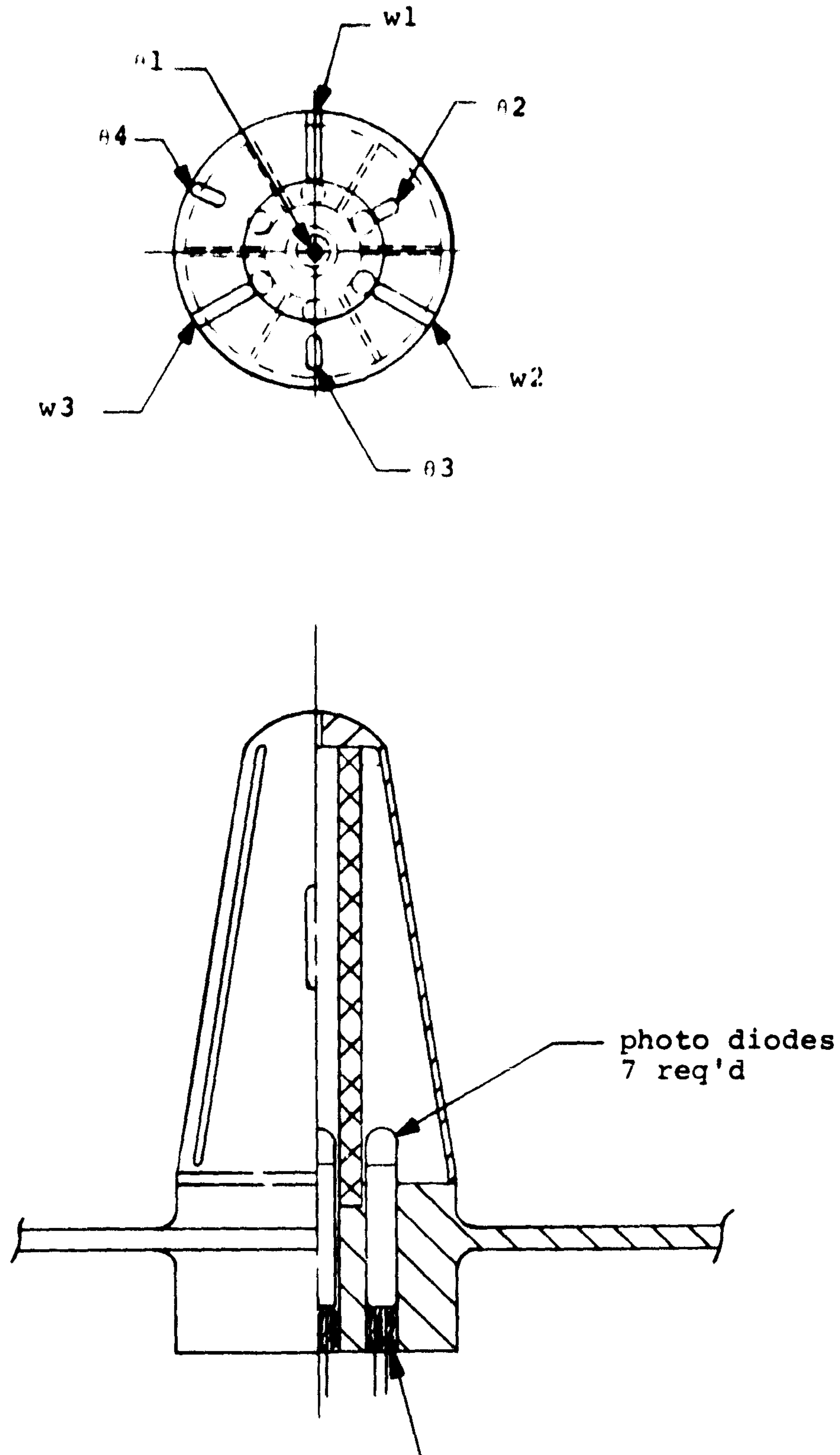

Fig. 10-1 Aspect sensor detector.

The three full-length slots are used to determine the spin rate (ω) and sense, and the photodiodes associated with these are identified as ω1, ω2 and ω3.

The central pin hole and the three slots with varied side position and length are used to obtain measurements of sun angle (θ), and their associated photodiodes are identified as θ1, θ2, θ3, and θ4.

10.1.1 The Detector Design

The ω1, ω2, and ω3 photodiode aperture slots are mechanically situated to provide light to their associated diode when the sun angle is greater than 0.5° and less than 91°. Rotation of the spacecraft will sequentially allow sunlight to illuminate ω1, ω2, and ω3 when the spacecraft rotation is counterclockwise as viewed from the solar-cell array (normal rotational sense during launch). The three electrical pulses generated by the photodiodes are digitally processed to provide a measurement of rate, since the time between each pulse represents one third of a revolution; and the sense of rotation by monitoring whether the sequence is ω1, ω2, ω3 or ω3, ω2, ω1.

The apertures provided for the measurement of θ are designed logarithmically to provide four incremental steps below 12° of sun angle, and three steps between 12° and 90°.

Figure 10-2 shows this logarithmic progression of θ diode view angles:

θ1 observes between 0° and 3.5°
θ2 observes between 1.8° and 12°
θ3 observes between 6.5° and 44°
θ4 observes between 24° and 90°

The overlap of view angles provides seven distinct measurement steps, which are:

$\theta 1 = 0^{\circ}$ to 1.8°
$\theta 1 \cdot \theta 2 = 1.8^{\circ}$ to 3.5°
$\theta 2 = 3.5^{\circ}$ to 6.5°
$\theta 2 \cdot \theta 3 = 6.5^{\circ}$ to 12°
$\theta 3 = 12^{\circ}$ to 24°
$\theta 3 \cdot \theta 4 = 24^{\circ}$ to 44°
$\theta 4 = 44^{\circ}$ to 90°

The pulses generated by the ω and θ photodiodes are shown in Fig. 10-3. The seven distinct pulse formats generated by the θ diodes can be processed and stored in a three-bit digital register as the numbers one through seven.

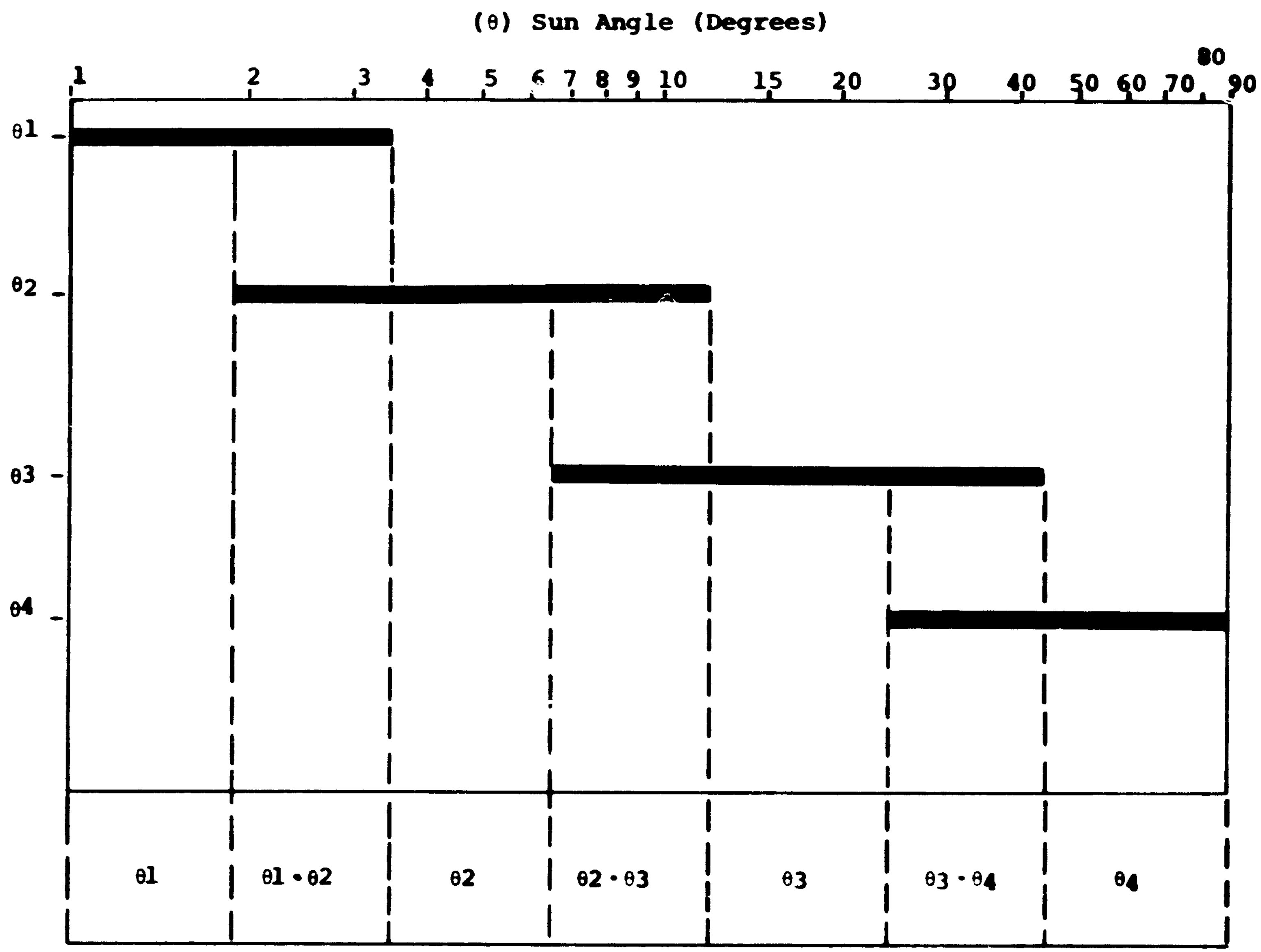

Fig. 10-2 Detector functional output.

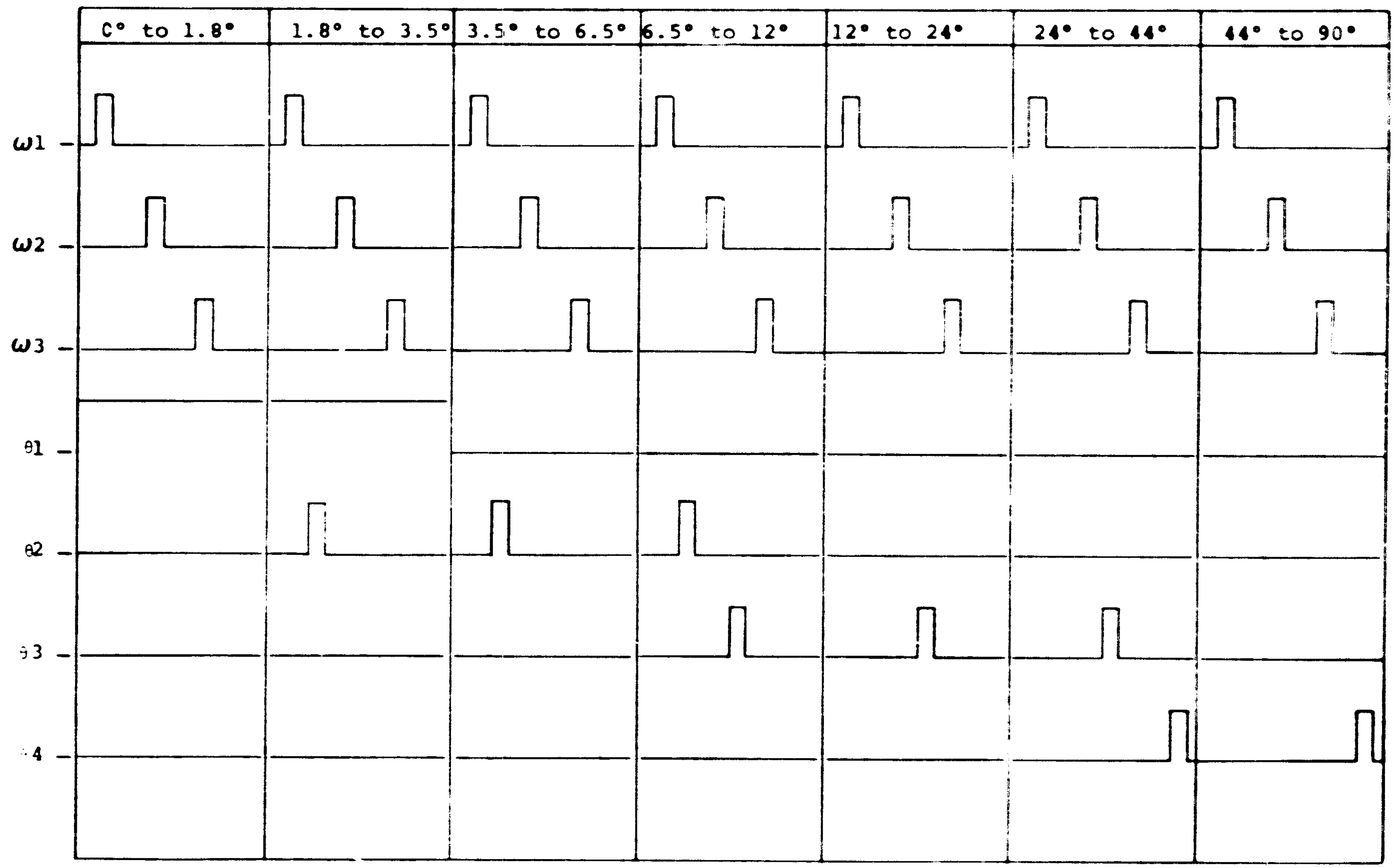

Fig. 10-3 Aspect sensor detector output format.

PRECEDING PAGE BLANK NOT FILMED

CHAPTER 11

11.0 SUNBLAZER SPACECRAFT POWER SYSTEM

11.1 Introduction

The fundamental consideration regarding the Sunblazer spacecraft power system is to generate at all times as much "useful" power per unit of mass as possible. In order to do this, the spacecraft is designed so that the solar cell panels are oriented towards the sun and operate at as low a temperature as practicable (see Chapter 9). The solar-cell energy conversion efficiency is maximized by adequately shielding the solar cells to prevent excessive degradation with time, and by operating the panels at the maximum power point throughout the orbit.

11.2 System Description

A simplified diagram of the power system appears in Fig. 11-1. The 640 (1 x 2 cm) n on p blue-shifted 1-Ω-cm solar cells will deliver approximately 19 W at $0^{o}C$ (1 AU), and 33 W at $70^{o}C$ (0.635 AU), if the solar-cell panel is operated at the maximum power point (MPP).*

There are two "L" converter units:** one low-power, which operates the tracking beacon and circuits that must be energized during the spacecraft orientation phase; and a high-power unit, which is switched on to supply the high-power pulsed transmitter when the spacecraft is oriented towards the sun.

A set of nickel-cadmium batteries, which is continually recharged from the low power "L" converter, is used as a source of initial energy to activate the solar-sail stepping motors and to run the tracking beacon. There are several different spacecraft operational modes which depend upon the amount of solar-cell power available (pointing angle with reference to the sun). These modes are controlled by the sensing power available, and

*State-of-the-art with matched selected cells.

**See Appendix 2

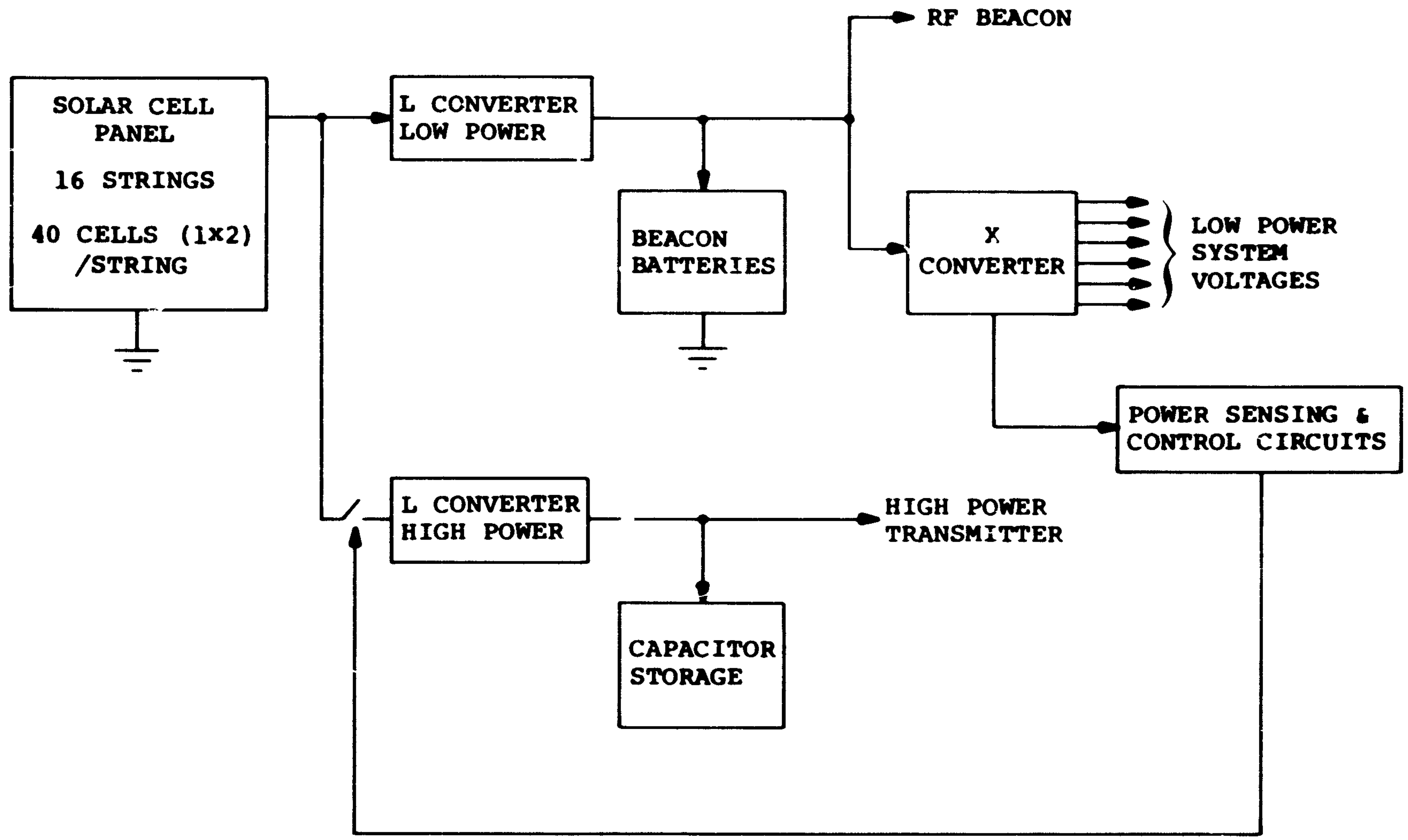

Fig. 11-1 Power system description.

by selection of the proper mode.

11.2.1 Solar-Cell Panels

Plate 2 shows how the individual solar cells are placed to form the Sunblazer solar panel. Since so much well-detailed material has been documented regarding solar-cell panel design, manufacture, operation, and testing for many different space applications, it is not necessary to delineate a set of solar-cell panel specifications in this report. When the Sunblazer panels are manufactured the specifications will be such that: 1) state-of-the-art cells will be used; and, 2) strict compliance with acceptable manufacturing practices (materials and workmanship), as described in various NASA documents, will be enforced.

Special aspects of the Sunblazer panels and mission are:

1. The relatively small number of solar cells per space-craft (640) should enable the panel manufacturer to select cells from the upper portion of the distribution curve in order to obtain higher energy efficiency than is feasible with large arrays, and still maintain adequate yields.
2. Better control over initial cell selection and matching is possible (that is, tighter selection limits can be set on various cell characteristics), with fewer cells, thereby decreasing the mismatch loss of this array.
3. Flat arrays, where the sun angle to all cells on the array is the same, further decreases the mismatch loss when compared to cylindrical arrays.

The Sunblazer array is made up of 16 parallel strings with 40 cells per string. Table 11-I shows the nominal current and voltage output of the array.

Table 11-I

Nominal current and voltage output

of Sunblazer array

1 AU				0.635 AU			
T_{AU}	I	V	P	T_{AU}	I	V	P
5°C	0.96A	20V	19.2 watts	75°C	2.3A	14.1V	33 watts

11.2.2 Power Converters

11.2.2.1 "L" Converter

The problem of utilizing the maximum available power from a power-limited source such as a solar-cell array can be solved by providing an adaptive dc-to-dc converter, which automatically adjusts its input parameters so as to take the maximum power from the source.

There are several possible approaches to the problem of providing an adaptive peak-power-seeking converter. Perhaps the most obvious approach is to sense the power drawn from the source, and to adjust the input parameters so as to maximize this power. If this power-sensing approach is used, the peak-power point can be tracked by continuously varying the converter input parameters and by reversing the sense of parameter variation whenever the sensed power begins to drop. This scheme causes the converter to dither its operation in a small range about the true peak-power point.

A more subtle approach is to use the principle of impedance matching. One notable characteristic of a solar-cell array is the high degree of convexity of its V-I characteristic. Because of this high degree of convexity, it is possible to choose an impedance which will define a point that remains near the peak-power point over a wide temperature and illumination range. A theory of an adaptive converter based on this fact has been discussed in detail in Appendix 2. This conversion technique has the difficulties of a number of possible "latch-up" conditions which must be avoided, and also of doing only an approximate job of tracking the true peak-power point. In a study of techniques to eliminate the aforementioned latch-up conditions with a minimum of extra complexity, an equally simple and very similar system was developed, which would both eliminate the latch-up conditions and provide true peak-power tracking.

It can be shown that, when the static impedance of a load is equal to the incremental impedance of the source to which it is connected, the power being transferred is at a maximum. If the dynamic V-I characteristic of a source is equivalent to the power-determining dc V-I characteristic, then the incremental impedance of the source can be determined by allowing some ripple current to flow in the source, and observing the ratio of the ΔV and ΔI produced at the source.

The static input impedance of the converter is of course determined by the ratio V/I, the input voltage to the input current. If $\frac{\Delta V}{\Delta I} = \frac{V}{I}$, then maximum power is being transferred. Rearranging this equation gives the peak-power condition as met when $\frac{\Delta V}{V} = \frac{\Delta I}{I}$. This form of the equation suggests the use of a converter in which ΔV and ΔI are controlled to be a fixed fraction of V and I respectively.

By using an inductive flyback "boost" converter, in which the state of the power switch is controlled by a flip-flop that changes state whenever the input voltage or current falls a fixed percentage of the pre-existing input voltage or current, peak-point power conversion can be accomplished.

The "L" converter that has been built (Fig. 11-2) utilizes this principle. Q7 is the power switch, and Q5 and Q6 act as a high-current-gain driver to minimize the load on the flip-flop.

Transistors Q8, Q9, Q10, and Q12 form the flip-flop, which is set or reset through clamped coupling networks that remove the base drive from the flip-flop's input transistors whenever the voltage at the input to the coupling network has fallen a given percentage of its initial value. Q1, Q2, Q3, and Q4 form a linear amplifier, which amplifies the small voltage drop across the current-sensing resistor R1 to a level where it can be coupled directly to the flip-flop. A dual FET input stage is used in this amplifier to eliminate the need for a negative supply voltage to obtain the near-zero input voltage offset that is required in this application. D5 and Q11 form a series regulator to provide control-circuit power.

For this converter $\frac{\Delta V}{V} = \frac{\Delta I}{I} = 0.1$. It was found that this was a nearly optimum figure, in that a smaller value would require a correspondingly larger inductor, thus increasing the size and weight of the package; and a larger value would result in less efficient peak-point conversion because of the larger per-cycle variations from the true peak-power point.

It is interesting to note that this method of tracking the peak-power point of a solar-cell array or other electrical-power source does not depend on the source having a convex V-I characteristic or any other special nonlinear V-I characteristic. It will seek the maximum power point and operate nicely, for example, with a source composed of a constant emf and a resistor.

11.2.2.2 "X" Converter

Basically, then, the "X" converter consists of two converters operated at 10 kHz, of which one is a standard Royer circuit. The primary voltage is supplied by a battery through a series regulator. The secondary supplies base drive to the transistors of the second converter, and a rectified dc input to a second series regulator. This provides the required 1%-regulated voltage at output. (See Fig. 11-3)

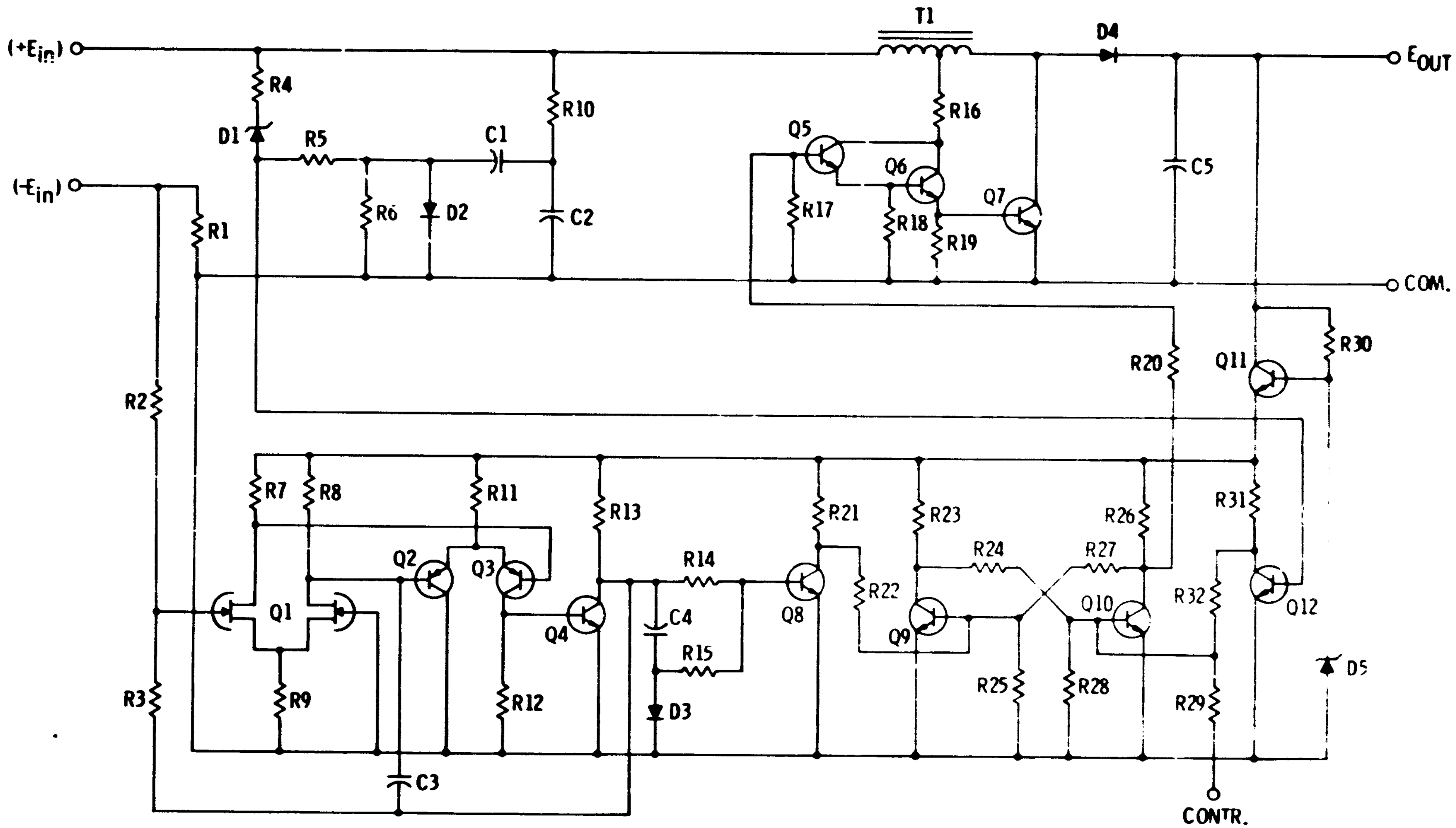

Fig. 11-2 "L" converter.

Table 11-II

"L" Converter parts list.

ITEM	CODE	DESCRIPTION	MANUFACTURER	MFG PART NO.
1	R1	Resistor 0.24 Ω 3 W formed in breadboard model from two 0.47 Ω resistors in parallel, each being:	IRC	Type BWH
2	R2	Resistor 15K 5%	Ohmite	RC07GF
3	R3	Resistor 300K 5%	Ohmite	RC07GF
4	R4, R14	Resistor 100K 5%	Ohmite	RC07GF
5	R5, R13 R15, R17 R29, R30	Resistor 10K 5%	Ohmite	RC07GF
6	R6, R20	Resistor 1.5K 5%	Ohmite	RC07GF
7	R7, R8	Resistor 47K 5%	Ohmite	RC07GF
8	R9	Resistor 2.7K 5%	Ohmite	RC20GF
9	R10, R19	Resistor 0.1K 5%	Ohmite	RC07GF
10	R11	Resistor 9.1K 5%	Ohmite	RC20GF
11	R12	Resistor 4.7K 5%	Ohmite	RC07GF
12	R16	Resistor 5.6 Ω 10%	Ohmite	RC20GF
13	R18	Resistor 1.8K 5%	Ohmite	RC07GF
14	R21, R23 R31	Resistor 62K 5%	Ohmite	RC07GF
15	R22, R24, R32	Resistor 18K 5%	Ohmite	RC07GF
16	R25, R28	Resistor 27K 5%	Ohmite	RC07GF
17	R26	Resistor 3K 5%	Ohmite	RC07GF
18	R27	Resistor36K 5%	Ohmite	RC07GF
19	Q1	Transistor	Texas Instruments	2N5045
20	Q2, Q3	Transistor	Solitron Devices	2N2605
21	Q4, Q8, Q9, Q10, Q11, Q12	Transistor	Solitron Devices	2N930
22	Q5	Transistor	Texas Instruments	2N718A
23	Q6	Transistor	Texas Instruments	2N4000
24	Q7	Transistor	Texas Instruments	2N3421
25	D1	Zener Diode	Motorola	1N746
26	D2, D3	Diode	General Electric	1N4444
27	D4	Rectifier	Unitrode	UTR4410
28	D5	Zener Diode	Motorola	1N968B
29	C1, C4	Capacitor 0.022 μF	Cornell-Dubilier	DMF1S22
30	C2	Capacitor 0.01 μF	Cornell-Dubilier	DMF2S1
31	C3	Capacitor 10 pF	Sprague	10TCC-Q10
32	C5	Capacitor 0.22 μF	Cornell-Dubilier	DMF1P22
33	T1	Tapped Inductor	Wilmore Electronics	Special

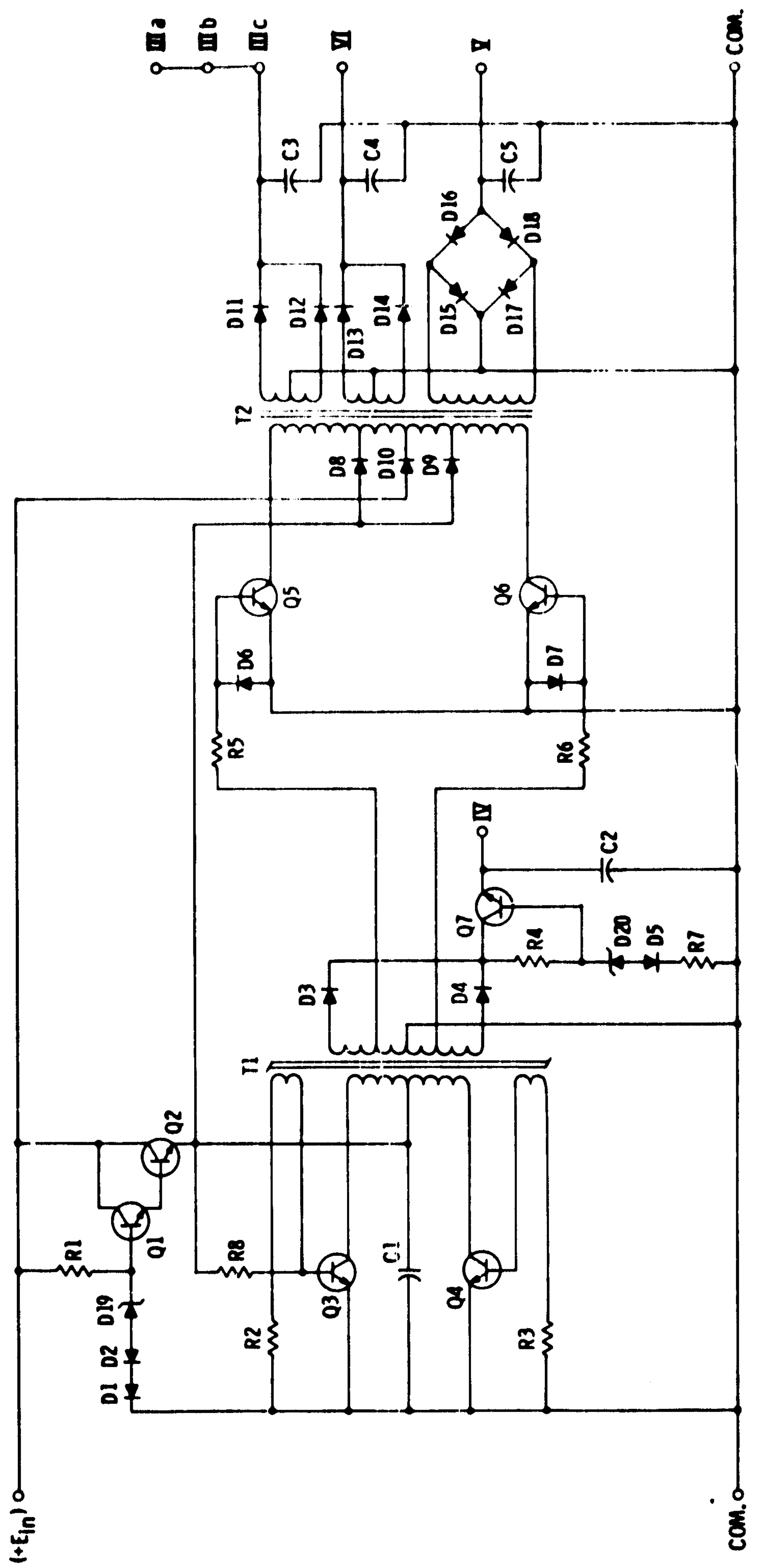

Fig. 11-3 "X" converter.

Table 11-III

"X" Converter parts list.

ITEM	CODE	DESCRIPTION	MANUFACTURER	MFG PART NO.
1	C1	1.0 μF 50 V capacitor	Kemet	K1J50KS
2	C2, C4	0.33μF 35 V capacitor	Kemet	KR33J35KS
3	C3	1.5 μF 20 V capacitor	Kemet	K1R5J20KS
4	C5	0.5 μF 600 V		
5	D1, D2, D3, D4, D5, D13, D14	Diode	General Electric	1N4444
6	D6, D7, D10	Diode	General Electric	1N645
7	D8, D9, D11, D12	Diode	Unitrode	UTR12
8	D15-D18	Bridge Rectifier	Unitrode	UBR5
9	D19	Zener Diode	Motorola	1N971B
10	D20	Zener Diode	Motorola	1N4104
11	R1, R8	Resistor 82K	Ohmite	RC20GF
12	R2, R3	Resistor 2400 Ω	Ohmite	RC20GF
13	R4	Resistor 5600 Ω	Ohmite	RC20GF
14	R5, R6	Resistor 120 Ω	Ohmite	RC20GF
15	R7	Resistor 0-2K (select)	Ohmite	RC20GF
16	Q1, Q7	Transistor	Solitron	2N930
17	Q2, Q3, Q4, Q5, Q6	Transistor	RCA	2N2405
18	T1	Transformer	Wilmore	Special
19	T2	Transformer	Wilmore	Special

11.3 Energy Storage Tests

A transistorized 8 kW dc switch was designed to enable capacitor-pulse-discharge testing. The overall test configuration simulated the spacecraft power system, since it incorporated a Solar Array Simulator (SAS), a prototype "L" converter, and eight parallel-connected capacitors (9000 μF, 40 V each).

The SAS is powered by a 35-volt, 0-3 A power supply, and biased by a 6-V battery. The SAS uses solar cells, of the type to be used in the spacecraft, in the feedback path of a high-power operational amplifier, such that the amplifier's output is a scaled-up representation of the voltage-current characteristics of the solar cells.

The frequency-response characteristics of this closed-loop amplifier are so much higher than the frequencies involved in the maximum-power-seeking "L" converter that the accuracy of both the dc simulation and of the dynamic simulation is excellent.

Two controls are provided to allow independent adjustment of the SAS output voltage and current, in order to simulate spacecraft attitude and/or orbital positions.

The "L" converter receives the SAS output power, and essentially transforms the array into a current source, which is capable of charging the energy-storage capacitors to any desired voltage amplitude, dependent only on the duty cycle of the pulse format and the available solar-cell power.

This stored energy is then transferred into a resistive load, by the switch which is driven into conduction by a pulse train similar to the spacecraft's RF transmission format.

The load resistor used is four parallel lengths of nichrome resistance wire (zero thermal coefficient of resistance). Resistance is measured on a General Radio bridge, and is then rechecked dynamically by monitoring its $\frac{E}{I}$ characteristics. Test-load resistances used are generally in the 0.3 to 0.5 Ω range. With this load resistor of known value, the various parameters of the energy-storage system can be empirically observed.

The total capacitance of the 8 paralleled capacitors can be interpreted by observing the time required to discharge to 36.8% of the initial voltage through the load resistor. Fig. 11-4 shows such a discharge curve, where E =5V/cm, and T = 5 ms/cm, E_0 = 40 V, E_f = 40 x 0.368 = 14.72 V. This occurs at 6.2 cm x 0.5 x 10^{-3} sec = 0.031 sec.

$$C = \frac{T}{R} = \frac{0.031}{0.46\Omega} = 0.06739 \text{ F} = 67,390 \ \mu\text{F}$$

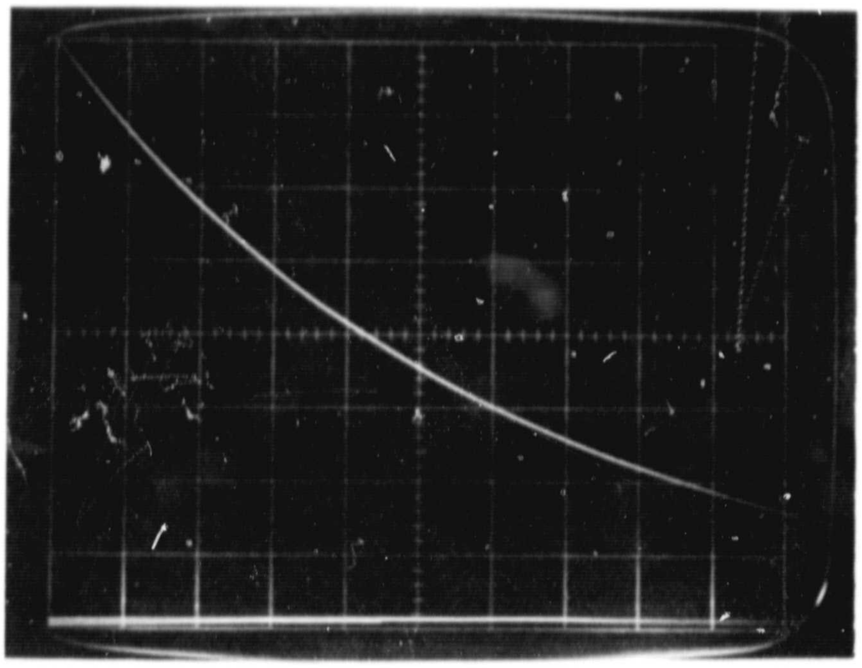

5 volts/cm

5 msec./cm

$R_L = 0.46\Omega$

Fig. 11-4 Capacitor discharge.

11.3.1 Interpretation of a Typical Pulsed Power Test

The "L" converter is designed to track the varying peak power of the solar-cell array as the spacecraft travels nearer to the sun. To observe this unique characteristic of the converter, the Solar Array Simulator (SAS) was energized and loaded by a variable resistor. The two controls of the SAS were advanced in position increments, and the peak-power point of each control setting was determined by observation of the maximum voltage and current obtainable (peak power) at the load resistance. These data provided the SAS output peak-power curve shown in Fig. 11-5.

With the SAS now supplying power to the "L" converter, which in turn charges a paralleled capacitor bank that is pulsed-discharged by the dc switch, an observation of the converter and capacitor characteristics can be made.

By setting the E and I dial controls of the SAS to positions similar to those used in the dummy-load test, the duty cycle of the pulse format is changed to allow an instantaneous amplitude of 45V on the capacitors at the beginning of the pulse discharge. In this manner, the data shown in Table 11-IV were obtained, and the indicated power levels have been plotted in Fig. 11-5 with the dummy-load power curve.

Since the load resistor's value has been carefully determined, the amount of capacitance in the energy storage can be determined, and the joule distribution in the system can be examined.

$$\text{The capacitance} = C = \frac{t}{\ln\frac{V_o}{V_f} \times R_L}$$

$$C = \frac{0.003 \text{ sec}}{\ln\frac{45}{40} \times 0.39} = \frac{0.003}{0.0442} = 67,876\ \mu F$$

which is in agreement with the C determined previously with a different R_L by the time-constant method.

The energy delivered by the capacitors can be determined by the difference in the joules stored in the bank before and after the discharge pulse.

$$J_o = \frac{Cv^2}{2} = \frac{678 \times 10^{-4} \times 45^2}{2} = 68.65$$

$$J_f = \frac{678 \times 10^{-4} \times 40^2}{2} = 54.24$$

$$J_o - J_f = 68.65 - 54.24 = 14.41$$

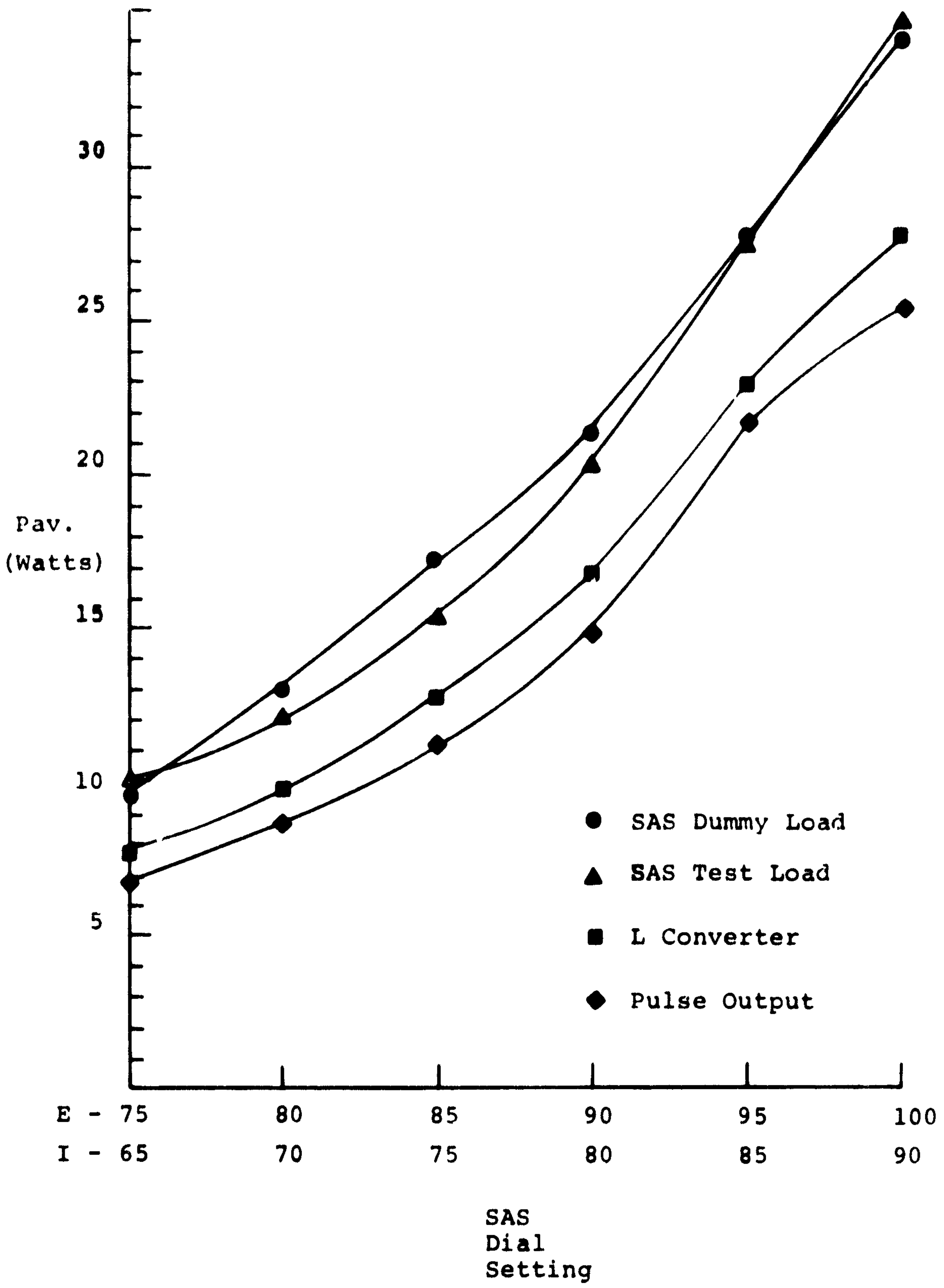

Fig. 11-5 "L" converter pulsed power tests.

Joules in the pulse = 4642 W × 0.003 s = 13.93.

Joules dissipated in capacitors = 14.41 - 13.93 = 0.48

$$\text{Watts dissipated during pulse} = \frac{0.48\text{J}}{3 \times 10^{-3}\text{sec}} = 160\text{W}$$

Average watts dissipated at 12-W input = $160 \times 183 \times 10^{-5} = 0.29$ W

Average watts dissipated at 27.6-W input = $160 \times 468 \times 10^{-5} = 0.75$ W

Assuming 0.5-W average dissipation per capacitor bank, the average power dissipated per capacitor =

$$\frac{0.5\text{W}}{8 \text{ capacitors}} = 0.062\text{W}$$

The average efficiency of the capacitors is determined by

$$\frac{P_{av}}{P_L} \quad \text{and is } 89.7\%$$

The discharge efficiency of the capacitors is determined by

$$\frac{J_{load}}{J_{del}} = \frac{13.93}{14.41} = 97\%$$

The recharge efficiency must then be:

$$\frac{\text{Total Av. Eff.}}{\text{Discharge Av Eff}} = \frac{89.7\%}{97.0\%} = 92.5\%$$

Table 12-V indicates a requirement of 4370 W dc input power to the RF sub-system.

The excess pulse power delivered in test = 4642 W - 4370 W = 272 W.

The average excess power at 12-W input = 272 W × 183 × 10^{-5} = 0.5 W.

The average excess power at 27.6-W input = 272 × 468 × 10^{-5} = 1.28 W.

The average excess power for use in operating the "X" converter and low-level power system over the test input-power range is

$$\frac{1.28 + 0.5}{2} = 0.89 \text{ W}$$

The average power delivered to the load in this test has been plotted versus a duty cycle which provides a peak amplitude of 45 volts (in Fig. 11-6). It can be observed that a duty cycle of 3×10^{-3} will deliver 14 W to an equivalent load of 0.39Ω.

With an RF sub-system requirement of 4370 W, the equivalent load resistor would be:

Table 11-IV

Capacitor test results.

SAS Dial Settings		SAS Output			"L" Converter Output			Pulse Amplitude			Duty Cycle	Pulse P_{av}
I	E	I	E	P	I	E_{av}	P	E_o	E_{av}	E_f		
70	80	0.75	16.1	12.08	0.23	42.5	9.78	45	42.5	40	0.00183	8.50 W
75	85	0.9	16.8	15.12	0.3	42.5	12.75	45	42.5	40	0.00242	11.24
80	90	1.13	18.1	20.45	0.395	42.5	16.79	45	42.5	40	0.00319	14.80
85	95	1.43	19.3	27.60	0.54	42.5	22.95	45	42.5	40	0.00468	21.73

Pulse width = 3 ms

$R_L = 0.39\Omega$

$$\text{Average Peak Pulse Power} = \frac{E_0^2 + E_{av}^2 + E_f^2}{3 \times 0.39\Omega} = 4642 \text{ W}$$

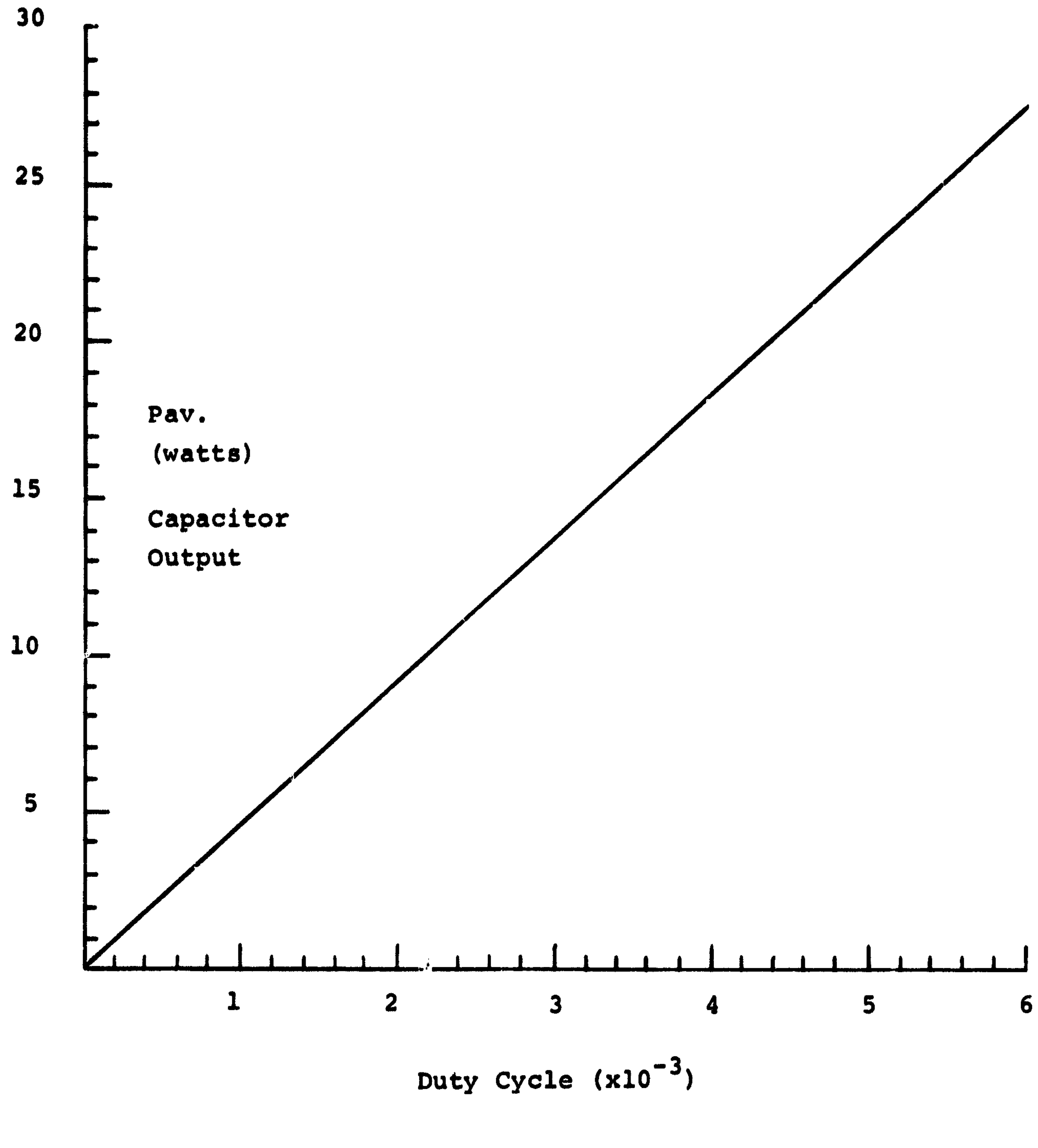

Fig. 11-6 Capacitor power output vs duty cycle.

$$R_L = \frac{E_{av}^{\ 2}}{P} = \frac{42.5^2}{4370} = 0.4133\Omega$$

rather than the 0.39Ω load used in the test.

11.3.2 Capacitor Vacuum Test

Twelve specially-designed capacitors were purchased from Sprague Electric Company for evaluation as energy-storage devices for a pulsed-discharge system operating in a vacuum.

Three of these capacitors (A, B and C) were operated in a pressure equal to 1×10^{-5} torr, and were delivering about 2kW pulses of 3 ms in length at a duty cycle of 0.004 from October 25, 1967 to February 29, 1968 (4 months).

After the construction of the high-power switch, ten capacitors in parallel were tested at the 4-kW pulse amplitude, 3-ms width and a 0.003 duty cycle at 1×10^{-5} torr from March 8, 1968 to May 27, 1968 (2 1/2 months). Three of the capacitors in this group of ten were the original A, B and C which showed no weight loss after 6 1/2 months exposure to low pressure.

11.3.3 Internal Pressure Relief Test

The Sprague capacitors were designed with the container scored, intended to perform the venting in case of high internal pressure. This design was selected over the standard vent, which is a thin diaphragm of plastic, usually positioned as a hole cover in the terminal plate of the capacitor.

To check the proper functioning of the scored can vent, a selected capacitor was overcharged by 150 percent (60V), and within one hour the scoring fractured slightly, developing a relatively small orifice which provided a controlled exhaust of the artificially-generated internal pressure.

11.4 Power System Summary

The power system consists of 640 1 × 2 cm solar cells in 16 parallel strings of 40 cells each. Because the spacecraft is solar-oriented, the number of cells per spacecraft is kept to a minimum and it is economically feasible to select only the cells of highest performance, and carefully match cell performance, to maximize the energy-conversion efficiency. This design allows minimum power per unit mass. The power converters have been designed to track automatically the solar cell panel V-I characteristics over the entire orbit (see Appendix 2). The design of the spacecraft energy-storage system, which is based on considerable analysis (Appendix 1), utilizes eight capacitors and has a redundancy factor greater than two. That is, only three capacitors in parallel are required to operate the system.

The prototype of the entire Sunblazer power system, utilizing a solar-cell panel simulator, has been bench-tested, and the design proven.

CHAPTER 12

12.0 RF SUBSYSTEM

The primary function of the Sunblazer electronics system is to generate pulse signals which will be used to probe the Solar Corona. Three subsystems, digital, RF, and power, are involved. (See Fig. 12-1)

The power subsystem converts the solar energy into electrical energy, maintains the charge on the capacitor package used for energy storage, and provides and regulates the voltages which are necessary for operation of the transmitter and digital subsystems.

Signal generation and housekeeping information-processing are handled by the digital subsystem.

The RF subsystem consists of a 2 kW transmitter which generates this power at three discrete frequencies, 70 MHz, 75MHz, and 80 MHz, which are necessary for the main experiment. In order to phase-lock the RF pulses and their envelope, a common clock drives the digital and RF subsystems. The 2 kW RF power level is achieved by cascading amplifiers of progressively higher power-handling capabilities, with the ultimate amplification being produced in the final stages by the paralleling of several single-stage amplifiers of one type, called the basic-power amplifier.

12.1 RF Subsystem Functional Description

The Sunblazer electronics system diagram print (see drawing No. 106-615, Fig. 12-2) shows the relationship of the RF subsystem to the digital and power subsystems. The power supply delivers to the transmitter the following required dc bias voltages: 10V, 10V regulated, 30V and 45V.

The RF chain starts with a 5 MHz crystal oscillator (Fig. 12-5). The output of the oscillator is fed into a two-stage feedback amplifier to provide load isolation and to bring its microwatt level up to about 1 mW.

The feedback amplifier drives a saturated 5-MHz line driver which provides a stable 6.0 mW with respect to variations in temperature.

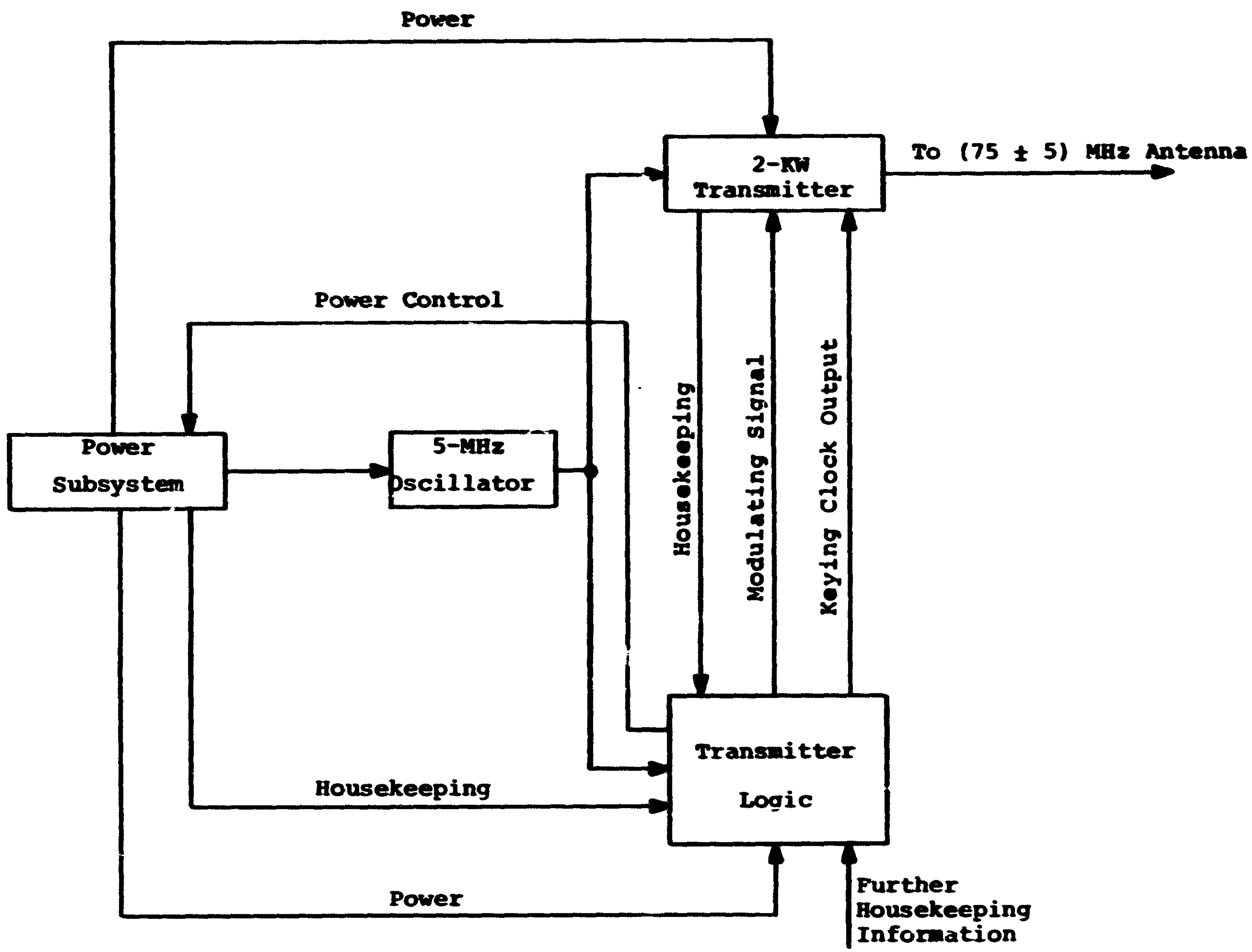

Fig. 12-1 Sunblazer electronics system.

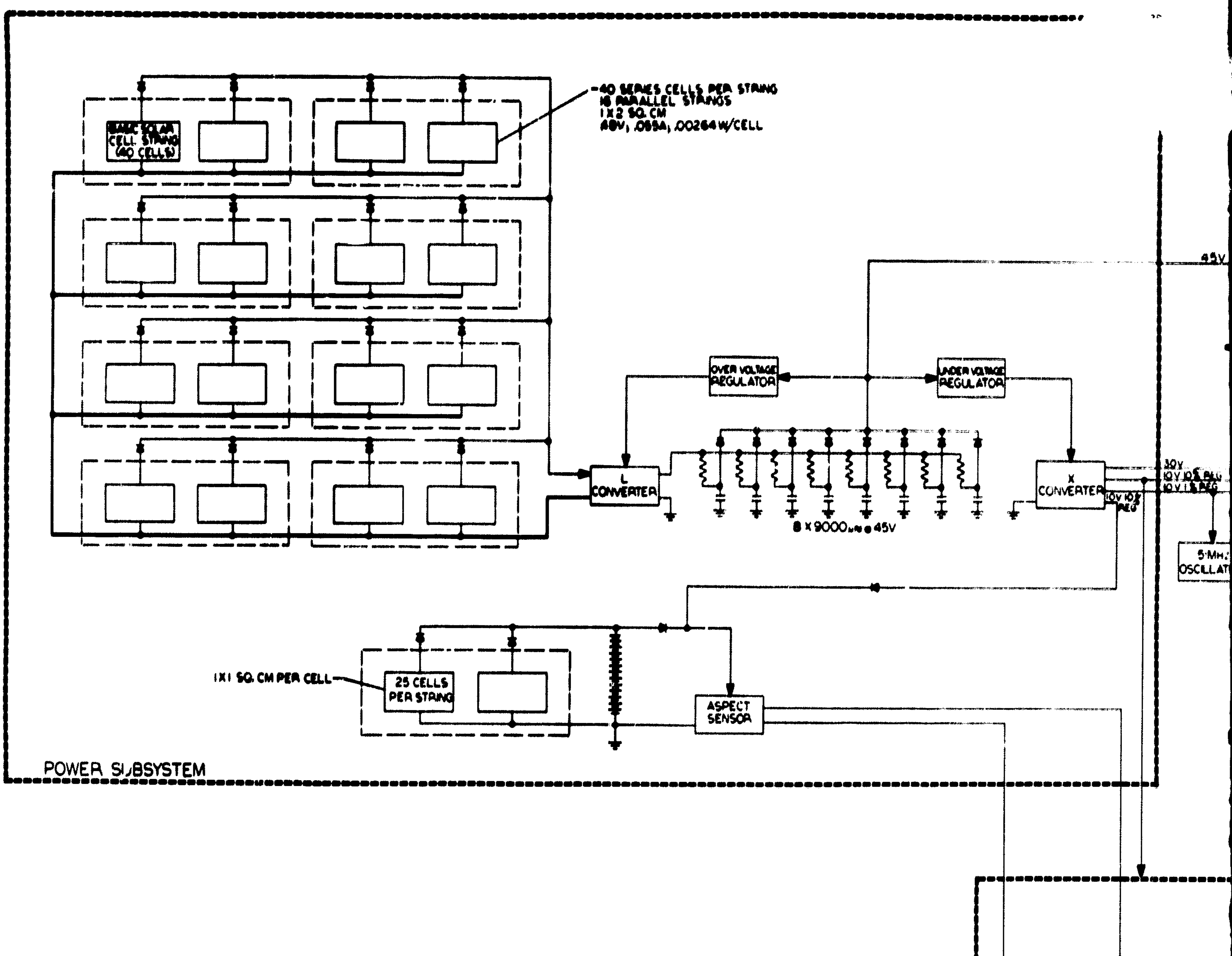

NOTES:
1. BA IS A 75W BASIC AMPLIFIER WITH 8DB POWER GAIN.
2. Q IS A BASIC QUAD WITH 4 PARALLELED BASIC AMPLIFIERS, COMBINER AND DIVIDER NETWORKS.
3. HPN AND LPN ARE HIGH AND LOWPASS POWER COMBINERS AND DIVIDERS WITH $\eta = 95\%$.
4. THE 3DB HYBRIDS ARE ASSUMED TO HAVE $\eta = 97\%$.

FOLDOUT FRAME 1

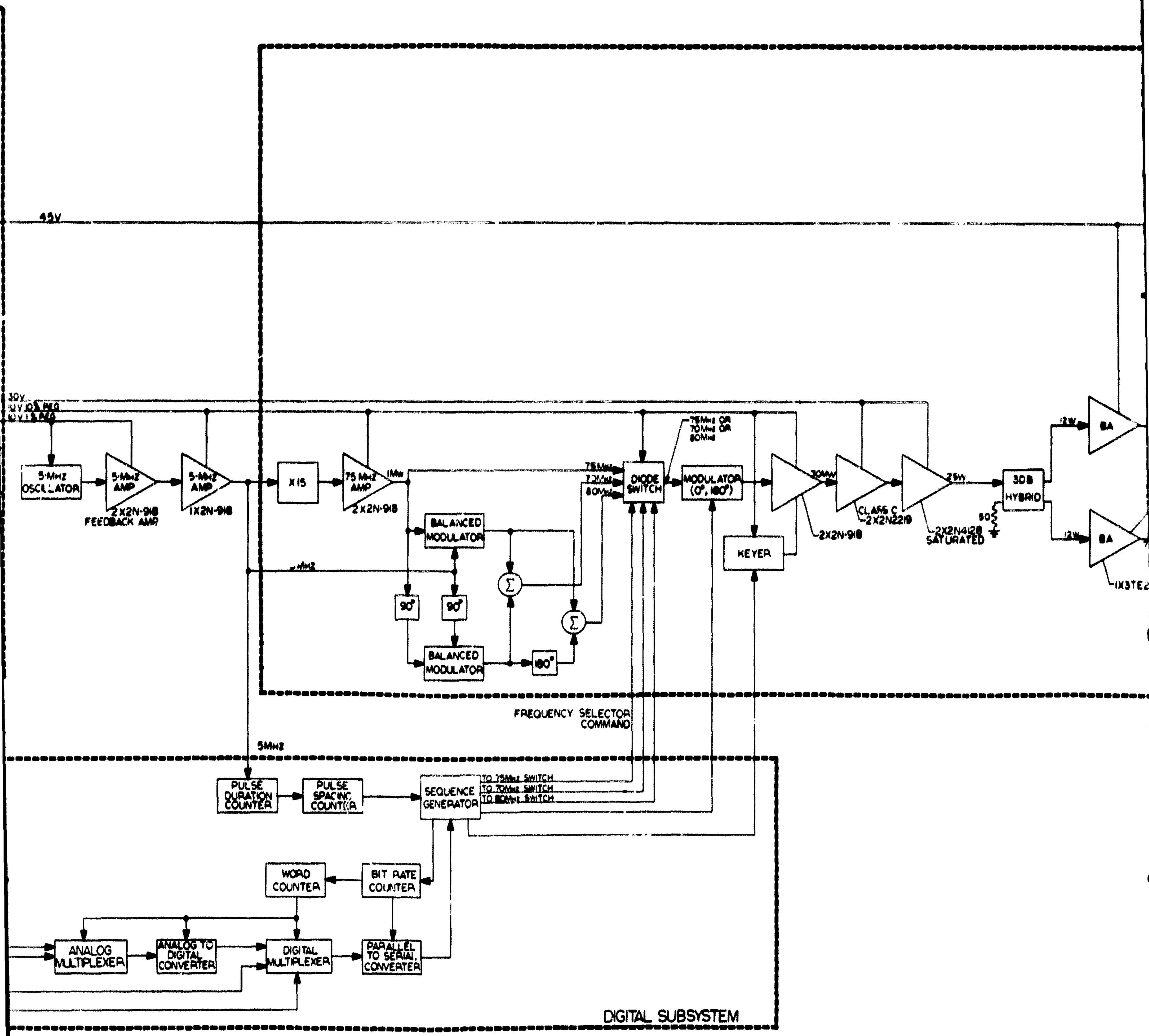

FOLDOUT FRAME 2

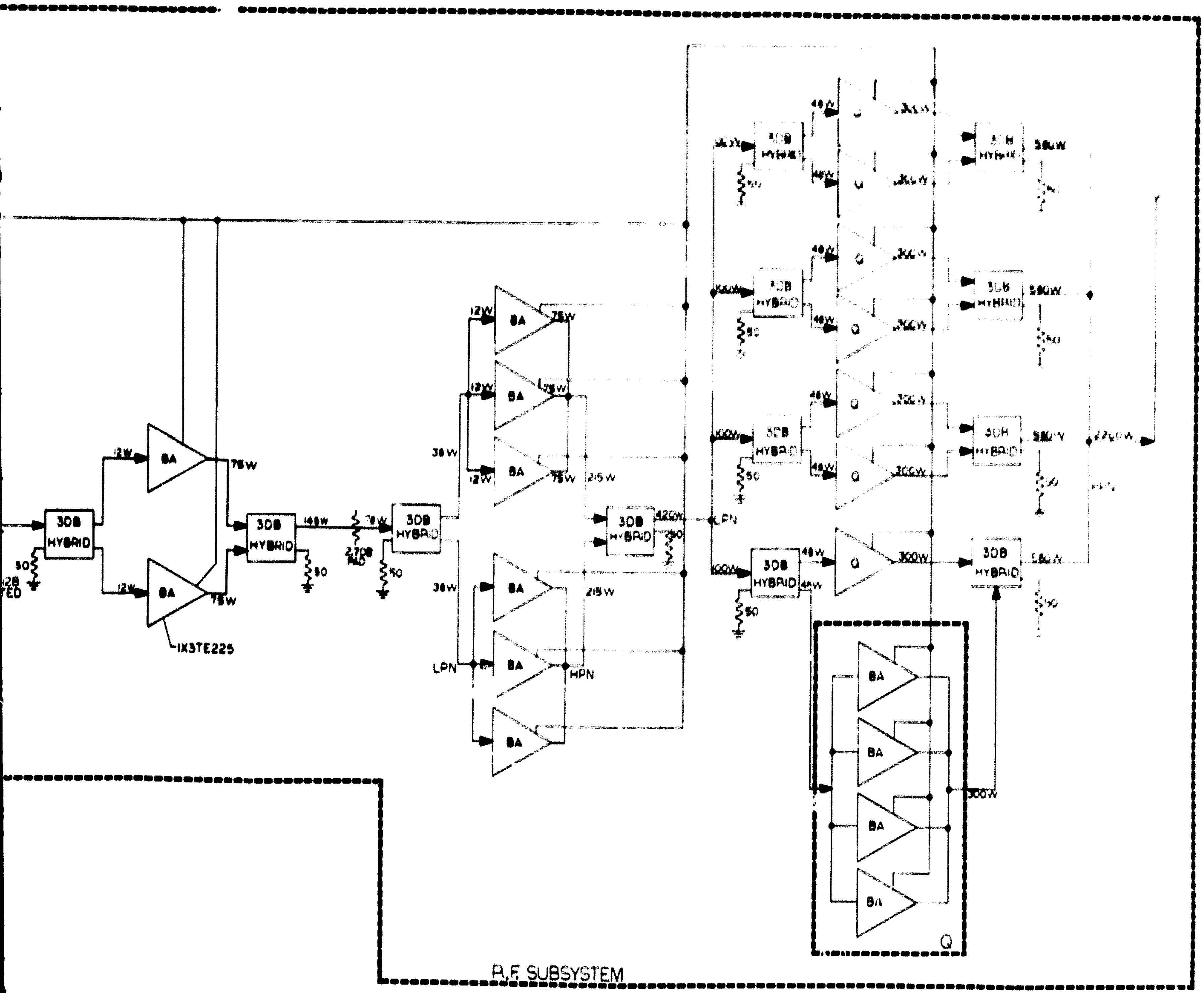

Fig. 12-2 Spacecraft electronics system diagram.

FOLDOUT FRAME 3

...ECEDING PAGE BLANK NOT FILMED.

This power is divided by three, and distributed to the digital subsystem (clock signal), to the sidebands generator (as a-m modulating signal), and to the x 15 frequency multiplier (Fig. 12-6).

The 75 MHz output of the frequency multiplier is further amplified to 4.0 mW by the two-stage 2N918 RF amplifiers.

This power is divided by two: one part of it constitutes the high-frequency component in the sidebands generator, the other makes 75 MHz available at the diode switch input port.

The mixing of 75 MHz and 5 MHz signals is processed in the sidebands generator whose 70 MHz and 80 MHz outputs are then also fed to the diode switch input.

Thus, three discrete frequencies, 70 MHz, 75 MHz, 80 MHz, are available in CW mode at the diode switch input port.

The diode switch, which is normally in the "off" condition (i.e., no signals reach the modulator), is activated through frequency-selecting gated signals generated by the digital subsystem. In this manner, transmission through the main chain is made possible at any of these frequencies.

The selected frequency is fed into a phase modulator where it is multiplied by +1 or -1 in order to generate a desired code word. The command to this 0° or 180° phase shifter is also generated in the logic subsystem.

In order to increase the overall dc-to-RF efficiency of the system, the 2 kW transmitter is turned on only when a signal is to be transmitted. This is realized by keying (Fig. 12-8) the 10V biasing voltage of the two-stage 2N918 amplifier, which brings its own RF output power level to 30.0 mW.

The keyer also phase-locks any RF signal with its envelope.

Thus, the transmitter must operate under a pulsed condition. At the present time, the pulse format is fixed as a 3 ms pulse occuring every second. This corresponds to a duty cycle of

$$\text{Duty cycle} = \frac{3\ \text{ms}}{1\ \text{s}} \times 100\% = 0.3\%$$

A fact worth noting at this point is the capability of this new Sunblazer transmitter system to generate (if necessary) three different intrapulse coding schemes by properly activating the diode switch and the modulator. We can define these groups as follows (Fig. 12-3):

Group 1: Code words generated at one frequency by means of 0° and 180° phase shifter (binary code).

<u>Binary Coding</u>

Group 1: The transmission frequency during a code word is either 70 MHz or 75 MHz or 80 MHz. Code words are obtained by 0° or 180° phase shift of the transmission frequency. Assuming that all the code words have a length of n digits the total amount of words generated in this way is 2^n.

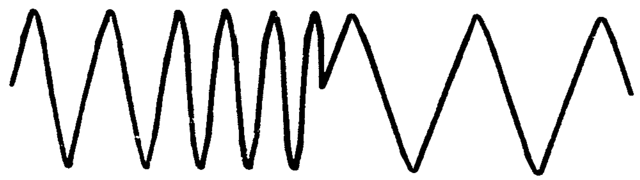

75 MHz 80 MHz 70 MHz 70 MHz

<u>Ternary Coding</u>

Group 2: A sequency of 3 discrete frequencies corresponding to the desired code word is transmitted. In this type of transmission the 0° or 180° Modulator is not activated such that all the transmission occurs either at 0° or at 180°. The total amount of words generated in this way is 3^n.

0° 75 MHz, 180° 80 MHZ, 180° 70 MHz, 0° 70 MHz

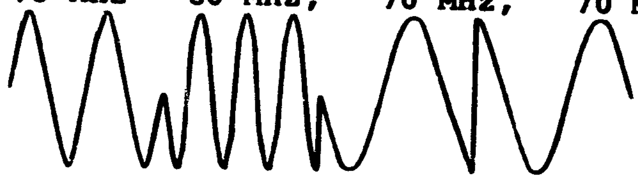

<u>Six-ary Coding</u>

Group 3: It is the situation of group 2 out with the modulator activated. Thus the total amount of words which could be transmitted in this way is 6^n, n being the number of digits per word.

Fig. 12-3 Different intrapulse coding schemes.

Group 2: Code words generated at a constant phase (all 0° or all 180° phase shifted) by means of a sequence of different frequencies (ternary code).

Group 3: Code words generated from the combination of the two previous groups.

The 30 mW peak power at the output of the two-stage 2N918 amplifiers is connected to a cascaded two-stage 2N2219 and a saturated two-stage 2N4128, the output of which brings the power level up to 25 W. The use of a saturated system at this point is to preserve the output level, and consequently to provide a constant drive to the RF chain, which is thereby isolated from the fluctuations in the low-level power. To establish load isolation and to prevent amplifier oscillations, a 3 dB hybrid (Fig. 12-12) is used as a two-way power divider. This provides 25 W RF input power, the required drive to the two paralleled 3TE225 basic amplifiers (Fig. 12-11).

The outputs of both basic amplifiers are combined and padded down to give a drive level of 78 W. A second paralleling of six basic amplifiers by means of 3 dB hybrids (which have an efficiency of 97% and a minimum isolation between the two output ports of -30 dB) and three-way power combiner-divider networks (Fig. 12-9) brings the power level up to 420 W.

In the final stage, 32 basic amplifiers are paralleled by using the same techniques to provide 2200 W RF power to the antenna.

One of the major characteristics of the transmitter chain which is to be emphasized is the requirement of a 10 MHz bandwidth with a center frequency of 75 MHz starting at the output of the modulator and continuing through all the supplementary circuitry to the antenna.

12.2 Generation of the Three Discrete Frequencies

Figure 12-4 is a block diagram of the frequency-generator system. Set f_m = 5 MHz as the modulating frequency and f_c = 75 MHz as the carrier frequency, with f_c obtained from f_m by the x15 frequency multiplication.

Thus, $\cos 2\pi f_c t$ is made available at the output of the system. In order to generate the sideband frequencies, i.e., $\cos 2\pi (f_c - f_m)t$ and $\cos 2\pi (f_c + f_m)t$, we feed both $\cos 2\pi f_c t$ and $\cos 2\pi f_m t$ into two balanced modulators, as indicated in Fig. 12-4. The upper balance modulator has then an output

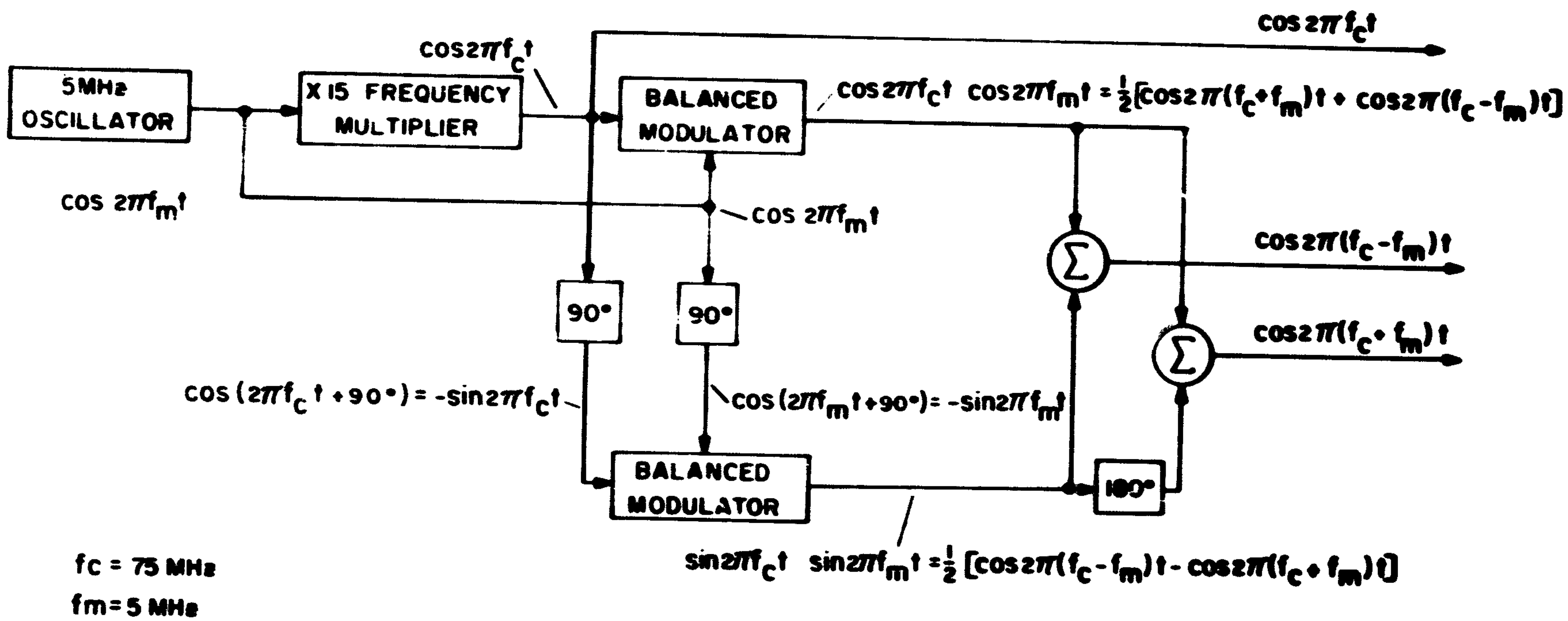

Fig. 12-4 Block diagram for generation of the (75 ± 5) MHz bandwidth.

$$\cos 2\pi f_c t \cos 2\pi f_m t = 1/2 \left[\cos 2\pi (f_c + f_m)t + \cos 2\pi (f_c - f_m)t\right] \quad (12.1)$$

The lower-balance modulator gives an output

$$\sin 2\pi f_c t \sin 2\pi f_m t = 1/2 \left[\cos 2\cdot (f_c - f_m)t - \cos 2\cdot (f_c + f_m)t\right] \quad (12.2)$$

The addition of (12.1) and (12.2) delivers the lower sideband signal $\cos 2\pi(f_c - f_m)t$. In order to obtain the upper sideband signal, (12.2) must be subtracted from (12.1). This is done by the 180° phase-shifter and combiner networks. One should note that in this mathematical analysis, for reasons of simplicity, the amplitudes of the signals have been deliberately assumed to be equal to unity. In a practical case, however, one should take into consideration the different amplitude levels and, therefore, design the mixer so that an optimum cancellation of unwanted frequency components on each of the three frequency chains can be achieved.

12.3 RF and dc Power Profile of the 2 kW Transmitter

Table 12-I indicates the estimated RF and dc power requirements for each section of the transmitter. It is assumed that:

1. Combiner-divider networks have 95% efficiency,
2. 3 dB hybrids have 97% efficiency,
3. Basic amplifiers have 8 dB gain with 75 W RF output 45 V B+ level and 70% dc-to-RF efficiency.

The sections are sequentially listed from the high RF output power level (i.e., required power for transmission) to the low end (i.e., oscillator).

12.4 Circuit Information

It is obvious that some of the circuitry designed for the previous 650 W transmitter may be useful in the present 2 kW version. With the exception of the 70 MHz and 80 MHz frequency generators, the circuitry for the low-level power remains basically unchanged (see Fig. 12-2, drawing no. 106-615). No major circuit modifications except broadbanding, which is present at the output of the 2X2N4128 saturated stages, are introduced up to the 25 W level.

Generation of broadbanded higher RF power by the use of ITT 3TE225 transistors and new broadband matching and paralleling techniques makes the high

Table 12-I

DC to RF conversion table

for the different sections of the transmitter.

Quantity	Section Description	RF Input Power (W)	RF Output Fower (W)	n = RFout / DCin (%)	RF Input Power (W)	B+ (V)	Idc (A)
	Antenna (assuming no losses)	2200	2200				
1	4-way Power Combiner (HPN)	2320					
32	Paralleled Basic Amplifiers (8 b·sic quads x 4 basic amplifiers/quad)		2400	70	3430	45	76.5
4	3dB Hybrid Power Dividers	400	384				
1	4-way Power Divider (LPN)	420					
1	3dB Hybrid Power Combiner	430					
6	Paralleled Basic Amplifiers	72	450	70	645	45	14.3
1	3dB Hybrid Power Divider	78	76				
1	3dB Hybrid Power Combiner		145				
2	Paralleled Basic Amplifiers	24	150	70	214	45	4.76
1	3dB Hybrid Power Divider	25					
	The 45V section of the transmitter has the following features:	25	2200	51.4	4289	45	≈96
	The 30V section of the transmitter consisting of 2x2N2219 and 2x2N4128 has the following features:	0.03	20	25	80	30	≈2.76
	The 10V sections of the transmitter consume a very small amount of power compared to the 30V and 45V sections. Therefore, they don't affect the overall efficiency of the system.				Max. 1	10	0.1
	2KW Transmitter Data		2200	50.5	4370		

RF power section of the 2 kW transmitter unique.

12.4.1 5 MHz Crystal Oscillator

The following block diagram briefly explains the theory of oscillators.

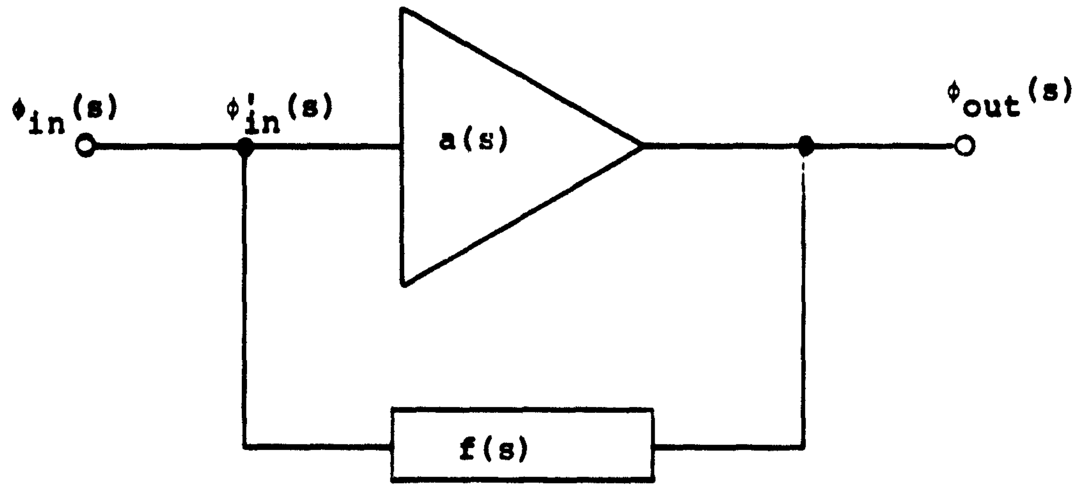

a(s) and f(s) are the network functions of both the active and passive networks. a(s) is the forward transmission; f(s) is the feedback network. $\phi(s)$ represents the Laplace transform of the signal, which can be either a voltage or a current.

The following equations can be written:

$$\phi_{out}(s) = a(s)\ \phi'_{in}(s)$$

$$\phi'_{in}(s) = \phi_{in}(s) + \phi_{out}(s) \cdot f(s)$$

The overall gain of the system is:

$$A(s) = \frac{\phi_{out}(s)}{\phi_{in}(s)} = \frac{a(s)}{1 - a(s)\,f(s)} \qquad (12.3)$$

Oscillations take place when $A(s) = \infty$

$a(s)\,f(s) = 1$ therefore,

$|a(s)\,f(s)| = 1$ and,

angle $a(s)\,f(s) = 0^{\circ}$ or 360°

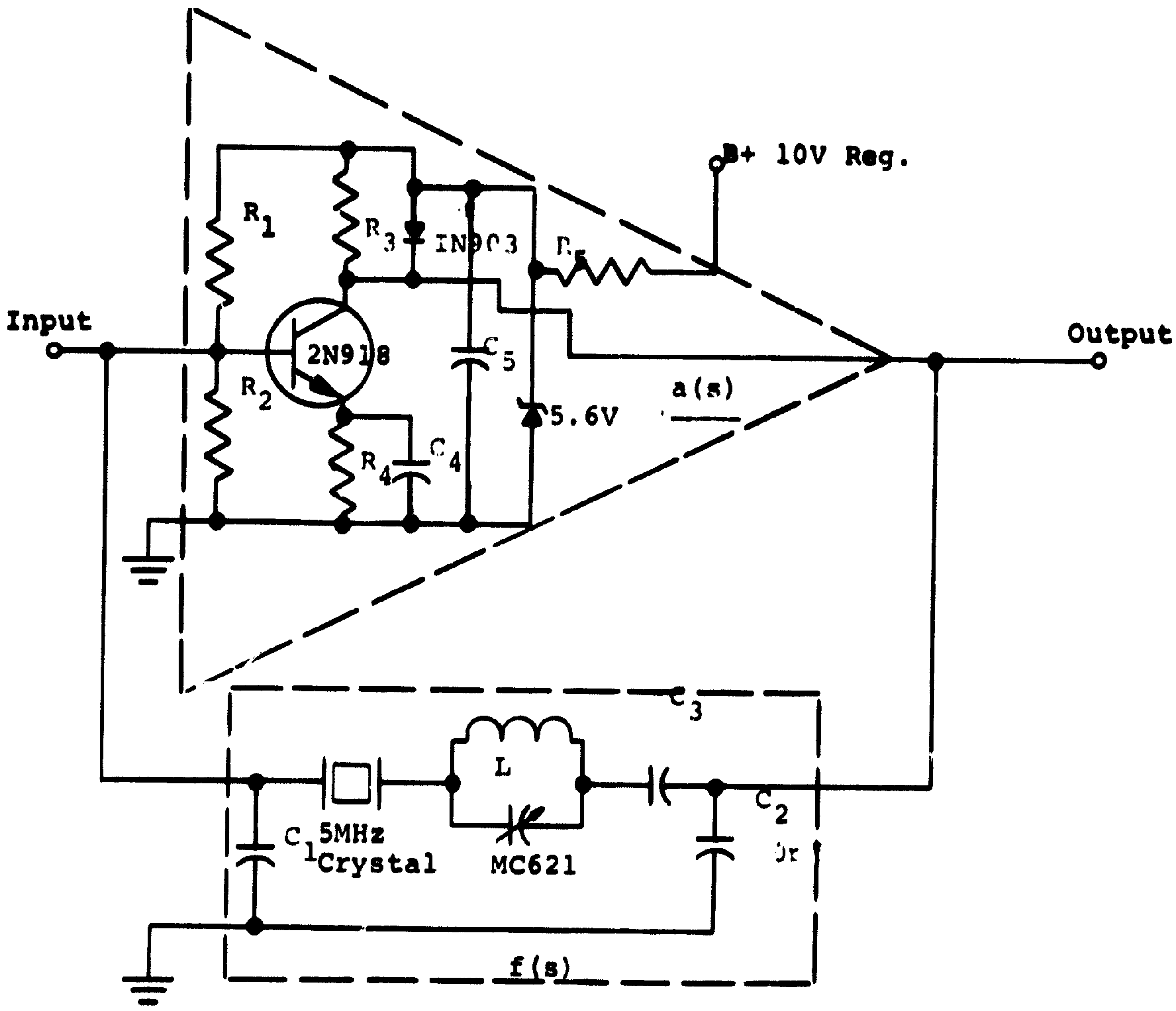

Fig. 12-5 5 MHz crystal oscillator.

Figure 12-5 shows the circuit of the 5 MHz crystal oscillator designed according to the principles previously presented. The variable capacitor MC621 in the f(s) passive circuitry provides an adjustment in frequency over a range of approximately 20 ppm. Frequency variations with temperature are limited to 30 ppm by the crystal. Double regulation (10V reg. and 5.6V zener diode) is used to dc-bias the oscillator, thereby minimizing frequency shifts caused by dc voltage variations.

12.4.2 ×15 Frequency Multiplier

The device used to achieve frequency multiplication is a step-recovery diode (Fig. 12-6) which has in the off condition an abrupt recovery time (see the characteristic curves Fig. 12-7.).

According to the Fourier analysis of periodic functions the output of the step-recovery diode contains several harmonics of 5 MHz.

The use of the 2 dB pad at the input helps to stabilize the operation of the multiplier with temperature variations. The series-resonant circuit, L_1 C_1, provides a clean 5 MHz input to the diode which is operated far below its cut off frequency. The operating point of the diode is defined by R_b. At the output, L_2, C_2, L_3, C_3 and C_4 constitute filtering and matching networks for 75 MHz.

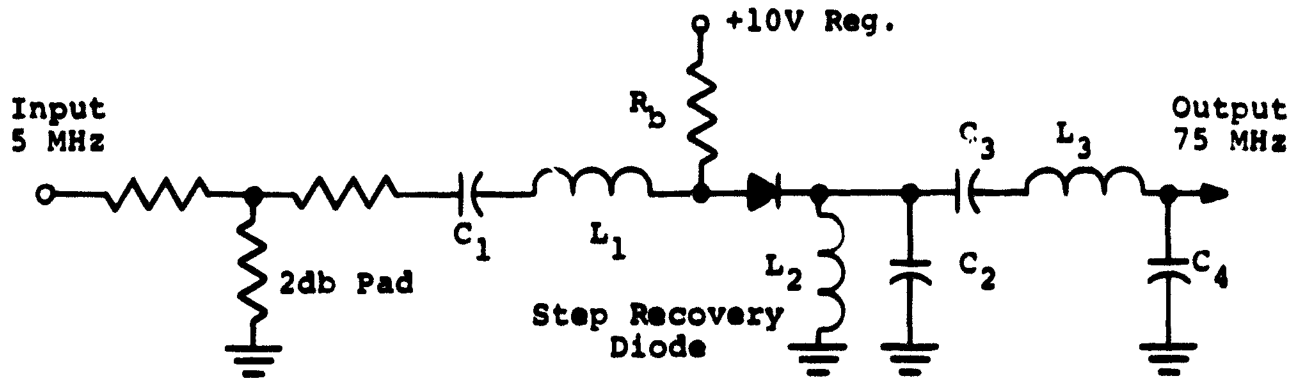

Fig. 12-6 5 MHz to 75 MHz frequency multiplier.

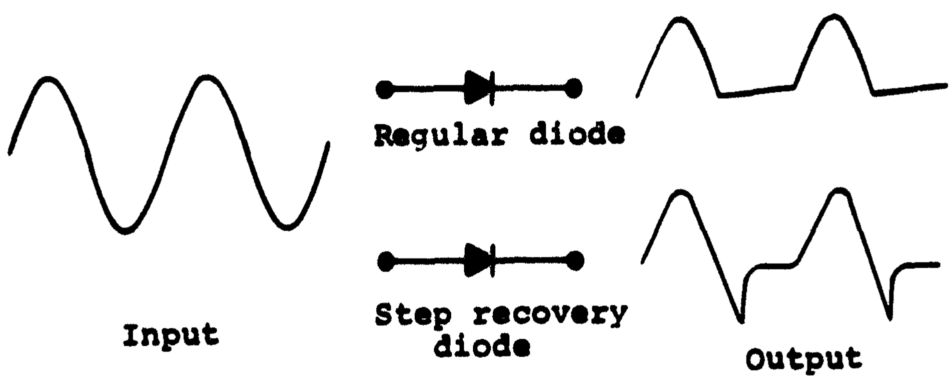

Fig. 12-7 Comparison of the output waveforms of regular and step recovery diodes.

12.4.3 10V Bias Keying Network

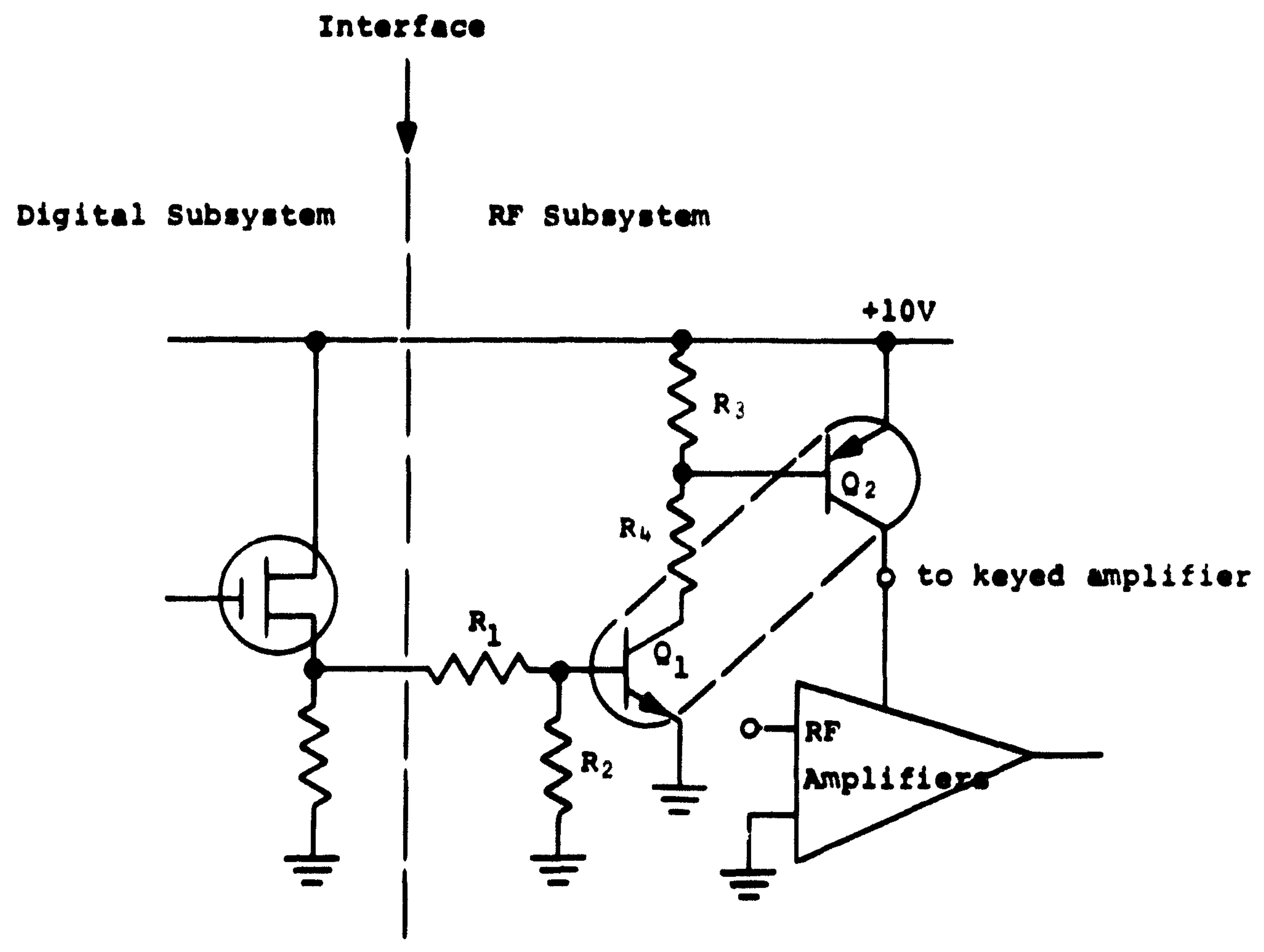

Fig. 12-8 Keying network.

R_1 through R_4 are biasing resistors determining the simultaneous switching levels of both switching transistors Q_1 and Q_2. A positive pulse fed into the input of the keying network turns on Q_1 and Q_2 and causes a 10V bias level to appear at the keyed RF amplifiers.

12.4.4 N-Way Power Divider or Combiner Networks

Power-divider or -combiner networks differ, as their names indicate, only in their application. Both could be represented by the same black box with a one-port on one side and an N-port on the other. In the case of a divider network, for example, power is fed into the box through the single port, and an N-way power division is obtained at the output.

This type of network requires the following features:

1. For the designed frequency, it must introduce the same phase shift for all N-ways. (Equiphase signals)
2. For the designed frequency, all the N-ways must be equally loaded. (Equiamplitude signals)
3. The network must be applicable for any value of N. (N could be odd or even)
4. In order to minimize the effect of errors (short circuit, mismatch, open circuit) from one channel to the other, a good isolation between the individual N-way ports is necessary.
5. It must have a low insertion loss.

Figure 12-9 shows a network designed with 95% efficiency and a minimum isolation of -30 dB.

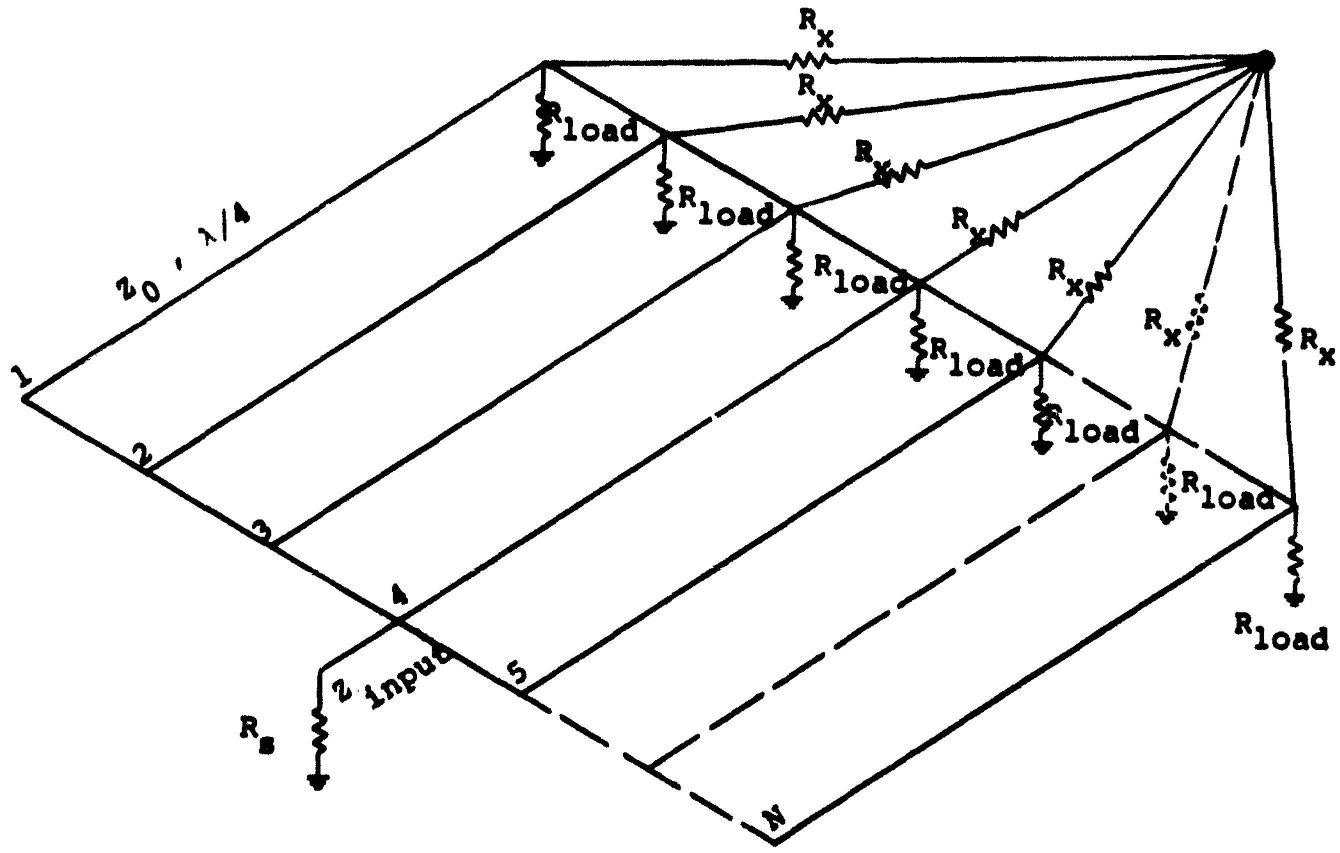

Fig. 12-9 N-way power-divider or combiner networks.

The transmission lines have a characteristic impedance of Z_o and a length of $\lambda/4$. They can be synthesized with lumped LC networks in highpass (HPN) or low pass (LPN) configurations. The analytical relations are:

$$R_x = R_{load}$$

$$Z_o = \sqrt{N}\, R_{load}$$

$$R_s = Z_{input} = \frac{\frac{Z_o^2}{R_{load}}}{N} = R_{load}$$

12.4.5 Basic Amplifiers

Some of the major factors which prescribe limitations in designing a spacecraft transmitter are the following:

1. Weight: The weight of the transmitter must be held to a minimum because of the limited payload capabilities of the launch vehicle used.
2. Volume: In order to locate all the electronic subsystems in the volume available in the spacecraft, the circuitry has to be as miniaturized as possible.
3. Power: Regardless of these physical limitations, the transmitter is required to deliver the maximum possible high-frequency output power.

These arguments justify the importance of the curves RF power out vs frequency (Fig. 12-10) for different types of transistors, and the selection of ITT 3TE225 devices as typical for application in the basic amplifier.

Besides their high RF-output power capability, the 3TE225's assure a high dc-to-RF efficiency. This feature has two advantages. First, for a given RF output power, the selected transistors reduce the high dc power requirement. Second, due to the smaller internal power dissipation of the device, an increase in its longevity is anticipated. Several tests and measurements on these devices show the possibility of achieving efficiencies of 80% in a large signal, class C, pulsed operation.

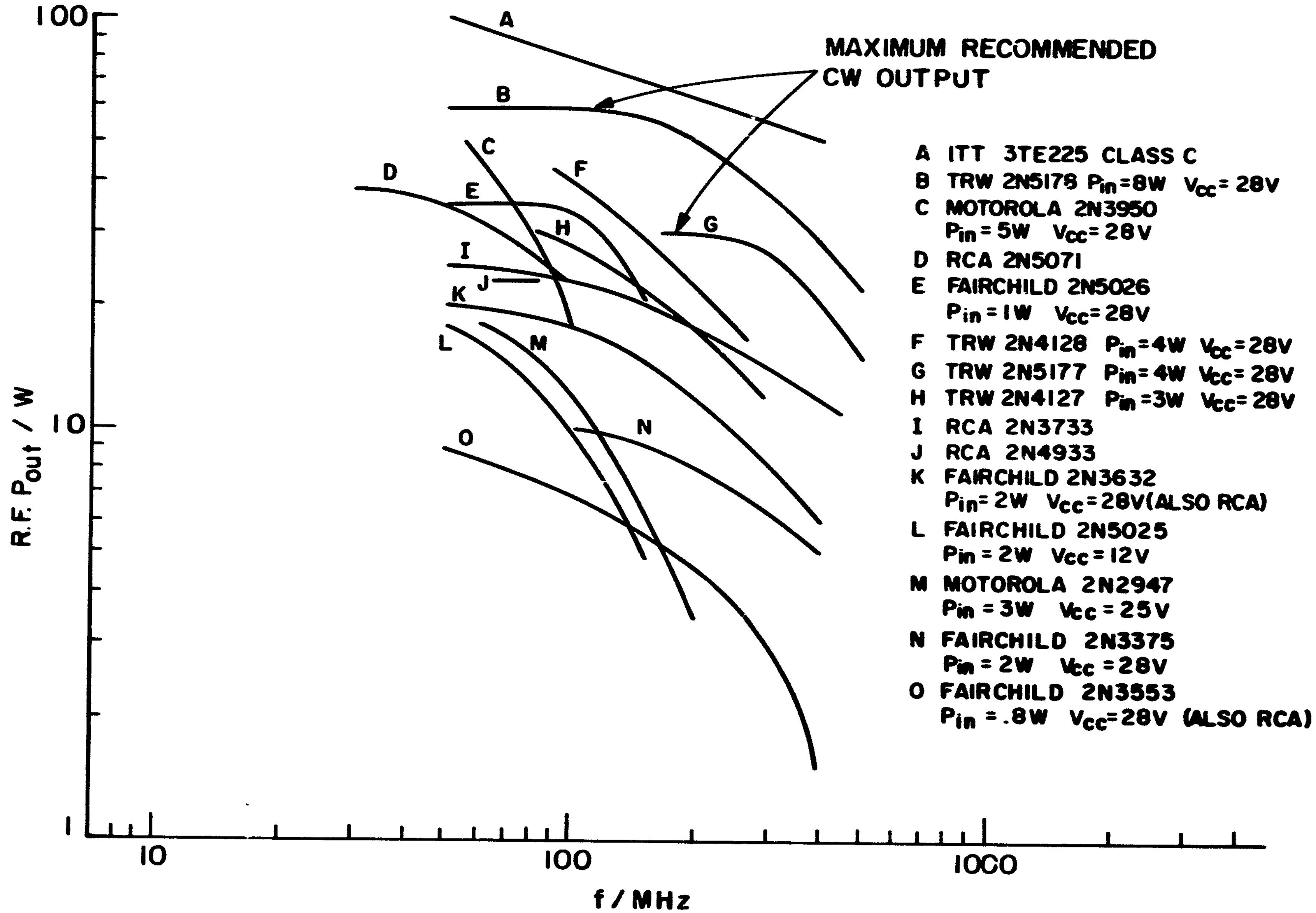

Fig. 12-10 Transistor power vs frequency curves.

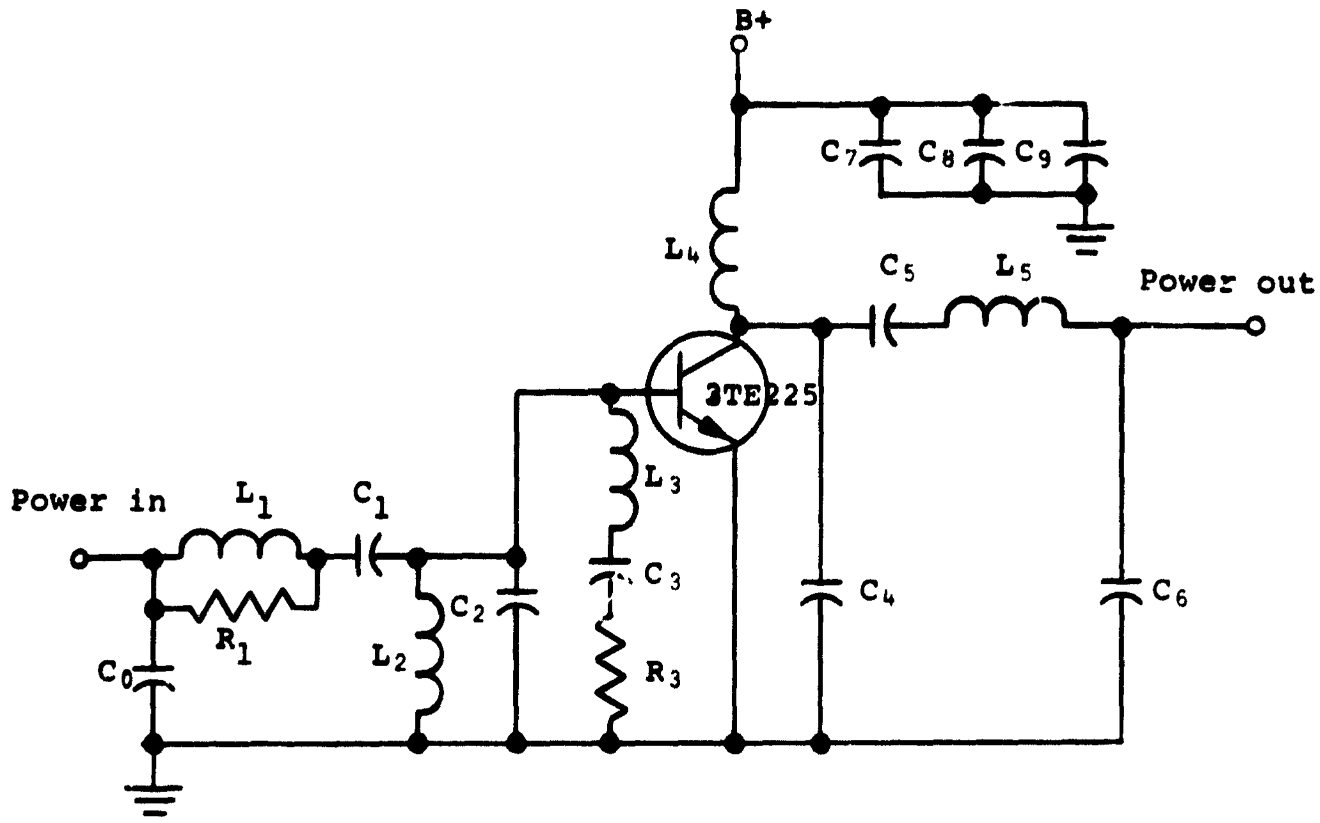

Fig. 12-11 Basic amplifier.

Figure 12-11 represents the circuitry of the basic broadband amplifier. The components C_0, R_1, L_1, C_1, L_2, C_2 constitute a low Q and, therefore, a broadband matching network. Matching is done at 50Ω.

The components R_3, L_3, C_3 constitute a notching filter designed for the center frequency. Its function is to reduce the level of the RF-output power of the basic amplifier at the center frequency to the power levels at the sideband frequencies. The 75 MHz resonating output network is mainly constituted by L_4, C_4 and the output capacitance of the device. C_5, L_5, C_6 represent the matching network at the output. In addition, C_7, C_8, C_9 are bypass capacitors and C_1, C_5 also have dc blocking functions.

The design goal is to obtain, with amplifier circuit under class C operation, a pulsed output power of 75 W with a B+ = 45 V, and dc-to-RF efficiency of 70 percent.

12.4.6 3 dB Quadrature Hybrid Circuits[1]

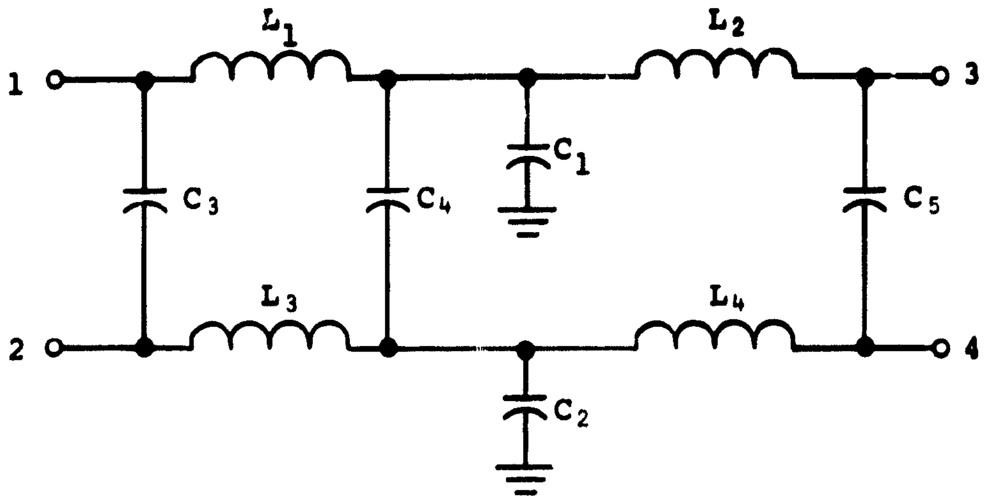

Fig. 12-12 3 dB quadrature hybrid.

The lumped circuit realization of the quadrature hybrid is given in Fig. 12-12. In the figure all the inductances are equal to a value L, where L is given by

$$L = \frac{Z_o}{\omega} \tag{12.4}$$

and Z_0 is the characteristic impedance of the transmission line system in which the coupler is used and ω is the design frequency. The capacitors C_1 and C_2 are equal, and related to the characteristic impedance by

$$Z_o = \frac{1}{\omega C_1} = \frac{1}{\omega C_2} \tag{12.5}$$

The capacitors C_3, C_4 and C_5 are equal to $\frac{C_1}{2}$.

The operation of the circuit is outlined below. If points 2, 3, and 4 are terminated to ground by the characteristic impendance Z_o, and the circuit driven by a matched generator at point 1 to ground, power is divided equally and without loss between the loads connected at points 3 and 4. Point 2 is decoupled. On the other hand, if point 2 is driven, point 1 is decoupled, but again power is divided equally between the loads connected at points 3 and 4. Since the circuit is symmetric, points 3 or 4 may be driven with similar power-division characteristics. In any case, the voltages at the output points are always 90^o out of phase.

The design of the circuit is based on a scattering matrix representation of the coupler. The components L_1, L_2 and C_1 form an equivalent circuit of a quarter-wavelength transmission line of characteristic impedance Z_o. The components L_3, L_4 and C_2 form an identical circuit. If points 1 and 2 are driven in phase, an equivalent circuit of a quarter-wavelength line of characteristic impedance $Z_o/2$ results. Now, if points 1 and 2 are driven 180^o

out of phase, inductors L_1, L_3, and capacitors C_3, C_4 form the equivalent circuit of a quarter-wavelength transmission line of characteristic impedance $2Z_0$. Under this driving condition, there is a similar circuit formed by inductors L_2, L_4 and capacitors C_5 and the series combination of C_1, C_2. Since these two identical quarter-wavelength circuits are in cascade, the total electrical length under this out-of-phase excitation is 180°. By satisfying the above impedance and phase conditions, all of the requirements (at a single frequency) for a 3 dB quadrature hybrid have been satisfied.

An experimental circuit was constructed for a center frequency of 75 MHz, and the observed insertion loss was less than 1 dB, the phase angle between the equal outputs was approximately 90°, and the output at the decoupled port was 20 dB below the input. A usable bandwidth of 20 MHz was observed, and the input VSWR was 1.1.

12.5 Construction Techniques

In order to build a transmitter capable of withstanding the shock and vibration of the launch, to keep the individual stages or sections isolated from each other, both thermally and electrically, and to prevent oscillation and reduce spurious output signals, the approach generally used in the past has been to build the individual stages into compartments which have been milled out of a large piece of metal such as brass, aluminum, magnesium or some other suitable material (point-to-point component mounting), then to put covers on the top and bottom to shield these circuits from the next black box.

The other alternative has been to build the transmitter on one or more printed circuit boards provided with shields mounted in appropriate places, then to mount these boards into boxes, and, in some cases, to foam-encapsulate the transmitter, then readjust the many variable components to compensate for the effects of the foam and the proximity of the box. Either of these methods, while proven reliable and effective, is satisfactory for a transmitter consisting of a dozen or so stages, but rapidly becomes impractical for space application because of size and weight considerations.

Consider for a moment a 2200 W transmitter consisting of 55 stages starting with a precision oscillator producing a few μW, built by milling out compartments from a block of aluminum. It is not difficult to imagine the remaining aluminum, with no RF parts included, weighing more than our entire transmitter, not to mention the volume taken up by a transmitter that approaches the total volume of our spacecraft. If, instead, printed circuit boards with strategically-located shields were used and then mounted in boxes, an improvement would be achieved; but the configuration would still be too large and too heavy for this application. Clearly, a different approach is needed.

The solution proposed is to use the printed circuit boards themselves as shields between the various circuits. When laying out the printed circuit boards, which are 5.14" x 1.98" cards that mate with the approximately 5" x 5" vertical member in each plug, care is taken to keep all printed lines on one side (component side) of the board, while the paths of ground current (input and output) of the stage are isolated as much as possible, both to reduce magnetic coupling between inductors in the input and output by physical placement and/or orientation and to keep lead lengths as short as possible. Further, as much unbroken copper as possible is left on both sides of the printed board, and this area is connected to ground potential. (Enough copper is etched away around printed wires and terminals to make the necessary connections, and the rest is left.) The result is that we have left about 80% to 90% of the copper on the reverse side of the board and a large amount on the component side to act as a shield from the circuit below and provide low-inductance ground paths. The vertical member upon which the circuit boards are stacked, one above the other, forms an effective shield from the circuit on the adjacent side of the vertical member. The result of this stacking leaves us with a pair of compartments between each pair of printed circuit boards, isolated from its neighboring compartment by the ground plane on its own reverse side, the ground plane on the board above, the vertical member, the side wall of the compartment, the end wall of the compartment, and the compartment shield. The 34 such compartments within which the circuits are constructed give excellent isolation between stages. This type of structure provides a common electrical ground for all cards, serves as a heat sink, and provides mechanical strength for launch environment. (Fig. 12-13)

This construction technique, coupled with the fact that we have reduced the number of variable components (which are heavy and large) to the bare minimum (one variable capacitor in the entire system) by careful measurement and substitution methods, taking into account the stray capacitance and lead inductances of components, printed lines and terminals, therefore makes the circuit boards an integral part of the RF circuit (an accomplishment in itself) and has permitted packing of VHF circuits much in the manner in which on would package low-frequency circuits. Further, we are able to construct these circuits with components out of stock, with a minimum of selection and with minor trimming to compensate for gain and phase variations due to device variations.

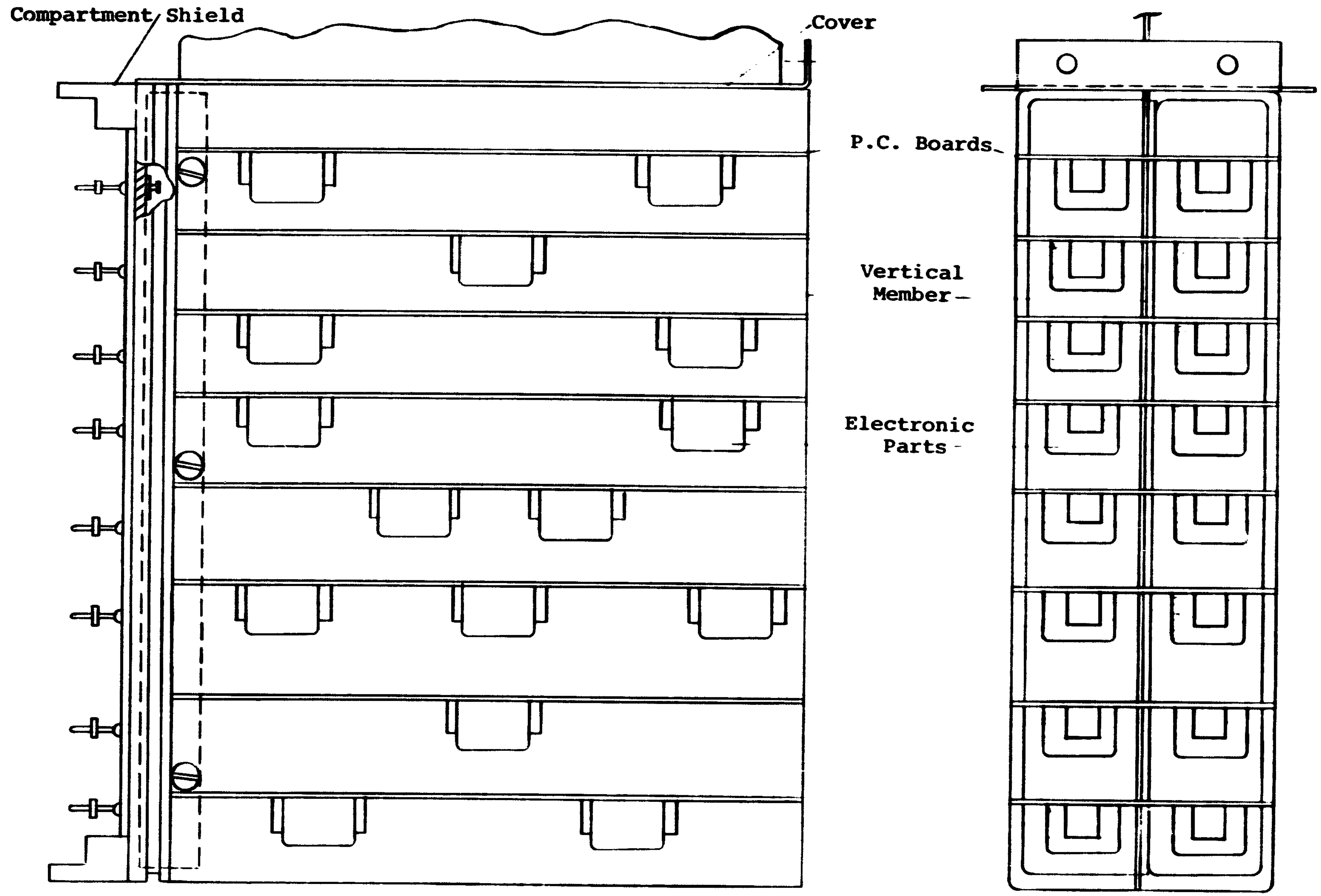

Fig. 12-13 RF circuit packaging.

By the use of the above techniques we have effected a substantial reduction in the overall size and weight requirements for the transmitter, and at the same time preserved the mechanical integrity of the spacecraft.

12.6 The 50-Watt Beacon Transmitter

Located in the rear section of the Hub is an auxilliary 50 W, battery-powered transmitter which provides a tracking beacon and pertinent telemetry during solar acquisition of the spacecraft.

The pulsed 75 MHz signal provided by this beacon transmitter is encoded by pulse-width modulation to provide orientation data from the aspect sensor, along with selected deployment, voltage, and temperature information.

The beacon transmitter is shown in Fig. 12-14a and consists of one class A stage and three cascaded class C amplifiers, with the final stage producing 50 watts. The drive signal for the beacon is provided by the same oscillator and multiplier which drives the main transmitter, and its output signal is radiated by one pair of sails.

A single-pole, single-throw, solid-state switch, operated by a digital command, is provided to prevent damage to the beacon transmitter's final amplifier due to voltage induced in the sail by the main transmitting antenna. The switch has an isolation of 45 dB, and an insertion loss of less than 0.2 dB, and is connected between the beacon final amplifier and the sails.

The switch-control circuitry is shown in Fig. 12-14b. The switch passes an RF signal when zero voltage is applied to the base of Q_1; then transistors Q_1, Q_2, Q_3 are cut off, leaving the control diode back-biased at -300 volts. In this condition, the beacon signal is transmitted. If, on the contrary, a positive voltage is applied to the base of Q_1, transistors Q_1, Q_2 and Q_3 conduct from the 10 V supply, forward biasing the control diode, and thus disconnecting the sails from the beacon transmitter.

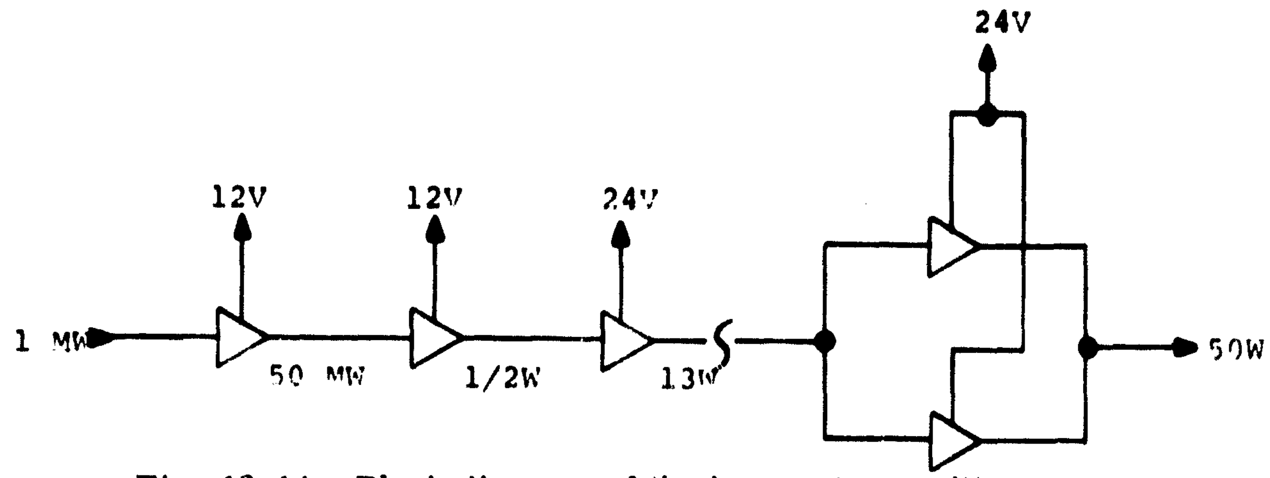

Fig. 12-14a Block diagram of the beacon transmitter.

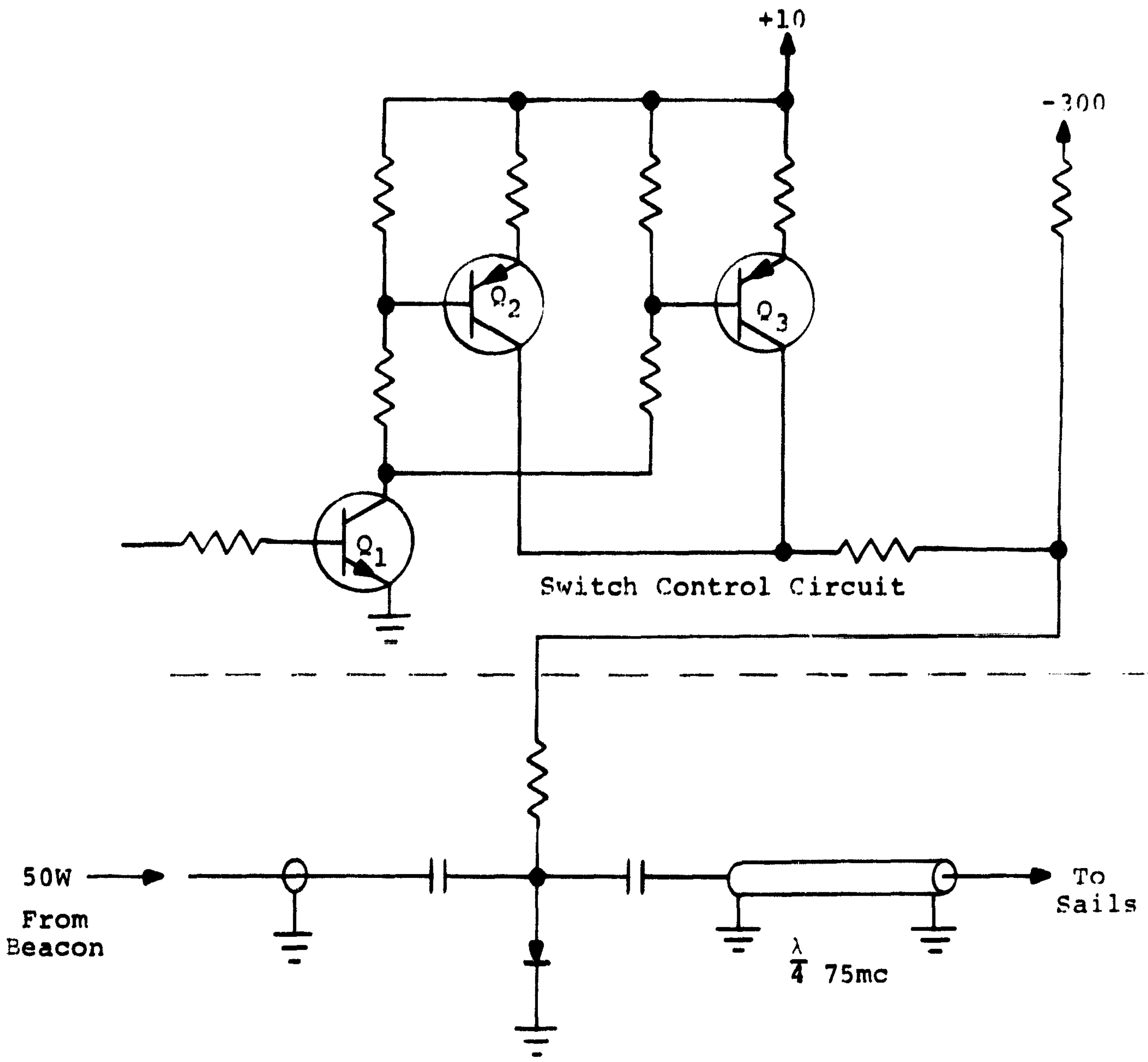

Fig. 12-14b Beacon antenna switch.

Table 12-II

Basic parameters of beacon transmitter.

Stage	dc Supply	Drive Level	Output	η	Trans-ister Type	Class	Gain
First	12V	1 mW	50 mW	40%	2N918	A	17.0 dB
2nd	12V	50 mW	1/2 W	60%	2N3924	C	10.0 dB
3rd	24V	1/2 W	13 W	70%	2N4128	C	14.0 dB
4th	24V	3.6 W	50 W	70%	Pair 3TE225	C	11.5 dB
Switch	Insertion Loss	Iso-lation	Forward Bias Current		Reverse Bias Voltage		
	< 0.2 dB	45 dB	20 ma		-300V		

12.7 The Spacecraft Integrated Antenna System

12.7.1 Introduction

There are several alternatives for the spacecraft antenna system, varying in complexity from a simple monopole to an elaborate array, each with its own degree of complexity in deployment and feed system. For this initial launch, however, it is desirable to use something consistent with gain and pattern requirements of the experiment, and as simple in deployment and feed as possible.

Figure 12-15 represents the Sunblazer spacecraft with the antenna systems under consideration. Radiation of the pulsed 2kW main transmitter signal at the 70 MHz, 75 MHz and 80 MHz frequencies is achieved by a pair of rods, each with a length L, mounted perpendicular to the spin axis on each side of the spacecraft solar-cell platform. The separation between these two links of the dipole thus formed is shown as 2d, which is equal to the diameter of the platform. The 75 MHz, 50 W beacon-pulsed signals are transmitted from a pair of sails which act as dipoles, but whose major function is to stabilize the dynamic motion of the spacecraft in conjunction with another set of sails mounted in an orthogonal axis. In the deployed configuration, the sails are canted forward by an angle of 70° with respect to the spin axis. Furthermore, sighting along the spin axis shows that any pair of sails to be used as the beacon antenna is displaced from the main transmitter antenna by an angle of 45°.

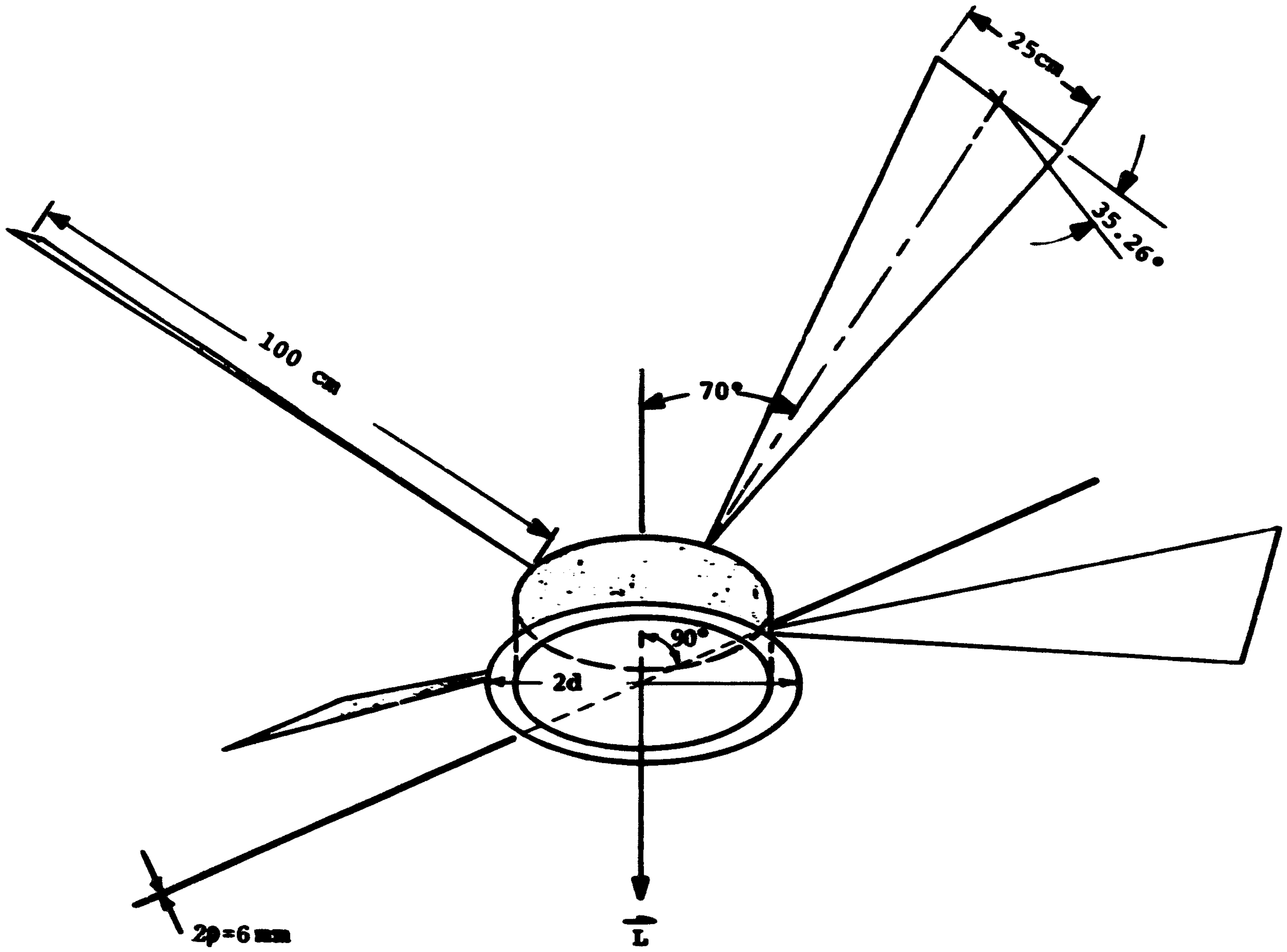

Fig. 12-15 Spacecraft projection.

12.7.2 Main Transmitter Antenna

There are two problems of major importance:

1. Matching each antenna to its transmitter.
2. Antenna patterns over the 10 MHz bandwidth.

These problems require the calculation of the input impedance $Z_s = R_s + jX_s$ of the antenna, the $\vec{E}$-field, $\vec{H}$-field, and $\vec{S}$ pattern analysis over the 10 MHz bandwidth, for different rod lengths L and the given spacing 2d.

Maxwell's equations for electromagnetic waves varying sinusoidally in time are

$$\nabla \times \vec{E} = -j\omega\mu\vec{H} \qquad \text{(a)}$$

$$\nabla \times \vec{H} = \vec{J} + j\omega\epsilon\vec{E} \qquad \text{(b)}$$

$$\nabla \cdot \vec{H} = 0 \qquad \text{(c)}$$

$$\nabla \cdot \vec{E} = \frac{\rho}{\epsilon} \qquad \text{(d)} \qquad (12.6)$$

Here any vector $\vec{V} = \vec{V}(\vec{r}_o, t) = \text{Re}\left[\underline{V}e^{j(\omega t - kr_o)}\right]$

$$\text{and} \qquad \vec{V} = \underline{V}e^{-jkr_o} \qquad (12.7)$$

The electric field $\vec{E}$ and the magnetic field $\vec{H}$ at each point in space are given by the solutions of Eq (12.6).

The solutions are

$$\vec{H} = \nabla \times \vec{A}$$

$$\vec{E} = -j\omega\mu\vec{A} - \nabla\phi \qquad (12.8)$$

where the retarded vector potential is defined as

$$\vec{A}(x, y, z) = \frac{1}{4\pi} \int_{V'} \frac{\vec{J}(x', y', z')e^{-jkr}}{r} dV' \qquad (12.9a)$$

and the retarded electric potential is defined as

$$\phi(x, y, z) = \frac{1}{4\pi\epsilon}\int_{V'} \frac{\rho(x', y', z')e^{-jkr}}{r}\, dV' \tag{12.9b}$$

One has to remark here that ϕ can be obtained from $\overleftrightarrow{A}$ by using the Lorentz condition, i.e.:

$$\phi = \frac{-1}{j\omega\epsilon}\nabla\cdot\overleftrightarrow{A} \tag{12.9c}$$

In calculating the solution for an antenna with a given current distribution, one assumes it is composed of several very short dipoles of different constant-current distributions. The scalar and vector potentials at any point in space, due to a very short dipole of length 2ℓ and constant-current distribution I_o located at the origin of a coordinate system along the z-axis, are given by the following equations:

$$\phi = \frac{2\ell I_o}{j\omega 4\pi\epsilon}\left[j\frac{\omega}{cR} + \frac{1}{R^2}\right]\cos\theta\, e^{-jkR} \tag{12.10a}$$

$$\overleftrightarrow{A} = \frac{2\ell I_o}{4\pi}\,\frac{e^{-jkR}}{R}\,\hat{z} = A_z\,\hat{z} \tag{12.10b}$$

where $\vec{R}$ is the radius vector from the origin of the coordinate system to the point in space, θ is the angle between the positive z-axis and the vector $\vec{R}$,

$$c = \frac{1}{\sqrt{\mu_o\epsilon_o}} = 3 \times 10^{10}\ \frac{cm}{sec},$$

and $$k = \frac{2\pi}{\lambda}\ .$$

Consider the dipole system represented in Fig. 12-16. The current distribution is given by

$$I_z(z') = I_o \sin k(h-|z'|) \tag{12.11}$$

For any point in space, Eq (12.10) may now be written for an incremental dipole of length dz':

$$d\phi = \left\{\frac{dz'\, I_o \sin k\,(h-z')}{j\omega 4\pi\epsilon}\left[\frac{j\omega}{cr_1} + \frac{1}{r_1^2}\right]\frac{z-z'}{r_1}\,e^{-jkr_1}\right. \tag{12.12a}$$

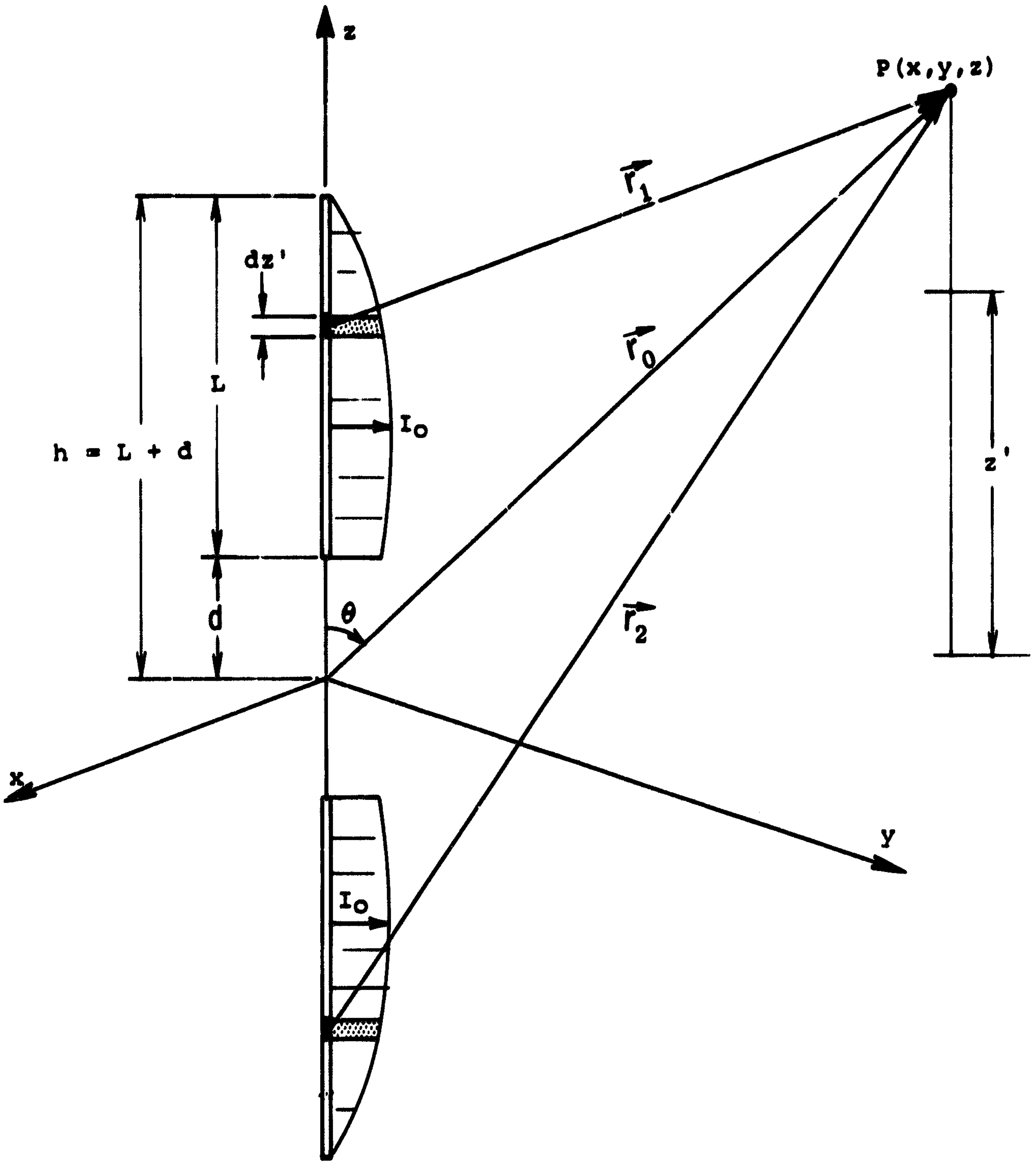

Fig. 12-16 Determination of ϕ and A for any point in space.

$$+ \frac{dz' I_o \sin k(h+z')}{j\omega 4\pi\epsilon} \left[\frac{j\omega}{c r_2} + \frac{1}{r_2^2}\right] \frac{z+z'}{r_2} e^{-jkr_2} \Bigg\}$$

$$d\overleftrightarrow{A} = \frac{dz' I_o \sin k(h-z')}{4\pi} \frac{e^{-jkr_1}}{r_1} + \frac{dz' I_o \sin k(h+z')}{4\pi} \frac{e^{-jkr_2}}{r_2} \qquad (12.12b)$$

By making the assumption that r_1, r_2, $r_o >> 2L + 2d$, one obtains the following simplified expressions:

$$r_{1,2} = r_o \mp z' \cos\theta \qquad (12.13)$$

$$\frac{z-z'}{r_1} = \frac{z+z'}{r_2} = \frac{z}{r_o} = \cos\theta$$

Equations (12.12) and (12.13) together give the expressions of the scalar and vector potentials for a separated dipole:

$$\phi = \frac{I_o \cos\theta}{4\pi\epsilon c} \frac{e^{-jkr_o}}{r_o} \left[\int_d^h \sin k(h-z') e^{jkz'\cos\theta} dz'\right.$$

$$\left. + \int_{-h}^{-d} \sin k(h+z') e^{jkz'\cos\theta} dz'\right]$$

$$+ \frac{I_o \cos\theta}{4\pi\epsilon j\omega} \frac{e^{-jkr_o}}{r_o^2} \left[\int_d^h \sin k(h-z') e^{jkz'\cos\theta} dz'\right.$$

$$\left. + \int_{-h}^{-d} \sin k(h+z') e^{jkz'\cos\theta} dz'\right]$$

$$\overleftrightarrow{A} = \frac{I_o}{4\pi} \frac{e^{-jkr_o}}{r_o} \left[\int_d^h \sin k(h-z') e^{jkz'\cos\theta} dz'\right.$$

$$\left. + \int_{-h}^{-d} \sin k(h+z') e^{jkz'\cos\theta} dz'\right]$$

and finally

$$\phi\ (\vec{r}_o) = \frac{I_o}{4\pi\epsilon}\ \cos\theta\ F(\theta, h, d, \lambda)\ \left[\frac{1}{cr_o} + \frac{1}{j\omega\, r_o^2}\right] e^{-jkr_o} \tag{12.14a}$$

$$\overleftrightarrow{A}(\vec{r}_o) = \frac{I_o}{4\pi}\ F(\theta, h, d, \lambda)\ \frac{e^{-jkr_o}}{r_o}\ \hat{z} \tag{12.14b}$$

where

$$F(\theta, h, d, \lambda) = \Big[2\Big\{\cos\left[kh\cos\theta\right] - \cos kL\cos\left[\kappa d\cos\theta\right]$$

$$+ \cos\theta\sin kL\sin\left[kd\cos\theta\right]\Big\}\Big] \Big/ k\ \sin^2\theta \tag{12.14c}$$

Equations (12.8) and (12.14), solved for a spherical coordinate system, give the component values for the $\overleftrightarrow{E}$ and $\overleftrightarrow{H}$ fields:

$$H_{r_o}(r_o, \theta, \phi) = H_\theta(r_o, \theta, \phi) = 0,$$

$$H_\phi(r_o, \theta, \phi) = \frac{I_o}{4\pi}\sin\theta\left\{j\frac{k}{r_o}\ F(\theta, h, d, \lambda) - \frac{1}{r_o^2\sin\theta}\ \frac{\partial}{\partial\theta}\left[F(\theta, h, d, \lambda)\cos\theta\right]\right\} e^{-jkr_o}, \tag{12.15}$$

and

$$E_{r_o}(r_o, \theta, \phi) = \frac{I_o}{4\pi}\cos\theta\ F(\theta, h, d, \lambda)\left\{2\sqrt{\frac{\mu_o}{\epsilon_o}}\ \frac{1}{r_o^2} - \frac{2j}{\omega\epsilon r_o^3}\right\} e^{-jkr_o},$$

$$E_\theta(r_o, \theta, \phi) = \frac{I_o}{4\pi}\sin\theta\left\{\sqrt{\frac{\mu_o}{\epsilon_o}}\ j\frac{k}{r_o}\ F(\theta, h, d, \lambda) - \sqrt{\frac{\mu_o}{\epsilon_o}}\ \frac{1}{r_o^2\sin\theta}\ \frac{\partial}{\partial\theta}\left[F(\theta, h, d, \lambda)\cos\theta\right]\right.$$

$$\left. + \frac{j}{\omega\epsilon r_o^3}\ \frac{1}{\sin\theta}\ \frac{\partial}{\partial\theta}\left[F(\theta, h, d, \lambda)\cos\theta\right]\right\},$$

and

$$E_\phi(r_o, \theta, \phi) = 0. \tag{12.16}$$

The average power density is therefore given by

$$\overleftrightarrow{S}(r_o, \theta, \phi) = \frac{1}{2}(\overleftrightarrow{E} \times \overleftrightarrow{H}^*)\ .$$

Thus,

$$S_{r_o}(r_o, \theta, \phi) = \frac{I_o^2 \sin^2\theta}{32\pi^2} \left\{ \sqrt{\frac{\mu_o}{\epsilon_o}}\, k^2 \, \frac{F^2(\theta, h, d, \lambda)}{r_o^2} \right.$$

$$+ \left[\sqrt{\frac{\mu_o}{\epsilon_o}}\, \frac{1}{\sin\theta}\, \frac{\partial}{\partial\theta}\left[F(\theta, h, d, \lambda)\cos\theta\right]\right]\left[F(\theta, h, d, \lambda) + \frac{1}{\sin\theta}\, \frac{\partial}{\partial\theta}\left(F(\theta, h, d, \lambda)\cos\theta\right)\right]\frac{1}{r_o^4}$$

$$\left. - \frac{j}{\omega\epsilon r_o^5 \sin^2\theta}\left[\frac{\partial}{\partial\theta}\left(F(\theta, h, d, \lambda)\cos\theta\right)\right]^2 \right\} ,$$

$$S_\theta(r_o, \theta, \phi) = \frac{I_o^2 \sin\theta\cos\theta}{32\pi^2}\, F(\theta, h, d, \lambda) \left\{ j\sqrt{\frac{\mu_o}{\epsilon_o}}\, \frac{2k}{r_o^3}\, F(\theta, h, d, \lambda) \right.$$

$$+ 2\sqrt{\frac{\mu_o}{\epsilon_o}}\left[F(\theta, h, d, \lambda) + \frac{1}{\sin\theta}\, \frac{\partial}{\partial\theta}\left(F(\theta, h, d, \lambda)\cos\theta\right)\right]\frac{1}{r_o^4}$$

$$\left. - \frac{2j}{\omega\epsilon r_o^5 \sin\theta}\, \frac{\partial}{\partial\theta}\left(F(\theta, h, d, \lambda)\cos\theta\right) \right\} ,$$

and

$$S_\phi(r_o, \theta, \phi) = 0 . \tag{12.17}$$

Considering only the far fields one obtaines from Eq (12.15), (12.16) and (12.17)

$$H_\phi(r_o, \theta, \phi) = \frac{I_o}{4\pi}\sin\theta\, j\, \frac{k}{r_o}\, F(\theta, d, h, \lambda) , \tag{12.18a}$$

$$E_\theta(r_o, \theta, \phi) = \frac{I_o}{4\pi} \sin\theta \sqrt{\frac{\mu_o}{\epsilon_o}}\, j\, \frac{k}{r_o} F(\theta, h, d, \lambda) \;, \qquad (12.18b)$$

and

$$S_{r_o}(r_o, \theta, \phi) = \frac{I_o^2 \sin^2\theta}{32\pi^2} \sqrt{\frac{\mu_o}{\epsilon_o}}\, \frac{k^2}{r_o^2}\, F^2(\theta, h, d, \lambda) \;. \qquad (12.18c)$$

Normalizing these to the peak value of the beam for a tuned dipole without separation, i.e. for

$$\theta = 90^\circ, \; 2d = 0, \; kL = \frac{\pi}{2}, \; h = L \,,$$

one obtains the following normalized quantities:

$$H_{\phi n}(r_o, \theta, \phi) = \frac{\sin\theta\, F(\theta, h, d, \lambda)}{F(\theta = 90^\circ, h = \frac{\lambda}{4}, 2d = 0, \lambda)} \quad \text{(in } \theta \text{ direction)} \;;$$

$$E_{\theta n}(r_o, \theta, \phi) = \frac{\sin\theta\, F(\theta, h, d, \lambda)}{F(\theta = 90^\circ, h = \frac{\lambda}{4}, 2d = 0, \lambda)} \quad \text{(in } \theta \text{ direction)} \;;$$

and

$$S_{r_o n}(r_o, \theta, \phi) = \frac{\sin^2\theta\, F^2(\theta, h, d, \lambda)}{F^2(\theta = 90^\circ, h = \frac{\lambda}{4}, 2d = 0, \lambda)} \quad \text{(in } r_o \text{ direction)} \;. \qquad (12.19)$$

Figures 12-17a, 12-17b, 12-17c, are plots of Eq (12.19) in polar coordinates for the special case of the antenna stem length of L = 100 cm ($\frac{\lambda}{4}$ at 75 MHz). The cases of 70 MHz, 75 MHz, and 80 MHz frequencies for the separation 2d = 0 and 2d = 46 cm are considered, and the electric field, magnetic field, and power density patterns are plotted.

In addition, in Fig. 12-18 an extreme case of the spacing 2d = λ = 400 cm is considered, showing effectively the variation of the patterns as a function of 2d.

The next important quantity which varies as a function of frequency and

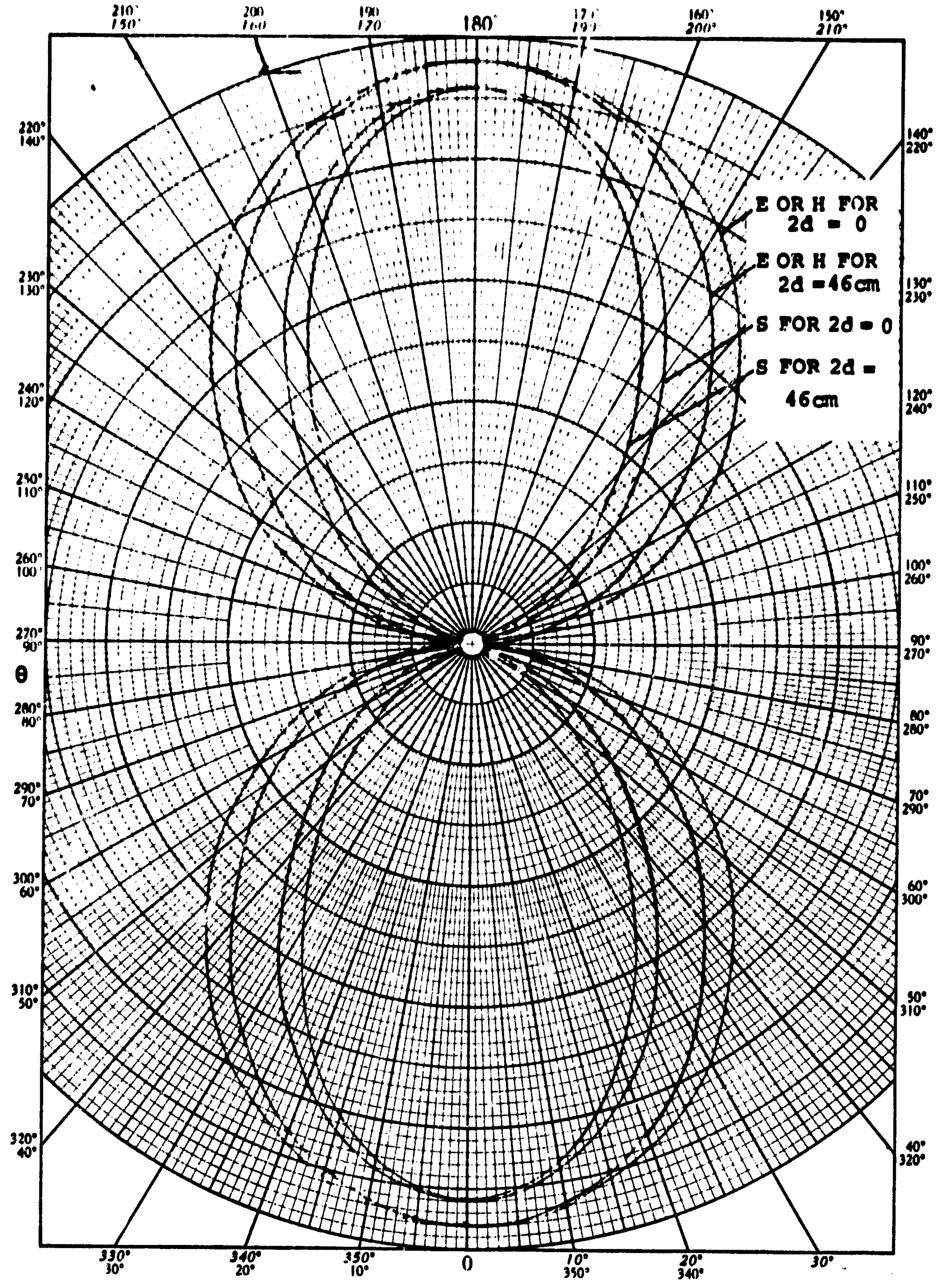

Fig. 12-17a Normalized |$\vec{E}$|, |$\vec{H}$|, and |$\vec{S}$| patterns for L=100cm and f=70 MHz.

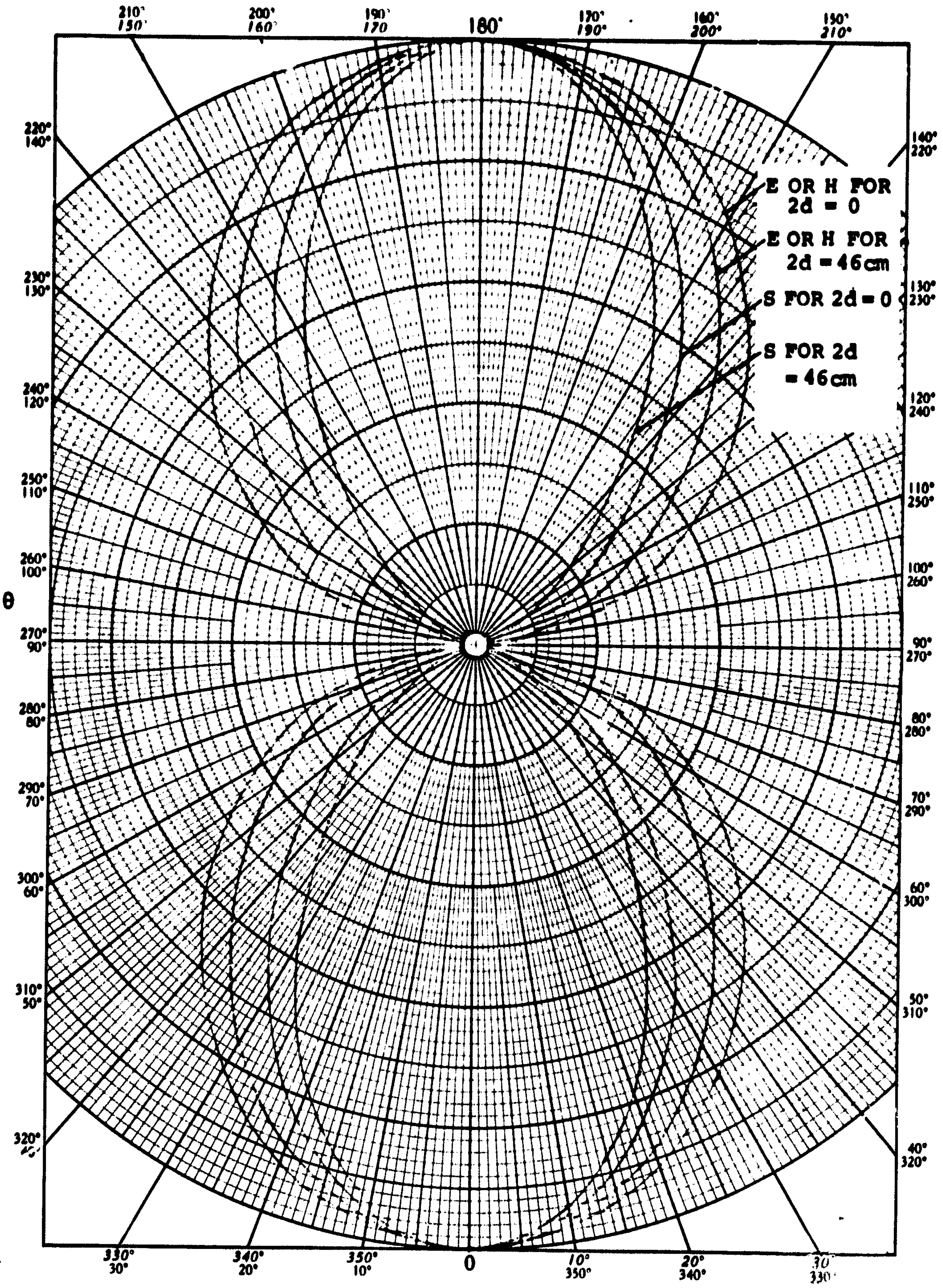

Fig. 12-17b Normalized $|\vec{E}|$, $|\vec{H}|$, and $|\vec{S}|$ patterns for L=100 cm and f=75 MHz.

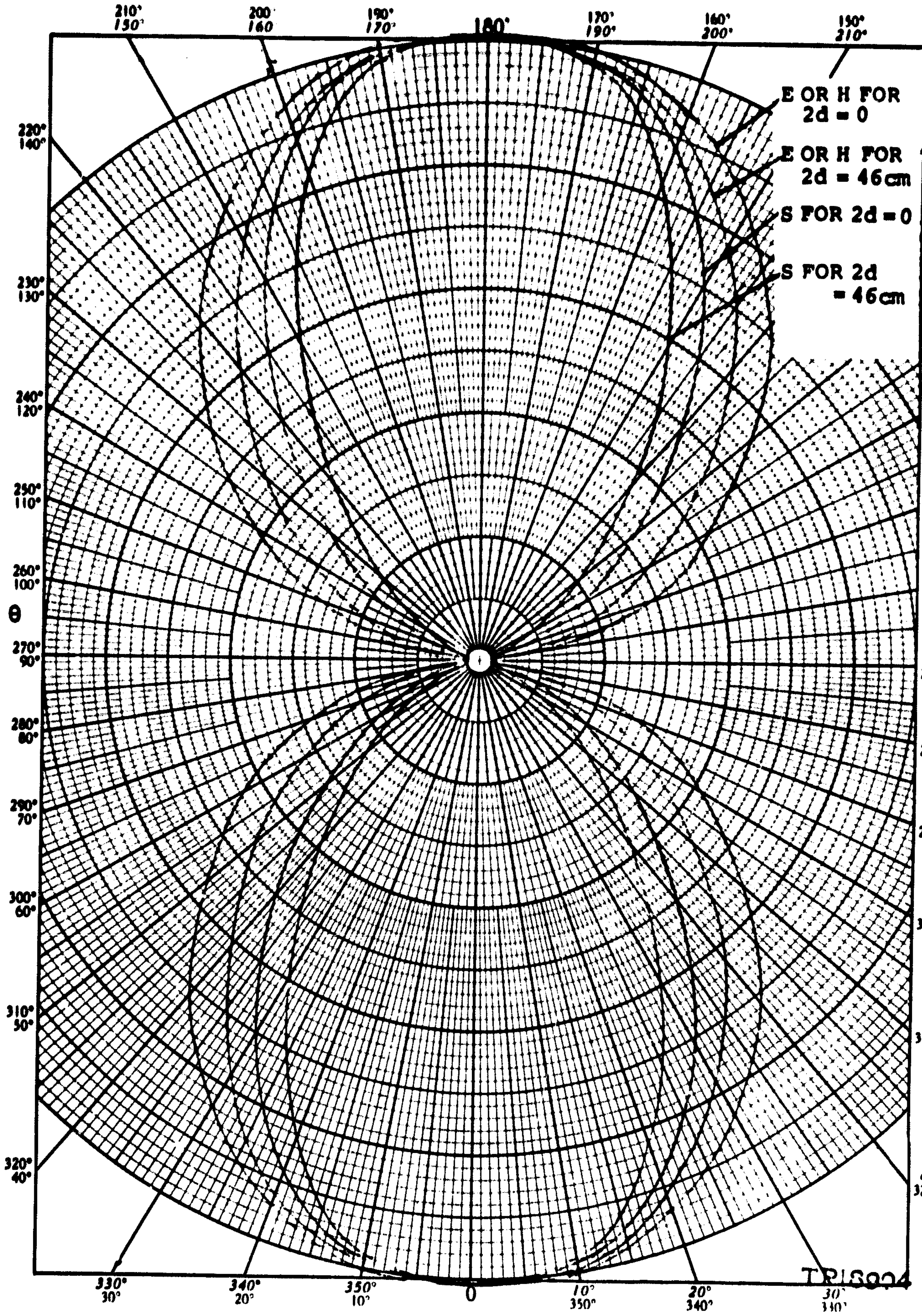

Fig. 12-17c Normalized $|\vec{E}|$, $|\vec{H}|$, and $|\vec{S}|$ patterns for L=100 cm and f=30 MHz.

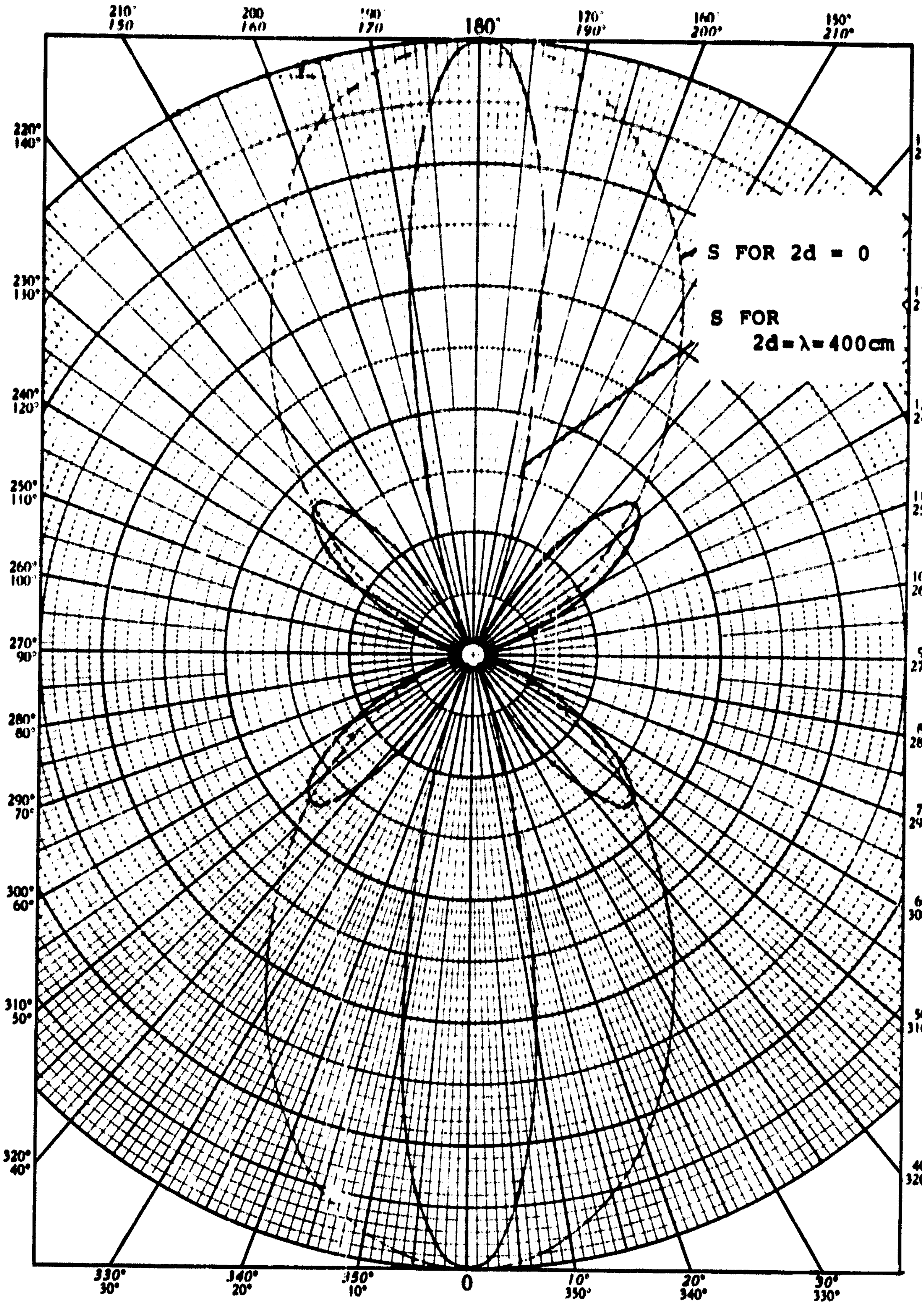

Fig. 12-18 Normalized $|\vec{S}|$ patterns for L=100 cm and f=75 MHz.

spacing is the input impedance at the antenna feedpoints A-B. This impedance can be defined as

$$Z_{A-B} = R_{A-B} + jX_{A-B} \tag{12.20}$$

and is called the radiation impedance of the antenna. In practice, the antenna will be connected to its transmitter as shown in Fig. 12-19. The 180° hybrid is necessary in order to create a dipole characteristic in the pair of rods. Matching Z_{A-B} at a specific frequency to the 180° hybrid output impedance $(50 + j0)\Omega$ therefore means a network design which compensates the effect of $j\frac{X_{A-B}}{2}$, and impedance transforms $\frac{R_{A-B}}{2}$ to 50Ω. The following equations give R_{A-B} and X_{A-B} as a function of frequency for a spacing $2d = 0$:

$$\begin{aligned}\frac{R_{A-B}}{\Omega} = 30\Big\{ & 2\Big[\mathrm{Si}\,(4kL) - 2\mathrm{Si}\,(2kL)\Big] \cot kL \\ & + 4\Big[E + \ln(2kL) - \mathrm{Ci}\,(2kL)\Big] \cot^2 kL \\ & - \Big[E + \ln(4kL) - \mathrm{Ci}\,(4kL)\Big]\Big[\cot^2 kL - 1\Big]\Big\}; \end{aligned} \tag{12.21a}$$

and

$$\begin{aligned}\frac{X_{A-B}}{\Omega} = -30\Big\{ & 2\Big[\ln\Big(\frac{L}{k\rho^2}\Big) - E + 2\mathrm{Ci}\,(2kL) - \mathrm{Ci}\,(4kL)\Big] \cot kL \\ & + \Big[\mathrm{Si}\,(4kL) - 2\mathrm{Si}\,(2kL)\Big]\Big[\cot^2 kL - 1\Big] - \frac{2}{\sin^2 kL}\,\mathrm{Si}\,(2kL)\Big\}. \end{aligned} \tag{12.21b}$$

Figures 12-20a (Real) and 12-20b (Imaginary) contain the results of Eq (12.21) for the case of

$$L = \frac{\lambda_{75\,\mathrm{MHz}}}{4} = 100\ \mathrm{cm}$$

It is possible to calculate the radiation impedance Z_{A-B} for the more general case of any spacing 2d and any rod length L by considering the total driving power at the feedpoints.

From the divergence law applied to the Poynting vector it follows

$$\oint_A (\vec{E} \times \vec{H}) \cdot d\vec{A} = \int_V \nabla \cdot (\vec{E} \times \vec{H})\, dV \tag{12.22}$$

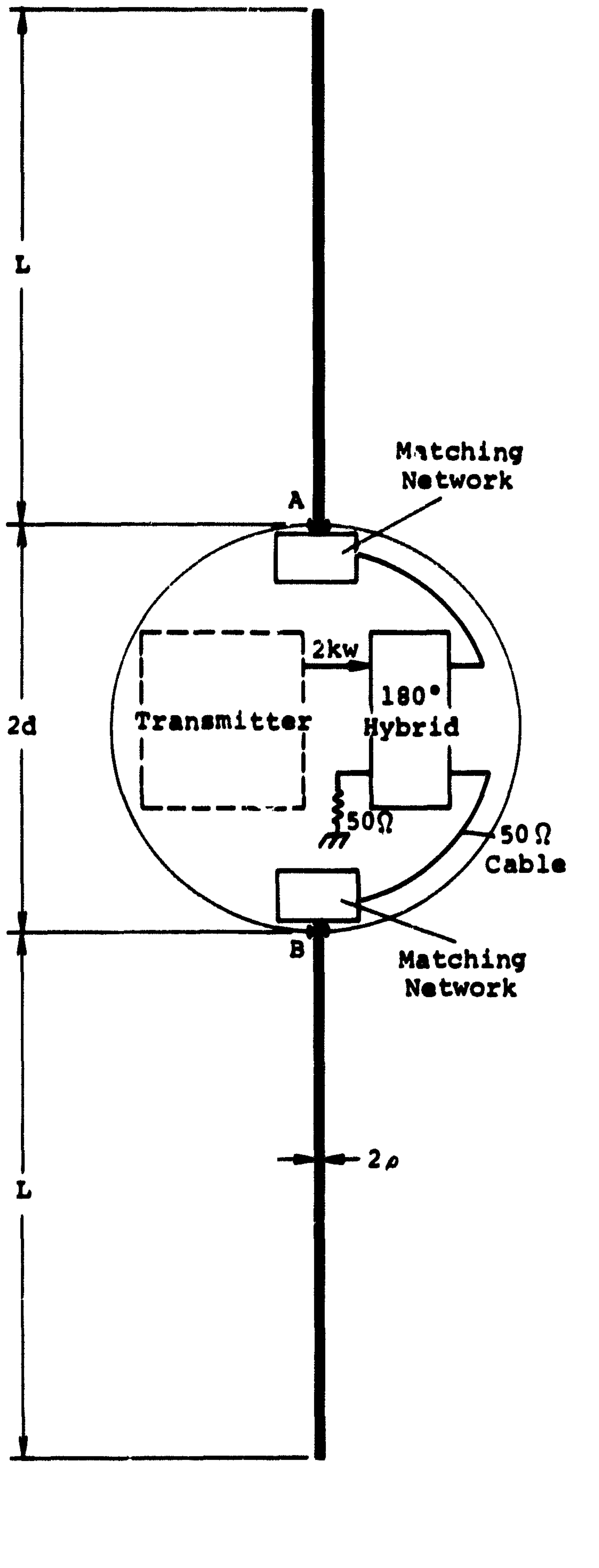

Fig. 12-19 Interface between transmitter and its antenna.

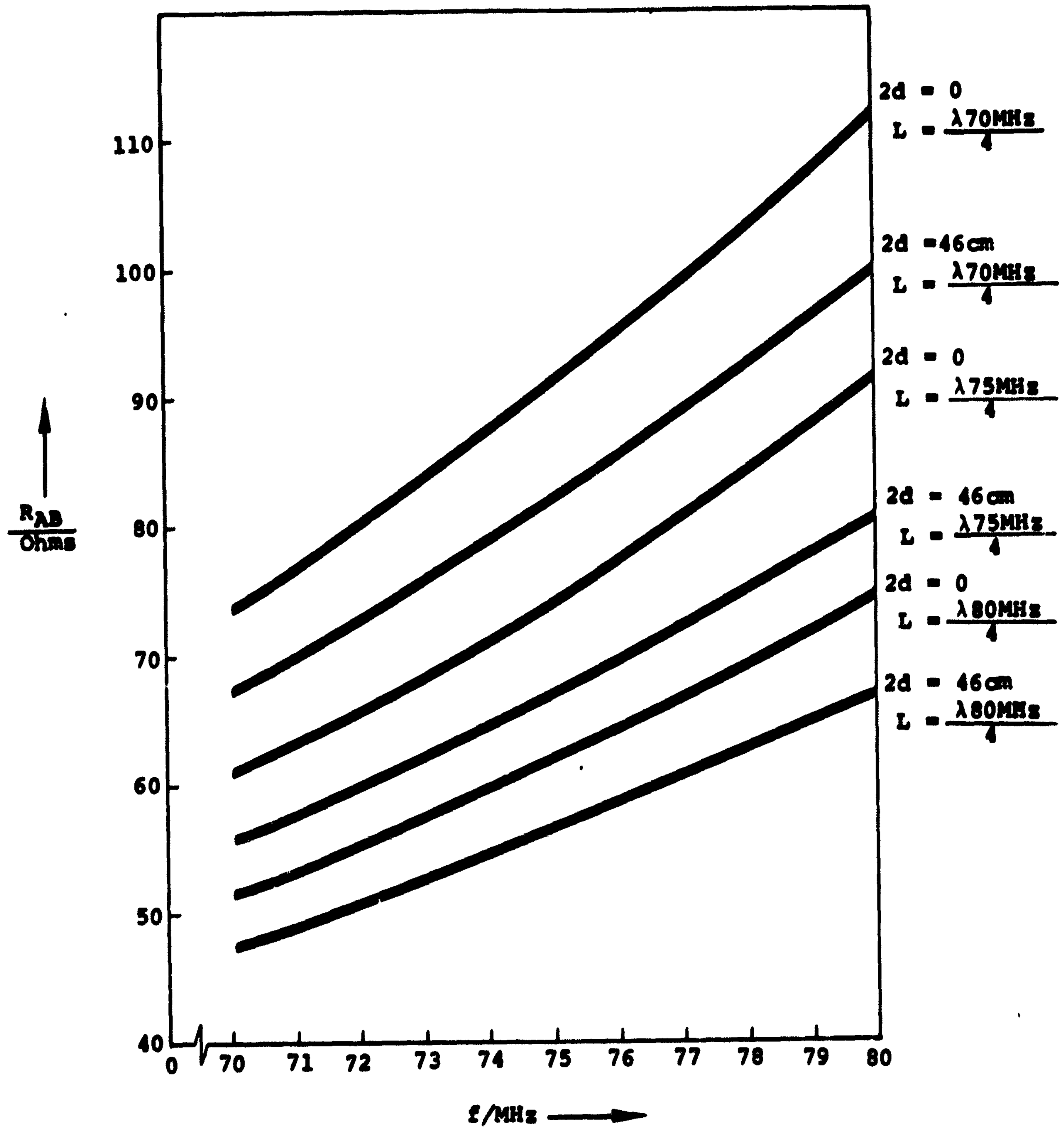

Fig. 12-20a Radiation resistance as a function of rod length, rod spacing and frequency.

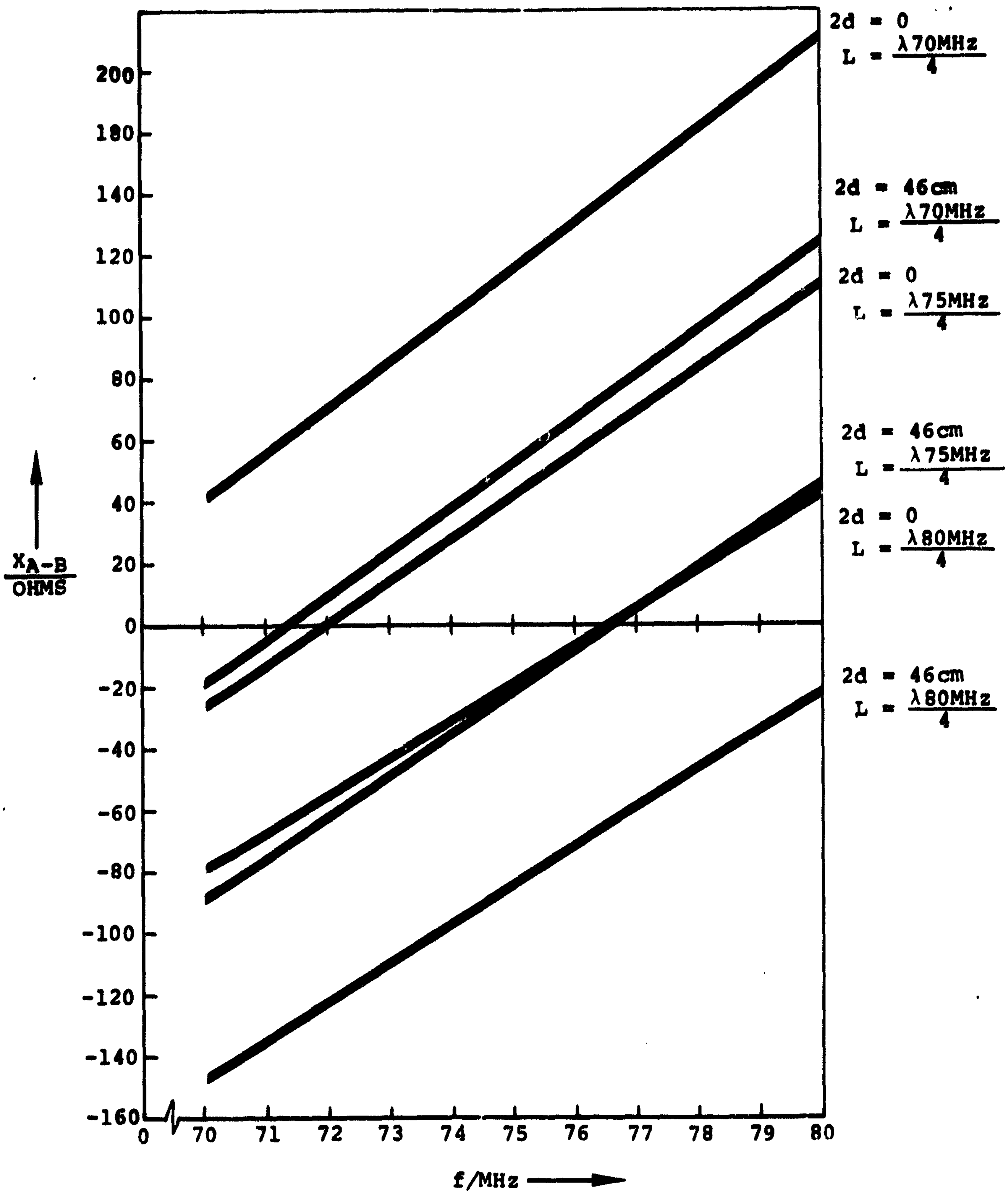

Fig. 12-20b Antenna reactance as a function of rod length, rod spacing and frequency.

setting

$$\nabla \cdot (\vec{E} \times \vec{H}) = \vec{H} \cdot \nabla \times \vec{E} - E \cdot \nabla \times \vec{H}$$

and using the results of Eqs (12.6), Eq (12.22) becomes

$$\oint_A (\vec{E} \times \vec{H})\, d\vec{A} = -\frac{\partial}{\partial t} \int_V \frac{1}{2} (\vec{H} \cdot \vec{B} + \vec{E} \cdot \vec{D})\, dV - \int_V \vec{J} \cdot \vec{E}\, dV \quad . \tag{12.23}$$

Ohm's law written in the form of Maxwell's equation is

$$\vec{J} = \sigma (\vec{E} + \vec{E}_e) , \tag{12.24}$$

where σ is the conductance of the material, $\vec{E}$ is the induced field, and $\vec{E}_e$ is the emf field (externally applied field).

Equations (12.23) and (12.24) solved for the total driving power P at the feedpoints give

$$P = \int_V \vec{J} \cdot \vec{E}_e\, dV = \frac{\partial}{\partial t} \int_V \frac{1}{2} (\vec{H} \cdot \vec{B} + \vec{E} \cdot \vec{D})\, dV + \int_V \frac{|\vec{J}|^2}{\sigma}\, dV + \oint_A (\vec{E} \times \vec{H}) \cdot d\vec{A} \; . \tag{12.25}$$

Assuming no losses in the antenna, and because the average of the energy contained in the volume, V, is constant in time for sinusoidally-varying quantities, Eq (12.23) and (12.24) break down to

$$P = \int_V \vec{J}\, \vec{E}_e\, dV = \oint_A (\vec{E} \times \vec{H}) \cdot d\vec{A} \tag{12.26a}$$

and

$$P = -\int_V \vec{J} \cdot \vec{E}\, dV \quad . \tag{12.26b}$$

Either Eq (12.26a) or (12.26b) can be used to calculate the impedance Z_{A-B}.

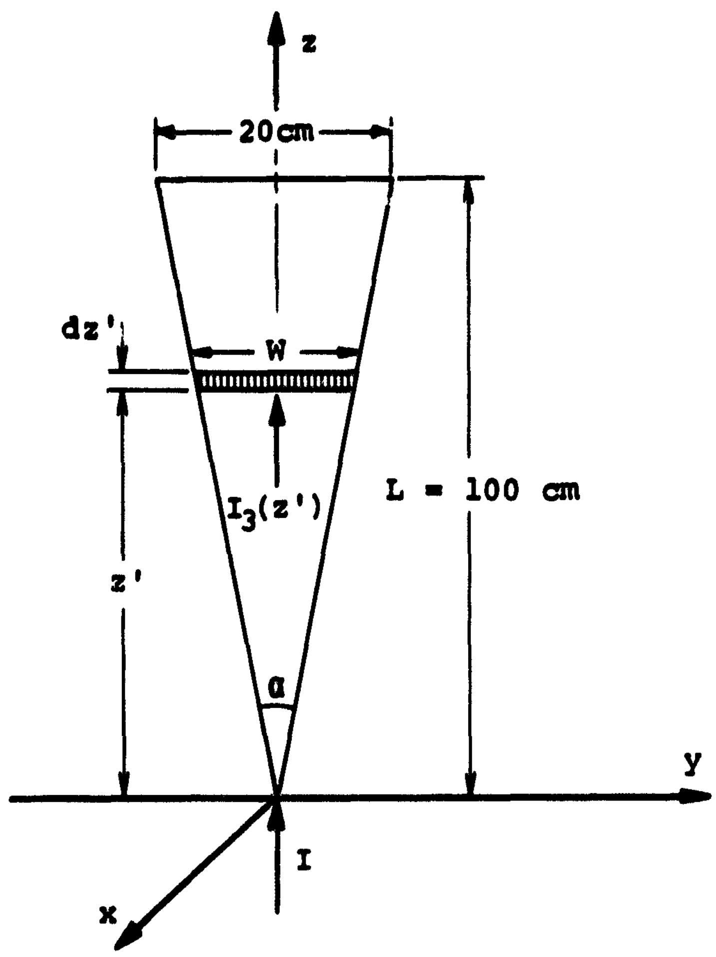

Fig. 12-21 Geometry and current distribution of a sail.

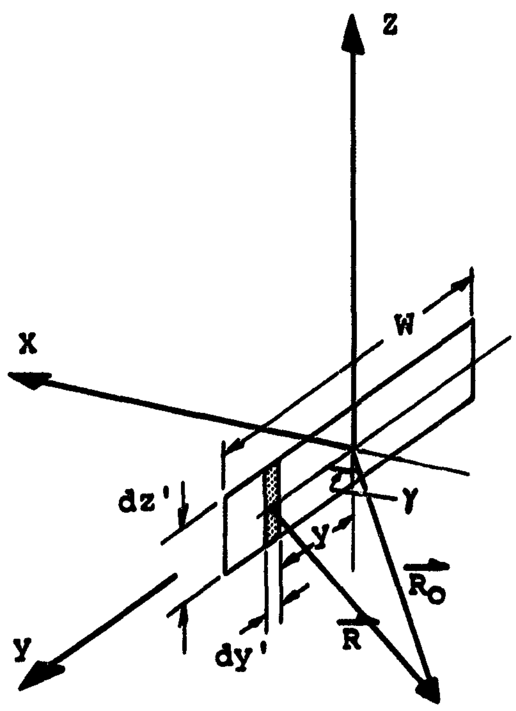

Fig. 12-22 Evaluation of the vector potential due to a current strip of width W and height dz′.

From (12.26a) it follows for R_{A-B} that

$$\frac{R_{A-B}(h, d, \lambda)}{\text{ohms}} = \frac{60\,\pi^2}{\lambda^2 \sin^2 kL} \int_{\theta=0}^{\pi} \sin^3\theta\, F^2(\theta, h, d, \lambda)\, d\theta \qquad (12.27)$$

From the condition of continuity of the tangential component of $\vec{E}$, and with the Eq (12.26b) and (12.11), it follows for $X_{A-B}^{(2)}$ that

$$\frac{X_{A-B}(h, d, \lambda)}{\text{ohms}} = -\frac{15}{\sin^2 kL} \int_0^{2kL} \Big[S_3(x)\sin x + S_4(x)\cos x$$

$$+ T_3(x)\cos(2kh - x) + T_1(x)\sin(2kh - x)\Big]\, dx\,, \qquad (12.28)$$

where

$$S_3(x) = \text{Si}(x) - \text{Si}(2kL-x)\,,$$

$$S_4(x) = \ln\left[\frac{x(2kL-x)}{k^4\rho^4}\right] + \text{Ci}(x) + \text{Ci}(2kL-x) - 2E\,,$$

$$T_3(x) = \ln\left[\frac{2k(L+2d)-x}{2k(2L+2d)-x}\right] + \text{Ci}\left[2k(L+2d)-x\right] - \text{Ci}\left[2k(2L+2d)-x\right],$$

and

$$T_1(x) = \text{Si}\left[2k(L+2d)-x\right] - \text{Si}\left[2k(2L+2d)-x\right].$$

R_{A-B} and X_{A-B} are plotted for various conditions in Fig. 12-20a (Real) and 12-20b (Imaginary).

12.7.3 Beacon Transmitter Antenna

For the study of the sail characteristics as an antenna set for the beacon transmitter, one starts again from the parameters of a very short dipole given in Eq (12.10a) and (12.10b). Figure 12-21 represents a sail in the (y-z) plane, with α a small angle such that $W \simeq z'\alpha$. Furthermore, the current density at z' is $\dfrac{I_z(z')}{W(z')}$. The first step is now to study the vector potential and the electric potential of such a narrow current strip of width W and length dz'. This can, however, be considered as constituted of several very short, parallel dipoles, all aligned next to each other along the y-axis and each carrying a current $\frac{I_z(z')}{W(z')} dy'$. This is again represented in Fig. 12-22.

For the small, short dipole, one may now write Eq (12.10b):

$$d\overleftrightarrow{A} = \frac{dz'}{4\pi} \frac{I_z(z')}{W(z')} dy' \frac{e^{-jkR}}{R} \hat{z}' \qquad (12.29)$$

With $R \simeq R_o - y' \cos\gamma$, it follows for the vector potential of the narrow current strip shown in Fig. 12-22 that

$$\overleftrightarrow{A} = \frac{dz'}{4\pi} \frac{I_z(z')}{W(z')} \frac{e^{-jkR_o}}{R_o} \hat{z} \int_{-\frac{W(z')}{2}}^{\frac{W(z')}{2}} e^{jky'\cos\gamma} dy'$$

and finally

$$\overleftrightarrow{A} = \frac{dz'}{4\pi} I_o \frac{e^{-jkR_o}}{R_o} \frac{\sin \frac{kW}{2}\cos\gamma}{\frac{kW}{2}\cos\gamma} \hat{z} \; . \qquad (12.30)$$

Analog considerations show that the expression for the electric potential at any point in space for a current strip of width, W, and length, dz', is

$$\phi = \frac{dz'}{4\pi j\omega\epsilon} I_o \left[j \frac{k}{R_o} + \frac{1}{R_o^2} \right] \frac{z}{R_o} \frac{\sin \frac{kW}{2}\cos\gamma}{\frac{kW}{2}\cos\gamma} \; . \qquad (12.31)$$

A comparison of the Eq (12.10a) and (12.10b) with Eq (12.30) and (12.31) shows that these two sets of equations differ only by the factor

$$\frac{\sin t}{t} \quad \text{where } t = \frac{kW}{2}\cos\gamma \; . \qquad (12.32)$$

The smaller W, the closer is t to 0 and, therefore, $\frac{\sin t}{t} \simeq 1$. In the worst case, where W = 20 cm, t becomes

$$t = \frac{2\pi}{\lambda_{75\ MHz}} \frac{20}{2} = \frac{2\pi}{400} \frac{20}{2} = 9^{o}$$

and

$$\frac{\sin t}{t} = \frac{0.156}{0.157} \simeq 1 .$$

Therefore, Eq (12.30) and (12.31) are similar to (12.10a) and (12.10b), hence the electromagnetic properties of a pair of sails are essentially the same as for a pair of rods. Consequently, the sails look like a pair of tilted rods, for which case the normalized patterns are given in Fig. 12-23 and 12-24*.

12.7.4 Mutual Coupling

The problem here is to determine how much of the 2 kW RF power of the main transmitter is received by the beacon antenna. This power in its turn will set the on-off characteristics (requirements) of the beacon antenna switch (see Section 12.6). The main function of the beacon antenna switch is to isolate the beacon transmitter from the main transmitter. Because of the relative complexity in geometry of the two antenna systems on the spacecraft, an analytical solution here would be quite cumbersome. The best way to determine the mutual effect is to measure the amount of power received by a pair of sails when the 2 kW transmitter is activated. However, in order to attain a qualitative feeling for the amount of the RF power coupled to the beacon antenna, a very simplified system was considered, in which the total power received by the beacon antenna was assumed to be composed of two separate parts.

That is:

Total RF received power = RF received power due to radiation $\left(\int \vec{S}d\vec{A}\right.$; physical aperture$\left.\right)$ + RF received power due to capacitive coupling.

For the geometry of Fig. 12-15 the radiation part of the RF received power was found to approximately 50 watts. As to the second term, the coupling capacity of the system was found to be about 0.52 pF. This corresponds at 80 MHz to a reactance of 4 kΩ. Thus, the RF power received at

* Computation of those patterns was made by M. Matsushita.

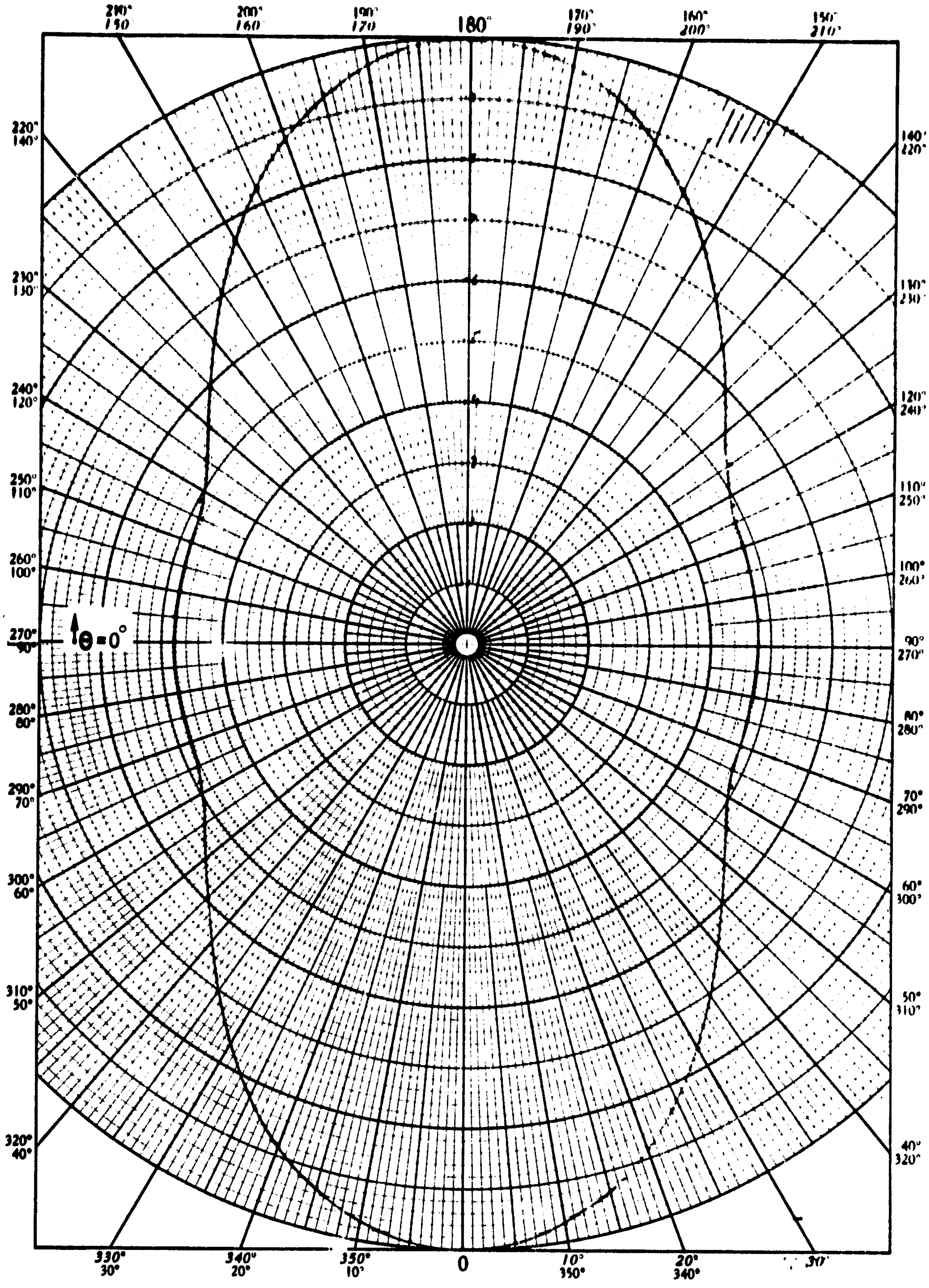

Fig. 12-23 Normalized $|\vec{H}|$ and $|\vec{E}|$ patterns for a dipole constituted by a pair of tilted rods.

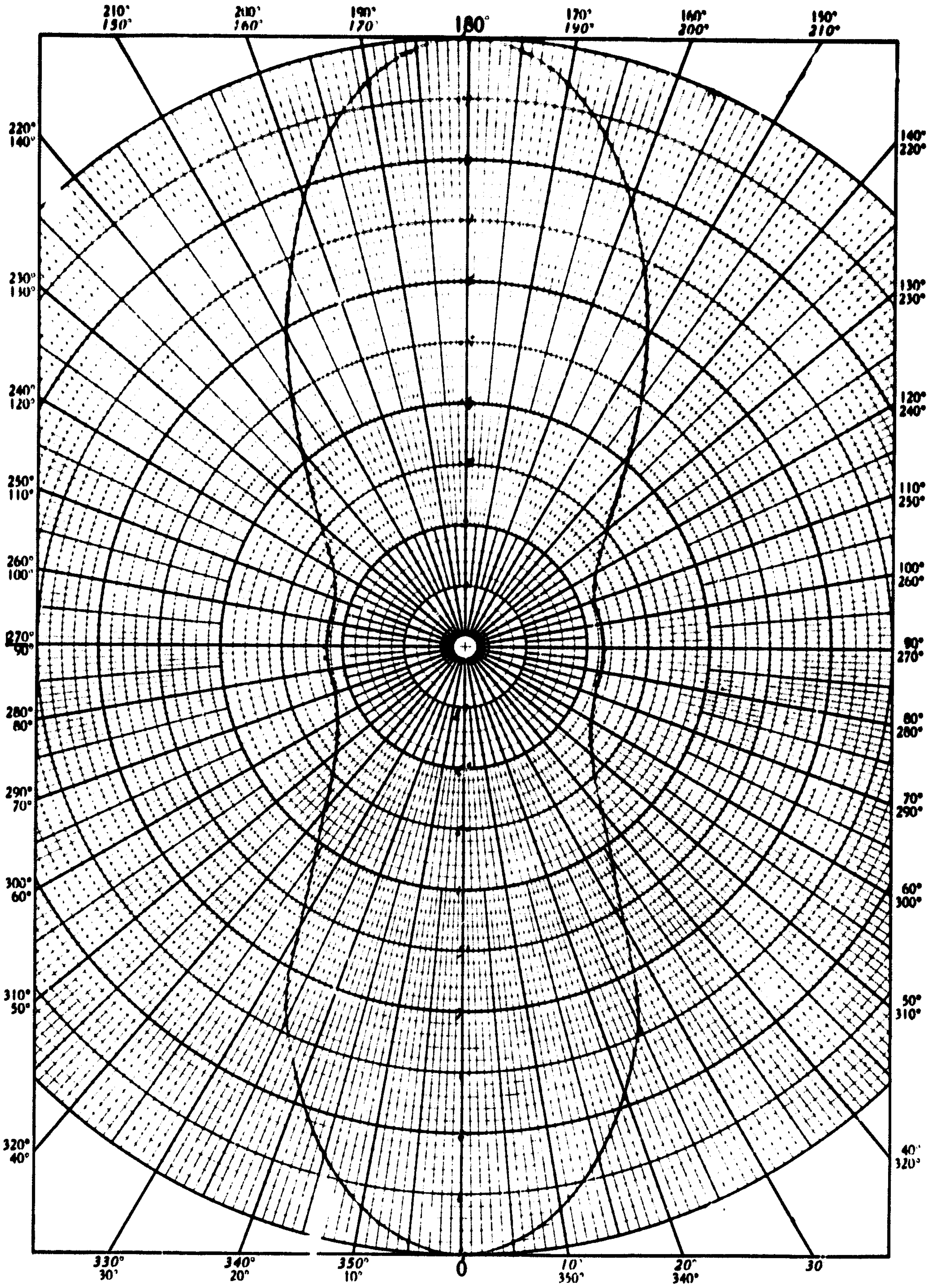

Fig. 12-24 Normalized $|\vec{S}|$ pattern for a dipole constituted by a pair of tilted rods.

the beacon in a 50Ω system due to capacitive coupling would be:

$$20 \log \left(\frac{4050}{50}\right) = 38 \text{ dB}$$

38 dB down as the 2 kW main transmitter power. This is approximately 0.3 W, which is essentially negligible when compared to the 50 W due to direct radiation.

In conclusion, there will therefore be a mutual coupling of approximately

$$\text{Coupling} = 10 \log \left(\frac{50}{2000}\right) = -16 \text{ dB}$$

-16 dB between the main and beacon antenna systems; and the design of the beacon antenna switching system has been based on the 50 W power level.

PRECEDING PAGE BLANK NOT FILMED.

REFERENCES

CHAPTER 1

(1) Harrington, J. V., Summary Report of Sunblazer Part I, Study of a Small Solar Probe -- Radio Propagation Experiment, MIT/CSR-PR-5255-5, 1965.

(2) Baker, R. H., and others, Summary Report of Sunblazer Part II, Spacecraft and Payload Design, MIT/CSR-PR-5255-5, 1965.

(3) James, J. C., R. H. Baker, and J. V. Harrington, Digitally Controlled Phased Array for the Reception of Sunblazer Signals, TR-66-3, 1966.

(4) Baker, R. H., J. V. Harrington, W. T. Higgins, and J. C. James, History and Design Summary, Sunblazer Phased Array, MIT/CSR, 1968.

(5) Goldstein, R. M., Jet Propulsion Laboratory Technical Report No. 32-1092, 1967.

(6) Hollweg, J. V., A Statistical Ray Analysis of the Scattering of Radio Waves by an Anisotropically Turbulent, Non-Homogeneous Solar Corona, MIT/CSR-T-67-6, 1967.

(7) Hollweg, J. V. and J. V. Harrington, "The Properties of Solar Wind Turbulence Deduced by Radio Astronomical Measurements" (paper to be submitted to the Journal of Geophysical Research, 1968).

(8) James, J. C., R. P. Ingalls, and L. P. Rainville, "Radar Echoes from Venus at 38 Mc/sec," Astronomical Journal 72, No. 8, p. 1047 1050, 1967.

CHAPTER 2

(1) Hollweg, J. V., MIT/CSR -T-67-6, 1967.

(2) Pindyck, R. S., Reception of Dispersed Barker Codes, MIT/CSR-T-67-1, 1967.

(3) Dutcher, G. L., A Communication Channel Model of the Solar Corona and the Interplanetary Medium, MIT/CSR-T-69-1, 1969.

(4) Goldstein, R. M., JPL Technical Report 32-1092, 1967.

CHAPTER 3

(No references cited)

CHAPTER 4

(1) Barton, D. R., Radar System Analysis, McGraw-Hill, 1964.

REFERENCES

CHAPTER 5

(1) Harrington, J.V., Proposal to NASA for Continued Work on the Sunblazer Ground Array, MIT/CSR, 1968.

(2) Wolff, E.A. Antenna Analysis, John Wiley and Sons, 1968, p. 243.

(3) Allen, J.L., The Theory of Array Antennas (with emphasis on radar applications), Lincoln Laboratory Technical Report 323, July 1963, p 10.

(4) Hansen, R.C. Microwave Scanning Antennas. Academic Press, 1964, p 29-35.

(5) Baker, R.H., and others, History and Design Summary, Sunblazer Phased Array, MIT/CSR, 1968.

(6) Allen, J.L., "Array Antennas: New Applications for an Old Technique," IEEE Spectrum, p. 115-130, November 1964.

CHAPTER 6

(No references cited)

CHAPTER 7

(No references cited)

CHAPTER 8

(1) Colombo, G., Passive Stabilization of a Sunblazer Probe by Means of Radiation Pressure Torque, MIT/CSR-TR-66-5, 1966.

(2) Peterson, C.A., Thermal Reradiative Effects in Spacecraft Attitude Control, MIT/CSR-T-66-3, 1966.

(3) Falcovitz, J., Attitude Control of a Spinning Sun - Orbiting Spacecraft by Means of a Grated Solar Sail, MIT/CSR-TR-66-17, 1966.

(4) Rossi, B. Optics. Reading: Addison-Wesley, 1965, p. 411-417.

(5) Koelle, H.H. Handbook of Astronautical Engineering. New York: McGraw-Hill, 1961, p. 8.36, 22.106.

(6) Sears, F.W., and M.W. Zemanski. Mechanics, Heat, and Sound. Cambridge: Addison-Wesley, 1955, p. 183-187.

(7) Goldstein, H. Classical Mechanics. Reading: Addison-Wesley, 1959, p. 6, 145.

(8) Ibid., p. 107.

(9) Ibid., p. 158.

(10) Ibid., p. 134.

(11) Ibid., p. 162.

(12) Halfman, R.L. Dynamics. Reading: Addison-Wesley, 1962, p. 220.

(13) Design Data Report Scout Fifth Stage, LTV Report No. 23.345, 1968.

(14) Steendal, R., Cone Angle of Fifth Stage, MIT/CSR Memorandum to R.H. Baker, October 1968.

(15) Collins, R.L., A Three-Dimensional Analysis of a Tangential Yo-yo Despin Device on a Rotating Body, NASA TN D-3848, 1967.

REFERENCES

CHAPTER 9

(1) Zerlaut, G.A., F.O. Rogers, and G. Noble, "The Development of S136 - Type Thermal - Control Coating Based on Silicate - Treated Zinc - Oxide" (Los Angeles: AIAA Third Thermophysics Conference, 1968) No. 68-790.

(2) NASA SP8005, Solar Electromatic Radiation, 1965.

(3) Greenberg, S.A., and D.A. Vance, Low Solar Absorptance and Emittance Surfaces Utilizing Vacuum Deposited Techniques, NASA CR-73039, Contract NAS2-3063, October 1966.

(4) Zerlaut, G.A., "Program to Select Thermal Control Coatings for Sunblazer," IIT Proposal 66-334U, January 1966.

(5) Haynes, G.A., "High Energy Radiation and Solar Cell Shields," NASA/LRC (Proceedings, Fourth Conference, Cleveland, Ohio, June 1968).

(6) Campbell, F.J., and R.J. Lambert, "Effects of Shielding on Electron Damage to Solar Cells, "(Proceedings, Fourth Photovoltaic Specialist Conference, June, 1964), Vol I, A-9-1, A-9-15.

(7) Riede, P.M., and D.I.J. Wang, "Characteristics and Applications of Some Superinsulations" (Houston: AICHE Annual Meeting, 1967).

(8) Cunnington, G. R., Jr., Zierman, C. A., Funai, A. I., and Lindahn, A., Performance of Multilayer Insulation System for Temperature to 700°K, Final Report, NAS2-2441, May 1967.

(9) Haviland, R. P., and C. M. House. Handbook of Satellite and Space Vehicles, D. Van Nostrand, Co., 1965, p. 214-226.

(10) Streed, E.R., and J.P. Kirkpatrick. Advanced Pioneer Thermal Control Concepts, NASA Ames Research Center.

(11) Brozek, A., Case Histories of Flares: The Large Flares of July 11, 12, 18 and 20, 1961, AAS-NASA on the Physics of Solar Flares, NASA SP-50, 1963, p 301-322.

CHAPTER 10

(No references cited)

CHAPTER 11

(No references cited)

CHAPTER 12

(1) Higgins, W. T., "Low Frequency Directional Couplers", Electronic Communicator (July-August, 1967).

(2) Labus, J., "Rechnerische Ermittlung der Impedanz von Antennen", Zeitschrift der Hochfrequenz und Elektroakustik, 41, 17, 1933.

ANALYSIS OF OPTIMAL ENERGY STORAGES

by

DIETER WILLNER

Dipl. - Ing.

Technical University of Berlin

(1965)

SUBMITTED IN PARTIAL FULFILLMENT OF THE

REQUIREMENTS FOR THE DEGREE OF

MASTER OF SCIENCE

and

ELECTRICAL ENGINEER

at the

MASSACHUSETTS INSTITUTE OF TECHNOLOGY

June, 1968

Signature of Author_ _

Department of Electrical Engineering, May 17, 1968

Certified by _

Thesis Supervisor

Accepted by _

Chairman, Departmental Committee on Graduate Students

ANALYSIS OF OPTIMAL ENERGY STORAGES

by

DIETER WILLNER

Submitted to the Department of Electrical Engineering on May 17, 1968, in partial fulfillment of the requirements for the Degrees of Master of Science and Electrical Engineer.

ABSTRACT

The problem investigated is the best design of energy storage systems to match a given power input - output relation. To consider a specific application a satellite system is selected and two models are investigated. These were a battery and a combined battery-capacitor storage. They were analytically investigated and optimized to yield a maximum number of pulses that can be transmitted under the condition that the voltage at the transmitter does not drop under a given minimum. In order to do so, assumptions and linearizations are necessary. The battery is modeled as a very large capacitor with internal resistance (as long as the voltage drop is limited to a certain small value). A periodic process is assumed and it is shown to have a steady state. The solutions of both models are calculated by computer and graphically compared.

It is found that the battery capacitor model has in general a higher pulse efficiency than the battery model. The reasons for this are discussed. The dependence of the solutions on the parameters are found and compared.

THESIS SUPERVISOR: David C. White
TITLE: Ford Professor of Engineering

ACKNOWLEDGEMENT

The author wishes to express his gratitude to all who helped in completing this project.

In particular, the author thanks Professor David C. White for supervising this thesis and for his many valuable ideas, and also Miss Linda Haney for typing the final copy.

This work was supported by the Ford Professorship of Professor David C. White for energy conversion in the School of Engineering. The computation was done on the Timesharing system of the M.I.T. Computation Center.

TABLE OF CONTENTS

TABLE OF CONTENTS (Continued)

CHAPTER I

I.1 Problem Statement

This investigation is concerned with optimizing an energy storage for an input - output relation, that appears quite frequently in applications where the input is continuous at low level and the output is in the form of large energy pulses. The problem of energy storage arises when the instantaneous power generation is lower than the instantaneous power requirements ($P_i > P_o$). Clearly over some average time interval the generated energy has to be higher than the required energy. That is

$$\int_{T_o}^{T_1} P_i \, dt > \int_{T_o}^{T_1} P_o \, dt$$

where P_i = generated power

P_o = required power

$T_1 - T_o$ = some time interval

Examples of this kind of application are satellite transmitters, remote pulse transmitters (weather stations) and stroboscopic lights. They often have the following input - output characteristic.

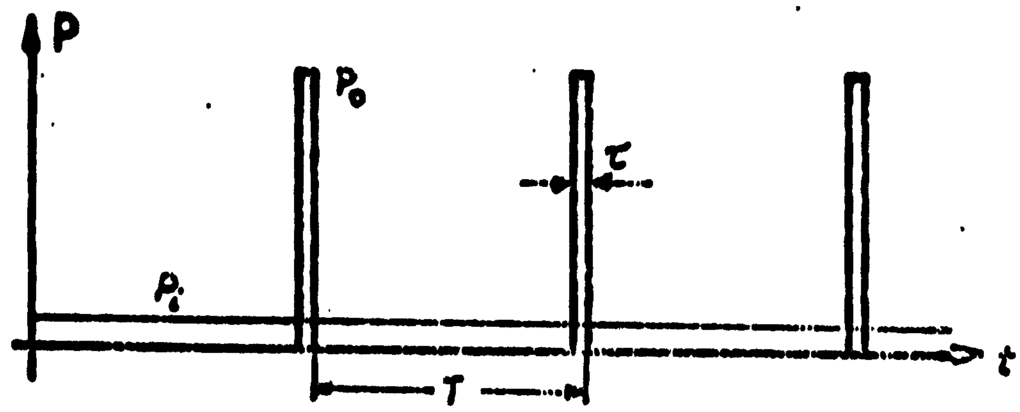

Figure 1

P_i is the power generated (usually by solar cells, batteries or very small reactors), P_o is the required power (or received power) by the load. If the process has a period T, then for

$$\int_t^{t+T} P_i \, dt > \int_t^{t+T} P_o \, dt \qquad \text{(for all t)}$$

simple energy storages like springs, capacitors or inductors are sufficient for storing energy, but in the case of

$$\int_{t_o}^{t_o+T} P_i \, dt < \int_{t_o}^{t_o+T} P_o \, dt \qquad \text{for some } t_o$$

we need storage elements with high energy capacity in which the energy is stored at $t < t_o$ like spinning masses, elevated masses in a gravitational field, batteries, or high magnetic fields stored using superconducting coils.

To evaluate the essential factors of such a system, we will design an energy storage system for a satellite. It should have a high reliability (this often means simplicity and redundancy in parts), high efficiency, and a low weight. Except for the required low weight, the other requirements occur in many other fields of application. The following overall network will be proposed:

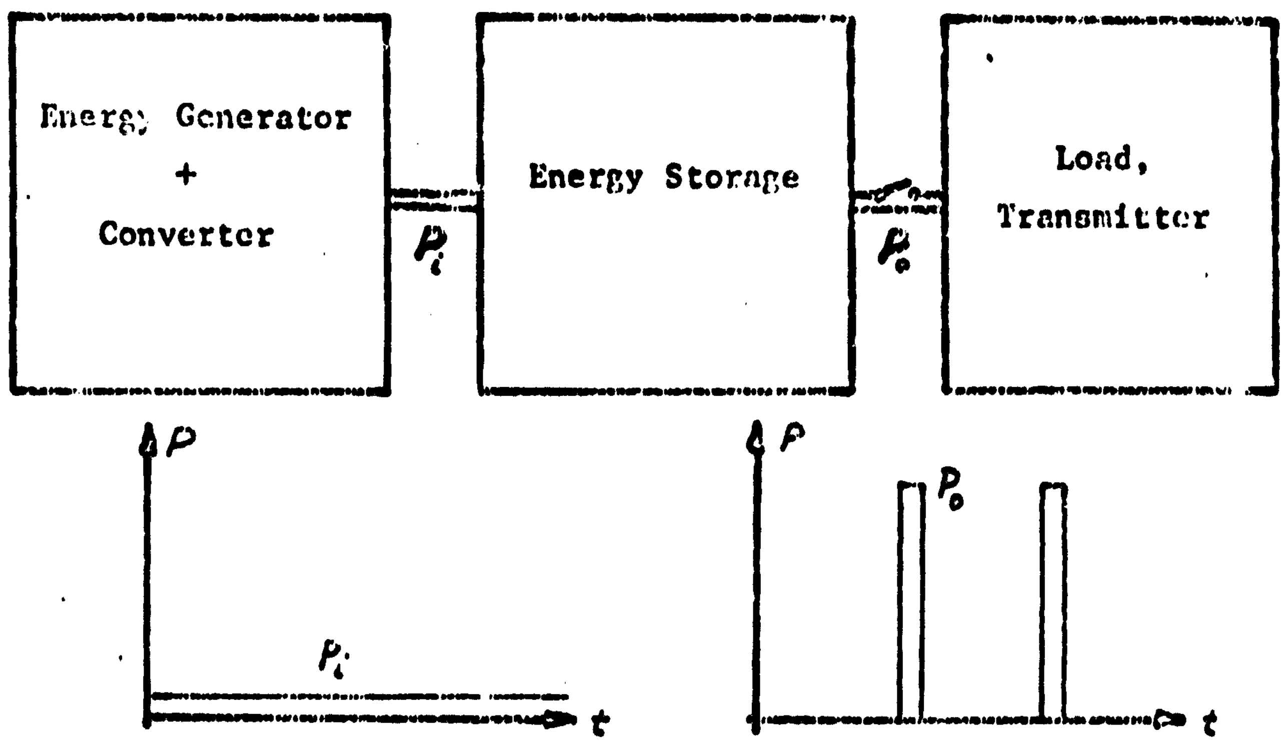

Figure 2

The transmitter is modeled as resistor (no inductive or capacitive reactance) with two states [R = R_d (discharge resistor) for $(T-\tau) < t \leq T$ and R = ∞ elsewhere].

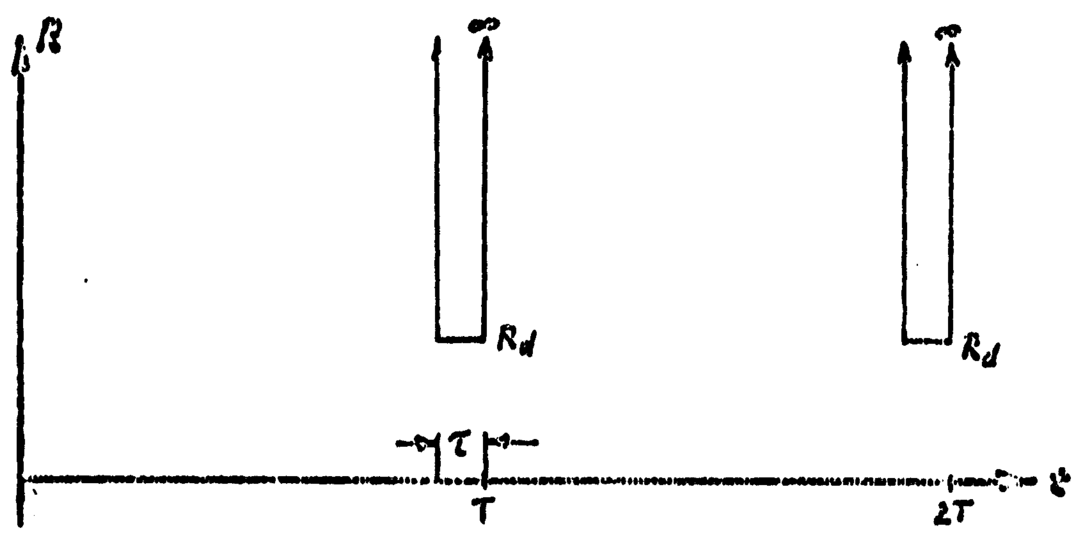

Figure 3

The energy storage system will be assumed to be a network of batteries, resistors or capacitors. We will show that inductors are not well suited for this purpose because their ratio of weight to stored energy is too large. This will be shown in the appendix. Storing energy in rotating devices is very tempting and certainly very effective for very large amounts of energy over short times, but for small amounts of energy the ratio of friction losses to stored energy is unfavorable. The energy storage we will consider consists of high reliability elements like capacitors (with negligible small internal resistance), batteries (with internal resistance), or a combination of both (linked by resistors).

I.2 Mathematical Model of the Battery

Since we want to investigate the storage systems analytically, we need a mathematical model for the battery that should be close to the behavior of real batteries. Batteries are assumed to have the following characteristics. [2], [3].

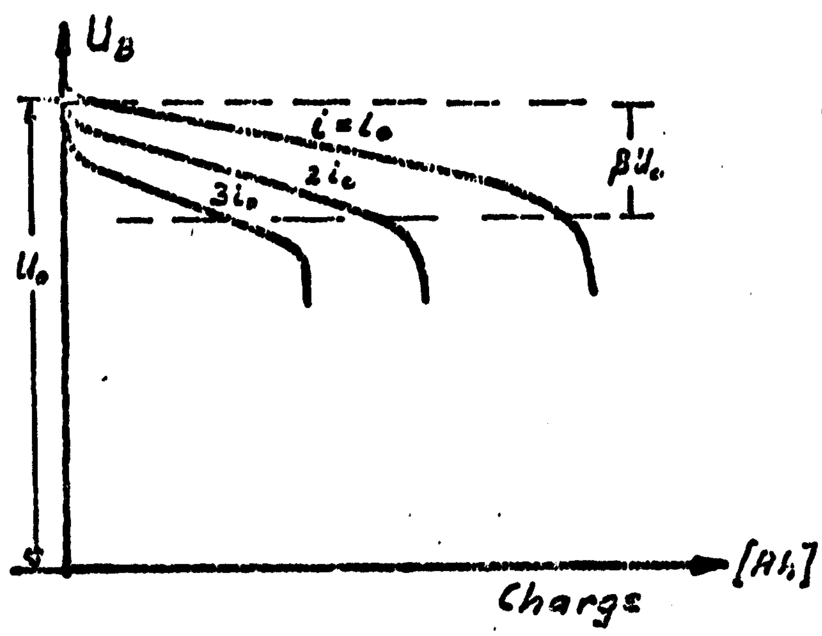

Figure 4.a

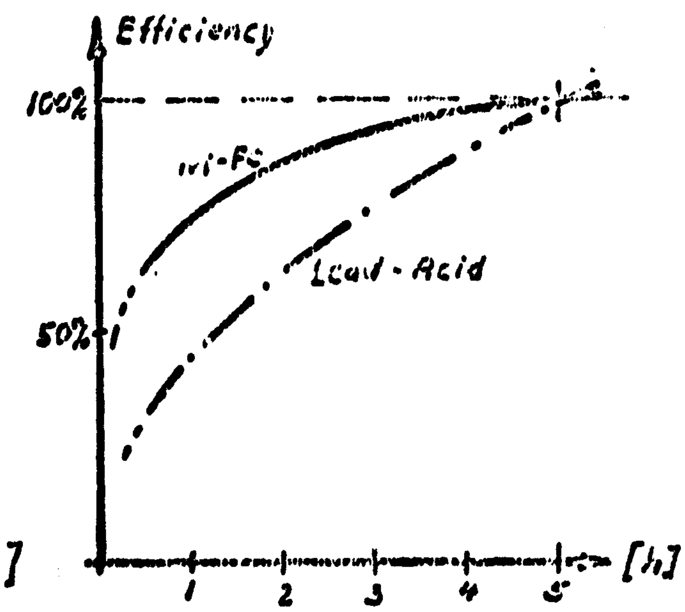

Figure 4.b

The characteristics for Ag-Zn, Ag-Cd, Ni-Cd and other types of batteries are very similar. The characteristics show that we can achieve highest efficiency when we discharge the battery at low currents. It looks as if the losses in the battery (due to polarization and internal resistance) are proportional to the decrease in efficiency. Using this observation we say that the efficiency is highest when the losses in the battery are lowest.

$$\text{Energy lost in battery} = \int_0^T I^2 R_i \, dt = \text{Min.}$$

where R_i = internal resistance

I = battery current.

We use the following model for the battery for $U_0 \geq U_B \geq \beta U_0$

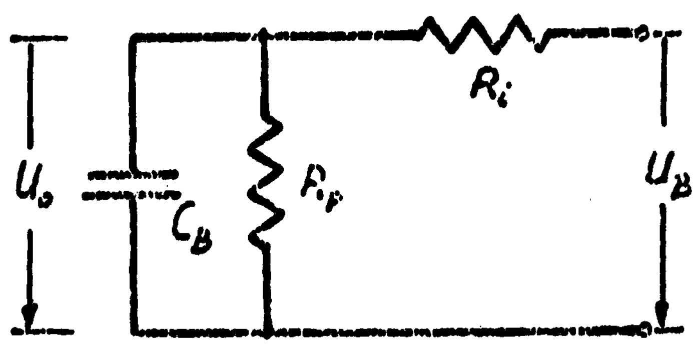

Figure 5

where C_B = very large

R_p = very large = ∞

R_i = internal resistance + equivalent for polarization losses.

β = voltage drop.

Instead of minimizing the loss energy we can maximize the output energy.

$$E_{out} = \int_0^T (U_0 I - I^2 R_i)dt = Max$$

Asking that the battery delivers a charge k in the time interval results in the following constraint:

$$k[Ah] = \int_0^T I dt$$

Using variational calculus (see appendix) we find that the output energy is a maximum for I = const. = k/T.

I.3 Practical Energy Storages

Since the load (in our case a transmitter) requires a high power we need an energy storage system output with very low resistance. A capacitor has practically no internal resistance but stores only small amounts of energy per pound. The battery with its very high storage capacity has internal resistance that is not negligible.

We will investigate two storage systems: one with a battery only, and the other one a combination of battery, resistor and capacitor.

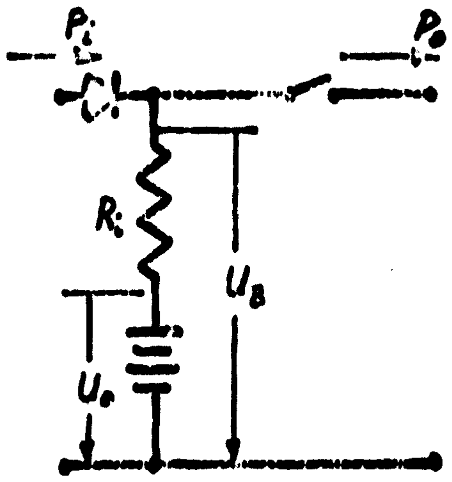

Model #1

Figure 6.a

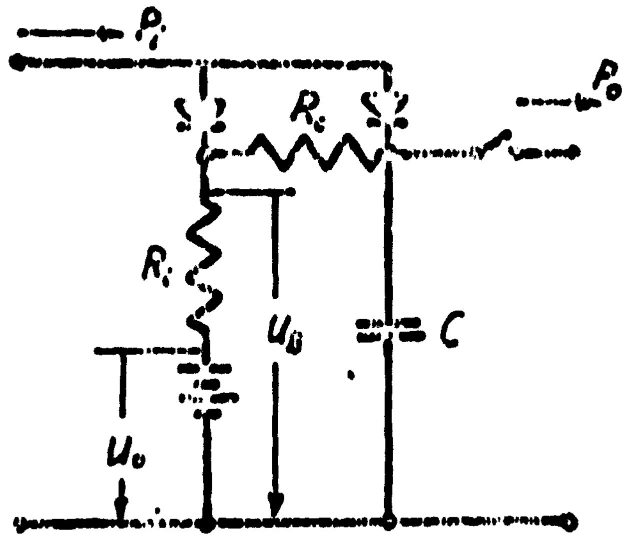

Model #2

Figure 6.b

Looking at Model #2 we ask if it is possible to gain over the performance of Model #1. There is an additional stage in the storage system and as shown in the appendix, we can get out only one-half of the energy supplied to charge the capacitor. This model is at best 50% efficient. First, consider Model #1 with its high current over very short times. If we take the total time (N τ, N = number of pulses, τ = pulse width) we might get a very short total discharging time (0 - 3 mintues as it turns out later), where the battery efficiency from Figure 4b, page 9 is very low.

Model #2 dissipates approximately the same amount of energy that it delivers to the load, but due to the slow discharging of the battery (0.05 - 2 hours) it will work in a region with much higher efficiency.

Both proposed models (battery only and battery, capacitor, resistor model) do not have constant discharge current. Model #1 (battery) delivers during a period T for τ seconds (with $\tau << T$)

a very high current. Model #2 (battery, capacitor, resistor) does the same, only that the high current is not delivered by the battery, but by the capacitor (with negligible internal resistance). The capacitor is then charged by the battery with a low (exponential) current (see Figure 7b).

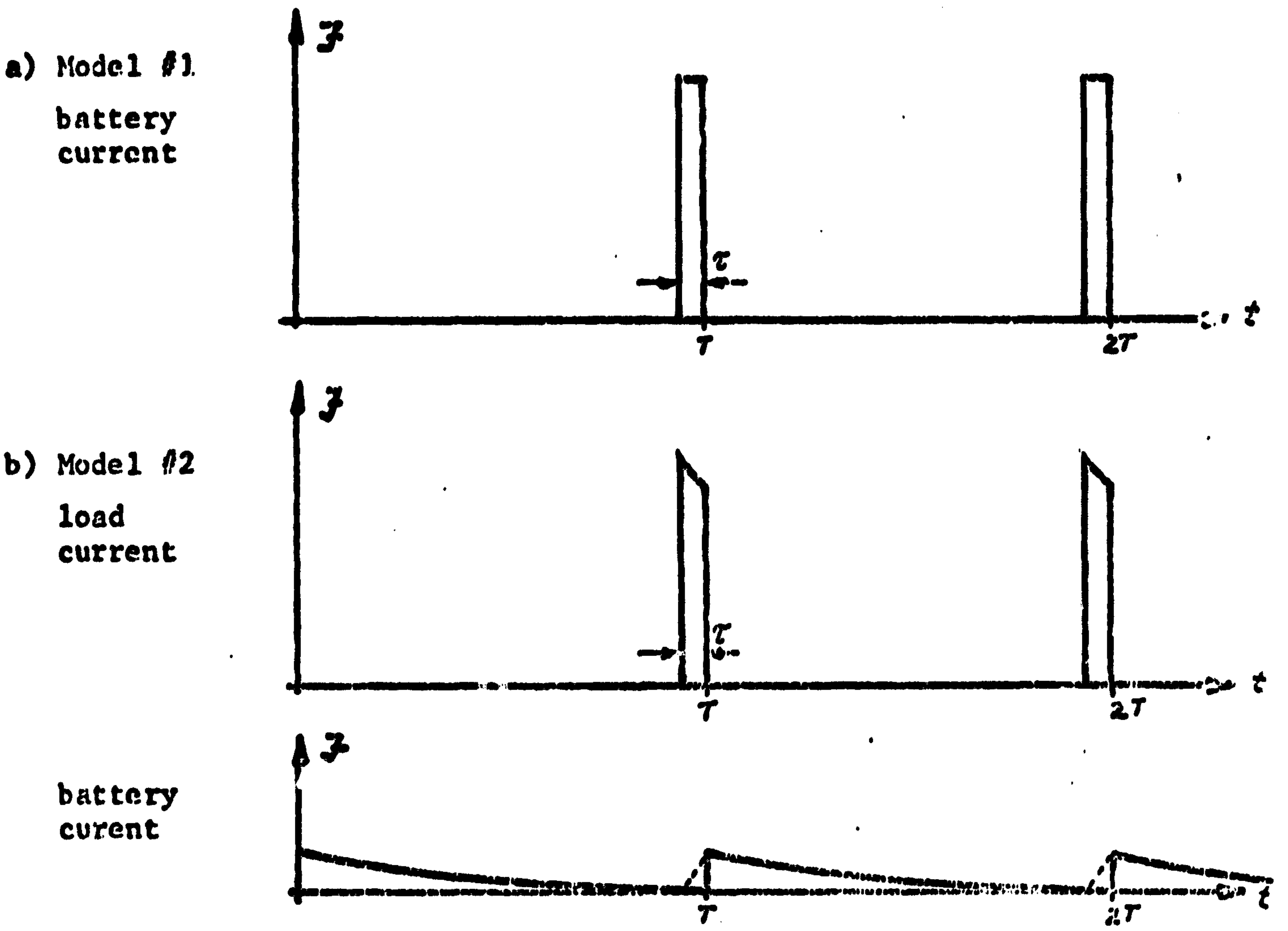

Figure 7

Though neither Model #1 nor #2 have a constant battery current, Model #2 has a low battery current, when we choose $R_i + R_c$ (the charge resistance between battery and capacitor) in the appropriate way.

I.4 Optimal Case Model

There are possibilities to discharge the battery with constant current $I = k/T$.

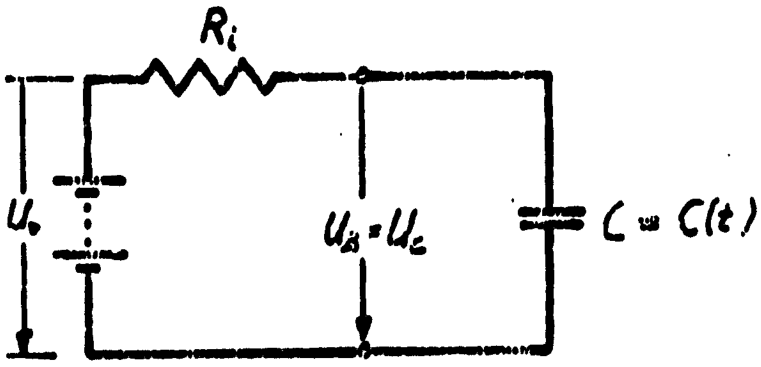

Figure 8

Assume $U_o = \text{const.}$

$$U_B = U_o - IR_i$$

$$I = \text{const.}$$

$$U_B = \text{const.}$$

$$I = \frac{dQ}{dt} = \frac{d}{dt}[CU_c] = \frac{dU_c}{dt}C + U_c\frac{dC}{dt}$$

$$Q = \text{charge of capacitor}$$

$$U_c = \text{const.} \longrightarrow \frac{dU_c}{dt} = 0$$

$$I = U_B\frac{dC}{dt} = \frac{k}{T} \text{ (from optimization)}$$

$$\longrightarrow dC = \frac{k}{U_B T}dt$$

or

$$C(t) = C_o t \;, \quad C_o = \frac{k}{U_B T}$$

for

$$t = T - \tau$$

and

$$\tau \ll T \longrightarrow t \approx T$$

$$C(T) = C_o T = \frac{k}{U_B}$$

$$U_B = U_o - IR_i = \frac{U_o T}{T+T_c}$$

where $T_c = R_i C$

then

$$C_o = \frac{k(T+T_c)}{U_o T}$$

$$I = \frac{U_o C_o}{T+T_c} = \text{const.}$$

This is a realizable solution. Varying the capacitor $C(t) = C_o(t)$ for $0< t \leq T$ produces a constant current. But since we need additional (mechanical) networks we need additional energy sources. Therefore this solution is not practical.

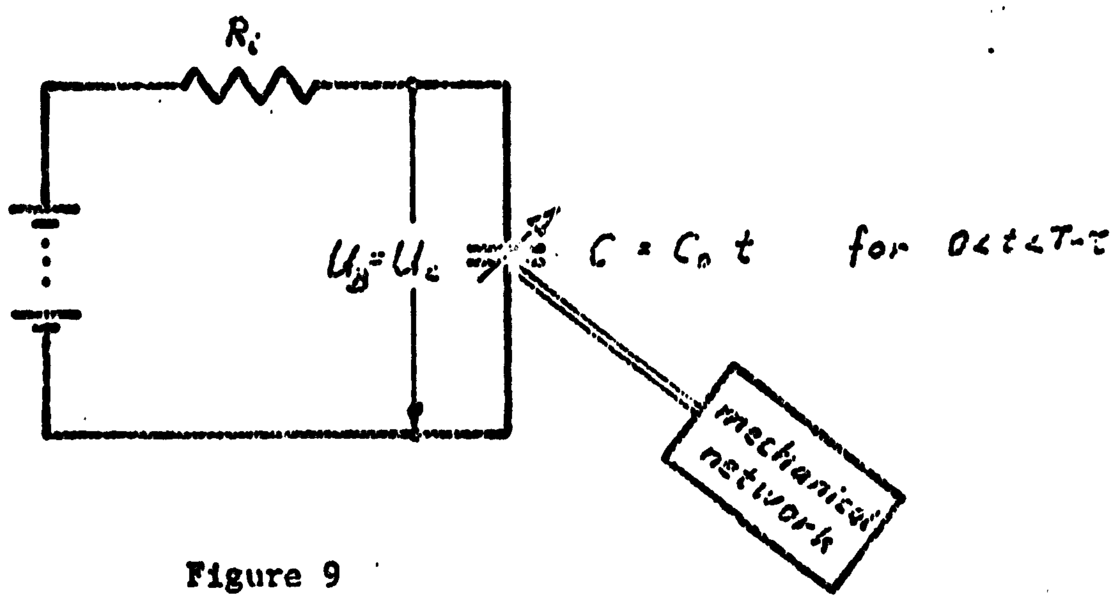

Figure 9

I.5 Conclusions

We are looking for an optimal energy storage system for given input - output relation. We say the system is optimal, when it delivers the maximum number of pulses at a given weight. Proposing several models we ruled out moving energy storages, capacitors and inductors, because of low storage capacity and proposed Model #1 and #2, which are investigated and compared in the following chapters.

CHAPTER II

II.1 Analysis of Model #1 and #2

Both Models can be represented in the following form:

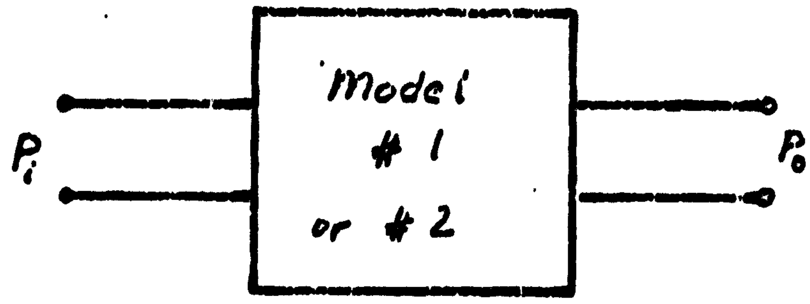

Figure 10

We want to find the number of pulses that each model can produce, provided that certain limits within the storage systems will not be exceeded. These limits will be that the voltage across the battery and the voltage across the load stay above certain values.

For this purpose we set $P_i = 0$ and calculate this number N. If it turns out that the total discharge time of the batteries (the time for N pulses) is short compared with the charging time, then we do not only get the pulse efficiency (number of pulses per loaded battery) but a number that is very close to the maximum number that we can send without time out for charging the batteries.

II.2 Model #1

Assumptions: (a) all elements are linear in the working range;

(b) switch S = ideal   R = 0 S closed
                        R = ∞ S open

Figure 11

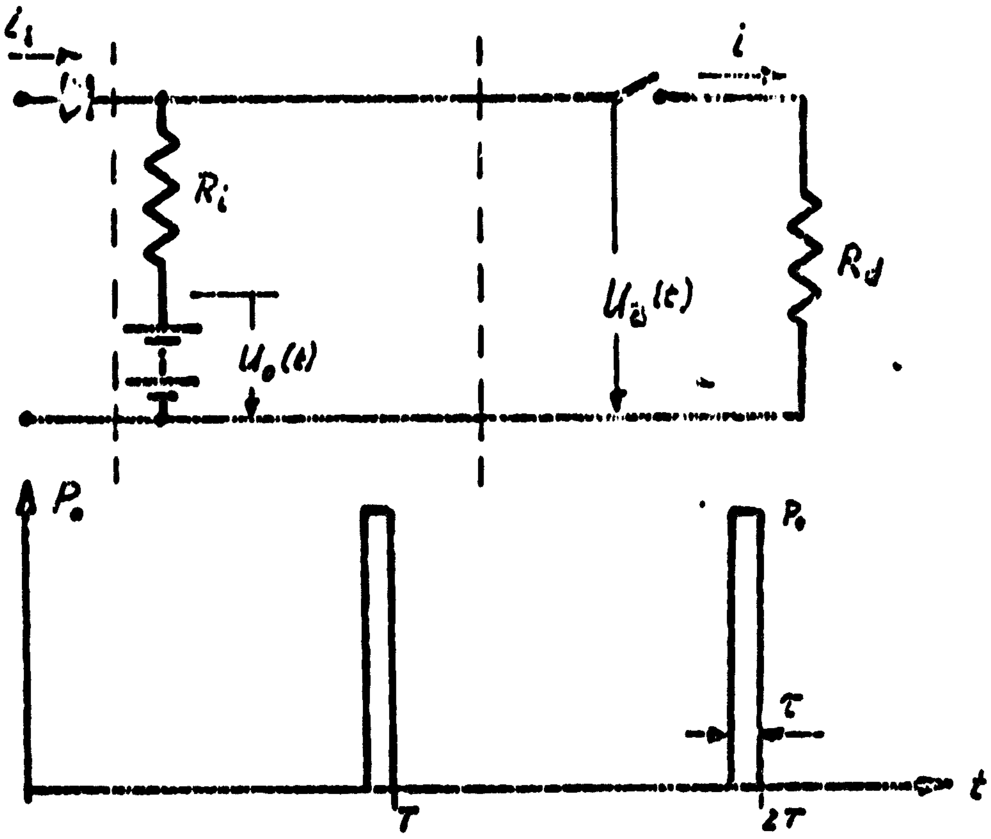

$$i_1 = 0 \longrightarrow P_1 = 0$$

We model the battery as a large capacitor with internal resistance. The battery emf is:

$$U_o(t) = U_o(0)[1-\alpha q(t)] \qquad (1)$$

where: $U_o(0)$ = battery voltage of the charged battery,

for $i = 0$,

and $t = 0$,

$U_o(t) = U_B(t)/_{i=0}$

$\alpha = 1/Q_B$

Q_B = total battery charge

$q(t) = \int_0^t i\,dt$ = charge delivered by the battery

$$Q_B = q(\infty) = \int_0^\infty i dt$$

Since the pulse width τ is constant and there is no charging, $i_i = 0$, we can substitute

$$t = n\tau \qquad (2).$$

where n is the number of pulses (we consider only the discharge time).

Substituting

$$U_o(t) = i(R_i + R_d)$$

and

$$R = R_i + R_d$$

$$i(R_i + R_d) = U_o(0)[1-\alpha q(t)].$$

The battery current is then

$$i(t) = \frac{U_o(0)}{R} \exp\left[-\alpha \frac{U_o(0)}{R} t\right] \qquad (3)$$

The charge taken out of the battery:

$$q(t) = \int_0^t i(t)dt = \frac{1}{\alpha}\left\{1-\exp\left[-\alpha \frac{U_o(0)}{R} t\right]\right\} \qquad (4)$$

The emf across the battery is:

$$U_o(t) = U_o(0)\exp\left[-\alpha \frac{U_o(0)}{R} t\right] \qquad (5)$$

The voltage across the battery is:

$$U_B(t) = U_o(t) - i(t)R_i \tag{6}$$

$$U_B(t) = \frac{R_d}{R_i + R_d} U_o(0) \exp\left[-\alpha \frac{U_o(0)}{R} t\right] \tag{7}$$

In order to protect the battery from destruction we limit the voltage drop β

$$\beta = \frac{U_o(0) - U_B(t)}{U_o(0)}$$

The allowable voltage drop β depends very much on the type of battery, but seldom exceeds 0.15 - 0.20. Usually the battery is recharged for $\beta \geq 0.1$.

The minimum voltage is

$$U_{B\,min}(t) = (1-\beta)U_o(0) \tag{8}$$

Inserting (8) in (7)

$$1-\beta = \frac{U_{B\,min}(t)}{U_o(0)} = \frac{R_d}{R_i + R_d} \exp\left[-\alpha \frac{U_o(0)}{R} t\right] \tag{9}$$

From this equation we can determine the total discharge time t:

$$t = \frac{R}{\alpha U_o(0)} \ln\left[\frac{R_d}{R_i + R_d} \frac{1}{1-\beta}\right] \tag{10}$$

Inserting (2), $t = N\tau$ into (10) we obtain the number of pulses:

$$N = \frac{t}{\tau} = \frac{R}{\alpha U_o(0)\tau} \ln\left[\frac{R_d}{R_i+R_d}\,\frac{1}{1-\beta}\right] \quad (11)$$

In the case where the allowable voltage drop at the load (κ) is less than the allowed voltage drop at the battery (β), we set $\beta = \kappa$. There are the following two cases:

(a) $\beta < \kappa$ choose β

(b) $\beta \geq \kappa$ set $\beta = \kappa$

Optimization of N

In order to have positive N it follows from (11)

$$\frac{R_d}{R_i+R_d}\,\frac{1}{1-\beta} \geq 1$$

$$\longrightarrow R_i \leq \frac{\beta}{1-\beta} R_d \quad (12)$$

Where is the maximum of N with respect to R_i?

$$\frac{dN}{dR_i} = \frac{\partial N}{\partial R}\,\frac{dR}{dR_i} = 0$$

since

$$R = R_i + R_d$$

$$\longrightarrow dR = dR_i$$

and

$$\frac{dN}{dR_i} = 0 = \frac{1}{\alpha U_o(0)\tau}\left\{\ln\left[\frac{R_d}{R}\,\frac{1}{1-\beta}\right]-1\right\} = 0$$

Then the maximum $\left(\frac{d^2N}{dR_1^2} \le 0 \right)$ occurs for

$$R_1 = R_d\left[\frac{1}{e(1-\beta)} - 1\right] \tag{13}$$

where e = base of natural logarithm.

For most applications $\beta \le 0.2$

$$R_1 \le - 0.54\ R_d$$

For all

$$R_1 \ge R_d\left(\frac{1}{e(1-\beta)} - 1\right)$$

$$\longrightarrow \quad \frac{dN}{dR} \le 0$$

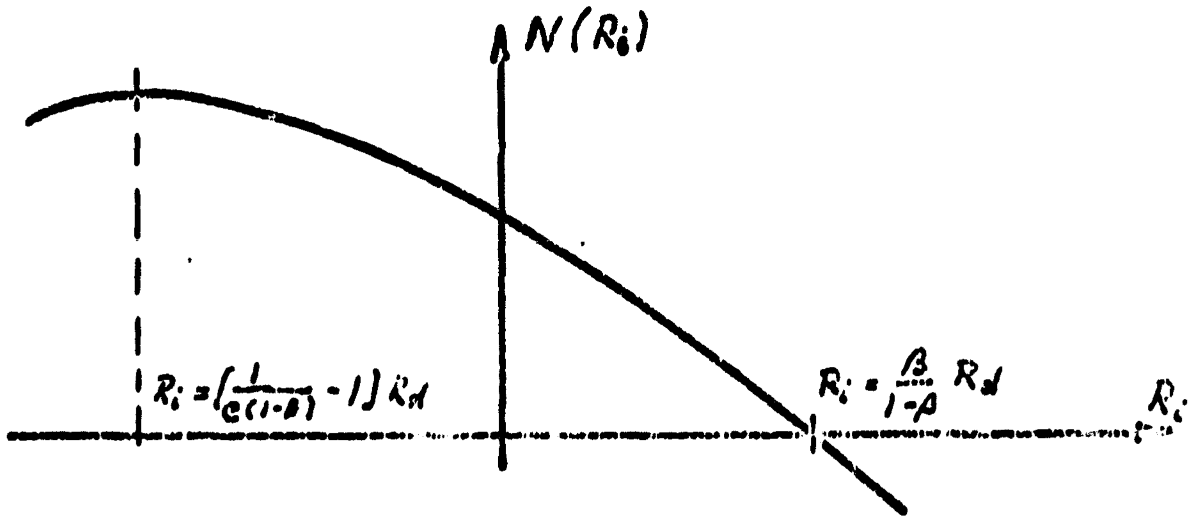

Figure 12

Therefore we conclude that the feasible maximum occurs for $R_1 = 0$ or R_1 as small as possible. In other words the better the battery (R_1 is small) the higher the number of pulses.

II.3 Model #2

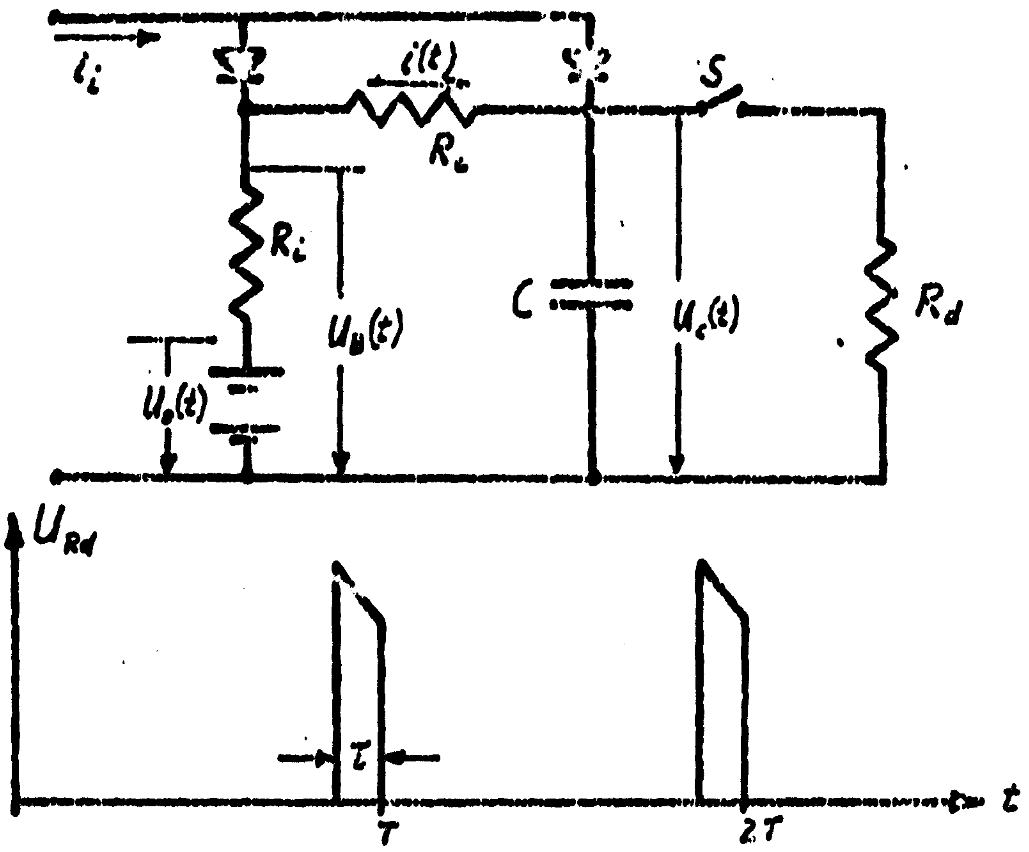

Figure 13

Assumptions: (a) all elements are linear in the working range;

(b) switch S is ideal $R = 0$ S closed

$R = \infty$ S open

We assume that the system has performed n periods, where one period is the time t:

$$mT < t \leq (m+1)T$$

where the capacitor will be alternately charged and discharged.

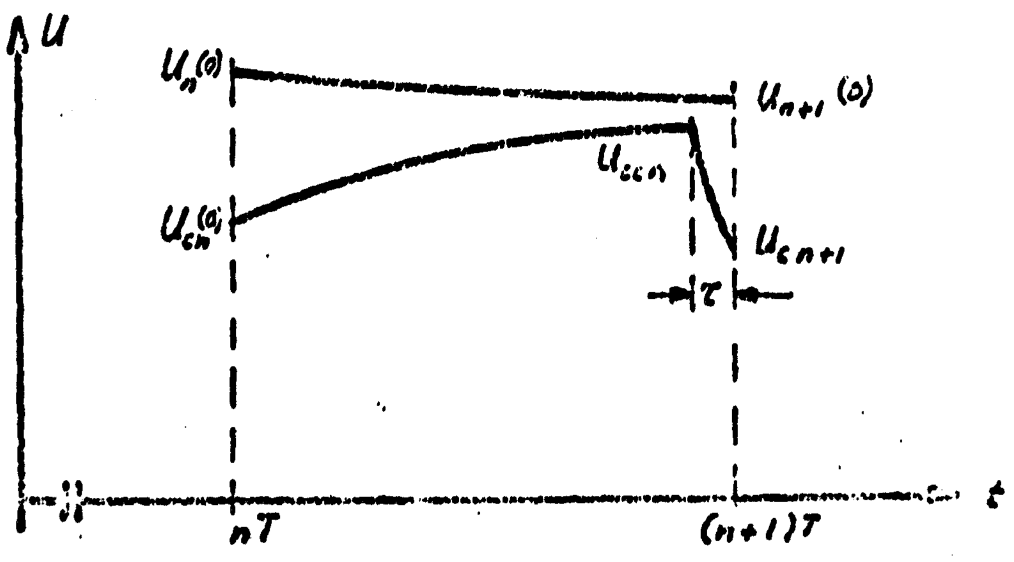

Figure 14

Let us assume: $i_i = 0$

charge resistance $= R = R_i + R_c$

battery emf $= U_o(t) = U_o(0)[1-\alpha q(t)]$

charge $= q(t) = \int_o^t i(t)dt$

battery constant $= \alpha = 1/q(\infty)$

and for

$$nT \leq v \leq (n+1)T$$

let

$$v = nT + t$$

This implies

$$t = v(\text{mod } T) \qquad (14)$$

Rewrite:

the battery emf $= U_o(v) = U_o(nT+t) = U_n(t)$

the battery voltage $= U_B(v) = U_B(nT+t) = U_{Bn}(t)$ (15)

the capacitor voltage $= U_c(v) = U_c(nT+t) = U_{cn}(t)$

U_{ccn} = maximum capacitor voltage during the n'th period.

II.3.1 Switch S Open

When the switch S is open, we can write the following equation for the n'th period:

$$U_o(v) = U_n(t) = U_n(0)\left\{1-\alpha_n\int_o^t i(t)dt\right\}$$

$$= i(t)R + \frac{1}{C}\int_o^t i(t)dt + U_{cn}(0) \qquad (16)$$

If we solve this equation for teh current $i(t)$, we get the following result:

$$i(t) = \frac{U_n(0)-U_{cn}(0)}{R} \exp\left\{-\left[\frac{1}{RC} + \alpha_n \frac{U_n(0)}{R}\right] t\right\} \tag{17}$$

Assuming that $\tau << T$ then we can write $t = T-\tau \approx T$, and find the maximum voltage of the capacitor.

$$U_{ccn} = U_{cn}(T-\tau) \approx U_{cn}(T) = U_{cn}(0) + \frac{1}{C}\int_0^T i(t)dt$$

$$= U_{cn}(0) + \frac{1}{C} q_n(T) \tag{18}$$

where $q_n(T)$ = total charge delivered by the battery during the n'th cycle.

$$q_n(T) = \int_0^T i dt = \frac{U_n(0)-U_{cn}(0)}{\frac{1}{C} + \alpha_n U_n(0)} \left\{1-\exp\left[-\left(\frac{1}{RC} + \alpha_n \frac{U_n(0)}{R}\right)T\right]\right\} \tag{19}$$

If we substitute

$$\gamma_n^* = \exp\left[-\left(\frac{1}{RC} + \alpha_n \frac{U_n(0)}{R}\right)T\right] \tag{20}$$

we can write U_{ccn}

$$U_{ccn} = U_{cn}(0) + \frac{U_n(0)-U_{cn}(0)}{1 + \alpha_n U_n(0)C}\left(1-\gamma_n^*\right) \tag{21}$$

Invariance of γ_n^*, $\alpha_n U_n(0)C$

We will show that $\alpha_n U_n(0)C$, γ_n^* do not depend on n.

We know from the definition of $\alpha = \frac{1}{Q}$

$$\alpha_n = \frac{1}{Q_n}$$

where Q_n = total battery charge remaining in the battery after n periods;

Q = original charge.

$$Q_n = Q-q(n)$$

with

$$q(n) = \sum_{n=0}^{n} q_n(T)$$

then the battery voltage (assuming we extract q(n) during one period from the battery)

$$U_n(0) = U_o(0)[1-\alpha q(n)]$$

$$\alpha_n U_n(0) = \frac{U_n(0)}{Q_n} = \frac{U_o(0)[1-\alpha q(n)]}{Q-q(n)}$$

$$= U_o(0)\,\frac{1}{Q}\cdot\frac{Q-q(n)}{Q-q(n)}$$

$$\alpha_n U_n(0) = \alpha U_o(0)$$

the product $\alpha_n U_n(0)$ does not depend on n and similarly $\gamma_n^* = \gamma_o^* = \gamma^*$.

Then

$$U_{\epsilon cn} = U_{cn}(0) + \frac{U_n(0)-U_{cn}(0)}{1+\alpha U_o(0)}(1-\gamma^*) \qquad (22)$$

$$q_n(T) = \frac{U_n(0)-U_{cn}(0)}{\frac{1}{C}+\alpha U_o(0)}\left(1-\gamma^{\nu}\right) \qquad (23)$$

II.3.2 Switch Closed

Since we assumed that $\tau \ll T$, we conclude that the battery will not contribute to the current in R_d for $T-\tau \leq t \leq T$ and we have the following equivalent network:

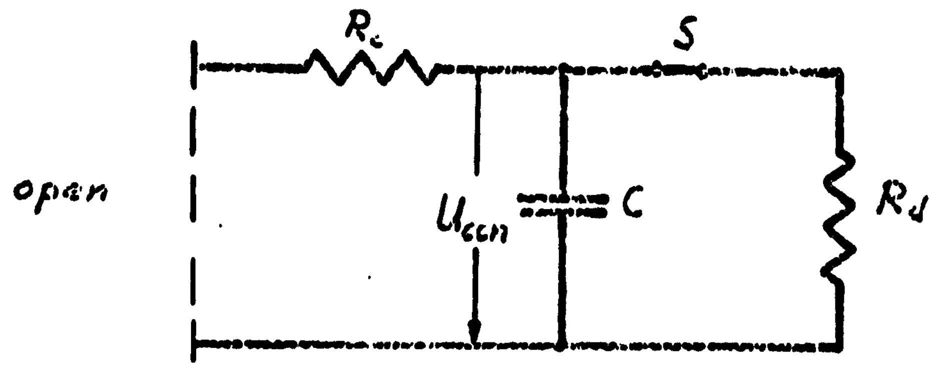

Figure 15

for $t \geq T-\tau$

$$U_{cn}(t) = U_{ccn}\exp\left(-\frac{t-(T-\tau)}{R_dC}\right) \qquad (24)$$

$$U_{cn}(T) = U_{c\,n+1}(0) = U_{ccn}\exp\left(-\frac{\tau}{R_dC}\right) \qquad (25)$$

substituting

$$\delta = \exp\left(-\frac{\tau}{R_dC}\right)$$

$$U_{c\,n+1}(0) = U_{ccn}\delta \qquad (26)$$

II.3.3 Steady State Solution

Now we have all the answers of the n'th period, given the initial conditions of the n'th period. We could continue and determine the initial conditions for the (n+1)'th period and calculate the (n+1)'th period. But for very large n we would spend too much time, therefore we try to determine the conditions of the n'th period, given the initial condition at t=0 for n=0.

Let us assume

$$U_{cn}(0) = \varepsilon_n U_n(0), \tag{27}$$

and we say the system is in <u>steady state</u> for

$$\varepsilon_n = \varepsilon_{n+1} \quad \text{for all } n(n = 0, 1, 2, \ldots) \tag{28}$$

We calculate $\varepsilon_{n+1} = \frac{U_{c\,n+1}(0)}{U_{n+1}(0)}$ with (27), (26), (25), (23), (22), (1)

$$\varepsilon_{n+1} = \frac{\delta\left\{U_{cn}(0) + \frac{U_n(0)-U_{cn}(0)}{1+\alpha U_o(0)C}(1-\gamma^*)\right\}}{U_n(0)\left\{1-\alpha_n\frac{U_n(0)-U_{cn}(0)}{\frac{1}{C}+\alpha U_o(0)}(1-\gamma^*)\right\}}$$

$$= \frac{\delta\left\{\frac{U_{cn}(0)}{U_n(0)} + \frac{1-\frac{U_{cn}(0)}{U_n(0)}}{1+\alpha U_o(0)C}(1-\gamma^*)\right\}}{1-\alpha_n U_n(0)\frac{1-\frac{U_{cn}(0)}{U_n(0)}}{\frac{1}{C}+\alpha U\;(0)}(1-\gamma^*)}$$

Before we continue we will make another substitution for the product $\alpha U_o(0)C$.

$$\alpha = 1/Q$$

$$Q = U_o(0)\,C_B \quad \text{battery charge}$$

$$C_B = \text{euqivalent capacitor}$$

$$\alpha U_o(0)C = \frac{U_o(0)C}{U_o(0)C_B} = \frac{C}{C_B} = \rho$$

Substitute

$$\alpha U_o(0)C = \alpha_n U_n(0)C = \rho \tag{29}$$

Since we assume there exists an $\varepsilon = \varepsilon_n$ then

$$\frac{U_{\varepsilon n}(0)}{U_n(0)} = \frac{U_{\varepsilon\, n+1}(0)}{U_{n+1}(0)} = \varepsilon$$

$$\varepsilon = \frac{\delta\left[\varepsilon + \frac{1-\varepsilon}{1+\rho}(1-\gamma^{\kappa})\right]}{1-\rho\frac{1-\varepsilon}{1+\rho}(1-\gamma^{\kappa})} \tag{30}$$

This gives the follwoing quadratic equation in ε

$$\varepsilon^2 + \varepsilon \underbrace{\frac{1+\rho\gamma - \delta(\gamma^{\kappa}+\rho)}{\rho(1-\gamma^{\kappa})}}_{p} - \underbrace{\frac{\delta}{\rho}}_{m} = 0 \tag{31}$$

which can be solved in the normal way

$$\varepsilon = -\frac{p}{2} \pm \sqrt{\frac{p^2}{4} - m}$$

Since all terms are independent of n, ε exists and $\varepsilon = \varepsilon_n$ for all n. For the case of constant battery voltage $U_o(0) = U_1(0) = \ldots = U_n(0)$, this implies infinite battery charge → α = C, ρ = 0,

then

$$\gamma^* = \exp\left[-\left(\frac{1}{RC} + \frac{\alpha U_o(0)}{R} \cdot T\right)\right] \quad .$$

$$\gamma^* = \exp\left(-\frac{T}{RC}\right) = \gamma$$

$$\varepsilon = \frac{1-\gamma}{\frac{1}{\delta} - \gamma} \qquad (32)$$

Approximation for later computation:

For most applications ρ << 1 and we can substitute

$$\varepsilon = \frac{1-\gamma}{\frac{1}{\delta} - \gamma}$$

without making large errors.

Now we know there exists an initial condition

$U_{co}(0) = \varepsilon U_o(0)$ so that

$U_{cn}(0) = \varepsilon U_n(0)$ for all n, but we have not found an easy expression for

$U_n(0) = f(U_o(0))$.

We assume there exists a ξ, such that

$$U_1(0) = \xi U_o(0)$$

or

$$U_n(0) = \xi^n U_o(0)$$

or

$$U_n(0) = \xi U_{n-1}(0)$$

$$\xi = \frac{U_n(0)}{U_{n-1}(0)} = \frac{U_{n-1}(0)(1-\alpha_n q_n)}{U_{n-1}(0)} = 1-\alpha_n q_n$$

with

$$\rho = \alpha_n U_n(0) C$$

$$q_n = (U_{\epsilon\epsilon n} - U_{\epsilon n}) C$$

$$U_{\epsilon\epsilon n} = \frac{1}{\delta} U_{\epsilon n+1}(0) = \frac{1}{\delta}\epsilon U_{n+1}(0)$$

$$U_{n+1}(0) = \xi U_n(0)$$

then

$$\xi = 1-\alpha_n q_n$$

$$= 1-\alpha_n\left[\frac{1}{\delta}\epsilon\xi U_n(0) - \epsilon U_n(0)\right] C$$

$$= 1-\rho\left(\frac{\epsilon}{\delta}\xi - \epsilon\right)$$

$$\xi = \frac{1+\epsilon\rho}{1+\frac{\epsilon}{\delta}\rho} \qquad (33)$$

With ξ we can determine all values for any given n, provided we start with $U^*_{\epsilon o}(0) = \epsilon U_o(0)$. But even if we don't start with $U^*_{\epsilon o}(0)$ we can use this formula; since this system behaves like a dynamic system with damping, every solution will converge to the steady state solution for every initial condition. For large n we will therefore neglect the effect of the initial condition and assume that the system is in steady state for all times.

$$U_n(0) = U_o(0)\xi^n \qquad (34)$$

We can calculate the minimum battery voltage, assuming that the minimum occurs at the beginning of a period.

$$U_{B\,min} = U_{cn} + (U_n - U_{cn})\frac{R_c}{R_1+R_c}$$

$$= U_o(0)\xi^n\left[(1-\varepsilon)\frac{R_c}{R_1+R_c} + \varepsilon\right] \qquad (35)$$

We limit the voltage drop at the battery to $\beta U_o(0)$

$$U_{B\,min} = (1-\beta)U_o(0) \qquad (36)$$

with (35) in (36)

$$1-\beta = \xi^n\left[\frac{R_c}{R_1+R_c}(1-\varepsilon) + \varepsilon\right]$$

or

$$N_B = \frac{1}{\ln\xi}\left\{\ln(1-\beta) - \ln\left[\frac{R_c}{R_1+R_c}(1-\varepsilon) + \varepsilon\right]\right\} \qquad (37)$$

Limiting the voltage drop at the capacitor to $\kappa U_o(0)$ leads to:

$$U_{c\,min} = U_{cn}(0) = \varepsilon U_n(0) = \varepsilon\xi^n U_o(0) = (1-\kappa)U_o(0) \qquad (38)$$

or

$$N_c = \frac{1}{\ln\xi}\ln\frac{1-\kappa}{\varepsilon} \qquad (39)$$

Now we have the number of pulses when we reach the minimum battery voltage or when we reach the minimum capacitor voltage. Clearly, we can take only the lower one of both.

$$N = \mathrm{Min}(N_B, N_C)$$

II.4 Conclusions

Assuming that we can model the battery as a large capacitor with internal impedance, we were able to calculate the number of pulses for Model #1 and Model #2. In order to do so for Model #2 we had to introduce

$$\varepsilon = \frac{U_{Cn}(0)}{U_n(0)}$$

and

$$\xi = \frac{U_n(0)}{U_{n-1}(0)}$$

A further difficulty in determining the number of pulses for Model #2 is that we obtained two results (36), (38) and we have to choose the smaller value of both. The reason for these two results is the one degree of freedom we have in choosing a combination of battery and capacitor, while in Model #1 everything is fixed. The assumption $\tau \ll T$ is not necessary for Model #1, but it is for #2. Therefore, for some $\tau > \tau_o$ (where τ_o is some limit for τ) the number of pulses for #2 will be in error and should only be used for $\tau \leq \tau_o$.

CHAPTER III

In Chapter II we derived the necessary formulas to determine the number of pulses for each Model. In this chapter we will use the formulas and calculate an optimal energy storage for the Sunblazer satellite. By varying different parameters we will find the sensitivity of each storage system to these parameters. Then we will propose a cost function to evaluate the "goodness" of each model and to make a comparison between sotrage systems easier and more meaningful.

III.1 Calculation of N

What are the specifications for satellite application? There will be a weight limit, which we will call W_t where t stands for total. The other specifications are the pulse period T, the pulse width τ, the minimum and maximum transmitter voltage U_{min}, $U_o(0)$. Since we want to have a high number of pulses, we will use high capacity elements like Ni-Cd batteries and electrolytic capacitors. These elements are also very reliable which is one of the requirements for space application. They have constant specific energy density (stored energy per kg) over wide voltage ranges. This is not true for capacitors, certainly not at a low voltage level. Therefore we assume to have a dc - dc energy converter without losses that shifts the voltage into a range, where the energy density is approximately independent of the voltage. We will choose the voltage

$$U_o(0) = 30 \text{ V}$$

(equals the operating voltage in the satellite),

the capacitor constant

$$\rho_c = 0.111 \text{ F/kg} ,$$

the battery constant

$$\rho_B = 4000 \text{ As/kg}$$

and the internal battery resistance constant

$$\rho_R = 60, R_i = \rho_R \cdot \frac{U_o(0)}{Q_b}$$

($U_o(0)$ = battery emf at t = 0, Q_b = total battery charge).
These constants are obtained by averaging the available empirical data from references as [1], [2].
Necessary wires, resistors and switches (transistors) are considered to be negligible in weight and are not included in the weight total. The computation has been done on a digital computer. The program is printed in the appendix.

III.2 Model #1

We use the formula

$$N = \frac{R_i + R_d}{\alpha U_o(0)\tau} \ln\left[\frac{R}{R_i + R_d} \frac{1}{1-\beta}\right]$$

Specifying

W_t = total weight

$U_o(0)$ = initial battery emf

τ = pulse width

β = allowable voltage drop at the battery

R_d = transmitter resistance

we can calculate

$$Q_b = W_t \rho_b$$

where

$$Q_B = \text{total battery charge}$$

and

$$\alpha = 1/Q_B$$

then

$$R_i = \rho_R \frac{U_o(0)}{Q_B}$$

and hence N which is in this case N_{max}.

III.2.1 Calculation of $N(W_t)$

Constant parameters are: R_d, τ, T, β, $U_o(0)$.

Variables are: W_t, $R_i = f(W_t)$.

R_i is small compared to R_d, therefore a change in R_i produces only minor changes in N. But R_i determines the region for which $N \geq 0$.

$$N \geq 0 \quad \text{for} \quad \frac{R_d}{R_i + R_d} \frac{1}{1-\beta} \geq 1 \qquad \text{from (12)}$$

substituting

$$R_i = \rho_R \frac{U_o(0)}{Q_B} = \frac{\rho_R U_o(0)}{\rho_b W_t}$$

$$W_t \geq \frac{\rho_R U_o(0)(1-\beta)}{\rho_\beta R_d \beta}$$

for

$$\beta \approx 0.15, \quad U_o(0) = 30 \text{ V}, \quad R_d = 1.0\Omega,$$

$$\rho_R = 60, \quad \rho_\beta = 4000$$

then

$$W_{to} = 2.55 \text{ kg}$$

If we substitute in (11)

$$\alpha = 1/Q = 1/\rho_\beta \cdot W_t$$

we see that N (neglecting change in R_i) is directly proportional to W . Therefore we can write

$$N = k_o + k_1 W_t$$

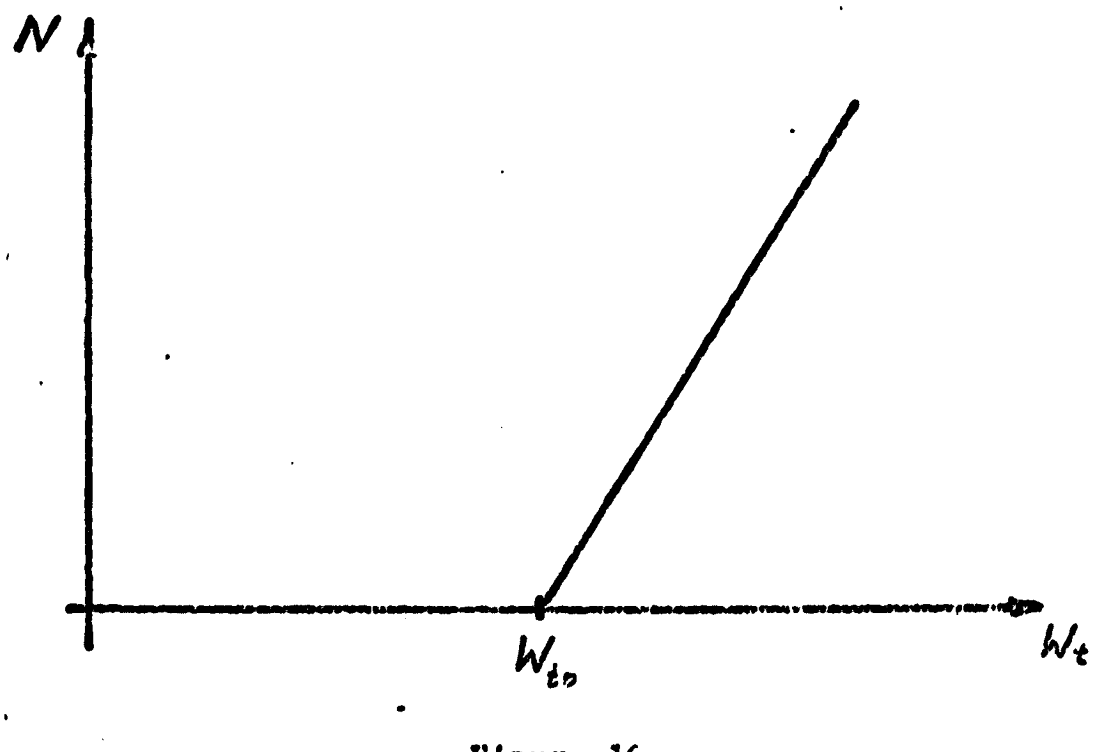

Figure 16

III.2.2 Calculation of $N(\tau)$

Fixed parameters are W_t, β, $U_o(0)$, R_d,

then

$$N(\tau) = N_o/\tau \text{ is a hyperbola}$$

with

$$N_o = \frac{R_i+R_d}{\alpha U_o(0)} \ln \frac{R_d}{R_i+R_d} \frac{1}{1-\beta}$$

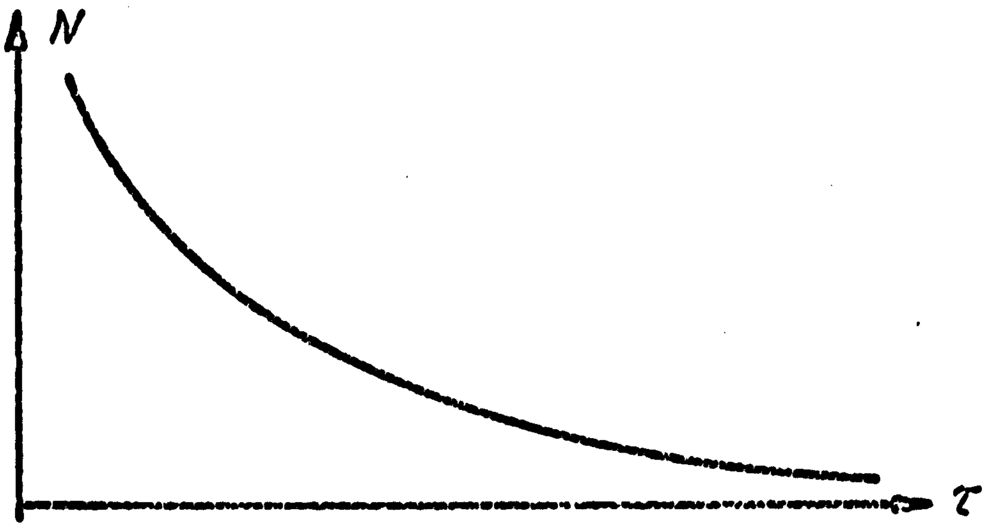

Figure 17

III.2.3 Calculation of $N(\beta)$

Fixed parameters are: W_t, $U_o(0)$, R_d, τ,

then

$$N(\beta) = N_1 (r + \ln \frac{1}{1-\beta})$$

$$= N_1 r - N_1 \ln[1-\beta]$$

where

$$N_1 = \frac{R}{\alpha U_o(0)\tau}, \qquad r = \ln \frac{R_d}{R_1+R_d}$$

$$N \geq 0 \quad \text{for} \quad \frac{R_d}{R_i + R_d} \cdot \frac{1}{1-\beta} \geq 1$$

$$N = 0 \quad \text{for} \quad \beta \leq \frac{R_i}{R_i + R_d} = \beta_o$$

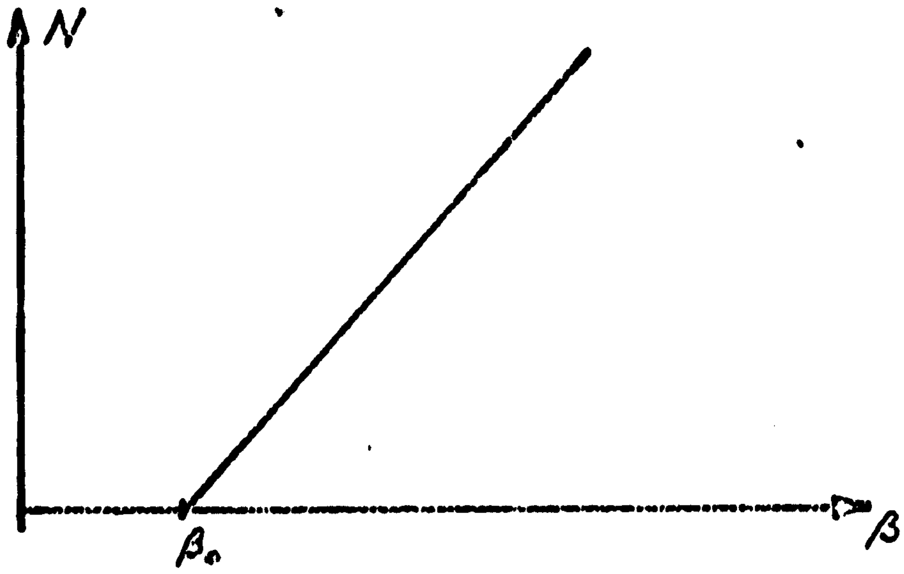

Figure 18

III.3 Model #2

We use the formulas (37) and (39)

$$N_B = \frac{1}{\ln\xi}\left\{\ln(1-\beta) - \ln\left[\frac{R_c}{R_i+R_c}(1-\varepsilon)+\varepsilon\right]\right\}$$

and

$$N = \frac{1}{\ln\xi}\ln\frac{1-\kappa}{\varepsilon}$$

where

$$\xi = \frac{1+\varepsilon\rho}{1+\frac{\varepsilon}{\delta}\rho}$$

$$\varepsilon = \delta\,\frac{1-\gamma}{1-\delta\gamma}$$

$$\gamma = \exp\left\{-\left(\frac{1}{RC} + \frac{\alpha U_o(0)}{R}\right)T\right\}$$

$$\delta = \exp\left(-\frac{T}{R_d C}\right)$$

We specify W_t, $U_o(0)$, τ, β, R_d like in Model #1 and additionally

T = pulse period

κ = allowable voltage drop at the capacitor

C = capacitor

R_c = additional charge resistor

From C we calculate

$$W_c = C/\rho_c$$

where W_c = weight of the capacitor,

$$W_B = W_t - W_c$$

where W_B = weight of battery.

III.3.1 <u>Calculation of $N_{B,C} = f(R_c)$</u>

We calculate and plot N_B, N_c = $f(R_c)$

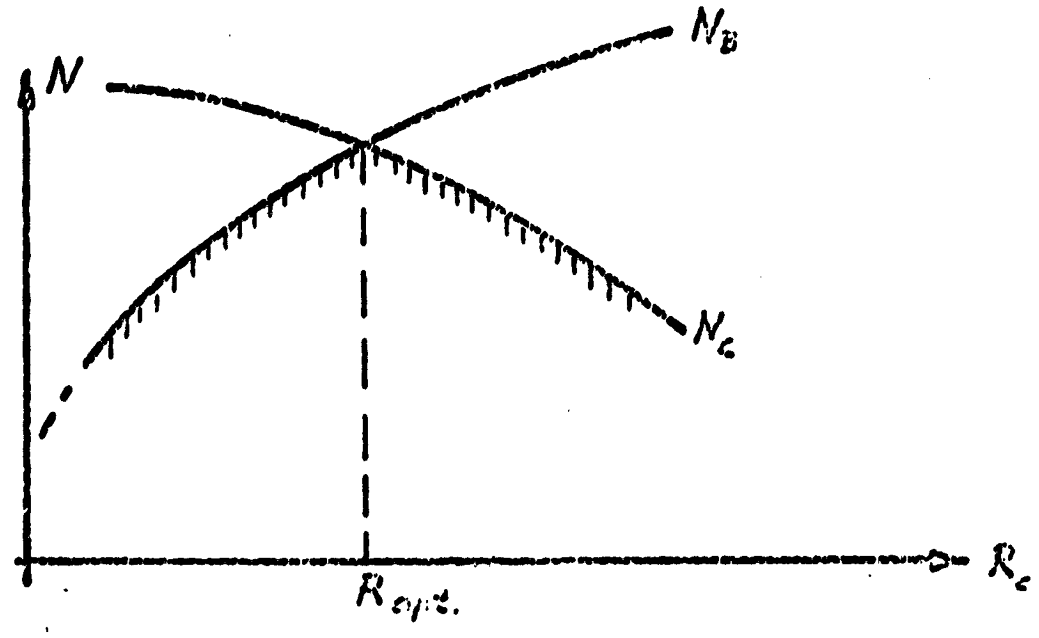

Figure 19

$N_B = f(R_c)$ is a monotonic increasing function of R_c, $N_c = g(R_c)$ is monotonically decreasing

$$N = \mathrm{Min}(N_B, N_c)$$

This implies that

$$N_{max} = \mathrm{Max}\ N$$

occurs for

$$N_B = N_c$$

By choosing an arbitrary R_c, we will generally not get the maximum, therefore we developed an algorithm that leads to the maximum.

We plot

$$N_c - N_B = f(R_c)$$

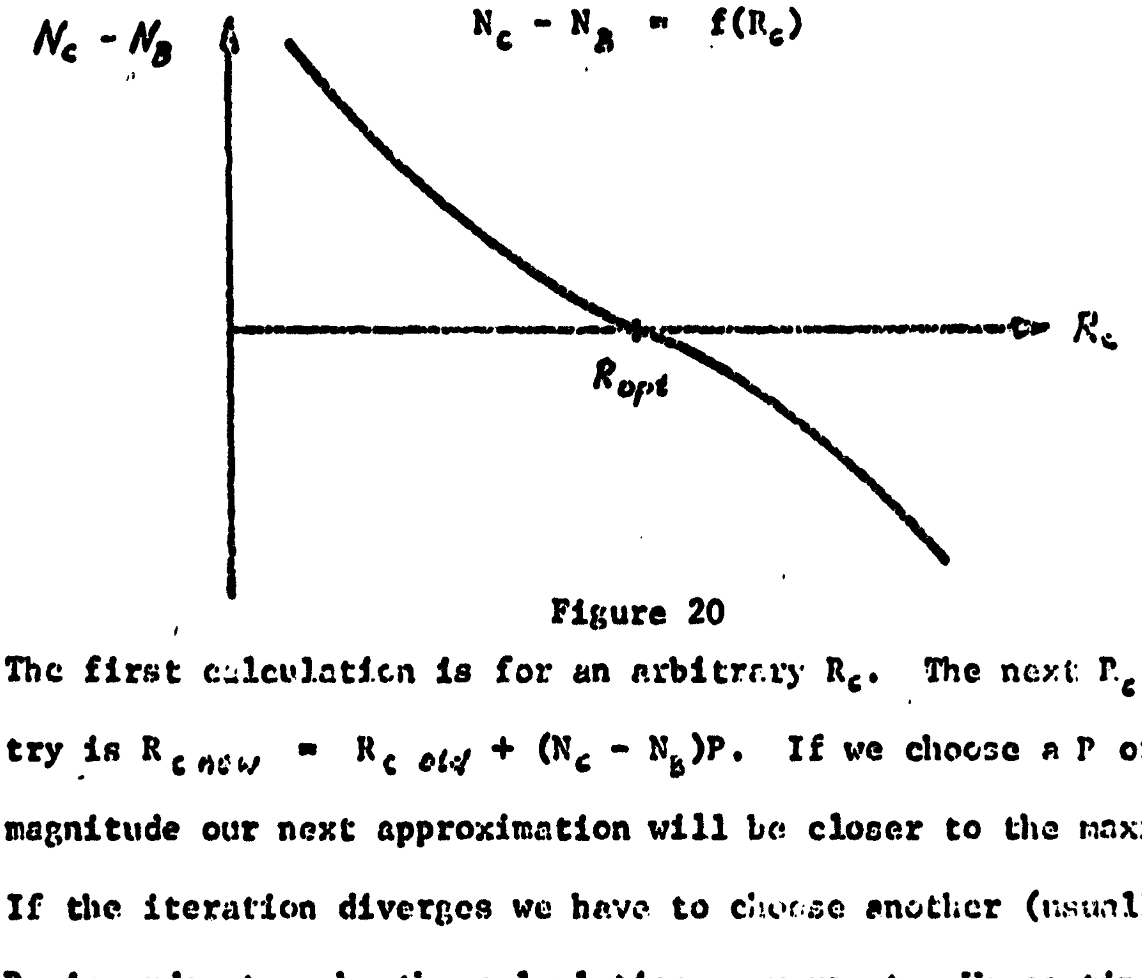

Figure 20

The first calculation is for an arbitrary R_c. The next R_c, we will try is $R_{c\,new} = R_{c\,old} + (N_c - N_B)P$. If we choose a P of right magnitude our next approximation will be closer to the maximum. If the iteration diverges we have to choose another (usually smaller) P, in order to make the calculation convergent. We continue until we find $N_B = N_c = N_{max}$.

III.3.2 Calculation of N(C)

Since the total weight splits into the weight for the battery and the weight for the capacitor, we have an infinite possibility to combine these two components under the condition that the total weight remains constant. Therefore we calculate $N = N(C)$ for various C. $N = N(C)$ is not just any $N(C)$ but $N_{max}(C)$, the maximum possible N (that means we try all possible (R_t) as in section III.3.1.). We plot $N = N_{max}(C)$ for W_t = constant.

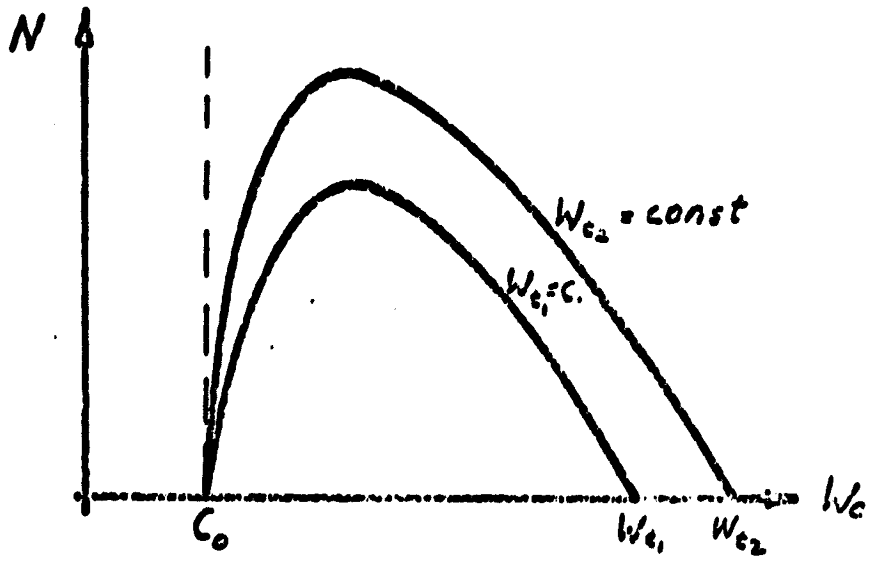

Figure 21

N(C) goes to zero for $C \to C_0$ and C = 100%. For W_c = 100% there is no battery left to charge the capacitor. For

$$C \leq C_0$$

$$\delta = \exp\left(-\frac{\tau}{R\ C}\right) \leq 1-\kappa$$

then

$$C_0 = -\frac{\tau}{R_d \ln(1-\kappa)}$$

with

κ = maximum voltage drop at the capacitor.

This implies that the voltage at R_d is smaller than the minimum voltage $(1-\kappa)U_o$ during the first pulse; therefore, N = 0. C_o depends only on τ, R_d, κ, but is independent of W_t and the other parameters. This explains why all N = $N_{max}(C_o)$ = 0 for all W_t.

III.3.3 Calculation of $N(W_t)$

Constant parameters are: R_d, β, κ, T, τ.

Variables are C, R_c, W_t.

Now we find the maximum of every W_t = constant from the diagram. That is

$$N = \max_{R_c, C} N = N_{max}(C, R_c)$$

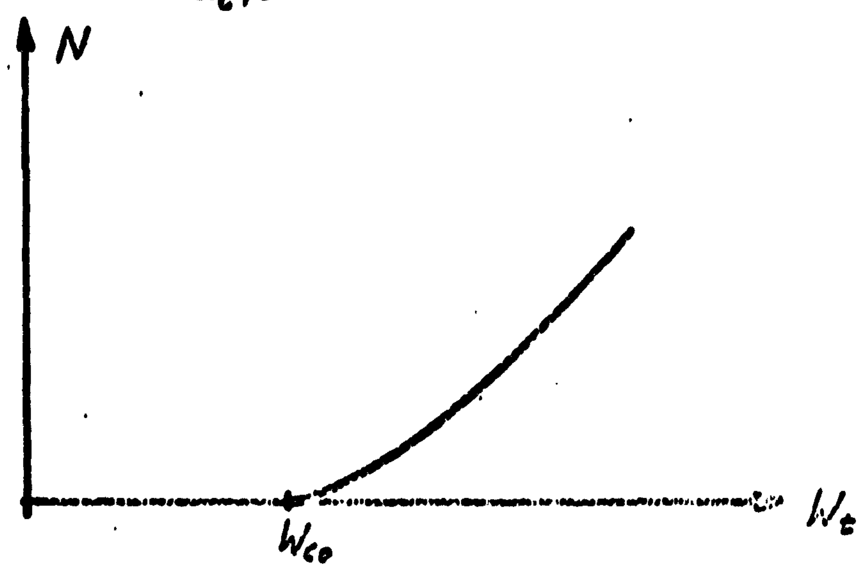

Figure 22

III.3.4 Calculation of $N(\tau)$

Constant parameters are: W_t, R_d, β, κ, T.

Variables are: R_c, C, τ.

$$N = \max_{R_c, C} N(\tau)$$

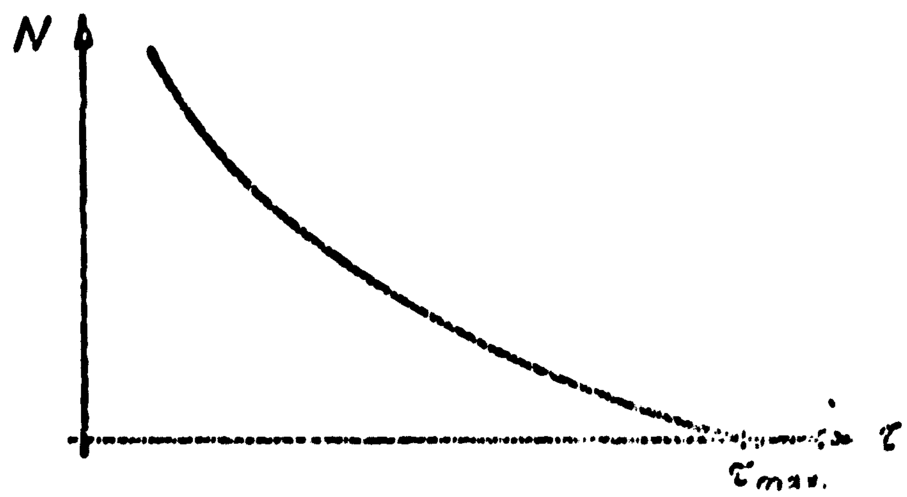

Figure 23

This curve has a hyperbolic character. Assuming that we draw constant power P from the capacitor during τ, then

$$E_o = P\tau \text{ per pulse.}$$

In W_t we can store E_{max}. Then the number of pulses we can get from the storage system is

$$N \approx \frac{E_{max}}{E_o} = \frac{E_{max}}{P\tau}$$

which is a hyperbola. For τ too large N goes toward zero ($N \to 0$). The minimum capacitor (as shown in III.3.2) $C_o = -\frac{\tau}{R\ \ln(1-\kappa)}$ is proportional to τ. For large τ the capacitor will weigh W_t, so that the battery gets smaller and smaller as τ increases.

$$N = 0 \text{ for } W_c = W_t = \frac{C}{\rho_c} = \frac{-\tau}{\rho_c R_d \ln(1-\kappa)}$$

So the maximum τ is:

$$\tau \leq - W_t \rho_c R_d \ln(1-\kappa)$$

with

$$\rho_c = 0.11, \quad R_d = 1.0, \quad \kappa = 0.7$$

then

$$\tau_{max} \approx 0.0396 \text{ sec/kg}$$

$$\tau_{max} \approx 0.04 \text{ sec/kg}$$

III.3.5 Calculation of $N(\beta)$

Constant parameters are: W_c, R_d, κ, τ, T.

Variables are: R_c, C, β.

$$N = \max_{R_c, C} N(\beta)$$

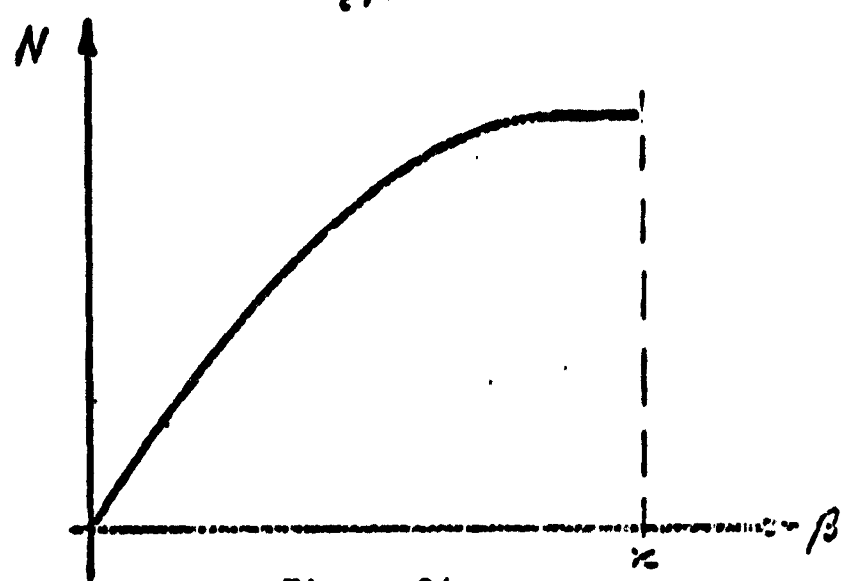

Figure 24

For small β, $N(\beta)$ is proportional to β. When β approaches κ ($\beta \to \kappa$) and large N (when the battery is already partially discharged) the difference between battery voltage and capacitor voltage is too small to charge the capacitor. Then the increase in N, $\Delta N \to 0$ as $\beta \to \kappa$.

III.4 Comparison between Model #1 and Model #2

In the sections III.2 and III.3 we have seen the dependence of N on each parameter. It would be ideal to have a function k (of all parameters), that tells us which combination of parameters and which model is the best. This function would be a cost function where the parameters are weighted by some factors and whenever this function is an extremum we would have a best or worst model.

In these applications nearly all parameters are fixed, like τ, T, W_t, R_d, $U_o(0)$, κ. Since we use Ni-Cd batteries the voltage drop β is fixed too, and we calculated N with $\beta = 0.15$ which is practically the upper limit. For Model #1 there is no optimization, because the battery is chosen as large as possible $W_B = W_t$. But for Model #2 we optimized over W_B, W_c, R_c ($W_t = W_B + W_c$) and found a maximum of N for a particular combination of W_B, W_c, R_c. Therefore the cost function for Model #2 is $N = N(W_c, R_c, W_B)$. Since this function is nonlinear and not explicitly solvable the optimization is not a straight forward procedure. It is done graphically. In the following we will assign N_2 to N for Model #2 and N_1 to N for Model #1. N_2 splits into N_{2B}, N_{2C} as in formulas (37) and (39) $N_B = N_{2B}$ and $N_C = N_{2C}$ respectively.

III.4.1 Optimization over R_c, $N_2 = N_2(R_c)$. Diagram 1

Constant parameters are: W_t, C, R_d, T, τ, β, κ.

For the optimal combination of W_c and W_B, N_{2C} and N_{2B} are plotted as functions of R_c in diagram (1) page 47. $N = Min(N_{2C}, N_{2B})$. We see that $N \approx N_{max}$ for a fairly wide range of R_c. We conclude

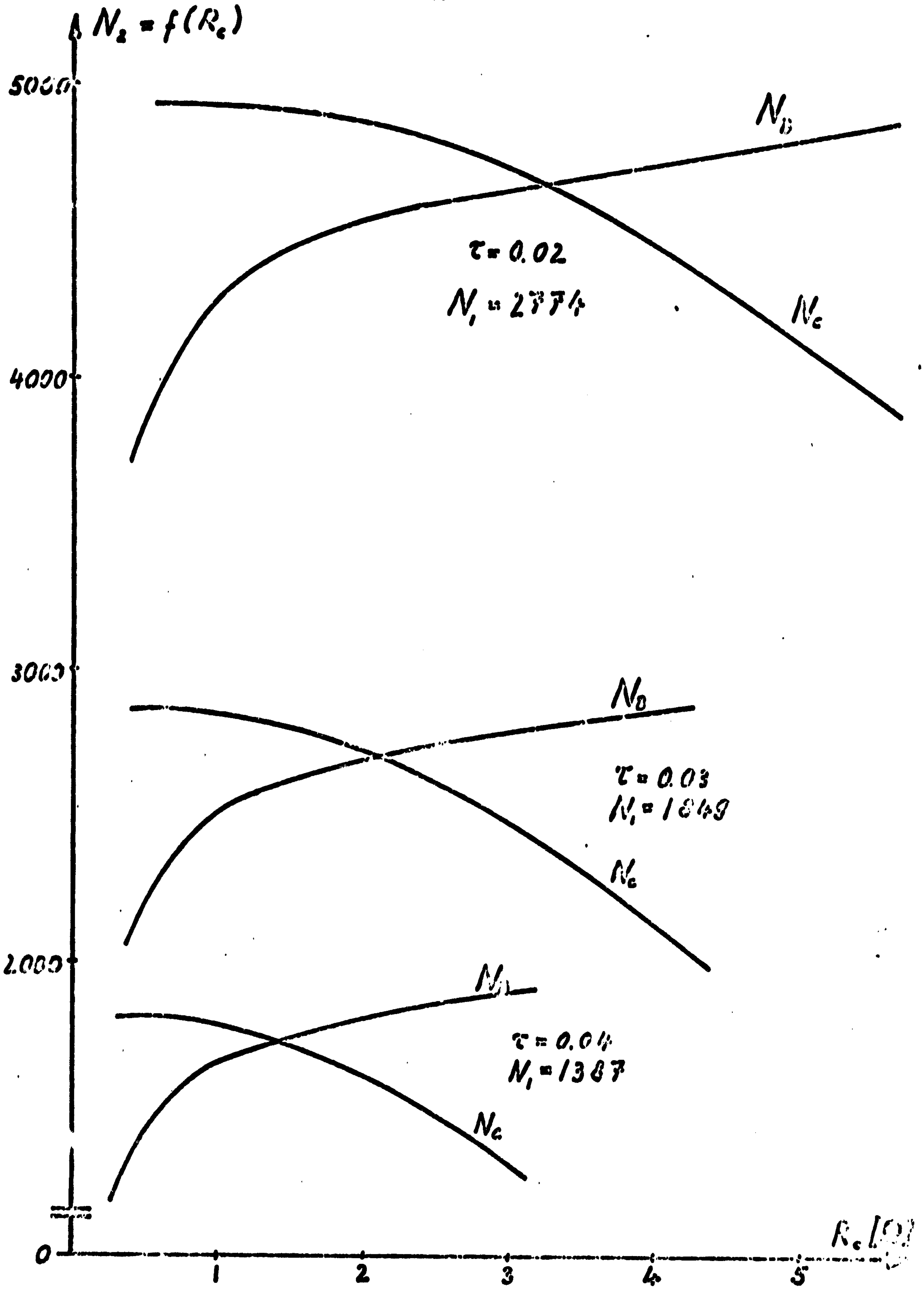

Diagram 1. N_{2B}, N_{2C} = $f(R_c)$

W_t = 5.0 kg, R_d = 1.0, T = 1.0, ε = 0.15, κ = 0.3

that an error in R_c is not very critical with respect to N_{max} as long as $R_c \approx R_{opt}$.

The diagram also shows the dependence of N_{2c}, $N_{2\ell}$ on R_c for different τ. To compare N_2 and N_1 the diagram also contains N_1.

III.4.2 Optimization over C, $N_2 = N_2(C)$. Diagrams 2, 4, 6

Constant parameters are: W_t, R_d, T, τ, β, κ.

For $R_c = R_{opt}$ diagram (2) page 49 shows the plot of $N_2 = N_2(W_c)$. W_c is directly proportional to C, so this diagram also represents $N_2 = N_2(C)$. The plot shows for all $C > C_o$ (see III.3.2) a very strong dependence of N_2 on C. Small deviations in C from C_{opt} result in large decreases of N_2, especially for $C_o < C < C_{opt}$. In the shaded areas $N_1 > N_2$.

Diagram (3) page 50 shows $W_B = f(W_c)$, with $W_B = W_t - W_c$ and the parameter N_2 = constant. This graph makes it easier to find the optimal W_c and N for any W_t given that R_d, β, τ, T, κ are fixed.

Diagrams (5,7) pages 52,54 represent $N_2 = N_2(C)$ and $W_B = f(W_c)$ as described above but for different τ. As τ increases the region with $N_2 > N_1$ decreases, because the capacitor grows larger and larger and cuts down on the battery size (see III.3.4).

III.4.3 Plot of $N = N(W_t)$. Diagram 8

Constant parameters are: R_d, T, τ, β, κ.

N_1, $N_2 = f(W_t)$ are as from III.2.1 and III.3.3 expected. $N_2 < N_1$ for all W but with τ increasing then $N_1 \to N_2$.

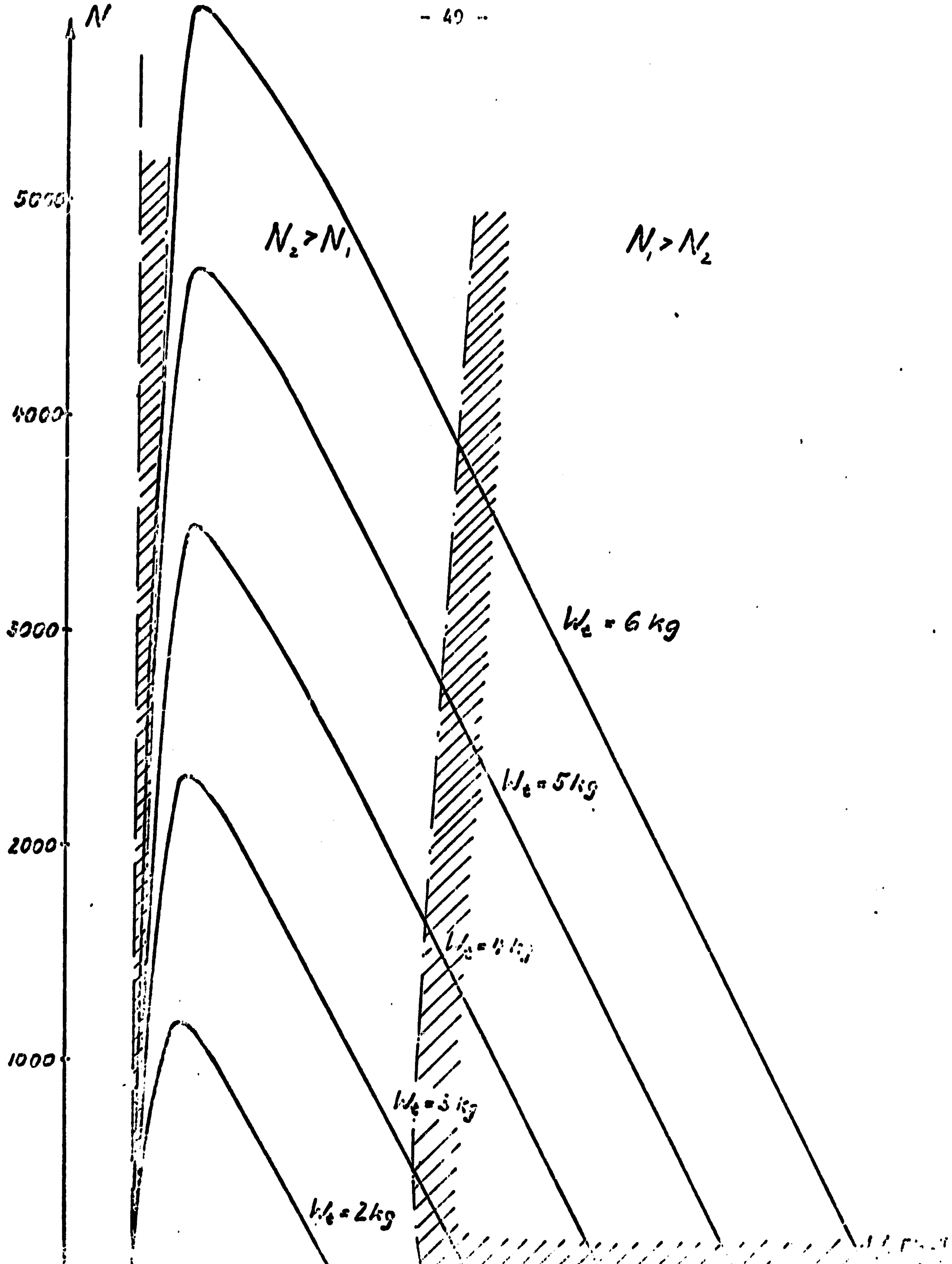

Diagram 2. $N_2 = f(W_c)$

$R_d = 1.0, \quad T = 1.0, \; \beta = 0.15, \; \kappa = 0.3, \; \iota = 0.02$

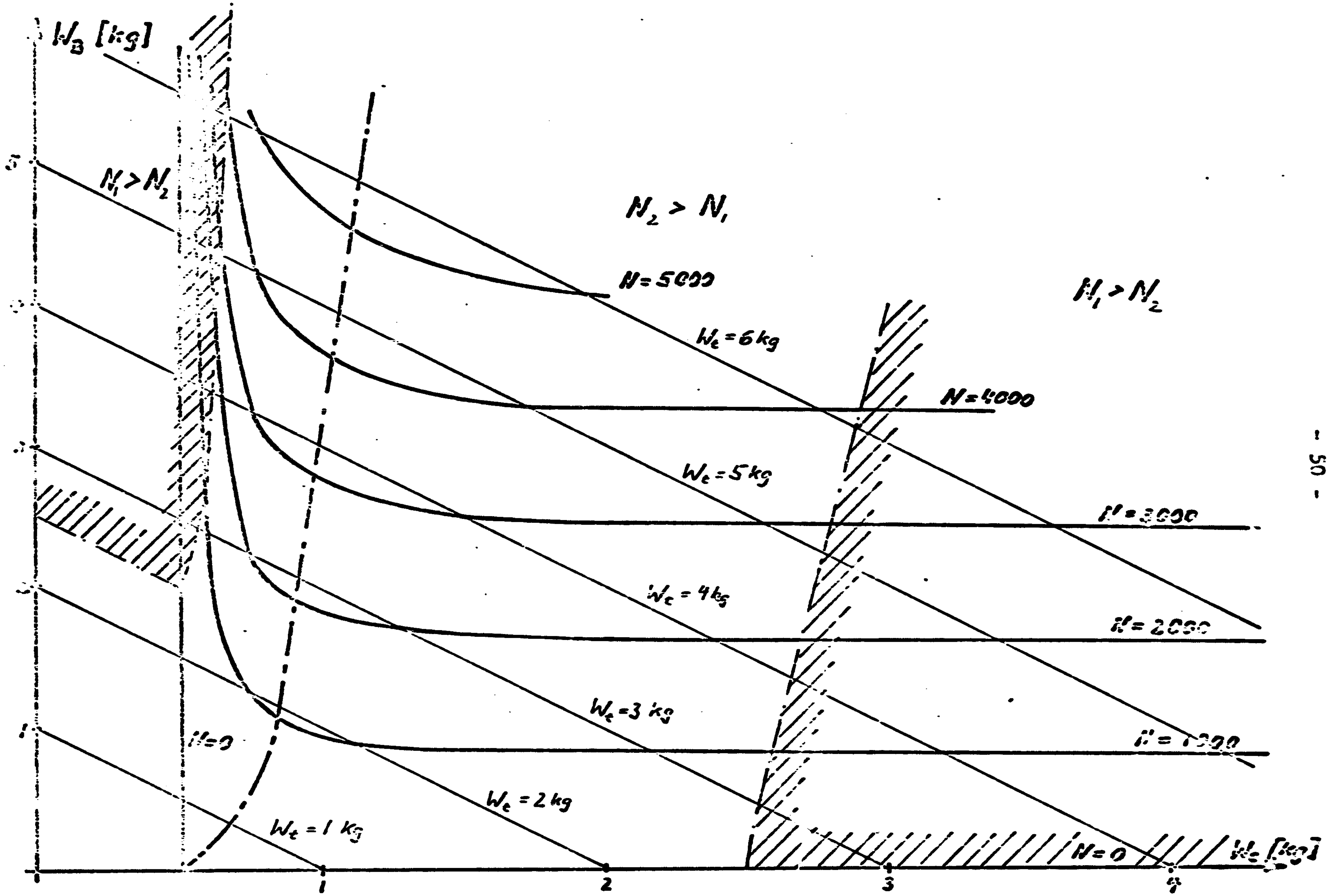

Diagram 3. $W_B = f(W_c)$

$R_d = 1.0$, $T = 1.0$, $\beta = 0.15$, $\kappa = 0.3$, $\tau = 0.02$

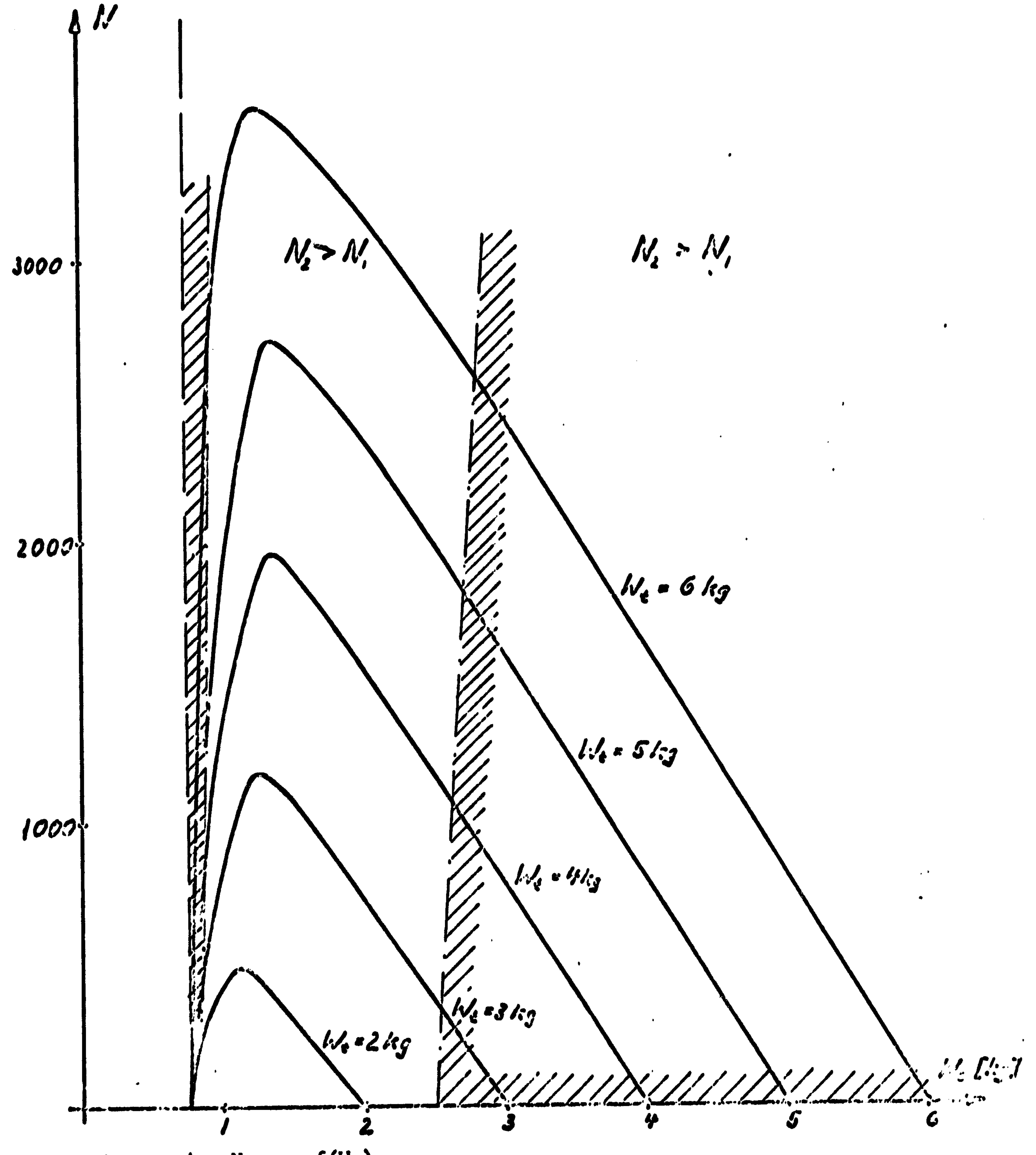

Diagram 4. $N_2 = f(W_c)$

$R_d = 1.0$, $T = 1.0$, $\beta = 0.15$, $\kappa = 0.3$, $\tau = 0.03$

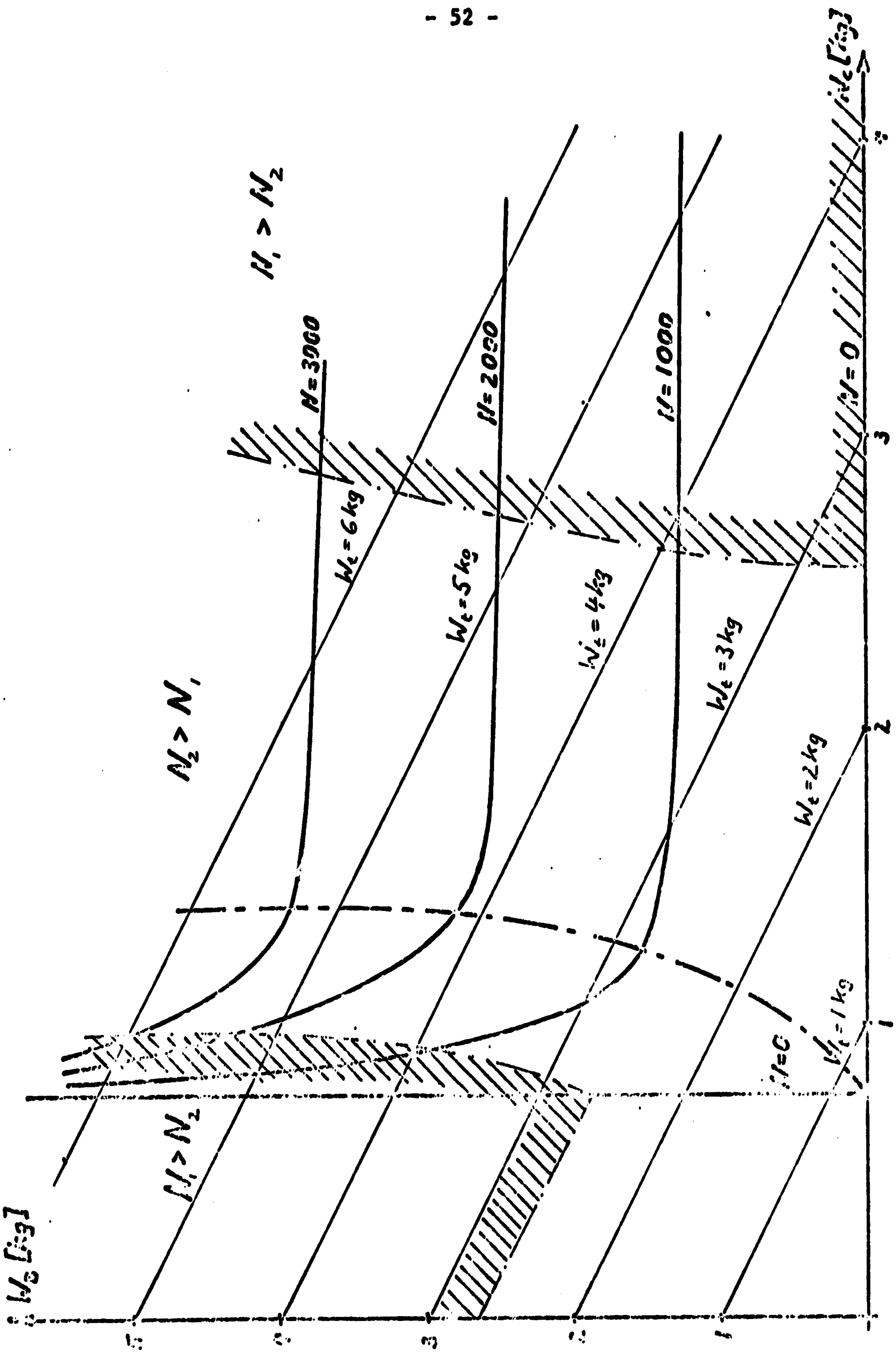

Diagram 5. $\hat{N}_B = f(W_c)$

$t_d = 1.0, \; ? = 1.0, \; \beta = 0.25, \; \kappa = 0.3, \; \tau = 0.03$

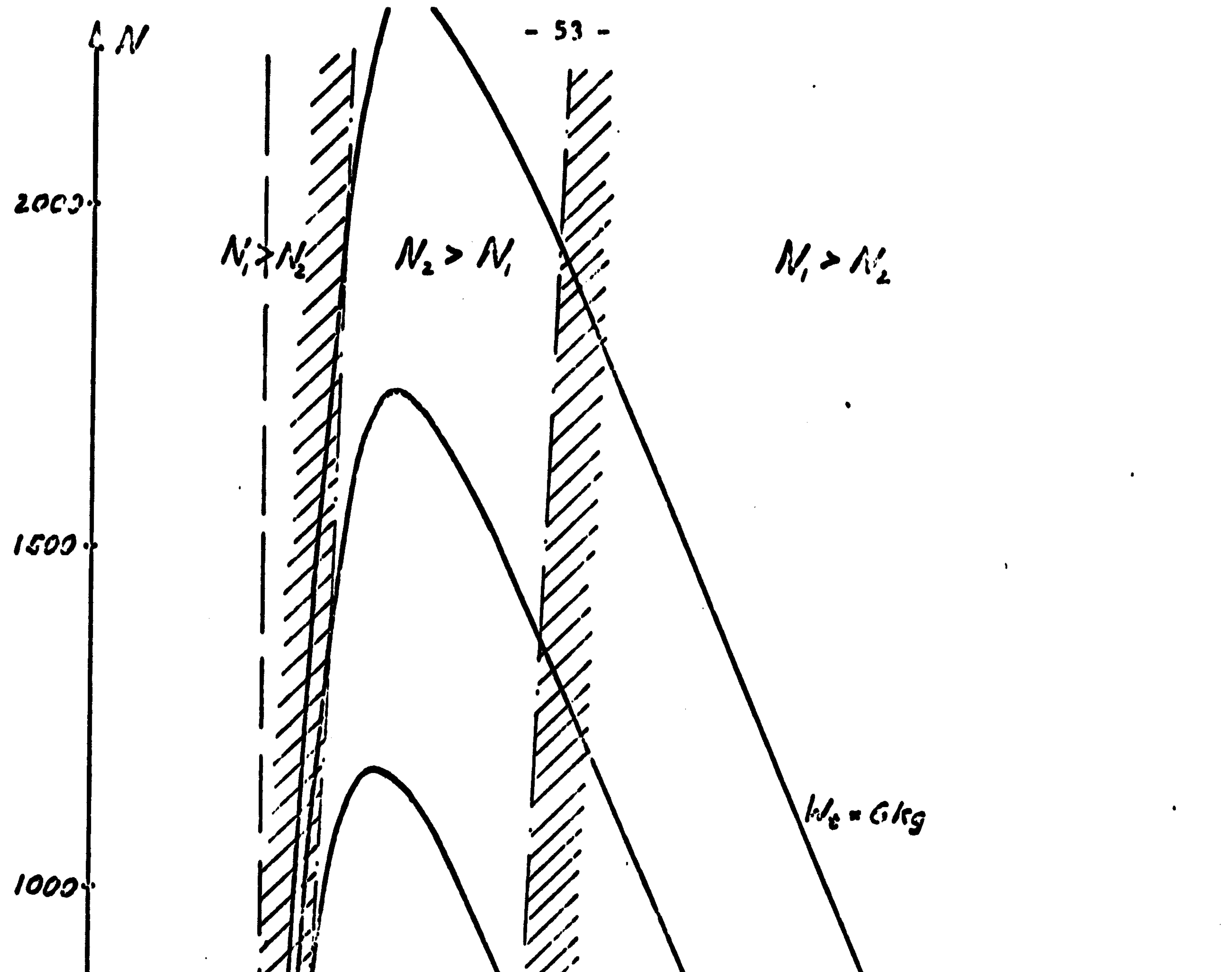

Diagram 6. $N_2 = f(W_c)$

$R_d = 1.0$, $T = 1.0$, $\beta = 0.15$, $\kappa = 0.3$, $\tau = 0.04$

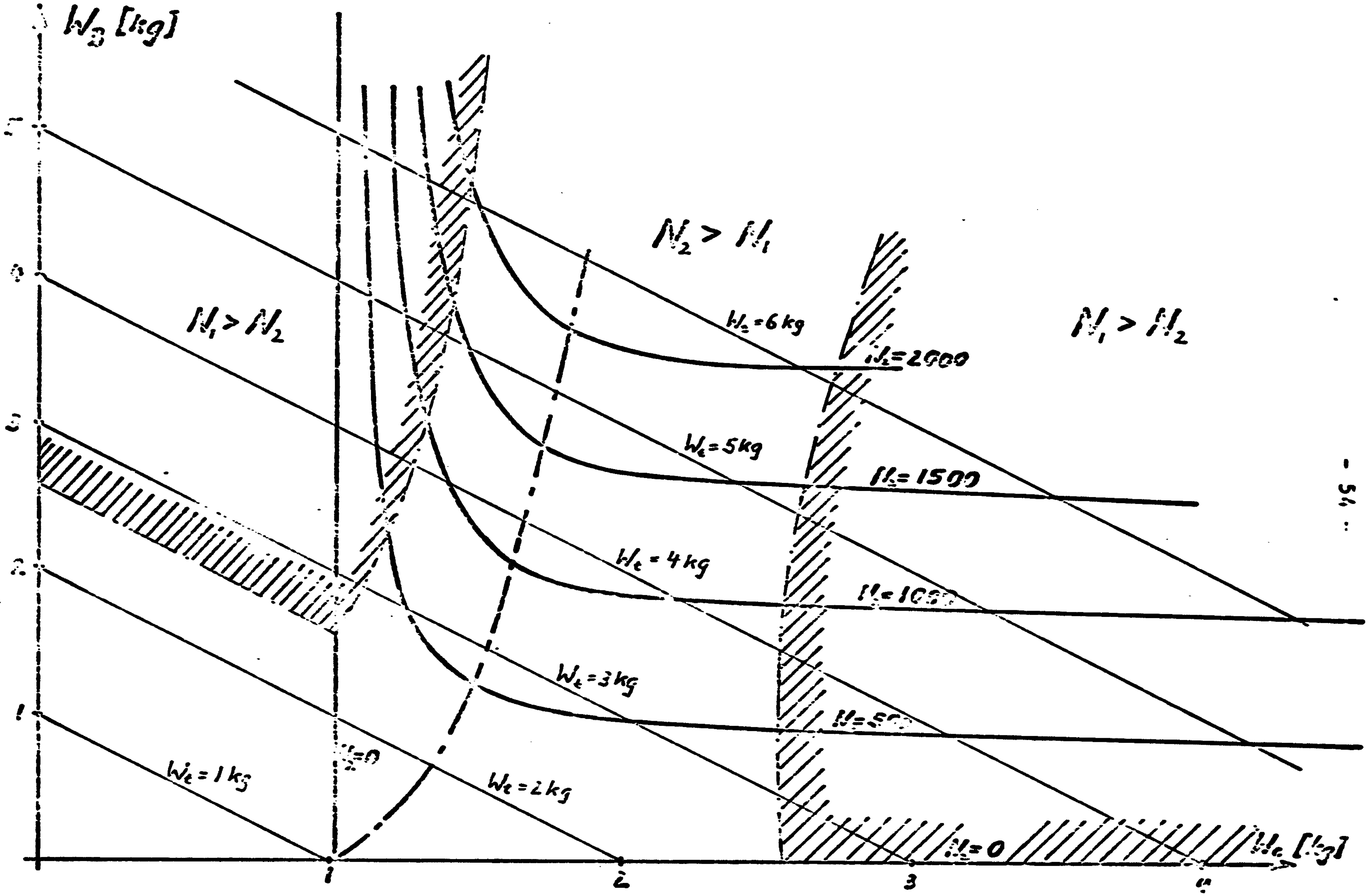

Diagram 7. $W_B = f(W_c)$

R_d = 1.0, I = 1.0, [illegible] = 0.25, [illegible] = 0.3, [illegible] = 0.04

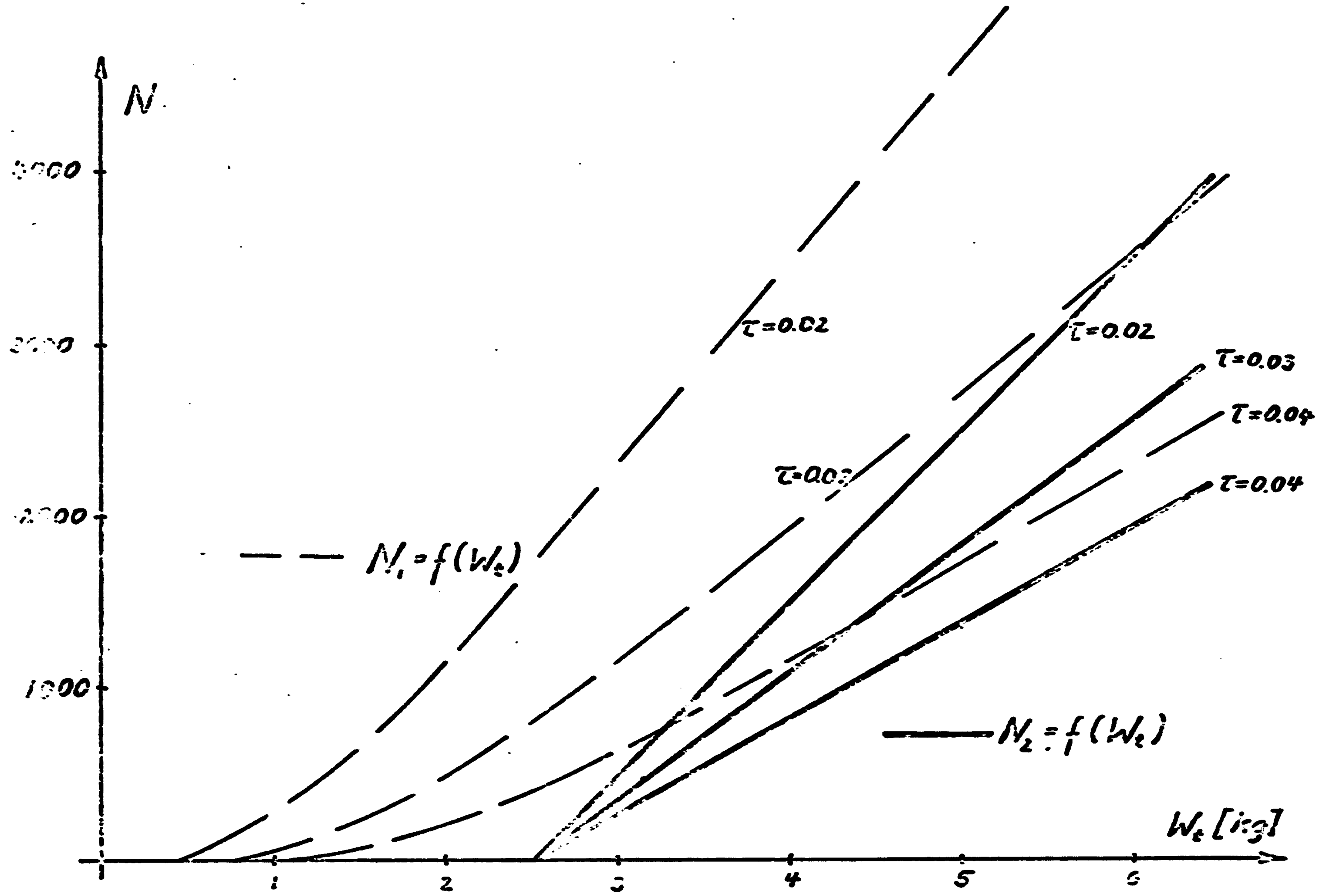

Diagram 8. N_2, N_1 = $f(W_t)$

$R_.$ = 1.0, T = 1.0, β = 0.15, κ = 0.3

III.4.4 Plot $N = N(\tau)$. Diagram 9

Constant parameters are: W_t, R_d, T, β, κ.

The diagram shows the plot of $N_1 = N_1(\tau)$ and

$$N_2 = \max_{W_b, W_c, R_c} N(W_b, W_c, R_c)$$

N_1 and $N_2 \rightarrow 0$ as τ gets large. But N_2 decreases faster than N_1 (see III.3.4). Since we made the assumption that τ << T, the calculation is valid only for small τ, but it shows the dependence of N on large τ. For large $\tau \rightarrow N_1 > N_2$.

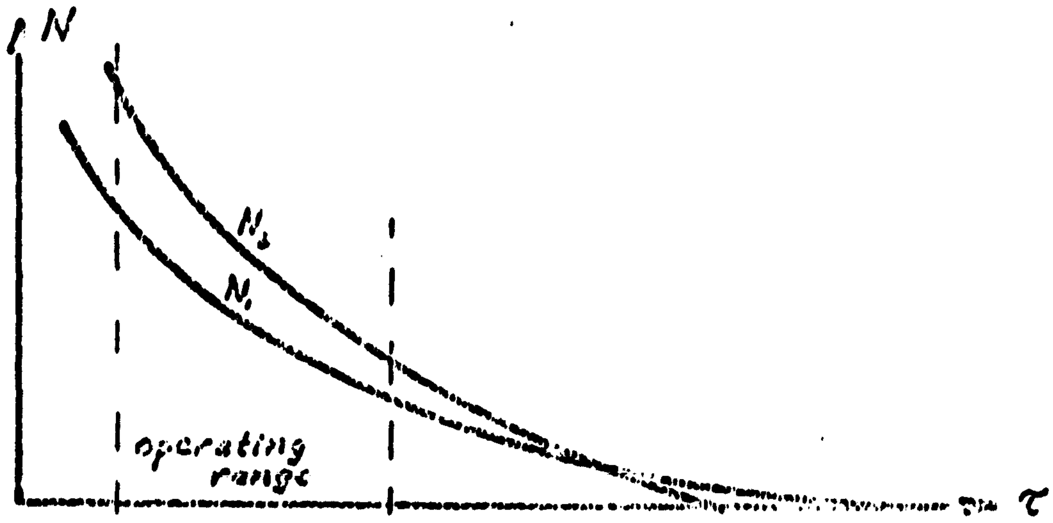

Figure 25

III.4.5 Plot of $N = N(\beta)$. Diagram 10

Constant parameters are: W_t, R_d, T, τ, κ.

In III.2.3 we found that $N_1(\beta) = 0$ for $R_i \geq R_d\frac{\beta}{1-\beta}$.

For small β, $N_1(\beta)$ rises approximately linearly because of $\ln\frac{1}{1-\beta} = -\ln(1-\beta) \approx \beta$. From III.3.5, we know that N_2 is a linear function of β for small β, but as $\beta \rightarrow \kappa$, $N \rightarrow$ constant.

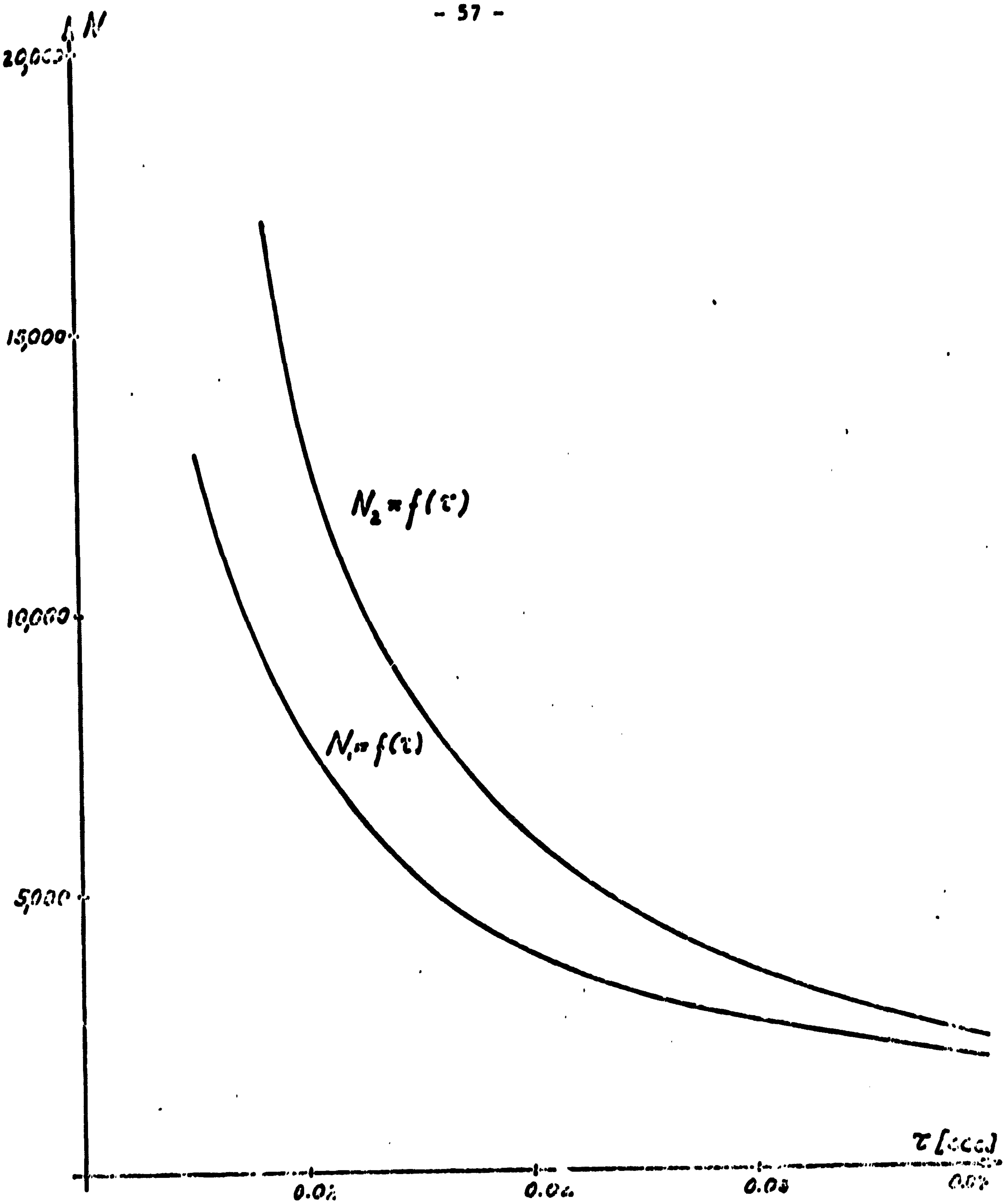

Diagram 9. $N_2, N_1 = f(\tau)$

$E_i = 6.0$, $R_a = 1.0$, $T = 1.0$, [illegible] $= 0.15$, [illegible] $= 0.3$

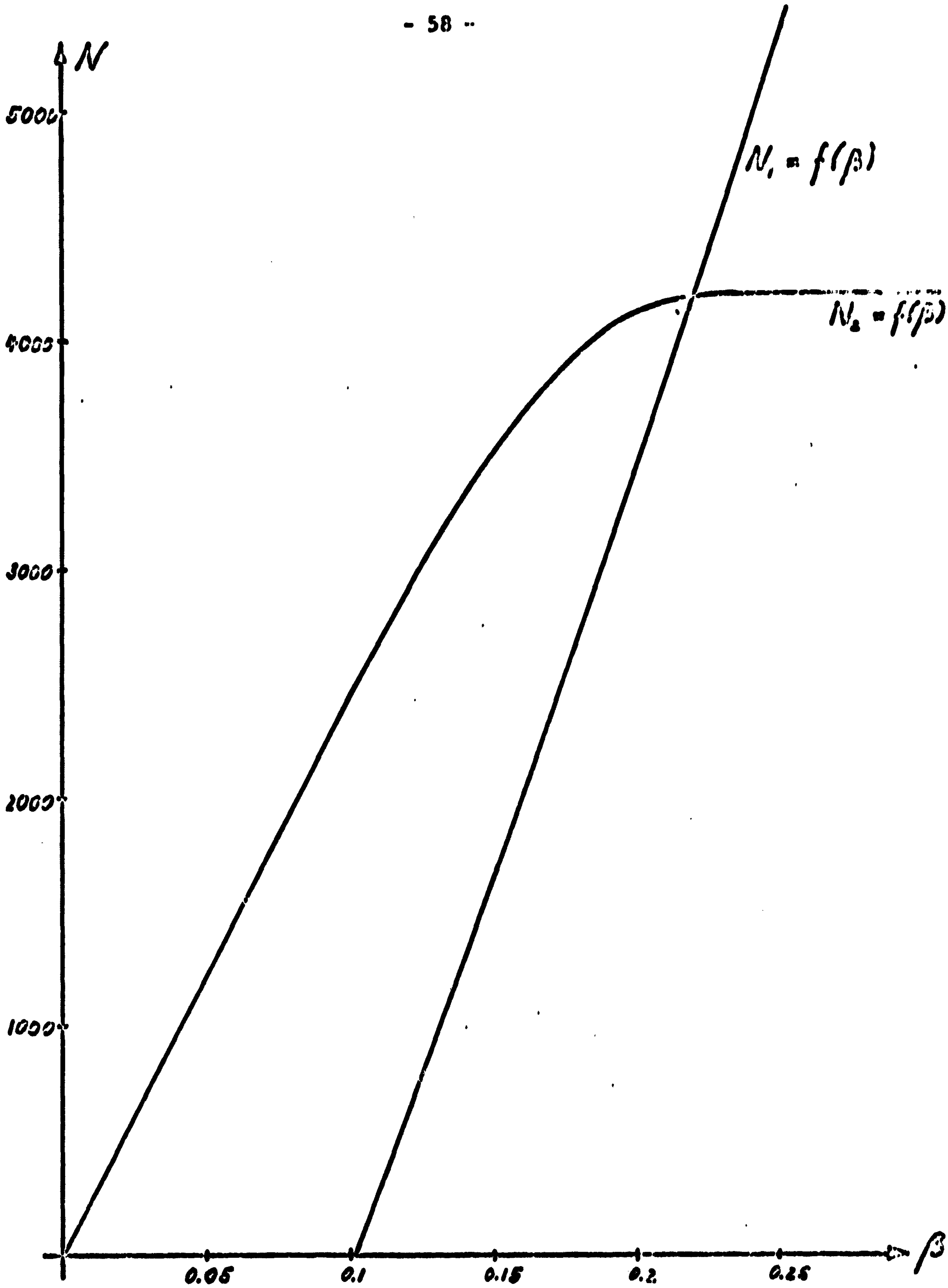

Diagramm 30. N_2, N_1 = f(β)

$W_t = 4.0$, $R_d = 1.0$, $T = 1.0$, $\tau = 0.02$, $\kappa = 0.3$

III.5 Conclusions

We established first the theoretical relations for Model #1 and #2, found the limits to different parameters and showed in section III.4 that the values obtained by calculation agreed with the expected plots. It is surprising that the dependence of N on the various parameters is in many cases linear or indirectly proportional in some regions, though it looks from the formulas as if we would have to expect much less linear dependence. The reason for this nearly linear dependence of N on the parameters is the linearization of the model and the small change of the parameters.

CHAPTER IV

IV.1 Conclusions

In Chapter III we compared Model #1 and Model #2. Model #2 has a higher number of pulses than #1 for almost every choice of the parameters, W_t, R_d, T, τ, β. Only in Diagram 10 N = N(β), we found $N_1 > N_2$; for all other cases we found $N_2 > N_1$. This was to be expected from the discussion in Chapter I. The total discharge time (T_d) for Model #1, $T_{d1} = N_1 \tau$ is small compared with the discharge time for Model #2

$$T_{d2} = N_2 T$$

Not only is $N_2 > N_1$, but $\tau \ll T$, so that $T_{d2} \gg T_{d1}$. Model #2 is especially advantageous for small total weight. Due to the relative high internal resistance of small batteries the battery voltage drops fast under the value of the minimum voltage for Model #1, not so for Model #2 where the extra storing stage (capacitor) can release the energy with only very small losses but draws itself only a small current from the battery. Though this stage is less than 50% efficient, Model #2 has a higher pulse efficiency than Model #1. We allow the voltage drop at the load to be higher than the one at the battery. Model #2 can handle this situation, Model #1 cannot, this is another reason why $N_2 > N_1$.

Since the total discharge times are small compared with the charging times (for $P_i \sim$ 1-5 W the charge time for a 5 kg energy storage with $Q_B \sim$ 200 Wh would run to approximately 30 - 6 hours since only $\delta Q_B = 0.15\, Q_B$ is taken out of the battery).

Now we see the main advantages of Model #2: 1) since the battery is smaller, the charging time is smaller; 2) since the pulse efficiency is larger than for Model #1, #2 does not need to be charged as often as #1; 3) for $i_i > 0$ we can directly charge the capacitor. In Model #1 we charge for $0 \leq t \leq T-\tau$ the battery and only for $T-\tau < t < T$, i_i contributes to the current in R_d. When we use Model #2 in a satellite, the satellite can transmit more information than a satellite equipped with Model #1. The first satellite in series of the Sunblazer satellites will be equipped with a capacitor (0.072 F, 1.8 kg) as energy storage. This is sufficient because it can be guaranteed that

$$\int_t^{t+T} P_i \, dt > \int_t^{t+T} P_o \, dt \, .$$

Further Sunblazer satellites will be equipped with more sophisticated energy storages that store energy over 22 hours and transmit signals for 2 hours per day. In that case Model #2 would be a good solution.

IV.2 Critique

This is a completely mathematical investigation. Though the assumptions made are justifiable from the engineer's point of view, the results should be supported by some experimental data. For larger τ it would seem to be worthwhile to investigate energy storages like spinning masses and ways to increase their ratio stored energy/losses. Where the total weight is not critical, but the system has to be very efficient, magnetic fields stored in superconducting coils might be better. These and many other possibilities to store energy have not been investigated, because of the low weight and the high reliability requirement.

CHAPTER V

APPENDIX

V.1 Efficiency of Capacitors

The capacitor C will be charged with constant voltage U_o over a resistor R_c.

The current is

$$i = \frac{U_o}{R_c}\exp\left[-\frac{t}{R_cC}\right]$$

The input energy

$$E_i = \int_0^\infty p\,dt = \int_0^\infty ui\,dt = \frac{U_o}{R_c}\int_0^\infty \exp\left[-\frac{t}{R_cC}\right]dt$$

$$= \frac{U_o^2}{R_c}R_cC = U_o^2C$$

Since the energy stored in the capacitor

$$E_s = \frac{1}{2}CU_o^2$$

The charge efficiency is

$$\eta = \frac{E_s}{E_i} = \frac{1}{2} = 50\%$$

V.2 Battery Current for Maximum Energy Output

$$E = \text{Max} \int_0^T (U_o - iR_i)\, i\, dt \tag{40}$$

where U_o = battery emf assumed constant.

R_i = internal resistance

i = battery current

$$\text{Constraint:} \quad k = \int_0^T i\, dt \tag{41}$$

Using Variational Calculus

$$\int F dx = \text{Max}$$

$$\text{Constraint:} \int G dx = \text{constant}$$

$$H = F - \lambda G$$

then Euler's equation

$$\frac{d}{dt}\left(\frac{\delta}{\delta (i)'} H\right) - \frac{\delta}{\delta i} H = 0$$

leads to

$$U_o - 2iR - \lambda = 0$$

where λ = constant

then

$$i = \frac{U - \lambda}{2R} = \text{constant} \qquad (42)$$

with (42) in (41)

$$i = \frac{k}{T} = \text{constant}$$

V.3 Comparison of Energy Densities

From [1] and numerous catalogs the energy densities are:

Capacitors	up to 25 Ws/kg
Chokes (inductors)	up to 0.5 Ws/kg
Ni-Cd batteries	up to 6×10^4 Ws/kg
Mercury batteries	up to 35×10^4 Ws/kg
Spinning masses (like gyroscopes)	up to 50×10^4 Ws/kg

Energy to loss ratio:

Conductors	2 - 5%	of stored energy
Capacitors	less than 0.1%	of stored energy
Batteries	less than 0.01%	of stored energy
Gyroscopes	less than 0.5%	of stored energy

The capacitor and battery energy density and loss percentages are more favorable than those of other elements.

V.4 Computer Program for N_1, N_{1B}, N_{2C}.

(Fortran II)

```
      READ 30,RD,CO,WT,RR,END
30    FORMAT (5F10.5)
      READ 32,UB,CK,TA,T,B
32    FORMAT (4F10.7,F10.2)
      ROC=0.111
      ROB=4000.
      WB=WT
      A=1/(WB*ROB)
      RI=A*UB*RR
      PRINT 42,B,RI
42    FORMAT (//2HB=,F6.5,3HRI=,F10.5///)
      T3=(RD/(RI+RD))/(1.0-B)
      IF (T3-1.0)50,50,55
50    CONTINUE
      PRINT 51
51    FORMAT(8HNBAT=0.0/)
      GO TO 56
55    T1=LOGF(T3)
      T2=(RI+RD)/(A*UB*TA)
      ANB=T1*T2
      PRINT 57,ANB
57    FORMAT (5HNBAT=,F10.0/)
56    CONTINUE
      C=CO
      OLD=0.0
      END=0.0
      J=0
58    J=J+1
65    C=C-0.02*CO
72      WC=C/ROC
      WB=WT-WC
      IF (WB) 130,130,82
82    AB=1/(WB*ROB)
      RI=AB*UB*RR
```

```
       RO=AB*C*HS
       RELC=HC/HB
75     R=2.0
       K=0
       GO TO 81
79     K=K+1
       IF (K-7) 80,80,43
43     CONTINUE
       PRINT 41
41     FORMAT (19HK,C,CO,ENB)
       READ 39,K,C,CO,ENB
39     FORMAT (I1,3F10.5)
       IF (K-7) 80,65,65
80     R=R+(ENC-ENB)/ENB
81     RC=R-RI
       G=EXPF(-T*(1.0+PO)/(R*C))
       D=EXPF(-T4/(PO*C))
       E=(1.0-G)/(1.0/D-G)
       X=(1.0+E*RO)/(1.0+E*RO/D)
       T5=LOGF(1.0-B)
       T6=LOGF(RC*(1.0-E)/R+E)
       ENB=(T5-T6)/LOGF(X)
       IF (ENB) 85,85,90
90     CONTINUE
       IF (R) 85,85,91
85     CONTINUE
       PRINT 86
86     FORMAT (9HHCAP=0.0 /)
       GO TO 79
91     ENC=LOGF((1.0-CK)/E)/LOGF(X)
       PRINT 93,ENB,ENC,C,RI,RC,RELC
93     FORMAT (2F10.0,4F10.5)
       IF (ENC)55,55,92
92     CONTINUE
       IF (ABSF(ENB-ENC)-20.)110,110,79
110    CONTINUE
       PRINT 120,ENB,ENC,C,RI,RC,RELC
120    FORMAT(2F10.0,4F10.5//)
       IF (J-55)125,125,130
125    CONTINUE
       GO TO 52
130    CONTINUE
       END
```

V.5 TABLES

τ (sec)	N_1	N_{2B}	N_{2C}	R_c (Ω)	R_i (Ω)	C (F)
0.02	2774	4010	4934	0.6	0.11	0.105
		4384	4929	1.2		
		4527	4903	1.8		
		4609	4834	2.4		
		4674	4723	3.0		
		4725	4572	3.6		
		4776	4396	4.2		
		4828	4200	4.8		
		4878	3986	5.4		
0.03	1849	2113	2861	0.4	0.125	0.154
		2446	2859	0.8		
		2577	2841	1.2		
		2652	2799	1.6		
		2704	2731	2.0		
		2747	2643	2.4		
		2784	2538	2.8		
		2819	2420	3.2		
		2853	2293	3.6		
0.04	1387	1185	1813	0.28	0.139	0.195
		1495	1811	0.56		
		1625	1803	0.84		
		1699	1780	1.12		
		1748	1743	1.40		
		1786	1693	1.68		
		1817	1632	1.96		
		1844	1563	2.24		
		1869	1487	2.52		

$\beta = 0.15$　　$R_d = 1.0$　　$W_t = 5.0$

$\kappa = 0.3$

Diagram 1, Page 47

N # of pulses	C [F]	C p.u. of W_t	C [kg]	R_i [Ω]	R_e [Ω]	R_i+R_e [Ω]
360	0.184	0.828	1.656	1.31	7.5	8.8
535	0.168	0.757	1.514	0.925	7.25	8.2
705	0.152	0.685	1.370	0.71	6.7	7.4
860	0.136	0.613	1.226	0.58	6.2	6.8
1015	0.12	0.54	1.08	0.40	5.0	5.5
1150	0.088	0.4	0.8	0.37	1.8	2.2
1140	0.104	0.47	0.94	0.42	3.9	4.3
865	0.074	0.33	0.66	0.34	0.75	1.1
635	0.067	0.30	0.6	0.32	0.54	0.86

$\beta=0.15$ $\tau=0.02$

$R_d=1.0$ $W_t=2.0$

$N_1=523$ $R_{11}=0.225$

Diagrams 2, 3, Pages 49, 50

N # of pulses	C [F]	C p.u. of [illegible]	C [kg]	R_i [Ω]	R_c [Ω]	R_i+R_c [Ω]
592	0.274	0.829	2.49	0.876	8.6	9.7
862	0.252	0.7[illegible]	2.37	0.617	8.33	8.95
1128	0.228	0.685	2.05	0.48	8.02	8.5
1389	0.204	0.613	1.84	0.39	7.65	8.04
1645	0.18	0.541	1.62	0.33	7.16	7.49
1855	0.16	0.479	1.44	0.288	6.62	6.91
2003	0.144	0.434	1.30	0.265	6.08	6.35
2143	0.129	0.388	1.16	0.245	5.37	5.61
2263	0.114	0.342	1.02	0.228	4.38	4.51
2321	0.099	0.297	0.89	0.213	2.68	2.89
1978	0.084	0.251	0.75	0.20	0.76	0.96
1660	0.076	0.229	0.69	0.195	0.49	0.635
1270	0.070	0.209	0.63	0.189	0.345	0.534

β=0.15 $\quad$ τ=0.02

R_d=1.0 $\quad$ W_t=3.0

N_1=523 $\quad$ R_{i1}=0.15

Diagrams 2, 3; Pages 49, 50

N # of pulses	C [F]	C p.u. of W_t	C [kg]	R_i [Ω]	R_c [Ω]	R_i+R_c [Ω]
1346	0.322	0.725	2.9	0.41	8.75	9.16
1660	0.294	0.662	2.65	0.33	8.6	8.93
1970	0.266	0.599	2.4	0.28	8.3	8.58
2278	0.238	0.536	2.14	0.24	8.1	8.34
2580	0.21	0.473	1.89	0.21	761	7.82
2860	0.182	0.41	1.64	0.19	7.1	7.29
3143	0.154	0.347	1.39	0.17	6.33	6.5
3380	0.1260.[illegible]	0.284	1.13	0.16	5.1	5.26
3496	0.101	0.228	0.91	0.146	2.7	2.85
3296	0.0924	0.208	0.83	0.142	1.16	1.30
2860	0.0836	0.188	0.75	0.139	0.536	0.675
2157	0.0736	0.166	0.66	0.135	0.298	0.433
1545	0.0672	0.151	0.6	0.133	0.214	0.347

β=0.15 τ=0.02
R_d=1.0 W_t=4.0

N_1=1650 R_{i1}=0.1125

Diagrams 2,3; Pages 49, 50

N # of pulses	C [F]	C p.u. of W_t	C [kg]	R_i [Ω]	R_c [Ω]	$R_i + R_c$ [Ω]
2102	0.368	0.663	3.32	0.267	9.03	9.27
2821	0.304	0.548	2.76	0.199	8.66	2.7
3518	0.24	0.432	2.16	0.158	8.05	8.21
3852	0.208	0.374	1.87	0.144	7.6	7.74
4167	0.176	0.317	1.58	0.132	6.96	7.09
4387	0.152	0.274	1.37	0.124	6.25	6.37
4634	0.12	0.216	1.08	0.115	4.83	4.95
4684	0.104	0.187	0.93	0.111	3.0	3.11
4671	0.101	0.182	0.91	0.110	2.51	2.62
4334	0.092	0.166	0.83	0.108	0.843	0.951
3002	0.075	0.134	0.67	0.104	0.25	0.35
2230	0.069	0.124	0.62	0.102	0.178	0.28

β=0.15 τ=0.02

R_d=1.0 W_t=5.0

N_1=2774 R_{11}=0.09

Diagrams 2, 3; Pages 49, 50

N # of pulses	C [F]	C p.u. of kVs	C [kg]	R_i [Ω]	R_c [Ω]	$R_i + R_c$ [Ω]
3381	0.368	0.553	3.32	0.168	9.0	9.17
3739	0.336	0.504	3.02	0.151	8.86	9.01
4091	0.304	0.456	2.73	0.138	8.64	8.78
4441	0.272	0.408	2.45	0.127	8.39	8.52
4778	0.24	0.36	2.16	0.117	8.05	8.17
5107	0.208	0.312	1.87	0.109	7.59	7.70
5413	0.176	0.264	1.52	0.102	6.94	7.04
5683	0.144	0.216	1.28	0.096	5.93	6.03
5872	0.112	0.168	1.01	0.09	3.92	4.01
5852	0.101	0.152	0.91	0.088	2.31	2.4
5374	0.092	0.139	0.833	0.087	0.68	0.77

$\beta=0.15$ $\tau=0.02$
$R_d=1.0$ $W_t=6.0$

$N_1=3879$ $R_{i1}=0.075$

Diagrams 2, 3; Pages 49, 50

N # of pulses	C [F]	C p.u. of k/e	C [kg]	R_i [Ω]	R_c [Ω]	R_i+R_c [Ω]
196	0.184	0.829	1.656	1.31	4.21	5.52
299	0.168	0.757	1.54	0.925	3.53	4.45
393	0.152	0.685	1.37	0.714	3.10	3.81
466	0.136	0.613	1.23	0.581	2.30	2.88
480	0.120	0.541	1.08	0.490	1.50	1.99
431	0.110	0.497	0.994	0.448	0.95	1.40
331	0.101	0.454	0.908	0.412	0.66	1.07
1.70	0.091	0.411	0.822	0.382	0.46	0.84

$\beta=0.15$ $\tau=0.03$

$R_d=1.0$ $W_t=2.0$

$N_1=0$ $R_{i1}=0.225$

Diagrams 4, 5; Pages 51, 52

N # of pulses	C [F]	C p.u. of W_t	C [kg]	R_i [Ω]	R_c [Ω]	$R_i + R_c$ [Ω]
361	0.276	0.829	2.49	0.876	5.6	5.94
532	0.252	0.757	2.27	0.617	4.76	5.38
700	0.228	0.684	2.06	0.476	4.40	4.88
863	0.204	0.613	1.84	0.387	3.99	4.39
1015	0.180	0.541	1.62	0.326	3.44	3.77
1141	0.156	0.468	1.405	0.282	2.61	2.89
1154	0.132	0.396	1.19	0.248	1.20	1.45
1023	0.119	0.359	1.08	0.234	0.69	0.92
865	0.110	0.332	1.0	0.224	0.49	0.71
635	0.101	0.303	0.92	0.215	0.35	0.57

$\beta=0.15$ $\tau=0.03$
$R_d=1.0$ $W_t=3.0$

$N_1=349$ $R_{11}=0.15$

Diagrams 4, 5; Pages 51, 52

N # of pulses	C [F]	C p.u. of W_t	C [kg]	R_i [Ω]	R_c [Ω]	R_i+R_c [Ω]
856	0.322	0.725	2.9	0.409	5.26	5.67
1059	0.294	0.662	2.65	0.333	5.03	5.36
1259	0.266	0.599	2.4	0.281	4.76	5.04
1451	0.238	0.536	2.15	0.242	4.42	4.66
1637	0.21	0.473	1.89	0.213	3.96	4.17
1805	0.182	0.410	1.64	0.191	3.31	3.50
1927	0.154	0.347	1.39	0.172	2.24	2.41
1697	0.126	0.284	1.14	0.157	0.61	0.87
1408	0.114	0.257	1.03	0.151	0.38	0.53
1075	0.104	0.235	0.94	0.147	0.26	0.41

$\beta=0.15$ $\tau=0.03$
$R_d=1.0$ $W_t=4.0$

$N_1=1106$ $R_{i1}=0.1125$

Diagrams 4, 5; Pages 51, 52

N # of pulses	C [F]	C p.u. of W_s	C [kg]	R_i [Ω]	R_c [Ω]	$R_i + R_c$ [Ω]
136	0.368	0663	3.32	0.27	5.45	5.72
1592	0.336	0.605	3.03	0.228	5.28	5.51
1820	0.304	0.548	2.74	0.199	5.05	5.25
2046	0.272	0.490	2.45	0.177	4.77	4.95
2262	0.240	0.432	2.16	0.159	4.40	4.56
2464	0.208	0.375	1.88	0.144	3.88	4.02
2640	0.176	0.317	1.58	0.132	3.06	3.19
2681	0.144	0.259	1.30	0.122	1.34	1.46
2367	0.128	0.232	1.16	0.117	0.52	0.64
2016	0.117	0.212	1.06	0.114	0.32	0.43

$\beta = 0.15$ $\tau = 0.03$

$R_d = 1.0$ $V_t = 5.0$

$N_1 = 1849$ $R_{i1} = 0.09$

Diagrams 4, 5; Pages 51, 52

N # of pulses	C [F]	C p.u. of W_t	C [kg]	R_i [Ω]	R_c [Ω]	R_i+R_c [Ω]
2198	0.368	0.552	3.32	0.168	5.45	5.62
2429	0.336	0.505	3.03	0.151	5.25	5.40
2655	0.304	0.456	2.73	0.138	5.03	5.17
2878	0.272	0.408	2.45	0.127	4.80	4.93
3083	0.24	0.36	2.16	0.117	4.37	4.49
3278	0.208	0.312	1.87	0.109	3.84	3.95
3443	0.176	0.264	1.57	0.102	3.01	3.11
3423	0.144	0.216	1.30	0.096	1.13	1.23
3277	0.138	0.207	1.24	0.095	0.71	0.81
2881	0.126	0.189	1.13	0.093	0.20	0.29

β=0.15 τ=0.03
R_d=1.0 W_t=6.0

N_1=2586 R_{i1}=0.075

Diagrams 4, 5; Pages 51, 52

N # of pulses	C [F]	C p.u. of W_t	C [kg]	R_i [Ω]	R_c [Ω]	$R_i + R_c$ [Ω]
106	0.184	0.828	1.656	1.31	2.54	3.85
163	0.168	0.757	1.54	0.925	2.04	2.97
197	0.152	0.685	1.37	0.714	1.50	2.21
171	0.133	0.601	1.202	0.564	0.88	1.42
100	0121	0.549	1.098	0.499	0.62	1.12

β=0.15 τ=0.04
R_d=1.0 W_t=2.0

N_1=0 R_{i1}=0.225

Diagrams 6, 7; Pages 53, 54

N # of pulses	C [F]	C p.u. of W_t	C [kg]	R_i [Ω]	R_c [Ω]	$R_i + R_c$ [Ω]
238	0.274	0.829	2.49	0.876	3.35	4.23
360	0.252	0.757	2.27	0.617	2.93	3.60
475	0.228	0.685	2.06	0.476	2.61	3.09
576	0.204	0.613	1.84	0.387	2.13	2.52
644	0.180	0.540	1.62	0.326	1.51	1.84
602	0.156	0.468	1.405	0.282	0.76	1.04
541	0.147	0.442	1.32	0.269	0.57	0.84
407	0.134	0.404	1.21	0.252	0.41	0.66

$\beta=0.15$ $\tau=0.04$

$R_d=1.0$ $W_t=3.0$

$N_1=262$ $R_{11}=0.15$

Diagrams 6, 7; Pages 53, 54

N # of pulses	C [F]	C p.u. of W_e	C [kg]	R_i [Ω]	R_c [Ω]	$R_i + R_c$ [Ω]
607	0322	0.725	2.9	0.409	3.47	3.88
752	0.294	0.662	2.65	0.333	3.21	3.54
893	0.266	0.599	2.4	0.281	2.91	3.19
1024	0.238	0.536	2.15	0.242	2.53	2.77
1135	0.210	0.473	1.89	0.213	1.99	2.20
1176	0.182	0.410	1.64	0.191	1.14	1.33
865	0.147	0.332	1.32	0.168	0.37	0.54
635	0.134	0.303	1.21	0.161	0.26	0.42

$\beta = 0.15$ $\tau = 0.04$
$R_d = 1.0$ $W_t = 4.0$

$N_1 = 829$ $R_{i1} = 0.1125$

Diagrams 6, 7; Pages 53, 54

N # of pulses	C [F]	C p.u. of W_t	C [kg]	R_i [Ω]	R_c [Ω]	$R_i + R_c$ [Ω]
980	0.368	0.663	3.32	0.267	3.65	3.92
1151	0.336	0.605	3.03	0.228	3.47	3.70
1315	0.304	0.548	2.74	0.199	3.19	3.39
1473	0.272	0.490	2.45	0.177	2.91	3.09
1616	0.240	0.432	2.16	0.159	2.46	2.62
1720	0.208	0.375	1.88	0.144	1.80	1.94
1645	0.176	0.317	1.58	0.132	0.69	0.82
1369	0.156	0.282	1.41	0.125	0.35	0.47
1087	0.142	0.257	1.28	0.121	0.23	0.35

$\beta=0.15$ $\tau=0.04$
$R_d=1.0$ $W_t=5.0$

$N_1=1387$ $R_{i1}=0.09$

Diagrams 6, 7; Pages 53, 54

N # of pulses	C [F]	C p.u. of W_t	C [kg]	R_i [Ω]	R_c [Ω]	R_i+R_c [Ω]
1602	0.368	0.553	3.32	0.168	3.63	3.80
1769	0.336	0.505	3.03	0.151	3.43	3.58
1928	0.304	0.456	2.73	0.138	3.18	3.32
2081	0.272	0.408	2.45	0.127	2.85	2.98
2218	0.240	0.360	2.16	0.117	2.40	2.52
2318	0.208	0.312	1.87	0.109	1.77	1.88
2128	0.176	0.264	1.57	0.102	0.53	0.63
1750	0.156	0.234	1.40	0.098	0.272	0.370
1379	0.143	0.214	1.28	0.095	0.187	0.282

$\beta=0.15$ $\tau=0.04$

$R_d=1.0$ $W_t=6.0$

$N_1=1939$ $R_{i1}=0.075$

Diagrams 6, 7; Pages 53, 54

β	N_1	N_2
0.05	0	1229
0.1	0	2453
0.15	1659	3500
0.20	3457	4152
0.25	5372	4214
0.30	7419	4215

Diagram 10, Page 58

$W_t = 4.0$, $R_d = 1.0$, $T = 1.0$,

$\iota = 0.02$, $\kappa = 0.3$

REFERENCES

1. Study of a Small Solar Probe (Sunblazer) Part II, PR-5255-5, July 1, 1965, Center of Space Research, M.I.T.

2. Hütte V/ a, Starkstromtechnik, 1957, p. 758, 763.

3. Fourteenth Annual Proceedings, Power Source Conference, 1960, p.79.

Power Requirements and Self-Optimizing Electronic Power Supply of a Small Solar Probe.

by

Richard H. Baker

Dr. Andreas Boehringer

TR-67-3

Power Requirements and Self-Optimizing Electronic Power Supply of a Small Solar Probe

by

Richard H. Baker

Dr. Andreas Boehringer

ABSTRACT

This report details the design of the basic power conditioning unit for the Sunblazer spacecraft. For light-weight spacecraft utilizing solar cells it is important to optimize the Power System over the full temperature and illumination range. The design discussed utilized optimal control techniques to match the temperature - illumination dependent array characteristics to a battery system. The result is an efficient lightweight converter with a minimum number of active components.

TABLE OF CONTENTS

APPENDIX 2

THEORTICAL STUDY OF A DC POWER CONVERTER FOR THE POWER SUPPLY OF A SMALL SOLAR PROBE (SUNBLAZER)

A. Performance Requirements

1. Input

The input of the dc power converter will be an array of series-parallel connected solar cells. In contrary to the output conditions the input conditions will change in a wide range (picture 1). As the sunblazer has to operate in an orbit with

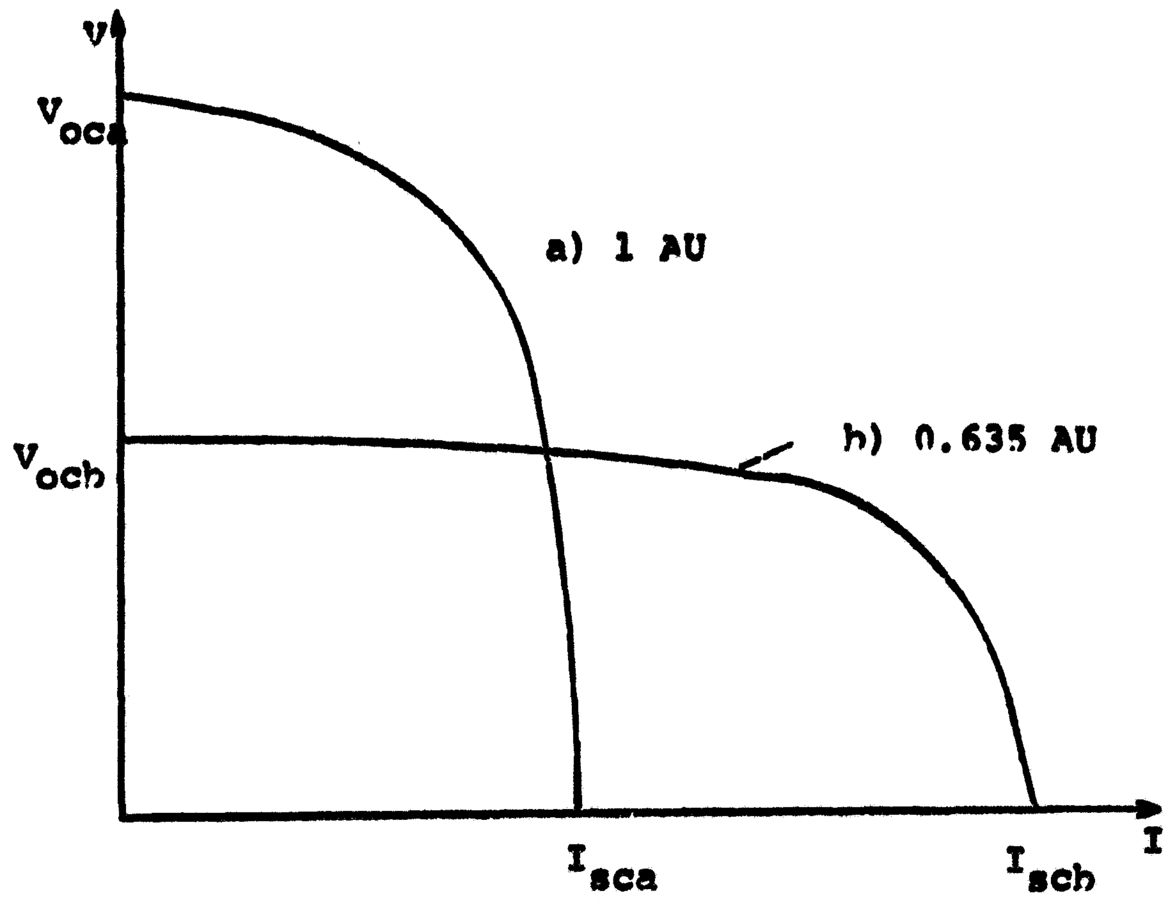

Picture A: Power Generation of Solar Cell Array

a) an aphelion of 1 AU and b) a perihelion of 0.625 AU the ratio of the shortcut currents (I_{sc}) of the solar cells is about

$$\frac{I_{sca}}{I_{scb}} = \frac{0.635^2}{1} = \frac{1}{2.5}$$

(The solar constant is inversely proportional to the square of the sun distance). The ratio of the open circuit voltages (on the basis of changing temperature will be about

$$\frac{V_{oca}}{V_{ocb}} = 1.9 \qquad \text{(see Appendix I)}$$

2. Output

As it can be seen today, the dc power converter will operate at its output on an array of series-parallel connected nickel-cadmium cells with a nearly constant voltage of E = 35V.

3. Operating Conditions

Since these substantial changes, shown above in the voltage-current characteristic of the solar batteries over the orbit, due to changes in temperature and solar constant, the power converter principally has to be designed in a way, which allows that it operates always at or close to Maximum Power Point (MPP), independent of the momentary power profile [1].

4. Reliability, Weight, Efficiency

a) The reliability of the power converter has to be as high as possible. Therefore the number of parts, especially semiconductors has to be as small as possible.

b) The weight has to be as small as possible.

c) The efficiency has to be as high as possible, however, efficiency is not quite as important as small weight.

Original material deleted because not applicable to present design requirements

B. Principle Design

1. Main Circuit and Switching Conditions

A good and simple way to match the conditions shown under A seems to be the following (picture 3).

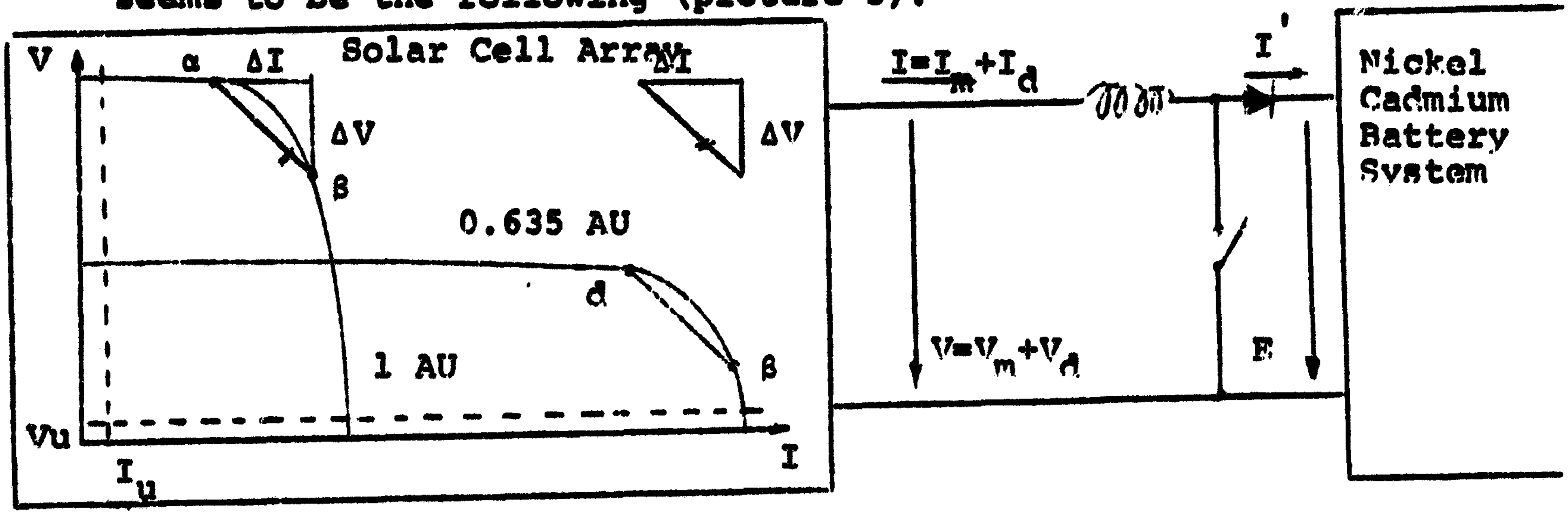

V_m, I_m :	Mean Values of Voltage and Current
V, I :	Actual Values of Voltage and Current
V_d, I_d :	Difference between actual Value and Mean Value

Picture 3: Principle Design of Main Circuit

The array of solar cells and the battery system are interconnected by only three components in the main circuits.

The switch S is turned on and off by a flip-flop which is triggered by the differences between actual value and mean value of voltage: $V_d = V - V_m$ and current: $I_d = I - I_m$ with the following trigger conditions:

$$V_d = -c_1 \cdot \Delta V \rightarrow \text{switch is turned off}$$

$$I_c = -c_2 \cdot \Delta I \rightarrow \text{switch is turned on}$$

where $\Delta V > 0$ and $\Delta I > 0$ are given values and $c_1 = \frac{1}{2}$ and $c_2 = \frac{1}{2}$, see C.4. For the following it shall be assumed that the solar cell array has come up to a point α, where the switch was closed.

Then it will run down to lower voltages and higher currents. V and herewith V_d is becoming smaller. When the circuit has reached point β, V_d has become equal to $-c_1 \cdot \Delta V$. Thus the switch is turned off.

When $E > V_m + (1-c_1) \cdot \Delta V$ (what <u>must</u> be), the current then will decrease and the voltage increase until V and I reach the point α, where I_d becomes equal to $-c_2 \cdot \Delta I$. Then the switch is closed and the described process starts again.

2. Choice of ΔV and ΔI

The ratio $\frac{\Delta V}{\Delta I}$ must be chosen so that in that situation where the power output of the solar cell array is at its lowest (1 AI) the power converter operates exactly at the MPP.

$$\text{For MPP: } V + I\frac{dV}{dI} = 0 \rightarrow \frac{\Delta V}{\Delta I} = \frac{V}{I}\Big|_{MPP}$$

ΔV (or ΔI) itself will be chosen to about 10 pct. of their mean values, thus providing an operation always close to the MPP. To those values (and for the same VI-characteristic) must be chosen the according values of c_1 and c_2, either by calculation (see C.4) or by experiment. However, this is not very important, since those values will be both very close to 1/2 and, for the practical design, can be taken to be exactly 0.5. Thus the power converter will operate in this point of the sunblazer orbit (1 AU) exactly around the MPP. In other points of the orbit, the system will not work exactly around the MPP, but very close to it. The power output of the converter will even though increase because the whole power output of the solar cell array there will be higher and because the power-current characteristic has a flat maximum in the MPP.

3. Principle Design of the Control Circuit

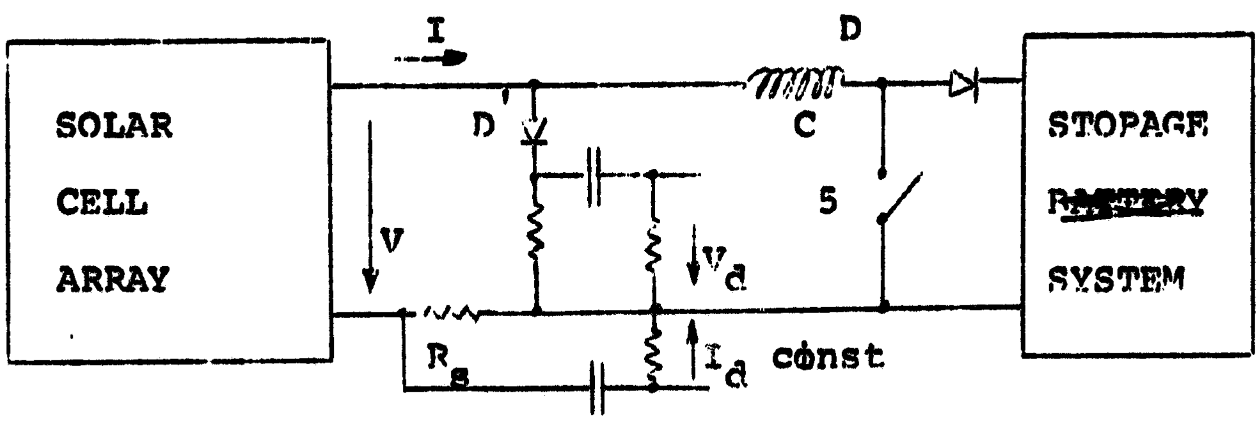

Picture 4· Principle Design of the Control Circuit

Picture 4 shows the principle design of the measuring circuit for V_d and I_d. For an enough sensitive flip flop the value of the shunt R_s can be kept so small, that this resistance will cause only an unessential influence on the efficiency of the whole system. The diode D' probably isn't necessary.

4. Start Up From Arbitrary Initial Conditions

If some failure happens to the system (for example, when the whole sunblazer turns around in space and V and I become zero for some time), the power converter must start to operate again properly, when the failure is over.

This can be guaranteed, when over an either-or circuit the flip flop is controlled too by two absolute values V_u and I_u (Picture 3), so that for the switching conditions must be written:

$$\left.\begin{array}{c} V_d = -c_1 \, \Delta V \\ \text{or} \\ V \leq V_u \end{array}\right\} \rightarrow \text{switch is turned off}$$

$$\left.\begin{array}{c} I_d = -c_2 \, \Delta I \\ \text{or} \\ I \leq I_u \end{array}\right\} \rightarrow \text{switch is turned on}$$

The value of I_u must be chosen higher than the current at that point, where the <u>stationary</u> characteristic E,I' of the storage battery and load intersects the voltage current profile of the solar cell array. But since there is concluded, that for a battery voltage less than 90% of its nominal value the load will be disconnected from the battery, I_u must be chosen only higher than the current at that point, where the stationary charging characteristic E,I' of the storage battery along intersects the voltage current profile of the solar cell array (at 1 AU). Thus it is reasonable to take I_u and V_u to about 10% of I_{MPP} and V_{MPP} (at 1 AU).

5. Stability

With the V_d, I_d control design the system will work stable only between the points α and β (as wanted), given by the VI-characteristic, ΔV and ΔI (and c_1 and c_2). Assumed, the system is out of this region and (for example) the mean values V_m and I_m, stored in the capacitors are $V_m = 0$ and $I_m = I_{sc}$ (very unfavorable conditions), the system will operate shortly between the points $\gamma(I = I_u)$ and $\varepsilon(I = I_{sc} - c_2 \cdot \Delta I)$.

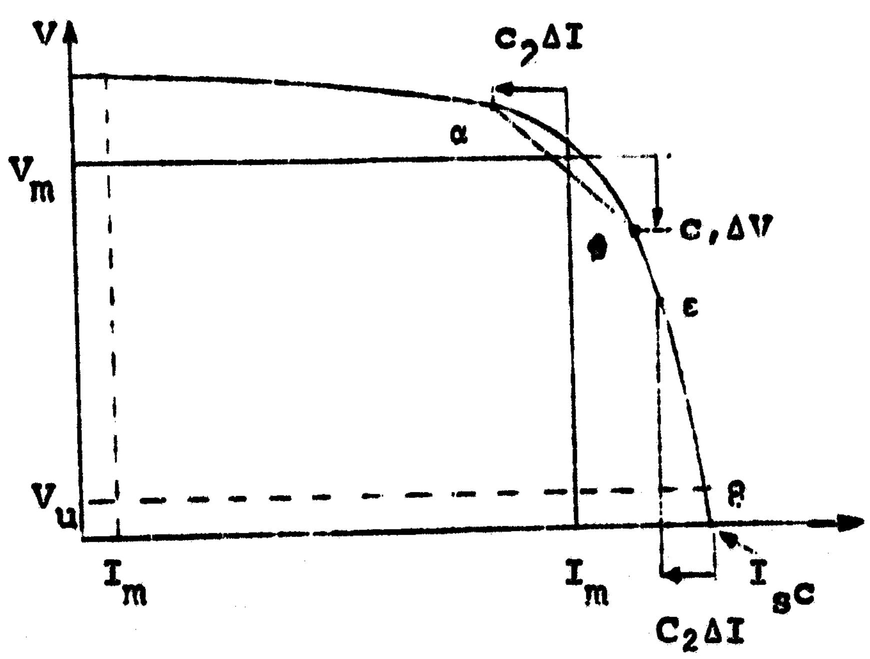

Picture 5 · Stability

But operating for some time in this circle will diminish I_m and enlarge V_{in}, so that both points ε and γ walk up on the VI-characteristic until α and β are reached. Thus, in short time, the system will come to work properly between α and β.

6. Overvoltage Protection of Switch and Storage Battery

a) To protect the switch (transistor) against overvoltage (when turned off) there should be a capacitor parallel to the storage battery (picture 6). Since the inner inductance of the nickel-cadmium cells is very small, this capacitor can be kept small too.

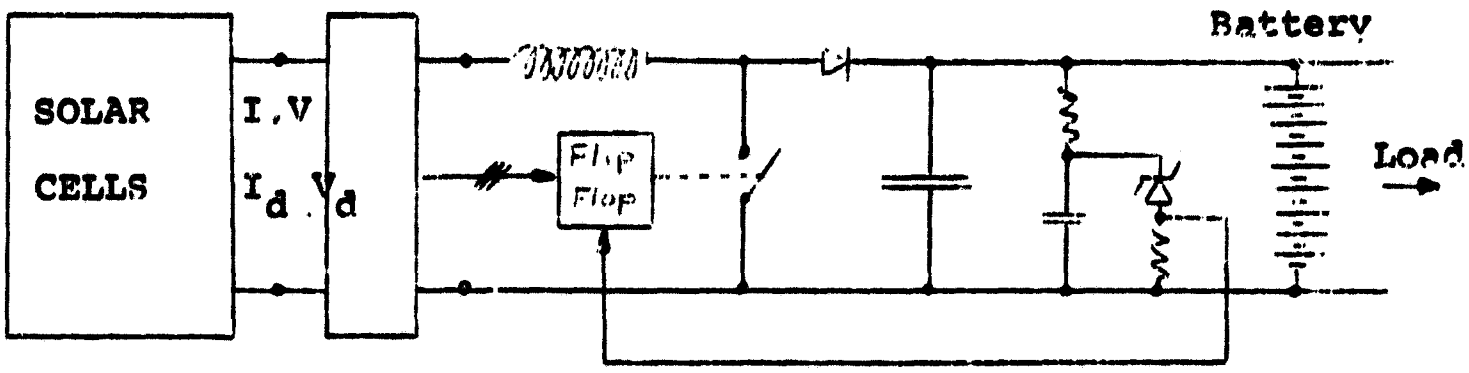

Picture 6 · Overvoltage Protection of Battery and Switch

b) To protect the battery system against overloading, the switch (by the flip flop) can be turned on all the time or turned off all the time (there is no important difference between these both possibilities), when the voltage of the battery exceeds its allowable value. This may be done, for example, by the circuit shown in picture 6.

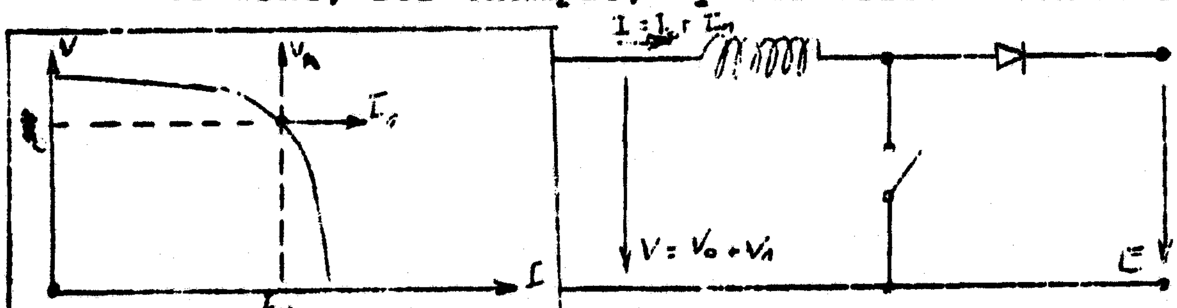

Picture 7 · Model for the simplified Calculation

C. Simplified Calculation

1. Introduction of deviations and normalized values

The differential equations for the simplified circuit shown in picture 7 are:

switch turned on: $V = L \cdot \frac{dI}{dt}$ (1a)

switch turned off: $V = L \cdot \frac{dI}{dt} + E$ (2a)

The circuit shall operate around a reference point P_o with the voltage V_o and the current I_o. Introducing the deviations of the actual values from there reference values:

$$V_1 = V - V_o \qquad (3)$$

$$I_1 = I - I_o \qquad (4)$$

the equations (1a) and (2a) become:

switch turned on: $V_1 + V_o = L \cdot \frac{dI_1}{dt}$ (1b)

switch turned off: $V_1 + V_o = L \cdot \frac{dI_1}{dt} + E$ (2b)

Introducing the normalized values

$$i_1 = \frac{I_1}{I_o} \text{ and } v_1 = \frac{V_1}{V_o}$$

they become

Switch turned on: $\frac{di_1}{dt} = v_1 + 1$ (1c)

Switch turned off: $\frac{di_1}{dt} = v_1 + 1 - e$ (2c)

with the abbreviations:

$$\left.\begin{aligned} \frac{V_o}{I_o} &= R_o \quad \frac{L}{V_o/I_o} = \frac{L}{R_o} = T_o \\ \frac{t}{T_o} &= t \quad \frac{E}{V_o} = e \ (>1) \end{aligned}\right\} \qquad (5)$$

2. Expansion of the given VI - Characteristic Into a Maclaurin Series

In the following calculation the original VI-profile of the solar cell array is expanded in a Maclaurin series in the reference point V_o, I_o. Since i_1 will always be small, it is reasonable to break off the series behind the second term:

$$V_1 = \frac{dv_1}{di_1}\Big|_o \cdot i_1 + \frac{1}{2} \frac{d^2v_1}{di_1^{\,2}}\Big|_o \cdot i_1^{\,2} \tag{6}$$

$$V_1 = a \cdot i_1 + b \cdot i_1^{\,2} \tag{7}$$

where $$a = \frac{dv_1}{dI_1}\Big|_o = \frac{d\frac{V_1}{V_o}}{d\frac{I_1}{I_o}}\Big|_{I_1=0} = \frac{dV}{dI}\Big|_{I_o} \cdot \frac{I_o}{V_o} = \frac{dV}{dI}\Big|_{I_o} \cdot \frac{1}{R_o} < 0 \tag{8}$$

and $$b = \frac{1}{2}\frac{d^2v_1}{dI_1^{\,2}}\Big|_o = \frac{1}{2}\frac{d^2\frac{V_1}{V_o}}{d(\frac{I_1}{I_o})^2}\Big|_{I_1=0} =$$

$$\frac{1}{2}\frac{d^2V}{dI^2}\Big|_{I_o} \cdot \frac{I_o^{\,2}}{V_o} = \frac{1}{2}\frac{d^2V}{dI^2}\Big|_{I_o} \cdot \frac{I_o}{R_o} < 0 \tag{9}$$

Thus the equations (1) and (2) become:

switch turned on: $$\frac{di_1}{dt} = 1 + ai_1 + bi_1^{\,2} \tag{1d}$$

switch turned off: $$\frac{di_1}{dt} + 1 - e + a_1 + bi_1^{\,2} \tag{2d}$$

where $a < 0$, $b < 0$ and $e > 1$.

Herefrom one may get the explicit equations $\tau = f(i_1)$ (Appendix II) and with the results of this calculation there can be shown, that for the given VI profile and $|i_1| \leq 0{,}05$ (what means $\frac{\Delta I}{I_o} = 0.1$) there is only a very small difference between b = 0 and b ≠ 0. Therefore it is reasonable to linearize the VI profile in P_o (i.e. to take b = 0).

3. Calculation for the Linearized VI Profile

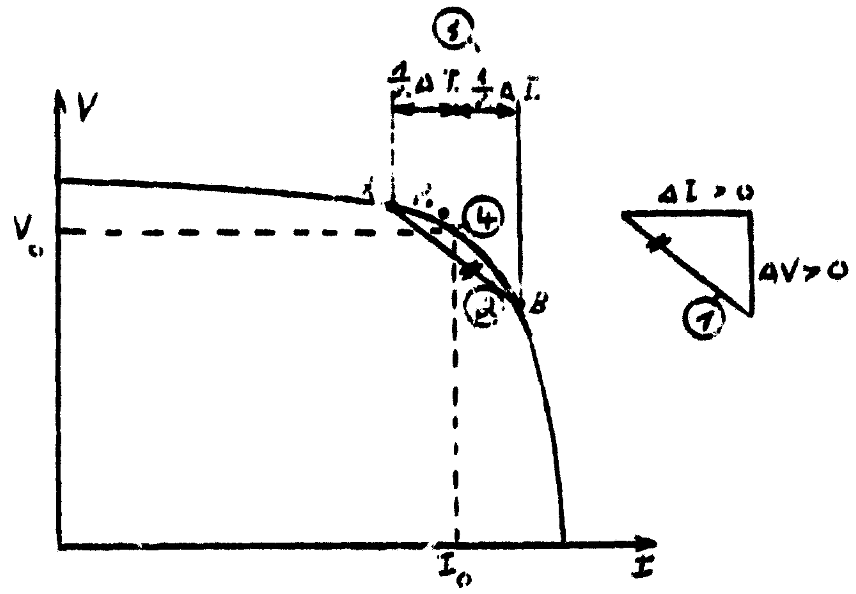

Picture 8 : Determination of Point P_o

It leads to an easy and well-arranged calculation when the point P_o for given VI characteristic and given ΔI and ΔV is determined by the way shown in Picture 8. (The numbers in the small circles show the sequence in which this point is determined).

Then can be written:

$$V_1 = -\frac{\Delta V}{\Delta I} \cdot I_1$$

$$\frac{V_1}{V_o} = -\frac{\Delta V/V_o}{\Delta I/I_o} \cdot \frac{I_1}{I_o}$$

$$v_1 = a \cdot i_1 \text{ with } a = -\frac{\Delta V}{\Delta I} \cdot \frac{I_o}{V_o} = -\frac{\Delta V}{\Delta I} \cdot \frac{1}{R_o} \qquad (10)$$

and
$$i_{1\alpha} = -\frac{1}{2}\frac{\Delta I}{I_o} = -\frac{1}{2}\Delta i$$

$$i_{1\beta} = +\frac{1}{2}\frac{\Delta I}{I_o} = +\frac{1}{2}\Delta i$$

Thus the equation (1) and (2) become:

switch turned on: $$\frac{di_1}{dt} = ai_1 + 1 \qquad (1e)$$

switch turned off: $$\frac{di_1}{dt} = ai_1 - (e - 1) \qquad (2e)$$

and their solutions:

switch turned on: $$\tau = \tau_o + \frac{1}{a}\ln(1 + ai_1) \qquad (1f)$$

switch turned off: $$\tau = \tau_o + \frac{1}{a}\ln(e - 1 - ai_1) \qquad (2f)$$

The normalized value for the time, the system needs to get from α to β switch turned on) is:

$$\Delta\tau_{\alpha\to\beta} = \Delta\tau\downarrow = -\frac{1}{a}\cdot\ln\frac{1 - \frac{1}{2}a\Delta i}{1 + \frac{1}{2}\quad\Delta i}$$

With (5) and (10) we get for the real time:

$$\Delta t\downarrow = \frac{L}{\Delta V/\Delta I}\cdot\ln\frac{1 + \frac{1}{2}\frac{\Delta V}{V_o}}{1 - \frac{1}{2}\frac{\Delta V}{V_o}}$$

or with an expansion into series for the logarithm:

$$\Delta t\downarrow = \frac{L}{\Delta V/\Delta I}\cdot L[\frac{1}{2}\frac{\Delta V}{V_o} + \frac{1}{3}(\frac{1}{2}\frac{\Delta V}{V_o})^3 + \frac{1}{5}(\frac{1}{2}\frac{\Delta V}{V_o})^5 + \ldots]$$

Since $\frac{1}{2}\frac{\Delta V}{V_o} << 1$: $\quad \Delta t = L \cdot \frac{\Delta I}{V_o}$ (11)

Analogues we get:

$$\Delta\tau_{\beta\to\alpha} = \Delta t\uparrow = -\frac{1}{a}\,\ln\frac{e - 1 - \frac{1}{2}a\Delta i}{e - 1 + \frac{1}{2}a\Delta i}$$

$$\Delta t\uparrow = \frac{L}{\Delta V/\Delta I}\,\ln\frac{1 + \frac{1}{2}\frac{\Delta V}{V_o}\cdot\frac{1}{e-1}}{1 - \frac{1}{2}\frac{\Delta V}{V_o}\cdot\frac{1}{e-1}}$$

and since

$$\frac{1}{2}\frac{\Delta V}{V_o}\cdot\frac{1}{e-1} << 1:$$

$$\Delta t\uparrow = L\cdot\frac{\Delta I}{V_o}\cdot\frac{1}{\frac{E}{V_o} - 1} \tag{12}$$

The time Δt for one cycle is

$$\Delta t = \Delta t\downarrow + \Delta t\uparrow = L\cdot\frac{\Delta I}{V_o}\left(1 + \frac{1}{\frac{E}{V_o} - 1}\right)$$

$$\Delta t = L\cdot\frac{\Delta I}{V_o}\cdot\frac{1}{1 - \frac{V_o}{E}}$$

and so the frequency

$$f = \frac{1}{\Delta t} = \frac{V_o}{\Delta I}\cdot\frac{1}{L}\left(1 - \frac{V_o}{E}\right)$$

$$f = \frac{E}{\Delta I}\cdot\frac{1}{L}\,\frac{V_o}{E}\left(1 - \frac{V_o}{E}\right) \tag{13}$$

The voltage across the coil is

$$V_{coil} = L\cdot\frac{dI}{dt}$$

The mean value of this voltage for the time when the switch is turned on therefore is:

$$\frac{1}{\Delta t\downarrow} \cdot \int_{t_\alpha}^{t_\beta} L \cdot \frac{dI}{dt} \cdot dt = \frac{1}{\Delta t\downarrow} \cdot L\,(I_\alpha - I_\beta)$$

$$= \frac{1}{\Delta t\downarrow} \cdot L \cdot \Delta I$$

Analogues the mean value of this voltage for the time when the switch is opened is:

$$\frac{1}{\Delta t\uparrow} \int_{t_\beta}^{t_\alpha} L \cdot \frac{dI}{dt}\, dt = \frac{1}{\Delta t\uparrow} \cdot L\,(I_\beta - I_\alpha)$$

$$= - \frac{1}{\Delta t\uparrow} \cdot L \cdot \Delta I$$

Therefore the <u>rectified</u> mean value for the whole cycle is:

$$V_{rm} = \frac{1}{\Delta t\downarrow + \Delta t\uparrow} (L \cdot \Delta I + L \cdot \Delta I)$$

$$V_{rm} = f \cdot 2 \cdot L \cdot \Delta I \tag{14}$$

or with (13)

$$V_{rm} = 2E \cdot \frac{V_o}{E} \left(1 - \frac{V_o}{E}\right) \tag{15}$$

4. Approximations for Time History of Current and Voltage

By taking the point V_o, I_o in the way shown in picture 8 the current will change during one cycle from $I_o + \frac{1}{2}\Delta I$ to $I_o - \frac{1}{2}\Delta I$ and back. During the switch is turned on (from α to β) the slope $\frac{dI}{dt}$ changes in the ratio

$$\frac{(\frac{dI}{dt})_\alpha}{(\frac{dI}{dt})_\beta} = \frac{V_o+V_{1\alpha}}{V_o+V_{1\beta}} = 1 + (\frac{V_{1\alpha}}{V_o} - \frac{V_{1\beta}}{V_o}) = 1 + \frac{\Delta V}{V_o}$$

Analogues, when the switch is turned off (from β to α) the slope $\frac{dI}{dt}$ changes in the ratio

$$\frac{(\frac{dI}{dt})}{(\frac{dI}{dt})} = \frac{E - V_o - V_1}{E - V_o - V_1} = 1 + (\frac{V_1}{V_o} - \frac{V_1}{V_o}) \cdot \frac{1}{\frac{E}{V_o} - 1}$$

$$= 1 + \frac{\Delta V}{V_o} \cdot \frac{1}{\frac{E}{V_o} - 1}$$

Since $\frac{\Delta V}{V_o}$ will be probably not bigger than about 0.1 and $\frac{E}{V_o}$ >1.5, the current will be a saw-tooth-function with nearly constant slope $\frac{dI}{dt}$ between two switching points (Picutre 9).

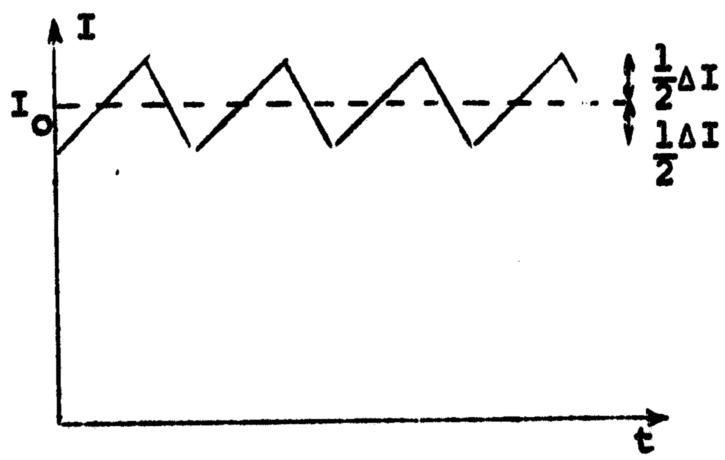

Picture 9: Time History of Current

The time history of the voltage belonging to this may be taken out of the original V,I profile. By integrating this voltage there can be obtained on even more exact current curve, hereto the voltage out of the original V,I-characteristic and so on.

Already the result of the first iteration will be very exact. Herefrom there can be obtained the mean values V_m and I_m and according to $V_\beta = V_m - c_1 \Delta V$, the exact value for c_1 and analogues, according to $I_\alpha = I_m - c_2 \Delta I$ the exact value for c_2 (VI-characteristic at aphelion, See B.2). But since these values will both be very close to 1/2, for the practical design they may be chosen to 1/2.

D. Choice of the System Parameters

1) Number of Series connected solar cells.

For the choice of the number of series connected solar cells two points are important.

a) For the sunblazer are provided 8 segments of solar cells, where on each can be placed between N=72 and N=82 cells. To get a simple wiring (the same in each segment) it is reasonable to provide in each segment a series connection c

$$N' = N \text{ or } \frac{1}{2}N \text{ or } \frac{1}{3}N \ldots$$

b) To get a small (light-weight) power coil and small power losses therein too, it is reasonable to keep the change of the switching frequency (over the orbit) as small as possible. According to equation (14) that would make it possible too, to get the power for load V (see A,5) out of a second winding on the power coil.

Following equations (13):

$$f = \frac{E}{\Delta I} \cdot \frac{1}{L} \cdot \frac{V_o}{E} \left(1 - \frac{V_o}{E}\right)$$

and (15)

$$V_{rm} = 2E \cdot \frac{V_o}{E} \left(1 - \frac{V_o}{E}\right)$$

for given E, ΔI and L the frequency and the rectified mean value at the power coil are direct proportional to

$$F = \frac{V_o}{E}\left(1 - \frac{V_o}{E}\right).$$

$F = F(\frac{V_o}{E})$ is shown in picture 10.

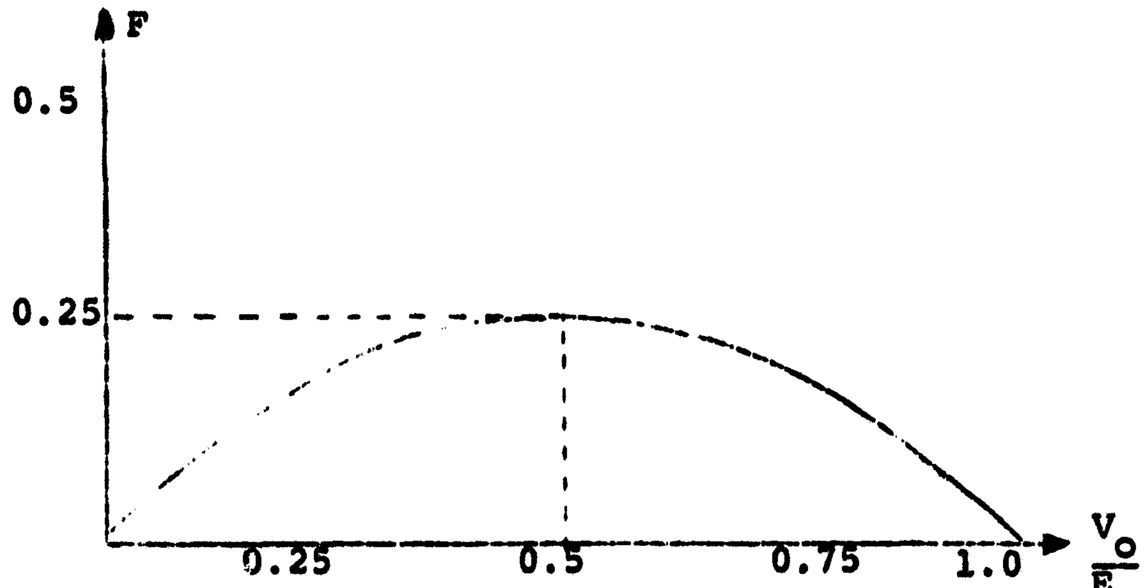

Picure 10: $F = F(\frac{V_o}{E})$

To get the smallest change in frequency, there should be

$$F(V_{o\,max}) = F(V_{o\,min})$$

i.e.

$$\frac{V_{o\,max}}{E}\left(1 - \frac{V_{o\,max}}{E}\right) = \frac{V_{o\,min}}{E}\left(1 - \frac{V_{o\,min}}{E}\right)$$

Therefrom one can get (for given $\frac{V_{o\,max}}{V_{o\,min}}$):

$$\left.\frac{V_{o\,max}}{E}\right|_{opt} = \frac{V_{o\,max}}{V_{o\,min}} \frac{\frac{V_{o\,max}}{V_{o\,min}} - 1}{\left(\frac{V_{o\,max}}{V_{o\,min}}\right)^2 - 1} \qquad (16)$$

For the given ratio $\frac{V_{o\,max}}{V_{o\,min}} = 1.9$ (See Appendix I)

one gets

$$\left.\frac{V_{0\,max}}{E}\right|_{opt} = 0.65$$

and

$$\left.\frac{V_{0\,min}}{E}\right|_{opt} = 0.344$$

For these both extreme cases the frequency will be the same. The highest frequency will occur at $\frac{V_0}{E} = 0.5$.

The ratio in which the frequency changes in this case therefore is:

$$\frac{F_{max}}{F(V_{0\,max})} = \frac{F_{max}}{F(V_{0\,min})} = \frac{0.228}{0.250} = 0.912$$

The rectified mean value of the voltage from a second winding would change only within ± 4,5%.

Number of series connected cells:

Assuming the lowest temperature is -20°C, one gets (Appendix I)

$$V_{0\,max} = [0.41 - \frac{0.0025}{°C}(-50°C)] \times N \text{ volts}$$
$$= 0.535 \times N \text{ volts.}$$

With $V_{0\,max}|_{opt} = 0.65 \cdot E = 22.8$ V therefrom results a number of series connected cells:

$$N_{opt}' = \frac{22.8V}{0.535V} = 43.$$

This number would require a total number of $N = 2N' = 86$ cells per segment (probably too big).

The following table shows the extreme values of F (which is proportional to the frequency and the rectified mean value of the voltage of a second winding on the power coil) for E= 35V, T_{max} = 72,°C, T_{min} = -28°C

N'	N	$\frac{V_{0\ max}}{E}$	$\frac{V_{o\ min}}{E}$	F_{min}	F_{max}	$\frac{F_{min}}{F_{max}}$	Approximate Change of F
36	72	0.550	0.290	0.206	0.250	0.823	±9%
38	76	0.581	0.306	0.212	0.250	0.850	±7.5%
40	80	0.606	0.322	0.218	0.250	0.871	±6.5%
42	84	0.641	0.338	0.224	0.250	0.898	±5%
43	86	0.658	0.346	0.227	0.250	0.909	±4.5%

However, there must be said that with changing the number of cells from N = 72 (as planned today), there will be some change of the temperature of the whole sunblazer and thus some change of $V_{0\ max}$ and $V_{o\ min}$ too.

2. ΔV, ΔI and Frequency.

The short-cut current of one string of solar cells at 1 AU will be I_{sc} = 0.06A.

The whole short-cut will be

$$a)\quad I_{sc}\big|_{1\ AU} = 8 \times 2.I_{sc}{}' = I\ A$$

and thus

$$b)\quad I_{sc}\big|_{0.635\ AU} = \frac{1}{0.635^2} = 2.5\ A$$

It seems reasonable to take $\Delta I = 0.1\ I_{sc}|_{1\ AU} = 0.1\ A$

and, according to A.3 $\Delta V = \Delta I \cdot \frac{V}{I}|_{MPP,\ 1AU} = 0.1\ A \cdot \frac{19.25\ V}{1\ A}$

$= 2.0\ V.$

To get a small coil, but at the same time small losses in the coil and the transistor, it seems reasonable to take a frequency of about

$$f = 50\ KHz.$$

3. <u>Design of Coil, Power Transistor and Power Diode</u>.

a) Following equation (13) the inductivity of the coil has to be:

$$L = \frac{E}{\Delta I} \cdot \frac{1}{f} \cdot F$$

with $F = 0.22$ $\quad f = 50\ KHz$

$E = 35\ V$ $\quad \Delta I = 0.1\ A$

one gets,

$$L = \frac{35\ V}{0.1\ A} \cdot \frac{1}{50} \cdot 10^{-3}\ sec. \ 0.22$$

$$L = 1.54\ mHy$$

If this inductivity should be too big, ΔI must be increased to about $\Delta I = 0.2\ A$ and/or the frequency to about 100 (200) KHZ.

The copper of the coil has to be chosen for $I_{max} = 2.5\ A$ and the air gap so that I_{max} the coil isn't yet in saturation.

b) Transistor: max. voltage: 40V

max. current: 2.5A

mean value of current: 2.5A

c) Diode: max. voltage: 35V

max. current: 2.5 A

mean value of current: 2.0 A

F. Losses

The main losses in the suggested circuit will be:

a) Copper and iron losses in the coil

b) Switching and conducting losses in the power transistor

c) Losses in teh drive circuit of the power transistor

d) Conducting losses in the diode.

For the final design of the coil and drive circuit there should be considered that the losses in point b) (0.635 A.U., high current low voltage) may be higher than in point a) (1 A.U., low current, high voltage) because in perihelion (0.635 A.U.) the output power will be higher than in aphelion (1 A.U.).

G. Summary

The proposed circuit for the dc power converter is very simple and therefore will be very reliable. In addition, it is easy to increase the reliability for example by dividing the solar cell array in two or four parts, each with its own converter and adding up the power in the storage battery through the power diodes.

It seems to be very important too that this system is self-adaptive and not a programmed one. It will work well also when the circumstances change, for example, the output of the solar cells as a result of mocrometeorite erosion or radiation effects.

H. APPENDICES

I. Ratio of the voltages in the MPP at 1 AU and 0.635 AU.

Given is: $V_{oa} = [0.41 - \frac{0.0025}{°C} (T_a - 22°C)]$ volts x N

$V_{ob} = [0.41 - \frac{0.0025}{°C} (T_b - 22°C)]$ volts x N

therefrom: $V_{oa} + V_{ob} = [0.82 - \frac{0.0025}{°C} (T_a + T_b - 44°C)]$ volts x N

$V_{oa} - V_{ob} = \frac{0.0025}{°C} (T_b - T_a)$ volts x N

Assuming, the mean value of the temperature will be $\frac{T_a + T_b}{2} = 22°C$ and the difference will be $T_b - T_a = 100°C$, we get:

$$\frac{V_{oa} + V_{ob}}{V_{oa} - V_{ob}} = \frac{0.82}{0.25}$$

or

$$\frac{V_{oa}}{V_{ob}} = 1.9.$$

The ratio of the voltages for open circuit (A.1) will be nearly the same:

$$\frac{V_{oca}}{V_{ocb}} = 1.9.$$

II. Calculation for a Parabolical Approximation of the VI-Characteristic

From C.2 equations (1d) and (2d) we get:

switch turned on: $d\tau = \frac{di_1}{1 + ai_1 + bi_1^2}$ (1f) switch turned off: $d\tau = \dfrac{di_1}{1 - e + ai_1 + bi_1^2}$ (26)

when $a,b < 0$ and $e > 1$.

For the solutions is important, whether the discriminant D is: $D > 0$ or $D < 0$.

switch turned on: $D_{on} = 4b - a^2$

switch turned off: $D_{off} = 4\,b(1 - e) - a^2$

Example from "Hoffman final report for Integral Glass Coatings for Solar Cells"

Page 45, curve 2, Solar Simulator

Maximum power point: $V_o = 420$ mV, $I_o = 61$ mA

Table for the points α and β (with $i_{1\alpha} = -\,i_{1\beta} = -\,\frac{1}{2}\frac{\Delta I}{I_o} = -0.05$)

$i_{1\alpha} = -0.05$	$I_\alpha = 57.95$ mA	$V_\alpha = 436$ mV	$V_{1\alpha} = 0.038$
$i_{1\beta} = +0.05$	$I_\beta = 64.05$ mA	$V_\beta = 394$ mV	$V_{1\beta} = -0.062$

These points must fit the equation

$$V_1 = ai_1 + bi_1^2$$

Point α: $V_{1\alpha} = 0.038 = -\,0.05a + 0.0025b$

Point β: $V_{1\beta} = -0.062 = +\,0.05a + 0.0025b$

Therefore:

$$a = -1,\ b = -\,4.8$$

Thus we get for the discriminant, when the switch is turned off:

$$D_{off} = 4b(1 - e) - a^2 = -\,19.2(1 - e) - 1$$

and with $e \geq 1.5,\ D_{off} > 0$

So we get for the solutions of (1f) and (2f):

switch turned on: $$\tau = \tau_o - \frac{2}{\sqrt{-D_{on}}} \text{ arc tan h } \frac{2bi_1+a}{\sqrt{-D_{on}}} \qquad (1g)$$

switch turned off: $$\tau = \tau_o' + \frac{2}{\sqrt{D_{off}}} \text{ arc tan } \frac{2bi_1+a}{\sqrt{D_{off}}} \qquad (2g)$$

The related value for th time, the system needs to get from α to β (switch turned on) is:

$$\Delta\tau_{\alpha\to\beta} = \Delta\tau\downarrow = -\frac{2}{\sqrt{-D_{on}}} \left[\text{arc tan h } \frac{2bi_{1\beta}+a}{\sqrt{-D_{on}}} - \text{arc tan h } \frac{2bi_{1\alpha}+a}{\sqrt{-D_{on}}}\right]$$

$$\Delta\tau\downarrow = -\frac{2}{\sqrt{-D_{on}}} \text{ arc tan h } \frac{2b\,(i_{1\beta} - i_{1\alpha})}{\sqrt{-D_{on}}\left[1 - \frac{a^2 + 4b^2 i_{1\beta} i_{1\alpha} + 2ab(i_{1\alpha}+i_{1\beta})}{-D_{on}}\right]}$$

and with $$i_{1\beta} - i_{1\alpha} = \frac{\Delta I}{I_o} = \Delta i$$

$$i_{1\beta} + i_{1\alpha} = 0$$

$$\Delta\tau\downarrow = -\frac{2}{\sqrt{-D_{on}}} \text{ arc tan h } \frac{2b\Delta i}{\sqrt{-D_{on}} - \frac{a^2 - (b\Delta i)^2}{-D_{on}}} \qquad (17)$$

and analogues:

$$\Delta\tau\uparrow = \frac{2}{\sqrt{D_{off}}} \left\{\text{arc tan } \frac{2bi_{1\alpha} + a}{\sqrt{D_{off}}} - \text{arc tan } \frac{2bi_{1\beta} + a}{\sqrt{D_{off}}}\right\}$$

$$\Delta\tau\uparrow = \frac{2}{\sqrt{D_{off}}} \text{ arc tan } \frac{2b\,(i_{1\alpha} - i_{1\beta})}{\sqrt{D_{off}}\left[1 + \frac{a^2+4b^2 i_{1\alpha} i_{1\beta} + 2ab(i_{1\alpha}+i_{1\beta})}{D_{off}}\right]}$$

$$\Delta\tau\uparrow = \frac{2}{\sqrt{D_{off}}} \text{ arc tan } \frac{-2b\Delta i}{\sqrt{D_{off}} + \frac{a^2 - (b\Delta i)^2}{\sqrt{D_{off}}}} \qquad (14)$$

Example: $\Delta i = 0.1 \quad a = -1$

$e = 1.5 \quad b = -4.8$

gives $\Delta\tau\downarrow = 0.1005$

$\Delta\tau\uparrow = 0.1989$

The corresponding values from equations (11) and (12) ($b = 0$) are:

$\Delta\tau\downarrow = 0.100$

$\Delta\tau\uparrow = 0.200$

As one can see, the difference is smaller than 1%.

__Literature:__ (1) Study of a Small Solar Probe (Sunblazer) Part II, Spacecraft and Payload Design, PR-5255, July 1, 1965.

Thermal Transfer and Radiation from a Thin Circular Plate Source--Thin Cylindrical Shell Radiator

I. Introduction

For the Sunblazer satellite, it is of interest to calculate the radiative properties of thin shells. In the configuration of Fig. 42, which is a simplified drawing of the Sunblazer satellite, there are two such shells. The first is the front plate, a thin plate which is covered with solar cells. The second is the cylinder, a thin shell which radiates excess heat into space.

II Summary

Assuming no radiative heat transfer within the cylinder, the temperature on the shells and the rate of radiation of the shells is determined solely by a dimensionless variable ζ, where:

$\zeta = 1/2 \, \frac{\epsilon\sigma}{Kt} \, T_e^3 \, x^2$

ϵ = Emissivity of shell (0.85 for aluminum)

$\sigma = 5.67 \; 10^{-12}$ watts/cm^2-°K^4

K - Conductivity of shell (2.05W/cm-°K for aluminum)

t - Thickness of shell

T_e = Temperature of shell at free end

X = Distance along shell (length on cylinder or radius on plate) [1]

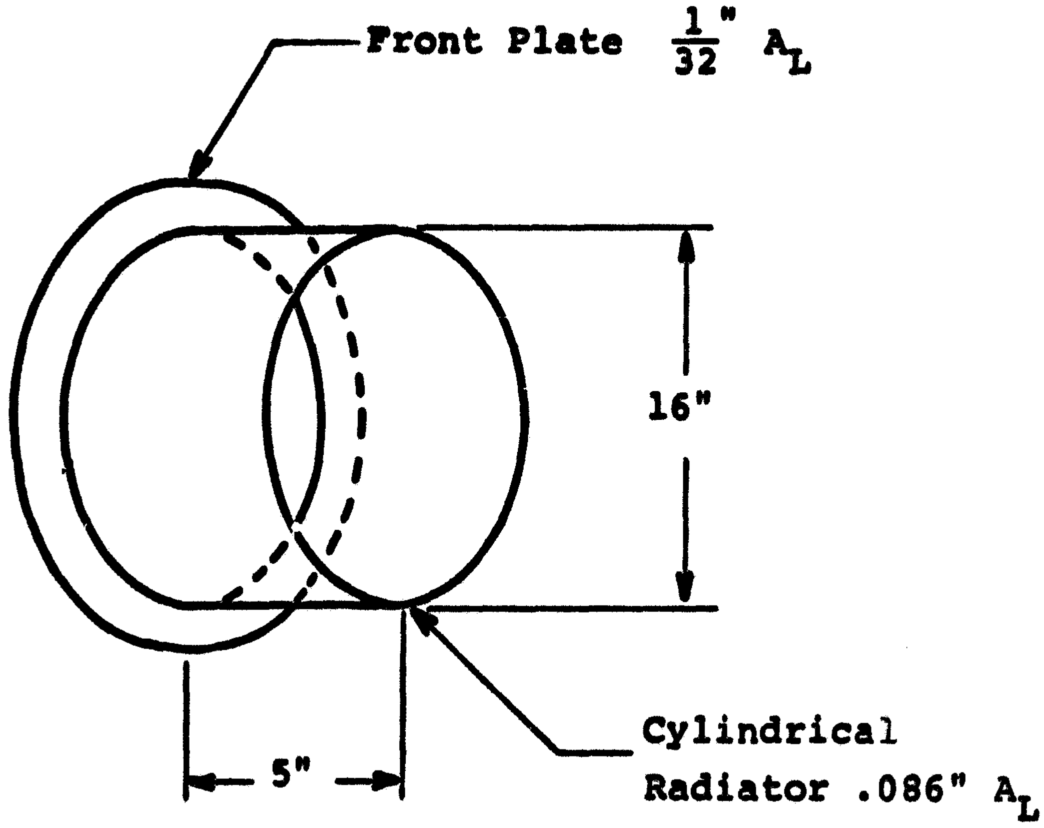

Figure 42

THE RADIATOR GEOMETRY

The smaller ζ is, the closer the system approximates an isothermal system. In terms of ζ, the temperature on the cylinder is given by:

$$T = T_o \; (1+\zeta+\frac{2}{3}\zeta^2+\frac{26}{45}\zeta^3+\frac{116}{315}\zeta^4+\frac{251}{1050}\zeta^5+....). \qquad [2]$$

The heat conducted down the cylinder is given by:

$$H = K2\pi rt \frac{dT}{dZ} = K\frac{4\pi rtT_o}{Z} \; (\zeta+\frac{4}{3}\zeta^2+\frac{78}{45}\zeta^3+\frac{464}{315}\zeta^3+...) \qquad [3]$$

$$H = 2\pi rZ\varepsilon\sigma T_o^4 \; (1+\frac{4}{3}\zeta+\frac{78}{45}\zeta^2+\frac{464}{315}\zeta^3+\frac{251}{210}\zeta^4...), \qquad [4]$$

where r = radius of cylinder.

The temperature on the plate is given by:*

$$T = T_o \; (1+\rho+\frac{1}{2}\rho\zeta+\frac{1}{3}\rho^2\zeta+\frac{1}{9}\rho\zeta^2+\frac{5}{48}\rho^2\zeta^2+\frac{1}{72}\rho\zeta^3+...) \qquad [5]$$

$$T = T_o + T_o \rho\Sigma_1, \qquad [6]$$

where

$$\rho = \frac{1}{4} \left[\frac{\varepsilon\sigma}{Kt} T_o^3 r^2 - \frac{\alpha Q}{KtT_o} r^2\right]. \qquad [7]$$

α = Absorptivity of front plate

Q = Heat flux per unit area incident on front plate

$$\Sigma_1 = 1+\frac{1}{2}\zeta+\frac{1}{3}\zeta^2+\frac{1}{72}\zeta^3+... \qquad [8]$$

The heat conducted out of the plate is given by:

$$H = K2\pi rt \frac{dT}{dr} = 4\pi KtT_o\rho\Sigma_2, \qquad [9]$$

where

$$\Sigma_2 = 1+\zeta+\frac{1}{3}\zeta^2+\frac{1}{18}\zeta^3+... \qquad [10]$$

* NOTE: For this calculation we have assumed a plate 16" in diameter, ending at the beginning of the cylinder. A slightly larger plate will have a similar temperature profile, depending similarly upon ζ.

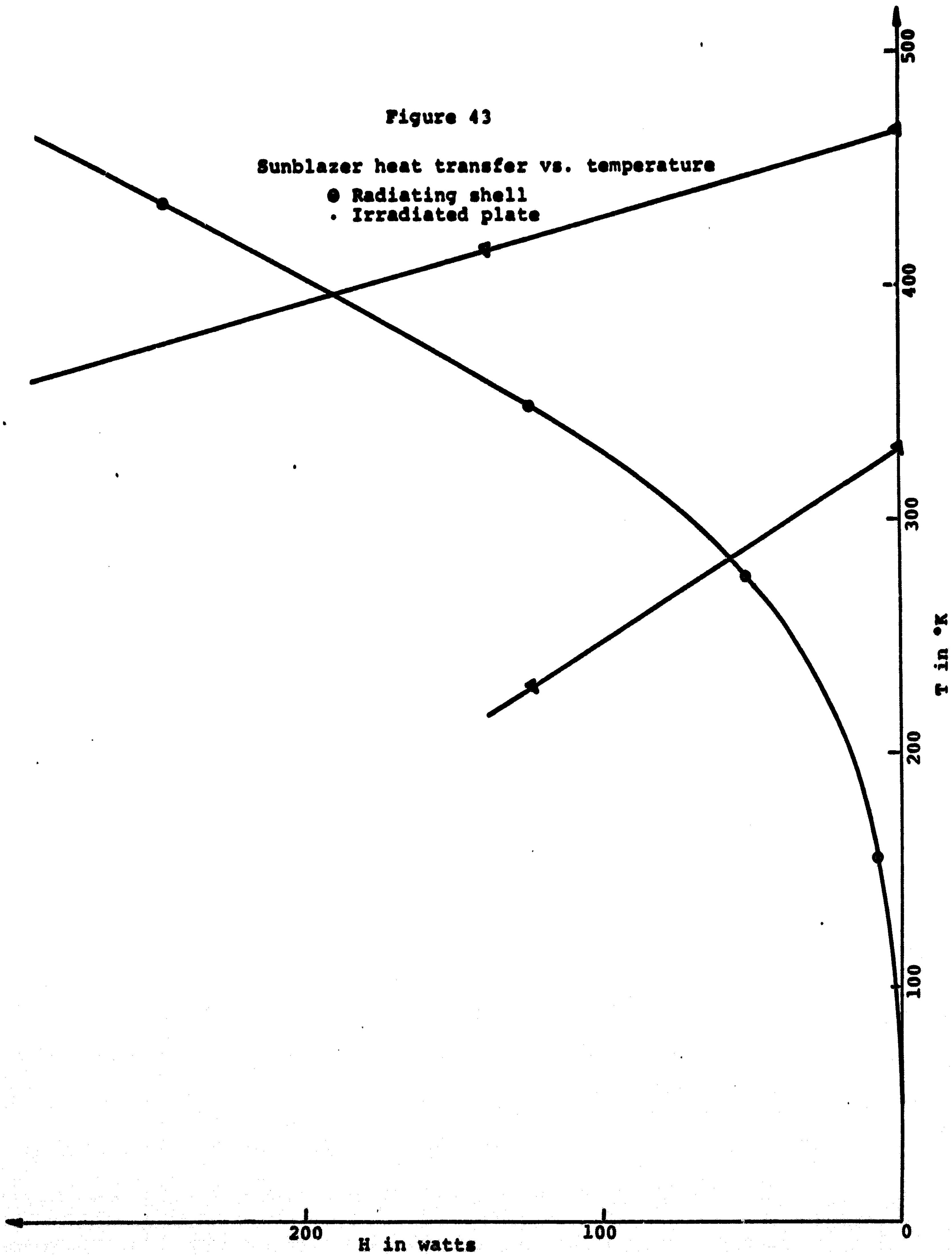

Figure 43

Sunblazer heat transfer vs. temperature

Defining

$$T_{\infty} = \sqrt[4]{\frac{\alpha Q}{\varepsilon\sigma}}\ , \qquad [11]$$

equations [6], [7], [10] and [11] can be solved to give

$$H = 8\pi K t \frac{\Sigma_2 \zeta}{1+2\Sigma_1 \zeta} \quad (T_{\infty}-T) \qquad [12]$$

and

$$\Delta T = \frac{2\Sigma_1 \zeta}{1+2\Sigma_1 \zeta} \quad (T_{\infty}-T). \qquad [13]$$

By plotting H vs. T from equations [2], [3] and [12], the common operating point of the cylinder and the plate can be found, as shown in Fig. 43.

Then the temperature rise along the cylinder and the plate can be found from equations [2] and [13]. The temperatures on the cylinder and plate have nearly parabolic dependence on distance, as shown in Fig. 44.

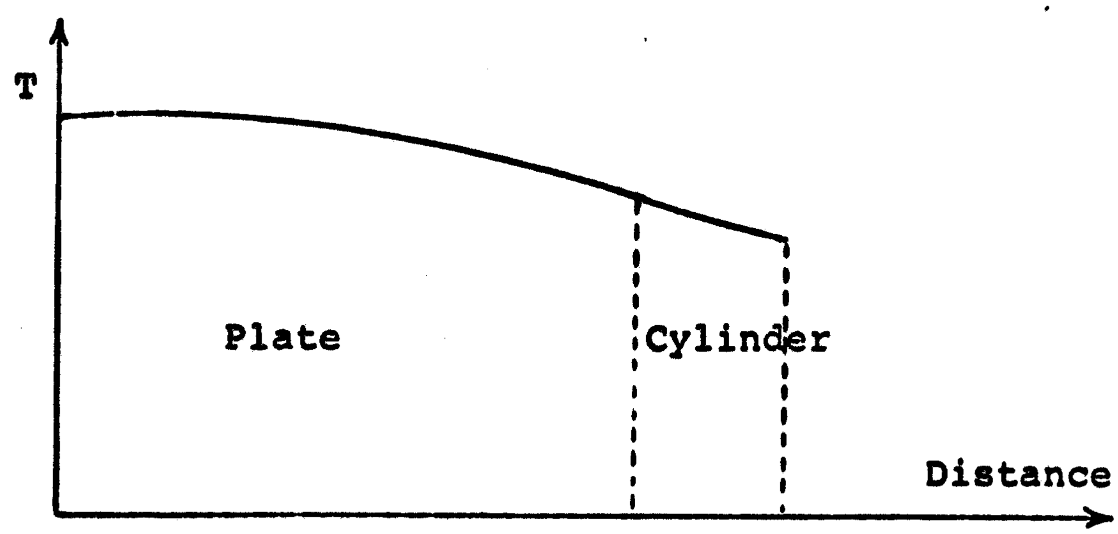

Figure 44. <u>Temperature profiles on cylinder and plate</u>

If the cylinder were at a constant temperature T, it would radiate heat at a certain rate R. The actual rate of radiation divided by R gives an efficiency

$$\eta_1 = \frac{1+\frac{4}{3}\zeta + \frac{78}{45}\zeta^2 + \frac{464}{315}\zeta^3 + \frac{251}{210}\zeta^4 + \ldots}{(T/T_o)^4}\ , \qquad [14]$$

which is shown in Fig. 45.

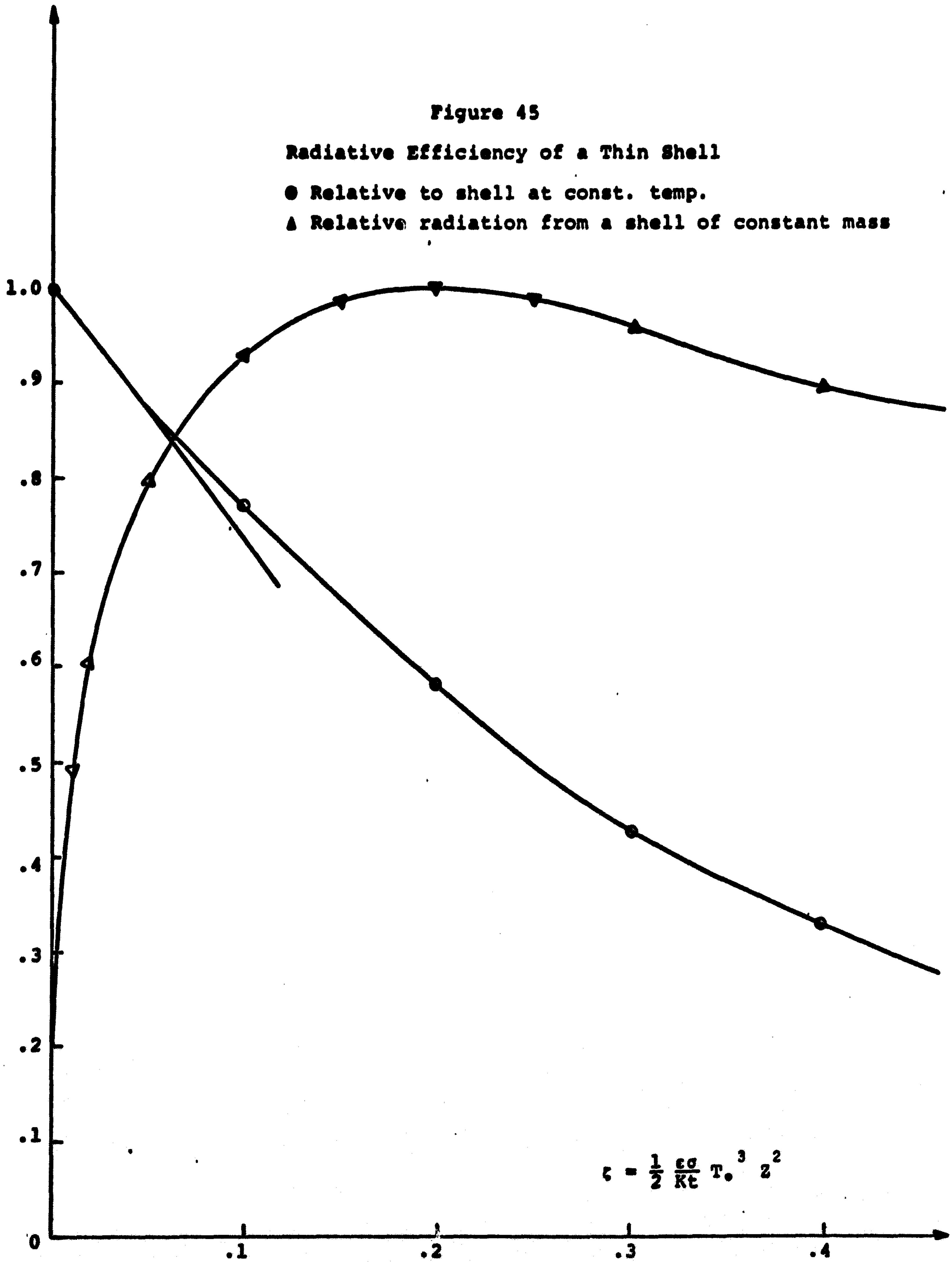

Figure 45
Radiative Efficiency of a Thin Shell
● Relative to shell at const. temp.
▲ Relative radiation from a shell of constant mass
1.0
.9
.8
.7
.6
.5
.4
.3
.2
.1
0
.1
.2
.3
.4
$\zeta = \frac{1}{2} \frac{\epsilon\sigma}{Kt} T_o^{3} z^{2}$

If we have cylinders of given mass and wish to maximize the heat radiated from the cylinder by optimizing the X to t ratio, we get the following equation,

$$\eta_2 = \frac{\zeta^{1/3}\ (1+\frac{4}{3}\zeta+\frac{78}{45}\zeta^2+\frac{464}{315}\zeta^3+\frac{251}{210}\zeta^4+\ldots)}{0.422(T/T_o)^3} \qquad [15]$$

Thus a cylinder of any mass will radiate a maximum amount of heat for $\zeta = 0.20$.

III Derivation of Equations

We have assumed no radiative heat transfer within the cylinder. This is a fairly good assumption because [1] in the inside of the cylinder contains electronic packages which obstruct heat flow, [2] the radiative heat transfer within the cylinder will be less than the conductive heat transfer and [3] given the above solution, we can easily obtain a good approximation to the complete solution by (a) assuming the given temperature distribution, (b) calculating the radiative heat inputs to the various areas of the shell, and then (c) re-calculating the temperature distribution (keeping (b) constant). This process could be iterated to obtain a closer approximation.

For the cylinder with no radiative heat transfer, the equation of heat balance is

$$\frac{d^2T}{dX^2} = \frac{\varepsilon\sigma}{Kt}\ T^4 \qquad [16]$$

Assuming a solution of the form

$$T = T_o\ (1+aX^2 + bX^4 + cX^6 + \ldots..) \qquad [17]$$

Expanding [16] and equating like powers of X leads directly to equation [2]. Differentiating [17], we get

$$\frac{dT}{dX} = \frac{2T_a}{X}\,(aX^2+2bX^4+3cX^6+\ldots) \qquad [18]$$

which is equivalent to [3].

For the front plate with heat input, from the sun, the equation of heat balance is

$$Kt\,\frac{d}{dr}\left(r\frac{dT}{dr}\right) - \varepsilon\sigma rT^4 + \alpha Qr = 0 \qquad [19]$$

By similar methods, we obtain Equations [5] through [13]. Because the front plate tends to equilibrium at a temperature near the maximum possible temperature, one of the properties of the solution is that the rate of heat conduction out of the plate is nearly a linear function of temperature drop.